WILEY

RADIO PROPAGATION
AND ADAPTIVE ANTENNAS FOR
WIRELESS COMMUNICATION LINKS

Terrestrial, Atmospheric, and Ionospheric

NATHAN
BLAUNSTEIN

•

CHRISTOS G.
CHRISTODOULOU

Radio Propagation and Adaptive Antennas for Wireless Communication Links

Radio Propagation and Adaptive Antennas for Wireless Communication Links

Terrestrial, Atmospheric and Ionospheric

Nathan Blaunstein and Christos Christodoulou

BICENTENNIAL
BICENTENNIAL
BICENTENNIAL
1807
WILEY
2007
BICENTENNIAL
BICENTENNIAL

*This book is dedicated to the authors' families, wives,
and children, and to the memory of their teachers*

Contents

Preface

This book deals with a variety of radio propagation phenomena in various environments and describes the most important characteristics of radio propagation in wireless communication links. Today we observe a conversion of existing wireless networks, labeled as the second generation (2G), third generation (3G), and fourth generation (4G) of wireless networks. To design such networks successfully, it is very important to predict the *propagation characteristics* of each radio channel used, to define the optimal location of subscribers, whether stationary or mobile, as well as the number of base stations, in order to provide high quality of service (QOS) for each individual subscriber located in a given area of service. These functions can be achieved by using smart antennas at one or both ends of a communication link. Accurate information about the physical propagation processes that occur in each specific link increases the performance of smart antennas and the efficiency of service (called grade of service, GOS) for each subscriber.

This book is intended for any scientist, practicing engineer and designer who is concerned with the operation and service of radio links, including personal, mobile, aircraft and satellite links. It examines different situations in the over-the-terrain, atmospheric, and ionospheric communication channels, including rural, mixed residential, and built-up environments for terrestrial links, atmospheric turbulences, and different kinds of hydrometeors (rain, clouds, snow, etc) for atmospheric links. For each channel we discuss the role of all kinds of obstructions on the corresponding propagation phenomena that influence the transmission of radio signals through such communication channels, in both line-of-sight (LOS) and obstructive non-line-of-sight (NLOS) propagation conditions along the radio path between the transmitter and the receiver antennas. The book also emphasizes how adaptive antennas, at the link terminals, can be utilized to minimize the deleterious effects of such obstructions.

The book introduces the reader to relevant topics in radio propagation in various media and their applications in smart communication networks. Multipath phenomena, path loss, large-scale or slow fading, and short-scale or fast fading are

thoroughly described. The phenomena treated include free-space propagation, propagation above an irregular terrain, in an inhomogeneous and stratified atmosphere and ionosphere, the reflection, and diffraction by various obstructions (hills, buildings, trees, hydrometeors, turbulences, plasma inhomogeneous structures, etc.), regularly or randomly distributed in an area of communication. Finally, the authors try to show how to create a unified approach for predicting the main propagation characteristics for different wireless communication channels using adaptive antenna systems. That means a full prediction of all propagation characteristics not only in space but also in azimuth, elevation, and time delay domains, without which adaptive antennas and their corresponding algorithms cannot be used successfully.

The structure of the book is as follows. The main parameters and characteristics of radio propagation links, as well as the challenges in using adaptive antennas, are briefly described in Chapter 1. Chapter 2 introduces the figures of merit and fundamentals of regular antennas. Chapter 3 introduces the physics of electromagnetic wave propagation in random media, based on the principles of statistical mechanics and quantum field theory, for applications in radio propagation above rough terrains, turbulent atmospheres, and ionospheric plasmas. In Chapter 4, we present the electrodynamics of radio propagation in free space, over smooth and rough terrains, based on Huygens principle and Fresnel-zone concept. All aspects of terrestrial radio propagation are covered in Chapter 5. First, we start with the description of the influence of a single building, its shape and roof or wall structures, on the radio pattern surrounding an antenna. Then, a general stochastic approach is used to perform a link budget for different kinds of outdoor communication links: rural, suburban, and urban on the basis of the physical aspects of the terrain features. In Chapter 6, the effects of the atmosphere and its features (clouds, fog, hydrometeors, rain, turbulences, etc.) on loss characteristics of any radio signal are described with examples on how to design a link budget for several specific land-atmospheric communication links. In Chapter 7, we give the reader information on how an inhomogeneous ionosphere, containing quasi-regular layers, large, average, and small sporadic plasma irregularities, affect radio wave propagation, focusing on path loss and fading. Indoor propagation is discussed in Chapter 8, where some models for practical applications in indoor communications are presented through numerous experimental data. Chapter 9 describes the main aspects of adaptive (or *smart*) antenna system technologies, such as antenna array and digital beamforming, focusing on their special applications in terrestrial, atmospheric, and ionospheric radio propagation for wireless mobile, personal, aircraft, and satellite communication links. In Chapter 10, a general, three-dimensional, stochastic approach is given to predict the joint angle-of-arrival, elevation-of-arrival, and time-of-arrival ray distribution and the corresponding power spectrum distribution in the space, angle, time, and Doppler frequency domains for different urban environments, using smart antenna technology. Here, we propose a new concept on how to predict the main propagation characteristics of the signal for wireless systems using smart antenna systems. In Chapter 11, the advantages and disadvantages of the proposed stochastic approach are discussed via a series of experiments carried out in

different built-up areas. Then, on the basis of a unified stochastic approach, a general algorithm that can be used to develop a link budget and to predict GOS, and which also has to optimize the capacity of the information data stream within different propagation channels, is presented. Chapter 12 concentrates on the design of cellular communication networks based on radio propagation phenomena. Several examples are presented and discussed. In Chapter 13, we verify the theoretical results described earlier by using more precisely arranged experiments carried out in different urban sites around the world. We do that by focusing our attention on the adaptive antenna operational characteristics in the space, angle, time, and frequency domains. Finally, Chapter 14 describes the different approaches, statistical or physical-statistical used today in land-satellite communication links, as well as for mega-cell map performance.

Fundamentals of Radio Communications

The purpose of this chapter is to familiarize the reader with the basic propagation characteristics that describe various wireless communication channels, such as terrestrial, atmospheric, and ionospheric for VHF to the X-band. Well-known standards in wireless communication [1–10] are introduced for the prediction of path losses and fading effects of any radio signal in various communication links, and finally, new possibilities that can be obtained using smart antennas are discussed.

1.1. RADIO COMMUNICATION LINK

Different radio communication links (land, land-to-air, air-to-air) covering different atmospheric and ionospheric conditions, include several components having a plethora of physical principles and processes, with their own independent or correlated working characteristics and operating elements. A simple scheme of such a radio communication link consists of a transmitter (T), a receiver (R), and a propagation channel. The main output characteristics of such a link depend on the conditions of radio propagation in different kinds of environments, as shown in Figure 1.1. According to Reference [6], there are three main independent electronic and electromagnetic design tasks related to this wireless communication network. The first task is the transmitter antenna operation including the specification of the electronic equipment that controls all operations within the transmitter. The second task is to understand, model, and analyze the propagation properties of the channel that connects the transmitting and receiving antennas. The third task concerns the study of all operations related to the receiver.

Wireless Propagation Channel
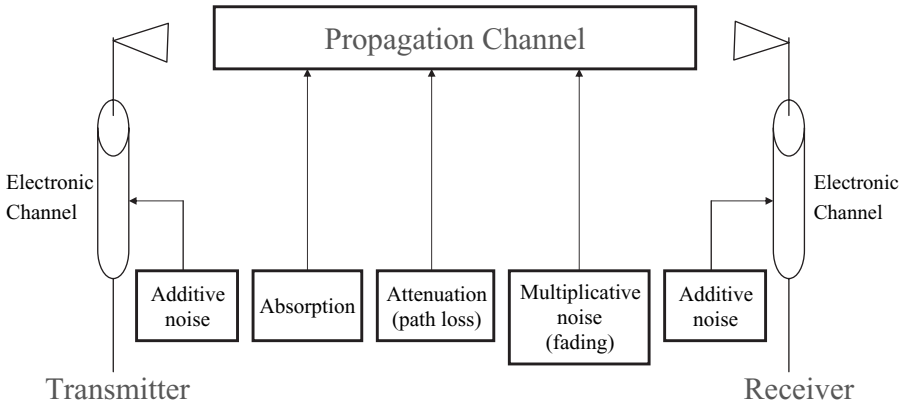
FIGURE 1.1. A wireless communication link scheme.

The propagation channel is influenced by the various obstructions surrounding antennas and the existing environmental conditions. Another important question for a personal receiver (or handheld) antenna is also the influence of the human body on the operating characteristics of the working antenna. The various blocks that comprise a propagation channel are shown in Figure 1.1.

Its main output characteristics depend on the conditions of radio wave propagation in the various operational environments where such wireless communication links are used. Next, we briefly describe the frequency spectrum, used in terrestrial, atmospheric, and ionospheric communications, and we classify some common parameters and characteristics of a radio signal, such as its path loss and fading for various situations, which occur in practice.

1.2. FREQUENCY BAND FOR RADIO COMMUNICATIONS

The *frequency band* is a main characteristic for predicting the effectiveness of radio communication links that we consider here. The optimal frequency band for each propagation channel is determined and limited by the technical re- quirements of each communication system and by the conditions of radio propagation through each channel. First, consider the spectrum of radio frequencies and their practical use in various communication channels [1–5].

Extremely low and *very low frequencies* (ELF and VLF) are frequencies below 3 kHz and from 3 kHz to 30 kHz, respectively. The VLF band corresponds to waves, which propagate through the wave guide formed by the Earth's surface and the ionosphere at long distances with a low degree of attenuation (0.1–0.5 per 1000 km [1–5]).

Low frequencies (LF) are frequencies from 30 kHz up to 3 MHz. In the 1950s and 1960s they were used for radio communication with ships and aircraft, but since then they are used mainly with broadcasting stations. Because such radio waves propagate along the ground surface, they are called ''surface'' waves [1–5].

High frequencies (HF) are those that are located in the band from 3 MHz up to 30 MHz. Signals in this spectrum propagate by means of reflections caused by the ionospheric layers and are used for communication with aircraft and satellites, and for long-distance land communication using broadcasting stations.

Very high frequencies (VHF) are located in the band from 30 MHz up to 300 MHz. They are usually used for TV communication, in long-range radar systems and radio navigation systems.

Ultra high frequencies (UHF) are those that are located in the band from 300 MHz up to 3 GHz. This frequency band is very effective for wireless microwave links, constructions of cellular systems (fixed and mobile), mobile–satellite communication channels, medium range radars, and other applications.

In recent decades, radio waves with frequencies higher than 3 GHz (C, X, K-bands, up to several hundred gigahertz, which in the literature are referred to as *microwaves*) have begun to be widely used for constructing and performing modern wireless communication channels.

1.3. NOISE IN RADIO COMMUNICATION LINKS

The effectiveness of each radio communication link—land, atmospheric, or ionospheric depends on such parameters, as [5]:

- noise in the transmitter and in the receiver antennas;
- noise within the electronic equipment that communicate with both antennas;
- background and ambient noise (cosmic, atmospheric, artificial man-made, and so forth).

Now let us briefly consider each type of noise, which exists in a complete communication system. In a wireless channel, specifically, the noise sources can be subdivided into *additive* and *multiplicative* effects, as seen in Figure 1.1 [6,7,10].

The *additive noise* arises from noise generated within the receiver itself, such as thermal noise in passive and active elements of the electronic devices, and also from external sources such as atmospheric effects, cosmic radiation, and man-made noise. The clear and simple explanation of the first component of additive noise is that noise is generated within each element of the electronic communication channel due to the random motion of the electrons within the various components of the equipment [5]. According to the theory of thermodynamics, the noise energy can be determined by the average background temperature, T_0, as [1–5]:

$$E_N = k_B T_0 \qquad (1.1)$$

where

$$k_{\mathrm{B}} = 1.38 \times 10^{-23}\,\mathrm{W} \times \mathrm{s} \times \mathrm{K}^{-1} \tag{1.2}$$

is Boltzman's constant, and $T_0 = 290\,\mathrm{K} = 17°\mathrm{C}$. This energy is uniformly distributed in frequency band and hence it is called ''white noise.'' The total effective noise power at the receiver input is given by the following expression:

$$N_{\mathrm{F}} = k_{\mathrm{B}} T_0 B_{\mathrm{W}} F \tag{1.3}$$

where F is the *noise figure* at the receiver. The noise figure represents any additional noise effects related to the corresponding environment, and it is expressed as:

$$F = 1 + \frac{T_{\mathrm{e}}}{T_0} \tag{1.4}$$

Here T_{e} is the effective temperature, which accounts all ambient natural (weather, cosmic noise, clouds, rain, and so forth) and man-made (industry, plants, power engine, power stations, and so forth) effects.

The *multiplicative noise* arises from the various processes inside the propagation channel and depends mostly on the directional characteristics of both terminal antennas, on the reflection, absorption, scattering, and diffraction phenomena caused by various natural and artificial obstructions placed between and around the transmitter and the receiver (see Fig. 1.2). Usually, the multiplicative process in the propagation channel is divided into three types: *path loss*, *large-scale* (or *slow fading*), and *short-scale* (or *fast fading*) [7–10]. We describe these three characteristics of the multiplicative noise separately in the following section.

1.4. MAIN PROPAGATION CHARACTERISTICS

In real communication channels, the field that forms the complicated interference picture of received radio waves arrives via several paths simultaneously, forming a multipath situation. Such waves combine vectorially to give an oscillating resultant signal whose variations depend on the distribution of phases among the incoming total signal components. The signal amplitude variations are known as the *fading* effect [1–4,6–10]. Fading is basically a spatial phenomenon, but spatial signal variations are experienced, according to the ergodic theorem [11,12], as temporal variations by a receiver/transmitter moving through the multipath field or due to the motion of scatterers, such as a truck, aircraft, helicopter, satellite, and so on. Thus we can talk here about space-domain and time-domain variations of EM field in different radio environments, as well as in the frequency domain. Hence, if we consider mobile, mobile–aircraft or mobile–satellite communication links, we may observe the effects of random fading in the frequency domain, that is, the
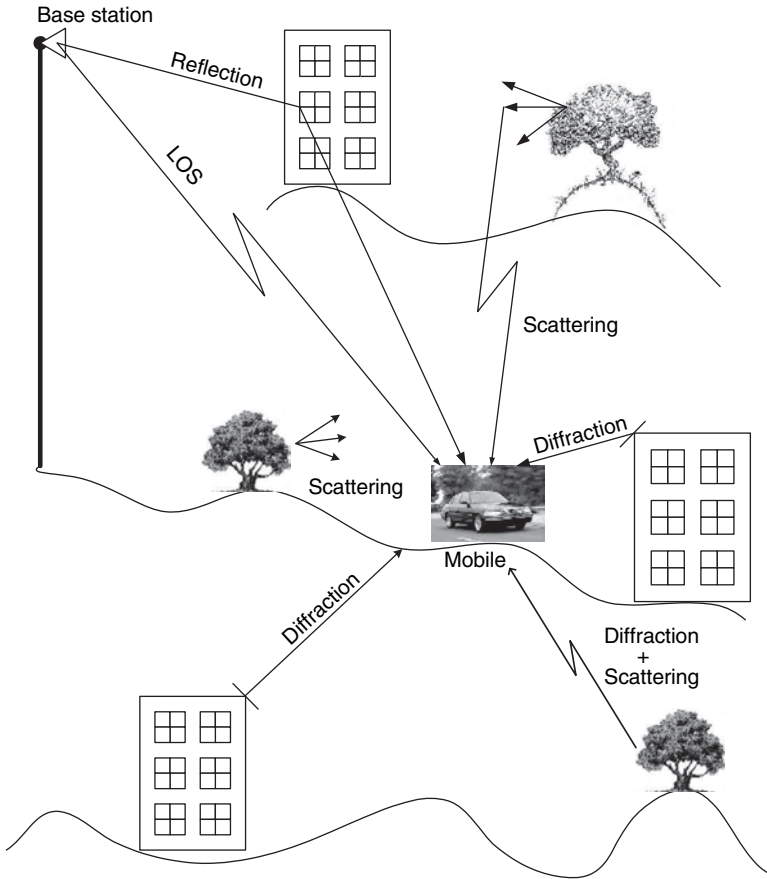
FIGURE 1.2. Multipath effects caused by various natural and artificial obstructions placed between and around the transmitting and the receiving antennas.

complicated interference picture of the received signal caused by receiver/ transmitter movements, which is defined as the ''Doppler shift'' effect [1–7,10].

Numerous theoretical and experimental investigations in such conditions have shown that the spatial and temporal variations of signal level have a triple nature [1–7,10]. The first one is the *path loss*, which can be defined as a large-scale smooth decrease in signal strength with distance between two terminals, mainly the transmitter and the receiver. The physical processes that cause these phenomena are the spreading of electromagnetic waves radiated outward in space by the transmitter antenna and the obstructing effects of any natural or man-made objects in the vicinity of the antenna. The spatial and temporal variations of the signal path loss are large and slow, respectively.

Large-scale (in the space domain) or *slow* (in the time domain) fading is the second nature of signal variations and is caused by diffraction from the obstructions

placed along the radio link surrounding the terminal antennas. Sometimes this fading phenomenon is called the *shadowing effect* [6,7,10].

During shadow fading, the signal's slow random variations follow either a Gaussian distribution or a lognormal distribution if the signal fading is expressed in decibels. The spatial scale of these slow variations depends on the dimensions of the obstructions, that is, from several to several tens of meters. The variations of the total EM field describe its structure within the shadow zones and are called *slow-fading* signals.

The third nature of signal variations is the *short-scale* (in the space domain) or *fast* (in the time domain) signal variations, which are caused by the mutual interference of the wave components in the multiray field. The characteristic scale of such waves in the space domain varies from half-wavelength to three-wavelength. Therefore, these signals are usually called *fast-fading* signals.

1.4.1. Path Loss

The path loss is a figure of merit that determines the effectiveness of the propagation channel in different environments. It defines variations of the signal amplitude or field intensity along the propagation trajectory (*path*) from one point to another within the communication channel. In general [1–3, 6–10], the path loss is defined as a logarithmic difference between the amplitude or the intensity (called *power*) at any two different points, $\mathbf{r}_1$ (the transmitter point) and $\mathbf{r}_2$ (the receiver point) along the propagation path in the medium. The path loss, which is denoted by L and is measured in decibels (dB), can be evaluated as follows as [5]:

– for a signal amplitude of $A(\mathbf{r}_j)$ at two points $\mathbf{r}_1$ and $\mathbf{r}_2$ along the propagation path

$$L = 10 \log \frac{A^2(\mathbf{r}_2)}{A^2(\mathbf{r}_1)} = 10 \log A^2(\mathbf{r}_2) - 10 \log A^2(\mathbf{r}_1)$$
$$= 20 \log A(\mathbf{r}_2) - 20 \log A(\mathbf{r}_1) \quad \text{[dB]} \tag{1.5}$$

– for a signal intensity $J(\mathbf{r}_j)$ at two points $\mathbf{r}_1$ and $\mathbf{r}_2$ along the propagation path

$$L = 10 \log \frac{J(\mathbf{r}_2)}{J(\mathbf{r}_1)} = 10 \log J(\mathbf{r}_2) - 10 \log J(\mathbf{r}_1) \quad \text{[dB]} \tag{1.6}$$

If we assume now $A(\mathbf{r}_1) = 1$ at the transmitter, then

$$L = 20 \log A(\mathbf{r}) \quad \text{[dB]} \tag{1.7a}$$

and

$$L = 10 \log J(\mathbf{r}) \quad \text{[dB]} \tag{1.7b}$$

For more details about how to measure the path loss, the reader is referred to References [1–3,6–10]. As any signal passing through the propagation channel, passes through the transmitter electronic channel and the electronic channel (see Fig. 1.1), both electronic channels together with the environment introduce additive or white noise into the wireless communication system. Therefore, the second main figure of merit of radio communication channels is the signal-to-noise ratio (SNR or S/N). In decibels this SNR can be written as:

$$\text{SNR} = P_R - N_R \quad [\text{dB}] \tag{1.8}$$

where P_R is the signal power at the receiver and N_R is the noise power at the receiver.

1.4.2. Characteristics of Multipath Propagation

Here we start with the general description of *slow* and *fast* fading.

Slow Fading. As was mentioned earlier, the *slow* spatial signal variations (expressed in decibels, dB) tend to have a lognormal distribution or a Gaussian distribution (expressed in watts, W) [1–4,6–10]. The probability density function (PDF) of the signal variations with the corresponding standard deviation, averaged within some individual small area or over some specific time period, depends on the nature of the terrain, of the atmospheric and ionospheric conditions. This PDF is given by:

$$\text{PDF}(r) = \frac{1}{\sigma_L \sqrt{2\pi}} \exp\left\{ -\frac{(r - \bar{r})^2}{2\sigma_L} \right\} \tag{1.9}$$

Here $\bar{r} = \langle r \rangle$ is the mean value of the random signal level, r is the value of the received signal strength or voltage envelope, and $\sigma_L = \langle r^2 - \bar{r}^2 \rangle$ is the variance or time-average power ($\langle r \rangle$ indicates the averaging operation of a variable r of the received signal envelope).

Fast Fading. In the case of stationary receiver and transmitter (*static multipath channel*), due to multiple reflections and scattering from various obstructions surrounding the transmitter and receiver, the radio signals travel along different paths of varying lengths, causing such fast deviations of the signal strength (in volts) or power (in watts) at the receiver.

In the case of a *dynamic multipath* situation, either the subscribers' antenna is in movement or the objects surrounding the stationary antennas are moving, so the spatial variations of the resultant signal at the receiver can be seen as temporal variations [11,12]. The signal received by the mobile at any spatial point may consist of a large number of signals having randomly distributed amplitudes, phases, and angles-of-arrival, as well as different time delays. All these features change the relative phase shifts as a function of the spatial location and, finally, cause the signal to fade in the space domain. In a dynamic (mobile) multipath situation, the signal
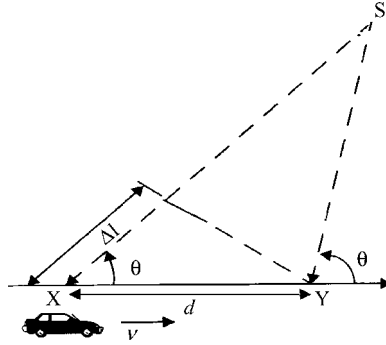
FIGURE 1.3. Geometry of the mobile link for Doppler effect estimation.

fading at the mobile receiver occurs in the time domain. This temporal fading is associated with a shift of frequency radiated by the stationary transmitter. In fact, the time variations, or dynamic changes of the propagation path lengths, are related to the Doppler effect, which is due to relative movements between a stationary base station (BS) and a moving subscriber (MS).

To illustrate the effects of phase change in the time domain due to the Doppler frequency shift (called the Doppler effect [1–4,6–10]), let us consider a mobile moving at a constant velocity v, along the path XY, as shown in Figure 1.3. The difference in path lengths traveled by a signal from source S to the mobile at points X and Y is $\Delta\ell = \ell\cos\theta = v\Delta\cos\theta$, where Δt is the time required for the moving receiver to travel from point X to Y along the path, and θ is the angle between the mobile direction along XY and direction to the source at the current point Y, that is, YS. The phase change of the resultant received signal due to the difference in path lengths is therefore

$$\Delta\Phi = k\Delta\ell = \frac{2\pi}{\lambda}\ell\cos\theta = \frac{2\pi v\Delta t}{\lambda}\cos\theta \tag{1.10}$$

Hence the apparent change in frequency radiated, or Doppler shift, is given by f_D, where

$$f_D = \frac{1}{2\pi}\frac{\Delta\Phi}{\Delta t} = \frac{v}{\lambda}\cos\theta \tag{1.11}$$

It is important to note from Figure 1.3 that the angles θ for points X and Y are the same only when the corresponding lines XS and YS are parallel. Hence, this figure is correct only in the limit when the terminal S is far away from the moving antenna at points X and Y. Many authors have ignored this fact during their geometrical explanation of the Doppler effect [1–4,10]. Because the Doppler shift is related to the mobile velocity and the spatial angle between the direction of mobile motion and the direction of arrival of the signal, it can be positive or negative depending on

whether the mobile receiver is moving toward or away from the transmitter. In fact, from Equation (1.11), if the mobile moves *toward* the direction of arrival of the signal with radiated frequency f_c, then the received frequency is increased, that is the apparent frequency is $f_c + f_D$. When the mobile moves away from the direction of arrival of the signal then the received frequency is decreased, that is the apparent frequency is $f_c - f_D$. The maximum Doppler shift is $f_{Dmax} = v/\lambda$, which, in our futher description will simply be denoted as f_m.

There are many probability distribution functions that can be used to describe the fast fading effects, such as, Rayleigh, Suzuki, Rician, Gamma, Gamma–Gamma, and so on. Because the Rician distribution is very general [1–4,10], as it includes both line-of-sight (LOS) together with scattering and diffraction with non-LOS, we briefly describe it in the following paragraph.

To estimate the contribution of each signal component, at the receiver, due to the dominant (or LOS) and the secondary (or multipath), the Rician parameter K is usually introduced, as a ratio between these components [1–4,10], that is,

$$K = \frac{\text{LOS} - \text{Component power}}{\text{Multipath} - \text{Component power}} \tag{1.12}$$

The Rician PDF distribution of the signal strength or voltage envelope r can be defined as [1–4,10]:

$$\text{PDF}(r) = \frac{r}{\sigma^2} \exp\left\{ -\frac{r^2 + A^2}{2\sigma^2} \right\} I_0\left(\frac{Ar}{\sigma^2} \right), \quad \text{for} \quad A > 0, r \geq 0 \tag{1.13}$$

where A denotes the peak strength or voltage of the dominant component envelope, σ is the standard deviation of signal envelope, and $I_0(\cdot)$ is the modified Bessel function of the first kind and zero-order. According to definition (1.12), we can now rewrite the parameter K, which was defined above as the ratio between the dominant and the multipath component power. It is given by

$$K = \frac{A^2}{2\sigma^2} \tag{1.14}$$

Using (1.14), we can rewrite (1.13) as a function of K only, [1–3,10]:

$$\text{PDF}(x) = \frac{r}{\sigma^2} \exp\left\{ -\frac{r^2}{2\sigma^2} \right\} \exp(-K) I_0\left(\frac{r}{\sigma} \sqrt{2K} \right) \tag{1.15}$$

For $K = 0$, $\exp(-K) = 1$ and $I_0(0) = 1$, that is, the worst case of the fading channel. The Rayleigh PDF, when there is no LOS signal and is equal to:

$$\text{PDF}(x) = \frac{r}{\sigma^2} \exp\left\{ -\frac{r^2}{2\sigma^2} \right\} \tag{1.16}$$
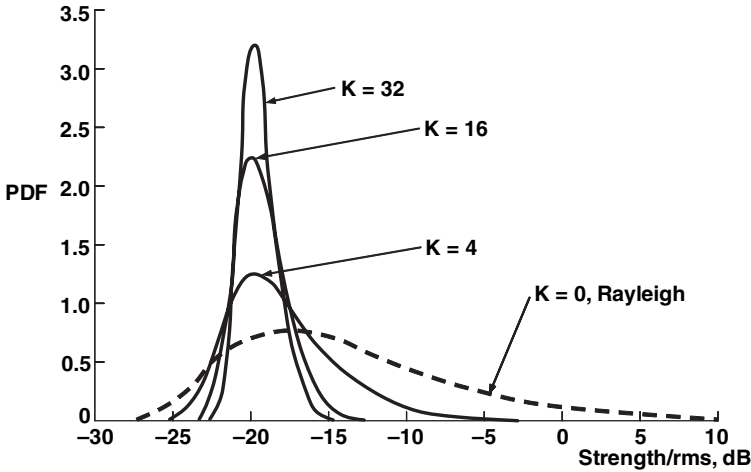
FIGURE 1.4. Rician PDF distribution versus ratio of signal to rms.

Conversely, in a situation of good clearance between two terminals with no multipath components, that is, when $K \to \infty$, the Rician fading approaches a Gaussian one yielding a ''Dirac-delta shaped'' PDF described by formula (1.9) (see Fig. 1.4). We will use these definitions in Chapter 5 for the link budget design inside a terrestrial radio communication system.

1.4.3. Signal Presentation in Wireless Communication Channels

To understand how to describe mathematically multipath fading in communication channels, we need to understand what kinds of signals we ''deal'' with in each channel.

Narrowband (CW) Signals. First of all, we consider a continuous wave CW or *narrowband* signals. A voice-modulated CW signal occupies a very narrow bandwidth surrounding the carrier frequency f_c of the radio frequency (RF) signal (e.g., the carrier), which can be expressed as:

$$x(t) = A(t)\cos[2\pi f_c t + \varphi(t)] \qquad (1.17)$$

where $A(t)$ is the signal envelope (i.e., slowly-varied amplitude) and $\varphi(t)$ is its signal phase. For example, for a modulated 1 GHz carrier signal by a wire signal of bandwidth $\Delta f = 2f_m = 8$ KHz, the fractional bandwidth is very narrow, that is, 8×10^3 Hz$/1 \times 10^9$ Hz $= 8 \times 10^{-6}$ or 8×10^{-4}%. Since all information in the signal is contained within the phase and envelope-time variations, an alternative form of a bandpass signal $x(t)$ is introduced [1,2,6–10]:

$$y(t) = A(t)\exp\{j\varphi(t)\} \qquad (1.18)$$
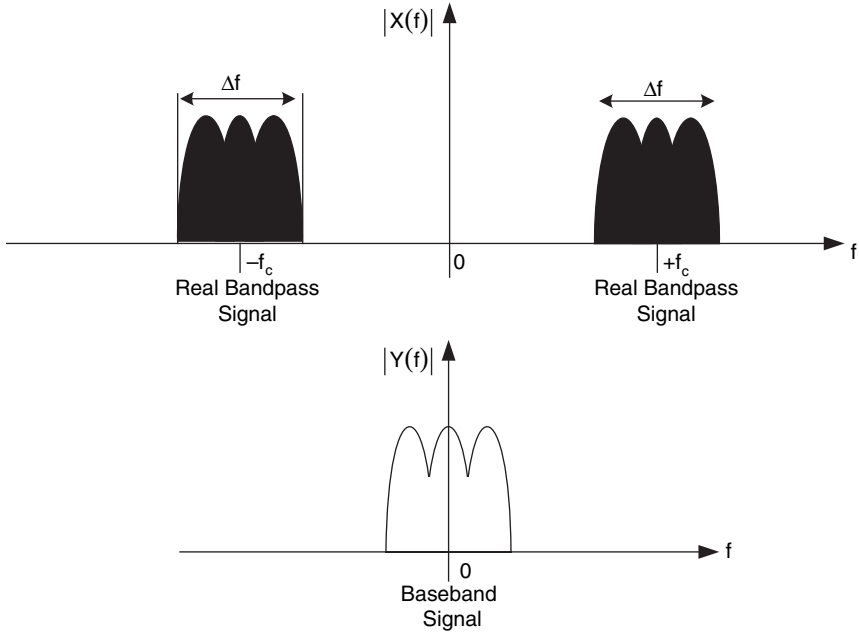
FIGURE 1.5. The signal power presentation of the frequency domain. Bandpath (upper figure) and baseband (lower figure).

which is also called the *complex baseband* representation of $x(t)$. By comparing (1.17) and (1.18), we can see that the relation between the *bandpass* (RF) and the *complex baseband* signals are related by:

$$x(t) = \text{Re}[y(t)\exp(j2\pi f_c t)] \tag{1.19}$$

The relations between these two representations of the narrowband signal in the frequency domain are shown schematically in Figure 1.5. One can see that the complex baseband signal is a frequency shifted version of the bandpass (RF) signal with the same spectral shape, but centered around a zero-frequency instead of the f_c [7]. Here, $X(f)$ and $Y(f)$ are the Fourier transform of $x(t)$ and $y(t)$, respectively and can be presented in the following manner [1,2]:

$$Y(f) = \int_{-\infty}^{\infty} y(t)e^{-j2\pi ft}dt = \text{Re}[Y(f)] + j\,\text{Im}[Y(f)] \tag{1.20}$$

and

$$X(f) = \int_{-\infty}^{\infty} x(t)e^{-j2\pi ft}dt = \text{Re}[X(f)] + j\,\text{Im}[X(f)] \tag{1.21}$$

Substituting for $x(t)$ in integral (1.21) from (1.19) gives:

$$X(f) = \int\limits_{-\infty}^{\infty} \mathrm{Re}\left[y(t)e^{j2\pi f_c t}\right]e^{-j2\pi ft}\,dt \tag{1.22}$$

Taking into account that the real part of any arbitrary complex variable w can be presented as:

$$\mathrm{Re}[w] = \frac{1}{2}[w + w^*]$$

where w^* is the complex conjugate, we can rewrite (1.22) in the following form:

$$X(f) = \frac{1}{2} \int\limits_{-\infty}^{\infty} \left[y(t)e^{j2\pi f_c t} + y^*(t)e^{-j2\pi f_c t}\right]e^{-j2\pi ft}\,dt \tag{1.23}$$

After comparing expressions (1.20) and (1.23), we get

$$X(f) = \frac{1}{2}[Y(f - f_c) + Y^*(-f - f_c)] \tag{1.24}$$

In other words, the spectrum of the real bandpass signal $x(t)$ can be represented by real part of that for the complex baseband signal $y(t)$ with a shift of $\pm f_c$ along the frequency axis. It is clear that the baseband signal has its frequency content centered around the "zero" frequency value.

Now we notice that the mean power of the baseband signal $y(t)$ gives the same result as the mean-square value of the real bandpass (RF) signal $x(t)$, that is,

$$\langle P_y(t) \rangle = \frac{\langle |y(t)|^2 \rangle}{2} = \frac{\langle y(t)y^*(t) \rangle}{2} \equiv \langle P_x(t) \rangle \tag{1.25}$$

The complex envelope $y(t)$ of the received narrowband signal can be expressed according to (1.18), within the multipath wireless channel, as a sum of phases of N baseband individual multiray components arriving at the receiver with their corresponding time delay, $\tau_i, i = 0, 1, 2, \ldots, N - 1$ [6–10]

$$y(t) = \sum_{i=0}^{N-1} u_i(t) = \sum_{i=0}^{N-1} A_i(t) \exp[j\varphi_i(t, \tau_i)] \tag{1.26}$$

If we assume that during the subscriber movements through the local area of service, the amplitude A_i time variations are small enough, whereas phases φ_i vary greatly

due to changes in propagation distance between the base station and desired subscriber, then there are great random oscillations of the total signal $y(t)$ at the receiver during its movement over a small distance. Since $y(t)$ is the phase sum in (1.26) of the individual multipath components, the instantaneous phases of the multipath components result in large fluctuations, that is, fast fading, in the CW signal. The average received power for such a signal over a local area of service can be presented according to References [1–3,6–10] as:

$$\langle P_{\mathrm{CW}}\rangle \approx \sum_{i=0}^{N-1} \langle A_i^2 \rangle + 2 \sum_{i=0}^{N-1} \sum_{i,j\neq i} \langle A_i A_j \rangle \langle \cos[\varphi_i - \varphi_j] \rangle \qquad (1.27)$$

Wideband (Pulse) Signals. The typical *wideband* or *impulse* signal passing through the multipath communication channel is shown schematically in Figure 1.6a according to [1–4]. If we divide the time-delay axis into equal segments, usually called bins, then there will be a number of received signals, in the form of vectors or delta functions. Each bin corresponds to a different path whose time-of-arrival is within the bin duration, as depicted in Figure 1.6b. In this case
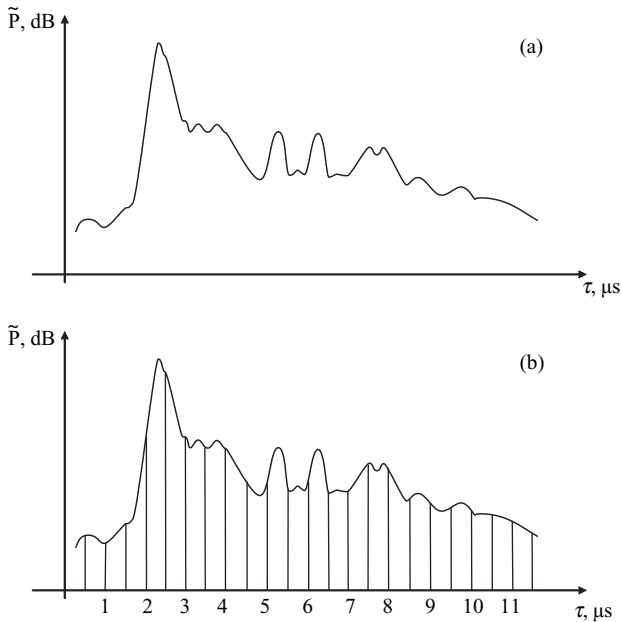
FIGURE 1.6. (a) A typical impulse signal passing through a multipath communication channel according to [1–4]. (b) The use of binds, as vectors, for the impulse signal with spreading.

the time varying discrete-time impulse response can be expressed as:

$$h(t, \tau) = \left\{ \sum_{i=0}^{N-1} A_i(t, \tau) \exp[-j2\pi f_c \tau_i(t)] \delta(\tau - \tau_i(t)) \right\} \exp[-j\varphi(t, \tau)] \quad (1.28)$$

If the channel impulse response is assumed to be time invariant, or is at least stationary over a short-time interval or over a small-scale displacement of the receiver/transmitter, then the impulse response (1.28) reduces to

$$h(t, \tau) = \sum_{i=0}^{N-1} A_i(\tau) \exp[-j\theta_i] \delta(\tau - \tau_i) \quad (1.29)$$

where $\theta_i = 2\pi f_c \tau_i + \varphi(\tau)$. If so, the received power delay profile for a wideband or pulsed signal averaged over a small area can be presented simply as a sum of the powers of the individual multipath components, where each component has a random amplitude and phase at any time, that is,

$$\langle P_{\text{pulse}} \rangle = \left\langle \sum_{i=0}^{N-1} \{A_i(\tau) | \exp[-j\theta_i] | \}^2 \right\rangle \approx \sum_{i=0}^{N-1} \langle A_i^2 \rangle \quad (1.30)$$

The received power of the wideband or pulse signal does not fluctuate significantly when the subscriber moves within a local area, because in practice, the amplitudes of the individual multipath components do not change widely in a local area of service.

Comparison between small-scale presentations of the average power of the narrowband (CW) and wideband (pulse) signals that is, (1.27) and (1.30), shows that when $\langle A_i A_j \rangle = 0$ or/and $\langle \cos[\varphi_i - \varphi_j] \rangle = 0$, the average power for CW signal and that for pulse are equivalent. This can occur when either the path amplitudes are uncorrelated, that is, each multipath component is independent after multiple reflections, diffractions, and scattering from obstructions surrounding both the receiver and the transmitter or the base station and the subscriber antenna. It can also occur when multipath phases are independently and uniformly distributed over the range of $\lfloor 0, 2\pi \rfloor$. This property is correct for UHF/X-waveband when the multipath components traverse differential radio paths having hundreds of wavelengths [6–10].

1.4.4. Parameters of the Multipath Communication Channel

So the question that is remains to be answered which kind of fading occurs in a given wireless channel.

Time Dispersion Parameters. First some important parameters for a wideband (pulse) signal passing through a wireless channel, can be determined, for a certain threshold level X (in dB) of the channel under consideration, from the signal

power delay profile, such as mean excess delay, rms delay spread and excess delay spread.

The *mean excess delay* is the first moment of the power delay profile of the pulse signal and is defined as:

$$\langle \tau \rangle = \frac{\sum_{i=0}^{N-1} A_i^2 \tau_i}{\sum_{i=0}^{N-1} A_i^2} = \frac{\sum_{i=0}^{N-1} P(\tau_i) \tau_i}{\sum_{i=0}^{N-1} P(\tau_i)} \qquad (1.31)$$

The *rms delay spread* is the square root of the second central moment of the power delay profile and is defined as

$$\sigma_\tau = \sqrt{\langle \tau^2 \rangle - \langle \tau \rangle^2} \qquad (1.32)$$

where

$$\langle \tau^2 \rangle = \frac{\sum_{i=0}^{N-1} A_i^2 \tau_i^2}{\sum_{i=0}^{N-1} A_i^2} = \frac{\sum_{i=0}^{N-1} P(\tau_i) \tau_i^2}{\sum_{i=0}^{N-1} P(\tau_i)} \qquad (1.33)$$

These delays are measured relative to the first detectable signal arriving at the receiver at $\tau_0 = 0$. We must note that these parameters are defined from a single power delay profile, which was obtained after temporal or local (small-scale) spatial averaging of measured impulse response of the channel [1–3,7–10].

Coherence Bandwidth. The power delay profile in the time domain and the power spectral response in the frequency domain are related through the Fourier transform. Hence, to describe a multipath channel in full, both the delay spread parameters in the time domain, and the *coherence bandwidth* in the frequency domain are used. As mentioned earlier the coherence bandwidth is the statistical measure of the frequency range over which the channel is considered "flat." In other words, this is a frequency range over which two frequency signals are strongly amplitude correlated. This parameter, actually, describes the time dispersive nature of the channel in a small-scale (local) area. Depending on the degree of amplitude correlation of two frequency separated signals, there are different definitions for this parameter.

The first definition is the *coherence bandwidth*, B_c, which describes a bandwidth over which the frequency correlation function is above 0.9 or 90%, and it is given by:

$$B_c \approx 0.02 \sigma_\tau^{-1} \qquad (1.34)$$

The second definition is the *coherence bandwidth*, B_c, which describes a bandwidth over which the frequency correlation function is above 0.5 or 50%, or:

$$B_c \approx 0.2\sigma_\tau^{-1} \tag{1.35}$$

There is not any single exact relationship between coherence bandwidth and rms delay spread, and equations (1.34) and (1.35) are only approximate equations [1–6,7–10].

Doppler Spread and Coherence Time. To obtain information about the time varying nature of the channel caused by movements, from either the transmitter/receiver or scatterers located around them, new parameters, such as the *Doppler spread* and the *coherence time*, are usually introduced to describe the time variation phenomena of the channel in a small-scale region. The Doppler spread B_D is defined as a range of frequencies over which the received Doppler spectrum is essentially nonzero. It shows the spectral spreading caused by the time rate of change of the mobile radio channel due to the relative motions of vehicles (and scatterers around them) with respect to the base station. According to [1–4,7–10], the Doppler spread B_D depends on the Doppler shift f_D and on the angle α between the direction of motion of any vehicle and the direction of arrival of the reflected and/or scattered waves (see Fig. 1.3). If we deal with the complex baseband signal presentation, then we can introduce the following criterion: If the baseband signal bandwidth is greater than the Doppler spread B_D, the effects of Doppler shift are negligible at the receiver.

Coherence time T_c is the time domain dual of Doppler spread, and it is used to characterize the time varying nature of the frequency dispersiveness of the channel in time coordinates. The relationship between these two-channel characteristics is:

$$T_c \approx \frac{1}{f_m} = \frac{\lambda}{v} \tag{1.36}$$

We can also define the coherence time according to [1–4,7–10] as the time duration over which two multipath components of receiving signal have a strong potential for amplitude correlation. One can also define the coherence time as the time over which the correlation function of two various signals in the time domain is above 0.5 (or 50%). Then according to [7,10] we get

$$T_c \approx \frac{9}{16\pi f_m} = \frac{9\lambda}{16\pi v} = 0.18\frac{\lambda}{v} \tag{1.37}$$

This definition is approximate and can be improved for modern digital communication channels by combining Equations (1.36) and (1.37) as the geometric mean between the two, this yields

$$T_c \approx \frac{0.423}{f_m} = 0.423\frac{\lambda}{v} \tag{1.38}$$
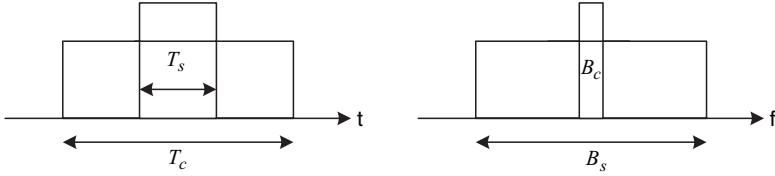
FIGURE 1.7. Comparison between signal and channel parameters.

The definition of coherence time implies that two signals arriving at the receiver with a time separation greater than T_c are affected differently by the channel.

1.4.5. Types of Fading in Multipath Communication Channels

Let us now summarize the effects of fading, which may occur in static or dynamic multipath communication channels.

Static Channel. In this case multipath fading is purely spatial and leads to constructive or destructive interference at various points in space, at any given instant in time, depending on the relative phases of the arriving signals. Furthermore, fading in the frequency domain does not change because the two antennas are stationary. The signal parameters, such as the signal bandwidth, B_s, the time of duration, T_s, with respect to the coherent time, B_c, and the coherent bandwidth, T_c, of the channel are shown in Figure 1.7. There are two types of fading that occur in the static channels:

A. *Flat slow fading* (FSF) (see Fig. 1.8), where the following relations between signal parameters of the signal and a channel are valid [7–10]:

$$T_c \gg T_s; \quad 0 \cong B_D \ll B_s; \quad \sigma_\tau \ll T_s; \quad B_c \sim \frac{0.02}{\sigma_\tau} \gg B_s \qquad (1.39)$$

Here all harmonics of the total signal are coherent.

B. *Flat fast fading* (FFF) (see Fig. 1.9), where the following relations between the parameters of a channel and the signal are valid [7–10]:

$$T_c \gg T_s; \quad 0 \cong B_D \ll B_s; \quad \sigma_\tau \leqslant T_s; \quad B_c \ll B_s \qquad (1.40)$$
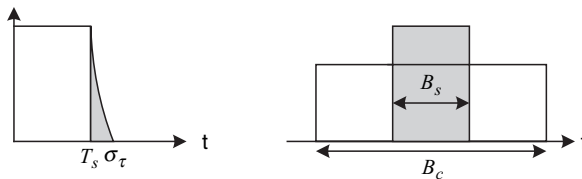
FIGURE 1.8. Relations between parameters for flat slow fading.
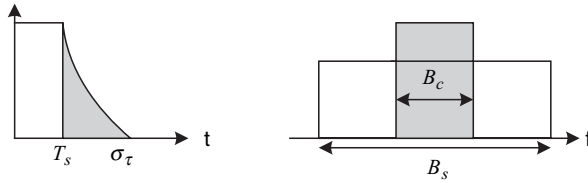
FIGURE 1.9. Relations between parameters for flat fast fading.

Dynamic Channel. There are two different types of fading also that occur in a dynamic (mobile) channel:

A. *Frequency selective fast fading* (FSFF) (see Fig. 1.10), when fast fading depends on the frequency. In this case following relations between the parameters of a channel and the signal are valid [7–10]:

$$T_c \ll T_s; \quad B_D \gg B_s; \quad \sigma_\tau \gg T_s; \quad B_c \ll B_s \qquad (1.41)$$

B. *Frequency selective slow fading* (FSSF) (see Fig. 1.11), when slow fading depends on the frequency. Therefore, the following relations between the parameters of a channel and the signal are valid [7–10]:

$$T_c > T_s; \quad B_D < B_s; \quad \sigma_\tau < T_s; \quad B_c \gg B_s \qquad (1.42)$$

Using these relationships between the parameters of the signal and of a channel, we can a priori define the type of fading which may occur in a wireless communication link (see Fig. 1.12).
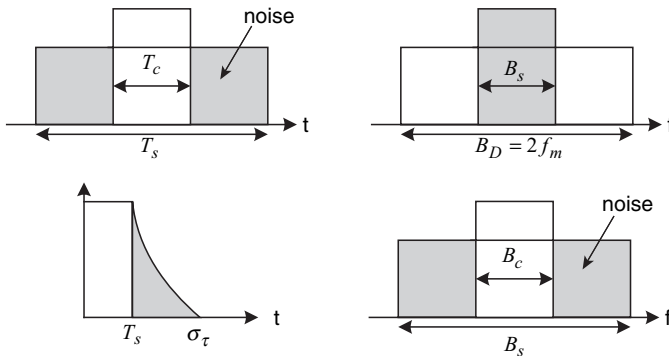
FIGURE 1.10. Relations between parameters for frequency selective fast fading.
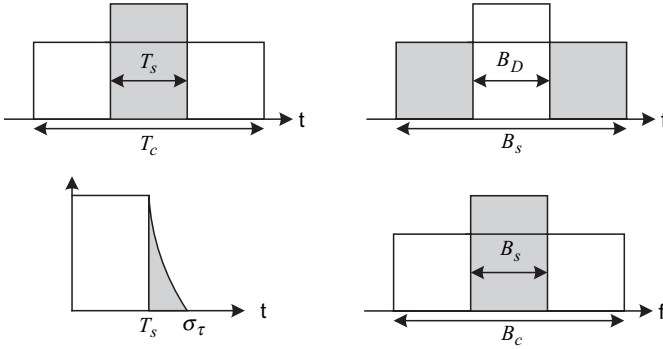
FIGURE 1.11. Relations between parameters for frequency selective slow fading.
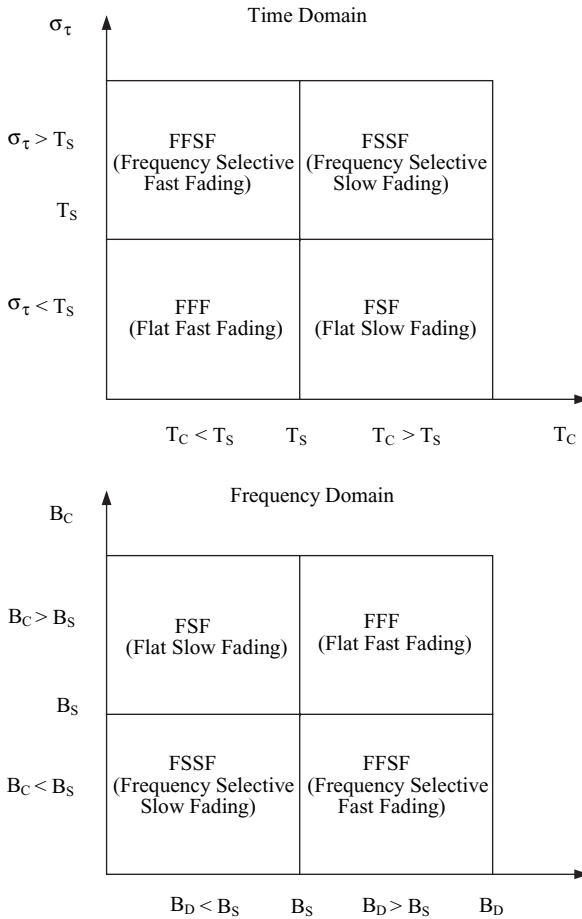
FIGURE 1.12. Common picture of different kinds of fading, depending on the relations between the signal and the channel main parameters.

1.5. PROBLEMS IN ADAPTIVE ANTENNAS APPLICATION

The main problem with land communication links is estimating the ratio between the coherent and multipath components of the total signal. That is, the Ricean parameter K, to predict the effects of multiplicative noise in the channel of each subscriber located in different conditions in the terrestrial environment. This is shown in Figure 1.13 for various subscribers numbered by $i = 1, 2, 3, \ldots$.

However, even a detailed prediction of the radio propagation situation for each subscriber cannot completely resolve all issues of effective service and increase quality of data stream sent to each user. For this purpose, in future generations of wireless systems, adaptive or smart antenna systems are employed to reduce interference and decrease bit error rate (BER). This topic will be covered in detail in Chapter 8. We present schematically the concept of adaptive (smart) antennas in Figure 1.14.
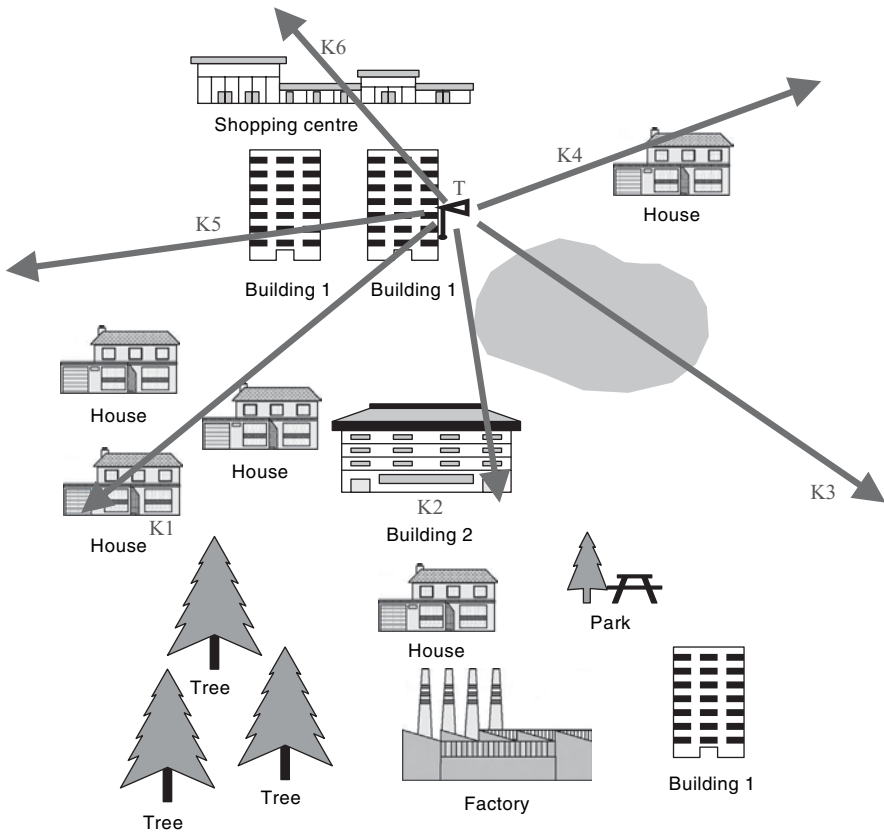
FIGURE 1.13. Scheme of various scenarios in urban communication channel.
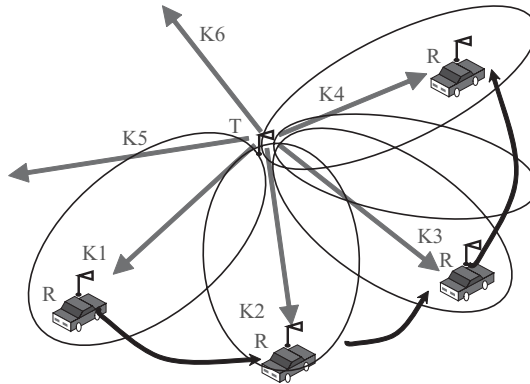
FIGURE 1.14. A scheme for using adaptive antennas for each user located in different conditions in a service area.

Even with smart antennas (see Chapter 8), we cannot totally cancel the effects of the environment, especially in urban areas, due to the spread of the antenna beam (see Fig. 1.14). Chapters 5 and 10 will focus on terrain effects where a thorough analysis of these effects on the design of wireless system will be presented.

BIBLIOGRAPHY

[1] Jakes, W. C., *Microwave Mobile Communications*, New York, John Wiley and Son, 1974.

[2] Steele, R., *Mobile Radio Communication*, IEEE Press, 1992.

[3] Stuber, G. L., *Principles of Mobile Communications*, Boston-London, Kluwer Academic Publishers, 1996.

[4] Lee, W. Y. C., *Mobile Cellular Telecommunications Systems*, McGraw Hill, New York, 1989.

[5] Blaunstein, N., *Radio Propagation in Cellular Networks*. Artech Houses, Boston-London, 1999.

[6] Blaunstein, N., and J. B. Andersen, *Multipath Phenomena in Cellular Networks*, Artech Houses, Boston-London, 2002.

[7] Saunders, S. R., *Antennas and Propagation for Wireless Communication Systems*, John Wiley & Sons, New York, 1999.

[8] Bertoni, H. L., *Radio Propagation for Modern Wireless Systems*, Prentice Hall PTR, New Jersey, 2000.

[9] Blaunstein, N., Chapter 12*, Wireless Communication Systems*, *Hanbook of Engineering Electromagnetics*, Edited by Rajeev Bansal, Marcel Dekker, NY, 2004.

[10] Rappaport, T. S., *Wireless Communications*, New York, Prentice Hall PTR, 1996.

[11] Leon-Garcia, A., *Probability and Random Processes for Electrical Engineering*, New York: Addison-Wesley Publishing Company, 1994.

[12] Stark, H., and Woods J. W., *Probability, Random Processes, and Estimation Theory for Engineers*, New Jersey, Prentice Hall, 1994.

Antenna Fundamentals

A radio antenna, transmitting or receiving, is an independent and yet integral component of any wireless communication system. An antenna acts as a transducer that converts the current or voltage generated by the feeding-based circuit, such as a transmission line, a waveguide or coaxial cable, into electromagnetic field energy propagating through space and vice versa. In free space, the fields propagate in the form of spherical waves, whose amplitudes are inversely proportional to their distance from the antenna. Each radio signal can be represented as an electromagnetic wave [1], that propagates along a given direction. The wave field strength, its polarization, and the direction of propagation determine the main characteristics of an antenna operation.

Antennas can be divided in different categories, such as wire antennas, aperture antennas, reflector antennas, frequency independent antennas, horn antennas, printed and conformal antennas, and so forth [2–10]. When applications require radiation characteristics that cannot be met by a single radiating antenna, multiple elements are employed forming ''array antennas.'' Arrays can produce the desired radiation characteristics by appropriately exciting each individual element with certain amplitudes and phases. The very same antenna array configurations, when combined with signal processing, lead to multiple-beam (switched beam) or adaptive antennas that offer many more degrees of freedom in a wireless system design than using a single antenna [11–14]. The subject antenna arrays, including adaptive arrays, will be studied in detail in Chapter 9. In this chapter, we introduce the basic concepts of antennas and some fundamental figures of merit, such as radiation patterns, directivity, gain, polarization loss, and so on, that describe the performance of any antenna.
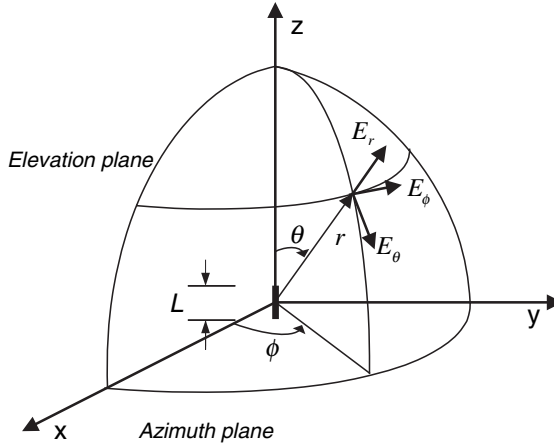
FIGURE 2.1. Spherical coordinate system for antenna analysis purposes. A very short dipole is shown with its no-zero field component directions.

2.1. RADIATION PATTERN

The radiation pattern of any antenna is defined as the relative distribution of electromagnetic energy or power in space. Because antennas are an integral part of all telecommunication systems, the radiation pattern is determined in the far-field region where no change in pattern with distance occurs. Figure 2.1 shows that if we place an antenna at the origin of a spherical coordinate system, the radiation properties of the antenna will depend only on the angles ϕ and θ along a path or surface of constant radius. A trace of the radiated (or received) power at a fixed radius is known as a *power pattern*, whereas the spatial variation of the electric field along the same radius is called the *amplitude field pattern*.

Although a 3-D visualization of an antenna radiation pattern is helpful, usually, a couple of plots of the pattern as a function of θ, for some particular values of ϕ, plus a couple of plots as a function of ϕ, for some particular values of θ, give sufficient information. For example, Figure 2.2(a) depicts the 3-D radiation pattern from an ideal or very short dipole. Figure 2.2(b) shows the *xy*-plane (azimuthal plane, $\theta = \pi/2$), called the principal *E*-plane cut, and Figure 2.2(c) is the *xz*-plane (elevation plane, $\phi = 0$) called the principal *H*-plane cut.

A typical antenna power pattern is shown in Figure 2.3. The upper part depicts a normalized polar radiation pattern in linear, whereas the bottom figure is actually the same pattern but in rectangular coordinates and in dB scale. The radiation pattern of the antenna consists of various parts, which are known as *lobes*. The *main lobe* (also known as *main beam* or *major lobe*) is the lobe containing the direction of maximum radiation. In the case of Figure 2.3 the main lobe is pointing in the $\theta = 0$ direction. Antennas can have more than one major lobe.
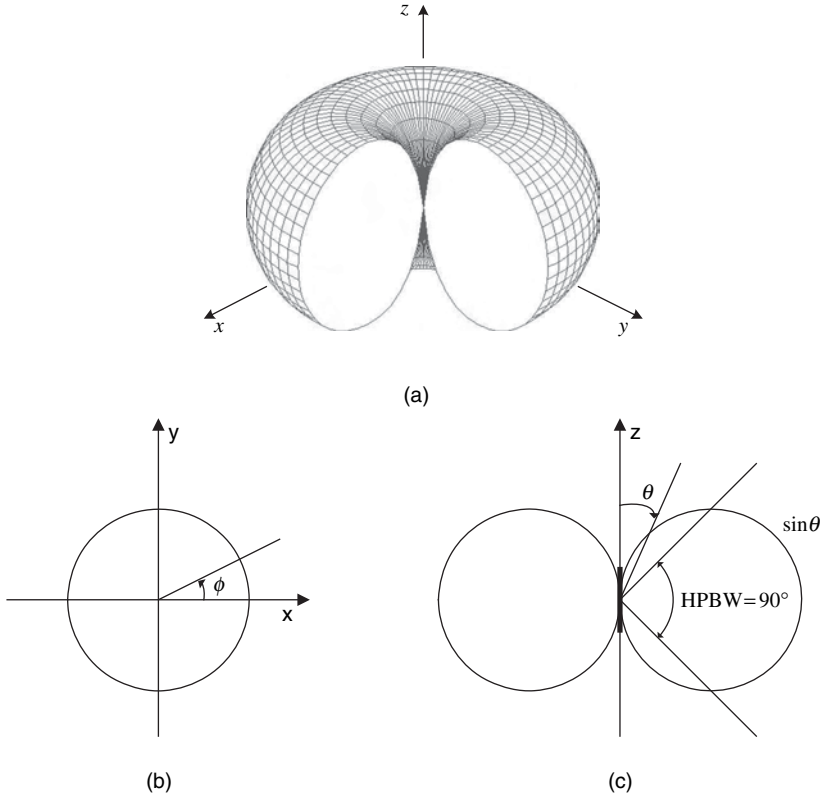
FIGURE 2.2. Radiation field pattern of far field from an ideal or very short dipole. (a) Three-dimensional pattern plot. (b) *E*-plane radiation pattern polar plot and (c) *H*-plane radiation pattern polar plot.

In Chapter 9, we will see that one can create multiple lobes to track several mobile users at the same time from a Base Station (BS). A *minor lobe* is any lobe other than the main lobe. Minor lobes are usually divided into *side lobes* and *back lobes*. The term side lobe refers to those minor lobes near the main lobe, and by a back lobe we refer to a radiation lobe that is in the opposite direction to that of the main lobe. Minor lobes usually represent radiation in undesired directions that can cause interference in a mobile environment, and they should be minimized. The ratio of levels of the largest side lobe over the major lobe is termed as the *side lobe ratio* or *side lobe level*.

Another term that characterizes a radiation pattern is its *half-power beamwidth* (HPBW) in the two principal planes. The HPBW is defined as the angular width of the main lobe within which the radiation intensity is one-half the maximum value of beam (see Fig. 2.3). Sometimes, we also use the *beamwidth between the first nulls* (BWFN) around the main beam. The 3-dB beamwidth plays a major role in the overall design of an antenna application. As the beamwidth of the radiation pattern

(a)

(b)
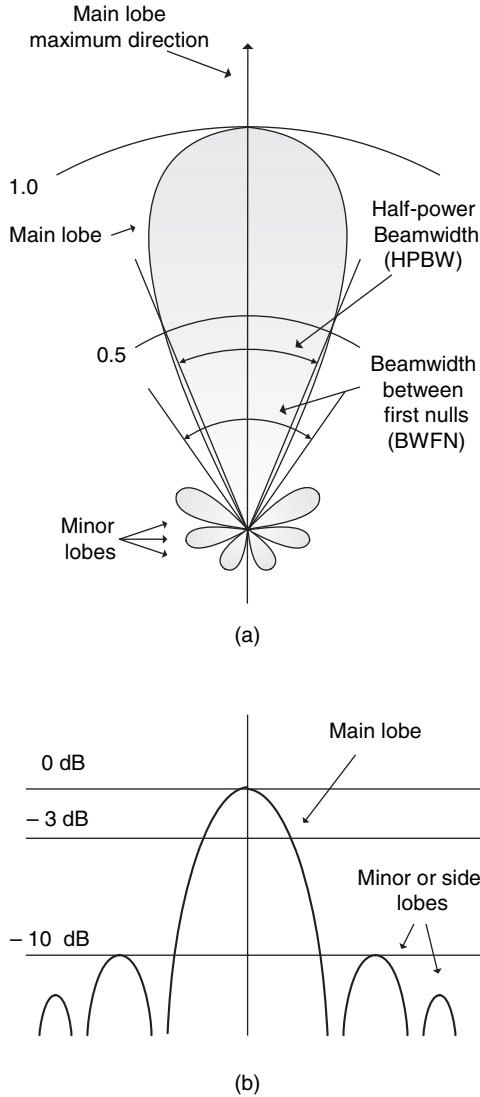
FIGURE 2.3. Antenna power patterns. (a) A typical polar plot in linear scale and (b) a plot in rectangular coordinates in decibel (logarithmic) scale. The associated lobes and beamwidths are also shown.

increases, the side lobe level decreases, and vice versa. So there is a trade-off between side lobe ratio and beamwidth of an antenna pattern.

Furthermore, the beamwidth of the antenna is also used to describe the resolution capabilities of the antenna to distinguish between two adjacent radiating sources or radar targets. That can play an important role when one uses an antenna to determine the angle-of-arrival of a radio source.

2.2. FIELD REGIONS OF AN ANTENNA

The space surrounding a transmitting antenna is divided into two main regions: the *near-field region* and the *far-field* region. The near-field region can be further subdivided into two regions: the *reactive near-field* and the *radiating near-field* [1].

Figure 2.4 shows these regions. The first region, which is the closest to the antenna, is called the reactive or induction near-field region. It derives its name from the reactive field that lies close to every current-carrying conductor. The reactive field, within that region, dominates all radiated fields.

For most antennas, the outermost boundary of this region is given by:

$$r > 0.62\sqrt{\frac{D^3}{\lambda}} \tag{2.1}$$

where r is the distance from the antenna, D is the largest dimension of the antenna, and λ is the wavelength.

Between this reactive near-field region and the far-field region, lies the radiating near-field region. Although the radiation fields dominate within this region, the angular field distribution still depends on the distance from the antenna. This region
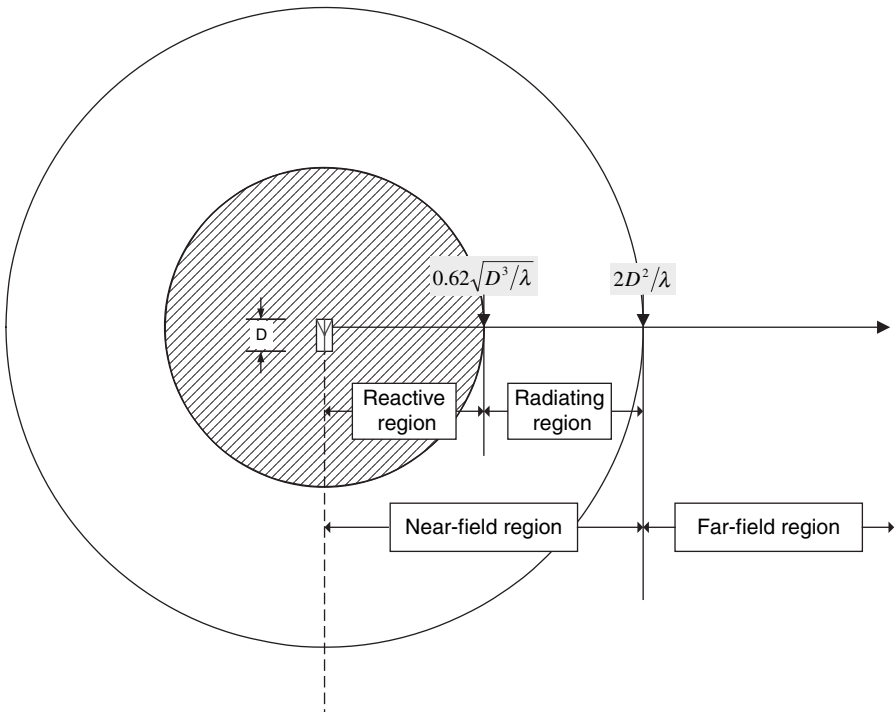
FIGURE 2.4. Field regions of an antenna and some common used boundaries.

is also called the Fresnel region, a terminology borrowed from the field of optics. The boundaries of this region are:

$$0.62\sqrt{\frac{D^3}{\lambda}} < r < \frac{2D^2}{\lambda}. \tag{2.2}$$

At the outer boundary of the near-field region, the reactive field intensity becomes negligible with respect to the radiated field intensity. The far-field or radiation region, also called the *Fraunhofer region,* begins at $r = \frac{2D^2}{\lambda}$ and extends outward indefinitely into free space. In this region the angular field distribution of the field of the antenna is not dependent on the distance from the antenna.

2.3. RADIATION INTENSITY

Radiation intensity is a far-field parameter that is used to determine the antenna power pattern as a function of angle:

$$\begin{aligned}
I(\theta, \phi) &= \mathbf{S}_{av} r^2 \\
&= \frac{r^2}{2\eta} |\mathbf{E}(r, \theta, \phi)|^2 \\
&= \frac{r^2}{2\eta} [|E_\theta(r, \theta, \phi)|^2 + |E_\phi(r, \theta, \phi)|^2] \\
&\approx \frac{1}{2\eta} [|E_\theta(\theta, \phi)|^2 + |E_\phi(\theta, \phi)|^2]
\end{aligned} \tag{2.3}$$

where $I(\theta, \phi)$ is the radiation intensity (W/unit solid angle); $\mathbf{S}_{av}$ is the Poynting vector (W/m^2); $E(r, \theta, \phi)$ is the total transverse electric field (V/m); $H(r, \theta, \phi)$ is the total transverse magnetic field (A/m); r is the distance from antenna to point of measurement (m); η is the intrinsic impedance of medium (Ω per square).

The averaged Poynting vector $\mathbf{S}_{av}$ in equation (2.3) is derived from:

$$\mathbf{S}_{av} = \frac{1}{2} \text{Re}(\mathbf{E} \times \mathbf{H}^*) \quad (\text{W/m}^2) \tag{2.4}$$

where the notation Re stands for the real part of the complex number and the * denotes the complex conjugate. Note that $\mathbf{E}$ and $\mathbf{H}$ in Equation (2.4) are the expressions for the radiated electric and magnetic fields.

Note that the radiation intensity is independent of distance since in the far field the Poynting vector is entirely radial, that is, the fields are entirely transverse and $\mathbf{E}$ and $\mathbf{H}$ vary as $1/r$. As the radiation intensity is a function of angle, it is related to the power radiated from an antenna per unit solid angle. The measure of a solid angle is
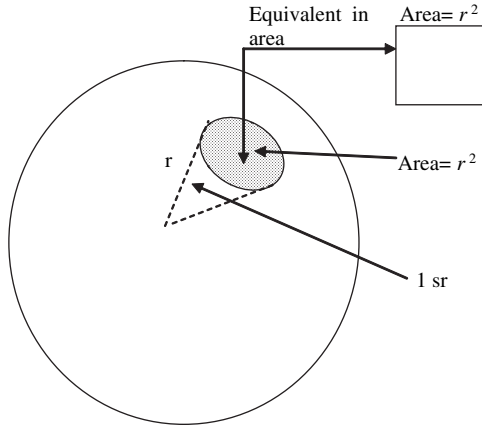
FIGURE 2.5. Definition of a solid angle and a steradian.

steradian, which is defined as the solid angle with its vertex at the center of a sphere of radius r, subtended by a spherical surface area equivalent to that of a square of size r^2 (see Fig. 2.5). But the area of a sphere of radius r is given by $A = 4\pi r^2$, so in a closed sphere there are $4\pi r^2/r^2 = 4\pi$ steradian (sr). For a sphere of radius r, an infinitesimal surface area dA can be expressed as:

$$dA = r^2 \sin\theta \, d\theta \, d\phi \ (m^2) \tag{2.5}$$

and hence the element of solid angle dΩ of a sphere is given by:

$$d\Omega = \frac{dA}{r^2} = \sin\theta \, d\theta \, d\phi \ (sr). \tag{2.6}$$

The total power that can be radiated is given by:

$$P_{rad} = \oiint_\Omega I(\theta, \phi) d\Omega = \int_0^{2\pi} \int_0^\pi I(\theta, \phi) \sin\theta \, d\theta \, d\phi. \tag{2.7}$$

Let us consider an *isotropic radiator* as an example. An *isotropic antenna* refers to a hypothetical antenna radiating equally in all directions and its power pattern is uniformly distributed in all directions. That means the radiation intensity of an isotropic antenna is independent of the angles θ and ϕ and the total radiated power will be:

$$P_{rad} = \oiint_\Omega I_i d\Omega = I_i \int_0^{2\pi} \int_0^\pi \sin\theta \, d\theta \, d\phi = I_i \oiint_\Omega d\Omega = 4\pi I_i \tag{2.8}$$

or $I_i = \frac{P_{rad}}{4\pi}$, which is the radiation intensity of an isotropic antenna.

Dividing $I(\theta, \phi)$ by its maximum value I_{max}, leads to the *normalized antenna power pattern,* that is,

$$I_n(\theta, \phi) = \frac{I(\theta, \phi)}{I_{\text{max}}(\theta, \phi)} \quad \text{(dimensionless)}. \tag{2.9}$$

2.4. DIRECTIVITY AND GAIN

An important parameter that indicates how well radiated power is concentrated into a limited solid angle is *directivity D.* The directivity of an antenna is defined as the ratio of the maximum radiation intensity to the radiation intensity averaged over all directions (i.e., with reference to the isotropic radiator). Thus, the average radiation intensity is found by dividing the total antenna radiated power r by 4π sr, or

$$D = \frac{I_{\text{max}}(\theta, \phi)}{I_{\text{av}}} = \frac{I_{\text{max}}(\theta, \phi)}{I_i} = \frac{I_{\text{max}}(\theta, \phi)}{P_{\text{rad}}/4\pi} = \frac{4\pi I_{\text{max}}(\theta, \phi)}{P_{\text{rad}}} \quad \text{(dimensionless)}. \tag{2.10}$$

The narrower the main lobe of the antenna radiation pattern, the larger the directivity of the antenna. Obviously, the directivity of an isotropic antenna is unity. Any other antenna will have a directivity larger than unity (i.e., larger than the isotropic), as shown in Figure 2.6.

Let us consider the directivity of a very short dipole, as an example. The average pointing vector for the dipole is given by [11]

$$\mathbf{S}_{\text{av}} = \frac{\eta}{2}\left(\frac{I_0 L \beta}{4\pi r}\right)^2 \sin^2 \theta \quad \text{W/m}^2 \tag{2.11}$$
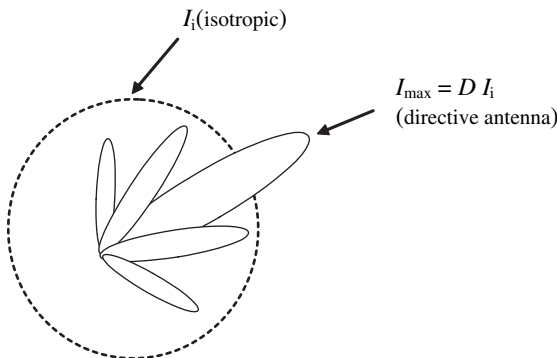
FIGURE 2.6. Directive pattern versus an isotropic one.

where L is the length of the short dipole, I_0 is the current flowing through the dipole, η is the wave impedance in free space, and $\beta = 2\pi/\lambda$. Using Equation (2.3) we can solve for the radiation intensity, and then we can use Equation (2.10) to obtain a directivity of 1.5. This occurs at the $\theta = 90°$ direction (see Fig. 2.2). Thus, in this direction, a very short dipole can radiate 1.5 times more power than the isotropic radiator. This is often expressed in decibels such that

$$D = 10\log_{10}(d) \quad \text{dB} = 10\log_{10}(1.5) = 1.76\,\text{dB}. \tag{2.12}$$

The *gain* of an antenna is closely associated with directivity, and it is defined as the ratio of the maximum radiation intensity in a given direction to the maximum radiation intensity produced in the same direction from a reference antenna with the same power input. Any convenient type of antenna can be taken as a reference antenna. Usually, the type of reference antenna is determined by the specific application, but the most commonly used one is the isotropic radiator, and thus we can write:

$$G = \frac{I_{\max}(\theta, \phi)}{I_i} = \frac{I_{\max}(\theta, \phi)}{P_{\text{in}}/4\pi} \quad \text{(dimensionless)} \tag{2.13}$$

where the radiation intensity of the isotropic radiator is equal to the input, P_{in}, of the antenna divided by 4π. As the gain of an antenna depends on how efficient it is in converting input power into radiated fields, we need to take into consideration its efficiency before we determine the actual gain. In general, *antenna efficiency* (ε) is defined as the ratio of the power radiated by the antenna to the input power at its terminals:

$$\varepsilon = \frac{P_{\text{rad}}}{P_{\text{in}}} = \frac{R_r}{R_r + R_{\text{loss}}} \quad \text{(dimensionless)} \tag{2.14}$$

where R_r is the *radiation resistance* of the antenna; R_r is an equivalent resistance in which the same current flowing at the antenna terminals will produce power equal to that radiated by the antenna. R_{loss} is the *loss resistance* due to any conductive or dielectric losses of the materials used to construct the antenna. So, if we include these losses, a real antenna will have radiation intensity

$$I(\theta, \phi) = \varepsilon I_0(\theta, \phi) \tag{2.15}$$

where $I_0(\theta, \phi)$ is the radiation intensity of the same antenna with no losses.

Using Equation (2.15) into (2.13) yields the definition of gain in terms of the antenna directivity:

$$G = \frac{I_{\max}(\theta, \phi)}{I_i} = \frac{\varepsilon I_{\max 0}(\theta, \phi)}{I_i} = \varepsilon D. \tag{2.16}$$

The values of gain range between zero and infinity, whereas for directivity the values range between unity and infinity. However, though directivity can be found either theoretically or experimentally, the gain of an antenna is almost always determined by a direct comparison of measurement against a reference, usually the standard gain antenna. Gain is expressed also in decibels, that is

$$G = 10 \log_{10}(g) \quad \text{dB.} \tag{2.17}$$

When we use the isotropic antenna as a reference then we use the dBi notation, which means decibels over isotropic.

2.5. POLARIZATION

2.5.1. Wave and Antenna Polarization

Polarization refers to the direction of the electric field component of an electromagnetic wave. The wave is called *linearly* or *plane polarized*, that is the locus of oscillation of the electric field vector within a plane perpendicular to the direction of propagation forms a straight line. On the contrary, when the locus of the tip of an electric field vector forms an ellipse or a circle, the wave is called an *elliptically* or *circularly polarized wave*, respectively. There is a tendency to refer to antennas as vertically or horizontally polarized, though it is only their radiations that are polarized. Next, we discuss the mechanics of various polarizations that we encounter in antenna communication systems.

2.5.2. Linear, Circular, and Elliptical Polarization

Consider a plane wave traveling in the positive z direction, with the electric field component along the x direction as shown in Figure 2.7(a). This wave is linearly polarized, in the x direction, and its electric field can be expressed as:

$$E_x = E_{x0} \sin(\omega t - \beta z). \tag{2.18}$$
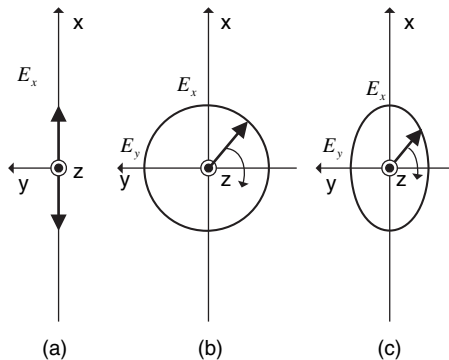
FIGURE 2.7. Polarization of a wave: (a) linear, (b) circular, and (c) elliptical.
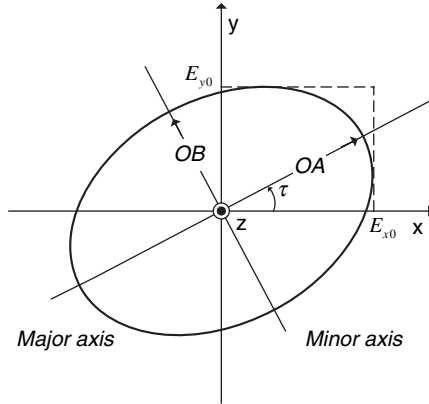
FIGURE 2.8. Polarization ellipse at $z = 0$ of an elliptically polarized electromagnetic wave.

In Figure 2.7(b) the wave has both a x and a y electric field component. If the two components E_x and E_y have the same magnitude, then the total (vector) electric-field rotates as a function of time with the tip of the vector forming a circular trace, and the wave is thus called circular polarized. Generally, the wave consists of two electric field components, E_x and E_y, of different amplitude ratios and relative phases that can yield an elliptically polarized wave, as shown in Figure 2.7(c). The polarization ellipse may have any orientation, which is determined by its tilt angle, as depicted in Figure 2.8. The ratio of the major to minor axes of the polarization ellipse is called the *axial ratio* (AR).

For any wave traveling in the positive z direction, the electric field components in the x and y directions can be written as:

$$E_x = E_{x0} \sin(\omega t - \beta z) \tag{2.19}$$
$$E_y = E_{y0} \sin(\omega t - \beta z + \delta) \tag{2.20}$$

where E_{x0} and E_{y0} are the amplitudes in x and y direction, respectively, and δ is the time-phase angle between them. By manipulating these two components we can show that [1,11]

$$\frac{E_x^2}{E_1^2} - \frac{2E_xE_y \cos \delta}{E_1E_2} + \frac{E_y^2}{E_2^2} = \sin^2 \delta. \tag{2.21}$$

Depending on the values of E_x, E_y, and δ, this equation can be expressed as the equation of an ellipse or of a circle.

The sense of rotation of a circularly or elliptically polarized wave plays an important role in a communication link. It is defined by the direction of rotation of the wave as it propagates towards or away from an observer along the direction of propagation. If, for example, a wave is moving away and its rotation is clockwise

then we say that the wave has a "clockwise" sense of rotation. The most common notation used today is that of the IEEE by which the sense of rotation is always determined observing the field rotation as the wave travels away from the observer. If the rotation is clockwise, the wave is *right-handed* or *clockwise circularly polarized* (RH or CW). If the rotation is counterclockwise, the wave is *left-handed* or *counterclockwise circularly polarized* (LH or CCW). The same applies to elliptically polarized waves.

The polarization state of an antenna is defined as the polarization state of the wave transmitted by the antenna. It is characterized by the sense of rotation and the spatial orientation of the ellipse, if it is elliptically polarized. If the receiving antenna has a polarization that is different from that of the incident wave, a *polarization mismatch* will occur. A polarization mismatch causes the receiving antenna to extract less power from the incident wave.

Polarization loss factor (PLF) is used as a figure of merit to measure the degree of polarization mismatch. It is defined as the square power of the cosine angle between the polarization states of the antenna in its transmitting mode and the incoming wave (see Fig. 2.9).

$$\text{PLF} = |\cos \gamma|^2$$

Generally, an antenna is designed for a desired polarization. The component of the electric field in the direction of the desired polarization is called the *co-polar component*, whereas the undesired polarization, usually taken in orthogonal direction to the desired one, is known as *cross-polar component*. The latter can be due to a change of polarization characteristics during the propagation of or scattering of waves that is known as *polarization rotation*.

An actual antenna does not completely discriminate against a cross-polarized wave due to structural abnormalities of the antenna. The directivity pattern obtained over the entire direction on a representative plane for cross-polarization with respect to the maximum directivity for the desired (co-polar) polarization is called *antenna cross-polarization discrimination* and plays an important factor in determining the antenna performance.
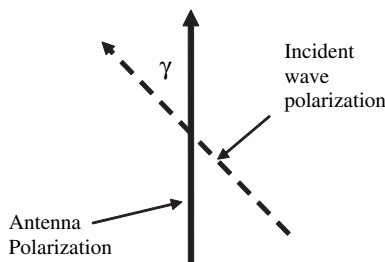
FIGURE 2.9. Definition of PLF.
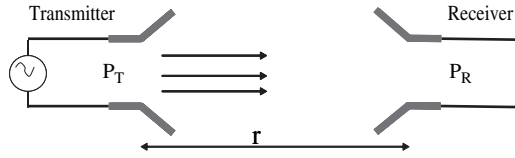
FIGURE 2.10. Transmitter and receiver antennas separated by range r.

2.6. TERMINAL ANTENNAS IN FREE SPACE

The equations in the previous section allow us to obtain a relation between the power at the transmitter and the power received at the receiver when both antennas are located in free space. This relation is called the *Friis transmission formula* [15]. For two antennas, shown in Figure 2.10, separated by a distance r, large enough so that we are in the far field of both antennas, we get:

The receiving antenna received a portion of the incident radiation, that is

$$P_R = A_R I_T \tag{2.22}$$

where I_T is the radiation intensity of the incident wave and A_R the effective area of the receiving antenna given by:

$$A_R = G_R \left(\frac{\lambda^2}{4\pi} \right). \tag{2.23}$$

Here, G_R is the gain of the receiving antenna, and $\left(\frac{\lambda^2}{4\pi} \right)$ is called the *free-space loss factor*. The received power can now be written as:

$$P_R = G_R \left(\frac{\lambda^2}{4\pi} \right) \frac{G_T}{4\pi r^2} P_T \tag{2.24}$$

with G_T being the gain of the transmitting antenna. If we also include polarization loss, then equation (2.24) becomes:

$$P_R = G_T \cdot G_R \left(\frac{\lambda}{4\pi r} \right)^2 P_T \cdot \text{PLF}. \tag{2.25}$$

This equation is called the Friis transmission formula, and it is very essential in designing a communication link between two antennas. Although this particular one is valid for free space only, we will later show how it can be adapted to take into account propagation conditions, other than free space.

2.7. ANTENNA TYPES

There is a large variety of antennas that are used in different branches of wireless communications. The simplest and most commonly used antennas are the *wire*

antennas that are used as *dipole*s, *loops*, or *helical* antennas. Another major antenna category is the *aperture* antennas that appear in the shape of *horns* or *reflectors*. Finally, *array* antennas are used extensively in communication as switched beam antennas or adaptive antennas. For more information on the design and analysis of antennas we refer the reader to several references [1–15], where all types of antennas, mentioned above, are fully described. Adaptive and multi-beam antennas will be studied in Chapter 9.

BIBLIOGRAPHY

[1] Balanis, C. A., *Antenna Theory: Analysis and Design*, 2nd ed., John Wiley & Sons, New York, 1997.

[2] Kraus, J. D., *Antennas*, 2nd ed., McGraw-Hill, New York, 1988.

[3] Chryssomallis, and C. G. Christodoulou, ''Antenna Radiation Patterns'' in *John Wiley Encyclopedia of Electrical and Electronics Engineering*, 2001.

[4] Drabowitch, S., A. Papiernik, H. Griffiths, J. Encinas, and B. L. Smith, *Modern Antennas*, Chapman & Hall, London, 1998.

[5] Kraus J. D. and R. Marhefka, *Antennas*, McGraw-Hill, New York, 2001.

[6] Stutzman W. L., and G. A. Thiele, *Antenna Theory and Design*, John Wiley and Sons, Inc., New York, 1981.

[7] Weeks, W. L., *Antenna Engineering*, McGraw-Hill, New York, 1968.

[8] Milligan, T. A., *Modern Antenna Design*, McGraw-Hill, New York, 1985.

[9] Johnson, R. C. (and H. Jasik, editor of first edition), *Antenna Engineering Handbook*, McGraw-Hill, New York, 1993.

[10] Lo, Y. T. and S. W. Lee (eds.), *Antenna Handbook: Theory, Applications and Design*, Van Nostrand Reinhold, New York, 1988.

[11] Siwiak, K., *Radiowave Propagation and Antennas for Personal Communications*, 2nd ed., Artech House, Boston-London, 1998.

[12] Vaughan, R., and J. Bach Andersen, *Channels, Propagation, and Antennas for Mobile Communications*, IEE, London, 2002.

[13] Bertoni, H. L., *Radio Propagation for Modern Wireless Systems*, Prentice Hall PTR, New Jersey, 2000.

[14] Saunders, S. R., *Antennas and Propagation for Wireless Communication Systems*, John Wiley & Sons, New York, 1999.

[15] Schelkunoff, S. A., and H. T. Friis, *Antenna Theory and Practice*, John Wiley & Sons, New York, 1952.

Fundamentals of Wave Propagation in Random Media

The subject of wave propagation through random media, terrestrial, atmospheric and ionospheric medium (e.g., plasma), has been investigated theoretically by many authors [1–30]. The problem of wave propagation through a random medium could be understood by using the statistical description of the wave field (electromagnetic and scalar) and quantum theory [31]. Because the problems of random equations are not tractable with standard mathematical tools, we must use some special methods such as Feynman's diagram method [1–4], the method of renormalization [5,7,22], etc.

The main goal of this chapter is to summarize the existing theoretical methods based on statistical and quantum theories and to explain how they can be applied in wave propagation solutions for future applications of radio communication problems.

In Section 3.1, we will briefly introduce the main equations and functions that describe stochastic processes in the random medium. In Section 3.2, we introduce the perturbation method [7,13,16–18,22] to describe the multi-scattering processes that a wave goes through by using Feynman's diagram procedure [1–4]. Here, we extend this method to non-Gaussian functions by means of a cluster expansion of the random refractive index. In Section 3.3, we introduce a one-dimensional random propagation equation having an exact solution, and already containing most features of the general theory. Section 3.4 describes a formal perturbation method and its approximations for a scalar wave equation with random refractive index, with or without time dependence. We also present several approximate procedures related to the perturbation method, such as Born's approximation [7,16–18,22], Keller's

expansion [14], Bourret's closure assumption [13], and Kraichnan's random coupling model [23]. In Section 3.5, we use a Taylor expansion [7,22] of the random refractive index, that is, we find the conditions under which it is possible to replace the random index by a mere random variable or a linear function with random coefficients. Section 3.6 describes the exact solution of the scalar wave equation through functional integration, and in Section 3.7, we introduce the vector electromagnetic wave equation with random index and harmonic time dependence. It is shown that at long wavelengths the effective phase velocity of electromagnetic waves increases because of the coupling between transverse and longitudinal waves. Section 3.8 describes wave propagation in a statistically inhomogeneous random medium. In Section 3.9, we describe more general propagation equations of plane waves in anisotropic random medium (namely, the ionospheric plasma, which is actually for problems of radiowave propagation in the ionosphere, see Chapter 7), the coupling between different wave modes and the subsequent energy transfer. It is shown that the energy transfer between different wave modes, for example, in a turbulent plasma, may be important even for weak random fluctuations of parameters, but it takes a very long time.

3.1. MAIN WAVE EQUATIONS AND RANDOM FUNCTIONS

A random medium is a medium whose parameters, such as pressure, density, temperature, and so forth are random functions of positon and time. This means that we are not describing the exact values of these parameters in the following section, but only the probability to find them between a given range of values at given intervals in space and time. A random medium can also be thought of as a collection of inhomogeneous media, each of which may be either continuous (turbulent medium) or discrete (medium with random inclusions). Next, we introduce the main equations that describe stochastic processes in a random medium.

3.1.1. Wave Equations

The propagation phenomena of linear waves in random medium is described by a linear differential equation with random coefficients. Let us consider a few examples.

A scalar wave equation can be presented in the following form:

$$\Delta \Psi(r,t) - \frac{n^2(r,t)}{c^2}\frac{\partial^2 \Psi(r,t)}{\partial t^2} = 0 \tag{3.1}$$

where $\Psi(r,t)$ is the wave field amplitude in the space and time domains, $n(r,t)$ is the refractive index, which is a random function of space (r) and time (t), and c is the wave velocity in free space.

A compact scalar wave equation with a source $g(r)$ can be presented as follows:

$$\Delta\Psi(r) - k^2 n^2(r)\Psi(r) = g(r). \tag{3.2}$$

Here, (3.2) is deduced from (3.1) assuming a harmonic time dependence $\sim\exp\{ickt\}\equiv\exp\{i\omega t\}$ and a time independent refractive index n, where $k = \frac{2\pi}{\lambda}$ is the wave number and λ is the wavelength. The source term $g(r)$ is assumed to be given and not randomised (e.g., deterministic). For mathematical convenience the wave number k is assumed to have a small positive imaginary part, which ensures that we are looking for the outgoing wave. Moreover, this imaginary part does not correspond to a decaying process and may be canceled after the correct solution has been found.

An Electromagnetic vector wave equation can be presented by the following form:

$$\Delta\mathbf{E}(r,t) - \nabla(\nabla\cdot\mathbf{E}(r,t)) - \frac{n^2(r,t)}{c^2}\frac{\partial^2\mathbf{E}(r,t)}{\partial t^2} = 0, \tag{3.3}$$

where $\mathbf{E}(r,t)$ is the vector presentation of electromagnetic field.

We shall always treat the refractive index as a time independent random function, which is equivalent to the assumption that the characteristic time of index fluctuations is much longer than the period of the propagating wave. The medium in such conditions will be taken statistically as homogeneous. This assumption excludes any medium where the turbulence is concentrated in a small volume of space. This restriction will be partially dropped in Section 3.9, where the scale of the inhomogeneity will be considered very large compared to the wavelength.

To conclude this subsection, let us show that the scalar wave Equation (3.1) and the reduced scalar wave Equation (3.2) may be treated simultaneously. Equation (3.1) corresponds to an initial value problem that is well known as the Cauchy problem and must be given as $\Psi(r,0)$ and $\frac{\partial\Psi(r,0)}{\partial t}$ in order to find $\Psi(r,t)$. Equation (3.2) corresponds to a radiation problem. Let us introduce the Laplace transform of the wave function $\Psi(r,t)$,

$$\Psi(r,q) = \int\limits_0^\infty \Psi(r,t)\cdot\exp\{i\cdot q\cdot t\}\cdot dt, \qquad \text{Im}(q) > 0. \tag{3.4}$$

It satisfies the following equation, which is the Laplace transform of (3.1):

$$\Delta\Psi(r,q) - \frac{q^2}{c^2}\cdot n^2(r)\cdot\Psi(r,q) = \frac{n^2(r)}{c^2}\left[i\cdot q\cdot\Psi(r,t=0) - \frac{\partial\Psi(r,t=0)}{\partial t}\right]. \tag{3.5}$$

Equations (3.5) and (3.2) are identical if one takes

$$q = c \cdot k, \quad \Psi(r, t = 0) = 0, \quad \frac{\partial \Psi(r, t = 0)}{\partial t} = -\frac{c^2}{n^2(r)} g(r). \quad (3.6)$$

We shall always choose these initial conditions for Equation (3.1) and treat (3.1) and (3.2) simultaneously, interchanging q and $c \cdot k$, whenever necessary.

3.1.2. Random Functions and Their Moments

A detailed treatment of stochastic processes may be found in [14–16]. By introducing any finite number of points $r_1, r_2, \ldots, r_n$, we assume that the mean value of random functions $\mu(r_1) \cdot \mu(r_2) \cdot \ldots \cdot \mu(r_n)$ always exists. A moment of order n for a random function is given by:

$$\langle \mu(r_1) \cdot \mu(r_2) \cdot \ldots \cdot \mu(r_n) \rangle = \int_{\Omega} \mu(r_1) \cdot \mu(r_2) \cdot \ldots \cdot \mu(r_n) \cdot P(d\omega). \quad (3.7)$$

A random function is often characterized by the infinite set of all its moments [16,24,25]. The random function $\mu(r)$ is centered if

$$\langle \mu(r) \rangle = 0 \quad (3.8)$$

This function is *stationary* if the joint distribution of any finite number of random variables $\mu(r_1) \cdot \mu(r_2) \cdot \ldots \cdot \mu(r_n)$ is invariant with respect to any simultaneous transfer of its arguments. For a space-dependent random function, it would perhaps be better to call it a *stationary homogeneous* random function (e.g., homogeneous turbulence [16]). If the random function is also real valued, the second order moment

$$\Gamma(r_1, r_2) = \langle \mu(r_1) \cdot \mu(r_2) \rangle \quad (3.9)$$

is called the covariance function.

   If the random function $\mu(r)$ is stationary, the covariance function $\Gamma(r)$ is only a function of $r = (r_1 - r_2)$, that is,

$$\Gamma(r_1, r_2) = \Gamma(r_1 - r_2). \quad (3.10)$$

The function $\Gamma(r)$ has a Fourier transform, which is a positive measure $\Gamma(k)$, called the *spectral measure* of the stationary random function, or *spectral density* function if it reduces to an ordinary function of wave number k. It is sometimes necessary to assume the existence of mean square derivatives of the random function $\mu(r)$ up to a given order; this subject will be discussed in Section 3.5.

Gaussian Random Function. A random function $\mu(r)$ is called Gaussian if the joint distribution of any finite number of random variables $\mu(r_1) \cdot \mu(r_2) \cdot \ldots \cdot \mu(r_n)$ is Gaussian [25]. This function is of great theoretical interest and has many practical applications, especially because of the following property:

> Any scalar linear functional of a Gaussian random function is a Gaussian random variable.

Furthermore, we note the important property of the moments of a *centered Gaussian random function*

$$\langle \mu(r_1) \cdot \mu(r_2) \cdots \mu(r_{2n+1}) \rangle = 0 \tag{3.11a}$$

$$\langle \mu(r_1) \cdot \mu(r_2) \cdots \mu(r_{2n}) \rangle = \underbrace{\sum \langle \mu(r_i) \cdot \mu(r_j) \rangle \langle \mu(r_k) \cdot \mu(r_m) \rangle \cdots}_{p \text{ factors}} \tag{3.11b}$$

Here the summation extends over all $\frac{(2 \cdot n)!}{2^n \cdot n!}$ partitions of $r_1 \ldots r_{2n}$ into pairs. For example, for $n = 2$ one can easily obtain from (3.11b)

$$\begin{aligned} \langle \mu(r_1) \cdot \mu(r_2) \cdot \mu(r_3) \cdot \mu(r_4) \rangle &= \langle \mu(r_1) \cdot \mu(r_2) \rangle \cdot \langle \mu(r_3) \cdot \mu(r_4) \rangle \\ &+ \langle \mu(r_1) \cdot \mu(r_3) \rangle \cdot \langle \mu(r_2) \cdot \mu(r_4) \rangle + \langle \mu(r_1) \cdot \mu(r_4) \rangle \cdot \langle \mu(r_2) \cdot \mu(r_3) \rangle. \end{aligned} \tag{3.12}$$

Fourier Transform (FT) of Stationary Random Functions. Let us consider random valued measures as the FT of stationary random functions. A stationary random function on real line, $\mu(\kappa, \omega)$, with continuous covariance function has a spectral representation of

$$\mu(\kappa, \omega) = \int\limits_{-\infty}^{\infty} dZ(k, \omega) \exp\{ik\kappa\}. \tag{3.13}$$

Here $Z(k, \omega)$ is a random function with orthogonal increments. This means that whenever the parameter values satisfy the following conditions [31]

$$\begin{aligned} &k_1 < k_2 \leq k_3 < k_4 \\ &\langle [Z(k_2) - Z(k_1)][Z(k_4) - Z(k_3)] \rangle = 0. \end{aligned} \tag{3.14}$$

The integral in (3.13) is a Stieltjes integral [1–4,7,16]. With this definition the Fourier transform of a stationary random function does not appear as another random function but as some *derivative* of a random function with orthogonal increments. The integral presentation of (3.13) can be generalized for the case of a three dimensional (3D) random function.

The Cluster Expansion of the Centered Random Function and Its FT. If the random function $\mu(r)$ is centered its covariance is also its two-point correlation

function, but this is not true for higher moments. As was shown in [1–4], the n-point correlation functions are not simultaneously correlated. We introduce therefore the correlation functions $h(r_1, r_2), h(r_1, r_2, r_3), \ldots, h(r_1, r_2, \ldots, r_p)$ through the following cluster expansions:

$$
\begin{aligned}
\langle \mu(r_1)\mu(r_2) \rangle &= h(r_1, r_2) \\
\langle \mu(r_1)\mu(r_2)\mu(r_3) \rangle &= h(r_1, r_2, r_3) \\
\langle \mu(r_1)\mu(r_2)\mu(r_3)\mu(r_4) \rangle &= h(r_1, r_2)h(r_3, r_4) + h(r_1, r_3)h(r_2, r_4) \\
&\quad + h(r_1, r_4)h(r_2, r_3) + h(r_1, r_2, r_3, r_4) \\
\langle \mu(r_1) \cdot \mu(r_2) \cdots \mu(r_p) \rangle &= \sum h(r_{i_1}, \ldots, r_{i_k})h(r_{j_1}, \ldots, r_{j_m})h(r_{l_1}, \ldots, r_{l_n}) \cdots
\end{aligned}
\tag{3.15}
$$

where the summation is extended over all parameters of the set $1, 2, \ldots, p$ into clusters of at least two points according to (3.11b). From (3.11) it follows that for a centered Gaussian random function, all correlation functions except the second order one vanish.

A graphic representation in terms of Mayer diagrams described in [1–4] may be helpful. The correlation function $h(r_1, r_2, \ldots, r_p)$ is represented by a set of p points connected by p lines:

$$
h(r_1, r_2) = \quad \quad h(r_1, r_2, r_3) = \quad \ldots\ldots\ldots
\tag{3.16}
$$

The cluster expansion is then written graphically. For example

$$
\langle \mu(r_1)\mu(r_2)\mu(r_3)\mu(r_4) \rangle = \quad + \quad + \quad + \quad .
\tag{3.17}
$$

This definition of correlation functions ensures that they vanish if the points $r_1, r_2, \ldots, r_p$ are not inside a common sphere of radius ℓ (see proof in [1–4]). We also need the FT of the correlation function as mentioned below:

$$
h(k_1, k_2, \ldots, k_p) = \frac{1}{(2\pi)^{3p}} \int h(r_1, r_2, \ldots, r_p) \exp\{-i(k_1 r_1 + \ldots + k_p r_p)\} d^3 r_1 \cdots d^3 r_p
\tag{3.18}
$$

If the random function $\mu(r)$ is stationary, this is not a function but a measure concentrated in the hyperplane $k_1 + k_2 + \ldots + k_p = 0$. Hence we write

$$
h(k_1, k_2, \ldots, k_p) = g(k_1, k_2, \ldots, k_p) \cdot \delta(k_1 + k_2 + \ldots + k_p)
\tag{3.19}
$$

and call the ordinary functions $g(k_1, k_2, \ldots, k_p)$ or simply the correlation functions in k-space. Using these functions, we can write the cluster expansion of the moments in k-space as

$$
\begin{aligned}
\langle \mu(k_1)\mu(k_2) \rangle &= g(k_1, k_2) \cdot \delta(k_1 + k_2) \\
\langle \mu(k_1)\mu(k_2)\mu(k_3) \rangle &= g(k_1, k_2, k_3) \cdot \delta(k_1 + k_2 + k_3) \\
\langle \mu(k_1)\mu(k_2)\mu(k_3)\mu(k_4) \rangle &= g(k_1, k_2) \cdot g(k_3, k_4) \cdot \delta(k_1 + k_2) \cdot \delta(k_3 + k_4) + \ldots
\end{aligned}
\tag{3.20}
$$

The moment $\langle \mu(k_1)\mu(k_2) \ldots \mu(k_p) \rangle$ is thus not only concentrated in the hyperplane $k_1 + k_2 + \ldots + k_p = 0$, but it appears as sums of products of terms that are concentrated in a hyperplane of lower dimensions.

3.1.3. Random Equations

A random equation such as

$$
\Delta \Psi(r) - k^2 n^2(r) \Psi(r) = g(r)
\tag{3.21}
$$

describes linear waves and does not constitute a linear problem because the mean solutions do not satisfy the mean equation. This is because

$$
\langle n^2(r)\Psi(r) \rangle \neq \langle n^2(r) \rangle \langle \Psi(r) \rangle.
\tag{3.22}
$$

In other words, the wave function and the refractive index are not statistically independent. If we try to evaluate $\langle n^2(r)\Psi(r) \rangle$, we must multiply (3.21) by $n^2(r)$ and average afterwards; this will yield the form $\sim \langle n^2(r_1)n^2(r)\Psi(r) \rangle$, and so on.

Keller [14] has obtained an equation for a functional generating the entire set of moments. This equation helps with new approximation procedures, but does not solve the problem. The fact that even the lowest order moment of the wave function $\langle \Psi(r) \rangle$ depends upon the infinite set of moments of the refractive index that seems to make the problem hopelessly difficult. However, it happens that in certain limiting cases, one may obtain solutions which do not depend upon the entire set of moments of the refractive index.

Therefore, the perturbation method described in Section 3.2 gives the Bourret's equation, which depends only on the mean value and the covariance of the refractive index. It is only valid for wavelengths that are longer compared to the range of index correlations. Conversely, for the random Taylor expansion (see Section 3.5), we need only the probability distribution of the refractive index and some of its derivatives at one fixed point. It is valid for wavelengths that are very short compared to the range of index correlations.

Another case of great interest is when $n^2(r)$ is a Gaussian random function. It is then possible to get an exact solution of (3.21) through functional integration, which gives all the moments of the wave functions in terms of a mean value and the

covariance of $n^2(r)$ (see Section 3.6). Unfortunately, this method cannot be generalized to other equations such as the electromagnetic wave equation of (3.3). Finally, it must be noted that no rigorous mathematical treatment of (3.21) has been presented till now. This is mainly because we are not able to solve linear partial differential equations with non-constant (e.g., variable) coefficients.

3.2. THE PERTURBATION METHOD FOR MULTIPLE SCATTERING

The multiple scattering perturbation method is a general method for studying propagation equations with linear coefficients. It has been first introduced by Bourret [13] and Furutsu [5,7,22], and studied later by Tatarskii et al. [16–18]. It is not a rigorous method and cannot be made rigorous because it relies on the use of a divergent series (see Section 3.4). Divergent series, however, have been used successfully, both in quantum field theory and in nonequilibrium statistical mechanics. Our aim is to show that the perturbation method and especially Bourret's approximation can be used to find uniform approximation of the mean wave function, when the wavelength is long compared to the range of index correlation. In this section, this will be proved rigorously for a one dimensional (1D) model that has an exact solution. It will also be justified for the scalar wave equation, using the method of extraction of the most divergent terms (terms which increase as some power t or R), and n-dimensional analysis of all perturbation terms. Such a method has been used previously by Ishimaru [24] in radio propagation, and by Balescu [25] in non equilibrium statistical mechanics. Here, to make things simple, we shall only consider the scalar wave equation

$$\Delta \Psi(r,t) - \frac{n^2(r)}{c^2}\frac{\partial^2 \Psi(r,t)}{\partial t^2} = 0 \tag{3.23}$$

together with the initial conditions

$$\Psi(r,0) = 0, \qquad \frac{\partial \Psi}{\partial t} = -\frac{c^2}{n^2(r)}j(r). \tag{3.24}$$

In Section 3.1, it was shown that this problem is equivalent to the random variable problem described by formula (3.2). We shall make the assumption that the refractive index $n(r)$ is a stationary random function of position and is time independent. The assumption of strict stationarity (i.e., not only for the two first moments) is essential. We separate now the constant mean value of $n^2(r)$ and its random part.

$$n^2(r) = \langle n^2(r)\rangle[1 + \varepsilon \cdot \mu(r)]$$
$$\langle \mu(r)\rangle = 0 \tag{3.25}$$

Here ε is a dimensionless small positive parameter characterizing the relative strength of index fluctuations. Equation (3.23) can now be rewritten as

$$\Delta \Psi(r,t) - \frac{1}{c^2}[1 + \varepsilon \cdot \mu(r)]\frac{\partial^2 \Psi(r,t)}{\partial t^2} = 0 \tag{3.26}$$

where $\langle n^2(r)\rangle$ has been incorporated into $\frac{1}{c^2}$.

The stationary random function is written in terms of its FT and $\mu(r)$, which is a random valued measure

$$\mu(r) = \int \exp\{ik \cdot r\}\mu(k)d^3k. \tag{3.27}$$

The Laplace transformation (LT) of (3.23), taking into account the initial conditions in (3.24) is:

$$\Delta \Psi(r,z) + \frac{z^2}{c^2}[1 + \varepsilon \mu(r)]\Psi(r,z) = j(r). \tag{3.28}$$

The FT of this equation is

$$\left[-k^2 + \frac{z^2}{c^2}\right]\Psi(k,z) + \frac{\varepsilon z^2}{c^2}\int \mu(k - k')\Psi(k',z)d^3k' = j(k). \tag{3.29}$$

Equations (3.28) and (3.29) are both of the type

$$(L_0 + \varepsilon L_1)\Psi = j \tag{3.30}$$

where L_0 is a non random operator whose inverse $G^{(0)} = L_0^{-1}$, called the unperturbed propagator (or unperturbed Green's function), is known, and L_1 is a random operator. In r-domain

$$L_0 = \Delta + \frac{z^2}{c^2}, \qquad G^{(0)}(r,r';z) = \frac{\exp\{iz|r - r'|\}}{-4\pi|r - r'|}, \qquad L_1 = \frac{z^2}{c^2}\mu(r) \tag{3.31}$$

acting as an integral convolution operator. In k-domain

$$L_0 = -k^2 + \frac{z^2}{c^2}, \qquad G^{(0)}(k;z) = \frac{c^2}{z^2 - c^2 k^2}, \qquad L_1 = \frac{z^2}{c^2}\mu(k - k') \tag{3.32}$$

acting as an integral convolution operator.

In r-domain L_1 is diagonal operator and L_0 is not; it is the converse in k-domain. The solution of (3.30) is now formally expanded in powers of ε yielding

$$\Psi = (L_0 + \varepsilon L_1)^{-1}j = L_0^{-1}j - \varepsilon L_0^{-1}L_1 L_0^{-1}j + \varepsilon^2 L_0^{-1}L_1 L_0^{-1}L_1 L_0^{-1}j + \dots \tag{3.33}$$

$(L_0 + \varepsilon L_1)^{-1} = G$ is called the *perturbed propagator* (or perturbed Green's function).

Let us represent the perturbation series for G with the aid of diagrams, which will be called *bare* diagrams to discriminate between them and other drossed diagrams to be introduced afterwards. We make the following conventions:

a) The unperturbed propagator $G^{(0)}(r, r')$ is represented by a solid line $\overline{r\,r'}$;
b) The random operator $-\varepsilon L_1$ is represented by a dot $\bullet$;
c) Operators act to the right.

If so, we may write

$$\mathrm{G} = \underline{\quad} + \underline{\quad\bullet\quad} + \underline{\quad\bullet\quad\bullet\quad} + \underline{\quad\bullet\quad\bullet\quad\bullet\quad} + \dots \qquad (3.34)$$

Let us write down explicitly a few terms of the perturbation series in r-domain

$$G(r,r';z) = G^{(0)}(r,r';z) - \varepsilon \frac{z^2}{c^2} \int G^{(0)}(r,r_1;z)\mu(r_1)G^{(0)}(r_1,r';z)d^3r_1$$

$$+ \varepsilon^2 \frac{z^4}{c^4} \iint G^{(0)}(r,r_2;z)\mu(r_2)G^{(0)}(r_2,r_1;z)\mu(r_1)G^{(0)}(r_1,r';z)d^3r_1 d^3r_2 \quad (3.35)$$

and in k-domain

$$G(k,k';z) = G^{(0)}(k;z)\delta(k-k') - \varepsilon \frac{z^2}{c^2} G^{(0)}(k;z)\mu(k-k')G^{(0)}(k';z)$$

$$+ \varepsilon^2 \frac{z^4}{c^4} \int G^{(0)}(k;z)\mu(k-k_1)G^{(0)}(k_1;z)\mu(k_1-k')G^{(0)}(k';z)d^3k_1 \quad (3.36)$$

where $\delta(k-k')$ is Dirac's measure.

In order to help the interpretation of bare diagrams, it is sometimes useful to introduce subscripts under certain elements:

$$G(r,r';z) = \underset{r \quad r'}{\underline{\quad}} + \underset{r \quad r_1 \quad r'}{\underline{\quad\bullet\quad}} + \underset{r \quad r_2 \quad r_1 \quad r'}{\underline{\quad\bullet\quad\bullet\quad}} + \dots\dots$$

$$(3.37)$$

$$G(k,k';z) = \underset{k \quad k'}{\underline{\quad}} + \underset{k \quad k_1 \quad k'}{\underline{\quad\bullet\quad}} + \underset{k \quad k_2 \quad k_1 \quad k'}{\underline{\quad\bullet\quad\bullet\quad}} + \dots\dots$$

If so, the dashed curve will connect the concrete points for which $\mu(r_1)$ and $\mu(r_2)$ (or $\mu(k - k_1)$ and $\mu(k_1 - k')$) are inside the integrals, that is,

$$\mu(r_1)\mu(r_2) \sim \underset{r_2 \quad r_1}{\bullet\!-\!-\!\bullet} \qquad (3.38)$$

or

$$\mu(k - k_1)\mu(k_1 - k') \sim \bullet\!-\!-\!-\!\bullet\,. \tag{3.39}$$
$$k_1$$

We now give the physical interpretation of the perturbation expansion. The r-space diagrams correspond to multiple scattering of the wave at points $r_1, r_2, \ldots, r_N$. The k-space diagrams correspond to multiple interactions between Fourier components of the wave and of the random inhomogeneities; at each vortex of a diagram a Fourier component k_p of the wave function interacts with a Fourier component $(k_{p+1} - k_p)$ of the random inhomogeneities, giving, as a result, a Fourier component $k_{p+1} \equiv k_{p+1} - k_p + k_p$ of the wave function. Both viewpoints are useful; the first one, particularly for single or double scattering and the second one for multiple scattering because of the wave vector conservation conditions.

In future description, we also need the expansion of the perturbed double propagator $G \otimes G^*$, that is, the tensor product of the perturbed propagator and its complex conjugate. In r-space

$$G \otimes G^* = G(r, r'; z)G^*(r_1, r_1'; z'). \tag{3.40a}$$

In k-space

$$G \otimes G^* = G(k, k'; z)G^*(k_1, k_1'; z'). \tag{3.40b}$$

This expansion can also be written in terms of diagrams:

$$\mathbf{G} \otimes \mathbf{G}^* = \quad \overline{} \quad + \quad \overline{\bullet} \quad + \quad \overline{} \quad + \quad \overline{\bullet} \quad + \quad \overline{\bullet\bullet} \quad + \cdots \tag{3.41}$$

If we make the convention that operators of the lower line are the complex conjugate of the usual ones, for example,

$$\overset{\displaystyle k \quad \overset{\bullet}{} \quad k'}{\underset{k_1 \quad \underset{\bullet}{} \quad k_1'}{}} = \varepsilon^2 \frac{z^2 z'^2}{c^r} G^{(0)}(k; z)\mu(k - k')G^{(0)}(k'; z)G^{(0)^*}(k_1; z')\mu^*(k_1 - k_1')G^{(0)^*}(k_1'; z')$$

$$\tag{3.42}$$

we can present the mean perturbed propagator as in [31].

The Mean Perturbed Propagator

Let us produce this propagator first in r-domain. We take the mean value of (3.34) in the following manner [31]

$$\langle G(r, r'; z)\rangle = \left\langle \overline{\underset{r \quad \quad r'}{}} \right\rangle + \left\langle \overline{\underset{r \quad r_1 \quad r'}{\bullet}} \right\rangle + \left\langle \overline{\underset{r \quad r_2 \quad r_1 \quad r'}{\bullet\bullet}} \right\rangle + \cdots . \tag{3.43}$$

Higher order diagrams contain moments of $\mu(r)$ such as $\langle\mu(r_1)\mu(r_2)\cdot\ldots\cdot\mu(r_p)\rangle$, which must be calculated before integration over $r_1, r_2, \ldots, r_p$, is performed.

To every partition we associate a dressed diagram constructed from the bare perturbation diagrams (the full procedure is described in [31]).

We can write down all diagrams up to the fourth order of perturbation

$$(3.44)$$

Such diagrams are called *Feynman diagrams* [1–4,7]. For random equations, they have been introduced by Bourret [13] in the case of Gaussian stochastic process, where only two point clusters are needed. If we want to write down explicitly the contribution of any diagram, we first write the multiple integral with $\mu(r_1)\cdot\mu(r_2)\cdot\ldots\cdot\mu(r_p)$ for the corresponding bare diagram, then replace $\langle\mu(r_1)\cdot\mu(r_2)\cdot\ldots\cdot\mu(r_p)\rangle$ by the product of the correlation functions corresponding to the clusters that appear in the diagram, and finally perform the integration over $r_1, r_2, \ldots, r_p$. For example in r-domain

$$= \varepsilon^4 \frac{z^8}{c^8} \int G^{(0)}(r, r_4)\mu(r_4)G^{(0)}(r_4, r_3)\mu(r_3)G^{(0)}(r_3, r_2)$$

$$\times \mu(r_2)G^{(0)}(r_2, r_1)\mu(r_1)G^{(0)}(r_1, r')d^3r_1 d^3r_2 d^3r_3 d^3r_4$$

$$(3.45a)$$

which accordingly to the above, shows:

$$= \varepsilon^4 \frac{z^8}{c^8} \int G^{(0)}(r, r_4)G^{(0)}(r_4, r_3)G^{(0)}(r_3, r_2)G^{(0)}(r_2, r_1)$$

$$\times G^{(0)}(r_1, r')h(r_1, r_2)h(r_3, r_4)d^3r_1 d^3r_2 d^3r_3 d^3r_4 \qquad (3.45b)$$

The same diagrams can be constructed in k-domain because the cluster expansion is valid in both spaces. It is preferable to express the FT of a correlation function that is singular, as a product of the original function and a δ-measure:

$$h(k_1, k_2, \ldots, k_p) = g(k_1, k_2, \ldots, k_p)\delta(k_1 + k_2 + \ldots + k_p). \qquad (3.46)$$

If we want to calculate a diagram in k-domain we first write the multiple integral with $\mu(k - k_p)\mu(k_p - k_{p-1})\cdot\ldots$ for the corresponding bare diagram, then replace $\langle\mu(k - k_p)\cdot\ldots\cdot\mu(k_1 - k')\rangle$ by the product of k-domain correlation functions and δ-measures corresponding to the clusters which appear in the diagram, and finally

perform in the integration over $k_1, k_2, \ldots, k_p$. For example

$$\overline{\underset{k\ \ k_3\ \ k_2\ \ k_1\ \ k'}{\bullet\!-\!\bullet\!-\!\bullet\!-\!\bullet\!-\!\bullet}} = \varepsilon^4 \frac{z^8}{c^8} \int G^{(0)}(k)\mu(k-k_3)G^{(0)}(k_3)\mu(k_3-k_2)G^{(0)}(k_2)$$
$$\times \mu(k_2-k_1)G^{(0)}(k_1)\mu(k_1-k')G^{(0)}(k')d^3k_1 d^3k_2 d^3k_3 \quad (3.47a)$$

or

$$\overline{\underset{}{\frown\ \frown}} = \varepsilon^4 \frac{z^8}{c^8} \int G^{(0)}(k)G^{(0)}(k_3)G^{(0)}(k_2)G^{(0)}(k_1)G^{(0)}(k')g(k-k_3,k_3-k_2)$$
$$\times g(k_2-k_1,k_1-k')\delta(k-k_2)\delta(k_2-k')d^3k_1 d^3k_2 d^3k_3. \quad (3.47b)$$

The vector differences $k_1 - k'$, $k_2 - k_1, \ldots$ and so forth, that appear as arguments of correlation functions, are called *transition vectors*. The wave vector conservation condition $k_1 + k_2 + \ldots + k_p = 0$ states that the sum of the transition vectors of a given cluster is zero. An immediate consequence of this is that any diagram has the same wave vector at both ends. In other words, the mean perturbed propagator is a diagonal operator in k-domain. It will be noted as $\langle G(k;z)\rangle$.

The Mean Double Propagator

If we assume the random function to be real, then the extension of the diagram technique to the mean double propagator is straightforward in r-space. To any bare double diagram, we associate as many dressed double diagrams as there are partitions of the whole set of upper and lower points into clusters, for example:
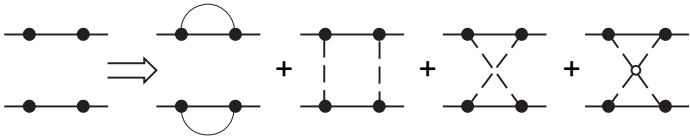
The explicit calculation of a diagram is performed exactly as for the mean propagator, remembering that operators in the lower lines are complex conjugate of the usual ones.

In k-space the situation is somewhat different, because the FT of a real function is not real but enjoys the property $f^*(k) = f(-k)$. When we calculate a diagram in k-domain, we must replace transition vectors appearing in the lower line by their opposite in the correlation functions. For example,

$$\overline{\underset{k_1\ \ \ k_1'}{\underset{\bullet\ \ \ \ \bullet}{\boxed{k\ \vdots\ k'}}}} = \varepsilon^2 \frac{z^2 z'^2}{c^4} G^{(0)}(k';z)G^{(0)}(k;z)G^{*(0)}(k_1';z')G^{*(0)}(k_1;z')$$
$$\times g(k-k',k_1'-k_1)\delta(k-k'+k_1'-k_1). \quad (3.48)$$

A consequence of the wave vector conservation condition is that the difference of the wave vectors appearing to the right and to the left of any double diagram is the same. If we take them as equal we obtain the following result: The mean spectral energy propagator $\langle |G(k, k'; z)|^2 \rangle$ satisfies a separate equation.

Mass Operator and Dyson Equation

Feynman diagram (single or double) is said to be unconnected if it can be cut into two or more diagrams, without cutting any dotted lines. The following diagrams are connected:
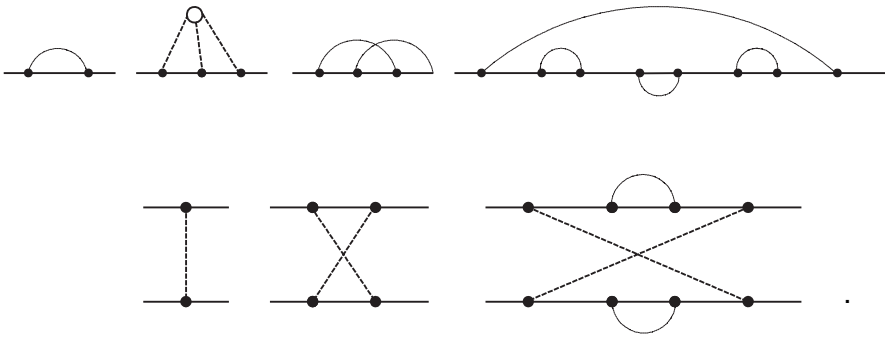
The following are unconnected (we give a possible cut),
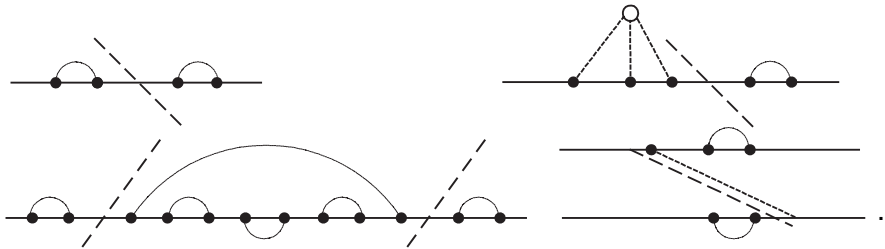
The strong lines at the end of a diagram are called its *terminals*. We can write any unconnected diagram as a product of connected diagrams without terminals and strong lines. The decomposition is unique for the single propagator, for example:
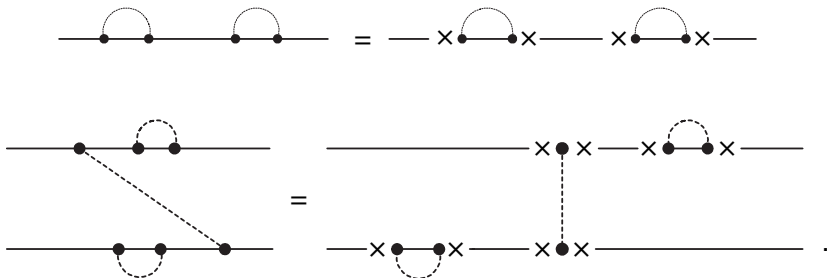
We now define the mass operator M as the sum of all connected diagrams without the terminals contributing to the single propagator:

$$(3.49)$$

In k-space M is a diagonal operator $M(k; z)$; in r-space, it is an integral convolution operator $M(r, r'; z)$. It is useful to introduce two new symbols for the mean perturbed propagator and the mass operator

Using the decomposition of unconnected diagrams into products of connected ones, the following expansion is easily derived:

This is formally equivalent to an equation called the Dyson equation in quantum field theory:

If $M(k; z)$ is known, then it is an ordinary equation for $\langle G(k; z)\rangle$ in k-space; solving it, we get

$$\langle G(k; z)\rangle = \frac{G^{(0)}(k; z)}{1 - G^{(0)}(k; z)M(k; z)}.$$

$$(3.50)$$

In order to find the double propagator counter part of the Dyson equation, we define the operator $\boxtimes$ as the sum of all connected double diagrams without the terminals. Using this operator the following expansion is derived for the mean double propagator [7]:

$$(3.51)$$

Equation (3.51) is formally equivalent to an equation sometimes called the [Bethe–Salpeter equation [22]:

$$\left\langle G \otimes G^* \right\rangle = \overline{\underline{}} + \overline{\underline{}}\boxtimes \left\langle G \otimes G^* \right\rangle . \tag{3.52}$$

If the mean perturbed propagator and the operator $\boxtimes$ are known, then it is an integral equation for the mean double propagator.

Before we show how to use all this perturbation formalism to get approximate solutions for the mean propagator and double propagator, we first study the one-dimensional (1D) random equation, which has an exact solution. It will help us outline what types of approximations are acceptable and what are not.

3.3. AN EXACT SOLUTION OF 1D-EQUATION

In this section, we study the one-dimensional equation:

$$\frac{\partial \Psi(x,t)}{\partial x} + \frac{1}{c}[1 + \varepsilon\mu(x)]\frac{\partial \Psi(x,t)}{\partial t} = 0 \tag{3.53}$$

where $\mu(x)$ is a real, centered, and stationary Gaussian random function with covariance function

$$\Gamma(x,x') = \langle \mu(x)\mu(x') \rangle \tag{3.54}$$

and the associated radiation problem

$$\frac{\partial \Psi(x)}{\partial x} - ik_0[1 + \varepsilon\mu(x)]\Psi(x) = \delta(x) \tag{3.55}$$

where $\delta(x)$ is Dirac's distribution at the origin. The wave number $k_0 = 2\pi/\lambda = 2\pi f/c$ is taken positive. Equations (3.53) and (3.55) can be treated simultaneously if we take the initial conditions

$$\Psi(x,0) = \frac{\delta(x)}{[1 + \varepsilon\mu(x)]} . \tag{3.56}$$

The LT of (3.53) and (3.55) are then identical by introducing z and ck_0.

The underlying physical problem is the following: The monochromatic source of frequency $\omega = 2\pi f = ck_0$ is radiating into a semi-infinite one-dimensional medium whose refractive index is $n(x) = 1 + \varepsilon\mu(x)$. Only propagation toward

$(x > 0)$ is considered; reflections are assumed to be negligible. Integration of (3.55) gives

$$\Psi(x) = Y(x)\exp[ik_0 x]\exp\left\{ik_0\int_0^x \varepsilon\mu(y)dy\right\} \tag{3.57}$$

where $Y(x)$ being Heaviside's step function [12].

To calculate now the mean value of the (3.57), the only random term is the second potential. For fixed x, $\int_0^x \varepsilon\mu(y)dy$ being a linear functional of the centered Gaussian random function $\mu(x)$, is a centered Gaussian random variable φ. If so, $\langle e^{ik_0\varphi}\rangle$ is the characteristic function of this random variable. As φ is Gaussian, that is,

$$\langle e^{ik_0\varphi}\rangle = e^{\frac{1}{2}k_0^2\langle\varphi^2\rangle} \tag{3.58}$$

we can evaluate now

$$\langle\varphi^2\rangle = \left\langle \varepsilon^2 \left|\int_0^x \mu(y)dy\right|^2\right\rangle = \varepsilon^2\int_0^x dy\int_0^y \Gamma(y-y')dy' \tag{3.59}$$

and finaly obtain [31]

$$\langle\Psi(x)\rangle = Y(x)\exp[ik_0 x]\exp\left\{-\frac{1}{2}k_0^2\varepsilon^2\int_0^x dy\int_0^y \Gamma(y-y')dy'\right\}. \tag{3.60}$$

The mean wave function is thus expressed in terms of the covariance function of the refractive index. Higher order moments such as $\langle\Psi(x)\Psi(x')\rangle$ are easily obtained, using the characteristic function of a multivariant Gaussian distribution [16]. We now introduce the covariance function

$$\Gamma(x-x') = \exp\left\{-\left|\frac{x-x'}{\ell}\right|\right\} \tag{3.61}$$

where ℓ is the range of index correlation. The mean wave function can now be calculated as:

$$\langle\Psi(x)\rangle = Y(x)\exp[ik_0 x]\exp\left\{-\varepsilon^2 k_0^2\ell^2\left(\frac{x}{\ell} + e^{-\frac{x}{\ell}} - 1\right)\right\}. \tag{3.62}$$

The dimensionless parameter which determines the behavior of the solution is $\varepsilon k_0 \ell$. There are two interesting limiting approximations:

a) $\varepsilon k_0 \ell \ll 1$. It is a long wavelength approximation ($\lambda \gg \ell$) and corresponds to weak interactions in quantum field theory. A uniform approximation for $\langle \Psi(x) \rangle$ is then

$$\langle \Psi(x) \rangle = Y(x) \exp[ik_0 x] \exp\{-\varepsilon^2 k_0^2 \ell x\}. \tag{3.63}$$

As follows from (3.63), the initial excitation is damped with an extinction length

$$x_{ex} = (\varepsilon^2 k_0^2 \ell)^{-1}. \tag{3.64}$$

Let us compare x_{ex} and the wavelength $\lambda \sim (k_0)^{-1}$

$$\frac{x_{ex}}{\lambda} \sim \frac{1}{\varepsilon^2 k_0 \ell} = \frac{1}{\varepsilon} \cdot \frac{1}{\varepsilon k_0 \ell} \gg 1. \tag{3.65}$$

The decaying is thus very slow; it is due to phase mixing and is not related to any dissipative mechanism. The mean wave function $\langle \Psi(x) \rangle$ can also be written as

$$\langle \Psi(x) \rangle = Y(x) \exp\{i(k_0 - i\varepsilon^2 k_0^2 \ell)x\}. \tag{3.66}$$

The effect of randomness on the mean wave function, as follows from (3.66), is simply a renormalization of the wave number. The renormalized wave number is now equal to $k = k_0 - i\varepsilon^2 k_0^2 \ell$, which has a small imaginary part (because $\varepsilon k_0 \ell \ll 1$). In the next section, we shall obtain this wave approximation as a sum of an infinite series extracted from the perturbation expansion of the mean propagator.

b) $\varepsilon k_0 \ell \gg 1$. It is a short wavelength approximation ($\lambda \ll \ell$) corresponding to strong interactions in quantum field theory. A uniform approximation for $\langle \Psi(x) \rangle$ is then

$$\langle \Psi(x) \rangle = Y(x) \exp[ik_0 x] \exp\left\{-\frac{1}{2}\varepsilon^2 k_0^2 x^2\right\}. \tag{3.67}$$

The initial excitation is damped again, with an extinction length $x_{ex} = (\varepsilon k_0)^{-1} \sim \lambda/\varepsilon$; the damping decay is more rapid than in the preceding case. This approximation is equivalent to a renormalization of the wave number because x^2 appears in the second exponent in (3.67).

Next we need the FT of the exact mean function (3.62)

$$\langle \Psi(k) \rangle = \int_{-\infty}^{\infty} \exp(-ik_0 x)\langle \Psi(x) \rangle dx$$

$$= \int_{0}^{\infty} \exp[i(k_0 - k)] \exp(\varepsilon^2 k_0^2 \ell^2 x) \exp(-\varepsilon^2 k^2 \ell x) \exp\left\{-\varepsilon^2 k_0^2 \ell^2 e^{-\frac{x}{\ell}}\right\} dx.$$

$$(3.68)$$

Expanding the last exponential term in a uniformly convergent series and integrating (3.68), yields:

$$\langle \Psi(x) \rangle = \exp(\varepsilon^2 k_0^2 \ell^2) \sum_{n=0}^{\infty} \frac{(-\varepsilon^2 k_0^2 \ell^2)^n}{n!} \frac{1}{ik - ik_0 + \varepsilon^2 k_0^2 \ell + n/\ell}. \qquad (3.69)$$

From (3.69), one can see that $\langle \Psi(k) \rangle$ has the poles $k_n = k_0 + i\varepsilon^2 k_0^2 \ell + in/\ell$, which correspond to more and more damped partial waves in r-space. If $\varepsilon k_0 \ell \ll 1$, we can approximate $\langle \Psi(k) \rangle$ by the first partial wave ($n = 0$) that gives again (3.66), apart from a factor $\exp(\varepsilon^2 k_0^2 \ell^2) \neq 1$.

3.4. APPROXIMATIONS OF THE PERTURBATION METHOD

In this section, we try to justify certain approximation procedures using the formal perturbation series of Section 3.2. We recall, once more, that the random function $\mu(r)$ is strictly stationary with respect to space transfer. Our investigations are only concerned with the mean propagator $\langle G \rangle$.

3.4.1. Low Order Approximations

In the section above, the mean wave function of the 1D-model was shown to be damped through destructive phase mixing; the damping length associated with this phenomenon is very large compared to the wavelength. It is therefore necessary to get approximate solutions for the mean propagator that are valid at long distances compared to the wavelength (radiation problem), and valid at long times compared to the period (initial wave problem). We show below the lower-order perturbation approximations to satisfy this condition, even the very small strength of random fluctuations ε.

The *Born approximation* for the mean propagator is the lowest order non vanishing approximation of the corresponding perturbation series, that is,

$$\langle G \rangle_{\text{Born}} = \frac{}{k} \quad + \quad \overset{k \,\bullet\!\!\frown\!\!\bullet\, k}{\underset{k'}{}} \qquad (3.70)$$

and explicitly in k-space as

$$\langle G \rangle = \frac{c^2}{z^2 - c^2 k^2} + \frac{\varepsilon^2 z^4 c^2}{(z^2 - c^2 k^2)^2} \int \frac{\Gamma(k - k')}{z^2 - c^2 k'^2} d^3 k' \tag{3.71}$$
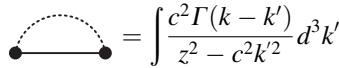
If so, $G(k - k') = g(k - k', k' - k)$ is the FT of the covariance function. The squared perturbed propagator appearing in the second term on the random homogeneous space of (3.71) is the consequence of the wave vector conservation conditions. This term has two double poles $z = \pm cK = \pm c|k|$. It is well known that such double poles will yield two contributions to the inverse Laplace transform $\langle G(k, t) \rangle$, proportional to $t \cdot \exp[icKt]$ and $t \cdot \exp[-icKt]$. In other words, the first perturbation term has a singular behavior, that is, it increases without any limit as $t \to +\infty$. As this prevents any damping of the mean propagator, we conclude:

The Born approximation is only a short time (or short distance) approximation.

Next, it will be useful to have a better knowledge of the time dependence of the Born approximation. Let us, for example, take the covariance function as

$$\Gamma(r) = \exp\left[-\frac{R}{\ell}\right], \qquad R \equiv |\mathbf{r}|. \tag{3.72}$$
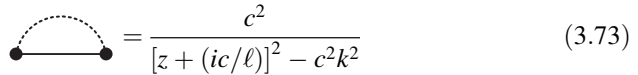
Here ℓ, as above, is the range of refraction index correlations. To evaluate the convolution integral

$$\overbrace{} = \int \frac{c^2 \Gamma(k - k')}{z^2 - c^2 k'^2} d^3 k'$$
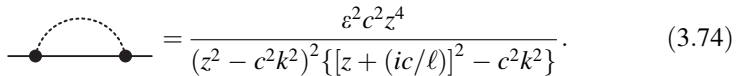
we note that it is the FT of

$$\exp\left[-\frac{R}{\ell}\right] \frac{\exp[izR/c]}{-4\pi R} = \frac{\exp\{(i/c) \cdot [z + (ic/\ell)]R\}}{-4\pi R}$$

and changing z into $z + (ic/\ell)$, yields

$$\overbrace{} = \frac{c^2}{[z + (ic/\ell)]^2 - c^2 k^2} \tag{3.73}$$

and

$$\overbrace{} = \frac{\varepsilon^2 c^2 z^4}{(z^2 - c^2 k^2)^2 \{[z + (ic/\ell)]^2 - c^2 k^2\}}. \tag{3.74}$$

Besides the double poles $z = \pm cK$, two other poles have appeared in (3.74): $z = \pm cK - ic/\ell$. The corresponding contributions to LT and $\langle G(k, t) \rangle$ are proportional to $\exp\{\pm icKt\} \cdot \exp\{ic(t/\ell)\}$. They are thus damped with a damping

time $t_d = \ell/c$. This damping time is the time the wave takes to travel a distance ℓ equal to the size of the scattering blobs. We call it, as in quantum field theory, the interaction time t_{int}. We turn back now to the perturbation series for the mean propagator, and show that, as we take more and more perturbation terms we get more and more divergent singular terms. The fourth order diagrams are (see Section 3.2):
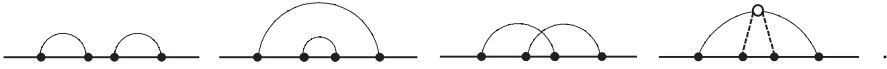
Because of the wave vector conservation condition, the same vector occurs in the middle and at the terminals of the diagram

The factor $G^{(0)}(k; z) = \frac{c^2}{z^2 - c^2 k^2}$ occurs thus twice in this diagram, producing singular terms proportional to $t^2 \cdot \exp[icKt]$ and $t^2 \cdot \exp[-icKt]$. More generally, any unconnected diagram that is the product of p connected diagrams produces singular terms proportional to $t^p \cdot \exp[icKt]$ and $t^p \cdot \exp[-icKt]$. We call them *the leading terms* of the diagram. Besides the leading terms, there are other singular terms with lower power of t, and also damped terms, with a damping time found to be always of the order of $t_{\text{int}} = \ell/c$. If the damping time of the mean propagator is much longer than t_{int}, the asymptotic time dependence of the mean propagator will be governed essentially by the leading terms.

Let us show that singular terms arise in the radiation problem too. We are now looking for $\langle G(r) \rangle$, whose FT may be obtained by changing z into ck_0 in $\langle G(k; z) \rangle$. Taking again the covariance function $\exp(-R/\ell)$, we obtain

$$\langle G(k) \rangle = \frac{1}{k_0^2 - k^2} + \frac{\varepsilon^2 k_0^2}{(k_0^2 - k^2)^2} \frac{1}{[(k_0 + i/\ell)^2 - k^2]} + \dots \tag{3.75}$$

This is only the function of $K = |k|$. Its inverse FT, $\langle G(R) \rangle$, can be obtained by a single integration

$$\langle G(R) \rangle = \frac{1}{(2\pi)^2} \int_0^\infty \frac{e^{iKR} - e^{-iKR}}{iKR} K^2 \langle G(k) \rangle \, dK. \tag{3.76}$$

In $\langle G(k) \rangle$ the poles $K = k_0$ appear again with increasing frequency, as we take more and more perturbation terms. As a consequence of this, we can write

$$\langle G(R) \rangle = e^{ik_0 R} \cdot [1 + AR + BR^2 + \dots] \tag{3.77}$$

where $A, B, \ldots$ do not depend on R. As we take the limit $\text{Im}(k_0) \to 0$, we obtain secular terms in R.

We conclude that no finite order approximation of the perturbation series can be used because it would diverge as $t \to \infty$ or $R \to \infty$. However, an infinite sum of singular terms may be non-singular; for example

$$\exp(-t^2) = \sum_{n=0}^{\infty} \frac{(-t^2)^n}{n!}. \tag{3.78}$$

But any finite sum has a singular behavior. If we want to do something with the formal perturbation series, we must thus use at least an infinite subseries. This result is independent of ε, the strength of refractive index fluctuations, because singular terms do only disappear for $\varepsilon = 0$.

3.4.2. Convergence of the Perturbation Expansion

A fundamental question arises now: Does the perturbation series converge? It is rather difficult to give a general answer to this question because we do not say what kind of convergence we expect (or do not expect). Let us first indicate that there is a proof [1–4] that the perturbation series for $G(r)$ (radiation problem) is the mean square convergent for Gaussian $\mu(r)$.

Let us consider the 1D-model. For $\varepsilon k_0 \ell \ll 1 (\ell \ll \lambda)$, we can write the mean propagator

$$\langle G(x, x') \rangle = Y(x - x') \exp\{ik_0(x - x')\} \exp\{-\varepsilon^2 k_0^2 \ell(x - x')\}. \tag{3.79}$$

The perturbation expansion, n of the mean propagator in power of ε is thus

$$\langle G(x, x') \rangle = Y(x - x') \exp\{ik_0(x - x')\} \sum_{n=0}^{\infty} \frac{[-\varepsilon^2 k_0^2 \ell(x - x')]^n}{n!}. \tag{3.80}$$

If x and x' are fixed, this is an analytic function of ε. This is of no interest because $\langle G(x, x') \rangle$ does not act as a multiplication but as an integral convolution operator. The convolution product of a bounded source function with $Y(x) \exp\{ik_0 x\} \times \exp\{-\varepsilon^2 k_0^2 \ell x\}$ is convergent, but the convolution product with $Y(x) \exp\{ik_0 x\} x^n$ is generally not convergent because of the singular behavior of this term.

As a last example, let us consider the convergence of the FT $\langle G(k) \rangle$ for the 1D-model. In Section 3.3, it was shown that

$$\langle G(x, x') \rangle = \exp(\varepsilon^2 k_0^2 \ell^2) \sum_{n=0}^{\infty} \frac{(-\varepsilon^2 k_0^2 \ell^2)^n}{n!} \frac{1}{[ik - ik_0 + \varepsilon^2 k_0^2 \ell + n/\ell]}$$

was a convergent, but this is not the perturbation series because ε appears in the denominator; $\langle G(k) \rangle$ acts as a multiplication. We ask if this is an analytic function of ε in some neighborhood of $\varepsilon = 0$ and all values of k.

For $n \geq 1$, $[ik - ik_0 + \varepsilon^2 k_0^2 \ell + n/\ell]$ is an analytic function of ε for $|\varepsilon| < \frac{n}{k_0 \ell^2}$ and all values of k. But for $n = 0$, $\varepsilon k_0 \ell \ll 1 (\ell \ll \lambda)$ is not an analytic function of ε in any neighborhood of $\varepsilon = 0$ because $k - k_0$ may vanish. We conclude that the perturbation expansion does not converge. However, it may be easily shown that for $\varepsilon k_0 \ell < 1 (\ell < \lambda)$ one can write

$$\langle G(x, x') \rangle = [ik - ik_0 + \varepsilon^2 k_0^2 \ell + n/\ell]^{-1} \{1 + \varepsilon^2 k_0^2 \ell^2 R(k, \varepsilon)\} \tag{3.81}$$

where $R(k, \varepsilon)$ is a bounded function of k and ε. This means that we can approximate $\langle G(k) \rangle$ uniformly by the first term of the series (3.69) for $k_0 \ell \ll 1$. This term, though not analytic, can be formally expanded in powers of ε:

$$\frac{1}{[ik - ik_0 + \varepsilon^2 k_0^2 \ell]} = \frac{1}{(ik - ik_0)} \sum_{p=0}^{\infty} \left(-\frac{\varepsilon^2 k_0^2 \ell}{ik - ik_0} \right)^p. \tag{3.82}$$

In the next section we shall do exactly the reverse: given a formal divergent series, we shall extract from it another divergent subseries whose formal sum is easy to calculate.

3.4.3. Bourret's Bilocal and Kraichnan's Random Coupling Models

We now describe two attempts to overcome the difficulty of divergent perturbation series. Both methods use the fact that there is certain infinite subseries of the formal perturbation series for the mean propagator, whose exact solution is possible. As it has been pointed by Kraichnan [23] in a fundamental paper on the dynamics of non linear stochastic systems, the use of subseries of the perturbation series is very dangerous because they may give unphysical results without any physical meaning. It will therefore be necessary to proceed very carefully. Let us now introduce briefly the first method.

Bourret's Bilocal Approximation. We take all diagrams whose connected parts have only two vertices; the resulting series is called the Bourret series and is denoted by $\langle G \rangle_B$ [13]:

$$\langle G \rangle_B = \text{———} + \overset{\frown}{\text{•—•}} + \overset{\frown}{\text{•—•—•}} + \overset{\frown}{\text{•—•—•—•}} + \cdots . \tag{3.83}$$

This series has been introduced by Bourret [13] for a Gaussian random function and also studied by Tatarskii et al. [16–18]. Recalling that the mass operator is the sum of all connected diagrams without terminals, we find that the Bourret series corresponds to the lowest order approximation of the mass operator. The corresponding Dyson's equation, which is immediately derived from (3.83) is

$$\langle G \rangle_B = \text{———} + \overset{\frown}{\text{•————•}} \langle G \rangle_B \tag{3.84}$$

This equation has also been derived by Keller [14], but his derivation must be considered incorrect because he treats the second term of the full perturbation series $(-\bullet-\bullet-)$ as a small perturbation. Before we discuss Bourret's approximation for the single propagator, let us give the corresponding double propagator approximation

$$<G\otimes G^*>_{\mathrm{B}} \; = \; \text{[diagram]} \; + \; \text{[diagram]} \; + \; \text{[diagram]} \; + \ldots . \qquad (3.85)$$

Bourret's equation (3.84) for the single propagator is easily solved in k-space; we shall not derive the corresponding solution for the radiation problem, because this may be found in [13,14,16–18]. It is also instructive to study the behavior of $\langle G(k,t)\rangle_{\mathrm{B}}$ for a given k, that is, the time dependence of an initial excitation proportional to $\exp\{ikr\}$. The main result is that the natural frequencies $\omega = \pm cK$ are renormalized. For an $\exp(-R/\ell)$ covariance function, the renormalized frequencies are:

$$\omega_r = \pm cK \mp \frac{\varepsilon^2 cK^3\ell^2}{2} - i\varepsilon^2 cK^4\ell^3. \qquad (3.86)$$

The damping time corresponding to the imaginary part of ω_r is $t_{\mathrm{d}} = \frac{1}{\varepsilon^2 cK^4\ell^3}$.

Bourret's derivation is based upon the following assumption [13]:

$$\langle \mu(r_1)\mu(r_2)\Psi(r_2)\rangle = \langle \mu(r_1)\mu(r_2)\rangle\langle\Psi(r_2)\rangle. \qquad (3.87)$$

Such closure assumptions have been studied by Kraichnan [23]; he has shown that they are generally not uniformly valid for $t \to \infty$. However, the examples considered by him are rather strong perturbations (such as a random oscillator). As we show below, the case $K\ell \ll 1$ corresponds to a weak perturbation. The damping time associated with the solution of Bourret's equation is $t_{\mathrm{d}} = \frac{1}{\varepsilon^2 cK^4\ell^3}$, and for $K\ell \ll 1$

$$t_{\mathrm{d}} \gg t_{\mathrm{int}} = \frac{\ell}{c}. \qquad (3.88)$$

Bourret's diagrams having p connected parts give a leading term proportional to $\varepsilon^{2p} \cdot t^p \cdot \exp(\pm icKt)$. For $t \sim t_{\mathrm{d}}$ this term becomes ε-independent. Any other diagram will give rise to uncompensated powers of ε and may thus be constructed as small. This is rather a poor justification of the Bourret's approximation, because we did not make a dimensional analysis of the diagram with respect to the other parameters c, K. Let us give the main lines of a more rigorous justification. The leading term of

$$\underbrace{\text{[diagram]}}_{P \; times} = \left[\frac{c^2}{z^2 - c^2 k^2}\right]^{p+1} \left(\text{[diagram]}\right)^p \qquad (3.89)$$

is easily found to be

$$i\left(\frac{c}{2K}\right)^{p+1} t^p \left[\exp(-icKt)\left(\lim_{z=ck+i0}\left(\text{}\right)^p\right) - \exp(ickt)\left(\lim_{z=-ck+i0}\left(\text{}\right)^p\right)\right]$$

(3.90)

and

$$\lim_{\eta\to0,\eta>0} z = cK + i\eta \Rightarrow \lim z = cK + i0.$$

The asymptotic time behavior of (3.89) depends thus only on

$$\lim_{z=\pm cK+i0}\left(\text{}\right)$$

and not on the whole z-dependence of . This is immediately generalized to any product of connected diagrams, whether it belongs to the Bourret series or not. In order to show that the Bourret's approximation is uniform, we only need to prove that for $z = \pm cK + i0$, is a good approximation of the mass operator $M(k; z)$. Following [31], it is easily found that for $z = \pm cK + i0$, a connected diagram L_p with p vertices and without terminals has the dimensional dependence

$$L_p(\varepsilon, c, K, \ell) \sim \varepsilon^p K^{2p} \ell^{2(p-1)} \Lambda_p(\ell K)$$

(3.91)

where $\Lambda_p(\ell K)$ being a non dimensional function of the non dimensional quantity ℓK. For small values of ℓK we can write

$$L_p \sim \varepsilon^p K^{2p} \ell^{2(p-1)}(1+O(\ell K) + \ldots)$$

(3.92)

for $\ell K \ll 1$ and $p > 2$, L_p is small compared to both $L_2 \sim \varepsilon^2 K^4 \ell^2$ and its first $O(\ell K)$ correction. This first order correction is necessary, because it is found that $\varepsilon^2 K^4 \ell^2$ does not contribute to the damping time, but only to the real frequency shift of the renormalized frequencies according to (3.86).

If the condition $\ell K \ll 1$ is violated, the contributions arising from the diagrams not belonging to the Bourret series become more and more important, and for $\ell K \gg 1$ Tatarskii [16–18] has shown that all diagrams with the same number of vertices are almost equal (this is only true for $t \ll t_{\text{int}}$, but as in this case $t_{\text{d}} \ll t_{\text{int}}$). If all these dimensional considerations are not very convincing, it is still possible to check the validity of Bourret's approximation on the 1D-model (see Section 3.4). The exact solution is described in Formula (3.62)

$$\langle \Psi(x)\rangle = Y(x) \exp[ik_0 x] \exp\left\{-\varepsilon^2 k_0^2 \ell^2\left(\frac{x}{\ell} + e^{-\frac{x}{\ell}} - 1\right)\right\}$$

(3.93)

The solution of Bourret's equation, which is an ordinary equation in k-space is:

$$\langle \Psi(k) \rangle_{\mathrm{B}} = \left[ik - ik_0 + \frac{\varepsilon^2 k_0^2}{ik - ik_0 + \dfrac{x}{\ell}} \right]^{-1}. \tag{3.94}$$

Taking the inverse FT, we get

$$\langle \Psi(k) \rangle_{\mathrm{B}} = Y(x) \frac{e^{ik_0 x}}{2\sqrt{\Delta}} \left\{ (1 + \sqrt{\Delta}) \exp\left[-\frac{1}{2\ell}(1 - \sqrt{\Delta})x \right] \right.$$
$$\left. - (1 - \sqrt{\Delta}) \exp\left[-\frac{1}{2\ell}(1 + \sqrt{\Delta})x \right] \right\} \tag{3.95}$$

where

$$\Delta = 1 - 4\varepsilon^2 k_0^2 \ell^2.$$

Expanding (3.94) for $\varepsilon k_0 \ell \ll 1$, we find

$$\langle \Psi(k) \rangle_{\mathrm{B}} = Y(x) e^{ik_0 x} \exp\{-\varepsilon^2 k_0^2 \ell x\}, \tag{3.96}$$

which is the uniform approximation (3.63), already found for the exact solution. If the condition $\varepsilon k_0 \ell \ll 1$ is not satisfied, Formulas (3.95) and (3.93) are not in agreement. For example, if $\varepsilon k_0 \ell \gg 1$, the Bourret's approximation gives

$$\langle \Psi(k) \rangle_{\mathrm{B}} = Y(x) e^{ik_0 x} \cos(\varepsilon k_0 x) \exp\{-x/2\ell\} \tag{3.97}$$

whereas the exact solution (3.67) is

$$\langle \Psi(x) \rangle = Y(x) e^{ik_0 x} \exp\left\{ -\frac{1}{2}\varepsilon^2 k_0^2 x^2 \right\}. \tag{3.98}$$

We conclude that:

The Bourret's approximation is a long wavelength approximation, uniformly valid for any random perturbation, whether Gaussian or not, and has a correlation range much shorter than the wavelength ($\ell \ll \lambda$)

This approximation can also be used for more general equations of random variables than the scalar wave equation, because the dimensional analysis is easily generalized. In Section 3.7 we apply it to the electromagnetic wave equation and in Section 3.8 to the coupled wave equation.

Let us consider now the Bourret's approximation for the double propagator. We have seen in Section 3.2 that the mean spectral energy propagator $\langle |G(k; z)|^2 \rangle$ and thus the mean spectral energy density $\langle |\Psi(k; z)|^2 \rangle$ satisfy a separate

equation. For the radiation problem, using the Bourret's approximation (3.85), this equation is

$$\langle|\Psi(k)|^2\rangle_B = |\langle G(k)\rangle_B|^2|j(k)|^2 + |\langle G(k)\rangle_B|^2\varepsilon^2 k_0^2 k_0^{*2}\int\Gamma(k-k')\langle|\Psi(k')|^2\rangle_B d^3k$$

(3.99)

where $\langle G(k)\rangle_B$ is the Bourret's approximation for the single propagator, and $j(k)$ is the FT of the source function. Equation (3.99) is an integral equation for the mean spectral energy density. As follows from Reference [13], the Bourret's approximation for $\langle G(k)\rangle$ is only valid for $K\ell \ll 1$, but the integral term of (3.99) relates the region of the spectrum that does satisfy this condition and the other one. Even if we assume that $j(k)$ is vanishing outside $K\ell \ll 1$, we do not know if some energy will not be transferred to the other part of the spectrum. Thus, there is a serious difficulty here, and it may be possible that the Bourret's approximation is never uniform for the mean double propagator. This question remains unanswered till date.

Kraichnan's Random Coupling Model. Given an equation of random variables, Kraichnan [23] showed that he can construct another equation which is related to it, but it can be reduced to a nonlinear nonrandom (e.g., deterministic) equation. This was achieved through the introduction of an additional random coupling between wave vectors, called by him the "random coupling model." The remarkable point is that its solution can be considered both as the exact solution of the model equation, as well as the approximate solution of the original equation. This ensures that if we can solve the model equation, the solution will be physically acceptable. Kraichnan's perturbation diagrams are somewhat different from what was presented previously, but the connection is easy to establish. Using notations, according to [31], the mean propagator of the random coupling model, which we denote by $\langle G(k)\rangle_K$, is the sum of all perturbation diagrams of the original problem such that there are:

  – there is no clusters of more than two points;
  – there are no intersecting dotted lines.

We give the first diagrams as

(3.100)

This expansion is easily found to be equivalent to a nonlinear but nonrandom equation (we use the symbol ===== for $\langle G \rangle_K$)

$$\overline{\overline{\quad\quad}} = \underline{\quad} \quad + \quad \overset{\frown}{\underset{\bullet\quad\quad\bullet}{\rule{3cm}{0.4pt}}} \quad . \tag{3.101}$$

The only difference with Bourret's equation (3.84) is that the mean propagator and not the unperturbed propagator appears under the dotted line. The equation for the mean propagator of the random coupling model is

$$< G \otimes G^* >_K = \; \overline{\overline{\quad\quad}} + \boxed{\underline{\quad\quad}} < G \otimes G^* >_K . \tag{3.102}$$

This linear equation can only be solved after the nonlinear Equation (3.101). All Bourret's diagrams are included in the random coupling model. Accordingly, we expect that it will give a better approximation. But the main reason for studying this model is that there is not a prior limitation to its validity such as $K\ell \ll 1$. The solution of the random coupling model for the wave equation would give at least a partial answer to important questions such as:

 – is there a damping effect of the mean propagator always?
 – how does the damping time vary with k?
 – what is the spectral mean energy distribution corresponding to a given excitation or a source function?

Let us write down the random coupling model equation for our 1D-model and the scalar wave equation. The 1D-model gives:

$$\langle G(k;z)\rangle_K = \frac{c}{ick - iz} + \frac{(\varepsilon iz)^2}{c(ick - iz)} \langle G(k;z)\rangle_K \int \Gamma(k - k')\langle G(k';z)\rangle_K d^3k'. \tag{3.103}$$

At the same time, the scalar wave equation is

$$\langle G(k;z)\rangle_K = \frac{c^2}{z^2 - c^2k^2} + \frac{\varepsilon^2 z^4}{c^2(z^2 - c^2k^2)} \langle G(k;z)\rangle_K \int \Gamma(k - k')\langle G(k';z)\rangle_K d^3k' \tag{3.104}$$

If $\Gamma(k - k') = \delta(k - k')$, Equations (3.103) and (3.104) are ordinary nonlinear equations which can be solved analytically. This case corresponds to a covariance function in r-space that is constant.

There are basically two possible iterations methods for the random coupling model equation:

a) by using Equation (3.101)

we can iterate it, considering the second term on the random homogeneous space as a perturbation. This gives

$$(3.105)$$

which cannot be used for long times because of the singular form.

b) A more interesting method is to write Equation (3.101) as

$$\langle G \rangle_K = \frac{G^{(0)}}{1 - G^{(0)} L(\langle G \rangle_K)} \tag{3.106}$$

where L is the linear operator

Equation (3.106) is then iterated giving

$$\langle G \rangle_K = \frac{G^{(0)}}{1 - G^{(0)} L\left(\dfrac{G^{(0)}}{1 - G^{(0)} L(\ldots)} \right)}. \tag{3.107}$$

This is the operator analogue of a continued fraction. For the 1D-model and the covariance function $\sim \exp(-|x|/\ell)$, it was possible to show that this iteration process converges for $|\varepsilon \ell z/c| < 1/2$ and to find its analytic continuation. The proof is somewhat artificial because we used the fact that for any function $f(k)$ is bounded and analytic in the half plane $\mathrm{Im}(z) < 0$

$$\int \Gamma(k - k') f(k') \mathrm{d}k' = f(k - i/\ell) \tag{3.108}$$

Hence we get a nonlinear finite difference equation, which is solved by means of a continued fraction. Unfortunately, it is not possible to extend this method to the scalar wave equation.

3.5. RANDOM TAYLOR EXPANSION AT SHORT WAVELENGTHS

In Section 3.4, we have found that in the limiting case $\varepsilon k_0 \ell \gg 1$, the random refractive index behaves as a mere random value and not as a random function. This is easily understood when ℓ is very large ($\ell \gg \lambda$), each realization (or sample) of the random index is a very slowly varying function that can be approximated by a constant. At an intermediate level, between the general random function and random variable, we could try to approximate a random function by a linear function or a quadratic function with random variables as coefficients. For example, constructing a limited random Taylor expansion of the random function. The random equation for this model is:

$$\frac{\partial \Psi(x)}{\partial x} - ik_0[1 + \varepsilon \mu(x)] \Psi(x) = \delta(x) \tag{3.109}$$

where $\mu(x)$ is a random function, $\delta(x)$ is Dirac's distribution at the origin, and the wave number $k_0 = 2\pi/\lambda = 2\pi f/c$ is taken, as in Section 3.3, to be positive. Here λ is the wavelength, f is the radiated frequency, and c is the velocity of light. We want to approximate the random function $\mu(x)$ by its random Taylor expansion [7,22]

$$\mu(x) = \mu(0) + x\mu'(0) + \frac{x^2}{2}\mu''(0) + \dots \tag{3.110}$$

where $\mu(0), \mu'(0), \mu''(0), \dots$ are not independent random variables. We cannot keep the covariance function $\exp\{-|x|/\ell\}$ because the corresponding random function is not mean square differentiable (see Reference [31]). As we do not need to specify the covariance Γ, we shall only assume that it has derivatives of all orders at $x = 0$ and that $\Gamma(0) = 1$. That leads us to an approximation for $\Psi(x)$, that is,

$$\frac{\partial \Psi(x)}{\partial x} - ik_0 \left[1 + \varepsilon\mu(0) + \varepsilon x\mu'(0) + \varepsilon\frac{x^2}{2}\mu''(0) \right] \Psi(x) = \delta(x). \tag{3.111}$$

It is solved for the mean wave function

$$\langle \Psi(x) \rangle = Y(x)e^{ik_0 x} \left\langle \exp\left[ik_0 \varepsilon x \left(\mu(0) + \varepsilon x\mu'(0) + \varepsilon\frac{x^2}{2}\mu''(0) \right) \right] \right\rangle. \tag{3.112}$$

As $\mu(x)$ is a Gaussian random function, the multivariate distribution of $\mu(0), \mu'(0), \mu''(0)$ is also Gaussian; it is thus determined by its second order moment such as $\langle(\mu(0))^2\rangle, \langle(\mu'(0))^2\rangle, \langle\mu(0)\mu'(0)\rangle$, and so forth. They are easily calculated in terms

of covariance function, for example

$$\langle \mu(0)\mu'(0) \rangle = \lim_{h \to 0} \frac{\langle \mu(0)\mu(h) \rangle - \langle \mu(0)\mu(0) \rangle}{h} = \Gamma'(0) \equiv 0 \qquad (3.113)$$

because Γ is an even function.

The mean value in (3.112) is easily related to the characteristic function of $\mu(0)$, $\mu'(0)$, $\mu''(0)$, and can be calculated in terms of Γ; this gives

$$\langle \Psi(x) \rangle = Y(x)e^{ik_0 x} \exp\left[-\frac{k_0^2 \varepsilon^2 x^2}{2} \left(1 + \frac{x^2}{12} \Gamma''(0) + O(x^3) \right) \right]. \qquad (3.114)$$

Let us compare this Equation to the exact solution as in (3.60)

$$\langle \Psi(x) \rangle = Y(x)e^{ik_0 x} \exp\left[-\frac{k_0^2 \varepsilon^2}{2} \int_0^x \int_0^y \Gamma(y - y') dy \, dy' \right]. \qquad (3.115)$$

Expanding the covariance function in power of x and integrating it we get exactly the same result as in (3.114). If the condition

$$\left| \frac{k_0^2 \varepsilon^2}{\Gamma''(0)} \right| \gg 1$$

is satisfied, we can use the so-called "random variable" approximation [31]

$$\langle \Psi(x) \rangle = Y(x)e^{ik_0 x} \exp\left[-\frac{k_0^2 \varepsilon^2 x^2}{2} \right]. \qquad (3.116)$$

An equivalent condition is that the damping length $x_d = 1/k_0 \varepsilon = \lambda/\varepsilon$ corresponding to this approximation should be much shorter than the range of random correlations $\ell = |\Gamma''(0)|^{-1/2}$. If it is satisfied, the wave cannot escape the region where the random index is properly approximated by a random variable. The "random variable" approximation is easily applied to any propagation equation because we only need to solve a partial differential equation with constant coefficients, and average afterwards. If we want a higher order approximation we must solve a partial differential equation with linear or quadratic coefficients. The case of linear coefficients can, in principle, be solved by means of a generalized Laplace transformation, but this is rather complicated. In Section 3.8 we shall apply the "random variable" method to the coupled wave equations at short wavelength.

Now we derive the short wave approximation for the scalar wave equation with point source:

$$\Delta \Psi(r) + k_0^2 [1 + \varepsilon \mu] \Psi(r) = \delta(r). \qquad (3.117)$$

We assume μ to be a centered Gaussian random variable and $\langle \mu^2 \rangle = 1$. Solving (3.117) we get

$$\Psi(r) = \frac{\exp\{ik_0(1 + \varepsilon\mu)R\}}{-4\pi R}, \qquad R = |r|. \tag{3.118}$$

Taking the mean value of this wave function we find

$$\langle \Psi(r) \rangle = \frac{\exp(ik_0 R)\exp\left(-\frac{1}{2}\varepsilon^2 k_0^2 R^2\right)}{-4\pi R}. \tag{3.119}$$

The damping due to phase mixing is thus exponential with a damping length

$$R_\mathrm{d} = (\varepsilon|k_0|)^{-1} > \lambda. \tag{3.120}$$

The condition $R_\mathrm{d} \ll \ell$ can be written as

$$\varepsilon|k_0|\ell \gg 1.$$

It is thus a short wavelength condition ($\ell \gg \lambda$). The result of (3.119) disagrees with a result derived by Tatarskii [16–18] for $|k_0|\ell \gg 1$. His mean wave function

$$\langle \Psi(r) \rangle = \frac{\exp(ik_0 R)}{-4\pi R} \cdot \frac{1}{(1 + \varepsilon^2 k_0^2 R\ell)^{1/2}} \tag{3.121}$$

has not an exponential decrease, but has a damping length of

$$R_\mathrm{d} = (\varepsilon^2 k_0^2 \ell)^{-1} \ll \lambda.$$

His result is expressed as a certain integral over the solution of the Bourret's equation (3.84), and this integral is calculated by the method of stationary phase. The expansion of the solution of the Bourret's equation used by Tatarskii is only valid for $|k_0|\ell \ll 1$. If the proper expansion is used, the result becomes identical with the one mentioned previously. This can also be checked on the 1D-model for which the calculation is easier.

3.6. AN EXACT SOLUTION OF THE SCALAR WAVE EQUATION

In References [1–4,16–18], it was suggested that functional space integration might be used to solve these random variables equations. It suggested that it would be necessary to generalize the Wiener measure to more general stochastic processes

besides the Brownian motion. Nevertheless, it was shown in [31] that the reduced scalar wave equation can be related to a complex version of the heat equation and solved via a complex Wiener measure. The method indicated here can also be used for the Schrodinger equation with a random potential. Let us show how by following Reference [31] one can obtain the solution of the reduced scalar wave equation with random refractive index

$$\Delta \Psi(r) + k_0^2[1 + \mu(r)]\Psi(r) = \delta(r) \tag{3.122}$$

where, once more, $\delta(r)$ is Dirac's distribution at the origin. Let us assume that the wave number k_0 has a small positive imaginary part and $\mu(r)$ is a centered Gaussian random function with covariance $\Gamma(r, r')$ that need not be stationary. In order to relate this equation to the heat equation, we introduce a new unknown function $\widetilde{\Psi}(r, \theta)$ such that

$$\Psi(r) = -\frac{i}{k_0} \int\limits_0^\infty \exp(ik_0\theta)\,\widetilde{\Psi}(r, \theta)\mathrm{d}\theta. \tag{3.123}$$

Because of the positive imaginary part of k_0, this integral is convergent if $\widetilde{\Psi}(r, \theta)$ is not increasing very fast at infinity. Equation (3.122) is now multiplied by k_0^2 and integrated by parts

$$k_0^2\Psi(r) = -\int\limits_0^\infty \widetilde{\Psi}(r, \theta)\frac{\partial}{\partial \theta}\exp(ik_0\theta)\mathrm{d}\theta = \widetilde{\Psi}(r, 0) + \int\limits_0^\infty \frac{\partial \widetilde{\Psi}(r, \theta)}{\partial \theta}\exp(ik_0\theta)\mathrm{d}\theta.$$
$$\tag{3.124}$$

Using (3.123) and (3.124) we can write

$$\Delta \Psi(r) + k_0^2\Psi(r) + k_0^2\mu(r)\Psi(r) \equiv -\frac{i}{k_0}\int\limits_0^\infty \exp(ik_0\theta)[\Delta\widetilde{\Psi} + k_0^2\mu(r)\widetilde{\Psi}]\mathrm{d}\theta + \widetilde{\Psi}(r, 0)$$

$$+ \int\limits_0^\infty \frac{\partial \widetilde{\Psi}(r, \theta)}{\partial \theta}\exp(ik_0\theta)\mathrm{d}\theta = \delta(r). \tag{3.125}$$

This is satisfied if we take

$$\frac{\partial \widetilde{\Psi}(r, \theta)}{\partial \theta} = \frac{i}{k_0}\Delta\widetilde{\Psi}(r, \theta) + ik_0\mu(r)\widetilde{\Psi}(r, \theta)$$
$$\widetilde{\Psi}(r, 0) = \delta(r). \tag{3.126}$$

Let us compare (3.126) to the perturbed heat equation

$$\frac{\partial \widetilde{\Psi}(r,\theta)}{\partial \theta} = \Delta \widetilde{\Psi}(r,\theta) + V(r)\widetilde{\Psi}(r,\theta) \tag{3.127}$$

and the Schrodinger equation

$$\frac{\partial \widetilde{\Psi}(r,\theta)}{\partial \theta} = \alpha \Delta \widetilde{\Psi}(r,\theta) + V(r)\widetilde{\Psi}(r,\theta). \tag{3.128}$$

The first equation (3.127) can be solved by functional integration for all functions $V(r)$ continuous and bounded from above, using the Wiener measure of the Brownian motion process. For the second equation (3.128) there is no Wiener measure. It is wellknown that for the Schrodinger equation this solution through functional integration, given first by Feynman [3,4], is only a formal extension of the heat equation case. Fortunately, it can be shown that all equations such as (3.128), where α has a positive real part can be rigorously solved with a complex Wiener measure. This is the case here because $\text{Re}(i/k_0) > 0$. Thus, the solution of (3.128) is

$$\widetilde{\Psi}(r,\theta) = \int_{\Omega} \exp\left[ik_0 \int_0^{\theta} \mu(\rho(\tau))d\tau\right] dW\left(\theta, r, \frac{i}{k_0}\right) \tag{3.129}$$

where Ω is the space of continuous function $\rho(\tau)$ such that $\rho(0) = 0$ and $\rho(\theta) = r$, and $dW(\theta, r, i/k_0)$ is the complex Wiener measure corresponding to the complex heat equation

$$\frac{\partial \widetilde{\Psi}(r,\theta)}{\partial \theta} = \frac{i}{k_0} \Delta \widetilde{\Psi}(r,\theta). \tag{3.130}$$

Expression (3.129) can also be written more explicitly as the limit of ordinary multiple integrals

$$\widetilde{\Psi}(r,\theta) = \lim_{n\to\infty} \left(\frac{4\pi i \Delta\tau}{k_0}\right)^{-\frac{3}{2}n} \int \cdots \int \exp\left\{\frac{ik_0}{4\Delta\tau}[r_1^2 + (r_2 - r_1)^2 + (r - r_{n-1})^2]\right\}$$
$$\times \exp\{ik_0\Delta\tau[\mu(r_1) + \mu(r_2) + \ldots + \mu(r_{n-1})]\}d^3r_1 d^3r_2 \cdots d^3r_{n-1} \tag{3.131}$$

where $\Delta\tau = \theta/n$, $(4\pi i \Delta\tau/k_0)^{-\frac{3}{2}n}$ is the $3n^{\text{th}}$ power of the square root of $4\pi i \Delta\tau/k_0$, which has a positive real part. A formal proof of (3.131) was presented in [31].

Now we calculate the mean value of $\widetilde{\Psi}(r, \theta)$ using (3.129) by interchanging the functional integration. Finally, we get:

$$\langle \widetilde{\Psi}(r, \theta) \rangle = \int_{\Omega} \left\langle \exp \left[ik_0 \int_0^{\theta} \mu(\rho(\tau)) d\tau \right] \right\rangle dW \left(\theta, r, \frac{i}{k_0} \right) \tag{3.132}$$

We shall now make use of the fact that $\mu(r)$ is a centered Gaussian random function. However, the Gaussian assumption can be dropped because we actually only need to know the characteristic function of $\mu(r)$:

$$F(\varphi(r)) = \left\langle \exp i \int \varphi(r)\mu(r) d^3r \right\rangle. \tag{3.133}$$

The following calculations are almost the same as those in Section 3.3 for the 1D-model. For a fixed curve $\rho(\tau)$, a linear functional of $\mu(r)$

$$\varphi = \int_0^{\theta} \mu(\rho(\tau)) d\tau \tag{3.134}$$

is a centered Gaussian random value and $\langle \exp[ik_0\varphi] \rangle$ is its characteristic function

$$\left\langle \exp \left[ik_0\varphi \right] \right\rangle = \exp \left\{ -\frac{1}{2} k_0^2 \langle \varphi^2 \rangle \right\} \tag{3.135}$$

where

$$\langle \varphi^2 \rangle = \int_0^{\theta} \int_0^{\tau} \langle \mu(\rho(\tau))\mu(\rho(\tau')) \rangle d\tau \, d\tau' = \int_0^{\theta} \int_0^{\tau} \Gamma(\rho(\tau), \rho(\tau')) d\tau \, d\tau'. \tag{3.136}$$

Turning back to the initial Equation (3.132), we get

$$\langle \widetilde{\Psi}(r) \rangle$$

$$= -\frac{i}{k_0} \int_0^{\infty} d\theta \exp(ik_0\theta) \int_{\Omega} \left\langle \exp \left[-\frac{1}{2} k_0^2 \int_0^{\theta} \int_0^{\tau} \Gamma(\rho(\tau), \rho(\tau')) d\tau \, d\tau' \right] \right\rangle dW \left(\theta, r, \frac{i}{k_0} \right) \tag{3.137}$$

that solves the problem. This functional integral can also be approximated for numerical purposes, for example, by multiple integrals:

$$\langle \widetilde{\Psi}(r) \rangle_n = -\frac{i}{k_0} \int_0^\infty d\theta \exp(ik_0\theta) \left(\frac{4\pi i \Delta\tau}{k_0} \right)^{-\frac{3}{2}n}$$

$$\int \cdots \int \exp\left\{ \frac{ik_0}{4\Delta\tau} [r_1^2 + (r_2 - r_1)^2 + (r - r_{n-1})^2] \right\}$$

$$\times \exp\left\{ -\frac{1}{2} k_0^2 (\Delta\tau)^2 \sum_{i,j=1}^{n-1} \Gamma_{i,j} \right\} d^3r_1 d^3r_2 \cdots d^3r_{n-1} \qquad (3.138)$$

where $\Gamma_{i,j} = \Gamma(r_i, r_j)$ and $\Delta\tau = \theta/n$. The extension to higher order moments is straightforward, using characteristic functions of multivariate Gaussian distributions.

Approximate Evaluations of the Functional Integral (3.137)

a) Short Wavelength Approximation. If the range of the covariance function is much longer than the wavelength, we use a functional saddle point method to approximate the function

$$\exp\left[-\frac{1}{2} k_0^2 \int_0^\theta \int_0^\tau \Gamma(\rho(\tau), \rho(\tau')) d\tau \, d\tau' \right] \qquad (3.139)$$

by a quadratic function of $\rho(\tau) - \rho_0(\tau)$, where $\rho_0(\tau)$ is the function that makes the exponent stationary. It is then possible to calculate exactly this approximate functional integral.

b) Long Wavelength Expansion. The multiple integral (3.138) reminds us of the formula for the partition function of a gas in thermodynamic equilibrium. We can write

$$\exp\left\{ -\frac{1}{2} k_0^2 (\Delta\tau)^2 \sum_{i,j=1}^{n-1} \Gamma_{i,j} \right\} = \prod_{i,j=1}^{n-1} (1 + F_{ij}) = 1 + \sum F_{ij} + \sum\sum F_{ij} F_{ikl} + \dots$$

$$(3.140)$$

with

$$F_{ij} = \exp\left\{ -\frac{1}{2} k_0^2 (\Delta\tau)^2 \Gamma_{i,j} \right\} - 1. \qquad (3.141)$$

The resulting integrals are then represented by the Mayer's diagrams [3,4]. This method can also be related to the perturbation method of Section 3.2.

3.7. THE ELECTROMAGNETIC WAVE EQUATION

In this section we consider the full electromagnetic wave equation with a random refractive index

$$\Delta \mathbf{E}(\mathbf{r}) - \nabla(\nabla \cdot \mathbf{E}(\mathbf{r})) + k_0^2[1 + \varepsilon\mu(\mathbf{r})]\mathbf{E}(\mathbf{r}) = \mathbf{j}(\mathbf{r}). \qquad (3.142)$$

where $\mathbf{j}(\mathbf{r})$ is related to the actual current density $\mathbf{j}^*(\mathbf{r})$ by $\mathbf{j}(\mathbf{r}) = -i\omega\mu_0\mathbf{j}^*(\mathbf{r})$, ω is the angular frequency, $\omega = 2\pi f$, and $\mu_0 = 4\pi \cdot 10^{-7}$ is the permeability of free space. This equation is not equivalent to the reduced scalar wave equation because of the term $\nabla(\nabla \cdot \mathbf{E}(\mathbf{r}))$, which is important when the refractive index changes much over a wavelength. We shall therefore only consider the case of long wavelengths such that $|k_0|\ell \ll 1$, and use the Bourret's approximation. This problem has already been treated by Tatarskii [16–18] but the results presented here do not agree. Taking the FT of (3.142) we get

$$[(k_0^2 - k^2)\delta_{ij} + k_i k_j]\mathbf{E}_j(\mathbf{k}) + \varepsilon k_0^2 \int \mu(\mathbf{k} - \mathbf{k}')\mathbf{E}_i(\mathbf{k}'\mathrm{d}\mathbf{k} = \mathbf{j}_i(\mathbf{k}). \qquad (3.143)$$

The unperturbed propagator $G_{ij}^{(0)}(k)$ satisfies the following equation

$$[(k_0^2 - k^2)\delta_{ij} + k_i k_j]G_{jl}^{(0)}(k) = \delta_{il}. \qquad (3.144)$$

This equation is easily solved as

$$G_{jl}^{(0)}(k) = \frac{1}{[k_0^2 - k^2]}\left(\delta_{ij} - \frac{k_i k_j}{k_0^2}\right). \qquad (3.145)$$

The Bourret's equation for the mean perturbed propagator $\langle G_{jl}(k)\rangle$ is

$$\langle G \rangle = \quad \underline{\quad\quad} \quad + \quad \overset{\frown}{\underline{\bullet\quad\quad\bullet}} \langle G \rangle \qquad (3.146a)$$

or

$$\langle G(k)\rangle = G^{(0)}(k) + G^{(0)}(k)\varepsilon^2 k_0^4\left[\int \Gamma(k - k')G^{(0)}(k')\mathrm{d}^3 k'\right]\langle G(k)\rangle \qquad (3.146b)$$

where $\Gamma(k)$ is the FT of the covariance function. After a few transformations, Equation (3.146b) becomes [31]:

$$\left[(k_0^2 - k^2)\delta_{ij} + k_i k_j - \varepsilon^2 k_0^4 \int \frac{\Gamma(k - k')}{k_0^2 - k'^2}\left(\delta_{ij} - \frac{k_i' k_j'}{k_0^2}\right)\mathrm{d}^3 k'\right]\langle G_{jl}(k)\rangle = \delta_{il}. \qquad (3.147)$$

Let us now denote the tensor $T_{ij}(k)$ as:

$$T_{ij}(k) = \int \frac{\Gamma(k - k')}{k_0^2 - k'^2} \left(\delta_{ij} - \frac{k_i' k_j'}{k_0^2} \right) d^3k'$$

and assume that the covariance function is isotropic. Then the tensor $T_{ij}(k)$ is the convolution product of an isotropic tensor and an isotropic function; it is thus an isotropic tensor and can be written as:

$$T_{ij}(k) = \chi(k)\delta_{ij} + \mu(k)\frac{k_i k_j}{k_0^2}. \tag{3.148}$$

The Bourret's equation for the mean propagator becomes now

$$[(k_0^2 - k^2 - \varepsilon^2 k_0^4 \chi(k))\delta_{ij} + (1 - \varepsilon^2 k_0^2 \mu(k)k_i k_j)]\langle G_{jl}(k)\rangle = \delta_{il}. \tag{3.149}$$

Let us now find the free oscillations that satisfy

$$[(k_0^2 - k^2 - \varepsilon^2 k_0^4 \chi(k))\delta_{ij} + (1 - \varepsilon^2 k_0^2 \mu(k)k_i k_j)]\langle E_j(k)\rangle = 0. \tag{3.150}$$

There are two kinds of oscillations:

a) Transverse oscillations. Here $\langle \varepsilon \rangle$ and $\mathbf{k}$ are perpendicular. The dispersion equation is

$$k_0^2 - k^2 - \varepsilon^2 k_0^4 \chi(k) = 0. \tag{3.151}$$

b) Longitudinal oscillations. Here $\langle \varepsilon \rangle$ and $\mathbf{k}$ are parallel. The dispersion equation is

$$1 - \varepsilon^2 (k_0^2 \chi(k) + k^2 \mu(k)) = 0. \tag{3.152}$$

Let us also find the renormalized wave number $K_\perp$ for transverse waves. We take for this purpose the correlation function $\exp(-R/\ell)$. After some straightforward manipulations we find that for $k\ell \ll 1 (\ell \ll \lambda)$

$$\chi(K_\perp) = -\frac{2}{3}\ell^2(1 + 2iK_\perp\ell) + \frac{1}{3k_0^2} + O(\ell^4 K_\perp^2). \tag{3.153}$$

The dispersion equation for transverse oscillations is solved for the renormalized wave number

$$K_\perp = [k_0^2(1 - \varepsilon^2 k_0^2 \chi(k))]^{1/2} \approx k_0 \left[1 - \frac{1}{6}\varepsilon^2 + \frac{1}{3}\varepsilon^2 k_0^2 \ell^2 (1 + 2ik_0\ell) \right]. \tag{3.154}$$

We compare this result to the corresponding formula for the scalar wave equation obtained in References [16–18] or deduced from Keller's result [14] with a covariance function of $\exp(-R/\ell)$

$$K_\perp = k_0 \left[1 + \frac{1}{2}\varepsilon^2 k_0^2 \ell^2 (1 + 2ik_0\ell) \right]. \tag{3.155}$$

First of all, the imaginary part of $K_\perp$ in (3.155) has been reduced by factor $\sim(1/3)$ with respect to that in (3.154), the damping length of the mean wave have thus increased by 50%. Secondly, due to the additional negative term ($\sim \frac{1}{6}k_0\varepsilon^2$) in (3.154) compared with (3.155), the real part of $K_\perp$ is less than the real part of k_0 if $2k_0^2\ell^2 < 1$. As we assumed that $k\ell \ll 1 (\ell \ll \lambda)$, this is satisfied.

   We conclude that the effective phase velocity of transverse waves increases at long wavelengths, instead of decreasing as is the case for the scalar wave equation. This needs some explanation. There are two wave modes actually in this medium: the transverse mode, whose phase velocity is approximately ω/k_0, and the longitudinal wave mode, whose phase velocity is much longer (infinite in the nonrandom case). Due to the term $k_i k_j E_j$ of (3.143), the wave modes are coupled and part of the mean transverse wave has traveled part of its way as a longitudinal wave. The traveling time being thus decreased, the phase velocity is increased. Without this coupling it would be impossible to explain the increase of the phase velocity. As the additional term $\frac{1}{6}k_0\varepsilon^2$ does not depend on ℓ, it is possible that it corresponds rather to a diffraction effect by the scattering blobs (whose sizes are small compared to the wavelength), than to a volume scattering effect.

3.8. PROPAGATION IN STATISTICALLY INHOMOGENEOUS MEDIA

In this section we assume that the mean refractive index is constant through space, but that its random part is not strictly stationary with respect to space translations. The correlation functions $\Gamma(x, x')$ are functions of $(x - x')$ and also of $(x + x')/2$. We shall assume that this additional space dependence has a scale of variations h that is large compared to the wavelength. As there is no homogeneous turbulence in nature, this is a very common situation.

   The FT $\mu(k)$ of such a slowly varying random function does not satisfy the wave vector conservation condition

$$\langle \mu(k_1)\mu(k_2) \cdot \ldots \cdot \mu(k_p) \rangle = 0, \qquad \text{if} \quad k_1 + k_2 + \cdots + k_p \neq 0 \tag{3.156}$$

and does not give rise to any singular terms in the perturbation series. All arguments based upon the extraction of the leading singular terms seem to disappear suddenly. We show however that if the condition $\varepsilon^2 K^4 \ell^3 h \gg 1$ is satisfied, in addition to the usual condition $K\ell \ll 1$, nothing is changed, because we have pseudo singular terms. We assume that the additional space variation of the correlation functions $X(r_1, r_2, \ldots, r_n)$ is given by a factor $\exp\left[\frac{is(r_1+r_2+\ldots+r_n)}{r_1}\right]$, where $\mathbf{s}$ is given vector. This

is not of course the most general case, but it will be sufficient for our purpose. The scale of variation of this additional factor is $h = 1/|\mathbf{s}|$. The Fourier transform of $\exp\left[\frac{i\mathbf{s}(r_1+r_2+\ldots+r_n)}{r_1}\right] X(r_1, r_2, \ldots, r_n)$ is $X(k_1 + \frac{s}{n}, k_2 + \frac{s}{n}, \ldots, r_n + \frac{s}{n})$. The wave vector conservation condition becomes thus

$$k_1 + k_2 + \cdots + k_n + s = 0. \tag{3.157}$$

If we apply this to a connected diagram in k-space, such as
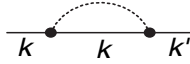
we find that

$$k - k' = s. \tag{3.158}$$

Because of the condition $h \gg \lambda$, which can also be written $|\mathbf{s}| < K$, the wave vectors at the terminals of a connected diagram are almost equal. Instead of a squared unperturbed propagator, the terminals of introduce a factor

$$\frac{c^2}{z^2 - c^2 K^2} \frac{c^2}{z^2 - c^2 K'^2} = \frac{c}{2(K^2 - K'^2)} \left[\frac{1}{K}\left(\frac{1}{z - cK} - \frac{1}{z + cK}\right) - \frac{1}{K'}\left(\frac{1}{z - cK'} - \frac{1}{z + cK'}\right) \right].$$
$$\tag{3.159}$$

Let us find the corresponding contribution to the inverse LT. It is proportional to

$$\frac{1}{(K^2 - K'^2)} \left[\frac{(e^{-icKt} - e^{ic'Kt})}{K} - \frac{(e^{-icK't} - e^{icK't})}{K'} \right] \tag{3.160}$$

then, using the fact that $K - K'$ is small compared to K, we approximate (3.160) by

$$\frac{1}{2K^2} \left[\frac{e^{-icKt}(1 - e^{ic(K-K')t})}{K - K'} - \frac{e^{-icKt}(1 - e^{-ic(K-K')t})}{K - K'} \right] \tag{3.161}$$

For $c(K - K') \ll 1$, we can make a Taylor expansion of (3.161) and find

$$-\frac{ic}{2K^2}(te^{-icKt} + te^{icKt}). \tag{3.162}$$

This expression is not really singular, because it is only valid for $c|K - K'|t \ll 1$; this condition can also be written $t \ll h/c$. If the damping time t_d, corresponding to the Bourret's approximation in the stationary case is small compared to h/c,

then because the expression behaves exactly as a singular term, we call it a pseudo secular term. As $t_d \sim \frac{1}{\varepsilon^2 c K^4 \ell^3}$, the condition $t_d \ll h/c$ can be written as

$$\varepsilon^2 K^4 \ell^3 h \gg 1 \qquad (3.163)$$

and because of $K\ell \ll 1$ and $\varepsilon^2 < 1$, h must be very large compared to the wavelength.

3.9. PROPAGATION IN HOMOGENEOUS ANISOTROPIC MEDIA

Waves in anisotropic media, such as ionospheric plasma in the presence of an ambient magnetic field (called *geomagnetic*), obey some partial differential equations that may be much more involved than the scalar wave equations. The wave function may have several components corresponding to a perturbed density, a perturbed velocity, a perturbed magnetic field, and so on (see Chapter 9). Instead of a single dispersion equation we may have several equations corresponding to different wave modes. The wave modes are defined to be the time harmonic functions of the propagation equations, with the boundary conditions taken into account. If we change the shape of the boundaries, we change also the nature of the wave modes.

3.9.1. Coupling Between Wave Modes

Here we shall only consider waves in free space because the eigenfunctions are easily found by means of a FT. Let us first consider the nonrandom case in order to introduce some definitions and notations.

Nonrandom Case. If the medium has constant parameters the propagation equations have constant coefficients. We assume that they can be written as a system of first order partial differential equations (this is the most frequent case) as:

$$\frac{\partial \Psi_j(r;t)}{\partial t} = b_{jlm} \nabla_l \Psi_m(r;t), \qquad l = 1, 2, 3, \qquad j, m = 1, 2, \ldots, n \qquad (3.164)$$

where n being the number of unknowns. Introducing now the FT

$$\Psi_j(k;t) = \int \exp(-ikr) \Psi_j(r,t) \mathrm{d}^3 r \qquad (3.165)$$

Equation (3.164) becomes

$$\frac{\partial \Psi_j(k;t)}{\partial t} = i b_{jlm} k_l \Psi_m(k;t) \qquad (3.166)$$

or in matrix notation

$$-i\frac{\partial \Psi(k;t)}{\partial t} = A(k)\Psi(k;t) \tag{3.167}$$

with

$$A_{jm}(k) = b_{jlm}k_l. \tag{3.168}$$

We assume that $A(k)$ is diagonalizable, that is, there exists a matrix $S(k)$ such that

$$S^{-1}(k)A(k)S(k) = D(k). \tag{3.169}$$

$D(k)$ being a diagonal matrix whose elements are the solution of the value equation

$$\det[\omega - A(k)] = 0.$$

This equation has n solutions (distinct or not)

$$\omega = \omega_j(k), \qquad j = 1, 2, \ldots, n.$$

We call Equation (3.169) the dispersion equation of the jth mode in an anisotropic medium. For mathematical convenience, we shall take n modes even if some of them are not physically distinct such as the x and y polarization of an electromagnetic wave $\sim E \exp(ikz)$ in an isotropic medium. We introduce the wave mode amplitude vector

$$Q(k;t) = S^{-1}(k)\Psi(k;t), \tag{3.170}$$

which satisfies the following diagonal equation

$$-i\frac{\partial Q(k;t)}{\partial t} = D(k)Q(k;t). \tag{3.171}$$

The jth component of $Q(k;t)$ is called the complex amplitude of the jth wave mode; it satisfies a separate propagation equation

$$-i\frac{\partial Q_j(k;t)}{\partial t} = \omega_j(k)Q_j(k;t) \tag{3.172}$$

without summation on j. We may conclude that in a nonrandom anisotropic medium different wave modes are uncoupled. We also define the spectral energy density of the jth wave mode:

$$E_j(k;t) = |Q_j(k;t)|^2. \tag{3.173}$$

If the medium is lossless, the frequencies $\omega_j(k)$ are real and the spectral energy densities remain constant. We shall see that in the random case there are energy transfers from one mode to another.

Random Case. Let us assume now that the parameters of the medium are stationary random functions of position and the medium is statistically homogeneous. Separating the mean values from the random part yields the random propagation equation as

$$\frac{\partial \Psi_j(r;t)}{\partial t} = b_{jlm}\nabla_l\Psi_m(r;t) + \varepsilon\delta b_{jlm}(r)\nabla_l\Psi_m(r;t) \tag{3.174}$$

where ε is a small parameter; $\delta b_{jlm}(r)$ are stationary centered random function of r. Taking the FT of (3.174) and using matrix notations, we have

$$-i\frac{\partial \Psi(k;t)}{\partial t} = A(k)\Psi(k;t) + \varepsilon\int \delta A(k-k')\Psi(k')\mathrm{d}^3k'. \tag{3.175}$$

$A(k)$ is defined by (3.168) and

$$\delta A_{jm}(k) = \delta b_{jlm}k_l. \tag{3.176}$$

Expression (3.175) is a random integral equation, which could be used as the starting point of a perturbation expansion. Following Reference [31], we first diagonalize $A(k)$ in order to obtain a set of coupled equations for the wave mode amplitudes. The wave modes are defined in the same way as for the nonrandom case, that is, as for $\varepsilon = 0$. This is perhaps somewhat artificial but is well justified if the parameter fluctuations are not too strong. The wave mode amplitude vector being defined by (3.170), we obtain a set of coupled integral equations

$$-i\frac{\partial Q(k;t)}{\partial t} = D(k)Q(k;t) + \varepsilon\int C(k,k')Q(k';t)\mathrm{d}^3k' \tag{3.177}$$

with

$$C(k,k') = S^{-1}(k)\delta A(k-k')S(k).$$

Using tensor notations, we get

$$-i\frac{\partial Q_j(k;t)}{\partial t} = \omega_l(k)\delta_{lj}Q_j(k;t) + \varepsilon\int C_{jl}(k,k')Q_l(k';t)\mathrm{d}^3k' \tag{3.178}$$

The random integral operator $C_{jl}(k,k')$ gives the coupling between wave modes for $j \neq l$, and the scattering (or self coupling) for $j = l$.

Equations (3.177) and (3.178) are fundamental equations for wave mode coupling, which we shall use as a starting point for the perturbation expansion and the random variable approximation (lowest order of a random Taylor expansion) in energy transfer.

3.9.2. Energy Transfer Between Wave Modes

Let us begin with the perturbation method at long wavelengths ($K\ell \ll 1$). The LT of $Q(k;t)$

$$\tilde{Q}(k;z) = \int_0^\infty \exp(izt)Q(k;t)\mathrm{d}t \tag{3.179}$$

satisfies

$$[-iz - iD(k)]\tilde{Q}(k;z) - i\varepsilon \int C(k,k')\tilde{Q}(k';z)\mathrm{d}^3k = Q(k,0). \tag{3.180}$$

This equation is of the type

$$(L_0 + \varepsilon L_1)Q = \mathbf{j} \tag{3.181}$$

considered in Section 3.2. As in this section, we introduce the unperturbed propagator

$$G^{(0)} = L_0^{-1} = [-iz - iD(k)]^{-1}, \tag{3.182}$$

which is a diagonal operator, and the perturbed propagator

$$G = (L_0 + \varepsilon L_1)^{-1}. \tag{3.183}$$

The diagram methods for the mean perturbed propagator and the mean double propagator are easily extended to this problem. The only differences being that the solid line and the dot are no more scalar operators but tensor (or matrix) operators. The only new feature is the coupling between wave modes (see Reference [31]). As we want to avoid unnecessary complications, we shall only take two wave modes and assume that there are no self-coupling terms and no losses. Thus we look at the following coupled wave equations:

$$-i\frac{\partial Q_1(k;t)}{\partial t} = i\omega_1(k)Q_1(k;t) + \varepsilon \int C_{12}(k,k')Q_2(k';t)\mathrm{d}^3k' \tag{3.184a}$$

$$-i\frac{\partial Q_2(k;t)}{\partial t} = i\omega_2(k)Q_2(k;t) + \varepsilon \int C_{21}(k,k')Q_1(k';t)\mathrm{d}^3k'. \tag{3.184b}$$

The medium being lossless, the total energy must be constant

$$\int [|Q_1(k;t)|^2 + |Q_2(k;t)|^2] d^3k = 0. \tag{3.185}$$

This implies that $\omega_1(k)$ and $\omega_2(k)$ are real and

$$C_{12}(k,k') = -C_{21}^*(k,k'). \tag{3.186}$$

We write now the Bourret's equation (see Section 3.4) for the mean propagator of Equation (3.181)

$$\langle G \rangle_{\mathrm{B}} = \underline{\quad\quad} + \underline{\quad\overset{\frown}{\quad\quad}\quad} \langle G \rangle_{\mathrm{B}}. \tag{3.187}$$

As there are only two modes, it is more convenient to have a scalar operator instead of a matrix one. For the unperturbed propagator being a diagonal matrix, it is sufficient to introduce, over the solid line, a superscript indicating the wave mode. Using this convention we write (3.187) as

$$\langle G_{11} \rangle_{\mathrm{B}} = \overset{1}{\underline{\quad\quad}} + \overset{1}{\underline{\quad}}\overset{2}{\overset{\frown}{\quad\quad}} \langle G_{11} \rangle_{\mathrm{B}}. \tag{3.188a}$$

$$\langle G_{22} \rangle_{\mathrm{B}} = \overset{2}{\underline{\quad\quad}} + \overset{2}{\underline{\quad}}\overset{1}{\overset{\frown}{\quad\quad}} \langle G_{22} \rangle_{\mathrm{B}}. \tag{3.188b}$$

As there are no self-coupling terms, $\langle G_{12} \rangle_{\mathrm{B}}$ and $\langle G_{21} \rangle_{\mathrm{B}}$ vanish. The consequence of the absence of self-coupling terms is thus the absence of coupling between the mean propagators (this is due to the fact that any Bourret diagram has an even number of vertices). But this will not prevent energy transfer between the wave modes, because the energy densities are calculated from the mean double propagator.

Let us find the behavior of $\langle G_{11} \rangle_{\mathrm{B}}$ for $t \gg t_{\mathrm{int}}$. It is determined by the scalar terms of the Bourret series and thus by

$$\lim_{z=-\omega_1(k)+i0} \overset{2}{\overset{\frown}{\quad\quad}} = i\beta_1(k). \tag{3.189}$$

In explicit from Equation (3.188a) becomes

$$[-iz - i\omega_1(k) - i\beta_1(k)]\langle G_{11} \rangle_{\mathrm{B}} = 1. \tag{3.190}$$

To derive this equation we have replaced $\underline{\quad\overset{\frown}{\quad}\quad}$ by $i\beta_1(k)$. Solving this equation we obtain

$$\langle G_{11}(k;t) \rangle = \exp\{i[\omega_1(k) + \beta_1(k)]t\}. \tag{3.191}$$

The frequency $\omega_1(k)$ has thus been renormalized. For the second wave mode from (3.188b) we find a similar result with $\beta_2(k) = -\beta_1^*(k)$.

Let us calculate $\beta_1(k)$. Writing

$$\langle B_{12}(k,k')B_{21}(k',k'')\rangle = \Gamma(k-k')\delta(k-k'') \qquad (3.192)$$

we obtain

$$\beta_1(k) = \lim_{\eta\to 0,\eta>0} \varepsilon \int \frac{\Gamma(k,k')}{\omega_1(k)-\omega_2(k)-i\eta}\mathrm{d}^3k'. \qquad (3.193)$$

$\Gamma(k,k')$ is a positive measure (FT of a covariance function), accordingly the imaginary part of $\beta_1(k)$ is positive and $\langle G_{11}(k;t)\rangle$ is damped. It is possible to evaluate this imaginary part by a dimensional analysis of (3.188a)

$$\left|\frac{\mathrm{Im}\beta_1(k)}{\omega_1(k)}\right| \sim \varepsilon^2 K^2 \ell^3 \ll 1. \qquad (3.194)$$

Now we turn our attention to the mean double propagator and calculate the mean spectral energy densities $\langle|Q_1(k;t)|^2\rangle$, $\langle|Q_2(k;t)|^2\rangle$. They do not satisfy any propagation equation but are deducible from $\langle\tilde{Q}_1(k;z)\tilde{Q}_1^*(k;z')\rangle$ and $\langle\tilde{Q}_2(k;z)\tilde{Q}_2^*(k;z')\rangle$, which satisfy the following equations of the Bourret's approximation

$$\left\langle\tilde{Q}_1(k;z)\tilde{Q}_1^*(k;z')\right\rangle = \underline{\underline{\frac{1}{\quad 1\quad}}}\tilde{Q}_1(k;0)\tilde{Q}_1^*(k;0) + \underline{\underline{\frac{1}{\quad 1\quad}}}\left\langle\tilde{Q}_2(k';z)\tilde{Q}_2^*(k';z')\right\rangle$$

$$(3.195a)$$

$$\left\langle\tilde{Q}_2(k;z)\tilde{Q}_2^*(k;z')\right\rangle = \underline{\underline{\frac{2}{\quad 2\quad}}}\tilde{Q}_2(k;0)\tilde{Q}_2^*(k;0) + \underline{\underline{\frac{2}{\quad 2\quad}}}\left\langle\tilde{Q}_1(k';z)\tilde{Q}_1^*(k';z')\right\rangle$$

$$(3.195b)$$

$\langle\tilde{Q}_1(k;z)\tilde{Q}_1^*(k;z')\rangle$ is the FT of $\langle\tilde{Q}_1(k;t)\tilde{Q}_1^*(k;t')\rangle$ with respect to t and t'. It is interesting to solve (2.195a) with the following initial conditions:

$$\begin{aligned}\tilde{Q}_1(k;0)\tilde{Q}_1^*(k;0) &= E_0\delta(k-k_0)\\ \tilde{Q}_2(k;0)\tilde{Q}_2^*(k;0) &= 0\end{aligned} \qquad (3.196)$$

for which the total initial energy of the wave is concentrated in the first wave mode with a single spectral line. Eliminating $\langle\tilde{Q}_1(k;z)\tilde{Q}_1^*(k;z')\rangle$ between (3.195a) and (3.195b) we obtain:

$$\left\langle\tilde{Q}_2(k;z)\tilde{Q}_2^*(k;z')\right\rangle = \underline{\underline{\frac{2\;\big|\;1}{2\;\big|\;1}}}E_0\delta(k'-k_0) + \underline{\underline{\frac{2\;\big|\;1}{2\;\big|\;1}}}\left\langle\tilde{Q}_2(k';z)\tilde{Q}_2^*(k';z')\right\rangle.$$

$$(3.197)$$

This integral equation can be solved by successive approximations. This method does not give singular terms because they have already been taken into account in the mean (single) propagators

$$
\underline{\underline{\frac{1}{\quad}}} = \frac{i}{z + \omega_1(k) + \beta_1(k)}, \qquad \underline{\underline{\frac{2}{\quad}}} = \frac{i}{z + \omega_2(k) + \beta_2(k)}. \tag{3.198}
$$

Let us calculate the lowest order approximation for $\langle \tilde{Q}_2(k;z)\tilde{Q}_2^*(k;z')\rangle$:

$$
\underline{\underline{\begin{array}{c|c} 2\,k & 1\,k' \\ \hline 2\,k & 1\,k' \end{array}}} E_0\delta(k'-k_0) = \frac{i}{[z+v_2(k)]}\frac{-i}{[z'^*+v_2^*(k)]}\varepsilon^2 E_0\Gamma(k,k_0)\;\frac{i}{[z+v_1(k_0)]}\frac{-i}{[z'^*+v_1^*(k_0)]}. \tag{3.199}
$$

We denote $v_1(k)$ and $v_2(k)$ the renormalized frequencies:

$$
\begin{aligned}
v_1(k) &= \omega_1(k) + \beta_1(k) \\
v_2(k) &= \omega_2(k) + \beta_2(k) = \omega_2(k) - \beta_1^*(k). \tag{3.200}
\end{aligned}
$$

Taking the inverse LT of (3.199), we obtain the following expression for the spectral energy density of the second mode as a function of time

$$
E_2(k;t) = \varepsilon^2\Gamma(k-k_0)\left|\frac{\exp(iv_2(k)t) - \exp(iv_1(k_0)t)}{v_2(k) - v_1(k_0)}\right|^2. \tag{3.201}
$$

The Born approximation would give the same result with the frequencies ω_1 and ω_2 instead of renormalized frequencies v_1 and v_2. Accordingly, it would be secular for any wave vector such that

$$
\omega_2(k) = \omega_1(k_0). \tag{3.202}
$$

This is now prevented by the imaginary part of $v(k)$. Let us assume that the real part of β_1 and β_2 have been incorporated into ω_1 and ω_2, and recall that the imaginary part of β_1 and β_2 are small compared to ω_1 and ω_2. It is then easily found that $E_2(k;t)$ can only be important for wave vectors which satisfy the coupling conditions:

$$
|\omega_2(k) - \omega_1(k_0)| < |\beta_1(k_0)|. \tag{3.203}
$$

and that the maximum of $E_2(k;t)$ occurs for $t \sim 1/|\beta_1(k_0)| \equiv t_{\rm d}$, which is the

damping time of the mean propagator. The maximum of $E_2(k;t)$

$$E_2(k;t_d) = \frac{\varepsilon^2 \Gamma(k,k_0)}{|\beta_1^2(k_0)|}.$$ (3.204)

If we want to obtain the total energy transfer from the first wave mode to the second one, we must integrate (3.204) over all wave vectors satisfying the coupling condition (3.203). As β_1 is proportional to ε^2, the total energy transfer is found to be independent of the strength of random fluctuations. A dimensional analysis of the total energy transfer shows that it is of order unity (i.e., independent of ε^2, c, K, ℓ etc.) for $t \sim t_d$. As t_d is proportional to ε^{-2}, the energy transfer may take a very long time for small random fluctuations.

Next we study the other limiting approximation of *short wavelengths* satisfying $\varepsilon K \ell \gg 1$. As we have seen in Section 3.5, we may treat the random parameters as mere random variables. The coupled wave Equations (3.184a and b) become now ordinary differential equations with a random parameter

$$\frac{\partial Q_1(t)}{\partial t} = i\omega_1 Q_1(t) + i\varepsilon b Q_2(t)$$ (3.205a)

$$\frac{\partial Q_2(t)}{\partial t} = i\omega_2 Q_2(t) + i\varepsilon b Q_1(t).$$ (3.205b)

We have dropped the wave vector dependence because there is no more coupling between different wave vectors. We shall assume that b is a real centered random variable. Equations (3.205a and b) describe a set of two randomly coupled oscillators. We solve (3.205) with initial conditions such that the initial energy of the wave is concentrated in the first mode, that is, $Q_1(0) = 1$ and $Q_2(0) = 0$. Using the LT, we get the following solutions

$$Q_1(t) = \frac{q_1 + \omega_1}{\sqrt{\Delta}} \exp\{-iq_1 t\} - \frac{q_2 + \omega_2}{\sqrt{\Delta}} \exp\{-iq_2 t\}$$ (3.206a)

$$Q_2(t) = \frac{-ib}{\sqrt{\Delta}} [\exp\{-iq_1 t\} - \exp\{-iq_2 t\}]$$ (3.206b)

with

$$\Delta = (\omega_1 - \omega_2)^2 + 4b^2 \varepsilon^2$$

$$q_{1,2} = \frac{-(\omega_1 - \omega_2) \pm \sqrt{\Delta}}{2}.$$

The mean energy of the second wave mode at time t is thus

$$E_2(t) = \langle |Q_2(t)|^2 \rangle = \left\langle \frac{2\varepsilon b^2}{(\omega_1 - \omega_2)^2 + 4b^2\varepsilon^2} \left(1 - \cos\left(t\sqrt{(\omega_1 - \omega_2)^2 + 4b^2\varepsilon^2} \right) \right) \right\rangle$$

(3.207)

or in terms of the probability density $P(b)$ of the random variable b

$$E_2(t) = \int_{-\infty}^{\infty} |Q_2(t)|^2 P(b) db.$$

(3.208)

Let us first assume that $\omega_1 = \omega_2$, then

$$E_2(t) = \frac{1}{2} \int_{-\infty}^{\infty} (1 - \cos 2bt) P(b) db$$

(3.209)

as $t \to \infty$ and then $E_2(t) \to \frac{1}{2}$. In the more general case $\omega_1 \neq \omega_2$, we take the probability density as

$$P(b) = \frac{\sigma}{\pi} \frac{1}{(b^2 + \sigma^2)}.$$

(3.210)

The asymptotic energy distribution is easily calculated by means of a LT.

$$\lim_{t \to \infty} \langle E_2(t) \rangle = \frac{1}{2} \frac{2\varepsilon\sigma}{[2\varepsilon\sigma + |\omega_2 - \omega_1|]} \leq \frac{1}{2}.$$

(3.211)

The condition of effective energy transfer is thus

$$|\omega_2 - \omega_1| \leq 2\varepsilon\sigma.$$

(3.212)

It is found that the time required to reach the equilibrium energy distribution is of the order of magnitude of $(\varepsilon\sigma)^{-1}$. The situation is the same as in the long wavelength approximation, that is:

We have an important energy transfer in a medium with very small random fluctuations, but this requires a very long time.

Also, we note that in the long time behavior of a random medium, energy transfer is always an important process between waves whose frequencies are not very different (see condition (3.203) at long wavelengths, and condition (3.212) at short wavelengths).

BIBLIOGRAPHY

[1] Dyson, F., ''The radiation theories of Tomonaga, Schwinger, and Feynman,'' *Phys. Rev.*, vol. 75, 1949, pp. 486–497.

[2] Foldy, L. L., ''The multiple scattering of waves. I. General theory of isotropic scattering by randomly distributed scatterers,'' *Phys. Rev.*, vol. 67, 1945, pp. 107–119.

[3] Lax, M., ''Multiple scattering of waves,'' *Rev. Modern Phys.*, vol. 23, 1951, pp. 287–310.

[4] Lax, M., ''Multiple scattering of waves. II. The effective field in dense systems,'' *Phys. Rev.*, vol. 85, 1952, pp. 621–629.

[5] Furutsu, K., ''On the group velocity, wave path and their relations to the Poynting vector of E-M field in an absorbing medium,'' *J. Phys. Soc. Japan*, vol. 7, 1952, pp. 458–478.

[6] Salpeter, E. E., and H. A. Bethe, ''A relative equation for bound-state problems,'' *Phys. Rev.*, vol. 84, 1951, pp. 1232–1239.

[7] Furutsu, K., ''On the statistical theory of electromagnetic waves in a fluctuating medium (I),'' *J. Res. NBS* (*Radio Prop.*), vol. 67D, 1963, pp. 303–323.

[8] Matsubara, T., ''A new approach to quantum-statistical mechanics,'' *Prog. Theoret. Phys.*, vol. 14, 1955, pp. 351–361.

[9] Martin, P. C., and J. Schwinger, ''Theory of many-particle systems (I),'' *Phys. Rev.*, vol. 115, 1959, pp. 1342–1349.

[10] Schwinger, J., ''On the Green's functions of quantized fields, I, II,'' *Proc. Natl. Acad. Sci.*, vol. 37, 1951, 452–455.

[11] Twersky, V., ''Multiple scattering of electromagnetic waves by arbitrary configurations,'' *J. Math. Phys.*, vol. 8, 1967, pp. 569–610.

[12] Buslaev, V. S., *in* Birman, M. Sh., ed., *Topics in Mathematical Physics*, Consultans Bureau, New York, vol. 2, 1968.

[13] Bourret, R. C., ''Fiction theory of dynamical systems with noisy parameters,'' *Can. J. Phys.*, vol. 43, 1965, pp. 619–627.

[14] Keller, J. B., ''Stochastic equations and wave propagation in random media,'' *Proc. Sympos. Appl. Math.*, vol. 13, Amer. Math. Soc., Providence, R. I., 1964, pp. 145–147.

[15] Chernov, L. A., *Wave Propagation in a Random Medium*, McGraw-Hill, New York, 1960.

[16] Tatarskii, V. I., *Wave Propagation in a Turbulent Medium*, McGraw-Hill, New York, 1961.

[17] Tatarskii, V. I., and M. E. Gertsenshtein, ''Propagation of wave in a medium with strong fluctuations of the refractive index,'' *JEFT*, vol. 17, 1967, pp. 548–563.

[18] Charnotskii, M. I., J. Gozani, V. I. Tatarskii, et al., *in* Wolf, E., ed., *Progress in Optics*, Elsevier, Amsterdam Holland, Vol. 32, 1993.

[19] Bassanini, P., ''Wave propagation in a one-dimensional random medium,'' *Radio Sci.*, vol. 2, 1967, pp. 429–436.

[20] Kieburts, R. B., ''Application of coherence theory to propagation of a quasi-monochromatic field in a random medium,'' *IEEE Trans. Antennas and Propag.*, vol. AP-15, No. 1, pp. 76–80.

[21] Brown, W. P. Jr, ''Propagation in random media-Cumulative effect of weak inhomogeneities,'' *IEEE Trans. Antennas and Propag.*, vol. AP-15, 1967, pp. 81–89.

[22] Furutsu, K., *On the Statistical Theory of Electromagnetic Waves in a Fluctuating Medium (II)*, NBS Monograph, No. 79, 1964, pp. 1–44.

[23] Kraichnan, R. H., ''Dynamics of nonlinear stochastic systems,'' *J. Math. Phys.*, vol. 2, 1961, pp. 124–148.

[24] Ishimaru, A., *Electromagnetic Wave Propagation, Radiation, and Scattering*, Prentice-Hall, Englewood Clifs, New Jersey, 1991.

[25] Balesku, R., *Equilibrium and Nonequilibrium Statistical Mechanics*, John Wiley and Sons, New York-London, 1975.

[26] Blaunstein, N, *Wireless Communication Systems*, Chapter 12 *in Handbook of Engineering Electromagnetics*, Ed. R. Bansal, New York, Marcel Dekker, 2004, pp. 417–481.

[27] Blaunstein, N., D. Katz, D. Censor et al., ''Prediction of loss characteristics in built-up areas with various buildings' overlay profile,'' *IEEE Anten. Propagat. Magazine*, vol. 43, 2001, pp. 181–191.

[28] Blaunstein, N., D. Censor, D. Katz, et al., ''Radio propagation in rural residential areas with vegetation,'' *J. Electromagnetic Waves and Applications*: *Progress In Electromagnetics Research*, PIER 40, 2003, pp. 131–153.

[29] Blaunstein, N., I. Z. Covacs, D. Katz, et al., ''Prediction of UHF path loss for forested environments,'' *Radio Science*, vol. 38, No. 3, 2003, pp. 1059–1075.

[30] Sonnenschein, E., N. Blaunstein, and D. Censor, ''Ray propagation in the presence of resonance heated ionospheric plasma,'' *Journal of Atmospheric, Terrestrial and Solar Physics*, vol. 60, No. 12, 1998, pp. 1605–1623.

[31] Blaunstein, N., ''Theoretical aspects of wave propagation in random media based on quanty and statistical field theory,'' *J. Electromagnetic Waves and Applications*: *Progress In Electromag. Research, PIER* 47, 2004, pp. 135–191.

Electromagnetic Aspects of Wave Propagation over Terrain

When both antennas are far from the ground surface a *free-space propagation* concept is usually used, which is based on the scalar (3.1) and (3.2) or vector (3.3) wave equation description, valid for infinite source-free homogeneous media. In Section 4.1, based on Green's theorem and the Huygen's principle, we introduce the Fresnel zone presentation that will be used for the description of terrain and other obstruction effects, such as reflection and diffraction on radio channels. In Section 4.2, we present the main formulas for path loss prediction for a free-space communication link. Next, in Section 4.3, the reflection phenomena due to a flat terrain are described [1–4]. Here, on the basis of Huygen's principle, Fresnel zone concepts, and stationary phase methods, we analyze all the reflection phenomena and give the main formulas for the resultant reflection coefficients. Section 4.4 deals with the electromagnetic aspects of radio wave propagation above a rough terrain. Here, the three methods of mathematical derivation of the field strength are presented to obtain the effects of radio wave scattering from ground surfaces with various roughnesses (large, medium and small) with respect to the wavelength. In Section 4.5, the effect of the ground curvature is considered by using Fock's theory of diffraction. Section 4.6 describes diffraction phenomena caused by a single obstruction placed on a flat ground surface.

4.1. WAVES PROPAGATION IN FREE SPACE

Let us rewrite Equations (3.1)–(3.3) by introducing the wave number k instead of refractive index n and the speed of light c, that is,

$$\nabla^2 \Psi(\mathbf{r}) - k^2 \Psi(\mathbf{r}) = 0. \tag{4.1}$$

Here Ψ represents each Cartesian component of the electric and magnetic fields of the wave and $k = \frac{2\pi}{\lambda}$, where λ is the wavelength.

4.1.1. A Plane, Cylindrical and Spherical Wave Presentation

The solution of Equation (4.1) is

$$\Psi(\mathbf{r}) = \exp\{i\mathbf{k} \cdot \mathbf{r}\} \tag{4.2}$$

The waves that satisfy the scalar equation (4.1) described by the solution (4.2) are called *plane waves*. The wave vector $\mathbf{k}$ denotes the direction of propagation of the plane wave in free space. For any desired direction in the Cartesian coordinate system, the corresponding solution can be immediately obtained from (4.1) and (4.2). For example, if the plane wave propagates along the x-axis, the solution of (4.1) is [1–3]

$$\Psi(x) = A \exp\{ikx\} + B \exp\{-ikx\} \tag{4.3}$$

This solution describes the waves propagating in the positive direction (with the sign "+") and the negative direction (with sign "−") along the x-axis with phase velocity $v_{\text{ph}} = \frac{2\pi f}{k} = \frac{c}{\sqrt{\varepsilon\mu}}$, where f is the radiated frequency. In free space, if the permittivity is $\varepsilon \equiv \varepsilon_0 \approx \frac{10^{-9}}{36\pi} \frac{F}{m}$ and the permeability is $\mu \equiv \mu_0 \approx 4\pi \cdot 10^{-7} \frac{H}{m}$, then the phase velocity in an ideal free space is simply the speed of light $c = 10^8$ m/s.

In the cylindrical coordinate system $\{\rho, \varphi, z\}$, the scalar wave equation, which describes the propagation of *cylindrical waves* in free space, can be written as in Reference [3]

$$\left(\frac{1}{\rho}\frac{\partial}{\partial\rho}\rho\frac{\partial}{\partial\rho} + \frac{1}{\rho^2}\frac{\partial^2}{\partial\varphi^2} + \frac{\partial^2}{\partial z^2}\right)\Psi(\mathbf{r}) = 0 \tag{4.4}$$

This equation has an approximate solution, which can be presented in the following exponential form [2–4]:

$$\Psi(\mathbf{r}) \approx \sqrt{\frac{2}{\pi k_\rho \rho}} \exp\left\{-i\frac{n\pi}{2} - i\frac{\pi}{4}\right\} \exp\left\{i\left[\frac{n}{\rho}(\rho\varphi) + ik_\rho\rho + ik_z z\right]\right\}. \tag{4.5}$$

Here, $\rho\varphi$ is the arc length in the φ direction, $k_\rho = \sqrt{k^2 - k_z^2}$, and n/ρ can be considered as the component of vector $\mathbf{k}$ if one compares the cylindrical wave

presentation as in (4.5) with that of a *plane wave* in (4.2). Consequently, (4.5) looks like a plane wave in the direction $k' = k_z z + k_\rho \rho$, when $\rho \to \infty$.

In the spherical coordinate system $\{r, \theta, \varphi\}$, the scalar wave equation, which describes propagation of *spherical waves* in free space, can be written as in References [1–3]

$$\left(\frac{1}{r^2} \frac{\partial}{\partial r} r^2 \frac{\partial}{\partial r} + \frac{1}{r^2 \sin^2 \theta} \frac{\partial}{\partial \theta} \sin \theta \frac{\partial}{\partial \theta} + \frac{1}{r^2 \sin^2 \theta} \frac{\partial^2}{\partial \varphi^2} + k^2 \right) \Psi(\mathbf{r}) = 0 \qquad (4.6)$$

As shown in [3], the spherical wave can be approximated by $\frac{\exp\{ikr\}}{r}$. Thus, one can represent the spherical wave as a plane wave, when $r \to \infty$.

4.1.2. Green's Function Presentation

Green's function is used in the description of any arbitrary source in an unbounded homogeneous medium, taking into account that each source $s(\mathbf{r})$ can be represented as a linear superposition of point sources. Mathematically this can be expressed as

$$s(\mathbf{r}) = \int d\mathbf{r}' s(\mathbf{r}') \delta(\mathbf{r} - \mathbf{r}') \qquad (4.7)$$

The scalar wave equation with the source in the right-hand side can be presented as

$$\nabla^2 \Psi(\mathbf{r}) - k^2 \Psi(\mathbf{r}) = s(\mathbf{r}) \qquad (4.8)$$

and the corresponding equation for the Green's function in an unbounded homogeneous medium can be presented as

$$\nabla^2 G(\mathbf{r}, \mathbf{r}') - k^2 G(\mathbf{r}, \mathbf{r}') = -\delta(\mathbf{r} - \mathbf{r}'). \qquad (4.9)$$

The solution of Equation (4.9) is [1–3]

$$G(r) = \frac{1}{4\pi} \frac{\exp\{ikr\}}{r} \qquad (4.10)$$

and the corresponding solution of (4.8) is

$$\Psi(\mathbf{r}) = - \int_V d\mathbf{r}' G(\mathbf{r}, \mathbf{r}') s(\mathbf{r}'). \qquad (4.11)$$

The geometry of the source $s(\mathbf{r})$ in a space with volume V is shown in Figure 4.1. Using Equation (4.10) one can easily obtain a general solution for the inhomogeneous
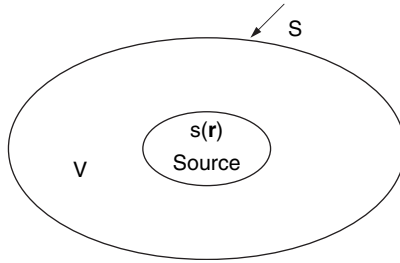
FIGURE 4.1. Geometrical presentation of a source $s(\mathbf{r})$ inside an arbitrary volume V bounded by a surface S.

Equation (4.8) given by

$$\Psi(\mathbf{r}) = -\int_V d\mathbf{r}' \frac{\exp\{ik|\mathbf{r} - \mathbf{r}'|\}}{4\pi|\mathbf{r} - \mathbf{r}'|} s(\mathbf{r}'). \qquad (4.12)$$

This presentation is valid for any component of an EM-wave, propagating in free space, and it satisfies the principle of linear superposition of *point sources* (4.7) for any real source of radiation.

4.1.3. Huygen's Principle

This concept is based on presenting the wave field far from any sources as shown in Figure 4.2. Here the point of observation A can be either outside the bounded surface S, as shown in Figure 4.2a, or inside, as shown in Figure 4.2b. In other words, according to Huygen's principle, each point at the surface S can be presented as an elementary source of a spherical wave, which can be observed at point A. Mathematically, the Huygen's concept can be explained by the use of Green's function. First, we multiply the homogeneous Equation (4.1) (without any source) by $G(\mathbf{r}, \mathbf{r}')$ and the inhomogeneous Equation (4.9) by $\Psi(\mathbf{r})$. Substracting the resulting equations from each other and integrating over a volume V containing
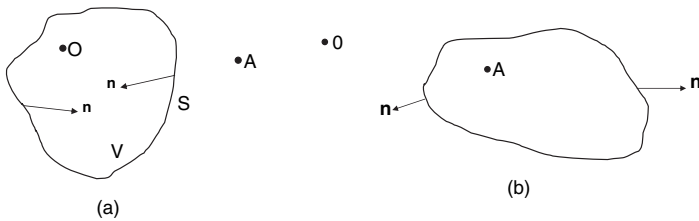
FIGURE 4.2. Geometrical explanation of the Huygen's principle in a bounded surface when the receiver is located at point *A* outside and inside the bounded surface and when the transmitter is located at point *O*.
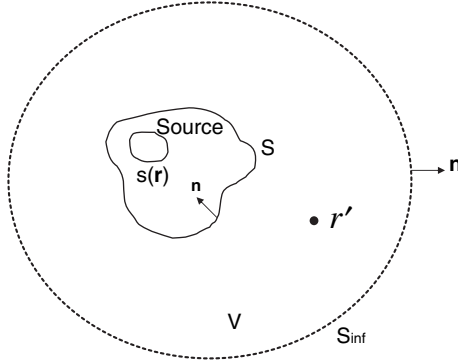
FIGURE 4.3. The geometry for derivation of Green's theorem for the two different boundary conditions at the bounded surface S; Neumann and Dirihlet.

vector $\mathbf{r}'$ (see Fig. 4.3), yields

$$\Psi(\mathbf{r}') = \int_V d\mathbf{r}\lfloor G(\mathbf{r}, \mathbf{r}')\nabla^2\Psi(\mathbf{r}) - \Psi(\mathbf{r})\nabla^2 G(\mathbf{r}, \mathbf{r}')\rfloor \qquad (4.13)$$

from which we can obtain *Green's theorem* or the *second Green formula* [1–3]:

$$\int_V d\mathbf{r}[G(\mathbf{r}, \mathbf{r}')\nabla^2\Psi(\mathbf{r}) - \Psi(\mathbf{r})\nabla^2 G(\mathbf{r}, \mathbf{r}')] = \oint_S ds\left[G(\mathbf{r}, \mathbf{r}')\frac{\partial\Psi(\mathbf{r})}{\partial\mathbf{n}} - \Psi(\mathbf{r})\frac{\partial G(\mathbf{r}, \mathbf{r}')}{\partial\mathbf{n}}\right]$$

$$(4.14)$$

This formula can be simplified using different boundary conditions on surface S. Using the relation between arbitrary scalar functions f and g: $fg \cdot \mathbf{n} = f\frac{\partial g}{\partial\mathbf{n}}$, we can write

$$\Psi(\mathbf{r}') = \oint_S ds\mathbf{n} \cdot [G(\mathbf{r}, \mathbf{r}')\nabla\Psi(\mathbf{r}) - \Psi(\mathbf{r})\nabla G(\mathbf{r}, \mathbf{r}')] \qquad (4.15)$$

Next, if we assume that $\mathbf{n} \cdot \nabla G(\mathbf{r}, \mathbf{r}') = 0$ at the boundary surface S, defined by the radius vector $\mathbf{r}$, Equation (4.15) becomes

$$\Psi(\mathbf{r}') = \oint_S ds\, G(\mathbf{r}, \mathbf{r}')\mathbf{n} \cdot \nabla\Psi(\mathbf{r}) \qquad (4.16)$$

If the boundary condition $\nabla G(\mathbf{r}, \mathbf{r}') = 0$ is applied at the surface S, then Equation (4.15) becomes

$$\Psi(\mathbf{r}') = -\oint_S ds\Psi(\mathbf{r})\mathbf{n} \cdot \nabla G(\mathbf{r}, \mathbf{r}') \qquad (4.17)$$
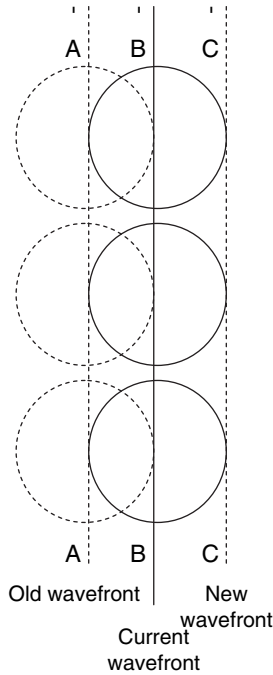
FIGURE 4.4. Geometry of plane wave-ray presentation of Huygens principle in free space.

Equations (4.15)–(4.17) are various forms of the Huygen's principle depending on the definition of the Green's function on the bounded surface S. Equations (4.16) and (4.17) state that only $\mathbf{n} \cdot \nabla \Psi(\mathbf{r})$ or $\Psi(\mathbf{r})$ need to be known, respectively, on the surface S in order to determine the solution of a wave function $\Psi(\mathbf{r}')$ at the observation point $\mathbf{r}'$.

In unbounded homogeneous media, as in free space, the Huygen's principle has a clear and physical explanation. Each spherical wave can be presented as a plane wave in the far field. In this case, the elementary spherical waves called wavelets, created by each virtual point source (the dimensions of which are smaller than the wavelength) can be represented by the straight line called wave fronts, as shown in Figure 4.4. Therefore, the phenomenon of straight-line radio wave propagation is the same as that of the light ray propagation in optics. This is the reason why sometimes in radio propagation the term ''ray'' is usually used instead of the term ''waves.''

4.1.4. The Concept of Fresnel Zones for Free Space

The Fresnel-zone concept is used to describe diffraction phenomena from obstructions in the path of two antennas based on the Huygen's principle. As the latter is useful both for free space and for various finite areas with obstructions, it is
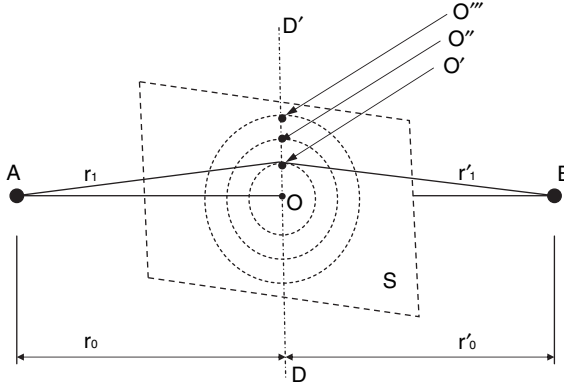
FIGURE 4.5. Fresnel-zone concept presentation in free space.

important to show both mathematically and physically the meaning of the Fresnel-zone concept when both terminal antennas are high enough that the LOS conditions are fully satisfied. In free space, on the basis Huygen's principle, instead of virtual point sources at an arbitrary surface S, as shown in Figures 4.2–4.4, we introduce virtual sources along some virtual wave front DD', as shown in Figure 4.5. In this figure, points A and B denote the position of the terminal antennas. The virtual plane S is the plane that covers each virtual source located at line DD' through which the plane S is passed. This imaginary plane is normal to the LOS path between two terminals, A and B, and passes across the point O at the line AB, as shown in Figure 4.5. For such geometry, the Green's theorem (4.14) can be rewritten for any vector namely, the Hertz-vector in [1–4] as

$$\Pi(\mathbf{R}) = \int_S ds \, \frac{\partial \Pi(\mathbf{R'})}{\partial \mathbf{n}} \frac{\exp\{ik|\mathbf{R} - \mathbf{R'}|\}}{|\mathbf{R} - \mathbf{R'}|} \tag{4.18}$$

where $|\mathbf{R} - \mathbf{R'}| = \mathbf{r'_1}$ is the distance from any point O_i $i = 1, 2, \ldots$, at the imaginary plane S and the observer at point B. If the radiation source located at point A is assumed to be point one with Green's function $G \sim \frac{e^{ikr_1}}{r_1}$, then for any point $O_i(O_1$ in Fig. 4.5), we have according by

$$\Pi(\mathbf{R}) = \frac{1}{2\pi} \int_S ds \left(\frac{1}{r_1} - ik\right) \frac{r_0}{r_1} \frac{\exp\{ik(r_1 + r'_1)\}}{r_1 r'_1} \tag{4.19}$$

as $\frac{\partial r_1}{\partial n} = -\frac{r_0}{r_1}$.

All distances denoted inside the integral are shown in Figure 4.5.

Because the wave in the far field (Fraunhofer zone) between the plane S and two terminals A and B, that is in the case of $r_1 \gg \lambda$ and $r_1' \gg \lambda$, $\frac{1}{r_1} \ll ik$, we have one term with fast oscillations $\sim \exp\{ik(r_1 + r_1')\}$, even for small changes of variable r, and a second term $\sim ik\frac{r_0}{r_1}$, with very slow variations of variable r. In this case, the well known method of stationary phase can be used to derive such an integral, containing both slow and fast terms inside the integrand. Following Reference [4], we can write

$$\Pi(B) \approx -\frac{ik}{2\pi r_0 r_0'} \exp\{ik(r_0 + r_0')\}$$
$$\times \iint dxdy \exp\left\{i\frac{k}{2}\left(\frac{1}{r_0} + \frac{1}{r_0'}\right)x^2\right\} \exp\left\{i\frac{k}{2}\left(\frac{1}{r_0} + \frac{1}{r_0'}\right)y^2\right\}. \tag{4.20}$$

Using

$$\int\limits_{-\infty}^{\infty} \exp\{i\alpha x^2\}dx = \sqrt{i\frac{\pi}{\alpha}},$$

we can rewrite equation (4.20) as [3]

$$\Pi(B) \approx -\frac{ik}{2\pi r_0 r_0'} \exp\{ik(r_0 + r_0')\}\frac{2i\pi r_0 r_0'}{k(r_0 + r_0')} = \frac{\exp\{ikr\}}{r} \tag{4.21}$$

where $r = r_0 + r_0'$ is the distance between the source located at point A and the observer located at point B. So, from Equation (4.21), if the source A at the plane S creates a field $\sim \frac{e^{ikr_1}}{r_1}$, then the virtual point source, at the observed point B uniformly distributed at S, will create a field $\sim \frac{e^{ikr}}{r}$. The same is valid for the direct wave from A to B. This is a main conclusion that results from the Huygen's principle. Moreover, additional analysis of Integral in (4.19) shows that the plane S can be split into concentric circles of arbitrary radii. From Figure 4.5, one can see that each wave path through any virtual point $O^{(i)}$ is longer than the direct path AOB, that is $AO^{(i)}B > AOB$. While passing from one circle to another, the real and the imaginary parts of the integrand in (4.19) change their sign. The boundaries of these circles satisfy the conditions [4–6]

$$k\{(r_1 + r_1') - (r_0 + r_0')\} = n\frac{\pi}{2}, \quad n = 1, 2, \ldots \tag{4.22}$$

These circles are usually called *Fresnel zones*. Their physical meaning is that only in the first central circle, the virtual sources at the plane S, which lie within the first zone, send to an observer B at point radiation with the same phase for each original wave. Sources from two neighboring zones send respective radiation in

anti-phase, that is, nulling each other. The radius of the corresponding circle for each Fresnel zone shown at the plane S in Figure 4.5 can be expressed in terms of a zone number n and the distance between points A and B and the imaginary plane S as [4–6]

$$h_n = \sqrt{\frac{n\lambda r_0 r_0'}{(r_0 + r_0')}} \tag{4.23}$$

from which the radius of the first Fresnel zone is

$$h_1 = \sqrt{\frac{\lambda r_0 r_0'}{(r_0 + r_0')}} \sim \sqrt{\lambda R} \tag{4.24}$$

R is the minimal range from each r_0 and r_0'. The width of each circle, Δh, can be easily obtained as in References [4–6]

$$\Delta h \approx \frac{\pi}{2k} \frac{R}{h} \sim \frac{h_1^2}{h} \ll h_1 \tag{4.25}$$

where $h = \sqrt{x^2 + y^2}$. From (4.23) and (4.25), the width of the circles decreases with an increase in the zone number n. At the same time, the area of these zones is not dependent on zone number n, that is,

$$2\pi h \Delta h \sim \frac{\pi}{2} \lambda R. \tag{4.26}$$

It is clear that the radius of each individual circle depends on the location of the imaginary plane with respect to points A and B, becoming largest at some point midway between A and B. Furthermore, from (4.22) the family of circles have a specific property: The path length from point A to point B via each circle is $n\frac{\lambda}{2}$ longer than the direct path AOB. Thus, for $n = 1$ (first zone) $AO^{(i)}B - AOB = \frac{\lambda}{2}$ the excess path length for the innermost circle is $\frac{\lambda}{2}$. Other zones will have an excess proportional to $\frac{\lambda}{2}$ with a parameter of proportionality $n = 2, 3, 4, \ldots$. The foci of the points, for which $AO^{(i)}B - AOB = n\frac{\lambda}{2}$, define a family of ellipsoids. The radii of ellipsoids are described by (4.23). Notice that in free space, without any obstructions, only the first ellipsoid is actual and determines the first Fresnel zone with a radius proportional to $\sqrt{\lambda R}$ according to (4.24). This ellipsoid covers an area between two terminal points, the transmitter (T) and the receiver (R) as shown in Figure 4.6. Therefore, despite the fact that in free space both reflection and diffraction phenomena are absent, which causes interference between neighboring zones, the concept of Fresnel zones based on Huygen's principle is very important. It describes the loss characteristics of radio wave passing along a channel of high deviation terminal antennas. This concept allows us to estimate conditions of direct
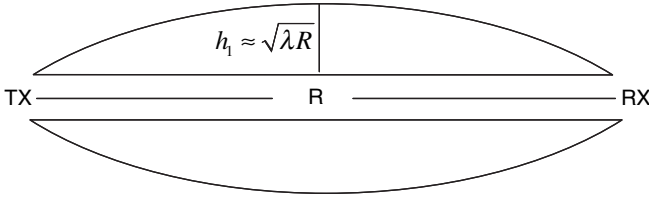
FIGURE 4.6. A free-space pattern of the first Fresnel zone covering both terminals, the transmitter T_X and the receiver R_X.

visibility or *clearance of the propagation channel* by using the right-hand term in (4.24) to evaluate the radius of the first Fresnel zone on the basis of the knowledge of the wavelength of the radiated wave and the range between the two terminal antennas. This is very important for link budget design in atmospheric channels where the terminal antennas are far from the Earth's surface. This aspect will be discussed in Chapter 6 when we deal with atmospheric communication links.

4.1.5. Polarization of Radio Waves

To understand the aspect of wave polarization, let us define this phenomenon. The alignment of the electric field vector **E** of a plane wave relative to the direction of propagation **k** defines the *polarization* of the wave (see Chapter 2). If **E** is transverse to the direction of wave propagation **k** then the wave is said to be TE-wave or *vertically* polarized. Conversely, when **H** is transverse to **k** the wave is said to be *TM*-wave or *horizontally* polarized. Both of these waves are *linearly polarized*, as the electric field vector **E** has a single direction along the entire propagation axis (vector **k**). If two plane linearly polarized waves of equal amplitude and orthogonal polarization (vertical and horizontal) are combined with a 90° phase difference, the resulting wave will be a *circularly polarized* (CP) wave, in which the motion of the electric field vector will describe a circle around the propagation vector.

The field vector will rotate by 360° for every wavelength traveled. Circularly polarized waves are most commonly used in land cellular and satellite communications, as they can be generated and received using antennas that are oriented in any direction around their axis without loss of power [1–3]. They may be generated as either right-hand *circularly polarized* or left-hand *circularly polarized*, depending on the direction of vector **E** rotation (see Fig. 4.7). In the most general case, the components of the combining waves could be of unequal amplitude, or their phase difference could be other than 90°. This combination result is an elliptically polarized wave, where vector **E** still rotates at the same rate as for circular polarized wave, but varies in amplitude with time. In the case of elliptical polarization, the axial ratio, $AR = E_{maj}/E_{min}$, is usually introduced (see Fig. 4.7). *AR* is defined to be positive for left-hand polarization and negative for right-hand polarization. Now let us turn our attention to the wave field polarization in the case of a free-space propagation channel.

Direction of wave along z-axis
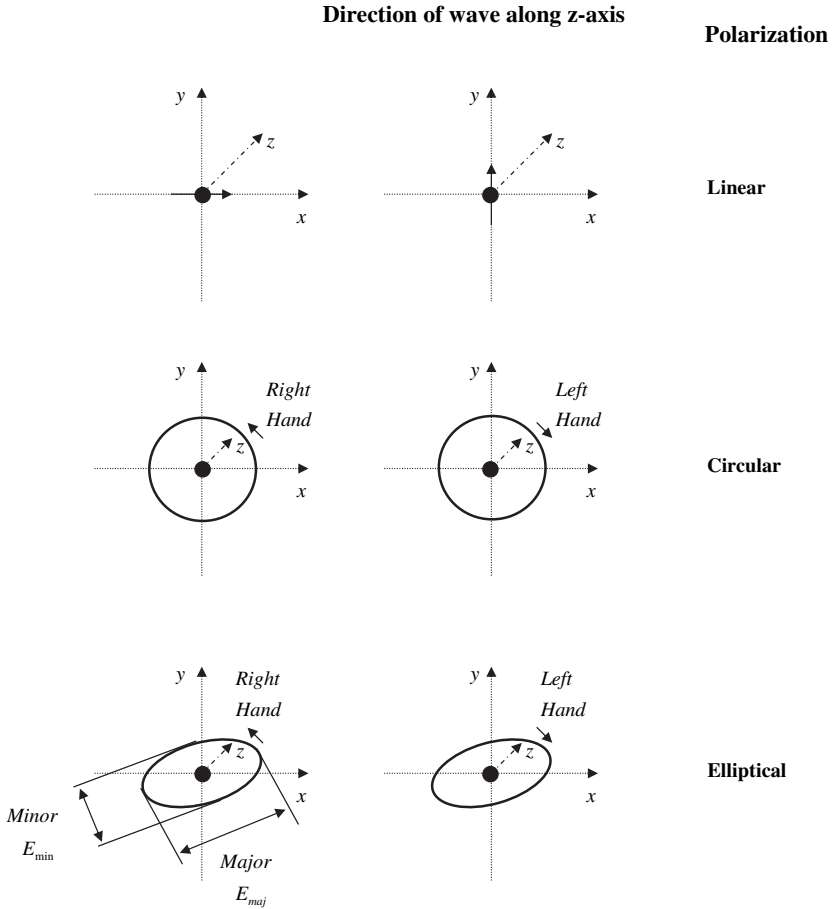
Polarization

FIGURE 4.7. Different kinds of field polarization.

4.2. PATH LOSS IN FREE SPACE

Let us consider a non isotropic source placed in free space as a transmitter antenna with P_T watts and a directivity gain G_T. At an arbitrary large distance r ($r \gg \lambda$, where $\lambda = cT = c/f$ is a wavelength) from the source, the radiated power is uniformly distributed over a surface area of a sphere of radius r. If P_R is the power at the receiving antenna, which is located at distance r from the transmitter antenna and has a directivity gain G_R, then the *path loss*, in decibels, is given by

$$L = 10 \log \frac{P_T}{P_R} = 10 \log \left[\left(\frac{4\pi r}{\lambda} \right)^2 \Big/ G_T G_R \right] = L_0 + 10 \log \left(\frac{1}{G_T G_R} \right) \qquad (4.27)$$

Here L_0 is the path loss for an isotropic point source (with $G_R = G_T = 1$) in free space and can be presented in decibels as

$$L_0 = 10 \log \left(\frac{4\pi f r}{c} \right)^2 = 20 \log \left(\frac{4\pi f r}{c} \right) = 32.44 + 20 \log r + 20 \log f \qquad (4.28)$$

where the value 32.44 is obtained from

$$32.44 = 20 \log \left(\frac{4\pi \cdot 10^3 (\text{m}) \cdot 10^6 (1/\text{s})}{3 \cdot 10^8 (\text{m/s})} \right) = 20 \log \left(\frac{40\pi}{3} \right)$$

Notice that all the above formulas are related to the well-known Friis' formula obtained in Chapter 2. In expression (4.28) the distance r is in kilometers (km), and frequency f is in megahertz (MHz). As the result, the path loss between the two directive antennas (receiver and transmitter) is given by

$$L_F = 34.44 + 20 \log d_{[\text{km}]} + 20 \log f_{[\text{MHz}]} - 10 \log G_T - 10 \log G_R \qquad (4.29)$$

It can be presented in a ''straight line'' form as

$$L_F = L_0 + 10\,\gamma \log d \qquad (4.30)$$

where $L_0 = 34.44 + 20 \log f - 10 \log G_T - 10 \log G_R$ and $\gamma = 2$.

4.3. RADIO PROPAGATION ABOVE FLAT TERRAIN

The simplest case of radio wave propagation over a terrain is one where the ground surface can be assumed to be flat and perfectly conductive. The assumption of ''flat terrain'' is valid for radio links between subscribers up to 10–20 km [4–8]. The second condition of a ''perfectly conductive'' soil medium can be satisfied only for some special cases, because the combination of conductivity σ and frequency ω such as $4\pi\sigma/\omega$, that appears in total formula of permittivity $\varepsilon = \varepsilon_{\text{ro}} - i4\pi\sigma/\omega$ play important role for high frequencies (VHF/L-band, usually used for terrain communication channel design) and finite sub-soil conductivity, as well as for small grazing angles of incident waves [1–8]. To introduce the reader to the subject of reflection from the terrain, we start with the simplest case of a perfectly conductive flat terrain.

4.3.1. Boundary Conditions at the Perfectly Conductive Surface

For a perfectly conductive ground surface the total tangential electric field vector is equal to zero, that is, $\mathbf{E}_t = 0$. Consequently, from $\nabla \times \mathbf{E}(\mathbf{r}) = i\omega\mathbf{H}(\mathbf{r})$ the normal

component of the magnetic field also vanishes, that is, $\mathbf{H}_n = 0$. At the same time, the tangential component of magnetic field $\mathbf{H}_\tau$ does not vanish because of its compensation by the surface electric current. The normal component of electric field $\mathbf{E}_n$ is also compensated by the electrical charge on the ground surface [1–8]. Thus, for the flat perfectly conductive ground surface, we have, $\mathbf{E}_\tau = 0$ and $\mathbf{H}_n = 0$, which in the Cartesian coordinate system can be rewritten as

$$E_x(x, y, z = 0) = E_y(x, y, z = 0) = H_z(x, y, z = 0) = 0 \qquad (4.31)$$

Here $\mathbf{E}_\tau$ is the tangential component of the electric field and $\mathbf{H}_n$ is the normal component of the electromagnetic wave with respect to the ground surface.

4.3.2. Areas Significant for Reflection

To obtain main Fresnel zones at the ground surface that are responsible for reflection, we again return to the Huygen's principle and the boundary conditions at the ground surface.

We consider in this section three typical positions of the terminal antennas: a) two antennas are higher than all terrain obstructions; b) one of the antenna is higher and the other is lower compared to the terrain obstructions; c) both antennas are lower than the terrain obstructions.

In the first case, the source is also placed above the ground surface at the point $O\ (x_0, y_0, z_0)$. Without any loss of generality, we choose the coordinate system to be such that $x_0 = 0$, $y_0 = y_A = 0$ (see Fig. 4.8). Using the main integral presentation of the total field in (4.14) and (4.15), for the atmosphere-earth boundary surface, and using the Hertz presentation of total field (that is, for $\widetilde{\Psi}(\mathbf{r}) \equiv \Pi(\mathbf{r})$), one can obtain the following result: According to this formula and the discussion presented above, in the situation over a flat terrain, the total field $\Pi(\mathbf{r}) = |\Pi(\mathbf{r})|$ at the observed point A is the superposition of the non disturbed field $\Pi_0(A)$ that describes the wave field in the unbounded homogeneous atmosphere, and the disturbed field $\Pi_1(A)$ that describes the reflection phenomenon caused by the virtual sources placed at the ground surface S (the area of integration in (4.15) or (4.16)). The integral on the surface S in (4.14)–(4.16) will always consist of products of the order of $\sim \frac{e^{ikr}}{r}\Pi(\mathbf{r})$ for any selected Green's function in the form of (4.10). Consequently, the field $\Pi(\mathbf{r})$ at the ground surface can also be considered as a product of the non disturbed field $\Pi_0(\rho) = |\mathbf{p}| \cdot \frac{e^{ik\rho}}{\rho}$ and some slowly changing attenuation function $W(\rho)$. In this case we can again return to the integral (4.19) from the product of a quickly oscillating function and a slowly changing function, and use the method of stationary phase for the description of zones at the surface S that gives minor contributions to wave the reflection phenomena from a flat ground surface. Next, consider the integral in (4.19). On the surface $S\ \{x, y, z = 0\}$ we find the point (x_0, y_0) at which this integral has some extremes. As seen from Figure 4.8, $r = \sqrt{(x_A - x)^2 + y^2 + z^2}$ and $\rho = \sqrt{x^2 + y^2 + z_0^2}$ means that the essential effect for the reflection phenomenon
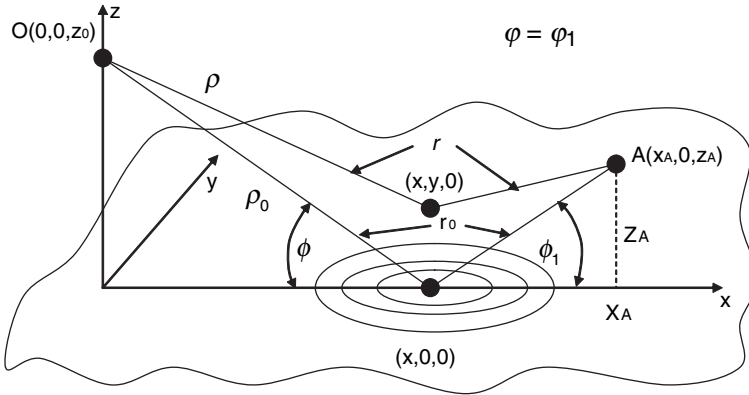
FIGURE 4.8. The Fresnel-zone reflected area presentation for one of the antenna located near the ground surface.

arises from the area that lies near the point of the specular reflection $(x_0, y_0, 0)$ [4–6]. Let us examine the behavior of the exponential function inside the integral in (4.20). First, to simplify things, we introduce new variables:

$$\varsigma = x - x_0, \quad \eta = y - y_0. \tag{4.32}$$

Assuming $\varsigma, \eta \ll r, \rho$, and expanding r and ρ into series, according to [4,6], we can obtain the phase function $\phi = k \cdot (r + \rho)$ in the exponent of integrand within (4.20) as:

$$\phi = k \cdot (r + \rho) \approx k \cdot \left\{ (r_0 + \rho_0) + \frac{\varsigma^2 \sin^2 \varphi + \eta^2}{2} \left(\frac{1}{r_0} + \frac{1}{\rho_0} \right) \right\} \tag{4.33}$$

where we define r_0' in the integrand inside (4.20) and ρ_0 according to geometry presented in Figure 4.8. The lines of equal phase $\phi(\varsigma, \eta) = $ const. have the form of ellipses placed around the point of the specular reflection (see Fig. 4.8). The following equation:

$$\frac{k}{2} \cdot \left(\frac{1}{r_0} + \frac{1}{\rho_0} \right) (\varsigma^2 \sin^2 \varphi + \eta^2) = m \frac{\pi}{2}, \quad m = 0, \ 1, \ 2, \ldots \tag{4.34}$$

or its strict mathematical presentation

$$\frac{\varsigma^2}{\dfrac{\pi \cdot m}{k \cdot \left(\dfrac{1}{r_0} + \dfrac{1}{\rho_0} \right) \cdot \sin^2 \varphi}} + \frac{\eta^2}{\dfrac{\pi \cdot m}{k \cdot \left(\dfrac{1}{r_0} + \dfrac{1}{\rho_0} \right) \cdot \sin^2 \varphi}} = 1 \tag{4.35}$$

is an equation of ellipses with semi-axes:

$$\text{along the } x\text{-axis:} \qquad a_m = \frac{1}{\sin \varphi} \sqrt{\frac{\pi \cdot m}{k} \frac{r_0 \cdot \rho_0}{(r_0 + \rho_0)}}$$

$$\text{and along the } y\text{-axis:} \qquad b_m = \sqrt{\frac{\pi \cdot m}{k} \frac{r_0 \cdot \rho_0}{(r_0 + \rho_0)}} \tag{4.36}$$

These ellipses are the real boundaries of the zones of specular reflection from a flat ground surface. For small grazing angles $(\varphi \to 0°)$ $a_m \gg b_m$, all ellipses are elongated along the x-axis, that is, along the direction of wave propagation. Earlier these ellipses were defined as the Fresnel zones, but now they are described when the specular reflection from the ground surface is taken into account. Approximate size of the reflecting areas in [4] were also estimated from

$$\text{along the } x\text{-axis:} \qquad 2a_R = \frac{4}{\sin \varphi} \sqrt{\lambda R} \tag{4.37a}$$

$$\text{and along the } y\text{-axis:} \qquad 2b_R = 4\sqrt{\lambda R} \tag{4.37b}$$

where R is the minimal value between the two distances, r_0 and ρ_0.

So far we have considered the situation when the antennas, transmitter, and receiver are above the earth surface. What happens if one of the points, for example, point A, lies close to the ground plane, that is, at $z = 0$?

In this second case $z_A \approx 0$ as shown in Figure 4.9, the term $(r + \rho)$ in the exponent of $\exp\{i \phi = \exp\{i \cdot k \cdot (r + \rho)\}$ in integral (4.20) has a minimum at point A, that is, when $x = x_A$, $y = y_A$. Also if we assume that $y_A \approx 0$ and introduce the polar coordinate system (r, α) with a center at point A (see Fig. 4.9), then

$$x = x_A + r \cdot \cos \alpha, \qquad y = r \cdot \sin \alpha \tag{4.38}$$

The r and ρ can be related as:

$$\rho \approx \rho_0 + r \cdot \cos \alpha \cdot \cos \varphi$$
$$i\phi \approx ik\rho_0 + i \cdot k \cdot r \cdot (1 + \cos \alpha \cdot \cos \varphi) \tag{4.39}$$

Using these expressions, one can again obtain for the fast oscillating term in the integral (4.19), the significant area where reflection occurs. The boundaries of this area are described by the following equation:

$$k \cdot r \cdot (1 + \cos \alpha \cdot \cos \varphi) = m\frac{\pi}{2}, \quad m = 0, 1, 2, \ldots \tag{4.40}$$

or

$$r = \frac{m \cdot \pi/2 \cdot k}{(1 + \cos \alpha \cdot \cos \varphi)} \tag{4.41}$$

Expression (4.41) describes a family of ellipses with their foci at the point $r = 0$ (point A). Their large semi-axis is elongated along the x-axis and is described by

$$a_m = \frac{m \cdot \pi}{2 \cdot k \cdot \sin^2 \varphi} \tag{4.42a}$$

and their small semi-axis is elongated along the y-axis and equals

$$b_m = \frac{m \cdot \pi}{2 \cdot k \cdot \sin \varphi} \tag{4.42b}$$

These ellipses are strongly elongated in the direction of the source, as shown in Figure 4.9. In this case the distance from point A to each successive ellipse is

$$(d)_{\alpha=\pi} = \frac{m \cdot \pi}{2 \cdot k \cdot (1 - \cos \varphi)} \tag{4.43}$$

and in the opposite direction to the source this value is

$$(d)_{\alpha=0} = \frac{m \cdot \pi}{2 \cdot k \cdot (1 + \cos \varphi)} \tag{4.44}$$

In the case of a wave incident with a small grazing angle $\varphi(\varphi \approx 0)$, several initial Fresnel zones will embrace most of the radio path between points O and A (the
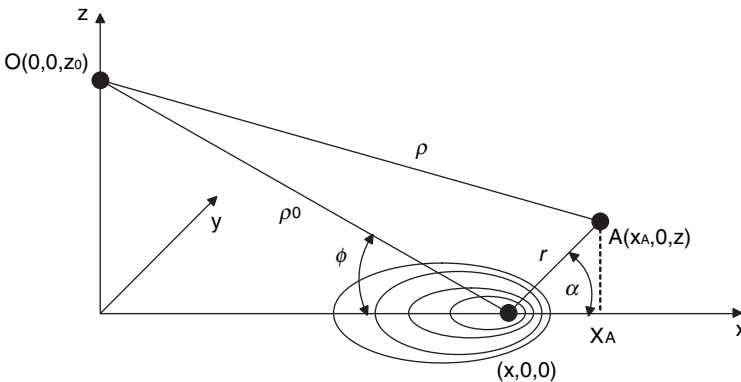
FIGURE 4.9. The Fresnel-zone reflected area presentation for both antennas located near the ground surface.
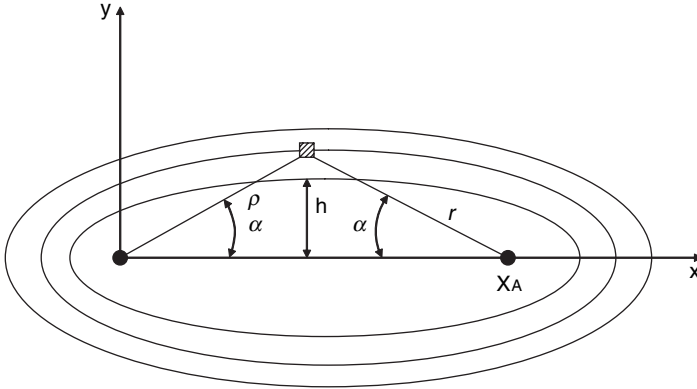
FIGURE 4.10. Specular reflection of the incident ray from a smooth flat terrain.

source and observer, respectively). Estimations carried out in Reference [4] showed that the area in front of an observer placed at point A, located near the Earth's surface, is very important for propagation. At the same time, the area behind the observer is not that significant. The conditions of propagation and hence of communication between points O and A become more effective with an increase in grazing angle φ or, of course, with a decrease of the range between the source and the observation point.

In the third case, the source and the observation point occurs when both are located near the earth's surface (let us say, in the plane $z = 0$, as shown in Fig. 4.10). In this case the position and the configuration of the Fresnel zones are determined by the earlier introduced condition of equality of phase of field oscillations, that is, $k \cdot (r + \rho) = $ const. But from this condition we can once more obtain the equations for the ellipses with their foci at points O (source) and A (observer). Because the minimum value of such a constant can be achieved for $(r + \rho) = x_A$, the boundaries of the Fresnel zones are determined by the following conditions:

$$k \cdot (r + \rho) = k \cdot x_A + m\frac{\pi}{2}, \quad m = 0, 1, 2, \ldots \tag{4.45}$$

The large semi-axis of each ellipse is

$$a_m = \frac{r + \rho}{2} = \frac{x_A}{2} + \frac{m \cdot \pi}{4 \cdot k} \tag{4.46}$$

Behind points O and A these ellipses are close to each other and are very elongated along the x-axis. The small semiaxis is

$$b_m = \frac{r + \rho}{2}\sin\alpha = \sqrt{\frac{m \cdot \pi}{k}\left(x_A + \frac{m \cdot \pi}{4 \cdot k}\right)} \approx \sqrt{\frac{m}{8}\lambda \cdot x_A} \tag{4.47}$$

for moderate values of m.

Thus we conclude that the ellipses depicted in Figure 4.10 are not real because $b_m \ll a_m$. If we now assume that $x_A \gg \lambda$ (for real radio paths designed above a flat terrain), then $x_A \gg b_m$ the specular reflection area is narrow enough. As shown in References [4,6], in this case only a few ellipses embrace the source (O) and observer (A) determine the significant area of specular reflection. The distances between neighboring ellipses behind points O and A are very small.

Thus, we have found the significant area of specular reflection from a flat terrain for various combinations of transmitter and receiver locations above the Earth's surface. We can combine all three cases of antenna positioning by analyzing more general situations for various positions of points O and A, and by introducing a system of rotating ellipsoids in space which have foci at these points. These ellipsoids can be described by [4]:

$$k \cdot (r + \rho) = k \cdot d + n \frac{\pi}{2}, \quad n = 0, 1, 2, \ldots \tag{4.48}$$

where d is the range between points O and A, whereas r and ρ are the distances from A and O to the current spatial point, respectively. Starting from any number $n = n_1$ these ellipsoids are crossed by the Earth's surface. The first point where the first contact with the ground surface takes place is the point of specular reflection

$$k \cdot (r_0 + \rho_0) = k \cdot d + n_1 \frac{\pi}{2} \tag{4.49}$$

The following values of $n = n_1 + m$, $m = 0, 1, 2, \ldots$, will give at the ground plane, the contours of the Fresnel reflection zones, as shown by Figures 4.8–4.10 for various elevations of the receiving and transmitting antennas.

4.3.3. Reflection Coefficients

Here, we present the expressions for the complex reflection coefficients (Γ) for waves with vertical (denoted by index V) and horizontal (denoted by index H) polarization [4–8].

For horizontal polarization:

$$\Gamma_H = |\Gamma_H| e^{-j\varphi_H} = \frac{\sin\psi - (\varepsilon_r - \cos\psi)^{1/2}}{\sin\psi + (\varepsilon_r - \cos^2\psi)^{1/2}} \tag{4.50a}$$

For vertical polarization:

$$\Gamma_V = |\Gamma_V| e^{-j\varphi_V} = \frac{\varepsilon_r \sin\psi - (\varepsilon_r - \cos\psi)^{1/2}}{\varepsilon_r \sin\psi + (\varepsilon_r - \cos^2\psi)^{1/2}} \tag{4.50b}$$
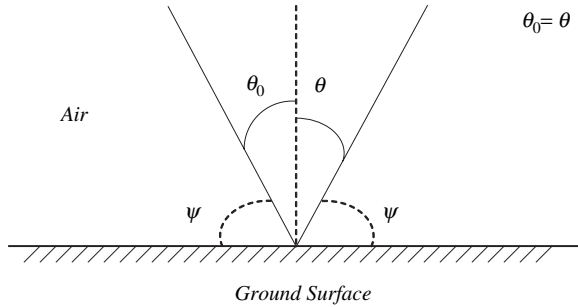
FIGURE 4.11. The Fresnel-zone reflected area presentation for two antennas placed above the ground surface.

Here, $|\Gamma_V|$, $|\Gamma_H|$ and φ_V, φ_H are the magnitude and phase of the reflection coefficient for vertical and horizontal polarization, respectively. $\psi = \frac{\pi}{2} - \theta_0$ is the grazing angle and θ_0 is the angle of wave incidence (see Fig. 4.11). The knowledge of the reflection coefficient amplitude and phase variations is a very important factor in the prediction of propagation characteristics for different situations in over-the-terrain propagation channels. In practice, for over-the-terrain wave propagation the ground properties are determined by the conductivity and the absolute permittivity of the sub-soil medium, $\varepsilon = \varepsilon_0 \varepsilon_r$, where ε_0 is the dielectric constant of vacuum, ε is the relative permittivity of the ground surface, and $\varepsilon_r = \text{Re}(\varepsilon) + \text{Im}(\varepsilon) = \varepsilon_{Re} - j60\lambda\sigma$. Here $\varepsilon_{Re} \equiv \varepsilon_{r0}$ and $\varepsilon_{Im} = 60\lambda\sigma$ are the real and imaginary parts of the relative permittivity of the sub-soil medium. Because both coefficients presented by (4.50a)–(4.50b) are complex values, the reflected wave will therefore differ in both magnitude and phase from the incident wave. Moreover, both coefficients in (4.50) differ from each other.

Thus, in the case of horizontal polarization, for $\varepsilon_r \to \infty$, $\sigma \to \infty$ (i.e., for a conductive ground surface), the relative phase of the incident and reflected waves, is nearly 180° for all angles of incidence. On the other hand, for very small grazing angles ($\psi \ll 90°$), as follows from (4.50a), the reflected and incident waves are equal in magnitude but differ by 180° in phase for all actual values of ground permittivity and conductivity, that is, $\Gamma_H = -1$, ($\alpha \ll \frac{\pi}{2}$), and $\varphi_H = 180°$.

From (4.50b) the reflection coefficient for a wave with vertical polarization does not change its properties compared to that of horizontal polarization in the case of a real conductive ground surface ($\varepsilon_c \gg 1, \sigma \gg 1$), and small grazing angles, that is, for $\psi \ll 90°$ $\Gamma_V = -1$, and $\varphi_V = 180°$. At the same time, for $\varepsilon_r \to \infty$, $\sigma \to \infty$ and $0 < \psi < 180°$, we get $\Gamma_V = 1$ (see (4.50b)). However, with an increase of angle ψ substantial differences appear, that is, both a rapid decrease of magnitude and phase of the reflected wave take place. For $\theta_0 \to \theta_{Br}(\psi \to 90° - \theta_{Br})$, where $\theta_{Br} = \tan^{-1}\sqrt{\varepsilon_r}$ is the Brewster angle, the magnitude $|\Gamma_V|$ becomes minimum and the phase φ_V reaches $-90°$. At values of ψ greater than the Brewster angle, $|\Gamma_V|$ increases again and the phase φ_V approaches zero, that is, $\Gamma_V \to 1$.

4.4. PROPAGATION ABOVE ROUGH TERRAIN UNDER LOS CONDITIONS

Now we consider EM-wave propagation above a rough terrain. Both terminal antennas, the transmitter and the receiver, are placed above the rough terrain in LOS conditions. Here the multi-scattering effects, caused by the terrain roughness, must be taken into account. The total field arrived at the receiving antenna is a superposition of the direct wave, the wave specularly reflected from the quasi-flat ground surface (which together with the direct wave form the coherent part of the signal total intensity, I_{co}), and the waves scattered in all directions from the irregularities of the terrain (which form the incoherent part of the signal total intensity, I_{inc}). In order to predict the propagation loss characteristics of the irregular ground surface and to estimate the role of each kind of wave in the total field, we use the Rayleigh rough-surface criteria and find the influence of each part in the signal total intensity at the receiver [9–14].

Next, we present expressions for both part of the total signal intensity, the coherent and incoherent, the reflected and scattered from the rough ground surface, respectively. These expressions take into consideration the various relations between the dimension of roughness, the wavelength of operation, and the angle of incidence. The interested reader is referred to the original works [15–27] for more details. Here we give recommendations on how to use these expressions for different frequency bands, for different terrain irregularities, and various positions of the receiving and transmitting antennas.

4.4.1. Scattering from a Rough Ground Surface

A rough terrain can be described, according to [9–14,16] by a ''relief function'' $z = S(x)$, as shown in Figure 4.12. If the roughness of arbitrary height z is distributed according to Gauss's law, with mean value $\bar{z}$ and a variance of σ^2, then the
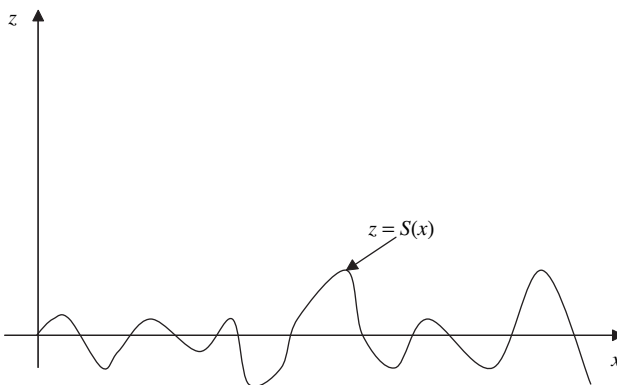
FIGURE 4.12. Relief function presentation for the rough terrain.

$\sigma \ll \lambda$ $\sigma \leq \lambda$ $\sigma > \lambda$ $\sigma \gg \lambda$
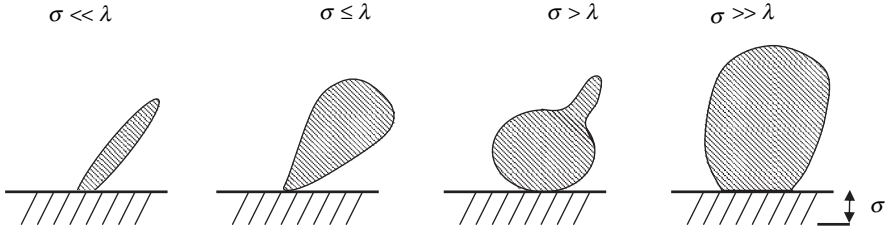
FIGURE 4.13. Different patterns of the scattered wave from a rough terrain.

probability density function, (PDF) (see definitions in Chapter 1), of roughness distribution is given by:

$$P_z = \frac{1}{\sqrt{2\pi\sigma}} \exp\left\{ -\frac{(z - \bar{z})^2}{2\sigma^2} \right\} \tag{4.51}$$

where the standard deviation of the ground surface roughness around its mean height $\bar{z}$ is $\sigma = \sqrt{\langle z^2 \rangle - \bar{z}^2}$. In Figure 4.13, the criterion of roughness of the terrain is presented schematically for various values of σ for a better understanding of the role of the reflected and scattered waves in the total field pattern. Thus, the case $\sigma = 0$ or $\sigma \ll \lambda$ (λ is a wavelength) describes pure reflection from a flat terrain; the case $\sigma \leq \lambda$ describes weak scattering effects from a gently rough surface, where the reflected wave is the dominant contributor to the total field pattern, that is, $I_{co} \gg I_{inc}$. In the cases of $\sigma > \lambda$ and $\sigma \gg \lambda$, the terrain is rough and irregular with an increased role in generating a significant scattered wave as a component of the total field pattern. The last two illustrations in Figure 4.13, show the $I_{co} \ll I_{inc}$ cases.

There are several approximate methods for the total field evaluation in radio propagation channels above a rough terrain. At present, there are three general approaches to solve the wave scattering problem that arises from the rough terrain:

a) the *perturbation technique* that applies to a surface which is slightly rough and whose surface slope is smaller than unity [4,9,21,25];

b) the *Kirchhoff approximation* that is applicable to a surface whose radius of curvature is much greater than a wavelength [4,9,13–20];

c) the *Rayleigh approximation* that is applicable to a surface whose curvature is at the same order as the wavelength [9–12].

We describe each approach briefly in the following section.

4.4.2. The Perturbation Solution

The perturbation method is applicable to a slightly rough surface that will be described herein. Let us consider the height of a rough surface to be given by some
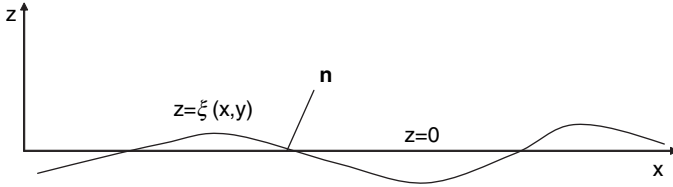
FIGURE 4.14. Geometrical presentation of weaker rough terrain described by the perturbation method.

function (see Fig. 4.14)

$$z = \varsigma(x, y) \tag{4.52}$$

We choose $z = 0$ so that (4.52) represents the deviation from the average height $\langle \varsigma(x, y) \rangle = 0$. Moreover, the perturbation method is valid when the phase difference due to the height variation is small, that is, when [4,9]

$$|k \cdot \varsigma(x, y) \cdot \cos \theta_i| \ll 1$$
$$\left| \frac{\partial \varsigma}{\partial x} \right| \ll 1, \qquad \left| \frac{\partial \varsigma}{\partial y} \right| \ll 1 \tag{4.53}$$

The boundary condition for the electric field at this surface requires that the tangential components of **E** vanish at the surface $z = \varsigma(x, y)$, that is,

$$\mathbf{E} \times \mathbf{n} = 0 \tag{4.54}$$

where **n** is the vector normal to the surface $z = \varsigma$ at point (x, y). If the surface profile (4.52) and the position of sources are known, then the problem is to determine the field in semi-space $z > 0$, given that the boundary conditions are known [9]. Let us consider the influence of roughness as a small perturbation, that is, the total field is

$$\mathbf{E} = \mathbf{E}^{(0)} + \mathbf{E}^{(1)} \tag{4.55}$$

where $\mathbf{E}^{(0)}$ is the field that could be derived for the condition $\varsigma = 0$, which a priory is well known using knowledge of specular reflection from smooth terrain obtained from two-ray model. The second term $\mathbf{E}^{(1)}$ that describes the field perturbations can be obtained from the wave equation using boundary conditions in (4.54). To present the solution of the perturbation term, let us consider two special cases, which are practical with regard to over-the-terrain propagation channels.

Let a *vertical dipole* be located at point O as shown in Figure 4.15. Its reflection from a flat surface at $z = 0$ and at the point O_1 according to the reflection theorem must also be directed vertically. By introducing the spherical coordinate systems $\{R, \vartheta, \varphi\}$ and $\{R_1, \vartheta_1, \varphi_1 \equiv \varphi\}$ for each dipole, we can present the components of
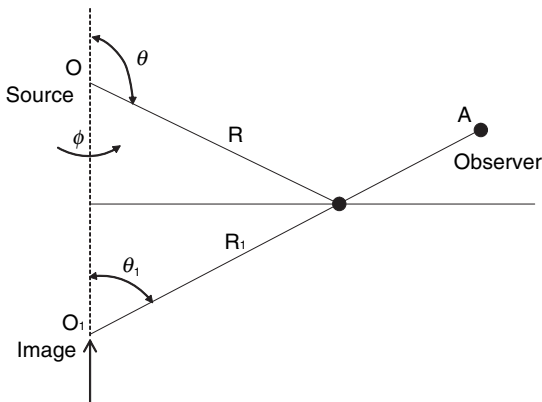
FIGURE 4.15. The geometry of a vertical dipole field scattered from a rough terrain.

the non perturbed field $\mathbf{E}^{(0)}$ as

$$
E_x^{(0)} = \left\{ -k_0^2 p \sin \vartheta \cos \vartheta \, \frac{e^{i(\omega t - k_0 R)}}{R} - k_0^2 p \sin \vartheta_1 \cos \vartheta_1 \, \frac{e^{i(\omega t - k_0 R_1)}}{R_1} \right\} \cos \varphi
$$

$$
E_y^{(0)} = \left\{ -k_0^2 p \sin \vartheta \cos \vartheta \, \frac{e^{i(\omega t - k_0 R)}}{R} - k_0^2 p \sin \vartheta_1 \cos \vartheta_1 \, \frac{e^{i(\omega t - k_0 R_1)}}{R_1} \right\} \sin \varphi \quad (4.56)
$$

$$
E_z^{(0)} = \left\{ k_0^2 p \sin^2 \vartheta \, \frac{e^{i(\omega t - k_0 R)}}{R} + k_0^2 p \sin^2 \vartheta_1 \, \frac{e^{i(\omega t - k_0 R_1)}}{R_1} \right\}
$$

Then, in the plane $z = 0(R = R_1, \vartheta = \pi - \vartheta_1)$

$$
E_x^{(0)} = E_y^{(0)} = 0, \qquad E_z^{(0)} = 2k_0^2 p \sin^2 \vartheta \, \frac{e^{i(\omega t - k_0 R)}}{R}. \qquad (4.57)
$$

Here p is the modulus of the momentum of the vertical dipole that is well known from the literature (see, for example, [4,9,11]). Because in practical terrain propagation case, the source and the observation point are far from the surface $z = 0$, we can present simple formulas for the perturbed part of the total field due to the terrain roughness in the case where the incident wave lies in the xy-plane (i.e., when $\varphi = 0$, $p \frac{e^{-ik_0 R}}{R} = q e^{-ik_0 x' \sin \vartheta}$, where q is constant):

$$
E_x^{(1)} = \frac{k_0^2}{2\pi}(2q) \int \left\{ ik_0 \cos^2 \vartheta + \sin \vartheta \, \frac{\partial \varsigma}{\partial x'} \right\} \frac{\partial}{\partial z} \frac{e^{-ik_0(\rho + x' \sin \vartheta)}}{\rho} \, dx' dy'
$$

$$
E_y^{(1)} = \frac{k_0^2}{2\pi}(2q) \int \left\{ \sin^2 \vartheta \, \frac{\partial \varsigma}{\partial y'} \right\} \frac{\partial}{\partial z} \frac{e^{-ik_0(\rho + x' \sin \vartheta)}}{\rho} \, dx' dy'
$$

$$
E_z^{(1)} = \frac{k_0^2}{2\pi}(2q) \int \left\{ ik_0 \frac{\partial \varsigma}{\partial x'}(\cos^2 \vartheta - \sin^2 \vartheta) + \left(\frac{\partial^2 \varsigma}{\partial x'^2} + \frac{\partial^2 \varsigma}{\partial x'^2} \right) \sin \vartheta \right. \qquad (4.58)
$$

$$
\left. + k_0^2 \cos^2 \vartheta \sin \vartheta \right\} \frac{e^{-ik_0(\rho + x' \sin \vartheta)}}{\rho} \, dx' dy'
$$

Here $\rho = \sqrt{(x - x')^2 + (y - y')^2 + (z - z')^2}$, in which x, y, z are the coordinates of the observed point. For small grazing angles ($\vartheta \to \frac{\pi}{2}$), that is, in the case of slipped incident waves, which is very actual in mobile and personal communication, these formulas can be significantly simplified, for example,

$$
\begin{aligned}
E_x^{(1)} &\approx -2k_0^2 \, q \, e^{-ik_0 x \sin \vartheta} \frac{\partial \varsigma}{\partial x} \\
E_y^{(1)} &\approx -2k_0^2 q \, e^{-ik_0 x \sin \vartheta} \frac{\partial \varsigma}{\partial x} \\
E_z^{(1)} &\approx \frac{k_0^2}{2\pi} (2q) \int \left(\frac{\partial^2 \varsigma}{\partial x'^2} + \frac{\partial^2 \varsigma}{\partial x'^2} - ik_0 \frac{\partial \varsigma}{\partial x'} \right) \frac{e^{-ik_0(\rho + x' \sin \vartheta)}}{\rho} \, dx' dy'
\end{aligned}
\tag{4.59}
$$

For a *horizontal dipole* located at the point O and oriented along the y-axis, its reflection vector from the flat surface $z = 0$ and at the point O_1 is oriented, in the opposite direction. The same approach, as above, allows us to present the perturbation part of the total field due to the terrain roughness for a horizontal dipole oriented along the y-axis

$$
\begin{aligned}
E_x^{(1)} &= 0 \\
E_y^{(1)} &= -\frac{k_0^2}{2\pi} (2q) \int (ik_0 \varsigma \cos \vartheta) \frac{\partial}{\partial z} \frac{e^{-ik_0(\rho + x' \sin \vartheta)}}{\rho} \, dx' dy' \\
E_z^{(1)} &= \frac{k_0^2}{2\pi} (2q) \int \left(ik_0 \frac{\partial \varsigma}{\partial y'} \cos \vartheta \right) \frac{e^{-ik_0(\rho + x' \sin \vartheta)}}{\rho} \, dx' dy'
\end{aligned}
\tag{4.60}
$$

Then, in the case of slipped waves (i.e., for small grazing angles ($\vartheta \to \frac{\pi}{2}$)) one can easily obtain from (4.60) very simple formulas for the perturbed part of the total field as

$$
\begin{aligned}
E_x^{(1)} &= 0 \\
E_y^{(1)} &= -2ik_0^3 \varsigma \, q \cos \vartheta \, e^{-ik_0 x \sin \vartheta} \approx 0 \\
E_z^{(1)} &= \frac{k_0^3}{2\pi} (2iq) \int \frac{\partial \varsigma}{\partial y'} \cos \vartheta \, \frac{e^{-ik_0(\rho + x' \sin \vartheta)}}{\rho} \, dx' dy'
\end{aligned}
\tag{4.61}
$$

A comparison between expressions (4.58)–(4.59) and (4.60)–(4.61), for both kinds of wave field polarizations, shows that the field of the horizontal dipole is less affected by the roughness of the terrain than that of the vertical dipole. The formulas presented here can predict the propagation characteristics over a rough terrain in conditions of direct visibility between the source and the observer if the profile $\varsigma(x, y)$ of the ground surface is known for each situation. Moreover, these formulas allow us to obtain the coherent and incoherent parts of the total field energy. In fact, the coherent power dominates in the case of a smooth surface and is determined by the use of the non perturbed field $\mathbf{E}^{(0)}$, the components of which are described

by (4.56). The incoherent power is determined by the perturbed field $\mathbf{E}^{(1)}$ described by (4.58)–(4.59) and (4.60)–(4.61) for both kinds of field polarizations.

The limitation of the perturbation method depends on the requirement of the "smallness" not only for $\nabla\varsigma$ but also for the Earth's surface deviations $\varsigma(x, y)$. But the last condition can be ignored, because, if we derive the second *perturbation* term $\mathbf{E}^{(2)}$ in Equation (4.55), we obtain for the case of vertical dipole the following condition [9,11]:

$$(|k_0 \cdot \varsigma \cdot \nabla\varsigma|)^{1/2} \ll 1 \qquad (4.62)$$

from which, assuming that $|\nabla\varsigma| \approx \varsigma/\ell$, where ℓ is the characteristic length of roughness, we obtain

$$\varsigma \ll \sqrt{\lambda \cdot \ell} \qquad (4.63)$$

Therefore, for sufficiently small slope angles, the described perturbation technique is valid even for deviations ς close to or larger than the wavelength λ.

4.4.3. Kirchhoff's Approximation

Now we consider the other limiting case when the characteristic size of the Earth's surface roughness significantly exceeds the wavelength size of the radiated field. In this case, the Kirchhoff approximation may be used to obtain a reasonably simple solution. What is very important to note is that this method requires the absence of shadow zones between all roughnesses and/or multi-reflection and multi-scattering between each part of the rough surface at $z = 0$. In other words, we assume that the surface S is slowly varying so that the radius of curvature is much greater than the wavelength (Fig. 4.16). At each point $\mathbf{r}$ on the quasi-smooth surface S, the wave field
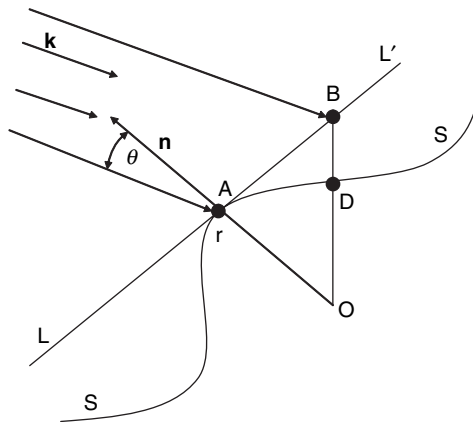
FIGURE 4.16. Geometrical presentation of a quasi-smooth terrain described by Kirchhoff's approximation.

is a superposition of the incident field $\mathbf{E}_0$ and the field $\mathbf{E}$ reflected from the plane LL'. This plane is tangential to the surface S at point $\mathbf{r}$, as shown in Figure 4.16. The scattered electromagnetic wave at the observation point R can be represented by the values of $\mathbf{E}$ and $\mathbf{H}$ on the surface S and by using the well-known Green's function presentation for the point source, $G = \frac{\exp\{ikR\}}{R}$, that is,

$$\mathbf{E}_i(\mathbf{r} \in S) = \mathbf{E}_0 \frac{\exp\{ikR_1\}}{R_1}, \qquad \mathbf{H}_i(\mathbf{r} \in S) = \mathbf{H}_0 \frac{\exp\{ikR_1\}}{R_1} \tag{4.64}$$

The final expression for the scattered filed is

$$\begin{aligned}
\mathbf{E}(\mathbf{R}) = \frac{ik}{4\pi} \int\limits_S \frac{e^{ik(R_1+R_2)}}{R_1 R_2} &\{[\mathbf{n} \times (\mathbf{H} - \mathbf{H}_0)] + [\mathbf{n} \cdot (\mathbf{E} - \mathbf{E}_0) \cdot \nabla_r R_2] \\
&- [\nabla_r R_2 \times \mathbf{n} \times (\mathbf{E} - \mathbf{E}_0)]\} \mathrm{d}s
\end{aligned} \tag{4.65}$$

Here, as follows from Figure 4.17, R_1 and R_2 are the distances from the current point $\mathbf{r}(x, y, z = 0)$ at the flat surface $z = 0$ to the source point O and the observation point R; $\widetilde{R}_1$ and $\widetilde{R}_2$ are the distances from the current point $\mathbf{r}(x, y, z)$ at the surface S over which the integration in (4.65) takes place; $\varsigma(\mathbf{r})$ is the height of the surface S at the arbitrary point $\mathbf{r}(x, y, z)$. If the source and observations point are located in the far-field zone relative to surface S, that is, $k\widetilde{R}_1 \gg 1$ and $k\widetilde{R}_2 \gg 1$, the integral in (4.65) for the scattered field in the direction $\mathbf{k}_s$ can be rewritten as

$$\begin{aligned}
\mathbf{E}(\mathbf{k}, \mathbf{k}_s) = \frac{ik}{4\pi} \frac{e^{ik(R_{10}+R_{20})}}{R_{10} R_{20}} \int\limits_{S_0} &\{[\mathbf{n} \times (\mathbf{H} - \mathbf{H}_0)] + [\mathbf{n} \cdot (\mathbf{E} - \mathbf{E}_0) \cdot \nabla_r R_2] \\
&- [\nabla_r R_2 \times \mathbf{n} \times (\mathbf{E} - \mathbf{E}_0)]\} \exp\{i[(\mathbf{k} - \mathbf{k}_s)\mathbf{r} + (k_z - k_{sz})\varsigma(\mathbf{r})]\} \frac{\mathrm{d}\mathbf{r}}{q_z}
\end{aligned} \tag{4.66}$$

Here R_{10} and R_{20} are the distances between the arbitrary point $\mathbf{r}(x, y, z = 0)$ on the surface S_0, which is the projection of rough surface S at the plane $z = 0$, and
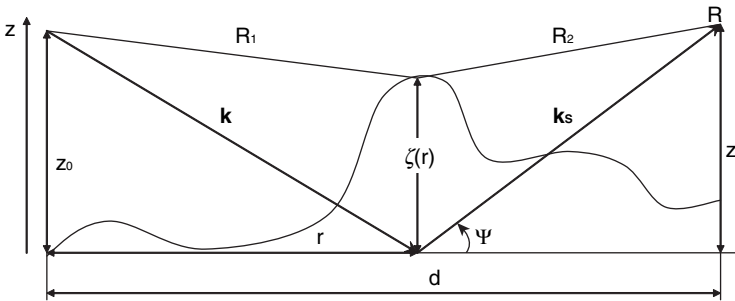
FIGURE 4.17. Reflection from a quasi-smooth terrain.

the source O and observed point R, respectively. For future analysis of the integral in (4.66), it is convenient to present the distances $\widetilde{R}_1$ and $\widetilde{R}_2$ through the vector $\mathbf{r}(x, y, z = 0)$ that lies on the flat surface $z = 0$ and the value of surface height $\varsigma(\mathbf{r})$ at this current point (see Figure 4.17):

$$\widetilde{R}_1 = \sqrt{r^2 + (z_0 - \varsigma)^2} \approx R_1 + \alpha_z \varsigma$$

$$\widetilde{R}_2 = \sqrt{(d - r)^2 + (z - \varsigma)^2} \approx R_2 + \beta_z \varsigma \qquad (4.67)$$

$$\text{where} \quad R_1 = \sqrt{r^2 + z^2}, \quad R_2 = \sqrt{(d - r)^2 + z^2};$$

$\alpha_z = -\frac{z_0}{R_1}$ and $\beta_z = \frac{z}{R_2}$ are the z-components of vectors $\mathbf{a} = \nabla_r R_1$ and $\mathbf{b} = -\nabla_r R_2$ (i.e., the projections of these vectors at the z-axis). We analyze the expression (4.66) that describes the scattered field for two cases that are useful in practice for over-the-terrain propagation by introducing some new variables according to References [9–14]: $\mathbf{q} = \mathbf{k}_s - \mathbf{k}$, $\mathbf{k} = k\mathbf{a} = k\nabla_r R_1$, $\mathbf{k}_s = k\mathbf{b} = -k\nabla_r R_2$.

In the case of a *perfectly conducting* Earth's surface, the expression (4.66) can be simplified taking into account that the electric and magnetic components of the electromagnetic field are mutually perpendicular, $\mathbf{H}_0 = \mathbf{k} \times \mathbf{E}_0 / k$, and that we concentrate only on the short-wave approximation ($q_z \varsigma \gg 1$), that is,

$$\mathbf{E}(\mathbf{k}, \mathbf{k}_s) \approx \frac{ik}{2\pi} \frac{e^{ik(R_{10} + R_{20})}}{R_{10} R_{20}} \frac{[\mathbf{b} \times (\mathbf{E}_0 \times \mathbf{q})]}{q_z} \int_{S_0} \exp\{-i[\mathbf{q} \cdot \mathbf{r} + q_z \varsigma(\mathbf{r})]\} d\mathbf{r}. \qquad (4.68)$$

After statistical averaging of integral (4.68), the average scattered field can be presented as

$$\langle \mathbf{E}(\mathbf{k}, \mathbf{k}_s) \rangle = \mathbf{E}^{(0)}(\mathbf{k}, \mathbf{k}_s) \Gamma_f(\psi) \qquad (4.69)$$

where

$$\mathbf{E}^{(0)}(\mathbf{k}, \mathbf{k}_s) = \frac{ik}{2\pi} \frac{e^{ik(R_{10} + R_{20})}}{R_{10} R_{20}} \frac{[\mathbf{b} \times (\mathbf{E}_0 \times \mathbf{q})]}{q_z} \int_{S_0} \exp\{-i\mathbf{q} \cdot \mathbf{r}\} d\mathbf{r} \qquad (4.70)$$

is the field reflected from area S_0 of the plane $z = 0$, and $\Gamma_f(\psi)$ is the effective reflection coefficient from the rough terrain, which for the surface S with a Gaussian distribution, can be presented as [21–27]

$$\Gamma_f(\psi) \approx \exp\{-2k^2 \varsigma^2 \sin^2 \psi\} \qquad (4.71)$$

Here, ψ is the slip angle (see Fig. 4.17). One can see that the effective reflection coefficient decreases exponentially with an increase of roughness height $\varsigma(\mathbf{r})$.

Now, by introducing the tensor coefficient of reflections $\Gamma^E_{j\ell} = -\delta_{j\ell} + 2n_jn_\ell$, where the double repeated index ℓ indicates the summation from 1 to 3, and $\delta_{j\ell}$ the unit tensor, (which equal 1, if $j = 1$, and 0, if $j \neq 1$) one can finally obtain from (4.68) the solution for the $\mathbf{E}_j$-component of the scattered field [9–14]:

$$\mathbf{E}_{j\ell}(\mathbf{k}, \mathbf{k}_s) \approx \frac{e^{ik(R_{10}+R_{20})}}{4\pi i R_{10}R_{20}} \frac{q^2}{q_z} \Gamma^{\mathrm{E}}_{j\ell} \cdot \mathbf{E}_{0\ell} \int\limits_{S_0} \exp\{-i[\mathbf{q} \cdot \mathbf{r} + q_z \varsigma(\mathbf{r})]\}d\mathbf{r} \qquad (4.72)$$

The same result can be obtained for the $\mathbf{H}_j$-component of the scattered field by introducing in (4.72) the following terms: $\mathbf{H}_{j\ell}$, $\mathbf{H}_{01}$ and $\Gamma^{\mathrm{H}}_{j\ell} = -\Gamma^{\mathrm{E}}_{j\ell}$, respectively.

A generalization of the problem for this case of scattering from the impedance rough surface for $(k \rightarrow \infty)$, gives the same result, as expressed in (4.72) for the perfectly conducting ground surface in terms of tensor:

$$\Gamma^{\mathrm{E}}_{j\ell} = \Gamma_{\mathrm{V}}\delta_{j\ell} - \frac{1}{\sin\vartheta}\{(\Gamma_{\mathrm{H}} + \Gamma_{\mathrm{V}}\cos\vartheta)n_jn_\ell + \cos\vartheta(\Gamma_{\mathrm{H}} + \Gamma_{\mathrm{V}})\alpha_jn_\ell\}$$
$$(4.73)$$
$$\Gamma^{\mathrm{H}}_{j\ell} = \Gamma_{\mathrm{V}}\delta_{j\ell} - \frac{1}{\sin\vartheta}\{(\Gamma_{\mathrm{V}} + \Gamma_{\mathrm{H}}\cos\vartheta)n_jn_\ell + \cos\vartheta(\Gamma_{\mathrm{H}} + \Gamma_{\mathrm{V}})\alpha_jn_\ell\},$$

which are significantly simplified for the case of the perfectly conducting surface and can be presented as

$$\Gamma^{\mathrm{H}}_{j\ell} = -\Gamma^{\mathrm{E}}_{j\ell} = \delta_{j\ell} - 2n_jn_\ell \qquad (4.74)$$

Here Γ_{H} and Γ_{V} are the reflection coefficients presented, previously, by formulas in (4.50) in Section 4.3 for the horizontal and vertical polarizations, respectively. Let us note that the expression in (4.72), allows us to treat scattering phenomena from a surface with arbitrary dielectric properties not only for the linearly polarized waves but also for the elliptically polarized waves. Thus, a linearly polarized wave, after undergoing scattering from the impedance rough surface, becomes elliptically polarized. But what is more interesting is that the depolarization phenomenon is not connected with the statistical properties of the rough terrain. It is completely determined by the inclination of the tangential plane G_r to the surface S at the points of specular reflection. The direction of vector $\mathbf{n}_0$ normal to this plane (and, hence the polarization of reflected field) is related to the direction of wave vector $\mathbf{k}$ of the incident wave and to the direction of the observation point $\mathbf{k}_s$ through the relation, $\mathbf{n}_0 = \frac{\mathbf{k}_s-\mathbf{k}}{|\mathbf{k}_s-\mathbf{k}|}$. Therefore, one can directly use the tensor presentation of the Fresnel reflection coefficients defined in (4.73) with the following conditions, such as $\mathbf{n} = \mathbf{n}_0$ and $\vartheta = \vartheta_0 = \cos^{-1}(\mathbf{n} \cdot \mathbf{b})$, $\mathbf{b} = -\nabla_r R_2$ for the evaluation of the scattered field for different kinds of polarization.

4.4.4. The Rayleigh Approximation

The use of Rayleigh approximation depends, not on the dimensions of surface roughness with respect to the wavelength, but mostly on the antenna elevation height. For the cases where the coherence length L between two nearby reflected rays is higher than λ, and the roughness is small compared to λ, that is, $\sigma \ll \lambda$ and $\sigma < \lambda$, the phase difference between field components becomes larger than $\pi/2$. Here the Rayleigh approximation is not as accurate as the Kirchhoff approximation. Sometimes the phase difference is close to $\pi/4$ and $\pi/8$. In that case a scalar Rayleigh factor in the coherent field can be introduced for such gently rough surfaces, which reduces the energy of the specularly reflected wave. These "above-the-terrain" propagation cases will be examined briefly below by using the effective Kirchhoff reflection coefficients and their corresponding effective permittivity of the rough terrain.

For the high-elevated antennas, the roughness is small compared to the wavelength ($\sigma < \lambda$). In this case of gentle rough ground surface, the two-ray model usually applied to smooth terrain and describes the coherent part of the signal, can be modified by introducing the reflection coefficient for vertical, Γ_{V}, and horizontal, Γ_{H}, polarization, as functions of the effective relative permittivity, ε_{reff} [15–27]

$$\Gamma_{V} = \frac{\varepsilon_{reff} \sin\psi - \sqrt{\varepsilon_{reff} - \cos^2\psi}}{\varepsilon_{reff} \sin\psi + \sqrt{\varepsilon_{reff} - \cos^2\psi}} \tag{4.75a}$$

$$\Gamma_{H} = \frac{\sin\psi - \sqrt{\varepsilon_{reff} - \cos^2\psi}}{\sin\psi + \sqrt{\varepsilon_{reff} - \cos^2\psi}} \tag{4.75b}$$

So, the modified coherent component of the total field intensity is

$$I_{co\,mod} = E_0^2 \left\{ \frac{e^{-jkr_1}}{r_1} + \Gamma_{V,H} \frac{e^{-jkr_2}}{r_2} \right\}^2 \tag{4.76}$$

where ψ is the grazing angle defined earlier, r_1 is the distance of the direct radio path between the antennas, r_2 is the distance from the transmitter to the point of reflection and from the point of reflection to the receiver, that is the radio path length of the reflected wave. The equivalent surface impedance is $\eta = \sqrt{\frac{\mu_r}{\varepsilon_{reff}}} \cong \frac{1}{\sqrt{\varepsilon_{reff}}}$, with the relative permeability $\mu_r \approx 1$, for all nonferromagnetic surfaces.

There are six distinct cases that can be considered here, three for each linear polarization, vertical and horizontal. These three asymptotic cases are valid

a) for short correlation lengths L and all grazing angles ψ;
b) for long correlation length L and large grazing angles ψ;
c) for long correlation length L and small grazing angles ψ.

So, for vertical polarization, the effective surface impedance η has a real part corresponding to a loss of power and an imaginary part corresponding to a reactive,

stored energy near the surface. Furthermore, the change in effective surface impedance for vertical polarization is strictly reactive for short correlation lengths ($\lambda \gg L$), resistive for large correlation lengths and large grazing angles ($\lambda \ll L$ and $\psi \gg \frac{1}{\sqrt{kL}}$), and a mixture of both for large correlation lengths and small grazing angles ($\lambda \ll L$ and $\psi \ll \frac{1}{\sqrt{kL}}$). For the case of a horizontally polarized field the surface impedance and the corresponding effective permittivity can be derived in a similar fashion.

In the case of low antenna elevation with respect to roughness, the criteria of $\sigma \geq \lambda$ and $\sigma \gg \lambda$ are generally valid and the Rayleigh scalar factor can be used as long as the criteria of the Kirchhoff approximation are fulfilled. In this case, instead of the specular reflection coefficients, we introduce the following effective reflection coefficients [9–16]

  a) for vertical polarization

$$\Gamma_V^{ef} = \Gamma_V \exp\left[-2\left(2\pi\frac{\sigma}{\lambda}\sin\psi\right)^2\right] \tag{4.77}$$

where $\exp\left[-2\left(2\pi\frac{\sigma}{\lambda}\sin\psi\right)^2\right]$ is the Rayleigh's factor; the coefficient Γ_V is defined by (4.50b) in Section 4.3 and can be reduced to

$$\Gamma_V = -1 + 2\psi\frac{\varepsilon_r}{\sqrt{\varepsilon_r - 1}} \tag{4.78}$$

  b) for horizontal polarization

$$\Gamma_H^{ef} = \Gamma_H \exp\left[-2\left(2\pi\frac{\sigma}{\lambda}\sin\psi\right)^2\right] \tag{4.79}$$

where Γ_H is defined by (4.50a) in Section 4.3 and can be reduced to

$$\Gamma_H = -1 + 2\psi\frac{1}{\sqrt{\varepsilon_r - 1}} \tag{4.80}$$

So, the use of each approximation strongly depends not only on the dimensions of rough structures with respect to the wavelength, but mostly on the terminal antenna elevations as well.

4.5. PROPAGATION ABOVE A SMOOTH CURVED TERRAIN

Let us now consider the case when the terrain is smooth but curved (see Fig. 4.18). In this case the degree of curvature and diffraction caused by the curved earth surface must be taken into account for the evaluation of field characteristics. In practice, for
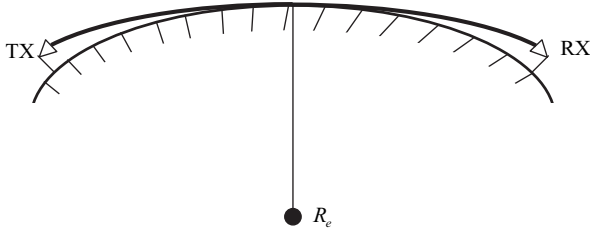
FIGURE 4.18. Geometrical presentation of radio path above a curved terrain.

land communications, it is very important to note that the influence of the curvature of the Earth's surface must be taken into account only for radio paths longer than 20–30 km.

Fock's Model. To take into account the terrain curvature and diffraction from the curved terrain, Fock, by introducing two special scales: the *range scale*, $L = (\lambda R_e^2/\pi)^{1/3}$, and the *height scale*, $H = 0.5 \cdot (\lambda^2 R_e/\pi^2)^{1/3}$, respectively, has determined the range of radio path, d, and the heights of both terminal antennas, h_T and h_R, using the dimensionless parameters $x = d/L$, $y_1 = h_T/H$, $y_2 = h_R/H$. The attenuation factor with respect to the flat terrain has a form [28]

$$F = 2\sqrt{\pi x} \left| \sum_{k=1}^{\infty} \frac{\exp(ixt_k)}{(t_k + p^2)} \frac{A(t_k + y_1)}{A(t_k)} \frac{A(t_k + y_2)}{A(t_k)} \right| \tag{4.81}$$

where

$$p = i(\pi R_e/\lambda)^{1/3}/\sqrt{\varepsilon_{r0} - i60\lambda\sigma} \tag{4.82}$$

$R_e = 6375$ km is the actual earth's radius. By $A(w)$ we denote a special airy function, which is related to the special Hankel's function of the order $1/3$ through

$$A(w) = \sqrt{\pi/3} \exp(-i2\pi/3) w^{1/2} H_{1/3}(2w^{3/2}/3) \tag{4.83}$$

Here t_k are the roots of

$$A'(t) - pA(t) = 0 \tag{4.84}$$

It can be shown that the value of t_k for finite values of p can be estimated as follows:

$$t_k(p) \approx t_k(0) + p/t_k(0), \qquad |p/\sqrt{t_k}| < 1 \tag{4.85a}$$

and

$$t_k(p) \approx t_k(\infty) + 1/p, \qquad |p/\sqrt{t_k}| > 1 \tag{4.85b}$$

Let us introduce the parameter $\bar{t}_k = t_k \cdot \exp(-2\pi/3)$. Next, we can compute the first set of roots $f_i(0)$ and $f_i(\infty)$ of Equation (4.84) as

$$
\begin{array}{ll}
\bar{t}_1(0) = 1.019, & \bar{t}_1(\infty) = 2.338 \\
\bar{t}_2(0) = 3.248, & \bar{t}_2(\infty) = 4.088 \\
\bar{t}_3(0) = 4.820, & \bar{t}_3(\infty) = 5.521 \\
\bar{t}_4(0) = 6.163, & \bar{t}_4(\infty) = 6.787 \\
\bar{t}_5(0) = 7.372, & \bar{t}_5(\infty) = 7.994
\end{array}
$$

For the UHF/X-frequency band, in the shadow zones due to ground surface curvature, where $|p| \gg 1$, we can write the attenuation factor as:

$$F = U(x)V(y_1)V(y_2) \tag{4.86}$$

The first term depends on the normalized range x between the antennas

$$U(x) = 2\sqrt{\pi x} \left| \frac{\exp(ixt_1)}{t_1 + p^2} \right| \tag{4.87}$$

but the second and the third terms are only functions of the antenna heights (*height parameters*)

$$V(y_{1,2}) = \left| \frac{H(t_1 + y_{1,2})}{H(t_1)} \right| \tag{4.88}$$

We must note that according to the above definitions, if both antennas are close to the ground surface (i.e., $y_{1,2} = 0$) then the "height product" $V(y_{1,2}) = 1$. Moreover, for $y_{1,2} < 1$, the "antenna height" factors $V(y_{1,2})$ (in decibels (dB)) are negative, otherwise they are positive. For $y_{1,2} < 1$ these factors can be approximated as

$$V(y_{1,2}) \cong 20 \log(y_{1,2}) [\text{dB}] \tag{4.89}$$

For $y_{1,2} \geq 1$, some estimates give us:

$$V(1) \cong 0 \, \text{dB}; \quad V(2) \cong 10 \, \text{dB}; \quad V(4) \cong 20 \, \text{dB}; \quad V(7) \cong 30 \, \text{dB}; \quad V(10) \cong 40 \, \text{dB}.$$

So, the above formulas allow us to compute, with great accuracy, the additional loss due to diffraction at the spherical ground surface both in the geometrical shadow zone and in zones of half shadowing. These formulas can be used to predict the diffraction losses of the wave field caused by the Earth's curvature. Once again, the effect of the Earth's curvature must be taken into account only for land radio cases with ranges of more than 10–20 km. At the same time we must note that for the long radio paths (more than 100 km) the real terrain profile of the path is obviously beyond the capabilities of the Fock's model.

4.6. EFFECT OF A SINGLE OBSTACLE PLACED ON A FLAT TERRAIN

Existing obstructions along the radio path leads to additional losses called diffraction losses, which are usually observed in rural areas where some arbitrary obstructions (such a hill, mountain etc.) exist. When there is a single obstacle between the transmitter and receiver, which can be modeled by a single "knife edge", losses of the wave energy take place. Such losses in the literature are called *diffraction losses* [29–36]. They can be obtained analytically by using the Fresnel complex integral based on the Huygen's principle discussed in Section 4.2. The total field E_{total} after diffraction from the obstruction can be presented in the following form:

$$E_{\text{total}} = E_0 \cdot \hat{D} \cdot \exp\{j\Delta\Phi\} \qquad (4.90)$$

where E_0 is the incident wave from the transmitter located in free space; $\hat{D}$ is the diffraction coefficient or matrix [29–36], $\Delta\Phi$ is the phase difference between the diffracted and direct waves mentioned above. The main goal of diffraction theory is to obtain parameters $\hat{D}$ and $\Delta\Phi$ by using an analytical deterministic approach based on complex Fresnel integral presentation [3]:

$$F(v) = \int_0^v \exp\left\{-i\frac{\pi}{2}v^2\right\}dv = -F(-v) \qquad (4.91)$$

To estimate the effect of diffraction around obstructions, we need a quantitative measure of the required clearance over any terrain obstruction, and, as was shown in Section 4.2, this may be obtained analytically in terms of Fresnel-zone ellipsoids drawn around both ends of the radio link, the receiver, and the transmitter (see Fig. 4.6). We discussed these zones when we presented free space propagation concepts and reflections from a flat terrain. Now, let us introduce the Fresnel-zone concept related to diffraction. We show this concept based on the illustration in Figure 4.19, where the cross-section radius of any ellipsoid with number n from the family at a distance r_0 and $r_0' = r - r_0$ was presented as a function of the parameters n, r_0, and r_0' by (4.23) in Section 4.2, which we repeat for convenience

$$h_n = \left[\frac{n\lambda r_0 r_0'}{(r_0 + r_0')}\right]^{1/2} \qquad (4.92)$$

The Fresnel integral in (4.91) gives the cumulative effect from several first Fresnel zones covered by the obstruction. In Figure 4.19, the Fresnel (also called *diffraction*) parameter v in (4.91) is presented by the following formula [29–36]:

$$v = h_n \cdot \left[\frac{2(r_0 + r_0')}{\lambda r_0 r_0'}\right]^{1/2} = (2n)^{1/2} \qquad (4.93)$$
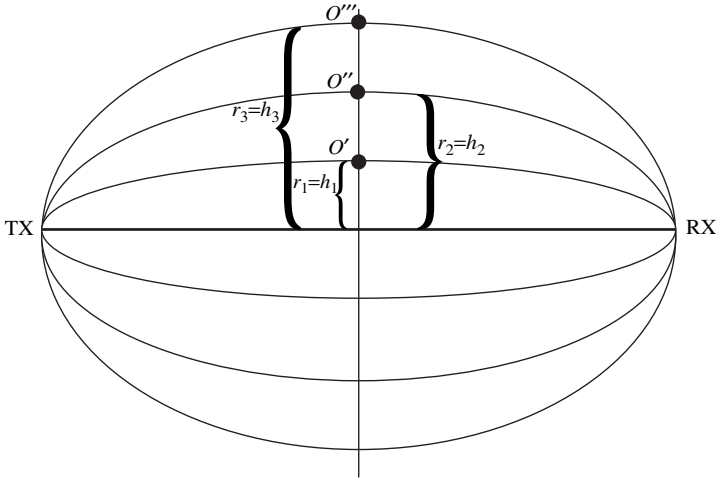
FIGURE 4.19. Geometrical presentation of the Fresnel zones in terms of ellipsoids.

From (4.92) and (4.93) one can obtain the physical meaning of the Fresnel–Kirchhoff diffraction parameter v. Thus, the diffraction parameter v increases with the number n of ellipsoids. All the above formulas are corrected for $h_n \ll r_0, r_0'$, that is, far from the terminal antennas. The volume enclosed by the ellipsoid and defined by $n = 1$ is known as the *first Fresnel zone*. The volume between this ellipsoid and the one that is defined by $n = 2$ is the *second Fresnel zone*. The contributions to the total field at the receiving point, from successive Fresnel zones, interfere by giving a very complicated interference picture at the receiver. If a virtual line OO' is placed at the middle of the radio path $TO'R$ (i.e., $TO' = O'R$, as shown in Fig. 4.19) then, if the height of the virtual point O' (the virtual source of diffraction) h increases from $h = h_1$ (corresponding to the first Fresnel zone) to $h = h_2$ (e.g., to the point O'' defining the limit of the second Fresnel zone), then to $h = h_3$ (i.e., to the point O''' defining the limit of the third *Fresnel zone*) and so on, the field at the receiver R will oscillate. The amplitude of oscillations would essentially decrease as a smaller amount of wave energy penetrates into the outer zone relative to the inner zone.

If, for example, some obstacles that we may model by a simple knife edge (with height above the line-of-sight line TOR, h, denoted in Fig. 4.20 as $OO^{(n)}$), lies between the receiver and the transmitter at distances r_0 and r_0', respectively, the Fresnel parameter can be presented as [1–8]

$$v = h\left[\frac{2(r_0 + r_0')}{\lambda r_0 r_0'}\right]^{1/2} = 2\left[\frac{\Delta r}{\lambda}\right]^{1/2} \qquad (4.94)$$

and the phase difference $\Delta\Phi$ between the direct ray from the source placed at the point O (denoted TOR) and the diffracted ray from the point $O^{(n)}$ (denoted
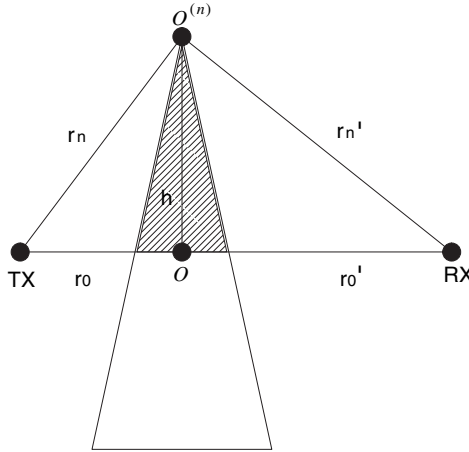
FIGURE 4.20. Geometrical presentation of the knife-edge diffraction.

TO$^{(n)}$ R) can be obtained in the standard manner by use of a simple presentation of the path difference, Δr, and the phase difference, $\Delta\Phi$, between these rays. From the geometry of the problem, shown in Figure 4.20, and using relationship (4.94) between Δr and v, the phase difference, $\Delta\Phi$, can be presented as

$$\Delta\Phi = \frac{2\pi}{\lambda}\Delta r = \frac{\pi}{2}v^2 \qquad (4.95)$$

From the above discussions, it is clear that any radio path in obstructive conditions requires a certain amount of a clearance around the central ray if free-space propagation is to occur. This effect can be understood by using the principle of *Fresnel clearance*, which is important in the design of point-to-point radio links, where communication is required along a single radio path. This clearance can be explained in terms of Fresnel zones. Thus, the first Fresnel zone (for $n = 1$) encloses all radio paths for which the additional path length Δr, defined in (4.94), does not exceed $\frac{\lambda}{2}$, and according to (4.95), a phase change is $\Delta\Phi_1 = \pi$. The second Fresnel zone (for $n = 2$) encloses all paths for which the additional path length Δr does not exceed $2\cdot\frac{\lambda}{2} = \lambda$, and correspondingly, $\Delta\Phi_2 = 2\pi$, and so on. The corresponding radius of the first Fresnel zone h_1 can be derived by setting $\Delta r = \frac{\lambda}{2}$ in (4.92). As a result,

$$h_1 = \left(\frac{\lambda r_0 r_0'}{r_0 + r_0'}\right)^{1/2} = \left(\frac{300\cdot r_0 r_0'}{fr}\right)^{1/2} \qquad (4.96)$$

where f is measured in gigahertz and $r = r_0 + r_0'$ in kilometer. The shape of the first Fresnel zone and the effect of the obstruction on the clearance are clearly illustrated
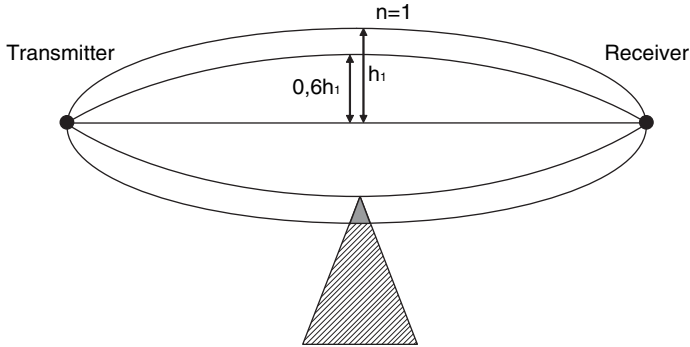
FIGURE 4.21. The clearance effect in the presence of knife-edge obstruction.

by Figure 4.21. The clearance due to the diffraction effect from the obstruction is about 60% of the first Fresnel zone, which normally in practice is considered an adequate value for the land rural point-to-point radio links. To finish this analysis, we must mention that the Fresnel-zone principle, as well as the clearance explanation is correct for the case where $r > r_0$, $r_0' \gg h_n$, which is adequate for the most practical cases of land radio link designs.

BIBLIOGRAPHY

[1] Jackson, J. D., *Classical Electrodynamics*, John Wiley & Sons, New York, 1962.

[2] Kong, J.A., *Electromagnetic Wave Theory*, John Wiley & Sons, New York, 1986.

[3] Dudley, D. G., *Mathematical Foundations for Electromagnetic Theory*, IEEE Press, New York, 1994.

[4] Al'pert, Ia. L., V. L. Ginsburg, and E. L. Feinberg, *Radio Wave Propagation*, State Printing House for Technical-Theoretical Literature, Moscow, 1953.

[5] Jakes, W. C., *Microwave Mobile Communications*, John Wiley and Sons, New York, 1974.

[6] Lee, W. Y. C., *Mobile cellular Telecommunications Systems*, McGraw Hill Publications, New York, 1989.

[7] Saunders, S. R., *Antennas and Propagation for Wireless Communication Systems*, John Wiley & Sons, New York, 1999.

[8] Steele, R., *Mobile Radio Communication*, IEEE Press, New York, 1992.

[9] Bass, F. G., and I. M. Fuks, *Wave Scattering from Statistically Rough Surfaces*, Pergamon Press, Oxford, 1979.

[10] Tatarskii, V. I., and M. I. Charnotskii, "On the universal behavior of scattering from a rough surface from small grazing angles," *IEEE Trans. Anten. Propagat.*, Vol. 46, No.1, 1995, pp. 67–72.

[11] Voronovich, A. G., *Wave Scattering from Rough Surfaces*, Springer-Verlag, Berlin, 1994.

[12] Backmann, P., and A. Spizzichino, *The Scattering of Electromagnetic Waves from Rough Surfaces*, Artech House, Boston-London, 1963.

[13] Felsen, L., and N. Marcuvitz, *Radiation and Scattering of Waves*, Prentice Hall, New Jersey, 1973.

[14] Ishimaru, A., *Electromagnetic Wave Propagation, Radiation, and Scattering*, Englewood Cliffs, Prentice-Hall, New Jersey, 1991.

[15] Miller, A. R., R. M. Brown, and E. Vegh, "New derivation for the rough-surface reflection coefficient and for the distribution of the sea-wave elevations," *IEE Proc.*, Vol. 131, Pt. H, No. 2, 1984, pp. 114–116.

[16] Ogilvy, J. A., *Theory of Wave Scattering from Random Rough Surfaces*, Bristol, IOP, 1991.

[17] Rice, S. O., "Reflection of electromagnetic waves from slightly rough surfaces," *Comm. Pure Appl. Math.*, Vol. 4, No. 3, 1951, pp. 351–378.

[18] Barrick, D. E., and W. H. Peake, "A review of scattering from surfaces with different roughness scales," *Radio Sci.*, Vol. 3, No. 7, 1968, pp. 865–868.

[19] Barrick, D. E., "Theory of HF and VHF propagation across the rough sea-Parts I and II," *Radio Sci.*, Vol. 6, No. 3, 1971, pp. 517–533.

[20] Barrick, D. E., "First order theory and analysis of MF/HF/VHF scatter from the sea," *IEEE Trans. Anten. Propagat.*, Vol. 20, No. 1, 1972, pp. 2–10.

[21] Wait, J. R., "Perturbation analysis for reflection from two-dimensional periodic sea waves," *Radio Sci.*, Vol. 6, No. 3, 1971, pp. 387–391.

[22] Valenzuela, G. R., "Scattering of electromagnetic waves from a slightly rough surface moving with uniform velocity," *Radio Sci.*, Vol. 3, No. 1, 1968, pp. 12–21.

[23] Valenzuela, G. R., "Scattering of electromagnetic waves from a tilted slightly rough surface," *Radio Sci.*, Vol. 3, No. 6, 1968, pp. 1057–1066.

[24] Valenzuela, G. R., "The effective reflection coefficients in forward scatter from a dielectric slightly rough surface," *Proc. IEEE*, Vol. 58, No. 12, 1970, pp. 1279–1285.

[25] Krishen, K., "Scattering of electromagnetic waves from a layer with rough front and plane back (small perturbation method by Rice)," *IEEE Trans. Anten. Propagat.*, Vol. 19, No. 4, 1970, pp. 573–576.

[26] Davies, H., "The reflection of electromagnetic waves from a rough surface," *Proc. IEEE*, Vol. 101, No. 2, 1954, pp. 209–214.

[27] Bullington, K., "Reflection coefficient of irregular terrain," *Proc. IRE*, Vol. 42, No. 11, 1954, pp. 1258–1262.

[28] Fock, V. A., *Electromagnetic Diffraction and Propagation Problems*, Pergamon Press, Oxford, 1965.

[29] Keller, J. B., "Diffraction by an Aperture," *J. Appl. Phys.*, Vol. 28, 1957, pp. 857–893.

[30] Keller, J. B., "Geometrical theory of diffraction," *J. Opt. Soc. Amer.*, Vol. 52, No. 1, 1962, pp. 116–131.

[31] James, G. L., *Geometrical Theory of Diffraction for Electromagnetic Waves*, 3-nd ed., Peter Peregrines, London, UK, 1986.

[32] Honl, H., A. W. Maue, and K. Westpfahl, *Theory of Diffraction*, Springer-Verlag, Berlin, 1961.

[33] Kouyoumjian, R. G., and P. H. Pathak, "An uniform geometrical theory of diffraction for an edge in a perfectly conducting surface," *Proc. IEEE*, Vol. 62, No. 9, 1974, pp. 1448–1469.

[34] Russel, S. T. A., C. W. Boston and T. S. Rappaport, "A deterministic approach to predicting microwave diffraction by buildings for micro cellular systems," *IEEE Trans. Anten. and Propag.*, Vol. 41, No. 12, 1993, pp. 1640–1649.

[35] Dougherty, H. T., and L. J. Maloney, "Application of diffraction by convex surfaces to irregular terrain situations," *Radio Phone*, Vol. 68B, Feb. 1964, p. 239.

[36] Anderson, L. J., and L. G. Trolese, "Simplified method for computing knife edge diffraction in the shadow region," *IRE Trans. Anten. Propagat.*, Vol. AP-6, July 1958, pp. 281–286.

Terrestrial Radio Communications

In this chapter, we consider wave propagation in various terrain environments based on the description of propagation characteristics such as the propagation (or path) loss, L, and the slope parameter γ that describe the signal decay law. These main parameters are very crucial in predicting land communication channels. First, in Sections 5.1 and 5.2, we introduce the reader into a brief description of the terrain features and various propagation situations in terrestrial communications related to the terminal antenna positions with respect to building rooftops. In Section 5.3, we continue the description of the propagation channel when the two antennas are placed on a flat terrain and under LOS conditions, when a free-space propagation concept can be used and is described by a two-ray model. In Section 5.4, we consider radio propagation in "hilly terrain," where we replace the hill by a "knife edge" and introduce Lee's empirical model. Section 5.5 describes how a single obstruction such as a building is placed above a flat terrain. In this case, on the basis of Keller's geometrical theory of diffraction (GTD), we present formulas that determine the electromagnetic field pattern reradiated by the building walls, corners, and roof for dipole transmitting antenna with vertical polarization. The electrical impedance properties of the building walls are taken into account here. Next, in Section 5.6, we present a unified approach on how to predict radio losses in rural forested links based on a stochastic model that describes multiscattering effects from trees. This model is compared with standard empirical, analytical, and statistical models. Section 5.7 describes radio propagation in mixed residential areas based on the same stochastic approach, but taking into consideration only a single scattering from houses and trees. Section 5.8 introduces the reader to the problems of radio propagation in

urban and suburban areas, where we consider two typical situations in the urban scene:

a) urban grid-plan buildings' distribution with straight crossing rows of streets, and

b) urban areas with randomly distributed buildings placed on a rough terrain.

Here, we present the unified stochastic approach that generalizes the stochastic models presented in Sections 5.6 and 5.7 by accounting for the buildings overlay profile and effects of diffraction from buildings' roofs. We compare this general model with those that are mostly used for predicting loss characteristics in such terrestrial communication links.

5.1. CHARACTERIZATION OF THE TERRAIN

The process of classifying *terrain configurations* is a very important stage in the construction of propagation models above the ground surface and, finally, in predicting the signal/wave attenuation (or "path loss", defined in Chapter 1) within each specific propagation channel.

These terrain configurations can be categorized as:

- flat ground surface;
- curved, but smooth terrain;
- hilly terrain;
- mountains.

The *built-up areas* can also be simply classified as [1–4]:

- rural areas;
- mixed residential areas;
- suburban areas;
- urban areas.

Several experiments carried out in different built-up areas have shown that there are many specific factors that must be taken into account to describe specific propagation phenomena, such as [1–4]:

– buildings' density or terrain coverage by buildings (in percentages);
– buildings' contours or their individual dimensions;
– buildings' average height;
– positions of buildings with respect to base station and mobile vehicles;
– positions of both antennas, receiver and transmitter, with respect to the rooftops height;

– density of vegetation, presence of gardens, parks, lakes, and so on;

– degree of "roughness" or "hilliness" of a terrain surface.

Recently, a new standard for terrain classification has been introduced for the analysis of urban topographic maps [1–4]. This standard is based on the following terrain characteristics:

(1) position and distribution of buildings regarding the observer;

(2) dimensions of buildings or useful built-up area;

(3) number of buildings at the tested area;

(4) height of ground surface and its degree of "roughness"; and

(5) presence of vegetation.

Using these specific characteristics and parameters of the terrain, we can easily classify various kinds of terrain by examining the topographic maps for each deployment of a radio communication system.

5.2. PROPAGATION SCENARIOS IN TERRESTRIAL COMMUNICATION LINKS

As remarked earlier, a very important characteristic of the propagation channel is the location/position of both antennas with respect to the obstacles placed around them. Usually there are three possible situations:

A. Both antennas, receiver and transmitter, are placed above the tops of obstacles (in a built-up area, this means that they are above the rooftop level) (Fig. 5.1a).

B. One of the antennas is higher than the obstacles' height (namely, the roofs), but the second one is lower (Fig. 5.1b).

C. Both antennas are below the tops of the obstacles (Fig. 5.1c).

In the first situation they are in *direct visibility* or LOS conditions. In the last two situations, one or both antennas are in *clutter* or obstructive conditions. In all these cases the profile of terrain surface is very important and may vary from flat and smooth to a curved surface and finally to a rough and hilly terrain.

5.3. PROPAGATION OVER A FLAT TERRAIN IN LOS CONDITIONS

Instead of using the complicated formulas in Section 4.2 to describe radio wave propagation above the flat terrain, the "two-ray" model can be used. Let us briefly describe this situation that widely occurs in land communication channels.
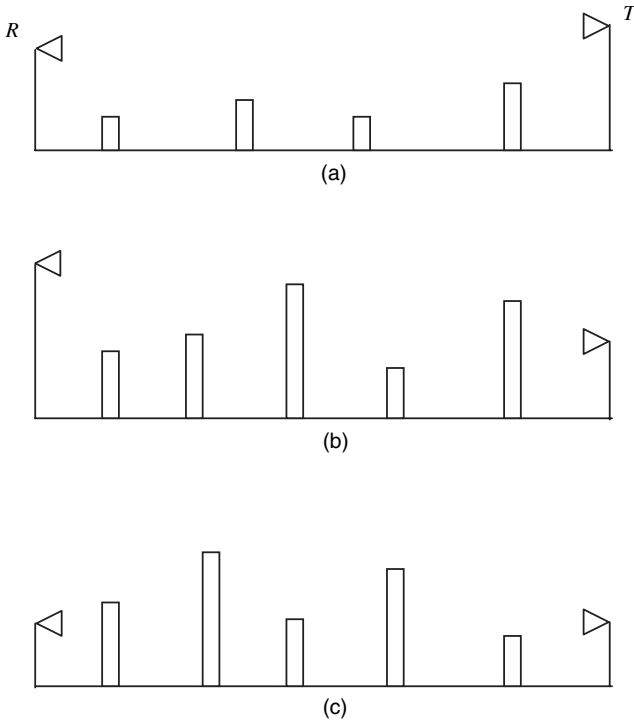
FIGURE 5.1. The three possible locations of the terminal antennas with respect to building height profile.

Two-Ray Model. The *two-ray* or *two-slope* model was first proposed in the early 1960s for describing the process of radio wave propagation over a flat terrain [1–6]. Let us briefly consider the two-ray model, which is based on the superposition of a direct ray from the source and a ray reflected from the flat ground surface, as shown in Figure 5.2. Earlier, in Chapters 2 and 3, the Friis' formula for the direct wave in free space was presented. We will rewrite it in the following form:

$$E = \sqrt{30G_{\mathrm{T}}G_{\mathrm{R}}P_{\mathrm{T}}}/r_1 \tag{5.1}$$

where r_1 is the radio path of direct wave as presented in Figure 5.2. The total field at the receiver is the sum of direct and received waves [7], that is,

$$E_{\mathrm{R}} = E_{\mathrm{T}}\left(1 + \frac{d}{d_1}\Gamma \mathrm{e}^{-jk\Delta d}\right) \tag{5.2}$$

here $\Gamma(\psi)$ is the reflection coefficient described by formulas (4.50a) and (4.50b) in Chapter 4 for horizontal and vertical polarization, respectively. $\Delta r = r_2 - r_1$ (see
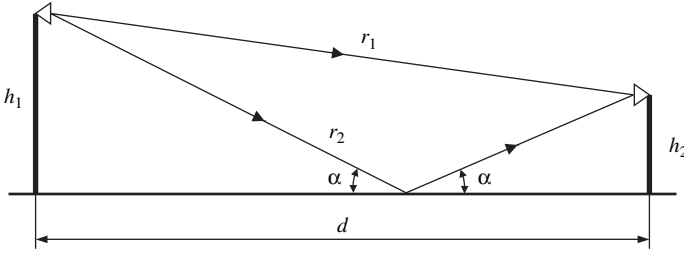
FIGURE 5.2. Geometrical presentation of the two-ray model.

Fig. 5.2) is the difference in the radio paths of the two waves, and $\Delta\varphi = k \cdot \Delta r$ is the phase difference between the reflected and direct waves, which can be presented according to the geometry, in Figure 5.2, as:

$$\Delta\psi = k\Delta d = \frac{2\pi}{\lambda}r\left[\left(1 + \left(\frac{h_R + h_T}{r}\right)^2\right)^{1/2} - \left(1 + \left(\frac{h_R - h_T}{r}\right)^2\right)^{1/2}\right] \quad (5.3)$$

where h_R and h_T are the receiver and transmitter antenna heights, respectively and r is the distance between them. For $r_1 \gg (h_T \pm h_R)$ and $r_2 \gg (h_T \pm h_R)$, using the assumption that $r_1 \approx r_2 \approx r$, the phase difference in (5.3) can be written as:

$$\Delta\varphi = \frac{4\pi h_R h_T}{\lambda \cdot r} \quad (5.4)$$

Furthermore, if we now assume that $G_R \approx G_T = 1$ (valid for isotropic or omnidirectional antennas, see Chapter 2) and that $\Gamma(\psi) \approx -1$ for the farthest ranges from the transmitter (i.e. small grazing angles), we can obtain the magnitude of the signal power at the receiver as [11]:

$$|P_R| = |P_T|\left(\frac{\lambda}{4\pi d}\right)^2 |1 + \cos^2 k\Delta d - 2\cos k\Delta d + \sin^2 k\Delta d|$$

$$= |P_T|\left(\frac{\lambda}{4\pi d}\right)^2 \sin^2\frac{k\Delta d}{2} \quad (5.5)$$

From Equation (5.5) one can determine the distance between a receiver and transmitter for which maximum power is received, taking into account the following conditions:

$$\frac{k\Delta r}{2} \approx \frac{\pi}{2}, \qquad \sin\frac{k\Delta r}{2} \approx 1 \quad (5.6)$$

This distance is called the *critical* or *break point range*, denoted by r_b, and is determined approximately by the following formula:

$$r_b \approx \frac{4h_R h_T}{\lambda} \tag{5.7}$$

Then, following definition of the *path loss* introduced in Chapter 1, and using

$$L = 20 \log |E_i| + 20 \log |1 + \Gamma e^{-jk\Delta d}| \tag{5.8}$$

we can easily obtain the path loss over a flat terrain by making use of the definition of break point range, r_b, and the mathematical description of the "straight line" (as (4.30) in Chapter 4) [7]

$$\text{for } r \leq r_b \quad L = L_b + 10\gamma \log\left(\frac{r}{r_b}\right), \quad \gamma = 2 \tag{5.9a}$$

$$\text{for } r > r_b \quad L = L_b + 10\gamma \log\left(\frac{r}{r_b}\right), \quad \gamma = 4 \tag{5.9b}$$

where L_b is the path loss in free space at the distance that equals the critical range that is, $r = r_b$, which can be calculated from the following formula [7]:

$$L_b = 32.44 + 20 \log r_{b[km]} + 20 \log f_{[MHz]} \tag{5.10}$$

From formulas (5.9a) and (5.9b), there are two modes of field intensity decay. One is $\sim r^{-q}, q = 2$ for $r \leq r_b$, and second is $\sim r^{-q}, q = 4$ for $r > r_b$. From the free space model, the range dependence between the two terminal antennas is $\sim r^{-2}$.

Also, for large distances between the antennas, that is $r > r_b$, we get from Equation (5.5) $\sin^2 \frac{k\Delta r}{2} \approx \left(\frac{k\Delta r}{2}\right)^2$ with $\Delta r = \frac{2h_R h_T}{r}$ (see formulas (5.3) and (5.4)). After some straightforward manipulations, we obtain the formula that describes the signal equation decay $\sim r^{-4}$, usually called the *flat terrain model* [1,2]:

$$L_F = 40 \log r_{[m]} - 20 \log h_T - 20 \log h_R. \tag{5.11}$$

From the two-ray model, the break point is within the range of $r_b = 150\text{--}300$ m from the source; at that point the $\sim r^{-2}$ mode transforms into the $\sim r^{-4}$ mode. This effect depends, according to (5.7), on both antennas' heights and the wavelength. Hence, the two-ray model covers both the free-space propagation model in close proximity to the source and the flat terrain propagation model at far ranges from the source. Most formulas above have been obtained for isotropic or omnidirectional antennas. For more directive antennas, their gain has to be included, as was done in Chapter 2 for Friis' formula.

5.4. PROPAGATION OVER A HILLY TERRAIN IN NLOS CONDITIONS

Formula (4.90) describes the effect of a hill, as a "knife-edge" obstruction, which was introduced in Section 4.5 to estimate the effect of diffraction losses. To accurately obtain the diffraction coefficient and the diffraction losses, the formula with the complex Fresnel integral presentation in (4.91) should be used. However, it is a very time consuming computational task [1–6], and so, *empirical* models are usually used instead. We present below a Lee's empirical model, on which most empirical and semi empirical models are based [36–40].

Lee's Model. A frequently used empirical model, developed by Lee [6], gives the following expressions for the "knife-edge" diffraction losses in decibel:

$$L(v) = L_\Gamma^{(0)} = 0 \text{(dB)}, \qquad\qquad v \le -0.8, \qquad\qquad (5.12a)$$

$$L(v) = L_\Gamma^{(1)} = 20\log(0.5 - 0.62 \cdot v)\text{(dB)}, \qquad -0.8 < v < 0, \qquad (5.12b)$$

$$L(v) = L_\Gamma^{(2)} = 20\log\{0.5\exp(-0.95v)\}\text{(dB)}, \quad 0 \le v < 1, \qquad (5.12c)$$

$$L(v) = L_\Gamma^{(3)} = 20\log[0.4 - (0.1184 - (0.38 - 0.1v)^2)^{1/2}]\text{(dB)}, \quad 1 < v \le 2.4, \qquad (5.12d)$$

$$L(v) = L_\Gamma^{(4)} = 20\log\left(\frac{0.225}{v}\right)\text{(dB)}, \qquad v > 2.4. \qquad (5.12e)$$

These formulas are used for the cases where several knife edges are placed along the radio path between the two terminal antennas. In this case a simple summation of the loss from each individual edge is obtained, according to Equation (5.12). This approach gives a sufficiently correct result (see results of corresponding empirical models described in References [41–44]).

5.5. EFFECT OF A BUILDING ON THE RADIO PROPAGATION CHANNEL

To design an effective radio communication link in a built-up environment with obstructive NLOS conditions, information about the influence of buildings on radio propagation is required. Knowledge of the total field distribution around a building, including diffraction from the building corners and reflection from its walls, is very important in order to predict the radio wave attenuation caused by the building.

In NLOS conditions, it is very important to examine the effects and contribution of all rays arriving at the receiving antenna after interaction with building corners and rooftops. To investigate the problem of radio wave diffraction from buildings, many strict and approximate models have been developed [5,6,9,11–13]. All these models are based on the assumption that all characteristic dimensions of buildings, as well as the ranges between the subscriber antenna and the base station antenna, are larger than the wavelength of the radiated signals. This fact allows us to use Keller's GTD [5,6,9] to describe the diffracted field caused by buildings.
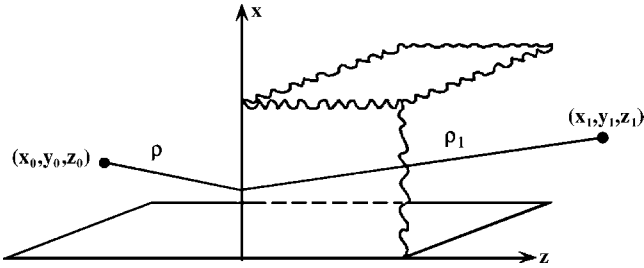
FIGURE 5.3. The transmitter and receiver locations near the building at the plane ground surface. Here (x_0, y_0, z_0) and (x_1, y_1, z_1) are the coordinates of the transmitting and receiving points, respectively.

In the following section, we examine these effects in the case of a vertical dipole.

5.5.1. The Electric Field of the Vertical Dipole

Let us consider a rectangular building illuminated by a vertical electric dipole placed at the point $\{x_0, y_0, z_0\}$ above a plane ground surface. A coordinate system is placed at an arbitrary point $\{x, y, z\}$, and the point of observation is placed at point $\{x_1, y_1, z_1\}$ (see Fig. 5.3). The dipole field is represented by the electric Hertz's vector [7,14]

$$\Pi^{(i)} = \frac{\mathbf{p} \exp\{ik\rho\}}{\rho} \tag{5.13}$$

where $\mathbf{p}$ is the moment of the electric dipole.

Using the relations between electric and magnetic field components and the Hertz's vector components for the field of the vertical electric dipole, we get [7]

$$E_x = -E_0 \frac{(x - x_0)(y - y_0)}{\rho^2} \frac{e^{ik\rho}}{\rho}$$

$$E_y = -E_0 \frac{(x - x_0)^2 + (z - z_0)^2}{\rho^2} \frac{e^{ik\rho}}{\rho} \tag{5.14}$$

$$E_z = -E_0 \frac{(y - y_0)(z - z_0)}{\rho^2} \frac{e^{ik\rho}}{\rho}$$

$$H_x = H_0 \frac{(z - z_0)}{\rho} \frac{e^{ik\rho}}{\rho}$$

$$H_y = 0 \tag{5.15}$$

$$H_z = H_0 \frac{(x - x_0)}{\rho} \frac{e^{ik\rho}}{\rho}.$$

In a spherical coordinate system, the source and observation coordinates can be written, respectively, as:

$$x_0 = \rho_0 \sin\theta_0 \sin\varphi_0; \quad y_0 = \rho_0 \cos\theta_0; \quad z_0 = \rho_0 \sin\theta_0 \cos\varphi_0;$$
$$x_1 = \rho_1 \sin\theta_1 \sin\varphi_1; \quad y_1 = \rho_1 \cos\theta_1; \quad z_1 = \rho_1 \sin\theta_1 \cos\varphi_1. \tag{5.16}$$

We also introduce the coefficient of reflection R from the plane ground surface, the formulation of which can be found in Chapter 4. The coordinate system is shown in Figure 5.3.

We will analyze the field diffracted at the edge and roof of the building and the loss of the diffracted field compared to the dipole field in free space, as well as changes of field polarization for both waves reflected from the walls and ground and those diffracted from the building edges.

5.5.2. Diffraction from the Edge of a Perfectly Conductive Building

To define the field diffracted from an ideal conductive edge of a building, we use Keller's method of GTD described in References [5,6,9,10]. The relationship between the field diffracted from a wedge and the incident field is [5,6]

$$\mathbf{E}_d = \frac{e^{ik\rho'}}{\sqrt{\rho'}} \mathbf{E}_o(P)\mathbf{D}_E \tag{5.17}$$

where $\mathbf{E}_0(P)$ is an incident wave field at point $P(x, y, z)$ on the edge of a building and the diffraction matrix $\mathbf{D}_E$ has the form:

$$\mathbf{D}_E = -\frac{2e^{i\pi/4}}{\sqrt{6\pi k}\sin\beta} \begin{bmatrix} \frac{1}{A_1} + \frac{1}{A_2} & 0 & 0 \\ -\frac{\cos\beta}{\cos\psi_0}\left[\frac{\sin(\psi - \psi_0)}{A_1} + \frac{\sin(\psi + \psi_0)}{A_2}\right] & \frac{\cos\psi}{\cos\psi_0}\left[\frac{1}{A_1} - \frac{1}{A_2}\right] & 0 \\ -\frac{\cos\beta}{\cos\psi_0}\left[\frac{\cos(\psi - \psi_0)}{A_1} + \frac{\cos(\psi + \psi_0)}{A_2}\right] & \frac{\sin\psi}{\cos\psi_0}\left[\frac{1}{A_1} - \frac{1}{A_2}\right] & 0 \end{bmatrix}$$
$$\tag{5.18}$$

The main parameters in expressions (5.17)–(5.18) are as follows:

$$\cos\beta = (y_1 - y_0)/[(y_1 - y_0)^2 + (b+a)^2]^{1/2}, \tag{5.19a}$$
$$\cos\psi_0 = (h - y_0)/a, \cos\psi = (y - h)/b, \tag{5.19b}$$
$$A_1 = 1 + 2\sin\frac{2}{3}(\psi - \psi_0), A_2 = 1 + 2\sin\frac{2}{3}(\psi + \psi_0), \tag{5.19c}$$
$$y = (by_0 + ay_1)/(a+b), \tag{5.19d}$$
$$a = [(l - x_0)^2 + (d - z_0)^2]^{1/2}, b = [(x_1 - l)^2 + (z_1 - d)^2]^{1/2}. \tag{5.19e}$$

Here, $2l$ is the building length, and $2d$ is its width. Let us take a cross-section of a vertical wedge at the plane $y = y_0 = y_1 = 0$ and get the coordinates x and z to zero at the vertical wedge. We do this to determine the diffracted field at an arbitrary point $\{x_1, y_1, z_1\}$ as a function of the distance from the source $\{x_0, y_0, z_0\}$. The derivations for the polar field components E_{dy} and $E_{d\varphi}$ are

$$E_{dy} = E_{dx}\sin\varphi + E_{dz}\cos\varphi, \qquad E_{d\varphi} = E_{dx}\cos\varphi + E_{dz}\sin\varphi \tag{5.20}$$

The detailed analysis of the relative diffracted field component E_{dy}/E_0 as a function of angles φ and φ_0, and comparison with those parameters for the reflected field, indicates that the diffracted field varies very smoothly in the azimuth domain. This leads to an attenuation of 30–35 dB compared to a dipole field E_0 in a free space. Recall that the attenuation for reflected waves is smaller and equals 10–15 dB compared to the dipole field in free space.

5.5.3. Diffraction at an Impedance Edge of a Building

Let us consider the same geometry as presented in Figure 5.3. In this case, the normal electric impedance $Z_{\pm}$ is introduced as a function of the dielectric parameters of the walls, ε; that is, $Z_{\pm} \sim \pm 1/\sqrt{\varepsilon}$, the "+" sign is determined from boundary conditions at the wedges: for angle $\varphi = 0$ we use "+" sign and for $\varphi = \pi/2$ we use "−" sign. The dipole is placed at point $\{x_0, y_0, z_0\}$ and is described by formulas (5.14)–(5.16). Using Keller's theory and the expression in (5.17), we obtain the diffraction matrix at an arbitrary point $\{x, y, z\}$ for the non zero impedance wedge:

$$
\mathbf{D}_E = \frac{2e^{i\pi/4}}{3\sqrt{2\pi k}}
\begin{bmatrix}
\frac{x(y-y_0)}{\rho^2}\varepsilon f & 0 & 0 \\[2mm]
0 & -\frac{\cos\varphi}{2\cos\varphi_0}g\frac{x^2+y^2}{\rho^2} & \frac{\cos\varphi}{2\sin\varphi_0}g\frac{z_0(y-y_0)}{\rho^2} \\[2mm]
0 & \frac{\sin\varphi}{2\cos\varphi_0}g\frac{x^2+y^2}{\rho^2} & -\frac{\sin\varphi}{2\sin\varphi_0}g\frac{z_0(y-y_0)}{\rho^2}
\end{bmatrix}
\tag{5.22}
$$

where

$$
f = \frac{\cos\frac{2}{3}(\varphi_0-\frac{\pi}{2})}{\eta(\varphi_0+\frac{\pi}{2})}\left[\frac{\eta(\varphi-\frac{9\pi}{4})}{\sin\frac{2}{3}(\varphi-\frac{9\pi}{4})-\sin\frac{2}{3}(\varphi_0+\frac{\pi}{2})}-\frac{\eta(\varphi-\frac{\pi}{4})}{\sin\frac{2}{3}(\varphi-\frac{\pi}{4})-\sin\frac{2}{3}(\varphi_0+\frac{\pi}{2})}\right],
$$

$$
g = \frac{\cos\frac{2}{3}(\varphi_0-\frac{\pi}{2})}{\eta(\varphi_0+\frac{\pi}{2})}\left[\frac{\eta(\varphi-\frac{9\pi}{4})}{\sin\frac{2}{3}(\varphi-\frac{9\pi}{4})-\sin\frac{2}{3}(\varphi_0+\frac{\pi}{2})}+\frac{\eta(\varphi-\frac{\pi}{4})}{\sin\frac{2}{3}(\varphi-\frac{\pi}{4})-\sin\frac{2}{3}(\varphi_0+\frac{\pi}{2})}\right],
$$

$$
\eta\left(\varphi_0+\frac{\pi}{2}\right) = \frac{1}{\cos^8\frac{\pi}{6}}\frac{\cos\frac{1}{6}(\varphi_0-\theta_+-\pi)\cos\frac{1}{6}(\varphi_0-\theta_++\pi)\cos\frac{1}{6}(\varphi_0+\theta_+-2\pi)\cos\frac{1}{6}(\varphi_0+\theta_+)}{\cos\frac{1}{6}(\varphi_0+\theta_+-\pi)\cos\frac{1}{6}(\varphi_0-\theta_+)} \rightarrow
$$

$$
\frac{\cos\frac{1}{6}(\varphi_0+\theta_--\frac{7\pi}{2})\cos\frac{1}{6}(\varphi_0+\theta_--\frac{3\pi}{2})\cos\frac{1}{6}(\varphi_0-\theta_--\frac{5\pi}{2})\cos\frac{1}{6}(\varphi_0-\theta_--\frac{\pi}{2})}{\cos\frac{1}{6}(\varphi_0-\theta_--\frac{3\pi}{2})\cos\frac{1}{6}(\varphi_0+\theta_--\frac{\pi}{2})}
$$

$$
\eta\left(\varphi-\frac{\pi}{4}\right) = \frac{1}{\cos^8\frac{\pi}{6}}\frac{\cos\frac{1}{6}(\varphi-\theta_++2\pi)\cos\frac{1}{6}(\varphi+\theta_++\pi)\cos\frac{1}{6}(\varphi+\theta_+-\pi)\cos\frac{1}{6}(\varphi-\theta_+)}{\cos\frac{1}{6}(\varphi-\theta_+-\pi)\cos\frac{1}{6}(\varphi+\theta_+)} \rightarrow
$$

$$
\frac{\cos\frac{1}{6}(\varphi+\theta_-+\frac{\pi}{2})\cos\frac{1}{6}(\varphi-\theta_--\frac{3\pi}{2})\cos\frac{1}{6}(\varphi+\theta_--\frac{5\pi}{2})\cos\frac{1}{6}(\varphi-\theta_-+\frac{\pi}{2})}{\cos\frac{1}{6}(\varphi+\theta_--\frac{3\pi}{2})\cos\frac{1}{6}(\varphi-\theta_--\frac{\pi}{2})}
$$

$$
\eta\left(\varphi-\frac{9\pi}{4}\right) = \frac{1}{\cos^8\frac{\pi}{6}}\frac{\cos\frac{1}{6}(\varphi-\theta_+-2\pi)\cos\frac{1}{6}(\varphi+\theta_+-3\pi)\cos\frac{1}{6}(\varphi+\theta_+-\pi)\cos\frac{1}{6}(\varphi-\theta_+)}{\cos\frac{1}{6}(\varphi-\theta_+-\pi)\cos\frac{1}{6}(\varphi+\theta_+-2\pi)} \rightarrow
$$

$$
\frac{\cos\frac{1}{6}(\varphi+\theta_--\frac{5\pi}{2})\cos\frac{1}{6}(\varphi+\theta_--\frac{9\pi}{2})\cos\frac{1}{6}(\varphi-\theta_--\frac{7\pi}{2})\cos\frac{1}{6}(\varphi-\theta_--\frac{3\pi}{2})}{\cos\frac{1}{6}(\varphi-\theta_--\frac{5\pi}{2})\cos\frac{1}{6}(\varphi+\theta_--\frac{7\pi}{2})}.
$$

Here, $\theta_\pm$ are the grazing Brewster's angles, which depend on the surface impedances

$$\sin\theta_\pm = \frac{Z_0}{Z_\pm} \qquad (5.23)$$

where Z_0 is the wave impedance in free space. Let us now consider the wedge cross-section at the plane $y = y_0 = 0$. In this case, using the relationships defined in (5.20) between the field components, we can examine the relative E_{dy}/E_0 component versus the direction of the source (which is determined by angle φ_0) and the direction of the observer (which is determined by angle φ). All other parameters are the same as in the previous case of a perfectly conductive wedge. The ratio $Z_0/Z_\pm$ in (5.23) was estimated as 0.05–0.1, which corresponds to brick building corners. Detailed analysis of E_{dy}/E_0 shows that the diffracted field decay is about 35–40 dB compared to the dipole field E_0 in free space, that is, 5–10 dB higher than the field diffracted from the perfectly conductive building corner. The spatial distribution of the diffracted field from the impedance wedge is completely irregular compared to that of perfectly conductive wedge. Moreover, the diffracted field pattern from a brick corner decreases sharply with a decrease in angle φ between the direction of the observer and the edge of the boundary. The field intensity decay for diffracted waves from building corners is two to three times higher than that of the corresponding reflected waves from the same building walls.

5.5.4. Diffraction from Roofs

Diffraction by a Flat Roof. Let us consider the wave from a vertical electric dipole placed at an arbitrary point $\{x_0, y_0, z_0\}$ on the flat roof of a building with imperfectly conducting (e.g., impedance) surface (see Fig. 5.4).

We have to find the secondary field diffracted by the edges of the roof, and estimate the diffracted field and its degree of depolarization. The rays falling on the
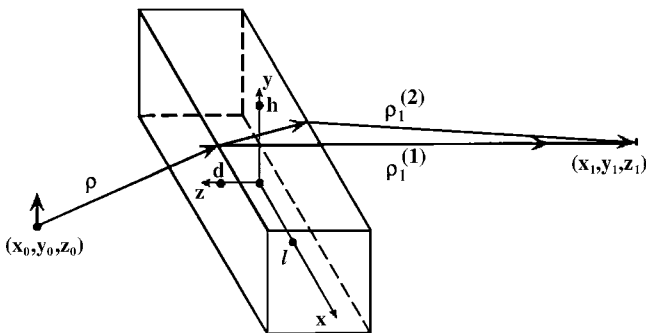
FIGURE 5.4. Diffraction from a flat roof.

roof edge create at the edge a cone of primary diffracted rays, which then fall on the next edge, creating a cone of secondary diffracted rays [10]. For the definition of secondary diffracted rays we again use Keller's theory [5,6], according to which the n-time-diffracted rays from the wedges are defined by the following expression:

$$\mathbf{E}_d^{(n)} = D_1 D_2 \ldots D_n \exp(ik\rho_0)/\lfloor \rho_0 (1 + \rho^{(n)}/\rho_0)^{1/2} \rfloor \mathbf{E}_0. \qquad (5.24)$$

Applying this formula to our specific case and taking the cross-section $y = y_0 = y_1 = 0$ for the vertical walls, we can easily analyze the components of the diffracted field. Then, using formulas (5.22)–(5.23), we can obtain the components of the secondary diffracted field from the roof of the building.

The analysis of components, $E_{dx}, E_{dy},$ and E_{dz} of the diffracted field, for different distances from the roof and different building height parameters of length and width indicates that the field decay caused by secondary diffraction from the roof of a building is of 60 to 80 dB compared to the field E_0 in free space for wavelengths between 10 to 30 cm. Therefore, we can neglect the effects of the secondary diffracted field in the total field distribution around a building in this frequency range.

Diffraction by an Oblique Roof. Now we consider a vertical electric dipole located at point $\{x_0, y_0, z_0\}$ on an oblique, imperfectly conducting roof (see Fig. 5.5). We again determine the field diffracted at the edge of the roof using Keller's theory [5,6] and estimate the decay of the diffracted field compared to the field E_0 in a free space. Using formulas (5.22)–(5.23) and taking the cross-section $y = y_0 = y_1 = 0$ for the vertical walls, we can easily analyze the components of the diffracted field.

The theoretical analysis shows that the field diffracted at the oblique roof varies smoothly; its attenuation is about 30–45 dB compared to the dipole field E_0 in a free space, which is approximately half than that from a flat roof. At the same time, the diffracted field decay for the concrete building's roof is approximately 10–15 dB, which is less than that for the brick building roof.
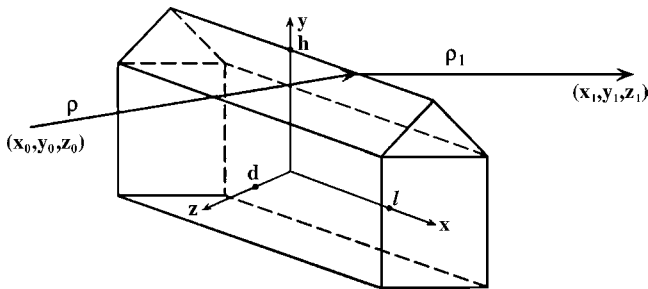
FIGURE 5.5. Diffraction from an oblique roof.
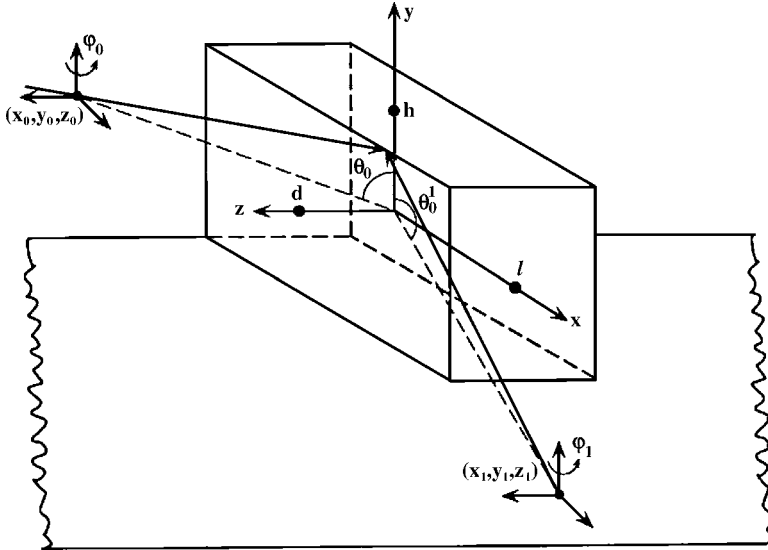
FIGURE 5.6. The complete scheme for the transmitter and receiver locations near a building at the plane ground surface.

5.5.5. Field Distribution Around a Building

Let us consider a building with impedance walls at $x = 2l$, $y = 2h$, $z = 2d$ illuminated by a vertical electric dipole placed at point $\{x_0, y_0, z_0\}$ above the plane ground surface. The coordinate system is considered to be located in the middle of the building and the observation point is at $\{x_1, y_1, z_1\}$ as shown in Figure 5.6.

The field components of a vertical electric dipole are given by expressions (5.14)–(5.19). We must find the reflected, diffracted, and the total field at the observation point for the electric dipole, as a transmitter, moving around the building. As all expressions for the diffracted field from the horizontal and the vertical edges of a building are the same, let us examine only one horizontal and one vertical edge of a building. Using Keller's theory and the formulas presented earlier, we can obtain the following expression for the horizontal edge "1" (see Fig. 5.7):

$$
\mathbf{E}_{d_1} = -\mathbf{E}_0 \mathbf{D}_{E_1} F(x) \frac{2\, e^{i\left[k\rho_1' + \frac{\pi}{4}\right]}}{\sqrt{6\pi k \rho_1'}\, \sin\beta_1} \frac{e^{ik\rho_1}}{\rho_1 [1 + \rho_1'/\rho_1]^{1/2}} \tag{5.25}
$$

Here $\mathbf{D}_E$ is the diffracted field matrix described by formula (5.22) and $F(x)$ is defined as:

$$
F(x) = \begin{cases} 0, & x < -l \\ 1, & -l < x < l \\ 0, & x > l \end{cases} \tag{5.26}
$$
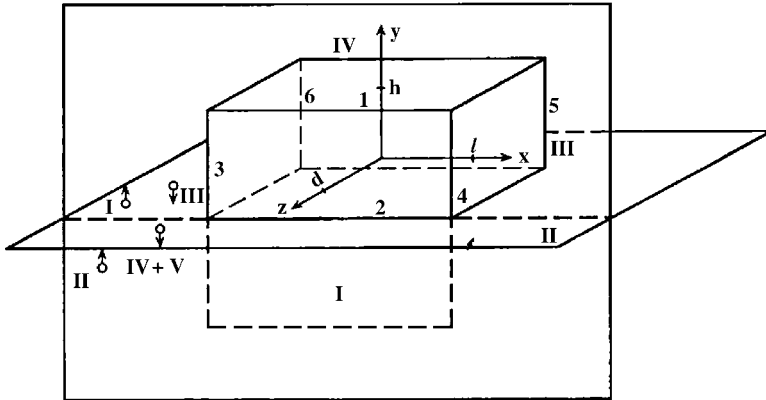
FIGURE 5.7. Reflections from the front wall and from the ground surface may be replaced by the image sources indicated by signs I, II, III, ...

since all horizontal edges have finite length. This formula is true for all horizontal edges, but for every edge we must change the coordinates of the vector from the observer to the receiver point and the values of their respective angles.

For the vertical edges we use (5.22)–(5.23). Now by introducing the function

$$F(y) = \begin{cases} 0, & y < -h \\ 1, & -h < y < h \\ 0, & y > h \end{cases} \quad (5.28)$$

which takes into account the finite height of building walls, we can obtain the following expression for the vertical edge "4" (Fig. 5.8):

$$\mathbf{E}_{d_4} = -\mathbf{E}_0 \mathbf{D}_{E_4} F(y) \frac{2\,e^{i\left[k\rho_4' + \frac{\pi}{4}\right]}}{\sqrt{6\pi k\rho_4'}\,\sin\beta_4} \frac{e^{ik\rho_4}}{\rho_4[1 + \rho_4'/\rho_4]^{1/2}} \quad (5.29)$$

Now, we turn our attention to the effects on ground reflection and building walls on radio wave propagations.

5.5.6. Total Wave Field Reflected from the Walls and the Ground Surface

The real properties of a ground surface and building walls can be considered by introducing the reflection coefficient R (see formulas (4.50) in Chapter 4). According to ray theory, we can replace the field reflected from the ground by an image source (II), symmetric to the real source (I) and illuminating the same area as the real source (see Fig. 5.7). The coordinates of this image source are $\{x_0, -(y_0 + 2h), z_0\}$. On the contrary, as the building is an ideal conductor, the field reflected from the wall
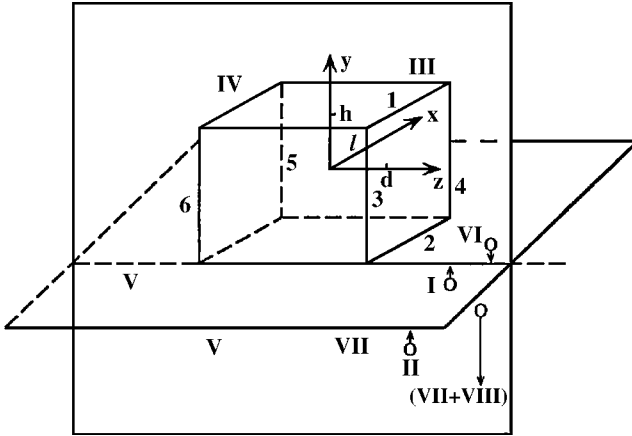
FIGURE 5.8. The same, as in Figure 5.7, but for reflections from the side wall.

with coordinates $\{(-l, l); (-h, h); d\}$ can be replaced by that from image source (III), symmetric to the real source (I) (see Fig. 5.7). Its coordinates are $\{x_0, y_0, -(z_0 + 2d)\}$, and the illuminated area can be determined from the coordinates of this source and the wall plane.

Taking into account reflections from the ground (image source II), we introduce a second reflection from the wall or image source (IV) symmetric to the source (II); its coordinates are $\{x_0, -(y_0 + 2h), -(z_0 + 2d)\}$, and they define the illuminated area on the wall. So, we end up having one real source (I) and three image sources (noted in Fig. 5.7 by II, III and IV, respectively). Moreover, one can take into account rays that undergo multiple reflections as shown in Figure 5.7.

Now we consider a real source that moves and illuminates not only the front wall but also the side wall (see Fig. 5.8). As the field is symmetric in the right and left directions, we can choose, for example, the side wall with coordinates $\{-l; (-h, h); (-d, d)\}$. The same geometrical constructions enable us to describe the field reflected from the side wall using the real source (I), the image source (II) (reflection from the ground), source (VI) (reflection from the wall), and the additional sources (VII + VIII) (second order reflection from the ground and the wall). All possible rays are shown in Figure 5.8.

Finally, we can determine all light and shadow zones around the perfectly conductive building. From the formulas introduced above, we note that the diffracted field is attenuated faster than the incident and reflected fields by a factor $\sim \pi k \rho' [1 + \rho'/\rho]^{1/2}$. This enables us to exclude the diffracted field in areas where incident and reflected waves also exist.

After determining all illuminated areas around the building, we can derive the total field intensity, taking into account the real and image sources mentioned above. In all formulas we use $y_0 = y_1 = y = 0$ and $\theta_0 = \theta_0' = \pi/2$. Taking into account the same form of field expressions in all illuminated areas, we describe, for example, the field in areas II, V, and VII, which are illuminated by real (I) and image (II) sources

(i.e., the first order reflection from the ground surface). Now to obtain the field intensity, let us introduce the vector of the field power [7]:

$$\mathbf{S} = c/8\pi \cdot \text{Re}[\mathbf{E}, \mathbf{H}^*] \tag{5.30}$$

where c is the speed of light. Using this formula, we can present all components of vector $\mathbf{S}$ in the following form:

$$S_x = -E_0 H_0 \left[\begin{matrix} R_g \\ R_w \end{matrix}\right] \frac{c}{8\pi} \left[(x_1 - x_0)^2 + (z_1 - z_0)^2\right] (x_1 - x_0) \left\{ \frac{1}{\alpha^3} + \frac{2\cos k\gamma}{\alpha^{3/2}\beta^{3/2}} + \frac{1}{\beta^3} \right\},$$
$$\tag{5.31a}$$

$$S_y = E_0 H_0 \left[\begin{matrix} R_g \\ R_w \end{matrix}\right] \frac{c}{8\pi} \frac{2h\lfloor (z_1 - z_0)^2 + (x_1 - x_0)^2 \rfloor}{\beta^{3/2}} \left[\frac{\cos k\gamma}{\alpha} + \frac{1}{\beta^{3/2}} \right], \tag{5.31b}$$

$$S_x = -E_0 H_0 \left[\begin{matrix} R_g \\ R_w \end{matrix}\right] \frac{c}{8\pi} [(x_1 - x_0)^2 + (z_1 - z_0)^2](z_1 - z_0) \left\{ \frac{1}{\alpha^3} + \frac{2\cos k\gamma}{\alpha^{3/2}\beta^{3/2}} + \frac{1}{\beta^3} \right\}.$$
$$\tag{5.31c}$$

Here $\alpha = \lfloor (x_1 - x_0)^2 + (z_1 - z_0)^2 \rfloor$; $\beta = \lfloor (x_1 - x_0)^2 + (2h)^2 + (z_1 - z_0)^2 \rfloor$; $\gamma = \sqrt{\beta} - \sqrt{\alpha}$; $k = 2\pi/\lambda$, λ is a wavelength; R_g and R_w are the reflection coefficients from the ground and wall, respectively. In the above expressions, the coefficient R_g is for the first order reflection from the ground surface, and R_w is the first order reflection from the building walls, defined by formula (4.50) from Chapter 4. Expressions (5.31a)–(5.31c) describe the total field power in the direct illuminated areas around the building. Using such an approach, we can determine the total field distribution in all areas surrounding a building, taking into account the direct field, multiple reflections from the ground, and the building walls, as well as the diffracted field from building roof and corners.

5.6. PROPAGATION IN RURAL FOREST ENVIRONMENTS

Vegetation presents another significant effect on radio wave propagation, such as scattering and absorption by trees with their irregular structure of branches and leaves. Predictions of signal decay in the case of irregular terrain at frequencies less than 500 MHz have been made by a number of authors [45–48] during the 1950s and 1960s. During the 1970s, vegetation and foliage losses have been reported [49–51] at frequencies up to 3 GHz but for relatively few paths. For forested environments [52–56], trees exhibit mainly absorbing and scattering effects and very little diffraction effects.

5.6.1. A Model of Multiple Scattering in a Forested Area

In References [57–60], a stochastic approach was proposed to investigate the absorbing and multiple scattering effects that accompany the process of radio wave
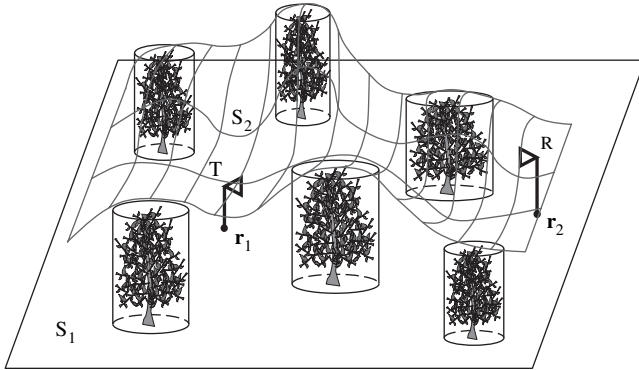
FIGURE 5.9. The profile of a forested nonregular area.

propagation through forested areas. This is a combination of probabilistic and deterministic approaches, which describe the random media scattering phenomenon. The geometrical optics approximation is used to account for propagation over a series of trees modeled as absorbing amplitude/phase screens with rough surfaces. This stochastic approach allows the designer to obtain the absorption effects from trees using their real physical parameters, such as permittivity and conductivity, as well as the random distribution of their branches and leaves.

The Forest Terrain Description. Let us consider an array of trees as cylinders with randomly distributed surfaces, all placed on a flat terrain (Fig. 5.9). Also assume that the reflecting properties of the trees are randomly and independently distributed, but they are statistically the same. The values of the reflection coefficient are complex with uniformly distributed phase in the range of $[0, 2\pi]$. Thus, the average value of the reflection coefficients is zero, that is $\langle \Gamma(\varphi_s, r_s) \rangle = 0$. The geometry of the problem is shown in Figure 5.10, where $A(\mathbf{r}_1)$ denotes the location of the transmitting antenna at height z_1, $B(\mathbf{r}_2)$ is the location of the receiving antenna at height z_2. Let us derive an average measure of field intensity for waves passing through the layer of trees after multiple scattering. In this case, we consider each tree as a phase amplitude cylindrical screen. Figure 5.9 shows an array of these (screens) placed at $z = 0$ (a flat surface S_1). The trees have an average height $\bar{h}$ and width $\bar{d}$ [60]. These trees are randomly and independently distributed and they are oriented in arbitrary directions at the plane $z = 0$ with equal probability and with average density v (per kilometer^2). In the case where both antennas are placed within the forest environment and are lower than the average tree height $\bar{h}$, that is $0 < z_2, z_1 < \bar{h}$, then the multiscattering effects are predominant and must be taken into account. In this case we can present the range of direct visibility (LOS under conditions) between the two terminal antennas as $\bar{\rho} = \gamma_0^{-1}$, where γ_0 is tree density

$$\gamma_0 = 2\bar{d}v/\pi \tag{5.32}$$
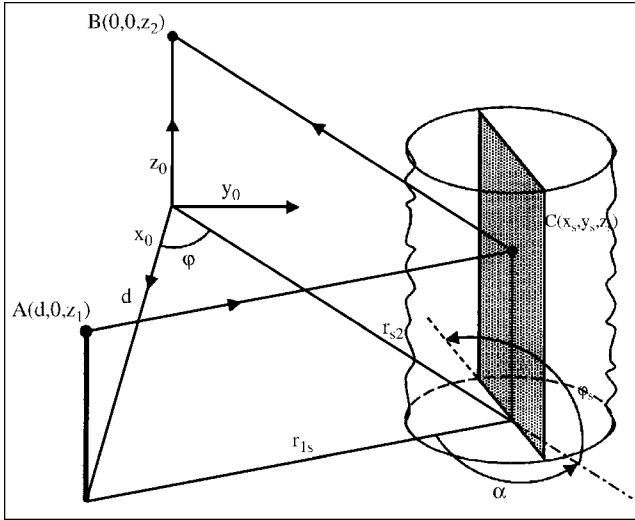
FIGURE 5.10. Scattering from a cylinder with a rough surface which is used to model a tree.

The "roughness" of a tree's surface is described by introducing a correlation function for the reflection coefficient Γ. We define the correlation function for the reflection coefficient Γ for ℓ_h, ℓ_h, $\ell_v \ll \bar{\rho}$, $\bar{d}$, $\bar{h}$ as [59,60]

$$K(\mathbf{r}_{2S}, \mathbf{r}_{1S}) = \langle \Gamma_{2S} \cdot \Gamma_{1S}^* \rangle = \Gamma \cdot \exp\left\{ -\frac{|\rho_{2S} - \rho_{1S}|}{\ell_h} - \frac{|z_{2S} - z_{1S}|}{\ell_v} \right\} \qquad (5.33)$$

where $\mathbf{r}_{2S}$ and $\mathbf{r}_{1S}$ are points at the surface of an arbitrary tree (see Fig. 5.10); Γ is the absolute value of the reflection coefficient, given by (4.50) in Chapter 4 for two kinds of field polarization, $\Gamma_{2S} = \Gamma(\mathbf{r}_{2S})$ and $\Gamma_{1S} = \Gamma(\mathbf{r}_{1S})$.

Average Field Intensity. Taking into account the wave field presentation and Green's theorem for our problem introduced in Chapter 4, we can present the field over the rough terrain using Green's theorem in integral form [57,58]

$$U(\mathbf{r}_2) = U_i(\mathbf{r}_2) + \int_S \left\{ U(\mathbf{r}_s) \frac{\partial G(\mathbf{r}_2, \mathbf{r}_s)}{\partial \mathbf{n}_s} - G(\mathbf{r}_2, \mathbf{r}_s) \frac{\partial U(\mathbf{r}_s)}{\partial \mathbf{n}_s} \right\} dS \qquad (5.34)$$

where $U_i(\mathbf{r}_2)$ is the incident wave field, $\mathbf{n}_s$ is the vector normal to the terrain surface S at the scattering point $\mathbf{r}_s$, $G(\mathbf{r}_2, \mathbf{r}_s)$ is the Green's function of the semi-space defined in Chapter 4, which we rewrite as [59,60]:

$$G(\mathbf{r}_2, \mathbf{r}_1) = \frac{1}{4\pi} \left\{ \frac{\exp[ik|\mathbf{r}_2 - \mathbf{r}_1|]}{|\mathbf{r}_2 - \mathbf{r}_1|} \pm \frac{\exp[ik|\mathbf{r}_2 - \mathbf{r}_1'|]}{|\mathbf{r}_2 - \mathbf{r}_1'|} \right\} \qquad (5.35)$$

Here $\mathbf{r}_1'$ is the point symmetrical to $\mathbf{r}_1$ relative to the Earth's surface S_1; $k = 2\pi/\lambda$, and λ is the wavelength. In integral (5.34), the random surface S (relief of the terrain with obstructions) is treated as the superposition of an ideal flat ground surface S_1 ($z = 0$) and rough surface S_2 is created by the tops of the obstructions (see Fig. 5.9). We construct the Green's function in the form of (5.35) to satisfy a general electrodynamic approach; that is, to describe both the vertical (sign "+" in (5.35)) and horizontal (sign "−" in (5.35)) polarizations with their corresponding boundary conditions. In fact, by introducing the Green's function (5.35) with the "+" sign in (5.34) we satisfy the Dirihlet boundary conditions at the flat (non disturbed) Earth's surface S_1 ($z = 0$). That means, $G_{z=0} = 2$ and $\frac{\partial u}{\partial \mathbf{n}_s} = 0$ (the same conditions were stated by (4.16a) in Chapter 4). At the same time, using the sign "−" we satisfy the Neumann boundary conditions at the plane $z = 0$: $G_{z=0} = 0$ and $u = 0$ (the same conditions were stated by (4.16b) in Chapter 4). Hence, if the source is described by formula (5.35), we can exclude the integration over the non disturbed surface S_1, assuming the surface S_1 is perfectly reflecting. Next, by using the well-known Kirchhoff's approximation described earlier, we can determine the scattered field $U_r(\mathbf{r}_s)$ from the forested layer as a superposition of an incident wave $U_i(\mathbf{r}_2)$, the reflection coefficient $\Gamma(\varphi_s, \mathbf{r}_s)$, and the shadow function $Z(\mathbf{r}_2, \mathbf{r}_1)$. The shadow function equals one, if the scattered point $\mathbf{r}_s$ inside the forested layer can be observed from both points $\mathbf{r}_1$ and $\mathbf{r}_2$ of the transmitter and receiver locations (as shown in Fig. 5.10), and equals zero in all other cases. Taking into account all these assumptions, the (5.34) can be rewritten as

$$U(\mathbf{r}_2) = Z(\mathbf{r}_2, \mathbf{r}_1)\widetilde{G}(\mathbf{r}_2, \mathbf{r}_1) + 2\int_{S_2} \{Z(\mathbf{r}_2, \mathbf{r}_s, \mathbf{r}_1)\Gamma(\varphi_s, \mathbf{r}_s)\widetilde{G}(\mathbf{r}_s, \mathbf{r}_1) \cdot (\mathbf{n}_s \cdot \nabla_s)\widetilde{G}(\mathbf{r}_2, \mathbf{r}_s)\}$$

$$(5.36)$$

where $\nabla_s = \left(\frac{\partial}{\partial x_s}, \frac{\partial}{\partial y_s}, \frac{\partial}{\partial z_s}\right)$, $\varphi_s = \sin^{-1}\left(\mathbf{n}_s \cdot \frac{\mathbf{r}_s - \mathbf{r}_1}{|\mathbf{r}_s - \mathbf{r}_1|}\right)$ (see Fig. 5.10), and $\widetilde{G}(\mathbf{r}_2, \mathbf{r}_1)$ is the normalized Green's function.

To solve (5.36), instead of using the Feynman diagrams for multiscattering problems (see Chapter 3, formula (3.44)), we present a solution in operator form through a set of Green's functions expansion as [60–62]

$$U_2 = Z_{21}\widetilde{G}_{21} + (Z_{2S}\bar{M}_{2S}\Gamma_S)Z_{S1}\widetilde{G}_{S1} + (Z_{2S}\bar{M}_{2S}\Gamma_S)(Z_{SS'}\bar{M}_{SS'}\Gamma_{S'})Z_{S'1}\widetilde{G}_{S'1} + \cdots$$

$$(5.37)$$

Here, $\bar{M}_{\alpha\beta}$ is an integral-differential operator that describes the expression inside the bracket in (5.37) and the variables $Z_{\alpha\beta}$, $\Gamma_{\alpha\beta}$ are the corresponding shadow and reflection coefficient functions denoted by indexes α and β. We also apply Twersky's approximation [63] to (5.36) and (5.37), which does not take into account mutual multiple scattering effects. Twersky's approximation states that the contributions of multiple scattered waves are additive and independent. This approximation together with that of $\langle \Gamma \rangle = 0$ makes it possible to obtain the coherent part of the total field

by averaging (5.36) over the reflecting properties of each tree and over all tree positions:

$$\langle U_2 \rangle = \langle Z_{21} \rangle \widetilde{G}_{21} \tag{5.38}$$

Z_{21} is the "shadowing" function that describes the probability of existence of some obstructions in the radio path of the two terminal antennas. As the contributions of the multiscattered waves are independent [63], we can represent the incoherent part of total field intensity (after averaging of (5.37)) as

$$
\begin{aligned}
\langle I_2 \rangle = \langle U_2 \cdot U_2^* \rangle &= \langle Z_{21} \rangle \widetilde{G}_{21} \cdot \widetilde{G}_{21}^* \\
&+ \langle \{ D_{2S,2\tilde{S}} + D_{2S',2\tilde{S}'} \cdot D_{S'S,\tilde{S}'\tilde{S}} \} \cdot Z_{S1} \cdot Z_{\tilde{S}1} \cdot \widetilde{G}_{S1} \cdot \widetilde{G}_{\tilde{S}1}^* \rangle
\end{aligned}
\tag{5.39}
$$

where $D_{S'S,\tilde{S}'\tilde{S}} = Z_{S'S} \cdot Z_{\tilde{S}'\tilde{S}} \cdot \hat{M}_{\tilde{S}'\tilde{S}} \cdot \hat{M}_{S'S} \cdot K_{S\tilde{S}}$.

For the conditions $\ell_h, \ell_v \ll \bar{d}, \bar{h}, \bar{\rho}$ and $k\ell_h, k\ell_v \gg 1$ for $0 < z_1 < \bar{h}$, we can integrate (5.39) over all variables of the type $\Delta \mathbf{r}_S = \mathbf{r}_{\tilde{S}} - \mathbf{r}_S$ at the surfaces of scattering trees. By manipulating the expression in (5.39), according to References [57,60], we obtain

$$\langle I_2 \rangle = \langle Z_{21} \rangle |\widetilde{G}_{21}|^2 + \langle \{ Q_{2S1} + Q_{2S'S} \cdot Q_{S'S1} + \ldots \} \cdot Z_{S1} |\widetilde{G}_{S1}|^2 \rangle \tag{5.40}$$

where $Q_{S''S'S} = Z_{S''S'} |\widetilde{G}_{S''S'}|^2 \sigma_{S''S'S}$. The cross-section area of scattering can be presented as [57,60]

$$\langle \sigma \rangle = \frac{\gamma_0 \Gamma}{4\pi} \cdot \sin^2 \frac{\alpha}{2} \cdot \frac{k\ell_v}{1 + (k\ell_v)^2 (\sin \vartheta' - \sin \theta')^2} \cdot \frac{k\ell_h}{1 + (k\ell_h)^2} \tag{5.41}$$

Let us now average (5.40) over all tree (screen) positions. The integration must be done over the surfaces of the screens as well as over their mirror surfaces $(-\bar{h} \le z, z', z'', \ldots \le \bar{h})$. The averaging over the screen orientations for each scattered point affects only the value of σ from (5.41). At the same time, the averaging over the number and position of all screens affects the "shadow" function Z. This approximation together with that of $\langle \Gamma(\varphi_s, r_s) \rangle = 0$ makes it possible to obtain the coherent part of the total field by accounting (5.38) [60]

$$\langle I_{\text{co}} \rangle = \frac{1}{(4\pi)^2} \frac{\exp(-\gamma_0 r)}{r^2} \left[2 \sin \frac{k z_1 z_2}{r} \right]^2 \tag{5.42}$$

For the incoherent part of total field intensity the expansion (5.39) can be presented in the operator form

$$\langle I_{\text{inc}}(\mathbf{r}_2) \rangle = 2 \{ Q + Q^2 + Q^3 + \ldots \} P(\mathbf{r}_2, \mathbf{r}_1) |\widetilde{G}(\mathbf{r}_2, \mathbf{r}_1)|^2 \tag{5.43}$$

where the effect of the integral operator on functions at the right-hand side of (5.43) can be presented by the following expression:

$$Qf(\mathbf{r}_2, \mathbf{r}_1) = \int_V (d\mathbf{r})P(\mathbf{r}_2, \mathbf{r})\frac{\langle\sigma(\mathbf{r}_2, \mathbf{r}, \mathbf{r}_1)\rangle}{|\mathbf{r}_2 - \mathbf{r}|}f(\mathbf{r}, \mathbf{r}_1) \qquad (5.44)$$

The product $d\mathbf{r} = dS \cdot dn$ defines the element of volume V of a plane parallel to the tree layer with width $2\bar{d}$, over which the integration of the right-hand side of (5.44) takes place. Using the same assumption for (5.44), as the one used in deriving (5.40), and setting $kz_2 \gg 1, z_2 < \bar{h}$, we can integrate (5.43) over variable z to get

$$(4\pi)^2|\rho_2 - \rho_1| \cdot \langle I_{inc}(\mathbf{r}_2)\rangle = 2\{q + q^2 + q^3 + \ldots\}g(\rho_2 - \rho_1) \qquad (5.45)$$

where

$$g(\rho_2 - \rho_1) = \frac{\exp\{-\gamma_0|\rho_2 - \rho_1|\}}{|\rho_2 - \rho_1|} \qquad (5.46)$$

If the integration is over ρ with infinite limits, the operator $\hat{q}$ becomes

$$\hat{q}f(\rho_2, \rho_1) = \frac{v \cdot \bar{d} \cdot \Gamma}{4\pi}\int (d\rho)\left[1 - \frac{\rho_2 - \rho}{|\rho_2 - \rho|} \cdot \frac{\rho - \rho_1}{|\rho - \rho_1|}\right]g(\rho_2 - \rho_1)f(\rho, \rho_1). \quad (5.47)$$

A detailed analysis of (5.45), taking into account (5.46) and (5.47), and using Laplace's method for $\gamma_0\rho \gg 1$ yields the incoherent part of the total field intensity or

$$\langle I_{inc}\rangle \approx \frac{\gamma_0\Gamma}{(4\pi)^2}\left[\frac{\Gamma^3}{4(8)^3}\frac{\exp(-\gamma_0 r)}{r} + \frac{\Gamma}{32}\left(\frac{\pi}{2\gamma_0}\right)^{1/2}\frac{\exp(-\gamma_0 r)}{r^{3/2}} + \frac{1}{2\gamma_0}\frac{\exp(-\gamma_0 r)}{r^2}\right] \qquad (5.48)$$

As

$$\langle I_{total}\rangle = \langle I_{co}\rangle + \langle I_{inc}\rangle \qquad (5.49)$$

we can evaluate the total path loss from

$$L_{total} = 10\log[\lambda^2(\langle I_{co}\rangle + \langle I_{inc}\rangle)] \qquad (5.50)$$

The third term in (5.48) is important for close ranges from the transmitter, whereas

$$r = r_{kr} < \frac{8^3}{\pi\gamma_0\Gamma^2} \approx 3\text{–}5\,\text{km} \qquad (5.51)$$

the first two terms are important only at long distances $r > r_{kr}$ from the transmitter.

5.6.2. Comparison with Other Models

The stochastic model described in the previous section is compared with Tamir's model [48–50]. The total field intensity for the range $0 < r < 1$–2 km in [48–50] is proportional to $r^{-2.5} - r^{-3}$. The same result can also be obtained from formulas (5.48)–(5.50). In fact, for zones far from the transmitter, the two last terms in (5.48) are the dominant terms and they predict a field intensity attenuation from $\frac{\exp(-\gamma_0 r)}{r}$ to $\frac{\exp(-\gamma_0 r)}{r^{3/2}}$ that can be expanded to $r^{-1.5} - r^{-3.5}$ [60]. Thus, the results obtained in References [48,50] are predicted by results of the stochastic model presented here. A good agreement was also with Weissberger's empirical model [64], that is based on numerous experiments in different forest environments. Comparisons with other statistical models have also shown that the stochastic model described here is more precise and covers the case of single scattering with a signal decay law of r^{-2} obtained in References [65–67] using the Born's approximation.

5.7. PROPAGATION IN MIXED RESIDENTIAL AREAS

Let us consider an array of houses and trees as blocks and cylinders with randomly distributed surfaces which are placed on a flat terrain. Such obstructions are mainly present in mixed residential areas. The characterization of the propagation properties of such environments has been thoroughly investigated in Reference [68] and briefly discussed in Reference [59].

5.7.1. Statistical Description of Mixed Residential Area

We assume that the reflecting properties of houses and trees are randomly and independently distributed, but they are statistically the same. The values of the reflection coefficients are complex with a uniformly distributed phase in the range $[0, 2\pi]$. Thus, we consider each house or tree as a phase-amplitude screen (see Fig. 5.11). The reflection properties of these screens are described by the complex reflection coefficient with a uniform distributed phase in the range $[0, 2\pi]$ and with correlation scales in horizontal, ℓ_h, and vertical, ℓ_v, directions, respectively. Both scales characterize the correlation function of the reflection coefficient, which can be presented as [68]:

$$K_\Gamma(\mathbf{r}_S, \mathbf{r}_S') = \Gamma(\varphi_S) \cdot \exp\left\{ -\frac{|\xi|}{\ell_v} - \frac{|\eta|}{\ell_h} \right\} \tag{5.52}$$

$\Gamma(\varphi_S)$ is the amplitude distribution of the reflection coefficient over angles φ_S. The absolute value of $\Gamma(\varphi_S)$ is defined by (4.50) in Chapter 4. In (5.52), to obtain $K_\Gamma(\mathbf{r}_S, \mathbf{r}_S')$, we introduce a new variable $\xi = |\mathbf{r}_S' - \mathbf{r}_S|$ and construct, at the surface of the reflected rough screen (Fig. 5.11), the local coordinate system $\{\xi, \eta\}$ with origin at point $\mathbf{r}_S$ and with axis 0ξ. The geometry of the problem is shown in Figure 5.12, where $A(\mathbf{r}_1)$ is the point of the transmitting antenna location at height z_1 and $B(\mathbf{r}_2)$ is the point of the receiving antenna location at height z_2. As was shown in
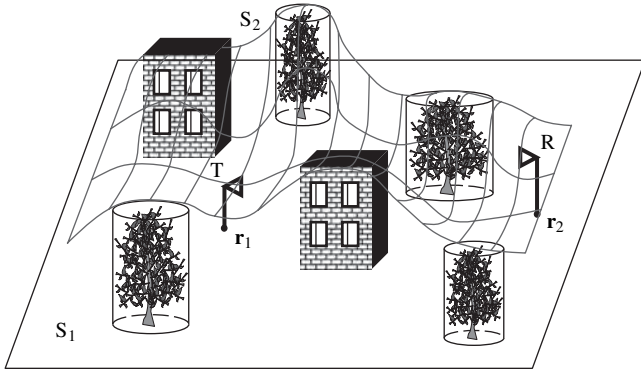
FIGURE 5.11. The profile of mixed residential area.

Reference [68], to derive an average measure of the field intensity for waves passing through the mixed layers of houses and trees, one needs to use the single scattering approach and take into account diffraction from building roofs. In this case, we consider that one of the antennas is higher than the average mixed-layer height, $\bar{h}$, that is $z_2 > \bar{h} > z_1$. The field component which passes through such a layer after multiple-scattering is smaller than that of the single scattering case. Thus, only a single-scattering problem with diffraction from the mixed layer tops should be considered here. Moreover, because in residential areas the height of the trees and houses are at the same level (i.e., uniformly distributed in the vertical plane), we can
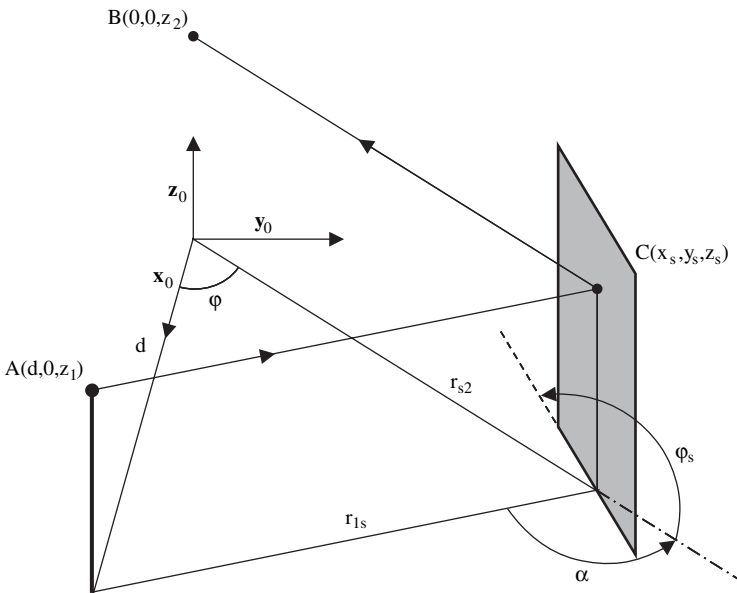
FIGURE 5.12. Scattering from a nontransparent screen that models a house.

exclude the influence of the terrain profile on propagation effects within such a channel, as was done previously for the forest environment.

5.7.2. The Average Field Intensity

Taking into account the basic description of signal strength in Equation (5.36), we determine the correlation function of the total field for the approximation of single scattering, $K(\mathbf{r}_2, \mathbf{r}_2') = \langle U(\mathbf{r}_2) U * (\mathbf{r}_2') \rangle$, in the following form [57,68]:

$$K(\mathbf{r}_2, \mathbf{r}_2') = 4k^2 \int_{S_2} dS_2 \int_{S_2} dS_2' \cdot \langle Z(\mathbf{r}_2, \mathbf{r}_S, \mathbf{r}_1) \cdot Z(\mathbf{r}_2', \mathbf{r}_S', \mathbf{r}_1) \cdot K_\Gamma(\mathbf{r}_S, \mathbf{r}_S')$$

$$\times \sin \psi_S \cdot \sin \psi_S' \cdot G(\mathbf{r}_2, \mathbf{r}_S) \cdot G(\mathbf{r}_S, \mathbf{r}_1) \cdot G^*(\mathbf{r}_2', \mathbf{r}_S') \cdot G^*(\mathbf{r}_S' \mathbf{r}_1) \rangle$$

(5.53)

To derive the correlation function, we must average expression (5.53) over the positions of the reflecting surfaces of the obstructions (houses and trees) and over their number and their reflecting properties. First, let us average Equation (5.53) over the reflection coefficient of each obstruction as a random screen over the phase interval $[0, 2\pi]$, and denote this result by $K_\Gamma(\mathbf{r}_2, \mathbf{r}_2')$. Assuming that the correlation scales introduced earlier are smaller than the obstructions sizes and the average distances between obstructions, that is ℓ_h, and $\ell_v \ll \bar{h}, \bar{d}, \bar{L}$, but $k\ell_h \gg 1$, $k\ell_v \gg 1$, we can integrate (5.53) over variables ξ and η and taking into account (5.52) we get

$$K_\Gamma(\mathbf{r}_2, \mathbf{r}_2') = 4k^2 \int_{S_2} dS_2 Z_{2S} \cdot Z_{2'S} \cdot \Gamma(\varphi_S) \cdot \sin^2 \psi_S \cdot |G_{2S}|^2 \cdot |G_{S1}|^2$$

$$\times \exp\{ik\ell \cos(\varphi - \varphi')\} \frac{4k\ell_h}{1 + (k\ell_h)^2(\cos\psi_s - \cos\varphi_s)^2} \cdot \frac{4k\ell_v}{1 + (k\ell_v)^2(\cos\theta_2 - \cos\theta_1)^2}$$

(5.54)

where $\ell = |\mathbf{r}_2' - \mathbf{r}_2|$; all angles, which are shown in Figure 5.11, can be defined as

$$\cos\varphi = \left(\frac{\mathbf{r}_2 - \mathbf{r}_1}{|\mathbf{r}_2 - \mathbf{r}_1|} \cdot \frac{\mathbf{r}_2 - \mathbf{r}_S}{|\mathbf{r}_2 - \mathbf{r}_S|} \right), \quad \cos\varphi' = \left(\frac{\mathbf{r}_2 - \mathbf{r}_1}{|\mathbf{r}_2 - \mathbf{r}_1|} \cdot \frac{\mathbf{r}_2 - \mathbf{r}_2'}{\mathbf{r}_2 - \mathbf{r}_2'} \right) \quad (5.55a)$$

$$\sin\theta_1 = (z_S - z_1)/|\mathbf{r}_S - \mathbf{r}_1|, \qquad \sin\theta_2 = (z_2 - z_S)/|\mathbf{r}_2 - \mathbf{r}_S| \quad (5.55b)$$

Then, by averaging (5.54) over the ensemble of obstructions that are randomly distributed at the ground surface for $k\ell_h \gg 1$, $k\ell_v \gg 1$ yields the expression for the average intensity as [68]:

$$\langle I(\mathbf{r}_2) \rangle \equiv K(\mathbf{r}_2, \mathbf{r}_2) = 4\gamma_0 \int_V (d\mathbf{r}) \exp\left\{ -\gamma_0 \left(r + \tilde{r} \frac{\bar{h} - z}{z_2 - z} \right) \right\} \Gamma\left(\frac{\alpha}{2} \right) \sin^2 \frac{\alpha}{2}$$

$$\times \frac{4k\ell_h |G(\mathbf{r}_2, \mathbf{r})|^2}{1 + (k\ell_h)^2(\cos\psi_s - \cos\varphi_s)^2} \frac{4k\ell_v |G(\mathbf{r}, \mathbf{r}_1)|^2}{1 + (k\ell_v)^2(\cos\theta_2 - \cos\theta_1)^2}$$

(5.56)

All parameters and functions presented in (5.56) have been described earlier. Here, the integration is over the layer volume $V \equiv \{x, y \in (-\infty, +\infty); z \in (0, \bar{h})\}$, and

$$r = \sqrt{(x - x_1)^2 + (y - y_1)^2}, \quad \tilde{r} = \sqrt{(x_2 - x)^2 + (y_2 - y)^2}. \tag{5.57}$$

In formula (5.56), the Green's functions were obtained according to the geometrical optics approximation, for $\ell_h, \ell_v \ll \bar{h}, \bar{d}, \bar{L}$, and $k\ell_h \gg 1, k\ell_v \gg 1$:

$$|G(\mathbf{r}_2, \mathbf{r})|^2 \approx \frac{1}{16\pi^2} \frac{1}{|\mathbf{r}_2 - \mathbf{r}_1|} \tag{5.58a}$$

$$|G(\mathbf{r}, \mathbf{r}_1)|^2 \approx \frac{1}{4\pi^2} \frac{1}{|\mathbf{r} - \mathbf{r}_1|} \sin^2 \frac{kzz_1}{|\mathbf{r} - \mathbf{r}_1|} \tag{5.58b}$$

Finally, using (5.58a) and (5.58b) in (5.56), for $(z_2 - \bar{h})/\bar{h} \gg \gamma_0 d \cdot e^{-\gamma_0 d}$ yields the following expression for the incoherent part of the total field intensity (for single scattering from each obstacle (Fig. 5.11)):

$$\langle I_{\text{inc}} \rangle = \frac{\Gamma}{8\pi} \cdot \frac{\lambda \cdot \ell_h}{\lambda^2 + [2\pi\ell_h \bar{L}\gamma_0]^2} \cdot \frac{\lambda \cdot \ell_v}{\lambda^2 + [2\pi\ell_v\gamma_0(\bar{h} - z_1)]^2} \frac{(z_2 - \bar{h})}{d^3} \tag{5.59}$$

This formula is more general than the ones obtained in References [57,58] because it accounts for the dimensions of obstructions in both the vertical and horizontal directions according to (5.52).

The average intensity of the field through the mixed layer is the sum of the intensity of the scattering wave defined in Equation (5.59) (incoherent part) and of the intensity of the coherent part $\langle I_{\text{co}} \rangle$ created by the wave coming from the source. The straightforward evaluation of (5.56) allows us to obtain $\langle I_{\text{co}} \rangle$ as [68]:

$$\langle I_{\text{co}} \rangle = \exp\left\{-\gamma_0 d \frac{\bar{h} - z_1}{z_2 - z_1}\right\} \left[\frac{\sin(kz_1z_2/d)}{2\pi d}\right]^2 \tag{5.60}$$

Finally, the corresponding path loss can be obtained by substituting expressions (5.59) and (5.60) in formulas (5.49) and (5.50), respectively.

5.8. PROPAGATION IN URBAN ENVIRONMENTS

Here, we consider two specific urban propagation environments observed from the topographic maps of most cities [69–83]:

  a) regularly distributed rows of buildings and streets, and;
  b) nonregularly distributed buildings, placed on a rough terrain with various orientations relative to the transmitting and receiving antennas.

In Section 5.8.1, we start with the multislit waveguide model, which was found to be in good agreement with experimental data for wave propagation in urban areas with regular cross-street grid layouts [69–71]. In Section 5.8.2, we discuss the situation when an array of buildings is randomly distributed at a rough terrain surface and we present the 3D stochastic multiparametric model obtained in Reference [76,77]. Then, in Section 5.8.3, we compare the stochastic model with the frequently used empirical, semi empirical and deterministic analytical models for predicting loss in various built-up areas [72–75, 78–83].

In order to understand the effect of a built-up environment on radio propagation in land communication links, researchers, first of all, have analyzed the role of concrete buildings on radio wave propagation relative to LOS propagation above both smooth and rough terrains. It was shown both theoretically and experimentally that the total field distribution surrounding a single, non transparent building is caused by rays diffracted and reflected from the building's corners and walls, as well as, by the waves bounced from the ground and then reflected from the walls [69–83] (see also discussions in Section 5.5).

In this case, the number of rays caused by diffraction is larger than the number of rays caused by reflection. The estimation of these diffracted rays has been carried out using several approaches [32–40] based on Keller's GTD [28–31] described in Section 5.5 for diffraction from wedges with different shapes and material. Using the results of these investigations, we can now tackle the problem of how an array of buildings affects the radio propagation in urban communication channels.

5.8.1. Propagation in Urban Areas with Regularly Distributed Rows of Buildings

Here, we consider several urban propagation environments. We start with the simplest case of EM-wave propagation in the urban scene, where both antennas are placed above a flat ground surface in conditions of LOS and below the rooftop level. As was shown in Section 5.3, in LOS, all propagation characteristics, as path loss and radio coverage, can be determined using the well known "two-ray" model. We will briefly discuss below the multislit waveguide model (for LOS propagation), which was found to be in good agreement with experimental data of wave propagation in urban areas with a regular cross-street grid layout [69–71].

Street Waveguide Model. As mentioned in References [59,69–71], the conditions of LOS propagation along a straight street on which a base station is located is of great importance in defining the coverage area for antennas located below because of the low path loss as compared to propagation over the rooftops. At the same time, a "multislit waveguide" model has been introduced recently for describing the propagation of EM-waves in a city scene with regularly planned streets, that is a model of straight streets with buildings lined up on the sides [69–71]. The street is seen as a planar multislit waveguide with a Poisson distribution of screens (building walls) and slits (intervals between buildings). The dielectric properties of the buildings'

Rays

Receiver

Building

Building

Building

Building

x

y

z

Transmitter

Image
source
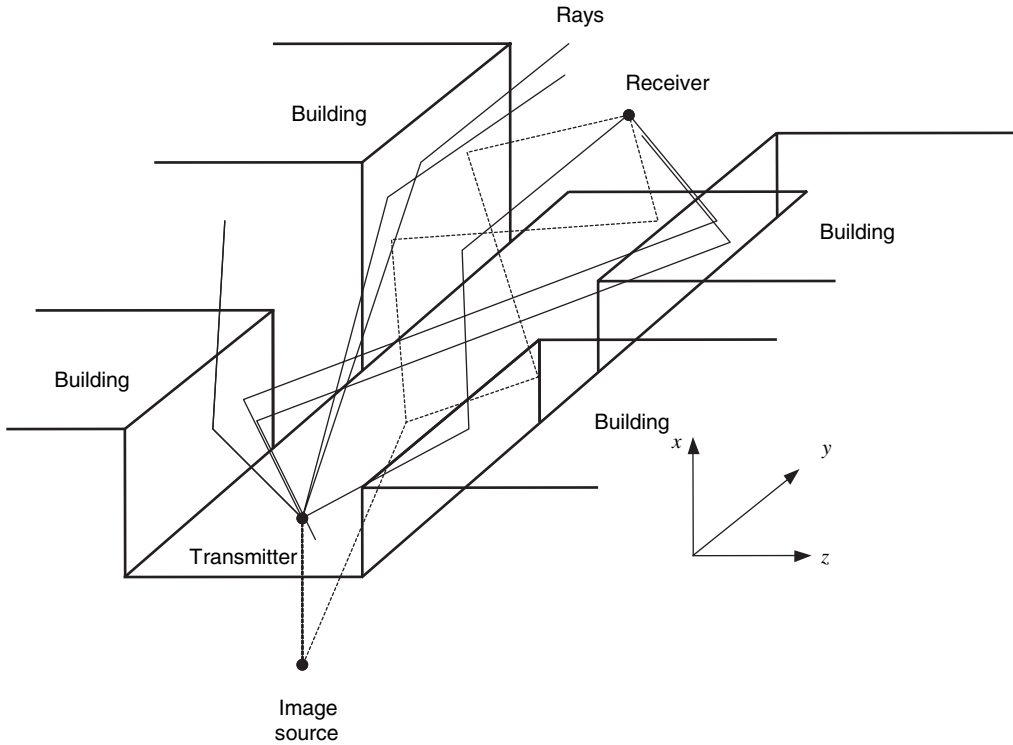
FIGURE 5.13. 3D presentation of the street waveguide model.

walls are taken into account by introducing the electrical impedance as a function of
their surface permittivity and conductivity. In Figure 5.13, a 3D-waveguide model of
a city region with regularly planned buildings, and with a receiver and transmitter is
shown. We notice that the condition h_T, $h_R < h_b$ is the main condition for the valid-
ity of the proposed street waveguide model [69–71]. Here, h_b is the height of the
buildings lining up the street, and h_T and h_R are the transmitter and receiver antenna
heights, respectively. The reflection from the ground surface is also considered using
an imaginary source. The projection of the waveguide on the zy-plane presents the
2D impedance parallel multislit waveguide with randomly distributed screens and
can be considered as a model of a city street (see Fig. 5.14). One waveguide plane
is placed at the waveguide (street) side $z = 0$, and the second one at $z = a$, where a is
a street width (Fig. 5.14). The screen length L_n and slit length l_n are distributed
according to Poisson's distribution with the average values of $\langle L \rangle = L$ and $\langle l \rangle = l$,
respectively [59,69–71]

$$f(L_n) = L^{-1} \exp\left\{-\frac{L_n}{L}\right\}, \qquad f(l_n) = l^{-1} \exp\left\{-\frac{l_n}{l}\right\} \qquad (5.61)$$
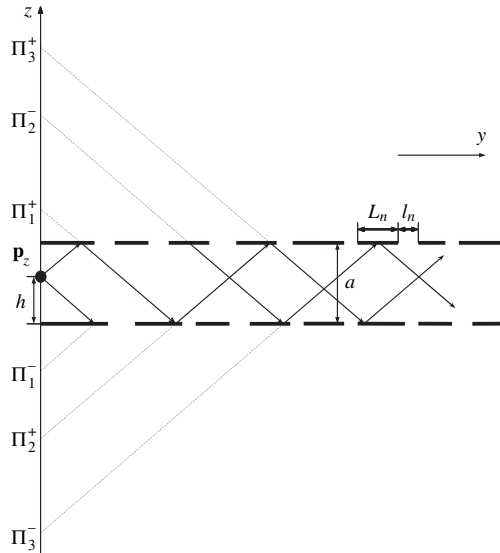
FIGURE 5.14. 2D presentation of the multislit street model with the width a.

The dielectric properties of a building's walls are usually described by the surface impedance:

$$Z_{EM} \sim \varepsilon_r^{-\frac{1}{2}}, \qquad \varepsilon_r = \varepsilon_{r0} - j60\lambda\sigma \tag{5.62}$$

In a real city scenario, the screen and the slit lengths are much greater than the radiation wavelength λ, that is, $L_n \gg \lambda$, $l_n \gg \lambda$. In this case we can make use of approximations provided to us from GTD. According to the GTD, the reflected and diffracted waves have the same nature, and the total field can be presented as a superposition of direct (incident) fields from the source and waves reflected and diffracted from the screens.

Path Loss Along the Straight Streets. Following the previously constructed model [69–71], we consider the resulting reflected and diffracted fields as a sum of fields reaching the observer from the virtual image sources Π_n^+ (for the reflections from plate $z = a$) and Π_n^- (for the reflections from plate $z = 0$), as shown in Figure 5.14.

Using some straightforward derivations presented in References [69–71], we can obtain the approximate expression for the path loss of the radio wave intensity at large ranges from the source ($r \gg a$):

$$L \approx 32.1 + 20\log_{10}f_0 - 20\log_{10}\left[\frac{(1 - \chi|R_n|)^2}{(1 + \chi|R_n|)^2}\right] + 17.8\log_{10}r - 40\log_{10}|\Gamma_g|$$

$$+ 8.6\left\{|\ln\chi|R_n||\left[\frac{\pi n - \varphi_n}{a}\right]\frac{r}{\rho_n^{(0)}a}\right\} \tag{5.63}$$

Here, $R_n = \frac{K_n - kZ_{EM}}{K_n + kZ_{EM}}$ is the coefficient of reflection for normal modes in the waveguide, φ_n is its phase, and $|R_n|$ is its modulus

$$|R_n| = \frac{\sqrt{[(\operatorname{Re} K_n)^2 + (\operatorname{Im} K_n)^2 - (kZ_{EM})^2]^2 + 4(\operatorname{Im} K_n)Z_{EM}^2}}{(\operatorname{Re} K_n + kZ_{EM})^2 + (\operatorname{Im} K_n)^2} \tag{5.64a}$$

$$\varphi_n = \tan^{-1} \frac{2\operatorname{Im}K_n kZ_{EM}}{(\operatorname{Re}K_n)^2 + (\operatorname{Im}K_n)^2 - (kZ_{EM})^2} \tag{5.64b}$$

where

$$\rho_n = (k^2 - K_n^2)^{1/2}$$

$$K_n = \pm\frac{\pi n}{a} + i\frac{\ln|\chi R_n|}{a} - \frac{\varphi_n}{a} = \operatorname{Re}K_n + i\operatorname{Im}K_n \quad n = 1, 2, 3, \ldots \tag{5.65}$$

Here, $\chi = \frac{L}{L+l}$ is the parameter of slit density. The expression for the ground reflection coefficient Γ_g is presented by (4.50) in Chapter 4. For a perfectly conductive waveguide, $Z_{EM} = 0$, $|R_n| = 1$, $\varphi_n = 0$ and

$$L \approx 32.1 + 20\log_{10} f_0 - 20\log_{10}\left[\frac{(1-\chi)^2}{(1-\chi)^2}\right] + 17.8\log_{10} r + 8.6\left\{|\ln\chi|\left[\frac{\pi n}{a}\right]\frac{r}{\rho_n^{(0)}a}\right\} \tag{5.66}$$

Like classical waveguides, most of the energy is conveyed by the first mode. Hence, taking $n = 1$ gives an accurate estimation of the resulting path loss along the street in LOS conditions. Using the two-ray model (see Section 5.3), we can also obtain from the proposed waveguide model the break point r_b, which determines the attenuation of the path loss as r^{-2}, for $r < r_b$, and varying as r^{-4}, for $r > r_b$ [69–71]. The formula for the break point r_b, that depends on the geometry of the streets and their structures, is given by:

$$r_b = \frac{4h_T h_R}{\lambda}\frac{[(1 + \chi|R_n|)/(1 - \chi|R_n|)][1 - h_b/a + h_T h_R/a^2]}{|R_n|^2} \tag{5.67}$$

In all the above formulas we assumed that the absolute values of the diffraction coefficients D_{mn} from the buildings corners are close to unity. Analyzing formula (5.67), one can see that for wide avenues, when $a > h_b > h_T, h_R$, and $\chi \to 0$, for $|R_n| \approx 1$, the break point is $r_b = \frac{4h_T h_R}{\lambda}$, that is, the same formula obtained from the two-ray model. Beyond the break point the field intensity attenuates exponentially [69–71]. This law of attenuation, obtained experimentally, states that the attenuation mode of field intensity beyond the break point is $\sim r^{-q}$, $q = 5$–7. This result does not follow from the two-ray model but can be explained using the waveguide model.

In the case of narrow streets, when $a < h_T$, $h_R < h_b$ and $\chi \to 1$, the range of the break point tends to go to infinity for the observed wavelength bandwidth

$\lambda = 00.1 - 0.3$ m used in wireless communication [69–71]. So, in the case of narrow streets the two-ray model cannot describe the absence of the break point and the two-mode field intensity decay. In the case of narrow streets, the multislit waveguide model predicts the exponential attenuation of the total field at the street level and compares well with numerous experimental data obtained in microcellular propagation channels (see detailed discussions in References [69–71]). Hence, the waveguide model is more general than the two-ray model and covers all situations occurred in the street scene.

5.8.2. Propagation Above Urban Irregular Terrain

In Sections 5.5–5.7, we dealt with propagation models that describe radio propagation above the irregular terrain, typical for rural environments containing obstructions such as hills, mountains, and trees. Some of these models adequately describe the situation in the urban scene, mostly in the suburban areas, where the effects of foliage, usually negligible in city centers, can be quite important. At the same time, the effects of trees are similar to those of buildings, introducing additional path losses and producing spatial signal variations.

In Section 5.8.1, we considered the case when both communicating antennas were located in LOS conditions, but assumed that the streets and buildings were uniformly distributed on a flat terrain. Now we will consider the situation where the buildings are randomly distributed over an irregular terrain, as is the main case of a city topography, and will present the 3D stochastic multiparametric model based on the same approach proposed for the forested and mixed residential areas.

Statistical Description of Urban Terrain. Let us consider an array of buildings randomly distributed on an irregular terrain. Using the approach in References [57–59], the coordinate system $\{x, y, z\}$ is placed at the plane $z = 0$ on the ground surface. The heights of the rough ground surface are described by the generalized function $Z(x, y)$ according to Shwartz [57–59] (see Fig. 5.15). The shadow function $Z(\mathbf{r}_2, \mathbf{r}_1)$, presented in integrals (5.36) and (5.53) for forested and mixed areas, will also be used for the urban environments. However, the situation in built-up areas is more complicated as we must also take into account the buildings' overlay profile and other specific features of the built-up terrain. In this case, the shadow function is a product of different probability functions which will be briefly presented below following the approach in References [76,77].

Probability of LOS between Subscribers. The next formula determines the probability that there is direct visible link between two arbitrary observers inside the layer of city buildings. Thus, if $\langle L \rangle$ is the average length of screens (buildings) surrounding points $A(\mathbf{r}_1)$ and $B(\mathbf{r}_2)$ (see Fig. 5.16), then the probability that there is no intersection of the line AB with any of the building screens is equal to [57,58]

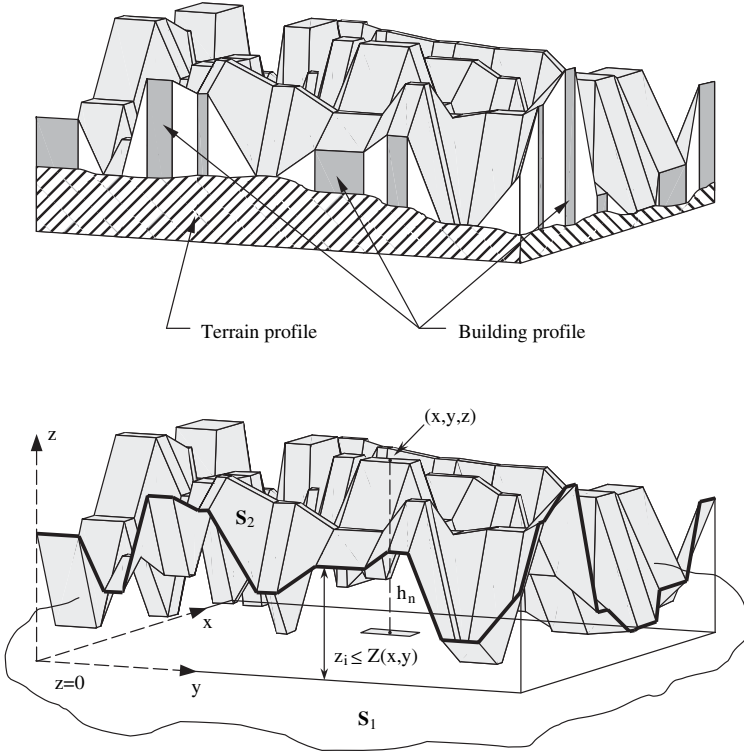$$P(\mathbf{r}_1, \mathbf{r}_2) \equiv P_{12} = \exp\{-2\langle L \rangle v r_{12}/\pi\} \tag{5.68}$$

FIGURE 5.15. The nonregular buildings' overlay profile $z = Z(x, y)$.
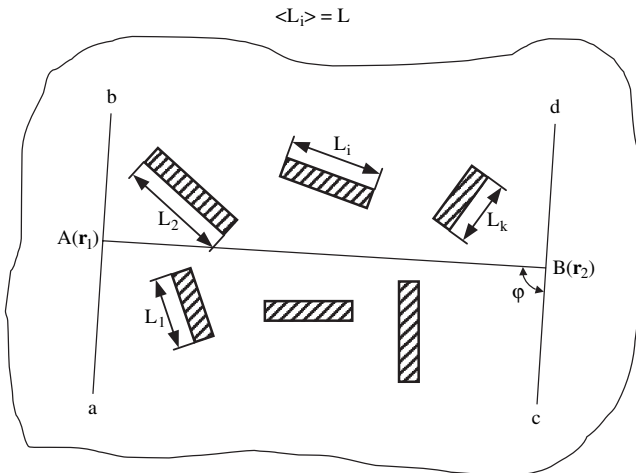
FIGURE 5.16. Line-of-sight conditions between terminal antennas in the urban scene.

from which we can easily define the one-dimensional building density parameter γ_0 (in km^{-1}) as

$$\gamma_0 = 2\langle L \rangle v / \pi. \tag{5.69}$$

Here, v is the density of buildings in the investigated area of $1\,km^2$. Parameter γ_0 determines the average minimal horizontal distance of LOS, $\bar{\rho}$ as $\bar{\rho} = \gamma_0^{-1}$ [57,58].

Influence of City Building Profile. The probability that the arbitrary subscriber antenna location is inside a built-up layer is described by the complimentary cumulative distribution function (CCDF) $P_h(z)$[CCDF $= 1 - $ CDF], which was introduced in References [76,77] as the probability that a point z is located below the buildings' roofs level.

$$P_h(z) = \int_z^\infty w(h_n) dh_n \tag{5.70}$$

Here, $w(h_n)$ is the probability density function which determines the probability that each subscriber antenna, stationary or mobile, with a vertical coordinate z is located inside the built-up layer, that is $z < h_n$, where h_n is the height of building with number n (see Fig. 5.15). Let us now consider the influence of a city buildings profile on the average field intensity. Here we use definitions introduced in References [76,77] to obtain a more general description of the built-up relief functions. Taking into account the fact that the real profiles of urban environments are randomly distributed, as shown in Figure 5.15, we can present, according to References [59,76,77], CCDF defined by (5.70) in the following form:

$$P_h(z) = H(h_1 - z) + H(z - h_1)H(h_2 - z)\left[\frac{(h_2 - z)}{(h_2 - h_1)}\right]^n, \quad n > 0, 0 < z < h_2 \tag{5.71}$$

where the function $H(x)$ is the Heaviside step function, which equals 1 for $x > 0$, and 0 for $x < 0$. Using this we can now introduce the built-up layer profile "between the two terminal antennas" that is described by the following function [77]:

$$F(z_1, z_2) = \int_{z_1}^{z_2} P_h(z) dz \tag{5.72}$$

To understand the influence of the built-up area relief on the signal intensity, let us first examine the height distribution function $P_h(z)$. The graph of this function versus height z of a built-up overlay is presented in Figure 5.17. For $n \gg 1$ $P_h(z)$ describes the case where the buildings are higher than h_1 (this is a very rare case as most buildings are at the level of a minimal height h_1). The case when all buildings
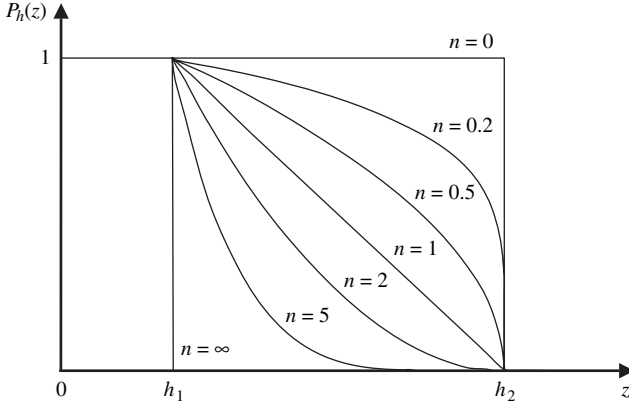
FIGURE 5.17. Buildings height distribution function $P_{\text{h}}(z)$ versus the current height z for various parameters n of built-up profile.

have heights close to h_2, (i.e., most buildings are tall), is given by $n \ll 1$. For n close to zero, or n approaching infinity, most buildings have approximately the same height h_2 or h_1, respectively. For $n = 1$ we have the case of building heights uniformly distributed in the range h_1 to h_2.

The same result is obtained from analyzing the built-up layer profile $F(z_1, z_2)$. For the case when the minimum antenna height is above the rooftop level, that is, $z_2 > h_2 > h_1$, then according to Reference [77] we get

$$F(z_1, z_2) = H(h_1 - z_1)\left[(h_1 - z_1) + \frac{(h_2 - h_1)}{(n+1)}\right]$$
$$+ H(z_1 - h_1)H(h_2 - z_1)\frac{(h_2 - z_1)^{n+1}}{(n+1)(h_2 - h_1)^n} \tag{5.73a}$$

and for the case where the minimum antenna height is below the rooftop level, that is $z_2 < h_2$, we derived [77]

$$F(z_1, z_2) = H(h_1 - z_1)\left[(h_1 - z_1) + \frac{(h_2 - h_1)^{n+1} - (h_2 - z_2)^{n+1}}{(n+1)(h_2 - h_1)^n}\right]$$
$$+ H(z_1 - h_1)H(h_2 - z_1)\frac{(h_2 - h_1)^{n+1} - (h_2 - z_2)^{n+1}}{(n+1)(h_2 - h_1)^n} \tag{5.73b}$$

From Equation (5.73) we can determine the average building height as

$$\bar{h} = h_2 - n(h_2 - h_1)/(n+1) \tag{5.74}$$

which reduces to

$$\bar{h} = (h_1 + h_2)/2 \tag{5.75}$$

for the case $n = 1$ of a uniformly distributed profile investigated in References [57,58].
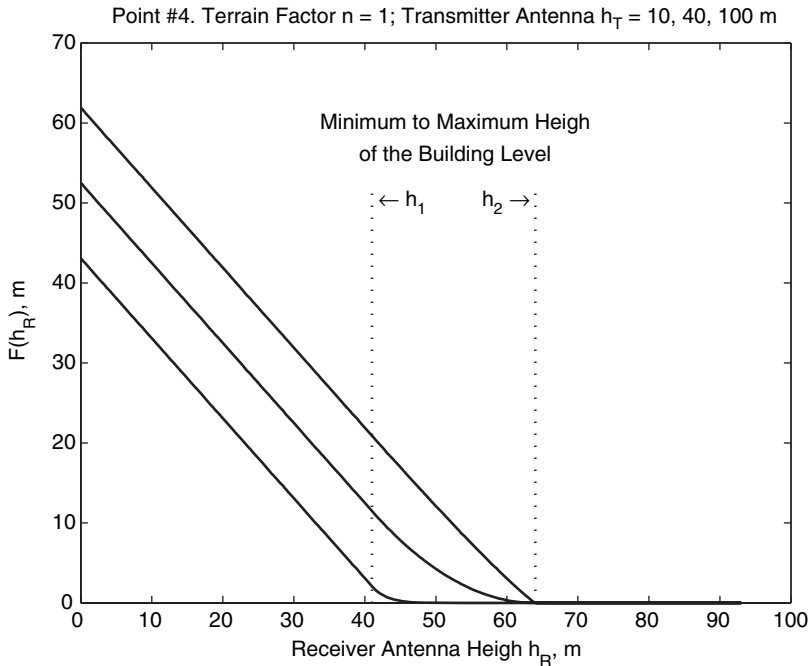
FIGURE 5.18. Distribution of $F(h_R)$ versus the receiver antenna height h_R for various heights of the transmitter antenna: $h_T = 10$, 40, and 100 m and h_1 and h_2 are the minimum and maximum of built-up relief.

As there are many geometrical factors in the built-up layer profile: the antenna heights z_1 and z_2, the minimum and maximum building heights h_1 and h_2, and the building relief that appear in formulas (5.73a) and (5.73b), we consider their effects on function $F(z_1, z_2)$ separately.

In Figure 5.18, $F(h_T; h_R, n) = F(z_1, z_2)$, given by expressions (5.73a) or (5.73b) for $z_2 > h_2 > h_1$ or $z_2 < h_2$, respectively, is depicted as a family of curves versus the receiving antenna height [77]. The discrete parameters are denoted by ";". These parameters are the transmitter antenna height, ranging between 10 m (bottom curve) to 100 m (top curve), and n. The minimum and maximum heights of the buildings overlay profile are indicated by the dotted vertical lines. We have chosen $n = 1$ which corresponds to a uniform distribution of building heights. By inspection of the displayed curves, it is obvious that for a constant transmitter antenna height, as the receiver antenna height increases, the value of $F(z_1, z_2)$ becomes smaller and the effect of the building layer on the path loss is reduced. Thus, for a transmitter antenna height $h_T = 40$ m, as the receiver antenna height h_R increases from 40 m (at the bottom level of rooftops) to 50 m (some intermediate building height value), $F(h_R)$ decreases sharply from 15 m to zero. A more gradual decrease for $F(h_R)$ is evidenced for higher transmitter antennas, (e.g., see curve for $h_T = 100$ m).
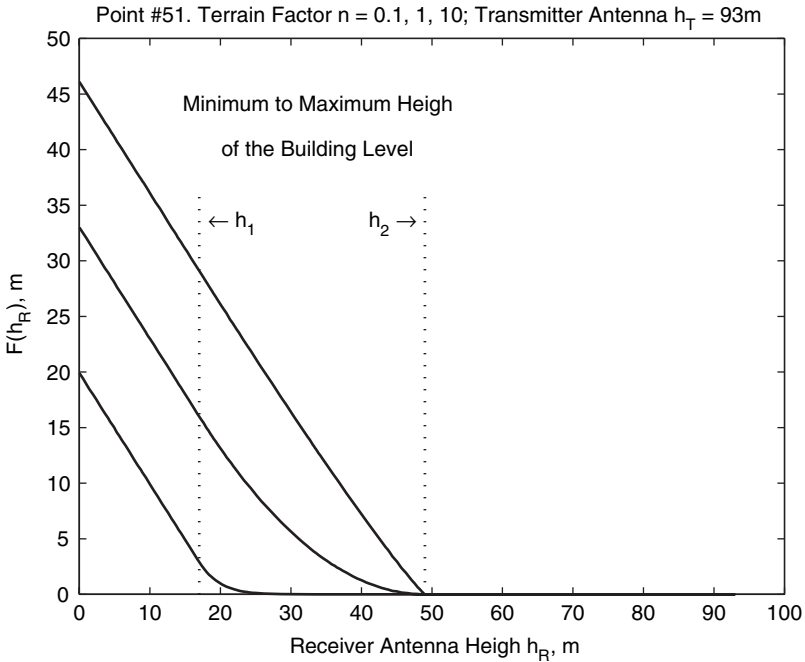
FIGURE 5.19. Distribution of $F(h_R)$ versus the receiver antenna height h_R (for a transmitter antenna $h_T = 93$ m), for various parameters $n = 0.1, 1, 10$.

In Figure 5.19, we examined the role of the parameter n on $F(h_T; h_R, n)$ at a constant transmitter antenna height $h_T = 93$ m. The values chosen were $n = 0.1, 1, 10$ that describe predominantly tall buildings, uniformly distributed heights, and predominantly low building heights, respectively. This provides a transition of the built-up area from that of typically residential area with predominantly small buildings (the bottom curve in Fig. 5.19 corresponding to $n = 10$), to that of a dense city center with predominantly tall buildings (the top curve in Fig. 5.19 corresponding to $n = 0.1$).

We therefore can state that the proposed method of characterizing the terrain and its associated building overlay provide good information regarding the nature of the profiles *vis-a-vis* the pertinent evaluation of terminal antennas, the transmitter, and the receiver.

Dimensions of the Reflected Surface Sections. Let us consider the case when LOS visibility exists between two points $\mathbf{r}_1$ and $\mathbf{r}_2$ (Fig. 5.16). Let us now determine the probability that given a point $A(\mathbf{r}_1)$, the horizontal segment inside the building (as a nontransparent screen) can be observed (see Fig. 5.20). If a horizontal segment with length l could be seen from point $\mathbf{r}_1$, a vertical segment with width l can be seen from this point as well. The vertical screen forms an angle Ψ with line AB. After
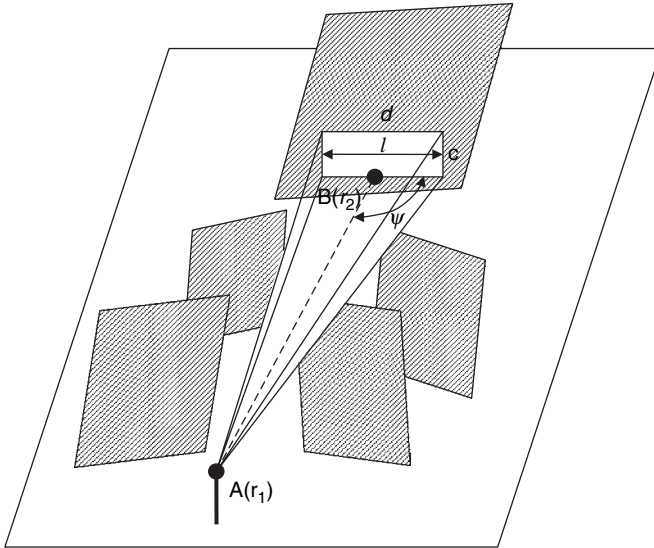
FIGURE 5.20. The screen at the building's wall with horizontal and vertical segments of length l, illuminated under the angle ψ by the source located at the point $A(\mathbf{r}_1)$.

some straightforward calculations we can obtain the probability of direct visibility of segment cd, with length l, from point A at a range of r_{12} as [57,58]:

$$P_{cd} = \exp(-\gamma_0\gamma_{12}r_{12} - v\varepsilon_{12}r_{12}|\sin\Psi|) \qquad (5.76)$$

where

$$\varepsilon_{12} = (z_2 - z_1)^{-1}\int_{z_1}^{z_2}(z - z_1)(z_2 - z_1)^{-1}P_h(z)[1 - XP_h(z)]^{-1}dz \qquad (5.77)$$

Here, the multiplier X in the integrand of (5.77) determines the probability of the event when the projection of the point $\mathbf{r}(x, y, z)$ on the plane $z = 0$ hits inside an arbitrary building (as shown in Fig. 5.15). When $X = 1$ and $z > z_1, z_2$, Equation (5.77) becomes to:

$$\varepsilon_{12} = (z_2 - z_1)^{-1}\int_{z_1}^{z_2}P_h(z)(z - z_1)(z_2 - z_1)^{-1}dz \qquad (5.78)$$

The Spatial Distribution of Scattering Points. The role of the single scattering case is very important when one of the antennas (mainly, the base station antenna)
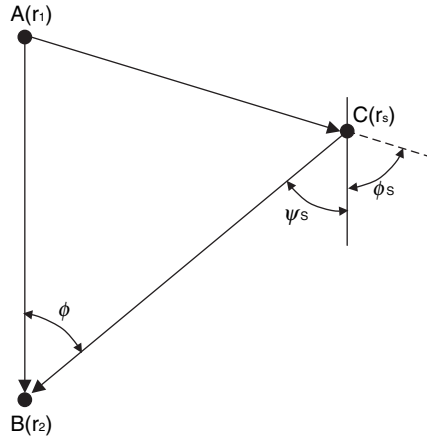
FIGURE 5.21. 2D-model of scattering from a nontransparent screen.

is above the roof level, and the other one is below it. This case is presented in Figure 5.21, where the reflected point C is inside the building contour of height h. The building orientation is determined by the angle Ψ_s and the vector $(\mathbf{r}_s - \mathbf{r}_1)$. The receiver (or transmitter) is placed at point $B(\mathbf{r}_2)$, and the transmitter (or receiver) is placed at point $A(\mathbf{r}_1)$. If we now introduce the polar coordinate system (r, φ) with point B as a base point on the plane $z = 0$ (Fig. 5.21), then for discrete distributed sources, the density of the scattered point distribution can be presented as follows [57–59]:

a) for $z_1, z_2 < h$

$$\mu(r, \varphi) = 0.5 v \gamma_0 \sin^2(\alpha/2)(r + \tilde{r}) \exp\{-\gamma_0(r + \tilde{r})\} \tag{5.79}$$

b) for $z_1 < h, z_2 > h$

$$\mu(r, \varphi) = (v\gamma_0 r/2h) \sin^2(\alpha/2) \exp\{-\gamma_0(r + \tilde{r})\} \int\limits_0^h [(r + \tilde{r}) \tag{5.80a}$$
$$- r((z_2 - h)/(z_2 - z))^2] \cdot \exp\{\gamma_0 r(z_2 - h)/(z_2 - z)\} dz$$

or for $\gamma_0 r \gg 1$

$$\mu(r, \varphi) = 0.5v \sin^2(\alpha/2)\{\gamma_0 hr(r + \tilde{r}) \exp[-\gamma_0(\tilde{r} + hr/z_2]/z_2\}$$
$$+ 0.5v \sin^2(\alpha/2)\{(z_2 - h)\tilde{r} \exp[-\gamma_0 r]/h\} = \mu_1(r, \varphi) + \mu_2(r, \varphi) \tag{5.80b}$$

where $\tilde{r} = (d^2 + r^2 - 2rd \cos\varphi)^{1/2}$; and h is the average building height. Comparing formulas (5.79) and (5.80b), one can see that the first summand in

(5.80b), $\mu_1(r, \varphi)$, is the same as that described in expression (5.79) for the case of $z_2 = h$. Both of these expressions describe *rare scatterers* which are distributed over a large area of a city, far from the receiver. The addition of significant changes in the scatterer distribution, for the case of $z_2 > h$, gives the second summand in (5.80b), $\mu_2(r, \varphi)$. For $z_2 = h$, its value is zero, but even some small increase of z_2 above h (i.e., when $z_2 > h$), yields a significant influence on the total scatterer distribution according to (5.70b). It describes the "illumination" of a small area near the upper boundary of a building layer, in the $\bar{\rho}$-region of a moving transmitter.

The Distribution of Reflected Points. In built-up areas, reflections are the most interesting single-scattering events described by geometrical optics. We can present the density of reflection points within a building layer as [57,58]:

$$\mu(\tau, \varphi) = \frac{v\gamma_0 d^3}{4} \frac{(\tau^2 - 1)}{(\tau - \cos \varphi)} P_h(z_c) \exp\{-\gamma_0 \gamma_{12} \tau d\} \qquad (5.81)$$

where $P_h(z_c)$ is described by (5.70) with variable

$$z_c = z_2 - \frac{(\tau^2 - 1)}{2(\tau - \cos \varphi)} \frac{(z_2 - z_1)}{\tau} \qquad (5.82)$$

Here, $\tau(\tau = (r + \tilde{r})/d)$ is the relative time of single-scattered waves propagating from the transmitter to the receiver through the built-up region using the function presentation (5.80b). We also assume that the height of point B (receiver) is higher than that of point A (transmitter) (i.e., $z_2 > z_1$), and is also higher than the average building height $\bar{h}$, that is $z_2 > \bar{h}$. The contribution from each level in the building layer, described by (5.81), is different than zero only for those values of τ and φ for which the coordinate z_c lies inside the building layer (i.e., $0 < z_c < h$). To obtain the average number of reflection points, we first integrate (5.81) over τ and then over φ. In other words, we analyze the distribution of reflection points $\mu(\tau, \varphi)$ in the angle-of-arrival (AOA) domain and in the time-of-arrival (TOA) domain assuming a uniform building layer. This also assumes that within this layer, the distribution of building heights is also uniform (i.e., $h_i = \bar{h} = $ constant). Next we introduce the nondimensional parameter $\varsigma = \frac{(z_2 - \bar{h})}{(z_2 - z_1)}$, which describes the effects of the difference between the terminal antennas compared with that for BS antenna with respect to average building height.

Let us now examine qualitatively how the distribution of these reflection points is changed at plane (x, y) (at the real terrain surface). We construct the regions G at which approximately 90% of reflected points are located. The boundaries of such a region consist of the arcs of ellipses with $\tau = \tau_{0.9}$, where $\tau_{0.9}$ is determined from the following relation:

$$\int_1^{\tau_{0.9}} d\tau \int_0^{2\pi} d\varphi \mu(\tau, \varphi) = 0.9 \int_1^{\infty} d\tau \int_0^{2\pi} d\varphi \mu(\tau, \varphi) \qquad (5.83)$$

and from the arcs of circles, the equation of which is

$$\tau^2 - 1 = 2\varsigma\tau(\tau - \cos\varphi) \tag{5.84}$$

Equation (5.84) can be presented by using the nondimensional coordinates $\xi = x/d$ and $\eta = y/d$ in the following form:

$$\left(\xi - \frac{\varsigma^2}{2\varsigma - 1}\right)^2 + \eta^2 = \left[\frac{\varsigma(1 - \varsigma)}{2\varsigma - 1}\right], \quad z_2 \geq h > z_1 \tag{5.85}$$

From Figure 5.22, we can see how the region G and its boundaries are changed with changes in the height factor ς from 0 to 1. In Figure 5.22, the region G and its boundaries (arcs of ellipses) are presented by the dotted curves, and the arcs of circles are presented by the continuous curves. These curves were constructed for the range of $d \approx 500$–600 m (between terminals), which is close to the conditions of most experiments carried out in built-up areas (see Chapter 11).

Estimations show that the region G is limited by a single ellipse with two foci, A and B, for $z_2 = h$ (i.e., $\varsigma \approx 0$). The distribution of the reflection points is maximum near these points (Fig. 5.22). The distribution of the reflection points does not equal
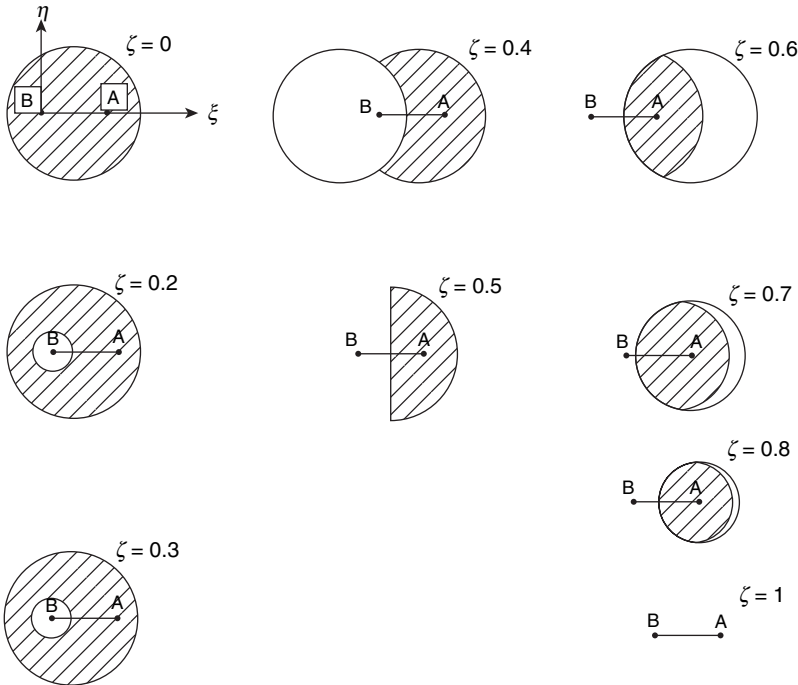

FIGURE 5.22. The region G and its boundaries change with changes in height factor ς from 0 to 1.

zero at the segment [AB] because there are some intersections of this segment with one of the arbitrary buildings (screens) that cross the path AB (see above Fig. 5.16). When the height of point B increases with respect to the rooftop height (i.e., when $z_2 > \bar{h}$), the region G, where these reflections are observed, is formed mainly around the transmitting point A. That means there is no reflection in the neighborhood of the receiving point B. Also, for $\varsigma = 0.2(\bar{h} = 20\,\text{m}, \ z_2 = 25\,\text{m})$, the region that is "prohibited" for reflections has the shape of a circle, the center and the boundary of which are determined by (5.84). Moreover, an increase in the height factor $\varsigma(z_2 > \bar{h})$ spreads this region (for $\varsigma = 0.4, h = 20\,\text{m}, z_2 = 33\,\text{m}$) to occupy the entire left half-plane (for $\varsigma = 0.5, h = 20\,\text{m}, z_2 = 40\,\text{m}$). Any further increase in $\varsigma(\varsigma \rightarrow 1)$ limits the reflections to the neighborhood of point A. (see in Fig. 5.22 the circles and arcs for $\varsigma = 0.6, z_2 = 50\,\text{m}$ and $\varsigma = 0.8, z_2 = 100\,\text{m}$).

Effects of Multiple Scattering form Obstructions. To analyze the multiple scattering phenomena caused by the buildings (e.g., nontransparent screens), we assume, as in References [76,77], that *the distribution of all obstructions placed above the rough terrain is satisfied by Poisson's distribution law.* Consequently, the probability of the event for at least one ray being received after *n*-time scattering from the randomly distributed screens is

$$P_n = 1 - \exp\{-\langle N_n(r)\rangle\}). \tag{5.86}$$

Here, the average number of *n*-time scattered rays from the screens can be obtained from the probability of the scattered points distribution $\mu_n(\mathbf{r}_0|\mathbf{r}_1, \mathbf{r}_2, \ldots \mathbf{r}_n)$:

$$\langle N_n(\mathbf{r}, \mathbf{r}_0)\rangle = \int \ldots \int \mu_1(\mathbf{r}_0|\mathbf{r}_1, \mathbf{r}_2, \ldots, \mathbf{r}_n) \ldots \mu_n(\mathbf{r}_0|\mathbf{r}_1, \mathbf{r}_2, \ldots, \mathbf{r}_n) d\mathbf{r}_n d\mathbf{r}_{n-1} \ldots d\mathbf{r}_1 \tag{5.87}$$

where

$$\mu_i(\mathbf{r}_0|\mathbf{r}_1, \mathbf{r}_2, \ldots, \mathbf{r}_n) = \exp\left\{-\gamma_0 \sum_{i=0}^{n} |\mathbf{r}_{i+1} - \mathbf{r}_i|\right\} \prod_{i=1}^{n} 0.5\gamma_0 v\{|\mathbf{r}_{i+1} - \mathbf{r}_i| + |\mathbf{r}_i - \mathbf{r}_{i-1}|\sin^2(\alpha_i/2)\}.$$

Here, the angle α_i is an angle between vectors $(\mathbf{r}_{i+1} - \mathbf{r}_i)$ and $(\mathbf{r}_i - \mathbf{r}_{i-1})$ for all $i = 1, 2, \ldots, n$; $(\mathbf{r}_0, \mathbf{r}_1, \mathbf{r}_2, \ldots, \mathbf{r}_n)$ are the radius-vectors of points $A, C_1, C_2, \ldots, C_n, B$, respectively (see Fig. 5.23). The examples of average values for once-, twice- and three-times-scattered rays from the randomly distributed buildings can be presented by using the MacDonald functions $K_n(w)$ of the order $n = 1; 2; 3$, respectively:

$$\langle N_1(r)\rangle = 0.25\pi vr^2 K_2(\gamma_0 r) \tag{5.88}$$

$$\langle N_2(r)\rangle = 9(\pi vr^2)^2 \{K_1(\gamma_0 r)/8! + (0.5\pi\gamma_0 r)^{-1/2} K_{7/2}(\gamma_0 r)/7!\} \tag{5.89}$$

$$\langle N_3(r)\rangle = 8(\pi vr^2)3\{K_5(\gamma_0 r)/10! + (0.5\pi\gamma_0 r)^{-1/2} K_{11/2}(\gamma_0 r)/11!\} \tag{5.90}$$
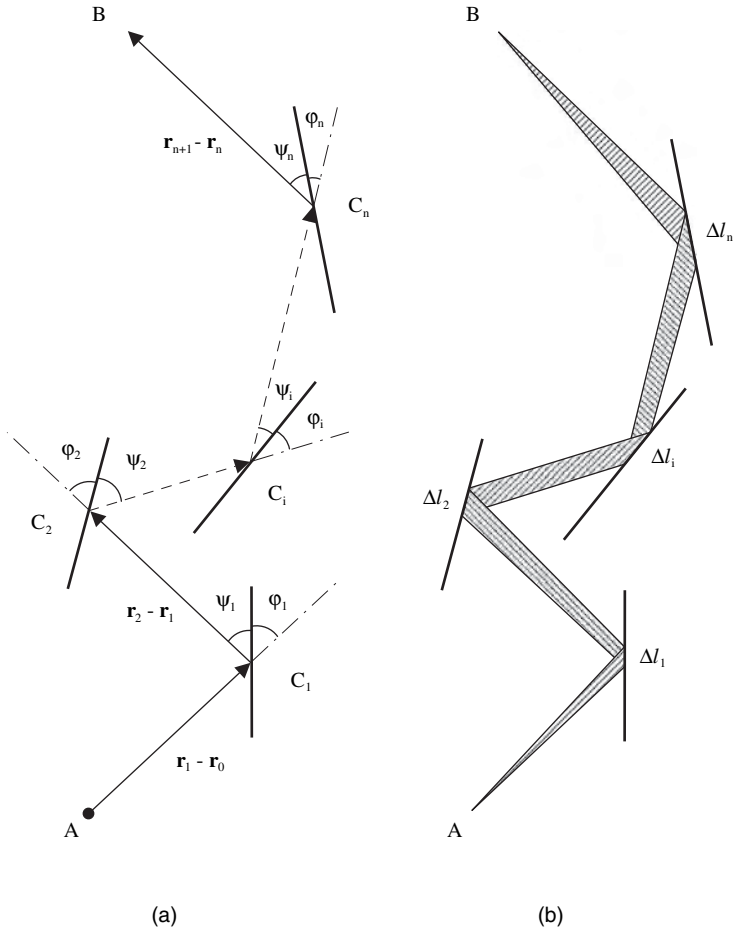
FIGURE 5.23. Geometry of multiple scattering by n randomly distributed buildings, as nontransparent screens.

The probability of occurrence for a single scattered wave (curve 1), a double scattered wave (curve 2), and a three-time scattered wave, calculated according to (5.86)–(5.90) and observed at the range of 1–2 km from the source, is presented in Figure 5.24. In microcellular conditions ($r < 1$–2 km) the probability of observing these rays at the receiver for single-to-three-times scattered waves is equal to the unity. For short ranges from the transmitter, only single scattered waves can be observed. On the other hand, in the far field, the effect of multiscattering becomes stronger than the single-scattering effect. All of the above mentioned probability formulas were substituted in the corresponding integral (5.54) instead of the shadow functions $Z_{\alpha\beta}$ for the signal field intensity evaluation.
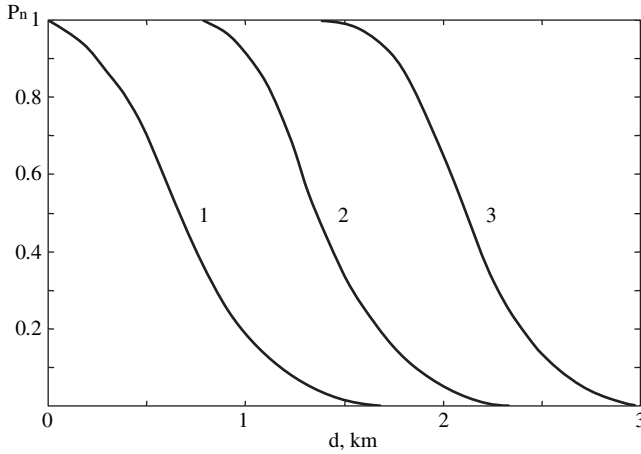
FIGURE 5.24. Probability of single, double and triple scattering versus distance d between the transmitting and receiving antennas.

3D Stochastic Model. The analysis used in Section 5.7 can be adopted to evaluate the average signal intensity distribution in the space domain in an urban communication channel. Here, all functions and parameters that describe the statistical properties of the rough built-up terrain and buildings, as scatterers (see Figs. 5.15) will be taken into account to derive Equation (5.54).

There is a difference between the mixed residential areas and the built-up areas with buildings larger than the wavelength and a corresponding correlation scale ℓ_h. It turns out that we can exclude the influence of the reflecting properties of these buildings' walls, in the horizontal directions, and describe the screens' reflecting properties only in the vertical plane (one-dimensional case, analyzed in Reference [57,58]) by rewriting (5.52) proportional to $\exp\{-|\xi|/\ell_v\}$. Also, in the case of the built-up terrain, as was mentioned above, we need to take into account the building layer profiles according to formulas (5.72)–(5.73). From Figures 5.18–5.19, one can see that this factor plays a significant role in signal power decay.

The theory of the average field intensity has been derived for 3D model in References [76,77], for the case of $\gamma_0 r_{12} = \gamma_0 d \gg 1$ and for the quasi-homogeneous built-up profiles. Similar to our treatment of the mixed residential areas, the expression for the incoherent part of the total field intensity can be presented, taking into account single and double diffracted waves shown in Figure 5.25a and 5.25b. Let us briefly examine the influence of diffraction phenomena caused by the buildings' rooftops on the field intensity attenuation. To account for this effect, we use the Huygens–Kirchhoff approximation described earlier. For the derivation of the diffraction field we introduce, according to Reference [57], the surface S_B of virtual sources that is normal to the building layer S and the surface of an infinite semi-sphere S_R that contains the source of radiation inside it, as shown in Figure 5.25a. The effect of all virtual sources placed inside the semi-sphere S_R is
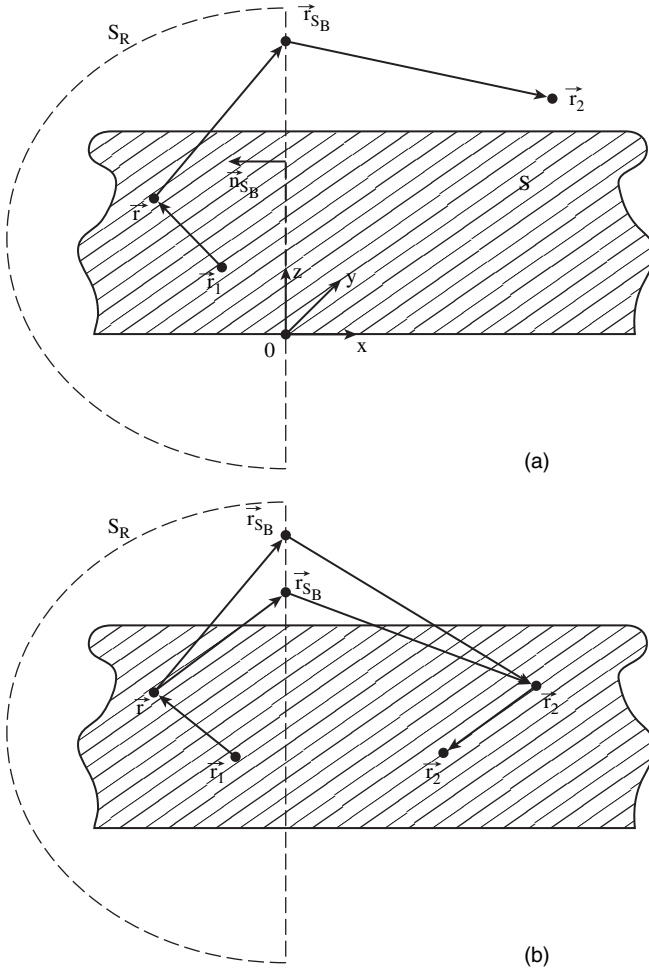
FIGURE 5.25(a). Geometry of single scattering and diffraction over a built-up layer. (b) Geometry of double scattering and diffraction over a built-up layer.

negligible, because it is limited to zero when the radius of this semi-sphere goes to infinity. Thus, the field at the receiver, presented by the Green's theorem (see Chapter 4) can be rewritten as:

$$U(\mathbf{r}_2) = 2ik \int_{S_B} \{U(\mathbf{r}_{S_B}) \cdot G(\mathbf{r}_2, \mathbf{r}_{S_B}) \cdot \cos \psi_{S_B}\} dS_B \qquad (5.91)$$

where $U(\mathbf{r}_{S_B})$ is the field at the surface S_B obtained by use of approximation (5.91) for single diffraction (see Fig. 5.25a); $\cos \psi_{S_B} = (\mathbf{n}_{S_B} \cdot (\mathbf{r}_2 - \mathbf{r}_{S_B})/|\mathbf{r}_2 - \mathbf{r}_{S_B}|)$, $\mathbf{n}_{S_B}$ is the unit vector normal to surface.

The average intensity of the received field $\langle I(\mathbf{r}_2) \rangle = \langle U(\mathbf{r}_2) \cdot U^*(\mathbf{r}_2) \rangle$ can be presented according to (5.91) as:

$$\langle I(\mathbf{r}_2) \rangle = 4k^2 \int_{S_B} dS_B \int_{S_B} dS_B' \cdot K(\mathbf{r}_{S_B}, \mathbf{r}_{S_B}') \cdot G(\mathbf{r}_2, \mathbf{r}_{S_B}') \cdot G(\mathbf{r}_2, \mathbf{r}_{S_B}) \cos \psi_{S_B} \cos \psi_{S_B}'$$

(5.92)

where $K(\mathbf{r}_{S_B}, \mathbf{r}_{S_B}')$ is the correlation function of the total field at points $\mathbf{r}_{S_B}$ and $\mathbf{r}_{S_B}'$, located at surface S_B, when the source is located at the point $\mathbf{r}_1$:

$$K(\mathbf{r}_{S_B}, \mathbf{r}_2') = 4k^2 \Bigg\langle \int_{S_B} dS_B \int_{S_B} dS_B' \cdot Z(\mathbf{r}_2, \mathbf{r}_{S_B}, \mathbf{r}_1) \cdot Z(\mathbf{r}_2', \mathbf{r}_{S_B}', \mathbf{r}_1) \cdot \Gamma(\varphi_{S_B}, \mathbf{r}_{S_B})$$

$$\times \Gamma^*(\varphi_{S_B}', \mathbf{r}_{S_B}') \cdot \sin \psi_{S_B} \cdot \sin \psi_{S_B}' \cdot G(\mathbf{r}_2, \mathbf{r}_{S_B}) \cdot G(\mathbf{r}_{S_B}, \mathbf{r}_1) \cdot G^*(\mathbf{r}_2', \mathbf{r}_{S_B}') \cdot G^*(\mathbf{r}_{S_B}', \mathbf{r}_1) \Bigg\rangle$$

(5.93)

Here, the reflection coefficient $\Gamma(\varphi_S, \mathbf{r}_S) = \Gamma \exp\left\{ -\frac{\xi}{l_v} \right\}$ and the shadow function $Z(\mathbf{r}_2, \mathbf{r}_1)$ are a superposition of all probability functions defined earlier. By averaging (5.93) over the spatial distribution of the nontransparent screens, over their number, and over the reflection properties of these screens, we obtain the following formula for the single-scattered field (single diffraction from the buildings rooftops) [76,77]:

$$\langle I(\mathbf{r}_2) \rangle = \frac{\Gamma \lambda l_v}{8\pi[\lambda^2 + (2\pi l_v \gamma_0 F(z_1, z_2))^2] d^3} [(\lambda d / 4\pi^3) + (z_2 - h)^2]^{1/2}$$

(5.94)

The same result can be obtained for twice-diffracted waves as shown in Figure 5.25b. Using the same presentation of average intensity of total field, as (5.56), we get:

$$\langle I(\mathbf{r}_2) \rangle = 4k^2 \int_{S_B} dS_B \int_{S_B} dS_B' \cdot K(\mathbf{r}_{S_B}, \mathbf{r}_{S_B}' | \mathbf{r}, \mathbf{r}_1) \cdot K(\mathbf{r}_{S_B}, \mathbf{r}_{S_B}' | \mathbf{r}', \mathbf{r}_1) \cos \psi_{S_B} \cos \psi_{S_B}'$$

(5.95)

where $K(\mathbf{r}_{S_B}, \mathbf{r}_{S_B}' | \mathbf{r}, \mathbf{r}_1)$ and $K(\mathbf{r}_{S_B}, \mathbf{r}_{S_B}' | \mathbf{r}', \mathbf{r}_1)$ are the correlation functions of the total field at the surface of the virtual sources of diffraction, which is determined by (5.93). Next, by averaging over (5.95), over the distribution of the nontransparent screens, over their number, and over the reflection properties of screens, we can

derive the formula for the double-scattered field as:

$$\langle I_{\text{inc}}(\mathbf{r}_2)\rangle = \frac{\Gamma^2\lambda^3 l_v^2}{24\pi^2\{\lambda^2 + [2\pi l_v\gamma_0 F(z_1,z_2)]^2\}^2 d^3}\left[\frac{\lambda d}{4\pi^3} + (z_2 - h)^2\right] \qquad (5.96)$$

Using (5.71) for the distribution function $P_{\text{h}}(z)$, the coherent part of the total field intensity can also be obtained as [76,77]:

$$\langle I_{\text{co}}(\mathbf{r}_2)\rangle = \exp\left\{-\gamma_0 d\frac{F(z_1,z_2)}{(z_2 - z_1)}\right\}\frac{\sin^2(kz_1z_2/d)}{4\pi^2 d^2} \qquad (5.97)$$

The difference between expressions (5.94) and (5.96), and those obtained for the forested and mixed residential areas, presented by (5.48) and (5.59), respectively, is that here we introduce single and double diffraction effects as well as a new relief function $F(z_1,z_2)$, given by formulas (5.73). This relief function is better suited to handle more realistic and more general cases of terrain and buildings overlay, as well as for different configurations of transmitter and receiver antennas. A comparison of formulas obtained in References [57,58] and Equations (5.94) and (5.96), shows that in References [57,58] the restricted case $n = 1$ of a uniform distribution profile was assumed, while Equations (5.94) and (5.96) give more latitude in describing more general distributions. Finally, the total average field intensity is written as:

$$\langle I_{\text{total}}\rangle = \langle I_{\text{inc}}\rangle + \langle I_{\text{co}}\rangle \qquad (5.98)$$

Hence, the path loss is presented as [76,77]:

$$L_{\text{total}} = 10\log\{\lambda^2(\langle I_{\text{inc}}\rangle + \langle I_{\text{co}}\rangle)\} \qquad (5.99)$$

Finally, the signal average intensity decay obtained in Sections 5.6–5.8, for various environments, is valid only for the case of an irregular but not curved terrain, and hence, they are only valid for radio links shorter than 10 km–20 km.

5.8.3. Comparison with Existing Models

Let us compare some results obtained from the stochastic, multiparametric model and those obtained from other well-known and frequently used models. For example, the empirical Okumura–Hata model [78,79], based on numerous measurements of the average power within the communication channel carried out in and around Tokyo, gives the path loss attenuation as a function of distance between "mobile-base station", d, by:

$$L(W) \propto d^{-\gamma}, \qquad \gamma = 3.0 - 3.8 \qquad (5.100)$$

The Walfisch-Ikegami semi-empirical model firstly discussed in Reference [80] developed gives a good path loss prediction for dense built-up areas of medium and large size cities. The model is based on the analytical approach, developed by Bertoni with colleagues in References [81–83], to derive the path loss in obstructive conditions. It was shown that the diffraction from the roofs and corners of buildings plays a significant role and the total field depends not only on the reflected waves but mainly on the diffracted waves. Following the work in Reference [5,81–83], the semi-empirical model developed by Walfisch and Ikegami considered two options for the base station locations: one above and one below the rooftops, in an environment with regularly distributed nontransparent buildings with various heights and different separation distances between them. Moreover, the semi-empirical model takes into account important urban parameters such as building density, average building height, and street width. The antenna height is generally lower than the average buildings height, so that the waves are guided mainly along the street. The path loss dependence on range is given as [5,80–83]:

$$L(W) \propto d^{-\gamma}, \qquad \gamma = 2.6 - 3.8 \qquad (5.101)$$

The stochastic model presented here, and the corresponding formulas (5.94) and (5.96), give the signal intensity decay law versus range between the terminal antennas as

$$L(W) \propto d^{-\gamma}, \qquad \gamma = 2.5 - 3 \qquad (5.102)$$

This result is very close to those predicted by the two other models mentioned above.

BIBLIOGRAPHY

[1] Jakes, W. C., *Microwave Mobile Communications*, John Wiley and Sons, New York, 1974.

[2] Lee, W. Y. C., *Mobile Cellular Telecommunications Systems*, McGraw Hill Publications, New York, 1989.

[3] Saunders, S. R., *Antennas and Propagation for Wireless Communication Systems*, John Wiley & Sons, New York, 1999.

[4] Steele, R., *Mobile Radio Communication*, IEEE Press, New York, 1992.

[5] Bertoni, H. L., *Radio Propagation for Modern Wireless Systems*, Prentice Hall PTR, New Jersey, 2000.

[6] Rappaport, T. S., *Wireless Communications*, Prentice Hall PTR, New York, 1996.

[7] Milstein, L. B., D. L. Schilling, R. L. Pickholtz et al., "On the feasibility of a CDMA overlay for personal communications networks," *IEEE Select. Areas in Commun.*, vol. 10, No. 4, 1992, pp. 665–668.

[8] Fock, V. A., *Electromagnetic Diffraction and Propagation Problems*, Pergamon Press, Oxford, 1965.

[9] Al'pert, Ia. L., V. L. Ginsburg, and E. L. Feinberg, *Radio Wave Propagation*, State Printing House for Technical-Theoretical Literature, Moscow, 1953.

[10] Bass, F. G., and I. M. Fuks, *Wave Scattering from Statistically Rough Surfaces*, Pergamon Press, Oxford, 1979.

[11] Voronovich, A. G., *Wave Scattering from Rough Surfaces*, Springer-Verlag, Berlin, 1994.

[12] Backmann, P., and A. Spizzichino, *The Scattering of Electromagnetic Waves from Rough Surfaces*, Artech House, Boston-London, 1963.

[13] Ishimaru, A., *Electromagnetic Wave Propagation, Radiation, and Scattering*, Englewood Cliffs, Prentice-Hall, New Jersey, 1991.

[14] Felsen, L. B., and N. Marcuvitz, *Radiation and Scattering of Waves*, IEEE Press, New York, 1994.

[15] Miller, A. R., R. M. Brown, and E. Vegh, ''New derivation for the rough-surface reflection coefficient and for the distribution of the sea-wave elevations,'' *IEE Proc.*, Pt. H, vol. 131, No. 2, 1984, pp. 114–116.

[16] Ogilvy, J. A., *Theory of Wave Scattering from Random Rough Surfaces*, London, 1987.

[17] Rice, S. O., ''Reflection of electromagnetic waves from slightly rough surfaces,'' *Comm. Pure Appl. Math.*, vol. 4, No. 3, 1951, pp. 351–378.

[18] Barrick, D. E., and W. H. Peake, ''A review of scattering from surfaces with different roughness scales,'' *Radio Sci.*, vol. 3, No. 7, 1968, pp. 865–868.

[19] Barrick, D. E., ''Theory of HF and VHF propagation across the rough sea-Parts I and II,'' *Radio Sci.*, vol. 6, No. 3, 1971, pp. 517–533.

[20] Barrick, D. E., ''First order theory and analysis of MF/HF/VHF scatter from the sea,'' *IEEE Trans. Anten. Propagat.*, vol. 20, No. 1, 1972, pp. 2–10.

[21] Wait, J. R., ''Perturbation analysis for reflection from two-dimensional periodic sea waves,'' *Radio Sci.*, vol. 6, No. 3, 1971, pp. 387–391.

[22] Valenzuela, G. R., ''Scattering of electromagnetic waves from a slightly rough surface moving with uniform velocity,'' *Radio Sci.*, vol. 3, No. 1, 1968, pp. 12–21.

[23] Valenzuela, G. R., ''Scattering of electromagnetic waves from a tilted slightly rough surface,'' *Radio Sci.*, vol. 3, No. 6, 1968, pp. 1057–1066.

[24] Valenzuela, G. R., ''The effective reflection coefficients in forward scatter from a dielectric slightly rough surface,'' *Proc. IEEE*, vol. 58, No. 12, 1970, pp. 1279–1285.

[25] Krishen, K., ''Scattering of electromagnetic waves from a layer with rough front and plane back (small perturbation method by Rice),'' *IEEE Trans. Anten. Propagat.*, vol. 19, No. 4, 1970, pp. 573–576.

[26] Davies, H., ''The reflection of electromagnetic waves from a rough surface,'' *Proc. IEEE*, vol. 101, No. 2, 1954, pp. 209–214.

[27] Bullington, K., ''Reflection coefficient of irregular terrain,'' *Proc. IRE*, vol. 42, No. 11, 1954, pp. 1258–1262.

[28] Keller, J. B., ''Diffraction by an Aperture,'' *J. Appl. Phys.*, vol. 28, 1957, pp. 857–893.

[29] Keller, J. B., ''Geometrical theory of diffraction,'' *J. Opt. Soc. Amer.*, vol. 52, No. 1, 1962, pp. 116–131.

[30] James, G. L., *Geometrical Theory of Diffraction for Electromagnetic Waves*, 2-nd ed., Peter Peregrines, London, UK, 1986.

[31] Honl, H., A. W. Maue, and K. Westpfahl, *Theory of Diffraction*, Springer-Verlag, Berlin, 1961.

[32] Kouyoumjian, R. G., and P. H. Pathak, ''A uniform geometrical theory of diffraction for an edge in a perfectly conducting surface,'' *Proc. IEEE,* vol. 62, No. 9, 1974, pp. 1448–1469.

[33] Russel, S. T. A., C. W. Boston, and T. S. Rappaport, ''A deterministic approach to predicting microwave diffraction by buildings for microcellular systems,'' *IEEE Trans. Anten. and Propag.*, vol. 41, No. 12, 1993, pp. 1640–1649.

[34] Dougherty, H. T., and L. J. Maloney, ''Application of diffraction by convex surfaces to irregular terrain situations,'' *Radio Phone*, vol. 68B, Feb. 1964, p. 239.

[35] Anderson, L. J., and L. G. Trolese, ''Simplified method for computing knife edge diffraction in the shadow region,'' *IRE Trans. Anten. Propagat.,* vol. AP-6, July 1958, pp. 281–286.

[36] Vogler, L. E., ''The attenuation of electromagnetic waves by multiple knife-edge diffraction,'' *NTIA Report*, 1981, pp. 81–86.

[37] Vogler, L.E., ''An attenuation function for multiple knife-edge diffraction,'' *Radio Sci.*, vol. 17, No. 9, 1982, pp. 1541–1546.

[38] Andersen, J. B., ''UTD multiple-edge transition zone diffraction,'' *IEEE Trans. Anten. Propagat.,* vol. 45, No. 7, 1997, pp. 1093–1097.

[39] Lee, S. W., ''Path integrals for solving some electromagnetic edge diffraction problems,'' *J. Math. Phys.*, vol. 19, No. 10, 1978, pp. 1414–1422.

[40] Bertoni, H. L., and J. Walfisch, ''A theoretical model of UHF propagation in urban environment,'' *IEEE Trans. Anten. Propagat.*, vol. 36, No. 12, 1988, pp. 1788–1796.

[41] Bullington, K., ''Radio propagation at frequencies about 30 Mc,'' *Proc. IRE*, vol. 35, No. 10, 1947, pp. 1122–1136.

[42] Epstein, J., and D. W. Peterson, ''An experimental study of wave propagation at 850 Mc,'' *Proc. IRE*, vol. 41, No. 5, 1953, pp. 595–611.

[43] *Atlas of Radio Wave Propagation Curves for Frequencies Between 30 and 10,000 Mc/s*, Radio Research Lab., Ministry of Postal Services, Tokyo, Japan, 1957, pp. 172–179.

[44] Deygout, J., ''Multiple knife-edge diffraction of microwaves,'' *IEEE Trans. Anten. Propagat.*, vol. 14, No. 4, 1966, pp. 947–949.

[45] LaGrone, A. H., and C. W. Chapman, ''Some propagation characteristics of high UHF signals in the immediate vicinity of trees,'' *IRE Trans. Anten. Propagat*, vol. AP-9, 1961, pp. 957–963.

[46] Tamir, T., ''On radio-wave propagation in forest environments,'' *IEEE Trans. Anten. Propagat.*, vol. AP-15, Nov. 1967, pp. 806–817.

[47] Sachs, D. L., and P. J. Wyatt, ''A conducting-slab model for electromagnetic propagation of lateral waves in an inhomogeneous jungle,'' *Radio Science*, vol. 3, Feb. 1968, pp. 125–134.

[48] Dence, D., and T. Tamir, ''Radio loss of lateral waves in forest environments,'' *Radio Science*, vol. 4, 1969, pp. 307–318.

[49] Reudink, D. O., and M. F. Wazowicz, ''Some propagation experiments relating foliage loss and diffraction loss at X-band and UHF frequencies,'' *IEEE Trans. on Commun.,* vol. COM-21, Nov. 1973, pp. 1198–1206.

[50] Tamir, T., ''Radio wave propagation along mixed paths in forest environments,'' *IEEE Trans. Anten. Propagat.,* vol. AP-25, 1977, pp. 471–477.

[51] Swarup, S., and R. K. Tewari, ''Depolarization of radio waves in jungle environment,'' *IEEE Trans. Anten. Propagat.*, vol. AP-27, Jan. 1979, pp. 113–116.

[52] Tewari, R. K., and S. Swarup, "An empirical result for the height gain in forest medium", *IEEE Trans. Anten. and Propagat.*, vol. AP-32, 1984, pp. 1265–1268.

[53] Vogel, W. J., and J. Goldhirsch, "Tree attenuation at 869 MHz derived from remotely piloted aircraft measurements," *IEEE Trans. Anten. and Propagat.*, vol. AP-34, 1986, pp. 1460–1464.

[54] Lebherz, M., W. Weisbeck, and K. Krank, "A versatile wave propagation model for the VHF/UHF range considering three dimensional terrain," *IEEE Trans. Anten. Propagat.,* vol. AP-40, 1992, pp. 1121–1131.

[55] Matzler, C., "Microwave (1-100 GHz) dielectric model of leaves," *IEEE Trans. Geoscience and Remote Sensing*, vol. 32, 1994, pp. 947–949.

[56] Seker, S., "Multicomponents discrete propagation model of forest," *IEE Proc. Microwave Anten. Propag.*, vol. 142, No. 3, 1995, pp. 357–363.

[57] Ponomarev, G. A., A. N. Kulikov, and E. D. Telpukhovsky, *Propagation of Ultra-Short Waves in Urban Environments*, Tomsk, USSR, Rasko, 1991.

[58] Blaunstein, N., "Distribution of angle–of–arrival and delay from array of building placed on rough terrain for various elevation of base station antenna," *Journal of Communic. and Networks*, vol. 2, No. 4, 2000, pp. 305–316.

[59] Blaunstein, N., "Wireless Communication Systems," in *Handbook of Engineering Electromagnetics*, Edited by R. Bansal, Chapter 12, Marcel Dekker, New York, 2004, pp. 417–481.

[60] Blaunstein, N., I. Z. Kovacs, Y. Ben-Shimol et al., "Prediction of UHF path loss for forest environments," *Radio Sci.*, vol. 38, No. 3, 2003, pp. 251–267.

[61] Furutsu, K., "On the statistical theory of electromagnetic waves in a fluctuating medium (I)," *J. Res. NBS*, vol. 67D (Radio Propagation), No. 3, 1963, pp. 303–323.

[62] Furutsu, K., *On the Statistical Theory of Electromagnetic Waves in a Fluctuating Medium* (II), National Bureau of Standards Monograph 79, Boulder, Co., USA, 1964.

[63] Twersky, V., "Multiple scattering of electromagnetic waves by arbitrary configurations," *J. Math. Phys.*, vol. 8, 1967, pp. 569–610.

[64] Weissberger, M. A., "An initial critical summary of models for predicting the attenuation of radio waves by trees," *ESD-TR-81-101*, EMC Analysis Center, Annapolis, MD, USA, 1982.

[65] Torrico, S. A., and R. H. Lang, "Bistatic scattering effects from a tree in a vegetated residential environment," *Proc. of National URSI Meeting*, Boulder, Colorado, 5–8 January, 1998, pp. 24–25.

[66] Torrico, S. A., H. L. Bertoni, and R. H. Lang, "Modeling tree effect on path loss in a residential environment," *IEEE Trans. Anten. Propagat.*, vol. 46, 1998, pp. 107–119.

[67] Lang, R. H., "Electromagnetic backscattering from a sparse distribution of lossy dielectric scatterers," *Radio Sci.*, vol. 16, 1981, pp. 15–30.

[68] Blaunstein, N., D. Censor, D. Katz et al., "Radio propagation in rural residential areas with vegetation," *J. Electromagnetic Waves and Applications*, vol. 17, No. 7, 2002, pp. 1039–1041; *Progress In Electromagnetic Research*, PIER 40, 2003, pp. 131–153.

[69] Blaunstein, N., and M. Levin, "VHF/UHF wave attenuation in a city with regularly spaced buildings," *Radio Sci.*, vol. 31, No. 2, 1996, pp. 313–323.

[70] Blaunstein, N., and M. Levin, "Propagation loss prediction in the urban environment with rectangular grid-plan streets," *Radio Sci.*, vol. 32, No. 2, 1997, pp. 453–467.

[71] Blaunstein, N., "Average field attenuation in the nonregular impedance street wave-guide," *IEEE Trans. Anten. and Propagat.*, vol. 46, No. 12, 1998, pp. 1782–1789.

[72] Xia, H. H., H. L. Bertoni, L. R. Maciel et al., "Radio propagation characteristics for line-of-sight microcellular and personal communications," *IEEE Trans. Anten. Propagat.*, vol. 41, No. 10, 1993, pp. 1439–1447.

[73] Rustako, A. J., Jr., N. Amitay, M.J. Owens et al., "Radio propagation at microwave frequencies for line-of-sight microcellular mobile and personal communications," *IEEE Trans. Veh. Technol.*, vol. 40, No. 2, Feb. 1991, pp. 203–210.

[74] Tan, S.Y., and H. S. Tan, "UTD propagation model in an urban street scene for microcellular communications," *IEEE Trans. Electromag. Compat.*, vol. 35, No. 4, Nov. 1993, pp. 423–428.

[75] Tan, S. Y., and H.S. Tan, "A theory of propagation path loss characteristics in a city street-grid scene," *IEEE Trans. Electromagn. Compat.*, vol. 37, Aug. 1995, pp. 333–342.

[76] Blaunstein, N., "Prediction of cellular characteristics for various urban environments," *IEEE Anten. Propagat. Magazine*, vol. 41, No. 6, 1999, pp. 135–145.

[77] Blaunstein, N., D. Katz, D. Censor et al., "Prediction of loss characteristics in built-up areas with various buildings' overlay profiles," *IEEE Anten. Propagat. Magazine*, vol. 43, No. 6, 2001, pp. 181–191.

[78] Okumura, Y., E. Ohmori, T. Kawano et al., "Field strength and its variability in the VHF and UHF land mobile radio service," *Review Elec. Commun. Lab.*, vol. 16, 1968, pp. 825–843.

[79] Hata, M., "Empirical formula for propagation loss in land mobile radio services," *IEEE Trans. Veh. Technol.*, vol. VT-29, 1980, pp. 317–325.

[80] Saleh Faruque, *Cellular Mobile Systems Engineering*, Artech House, Boston-London, 1994.

[81] Walfisch, J., and H. L. Bertoni, "A theoretical model of UHF propagation in urban environments," *IEEE Trans. Anten. and Propagat.*, vol. AP-38, 1988, pp. 1788–1796.

[82] Xia, H. H., and H. L. Bertoni, "Diffraction of cylindrical and plane waves by an array of absorbing half screens," *IEEE Trans. Anten. and Propagat.*, vol. 40, 1992, pp. 170–177.

[83] Bertoni, H. L., W. Honcharenko, L.R. Maciel et al., "UHF propagation prediction for wireless personal communications," *Proc. IEEE*, vol. 82, No. 9, 1994, pp. 1333–1359.

Effects of the Troposphere on Radio Propagation

Tropospheric effects involve interactions between radio waves and the lower layer of the Earth's atmosphere, covering altitudes from the ground surface up to several tens of kilometers above the Earth. These include effects of the gases composed in the air and hydrometeors such as rain, clouds, fog, pollutions, as well as various turbulent structures created by the turbulent wind streams both in vertical and in horizontal directions, gradient of temperature, moisture and pressure in layered atmosphere at the near-the-earth altitudes.

6.1. MAIN PROPAGATION EFFECTS OF THE TROPOSPHERE AS A SPHERICAL LAYERED GASEOUS CONTINUUM

6.1.1. Model of the Troposphere and Main Tropospheric Processes

Troposphere is the region of the Earth's lower atmosphere that surrounds the Earth from the ground surface up to 10–20 km above the terrain, where it continuously spreads to the stratosphere (20–50 km), and then to the thermosphere, usually called ionosphere (50–400 km). The effects of the latter on radio propagation will be presented in the next chapter. Now let us focus on the effects of troposphere on radio propagation starting with a definition of the troposphere as a natural layered air medium consisting of different gaseous, liquid, and crystal structures.

The physical properties of the troposphere are characterized by the following main parameters such as *temperature T* (in Kelvin), *pressure p* (in millibars or

in millimeters of Mercury), and *density* ρ (in particles per cubic meter or cubic centimeter). All these parameters significantly change with altitude and, seasonal and latitudinal variability and strongly depend on weather [1–9].

Content of the Troposphere. The troposphere consists of different kinds of gaseous, liquid, and crystal structures, including effects of gas molecules (atoms), aerosol, cloud, fog, rain, hail, dew, rime, glaze, and snow. Except for the first two components, the others are usually referred to as *hydrometeors* in past literature [10–24]. Furthermore, due to irregular and sporadic air streams and motions, such as irregular wind motions, the chaotic structures, defined as *atmospheric turbulences*, are also present in the troposphere [25–40].

Below, we present a brief decription of the various components that make up the troposphere [1–40].

Aerosol is a system of liquid or solid particles uniformly distributed in the atmosphere. Aerosol particles play an important role in the precipitation process, providing the nuclei upon which condensation and freezing take place. The particles participate in chemical processes and influence the electrical properties of the atmosphere. Actual aerosol particles range in diameter from a few nanometers to about a few micrometers. When smaller particles are in suspension, the system begins to acquire the properties of a real aerosol structure. For larger particles, the settling rate is usually so rapid that the system cannot properly be called a real aerosol. Nevertheless, the term is commonly employed, especially in the case of fog or cloud droplets and dust particles, which can have diameters of over 100 μm. In general, aerosols composed of particles larger than about 50 μm are unstable unless the air turbulence is extreme, as in a severe thunderstorm (see details in References [5,36]).

Hydrometeors are any water or ice particles that have formed in the atmosphere or at the Earth's surface as a result of condensation or sublimation. Water or ice particles blown from the ground into the atmosphere are also classified as hydrometeors. Some well-known hydrometeors are rain, fog, snow, clouds, hail, dew, rime, glaze, blowing snow, and blowing spray.

(A) Rain is the precipitation of liquid water drops with diameters greater than 0.5 mm. When the drops are smaller, the precipitation is usually called drizzle. The concentration of raindrops typically spreads from 100 to 1000 m^{-3}. Drizzle droplets usually are more numerous. Raindrops seldom have diameters larger than 4 mm, because as they increase in size they break up. The concentration generally decreases as diameters increase, except when the rain is heavy. It does not reduce visibility as much as drizzle. Meteorologists classify rain according to its rate of fall. The hourly rates relating to light, moderate, and heavy rain correspond to dimensions less than 2.5 mm, between 2.8 mm and 7.6 mm, and more than 7.6 mm, respectively. Less than 250 mm and more than 1500 mm per year represent approximate extremes of rainfall for all of the continents. Rainfall intensities greater than 30 mm in 5 min, 150 mm in 1 h, or 500 mm per day are quite rare, but these intensities, on occasions, have been more than double for the respective duration (see details in References [6,11–18,36]). Below we will discuss the effects of rain on radio propagation.

(B) Snow is the solid form of water that crystallizes in the atmosphere and falls to the Earth covering permanently or temporarily about 23% of the Earth's surface. At sea level, snow falls usually at higher latitudes, that is, above latitude 35° N and below 35° S. Close to the equator snowfall occurs exclusively in mountain regions, at elevations of 4900 m or higher. The size and shape of the crystals depend mainly on the temperature and the amount of water vapor available as they develop. In colder and drier air, the particles remain smaller and compact. Frozen precipitation has been classified into seven forms of snow crystals and three types of particles: graupel, that is, granular snow pellets, (also called soft hail), sleet, (that is partly frozen ice pellets), and hail, for example hard spheres of ice (see details in References [3,36]).

(C) Fog is a cloud of small water droplets near ground level and sufficiently dense to reduce horizontal visibility to less than 1000 m. The word ''fog'' may also refer to clouds of smoke particles, ice particles, or mixtures of these components. Under similar conditions, but with visibility greater than 1000 m, the phenomenon is termed a mist or haze, depending on whether the obscurity is caused by water drops or solid particles. Fog is formed by the condensation of water vapor on condensation nuclei that are always present in natural air. This happens as soon as the relative humidity of the air exceeds saturation by a fraction of 1%. In highly polluted air the nuclei may grow sufficiently to cause fog at humidities of 95% or less. Three processes can increase the relative humidity of the air: (1) cooling of the air by adiabatic expansion; (2) the mixing of two humid airstreams having different temperatures; and (3) the direct cooling of the air by radiation. According to the physical processes involved in the creation of fogs, there are different kinds of fogs that are usually observed: advection, radiation, inversion, and frontal. We do not enter deeply into the subject of their creation, because this is a subject of meteorology, for which readers may refer to special literature [3,7,24,36]. Here we will only analyze their influence on radio propagation.

(D) Clouds have the dimensions, shape, structure, and texture that are influenced by the kind of air movements that result in their formation and growth and by the properties of the cloud particles. In settled weather, clouds are small and well scattered. Their horizontal and vertical dimensions are only a kilometer or two. In disturbed weather they cover a large part of the sky, and individual clouds may tower as high as 10 km or more. Clouds often cease their growth only upon reaching the stable stratosphere, producing heavy showers, hail, and thunderstorms. Growing clouds are sustained by upward air currents, which may vary in strength from a few centimeters per second to several meters per second. Considerable growth of the cloud droplets with falling speeds of only about 1 cm/s, leads to their fall through the cloud, reaching the ground as drizzle or rain. Four principal classes are recognized when clouds are classified according to the kind of air motions that produce them: (1) layer clouds formed by the widespread regular ascent of air; (2) layer clouds formed by widespread irregular stirring or turbulence; (3) cumuliform clouds formed by penetrative convection; and (4) orographic clouds formed by ascent of air over hills and mountains. The reader who is interested in delving deeper into this subject can find information in References [7,21,24,36].
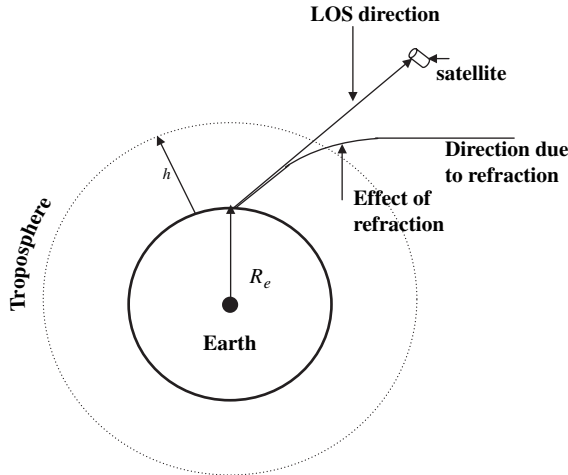
FIGURE 6.1. Displacement of the ray due to refraction.

(E) Atmospheric Turbulence is a chaotic structure generated by the irregular air movements in which the wind randomly varies in speed and direction. Turbulence is important because it churns and mixes the atmosphere and causes water vapor, smoke, and other substances, as well as energy, to become distributed at all elevations. Atmospheric turbulence near the Earth's surface differs from that at higher levels. Within a few hundred meters of the surface, turbulence has a marked diurnal variation, reaching a maximum about midday. When the sky is overcast, the low-level air temperature varies much less between day and night and turbulence remains nearly constant. At altitudes of several thousand meters or more, the frictional effect of the Earth's surface topography on the wind is greatly reduced and the small-scale turbulence, which is usually observed in the lower atmosphere, is absent.

Tropospheric Radio Phenomena. From investigations carried out in References [1,2,4,6], it follows that for clear gaseous atmosphere, even if hydrometeors are absent, fading phenomena of radio waves can prevent an availability of 99.999% at the paths of 5 km and more with the fade margin of 28 dB. However, there is a refraction effect observed in the troposphere, which can significantly decrease the efficiency of satellite communication links (see Fig. 6.1 according to References [25–30]).

Refraction occurs as a result of propagation effects of quasi homogeneous layered structures of the troposphere, as a gaseous continuum, that cause radio waves to propagate not along the straight radio paths but to curve slightly towards the ground (see Fig. 6.2 according to References [1,2,8]). This phenomenon is described below.

Moreover, the troposphere consists of a mixture of particles having a wide range of sizes and characteristics, from the molecules in atmospheric gases to the different kinds of hydrometeors such as raindrops, drops of snow, hail, drops of fogs, clouds and so forth. The main processes that caused the total wave
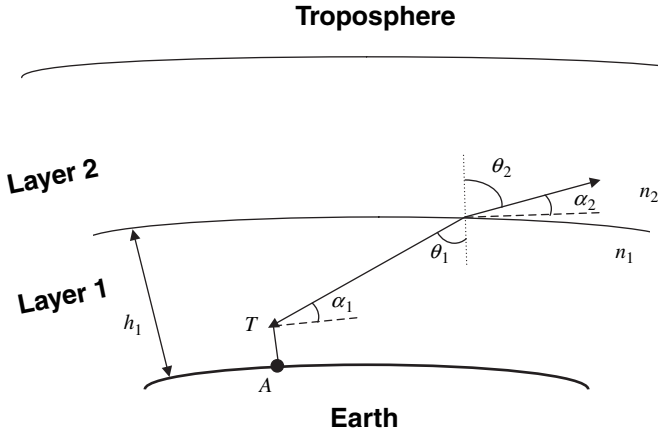
Troposphere

FIGURE 6.2. Refraction caused by the layered atmosphere.

loss (in decibels) are the absorption and the scattering, that is $L_{tot} = L_{abs} + L_{scat}$ [25–30].

Absorption (or *attenuation*) occurs as the result of conversion from radio wave energy to thermal energy within an attenuating particle, such as a gas molecule and different hydrometeors. We will consider this effect later for the gaseous layered atmosphere, as an air continuum, and for different kinds of hydrometeors.

Scattering occurs from the redirection of the radio waves into various directions so that only a fraction of the incident energy is transmitted onwards in the direction of the receiver [25–30]. This process is frequency-dependent, since wavelengths that are long compared to the particles' size will be only weakly scattered. The main influencing mechanisms in radio links passing through the troposphere are hydrometeors, including raindrops, fog, snow, clouds, and so on. For such kinds of obstructions of radio wave energy, the scattering effects are only significant to systems operating below 10 GHz [35]. The absorption effects also rise with frequency of radio waves, although not so rapidly. We will discuss the effect of scattering below.

To predict the effects of all such tropospheric structures on radio wave propagation through the atmosphere, we need some background knowledge about the concentration and size distribution of all kinds of structures, as well as their spatial and altitudinal distribution. We will briefly describe these questions below considering the effects of each kind of atmospheric content separately.

6.1.2. Tropospheric Refraction

As a first step we will consider the troposphere as a quasi-homogeneous gaseous layered medium, consisting of aerosol and molecules and atoms of gas. In other words, we consider the gaseous spherical medium around the Earth, the components of which are homogeneously distributed within the virtual layers along the height from the ground surface [32].

Refractive Index or Refractivity. The radio properties of the quasi homogeneous layered troposphere are characterized by the refractive index n, related to the dielectric permittivity of the air, ε_r, as $n = \sqrt{\varepsilon_r}$. The refractive index n of the Earth's atmosphere is slightly greater than 1, with a typical value at the Earth's surface of around 1.0003. Since the value is so close to unity, it is common to express the refractive index in N-units, usually called *refractivity* [1–3,30], which is the difference between the actual value of the refractive index and unit in parts per million:

$$N = (n - 1) \cdot 10^6 \tag{6.1}$$

Thus, at the ground surface the refractivity equals $N = N_S \approx 315$ N-units. In a real atmosphere, refractivity N varies with gas pressure and temperature and with water vapor pressure in the atmosphere. The variations of temperature, pressure, and humidity from point to point within the troposphere cause the variations of the refractivity N, which can be calculated according to the semiempiric Debye formula [1–9,30]

$$N = \frac{77.6}{T}(p_a + 4810\, p_w/T) \tag{6.2}$$

where T is the absolute temperature in Kelvin [K], p_a is the atmospheric pressure in millibars [mb], and p_w is the water vapor pressure in millibars [mb]. There are seasonal and daily variations of the refractivity measured at the surface of the ground, N_0.

More important is the decrease of the refractive index with height. Usually, we can neglect the horizontal variations of N and consider the troposphere as a quasi-homogeneous spherically layered medium. If so, the dominant variation of N is vertical with height above the Earth's surface: N reduces towards zero (n becomes close to unity) as the height is increased. The variation is approximately exponential within the first few tens of kilometers of the Earth's atmosphere, that is, this region is called the *troposphere* [1,2,30]:

$$N = N_S \exp\left\{-\frac{h}{H}\right\} \tag{6.3}$$

where h is the height above sea level, and $N_S \approx 315$ and $H = 7.35$ km are standard reference values; H is defined as the height scale of the standard atmosphere. Equation (6.3) is called the standard exponential model of the troposphere.

Tropospheric Refraction. The refractive index variations with height cause the phase velocity of radio waves to be slightly slower and closer to the Earth's surface, such that the ray paths are not straight but tend to curve slightly towards the ground. In other words, the elevation angle α_1 of the initial ray at any arbitrary point (see Fig. 6.2) is changed after refraction at angle α_2. The same situation will be at the next virtual layer of atmosphere with other refractive index n. Finally, the ray launched

from the Earth's surface propagates over the curve, whose radius of curvature, ρ, at any point, is given in terms of the rate of change of n with height [1,2,30]:

$$\rho = -\left(\frac{\cos \alpha_1}{n} \frac{dn}{dh}\right)^{-1} \tag{6.4}$$

As a result, a ray passing through the troposphere, instead of the apparent direction, propagates in a direction far from that towards the satellite. The resulting ray curvature is illustrated in Figure 6.1. The gradient of the refractivity is given by

$$g(h) = dN/dh$$

Usually it is assumed [1–9] that near the Earth's surface this gradient varies exponentially as

$$g_s(h) = -0.04 \exp(-0.136\,h),\,\text{km}^{-1} \tag{6.5}$$

Linear approximation. According to (6.5), the gradient depends nonlinearly with height. However, in the first approximation we can use the linear model, setting the gradient as a constant equal to its value at $h = 0$: $g = g(0)$. This occurs for small heights, when the standard atmosphere in (6.3) can be approximated as linear, as shown in Figure 6.3, and according to the following equation [1–9,30]:
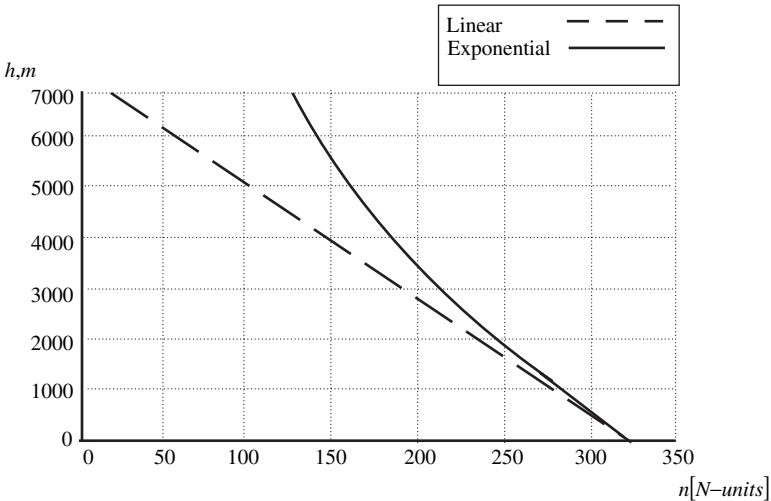
$$N \approx N_S - \frac{N_S}{H}h \tag{6.6}$$

FIGURE 6.3. Linear and exponential height dependence of the refractive index.

The refractivity thus has nearly a constant gradient of about -43 N-units per km. If so, the curvature of the ray trajectory is constant (this follows from (6.3) for $dn/dh = $ const.). A common way to take this factor into account is to introduce, instead of the actual Earth's radius, the effective Earth's radius [1–9,30]:

$$R_{\mathrm{eff}} = \kappa R_{\mathrm{e}} \qquad (6.7)$$

where $R_{\mathrm{e}} = 6375$ km, and κ is the Earth radius factor. As was shown in References [1,2], the large values of the κ-factor facilitate the propagation over long paths and small values may cause obstruction fading. In order to predict such fading, the statistics of the low values of the κ-factor have to be known. However, since the instantaneous behavior of the κ-factor differs at various points along a given path, an effective κ-factor for the path, κ_{e}, should be considered. In general, κ_{e} represents a spatial average and the distribution of κ_{e} shows less variability than that derived from point-to-point meteorological measurements. The variability decreases with increasing distance. The effective factor is given by [1,2,30]

$$\kappa_{\mathrm{e}} = \frac{1}{R_{\mathrm{e}}\dfrac{dn}{dh} + 1} \cong \frac{R_{\mathrm{e}}}{1 - \dfrac{R_{\mathrm{e}}}{\rho}} \qquad (6.8)$$

As the variation of refractive index is mostly vertical, rays launched and received with the relatively high elevation angles usually used in fixed satellite communication links (see Chapter 14) will be mostly unaffected. But for the near horizontal rays, where

$$\rho \approx -10^6/g \qquad (6.9)$$

we obtain

$$R_{\mathrm{eff}} = \kappa_{\mathrm{e}} R_{\mathrm{e}} \qquad (6.10)$$

where now the effective earth-radius factor is

$$\kappa_{\mathrm{e}} = (1 + 10^{-6} g R_{\mathrm{e}})^{-1} \qquad (6.11a)$$

Another form of this relation reads

$$\kappa_{\mathrm{e}} = \frac{0.157}{0.157 + g} \qquad (6.11b)$$

For the standard atmosphere and in limits of a linear model ($g = -3.925 \cdot 10^{-2}$ 1/km) one can immediately obtain from (6.11b) $\kappa_{\mathrm{e}} = 4/3$, so the effective radius from (6.10) is about 8500 km. Although the linear model leads to an excessive ray bending at high altitudes, this is not that important in our calculations, because the critical part of the trajectory is located near the ground antenna.

Usually, it is assumed that for the radio path with length d greater than about 20 km, the standard deviation of the effective gradient, g_e, tends to the normal distribution with the mean value g_0 as in standard atmosphere and rms deviation (see definitions of statistical parameters and distribution functions in Chapter 1):

$$\sigma_e \approx \frac{\sigma_0}{\sqrt{1 + d/d_0}} \tag{6.12}$$

where $d_0 \approx 13.5$ km for European climate conditions. Estimations show that for a radio path of length $d = 150$ km we have $\sigma_e \approx 0.3\,\sigma_0$, and for $d = 350$ km we have $\sigma_e \approx 0.2\,\sigma_0$. The reasonable estimate of σ_0 is $\sigma_0 \approx 0.04$.

In Chapter 1, the Gaussian probability density function (PDF) was introduced, the cumulative distribution function $F(x)$ of which can be presented by the error function (*erf*) in the following manner [30,33,34]:

$$F(x) = \frac{1}{2}\left[1 + \mathrm{erf}\left(\frac{x - m}{\sigma\sqrt{2}}\right)\right] \tag{6.13}$$

where the error function is defined as

$$\mathrm{erf}(x) = \frac{2}{\sqrt{\pi}} \int_0^x \mathrm{d}t\, e^{-t^2}$$

Then, the characteristic Q-function of the normal distribution is given by

$$Q = \sqrt{2}\,\mathrm{erfinv}(2t - 1) \tag{6.14}$$

where $\mathrm{erfinv}(x)$ is the inverse error function, and t is the time availability expressed in relative units (if t is in percentage there is a need to divide this value by 100%). Thus, for the 95% time availability we get $Q = 1.64$ (see References [30,33,34]) and

$$g_e \approx g_0 + 1.64\,\sigma_e \tag{6.15}$$

Therefore, $g_e \approx -0.020$ ($\kappa_e \approx 1.14$) for $d = 150$ km, and $g_e \approx -0.027$ ($\kappa_e \approx 1.21$) for $d = 350$ km. For the 99% time availability we get $Q = 2.33$ (see [30,33,34]) and

$$g_e \approx g_0 + 2.33\,\sigma_e \tag{6.16}$$

That leads to a $g_e \approx -0.012$ ($\kappa_e \approx 1.08$) for $d = 150$ km, and a $g_e \approx -0.021$ ($\kappa_e \approx 1.15$) for $d = 350$ km. We can see that for the real model of the spherical layered troposphere, the median value of κ_e differs from $4/3$, which follows from the linear model of the reflectivity profile.

Approximation Based on the Parabolic Equation Method. As shown above, the real troposphere is characterized by a nonregular inhomogeneous structure of the refractivity both in vertical and in horizontal directions. As a result, there are areas of space in which both constructive and destructive interference occur between multiple paths and other areas called "radio holes" through which no rays pass and where the signal level is very low. The boundary between two such areas forms a caustic along which the level of the signal may be very high.

As refraction conditions vary in time, a given point in space may be located alternatively in "radio holes" or in illuminated areas, which result in the sharp fluctuations of signal arriving at the receiver antenna. In many situations there are rather fast changes in the refraction conditions during multipath activity, and the characteristic time may reach only several seconds. In addition, the movement of the air vehicle may transform the slow fading to the fast one, as we observed in mobile terrestrial communication links (see Chapter 5). The combination of several rays that have been subjected to different propagation delays causes frequency selective fast fading (see definitions in Chapter 1), which may result in amplitude and phase variations inside the bandwidth of the transmission channel. The frequency selective fast fading in such cases may exceed $\pm(0.25\text{--}0.5)$ dB/MHz. It is known that the multipath mechanism exists mainly during periods of large negative values of the refractive index gradient and strong tropospheric stratification [1,2,8]. The angle-of-arrival deviations may be as large as $0.5\text{--}0.8°$ and even more in the vertical plane.

The usual technique, used for investigation of all these phenomena, is based on the geometric optics approximation and on a multiray model, which is not capable of describing radio holes and field behavior near caustics. For such purposes an exact model based on a parabolic type equation was developed and numerically investigated [39]. Why do we need to use such rigorous models? From the literature, the simplified theories, such as multiray model, do not offer an adequate description of the range-height structure of the field in the atmospheric radio channel, which may lead to significant errors in the link budget design accounting for the fading phenomena. On the contrary, the solution of the parabolic wave equation exhibits excellent robustness and accuracy for complicated problems involving vertically and horizontally varying refractive conditions [39].

Here, we do not concentrate on the details of numerical computations of path loss based on the parabolic equation technique, referring the reader to Reference [39] and to the bibliography mentioned there. We only point out that the two most popular approaches to numerically solve parabolic wave equations are the implicit finite differences and the Fourier split-step algorithms.

Derivations of the scalar Helmholtz equation, beginning with the Maxwell equations for both horizontal and vertical polarizations, are well known. Here we can use the so-called earth-flattening approximation to transform the spherical coordinate representation to pseudorectangular coordinates (x, z). Next, the Helmholtz equation is presented approximately in the form of a parabolic wave equation

$$\frac{\partial u}{\partial x} - i\sqrt{k^2 + \frac{\partial^2}{\partial z^2}}u - ik(q-2)u = 0 \qquad (6.17)$$

where x and z are horizontal (ground range) and vertical (altitude above the Earth's surface) coordinates, k is the free-space wave number, and $q(x,z)$ is the modified refractive index term defined as

$$q^2(x,z) \approx n^2(x,z) + 2z/R_{\text{eff}} \qquad (6.18)$$

In (6.18), $n(x,z)$ is the usual refractive index, and R_{eff} is the effective Earth's radius introduced above to take into account effects of a spherical layered troposphere. For vertical electric polarization, the envelope function, $u(x,z)$, is related approximately to the transverse tangential magnetic field as follows:

$$H_y(x,z) \approx \frac{n}{\sqrt{x}} u(x,z) e^{ikx} \qquad (6.19)$$

For horizontal electric polarization, the transverse tangential electric field $E_y(x,z)$ is related to $u(x,z)$ in a similar way. Using these expressions, we can evaluate total field solution for spherical-layered irregular atmosphere following Reference [39].

6.1.3. Wave Attenuation by Atmospheric Gaseous Structures

Let us consider the wave attenuation caused by the atmospheric gas, as a continuum of molecules of gases. Then, in the next sections we will consider all effects of hydrometeors, as most important in determining communication system reliability. The molecular absorption is due primarily to atmospheric water vapor and oxygen. Although for frequencies around 1–20 GHz this kind of attenuation is not large, it takes place as a permanent factor. The absorption in the atmosphere over a path length r is given by [4,5,30]

$$A = \int_0^r dr \gamma(r) \quad [\text{dB}] \qquad (6.20)$$

where $\gamma(r)$ is the specific attenuation consisting of two components:

$$\gamma(r) = \gamma_o(r) + \gamma_w(r) \quad [\text{dB/km}] \qquad (6.21)$$

where $\gamma_o(r)$ and $\gamma_w(r)$ are the contributions of oxygen and water vapor, respectively. At the ground level (where pressure is of 1013 mb) and at a temperature of 15°C they are approximated by [3–5,9]

$$\gamma_o = \left[7.19 \cdot 10^{-3} + \frac{6.09}{f^2 + 0.227} + \frac{4.81}{(f-57)^2 + 1.50} \right] f^2 \times 10^{-3} \quad [\text{dB/km}] \quad (6.22)$$

and

$$\gamma_w = \left[0.050 + 0.0021\rho + \frac{3.6}{(f-22.2)^2+8.5} + \frac{10.6}{(f-183.3)^2+9.0} \right] f^2 \rho \times 10^{-4} \quad [\text{dB/km}]$$

$$(6.23)$$

where f is the frequency [GHz], and ρ is the water vapor density [g/m³]. Other temperatures are taken into account by correction factors of -1.0% per °C from 15°C for dry air, and -0.6% per °C from 15°C for water vapor (attenuation increasing with decreasing temperature).

As in meteorology the measurable quantity is the relative humidity $\eta(T)$, we have to relate ρ with $\eta(T)$. The relative humidity is given by

$$\eta(T) = p/E(T) \tag{6.24}$$

where p is the water vapor partial pressure, [mb], and $E(T)$ is the saturation pressure, which is defined by the approximate formula [3–5,9]

$$E(T) \cong 24.1\Theta^5 10^{10-9.834\Theta} \tag{6.25}$$

where $\Theta = 300/T$. Finally, the values of p and ρ are related by

$$\rho \cong 216.7 \, p/T \tag{6.26}$$

The attenuation for a slant path can be estimated by using the exponential models with height scales of $h_o = 6 \, \text{km}$ and $h_w = 2 \, \text{km}$ for the dry air and water vapor, respectively. Such a model leads to

$$A_o = \gamma_o L_o, \qquad A_w = \gamma_w L_w \quad [\text{dB}] \tag{6.27}$$

where the effective path lengths are given by $(n = o, w)$

$$L_n = \frac{\sqrt{R_{\text{eff}} h_n}}{\cos \theta} [F(x_{n1}) - F(x_{n2}) \exp(-h_2/h_n)] \quad [\text{km}] \tag{6.28}$$

Here, as above, $R_{\text{eff}} = 8500 \, \text{km}$ is the effective Earth's radius,

$$\theta \approx \arctan h_2/d \tag{6.29}$$

is the elevation angle, and the values of x_{ni} are given by

$$x_{ni} = \cos \theta \left[z_n \tan^2 \theta + \sqrt{z_n^2 + 2\frac{h_i}{h_n} + \frac{h_i^2}{2R_{\text{eff}} h_n}} \right] \tag{6.30a}$$

$$z_n = \sin \theta \sqrt{R_{\text{eff}}/h_n} \tag{6.30b}$$

The function $F(x)$ is approximated by the expression [3–5,9]

$$F(x) = \frac{1}{0.661x + 0.339\sqrt{5.51 + x^2}} \tag{6.31}$$

Using these formulas, we find that the attenuation due to the water vapor dominates, and for typical European or North American summer weather conditions, the specific attenuation does not exceed 0.02 dB/km at sea level. This corresponds to the maximal attenuation of 7 dB for the horizontal path length of 350 km. Under summer conditions, the absorption due to oxygen does not exceed typically $8 \cdot 10^{-3}$ dB/km, which corresponds to 2.8 dB for the maximal distance. In winter, the oxygen contribution to the specific attenuation does not exceed 10^{-2} dB/km. The total attenuation at sea level due to atmospheric gases can be estimated as 0.025 dB/km. However, for slant paths the total attenuation does not exceed the value of 1 dB, but for the 99% level of probability it may be estimated as 2 dB.

As was mentioned above, gaseous molecules in atmosphere may absorb energy from radio waves passing through them, thereby causing attenuation. This attenuation is greatest for polar molecules such as water H_2O [30]. As was mentioned in Reference [30], the oppositely charged ends of such molecules cause them to align with the ambient electric field. Since the electric field of radio waves is changing in direction twice per cycle, realignment of such molecules occurs continuously, so a significant loss may result. At higher frequencies this realignment occurs faster, so the absorption loss has a general tendency to increase with frequency.

Nonpolar molecules, such as oxygen O_2, may also absorb wave energy due to the existence of magnetic moments. Here also the increase of absorption is observed with an increase of wave frequency [5,9,30]. But here several resonance peaks of absorption, each corresponding to different modes of molecule vibration, the lateral, the longitudinal and so forth, are occurring. The main resonance peaks of H_2O are around 22.3, 183.3, and 323.8 GHz, and of O_2 are around 60 GHz covering actually a complex set of closely spaced peaks that prevent the use of the band 57–64 GHz for practical satellite communication. The specific attenuation in decibels per kilometer for water vapor, γ_w, and for oxygen, γ_o, is given in Figure 6.4 according to References [5,9] for a standard set of atmospheric conditions. The total atmospheric attenuation L_a for a particular path is then found by integrating the total specific attenuation over the total path length r_T in the atmosphere [3–5,9,30]:

$$L_a = \int_0^{r_T} \gamma_a(l)dl = \int_0^{r_T} [\gamma_w(l) + \gamma_o(l)]dl \quad [\text{dB}] \tag{6.32}$$

This integration calculated for the total zenith $(\theta = 90°)$ attenuation carried out in References [5,9] is presented in Figure 6.5 by assuming an exponential decrease in
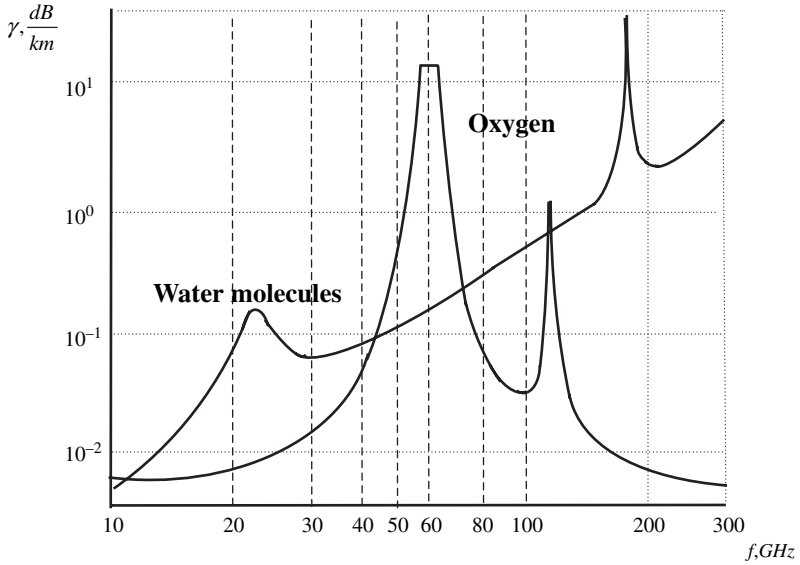
FIGURE 6.4. Attenuation versus frequency for water vapor and oxygen.
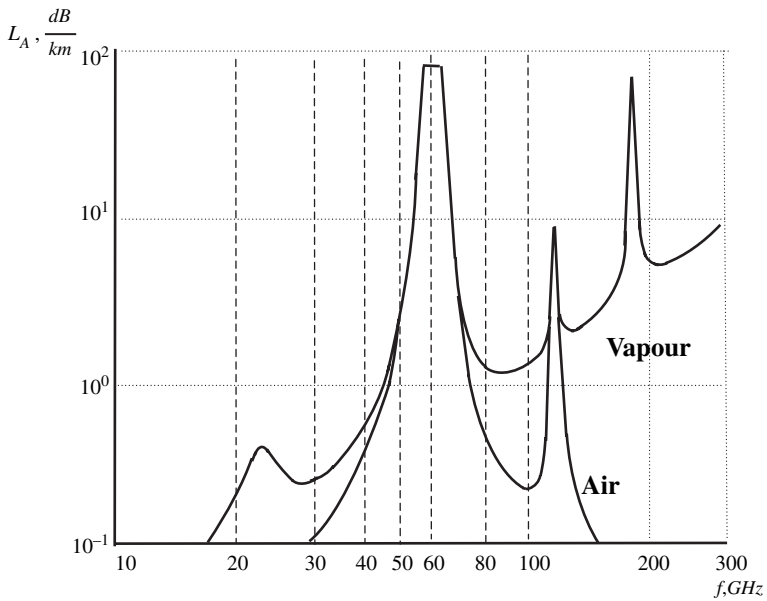

FIGURE 6.5. Attenuation versus frequency for gaseous atmosphere with water vapor and dry air.

gas density with height. The attenuation for inclined paths with an elevation angle $\theta > 10°$ can then be found from the zenith attenuation L_z as [5,9,30]

$$L_a = \frac{L_z}{\sin\theta} \qquad (6.33)$$

We must note that atmospheric attenuation results in an effective upper frequency limit for mobile satellite communications.

6.1.4. Scattering in the Troposphere by Gaseous Structures

Pure scattering occurs if there is no absorption of the radiation in the process, and hence, no loss of energy but only a redistribution of it [5,9,30]. Most of the scattering encountered in the atmosphere is essentially pure and is discussed in this section.

The attenuation due to scattering of the radio wave depends upon the pattern (or main lobe) of the receiving antenna. If the antenna pattern is very large, some field energy scattered at a very small forward angle will still be accepted and received. If the antenna pattern is very small, all scattered radiation can be rejected and only transmitted rays arrive at the receiver.

Theoretically, scattering can be treated using three separate approaches depending on the wavelength and the size of the particles causing the scattering. These approaches are Rayleigh scattering, Mie scattering, and Nonselective scattering.

Rayleigh Scattering applies when the radiation wavelength is *much larger* than the particle size. The volume scattering coefficient for Rayleigh scattering can be expressed as [25,27]

$$\sigma = \frac{(4\pi^2 N V^2 / \lambda^4)(n^2 - n_0^2)^2}{(n^2 + 2n_0^2)^2} \qquad (6.34)$$

where N is a number of particles per unit volume, [cm^{-3}]; V is the volume of scattering particles, [cm^3]; λ is a wavelength of radiation, [cm]; n_0 is the refractive index of the atmosphere in which molecules (atoms) of gases are suspended as particles; and n is a refractive index of scattering particles. For spherical water droplets in air, (6.34) becomes

$$\sigma = 0.827 \frac{N\sigma_S^3}{\lambda^4} \qquad (6.35)$$

where σ_s is the cross-sectional area of the scattering droplet. The expression (6.35) must be integrated over the range of λ and σ_s encountered in any given circumstance. As long as the particle diameter $2\sqrt{\sigma_s/\pi}$ is very small compared to λ, the same scattering can be experienced from a large number of small particles or a small number of large particles, accounting the product $N\sigma_s^3$ to be the same.

At the conditions of standard temperature and pressure the scattering coefficient is $\sigma_\lambda = 1.07 \times 10^{-3}\lambda^{-4.05}$ km^{-1} (λ in micrometers); σ_λ is the scattering coefficient for wavelength, [cm^{-1}].

Mie scattering is applicable when the particle size is *comparable* to the radiation wavelength. The Mie scattering-area coefficient is defined as the ratio of the incident wave front that is affected by the particle to the cross-sectional area of the particle itself. The scattering coefficient σ can be obtained from References [25,26]

$$\sigma = NK\pi a^2 \qquad (6.36)$$

where the value of K rises from 0 to nearly 4 and asymptotically approaches the value 2 for large droplets. For the almost universal condition in which there is a continuous size distribution in the particles, we have from Reference [25]

$$\sigma_\lambda = \pi \int_{a_1}^{a_2} N(a)K(a,n)a^2 da \qquad (6.37)$$

where $N(a)$ is a number of particles per cubic centimeter in the interval da, [cm^{-3}]; $K(a,n)$ is the scattering area coefficient; a is the radius of spherical particle, [cm^{-1}]; n is an index of refraction of particle. Many authors present a detailed treatment of scattering theory [25–27] for a wide variety of particle composition, size, and shape. The Mie scattering area coefficient is given in References [25–27].

Nonselective scattering occurs when the particle size is *very much larger* than the radiation wavelength. Large-particle scattering is composed of contributions from three processes involved in the interaction of the electromagnetic radiation with the scattering particles:

– reflection from the surface of the particle with no penetration;
– passage through the particle with and without internal reflections;
– diffraction at the edge of the particle.

In References [25–27] the combined effect of all three processes, including the interference encountered between the three components, is discussed. It is shown that for particles larger than about twice the radiation wavelength ($\alpha > 20$), the scattering-area coefficient becomes 2, which is the asymptotic value of scattering effect predicted by the Mie theory. Thus, the theoretical approach through diffraction, refraction, and reflection appears to have little contribution to the more general approach of Mie. Thus, for $\alpha < 20$, the Mie theory is valid, and for $\alpha > 20$ the two predictions converge on the value 2.

6.1.5. Propagation Clearance

The maximal distance r_0 of line-of-sight (LOS) propagation in a nonrefractive atmosphere and a spherical earth surface is given by [31]

$$r_0 = \sqrt{2R_{\text{eff}}}\left(\sqrt{h_1} + \sqrt{h_2}\right) = 3.57\left(\sqrt{h_1} + \sqrt{h_2}\right) \qquad (6.38)$$

where h_1 and h_2 are the heights of the antennas, [m]. When refraction is taken into account, we have [31]

$$r_0 = 3.57\sqrt{\kappa_e}\left(\sqrt{h_1} + \sqrt{h_2}\right) \quad [\text{km}] \qquad (6.39)$$

In practice, the term associated with the height of the ground-based terminal antenna ($h_1 < 10\,\text{m}$) can be neglected with respect to the height h_2 of the air vehicle antenna. Then, the latter formula may be easily inverted to obtain the minimal altitude of the object (air vehicle antenna), which is visible for a given distance d,

$$h_{2\,\text{min}} = 0.0785\,d^2/\kappa_e \quad [\text{m}] \qquad (6.40)$$

Although this dependence looks like a parabolic function, its behavior differs from pure parabolic because of the presence of κ_e, which is a function of distance.

Let us now present some examples on how refraction affects the range of direct visibility (LOS conditions) between two antennas within the tropospheric radio link. Thus, for a vehicle antenna at height of $h_2 = 2\,\text{km}$, we have from (6.11) and (6.39) that $r_0 = 178\,\text{km}$ for 95% availability, and $r_0 = 173\,\text{km}$ for 99% level. Similarly, for $h_2 = 6\,\text{km}$, we have $r_0 = 312\,\text{km}$ (availability is 95%) and 304 km (availability is 99%). On the contrary, knowledge of the range between antennas allows us to obtain the minimal height of air vehicle, from which LOS conditions are valid. Thus, the range of 350 km will be covered, according to (6.40) and taking into account (6.11) only for heights h_2 larger than 8 km.

Tropospheric radio paths are classified as *open* (correspond to the same LOS conditions as in terrestrial links described in Chapter 5), *semiopen*, and *closed* (correspond to the same NLOS conditions in terrestrial links). As was shown in Chapter 5, wave propagation takes place within the first Fresnel zone (ellipsoid) around the ray connecting the terminal/vehicle antennas. We will state this concept also for tropospheric radio links. Thus, the radius of the first Fresnel zone at a point between the transmitter and the receiver antennas is determined by the following formula

$$l_F(d_1, d_2) = \sqrt{\lambda d_1 d_2/(d_1 + d_2)} \qquad (6.41)$$

where d_1 and d_2 are the distances to the antennas at the point where the ellipsoid radius is calculated. The maximum value is achieved in the middle of the path ($d_1 = d_2 = L/2$) and is equal to (see Fig. 6.6)
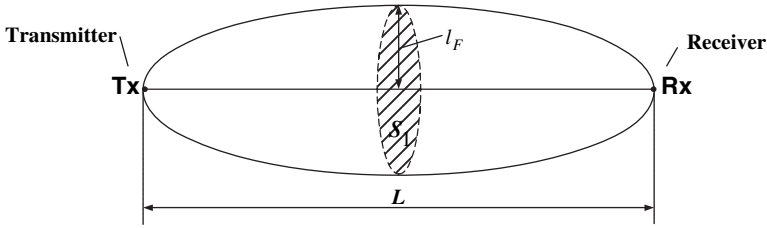
$$l_F = \sqrt{\lambda L/2} \qquad (6.42)$$

FIGURE 6.6. The line-of-sight (LOS) conditions; S_1 is the area of cross section of Fresnel's zone with radius l_F.

For example, for frequency 15 GHz and maximal distance of 150 km $l_F \approx 39$ m, and for frequency 13 GHz and distance of 350 km $l_F \approx 64$ m.

Using the Fresnel zone concept, we can determine all kinds of tropospheric radio links. Thus, we will state that for:

Open (or within the horizon) paths there are no obstacles located between the antennas (see Fig. 6.6). In this case the propagation of the wave is similar to that in free space (see Chapter 5), taking into account only the attenuation due to atmospheric gases and hydrometeors.

For semiopen (near the radio horizon) paths, the obstacles cover a part of the ellipsoidal cross section, and the effects of the obstacles can be important (see Fig. 6.7). However, the size of the first Fresnel zone is very small compared to the variability of the air vehicle antenna height, and this intermediate case is of much less importance.

For closed paths, including the hilly or mountainous terrain described in Chapter 5, the wave attenuation due to diffraction from such obstructions and due to the effects in the troposphere may exceed 300 to 350 dB, and the propagation is possible only by using the so-called troposcatter mechanism (this subject will be discussed later in Section 6.3).

6.1.6. Depolarization of Radio Wave in the Atmosphere

The polarization of a wave changes when passing through an anisotropic medium such as a cloud. As was shown by Saunders [30], a purely vertical polarized wave
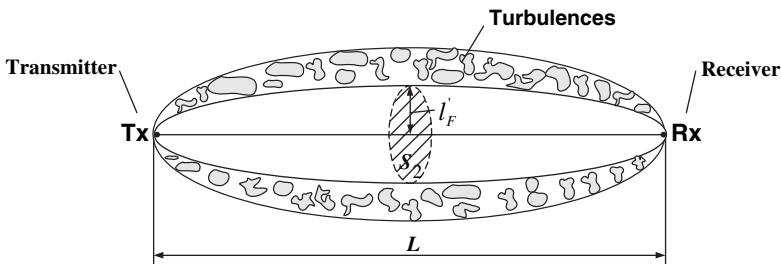

FIGURE 6.7. The non-line-of-sight (NLOS) conditions; S_2 is the area of cross section of the part of the Fresnel's zone with radius l_F.
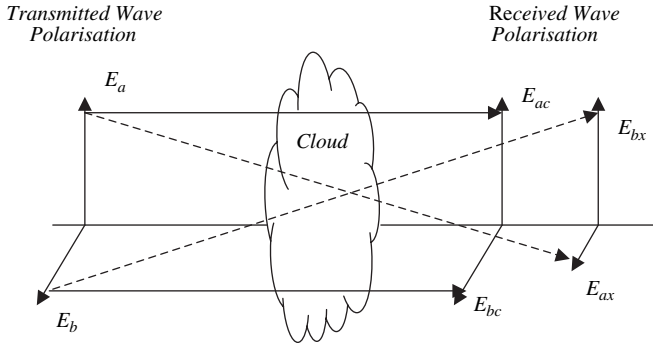
FIGURE 6.8. Depolarization of the transmitted wave caused by a cloud.

may obtain an additional horizontal component, or the right-hand circularly polarized (RHCP) wave may obtain an additional left-hand circularly polarized (LHCP) component. The extent of this depolarization may be measured by the *cross-polar discrimination* (XPD) and *cross-polar isolation* (XPI) terms, which can be presented schematically in Figure 6.8 according to Reference [30]. Essentially, the XPD term expresses how much of a signal in a given polarization is transformed into the opposite polarization caused by the medium, while the XPI term shows how much two signals of opposite polarizations, transmitted simultaneously, will interfere with each other at the receiver. As was also shown in Reference [30], depolarization is strongly correlated with rain attenuation and standard models of depolarization use this fact to predict XPD directly from the attenuation. One of such a model, described in Reference [30], gives

$$XPD = a - b \log L \tag{6.43}$$

where L is the rain attenuation (in watt), and a and b are constants $a = 35.8$ and $b = 13$. This formula is an accurate empirical predictor for frequencies below 10 GHz. Hydrometeors and tropospheric scintillation can be the additional source of signal depolarization in fixed satellite commu nication links (see Chapter 14).

6.2. EFFECTS OF THE HYDROMETEORS ON RADIO PROPAGATION IN THE TROPOSPHERE

6.2.1. Effects of Rain

The attenuation of radio waves caused by rain increases with the number of raindrops along the radio path, the size of the drops, and the length of the path through the rain.

Statistical-Analytical Models. If such parameters of rain, as the density and size of the drops are constant, then, according to Reference [30], the signal power P_r at

the receiver decreases exponentially with radio path r, through the rain, with the parameter of power attenuation in e^{-1} times, α, that is,

$$P_r = P_r(0) \exp\{-\alpha r\} \tag{6.44}$$

Expressing (6.44) in logarithmic scale gives

$$L = 10 \log \frac{P_t}{P_r} = 4.343 \alpha r \quad [\text{dB}] \tag{6.45}$$

Another way to estimate the total loss via the specific attenuation in decibels per meter was shown by Saunders in Reference [30]. He defined this factor as

$$\gamma = \frac{L}{r} = 4.343 \alpha \tag{6.46}$$

where now the power attenuation factor α can be expressed through the integral effects of the one-dimensional (1D) distribution of diameter D of the drops, denoted by $N(D)$, and the effective cross-section of frequency-dependent signal power attenuation by rain drops, $C(D)$ [dB/m], that is,

$$\alpha = \int_{D=0}^{\infty} N(D) \cdot C(D) \mathrm{d}D \tag{6.47}$$

As was mentioned in References [4,6,8,30], in real tropospheric situations, the drop diameter distribution $N(D)$ is not a constant value and one must account for the range dependence of the specific attenuation that is, the range dependence, $\gamma = \gamma(r)$, and integrate it over the whole radio path length r_R to find the total path loss

$$L = \int_{0}^{r_R} \gamma(r) \mathrm{d}r \tag{6.48}$$

To resolve Equation (6.48), a special mathematical procedure was proposed in Reference [11] that accounted for the drop size distribution. This procedure yields an expression for $N(D)$ as

$$N(D) = N_0 \exp\left\{-\frac{D}{D_m}\right\} \tag{6.49}$$

where $N_0 = 8 \cdot 10^3 \, \text{m}^{-2} \, \text{mm}^{-1}$ is a constant parameter [11], and D_m is the parameter that depends on the rainfall rate R, measured above the ground surface

in millimeters per hour, as

$$D_m = 0.122 \cdot R^{0.21} \text{ mm} \tag{6.50}$$

As for the attenuation cross-section $C(D)$ from (6.47), it can be found using the Rayleigh approximation that is valid for lower frequencies, when the average drop size is smaller compared to the radio wavelength. In this case only absorption inside the drops occurs and the Rayleigh approximation is valid giving a very simple expression for $C(D)$

$$C(D) \propto \frac{D^3}{\lambda} \tag{6.51}$$

Attenuation caused by rain increases more slowly with frequency approaching a constant value known as the *optical limit*. Near this limit, scattering forms a significant part of attenuation that can be described using the *Mie* scattering theory described above.

In general, Equation (6.47) can be solved directly using expressions (6.48)–(6.51). However, as the rainfall rate depend on the raindrop size distribution, on several antenna parameters (elevation angle, height, polarization, etc.), as well as on the geographical parameters (longitude and latitude) of the location of antennas it cannot be predicted strictly using some unified approach. In practical situations, an empirical model is used, where $\gamma(r)$ is assumed to depend only on rainfall R and wave frequency. Then according to References [4,6,8,9] we can obtain

$$\gamma(f, R) = a(f)R^{b(f)} \tag{6.52}$$

where γ has units dB/km; $a(f)$ and $b(f)$ depend on frequency [GHz]. For 15–70 GHz frequency band, $a(f)$ and $b(f)$ can be approximated by [4,6,8,9]

$$a(f) = 10^{1.203 \log(f) - 2.290}$$
$$b(f) = 1.703 - 0.493 \log(f) \tag{6.53}$$

In References [6,9,30], it was shown that for ground vehicle antenna elevation angles θ smaller than $90°$, it is necessary to account for the variation in the rain in the horizontal direction. This allows us to focus on the finite size of rain clouds, that is, on the areas called the *rain areas (or cells)* (see Fig. 6.9). In the case of finite rain sizes, the path length is reduced by using a reduction factor s. If so, the rain attenuation is [6,15]

$$L = \gamma s r_R = a(f)R^{b(f)} s r_R \tag{6.54}$$

Also, rain varies in time over various scales: *seasonal*, *annual*, and *diurnal*. All of these temporal variations are usually estimated by using (6.52) to predict the rain
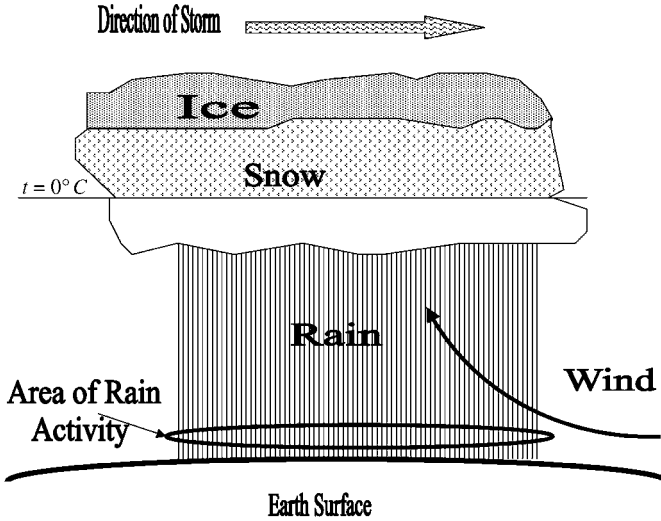
FIGURE 6.9. A rain cell with respect to snow, ice, and storm phenomena.

attenuation, $L_{0.01}$, that must not exceed 0.01% of the time. In this case, the rainfall rate, $R_{0.01}$, must not exceed 0.01% of the time during an average year. Using special corrections of this attenuation, in Reference [30] another approximate formula than (6.54) was presented by Saunders

$$L = aR_{0.01}^b s_{0.01} r_R \qquad (6.55)$$

where the following empirical expression for $s_{0.01}$ was evaluated in References [6,15,30]:

$$s_{0.01} = \frac{1}{1 + \dfrac{r_R \sin \theta}{35 \exp(-0.01 R_{0.01})}} \qquad (6.56)$$

Here, it was also shown that the empirical Expression (6.55) for attenuation can be corrected by introducing special relevant time percentage P, which is changed over the wide range from 0.001% to 1%, that is,

$$L_P = L_{0.01} \cdot 0.12 \cdot P^{-(0.546 + 0.043 \log P)} \qquad (6.57)$$

As was shown and discussed in References [6,15,30], the reference rainfall rate $R_{0.01}$ is strongly dependent on the geographical location: from around 30 mm/h in Northern Europe and countries at the same latitudes of USA, to 50 mm/h in Southern Europe, around the Mediterranean zone, and up to 160 mm/h in the equatorial zones.

Now using the semiempirical approach proposed in References [6,11,15,30], we can finally obtain the total path loss caused by rain as

$$L_{\text{total}} = L_{\text{FS}} + L \tag{6.58}$$

where L_{FS} is a path loss in free space (see Chapter 5):

$$L_{\text{FS}} = 32.44 + 20\,Log(r_c) + 20\,Log(f) \tag{6.59}$$

and r_c is the whole radio path between the ground surface and the frozen layer [km], where rain evolve into snow (see Fig. 6.9), and f is the frequency [MHz]. The loss parameter due to rain can be found either using the statistical approach with the formula (6.48) and (6.49) or using the empirical formulas (6.54)–(6.57). Formula (6.58) defines the *link budget* between the ground and the melting layer and can be calculated by adding the total rain attenuation L and the free space attenuation L_{FS}.

Empirical Models. There is another approach proposed by Crane [14] to estimate the rain attenuation effects on radio propagation in the atmosphere for open radio paths. The basic quantity, as before, is the rainfall rate R, the distribution of which can be evaluated by using the model for the yearly percentage of time [3,14]

$$P(R > r) = \frac{C_0}{87.6}[0.03\beta\,e^{-0.03r} + 0.2(1 - \beta)(e^{-0.258r} + 1.86\,e^{-1.63r})] \quad [\%] \tag{6.60}$$

where

$$\beta = C_m/C_0 \tag{6.61}$$

C_0 is the general yearly rain capacity, and C_m is the yearly rain capacity due to heavy rains with $R > 50\,\text{mm/h}$. For typical European and the U.S. climatic conditions we can predict $R = 1.7\,\text{mm/h}$ for time availability 99% and $R = 10.7\,\text{mm/h}$ for 99.9% level.

The radius of the rain drops varies from 0.1 to 3.6 mm. For the range of frequencies 5–30 GHz, the drops can be considered as rather small scatterers, and the attenuation rate decreases generally with the wavelength. The distribution of the drop scale in rain depends on the rainfall rate, type of cloud, wind velocity, temperature, height, and many other factors. The size distribution of rain drops may be modeled by Laws–Parsons, Marshall–Palmer, Best, Shifrin, or other distributions [9–11]. The presented approach is based on the Marshall–Palmer distribution. Specifically, in L/X-band frequency, the attenuation rate can be approximated by the relation

$$\gamma_r \approx 0.175c(t)R^{1.2}/\lambda^{2.5} \quad [\text{dB/km}] \tag{6.62}$$

where λ is the wavelength [cm], and $c(t)$ is the temperature correction factor, which is equal to 1 at 20°C. For $t = 0$°C we have $c(0) \approx 2$, for $t = 10$°C we have $c(10) \approx 1.3$ (the latter value is used for estimations presented below), and for $t = 30$°C we have $c(30) \approx 0.70$. The strong effect of the temperature is related to the temperature dependence of both real and imaginary parts of water permittivity. Obviously, the coefficient 0.175 in (6.60) is closely related to the distribution used. For other distributions, this coefficient may differ significantly up to 30% and even more, but comparison with experimental studies for rain attenuation, for rather long paths, shows that the value used in (6.60) may serve as a good approximation. At frequencies near 15 GHz ($\lambda = 2$ cm), we have $\gamma = 0.076$ dB/km for $R = 1.7$ mm/h and $\gamma = 0.69$ dB/km for $R = 10.7$ mm/h. At frequencies near 13 GHz ($\lambda = 2.308$ cm) we have $\gamma = 0.053$ dB/km for $R = 1.7$ mm/h and $\gamma = 0.48$ dB/km for $R = 10.7$ mm/h.

The field of rainfall rate is inhomogeneous in space and time. Rain observations by weather radars show short intervals of higher rain rate imbedded in longer periods of lighter rain. Also, such observations show small areas of higher rain rate imbedded in larger regions of lighter rain [12–18]. The geometrical characteristics of rain cells depend on the rain intensity and climate conditions, seasonal, annual and diurnal, which are related to the coordinates of the region.

The cell diameter appears to have an exponential probability distribution of the form [12–18]

$$P(D) = \exp(-D/D_0) \tag{6.63}$$

where D_0 is the mean diameter of the cell and is a function of the peak rainfall rate R_{peak}. For Europe and the United States, the mean diameter D_0 decreases slightly with increasing R_{peak} when $R_{\text{peak}} > 10$ mm/h. This relationship appears to obey the power law

$$D_0 = aR_{\text{peak}}^{-b}, \qquad R_{\text{peak}} > 10 \, \text{mm/h} \tag{6.64}$$

Values for the coefficient a ranging from 2 to 4, and the coefficient b from 0.08 to 0.25 have been reported. An example of the correlation between rainfall rate and the typical cell scale is given in Table 6.1 following the results obtained in Reference [30] according to the observations made in References [12–18].

The most difficult parameter in attenuation modeling is the *spatial distribution* of rain. As the precipitations are characterized by variations in both the horizontal and vertical directions, a correction factor is required in the modeling path lengths of rain attenuation. Here we use a simple prediction method on the basis of the so-called

TABLE 6.1. Rain Rate R for Different Rain Cells

R, mm/h	100	50	25	20	10	5
Rain Area, km	3	4	6	7	10	20

TABLE 6.2. Effective Path Length L_r and the Rain Attenuation F_r for Time Aviability of 99.0% and 99.9% for f = 156 Hz and the Antenna Height h_2 = 2 km

Distance, km	50	100	150
L_r, km (99.0% level)	22.6	26.6	28.2
L_r, km (99.9% level)	18.5	21.1	22.1
F_r, dB (99.0% level)	1.7	2.0	2.1
F_r, dB (99.9% level)	12.8	14.6	15.3

effective path length to take into account the non uniform profile of rain intensity along a given path. The effective path length L_r is the length of a hypothetical path obtained from radio data, dividing the total attenuation by the specific attenuation exceeded for the same percentage of time. The transmission loss due to attenuation by rain is then given by

$$A_r = \gamma_r L_r \tag{6.65}$$

The effective path length L_r can be estimated, instead of (6.50)–(6.52), according to the empirical model [10,11]

$$L_r = \frac{L_s}{1 + 0.0286\, L_h\, R^{0.15}} \tag{6.66}$$

where, neglecting the ray bending,

$$L_h = d, \qquad L_s = \sqrt{d^2 + h_2^2}, \qquad h_2 < h_r \tag{6.67a}$$

$$L_h = dh_r/h_2, \qquad L_s = h_r\sqrt{1 + d^2/h_2^2}, \qquad h_2 > h_r \tag{6.67b}$$

d is the horizontal component of the distance between antennas, h_r is the average rain height (approximately 3 km for European weather conditions), and h_2 is the height of the air vehicle antenna. An example of the corresponding calculations of rain attenuation (in dB) for the frequency 15 GHz and antenna height $h_2 = 2$ km are presented in Table 6.2, and for the frequency 13 GHz and antenna height $h_2 = 6$ km in Table 6.3.

TABLE 6.3. Effective Path Length L_r and the Rain Attenuation F_r for Time Aviability of 99.0% and 99.9% for f = 136 Hz and the Antenna Height h_2 = 6 km

Distance, km	100	200	300
L_r, km (99.0% level)	19.9	24.9	27.1
L_r, km (99.9% level)	16.8	20.1	21.8
F_r, dB (99.0% level)	1.3	1.6	1.8
F_r, dB (99.9% level)	8.5	9.8	10.6

Semi-Empirical Models. The first presented model used in satellite communications is a semi empirical model called "Lin-Chen" that was proposed in [17] to evaluate the extinction cross section (ECS) of raindrops by using the modified raindrop model for mean radius of drops calculation ranging from 0.25 to 3.5 mm. This wide-range model (from 0.6 to 100 GHz) is based on the compilation of experimentally obtained factors, numerical data, and on the volume integral equation formulation (VIEF) to obtain the empirical formula for calculating the ECS of raindrops. To derive the corresponding empirical formula that characterizes the ECS of raindrops, Q_t, it was assumed in [17] that it must be a function of such parameters, such as the radio frequency, f, the mean drops' radius, a_0, the complex dielectric permittivity, ε^*, and on the type of polarization of radio wave. Based on the VIEF evaluation of Q_t for raindrops with 14 different radii (from 0.25 to 3.5 mm) and wave polarizations, horizontal and vertical, the following criteria are formulated [17]:

1) for $f < f_c$, the ESC is increased as a bell-shape function;
2) for $f > f_c$, the ESC is increased rapidly and then, reaching to the maximum value, is increased slowly with an increase of radio frequency.

Here f_c is the critical frequency obtained by the least-square curve fitting of 364 sets on computed Q_t, [m^2], with empirical data available for 14 different radii of raindrops using VIEF method (see details in [17]). A simple formula that satisfies these two criteria is given by [17]

$$Q_t = 10^{-6} \left\{ \frac{A_1 \left(\frac{f}{f_c}\right)^2 + A_2^2}{\left[\left(\frac{f}{f_c}\right)^2 + 2.2\left[\left(\frac{f}{f_c}\right) - 1\right]\right]^2} [1 - U(f - 0.5f_0)] + [(A_3 f + A_4)(1 - e^{-A_5(f//f_0)})][U(f - 0.5f_0)] \right\}$$

(6.68)

where A_1, A_2, A_3, A_4, and A_5 are a function of type of polarization, the mean radius a_0 and the radio frequency f; $U(f - 0.5f_0)$ is a unit step function defined by

$$U(f - 0.5f_0) = \begin{cases} 0 & f < 0.5\,f_0 \\ 1 & f > 0.5\,f_0 \end{cases}$$

(6.69)

f_0 is a function of mean radius a_0 determined by curve fitting a group of 14 data sets expressed by

$$f_0 = 58.5866 a_0^{-1.04493}$$

(6.70)

Here, units of f_0 and a_0 are in gigahertz and millimeters, respectively. The empirical formula (6.68) was proposed for frequency ranges from 0.6 to 100 GHz. As f_c, the coefficients A_1, A_2, A_3, A_4, and, A_5, were determined by a least-squares curve fitting of 364 sets of Q_t with data available for 14 different raindrops using

the VIEF. These coefficients were expressed empirically in terms of raindrop parameters such as a_0, f, and polarization in the following manner. For the critical frequency

$$f_c = \frac{f_0}{(0.9076 + 0.209a_0)} \quad \text{(GHz)} \tag{6.71}$$

The coefficients A_1, A_2, A_3, A_4, and A_5 are given by [17]:
   for horizontal polarization:

$$
\begin{aligned}
A_1 &= 2.0 + 7.0 \times a_0 \\
A_2 &= 0.6 \times 10^{-5} + 3.245 \times 10^{-4} \times (a_0 \times f)^{1.89} \\
A_3 &= 0.0087 + 0.0383 \times a_0^{1.686} \\
A_4 &= -11.49 + 45.97 \times a_0 \\
A_5 &= 0.43 \times a_0^{1.05}
\end{aligned}
\tag{6.72a}
$$

   for vertical polarization:

$$
\begin{aligned}
A_1 &= 2.0 + 5.5 \times a_0 \\
A_2 &= 0.3 \times 10^{-5} + 3.245 \times 10^{-4} \times (a_0 \times f)^{1.31} \\
A_3 &= 0.0087 + 0.0236 \times a_0^{1.324} \\
A_4 &= -8.79 + 32.27 \times a_0^{1.324} \\
A_5 &= 0.46 \times a_0^{1.05}
\end{aligned}
\tag{6.72b}
$$

As above, the units of f and a_0 in (6.71) and (6.72) are in gigahertz and millimeters, respectively. Thus, (6.68) provides a frequency-dependent empirical formula for the Q_t for raindrops with the coefficients A_1, A_2, A_3, A_4, and A_5, expressed in (6.72a) and (6.72b) in terms of mean radius of raindrops and frequency.

   Now, on the basis of the study of isotropic or anisotropic spherical wave expansion, the specific rain attenuation A in dB/km can be expressed as [17]

$$A = 4.343 \times 10^3 \int_0^\infty Q_t(a)N(a)\mathrm{d}a \tag{6.73}$$

where $Q_t(a)$ is the ECS defined above and $N(a)\mathrm{d}a$ is the number of the density of raindrops with equivalent radius a in the interval da. As was mentioned earlier, analyzing the Saunder's model [30], the raindrop size distribution function $N(a)$ may have a great difference in different regions. There are many raindrop size distributions used in the calculation of possible specific attenuation values. As was shown in Reference [17], the raindrop size distribution in most rain cases is

described by a theoretical distribution having the negative exponential form

$$N(a) = N_0 e^{-\Lambda a} \quad [\text{m}^{-4}], \qquad \Lambda = \alpha R^{-\beta} \quad [\text{mm}^{-1}] \tag{6.74}$$

where N_0, α, and β are constants and R is the rain rate in millimeters per hour. For example, in the model described in Reference [18], $N_0 = 1.6 \times 10^4 \, \text{m}^{-3} \cdot \text{mm}^{-1}$, $\alpha = 8.2$, $\beta = 0.21$, and a is the raindrop radius in millimeters.

The specific rain attenuation of (6.73) can be obtained by substituting the empirical formula of Q_t and the negative exponential size distribution $N(a)$ into (6.73). Thus, an empirical formula for specific rain attenuation can be obtained by numerical calculation as

$$A = 4.343 \times 10^3 \sum_{k=1}^{K} Q_t(k\Delta a)N(k\Delta a)\Delta a \quad [\text{dB/km}] \tag{6.75}$$

where K is an integer number of $a_{\max}/\Delta a$; $a_{\max}$ and Δa are the maximum mean radius of a raindrop and the incremental radius respectively. It is clear that the value of specific rain attenuation A in (6.75) depends on the choice of the incremental radius Δa and the maximum mean radius $a_{\max}$. According to Reference [15], the smallest raindrop may be equivalent to those found in clouds, and the largest raindrops will not exceed 4 mm in radius, as raindrops with radius greater than 4 mm are unstable and break up. Therefore, we chose K to be 4 mm. The maximum mean radius of 4 mm will be adopted for the calculation of specific rain attenuation.

Finally, the knowledge of specific rain attenuation A allows us to calculate the total path loss introduced in (6.58), the LOS component in (6.59), and the rain loss excess L, as the product of the specific parameter A and the length of radio path through the layer containing rain, that is, $L = Ar_R$.

It is important to note that the International Telecommunication Union (ITU) has proposed to use the Saunder's model [30] as the most convenient rain attenuation model for terrestrial systems and for space-to-land links [4,6,9] for the following reasons:

– this model is a general model that does not depend on a particular place in the world, making it suitable for all places around the globe;
– it is not frequency constrained, that is it is a general model suitable for all communication frequencies used in land-satellite links, whereas most of the models are frequency depended in the X/Ku-band;
– it has a good processing time and can be easily implemented.

Therefore, it is interesting to compare the Saunder's model with the ''Lin-Chen'' and the Crane's semi-empirical statistical-empirical models.

To compare the ''Lin-Chen'' model with Saunder's model, both described above, take the root-mean-square (*rms*) value of a specific rain attenuation for the vertical

and horizontal polarizations expressed by

$$A_{\text{RMS}} = \sqrt{\frac{A_{\text{H}}^2 + A_{\text{V}}^2}{2}} \quad [\text{dB}/\text{km}] \tag{6.76}$$

It is quite reasonable to take the rms values for comparisons of rain attenuation, as some measurements are not stated by polarization factors. Here, we use the empirical formula that was given for the calculations of the ECS and three different drop size distributions:

(1) The first one is the Singapore raindrop size distribution model with the following parameters [15,16]:

$$N_0 = 6256.64 \lfloor \text{m}^{-3} \cdot \text{mm}^{-1} \rfloor, \quad \alpha = 5.44 \quad \beta = 0.197775 \tag{6.77a}$$

(2) The second one is the M–P raindrop size distribution model with the following parameters [18]:

$$N_0 = 16000 \lfloor \text{m}^{-3} \cdot \text{mm}^{-1} \rfloor, \quad \alpha = 8.2 \quad \beta = 0.21 \tag{6.77b}$$

(3) The third one is the J–T raindrop size distribution model with the following parameters [17]:

$$N_0 = 2800 \lfloor \text{m}^{-3} \cdot \text{mm}^{-1} \rfloor, \quad \alpha = 6 \quad \beta = 0.21 \tag{6.77c}$$

Next, we use the empirical Formula (6.75), obtained from the ''Lin-Chen'' model, and apply it to the three raindrop sizes mentioned above. Figures 6.10a and 6.10b show a comparison between the emprirical formula in (6.75) and the Saunder's model for a macrocell area ($r_R \geq 10$ km). Figures 6.11a and 6.11b are for microcell areas ($r_R \leq 2$–3 km). From Figure 6.10a, it is clear that there is a better match between the Saunder's model and the ''Lin-Chen'' model for the J–T and M–P drop size distributions rather than the ''Singapore'' raindrop size distribution at 12.5 GHz. At 30 GHz, from Figure 6.10b, a good match between the Saunder's and the ''Lin-Chen'' models is demonstrated for the M–P drop size distribution, but not for the J–T drop size distribution case. The same tendency is observed for microcell areas (see Figs. 6.11a,b). However, there is a significant difference in the achieved rain attenuation between the macro- and microcells, if we compare the Saunder's and the ''Lin-Chen'' model for the M–P drop size distribution.

Equation (6.62) was used to compare the Saunder's model to the Crane model, where a knowledge of specific rain attenuation A, allows us to calculate the rain loss excess L, as the product of the specific parameter A and the length of radio path through the layer containing rain, that is, $L = Ar_R$.

Comparisons of path loss caused by specific rain attenuation versus the rain intensity, [in mm/h], obtained from Saunder's model and the Crane model at

Macro Cell Link Budget Lin Chen Vs Saunders Model at 12.5 GHz

RMSSingapore -1
RMSMP -2
RMSJT -3
Saunders -4

Rain Attenuation [dB]

Rain Intensity [mm/h]

(a)

Macro Cell Link Budget Lin Chen Vs Saunders Model at 30 GHz

RMSSingapore -1
RMSMP -2
RMSJT -3
Saunders -4

Rain Attenuation [dB]
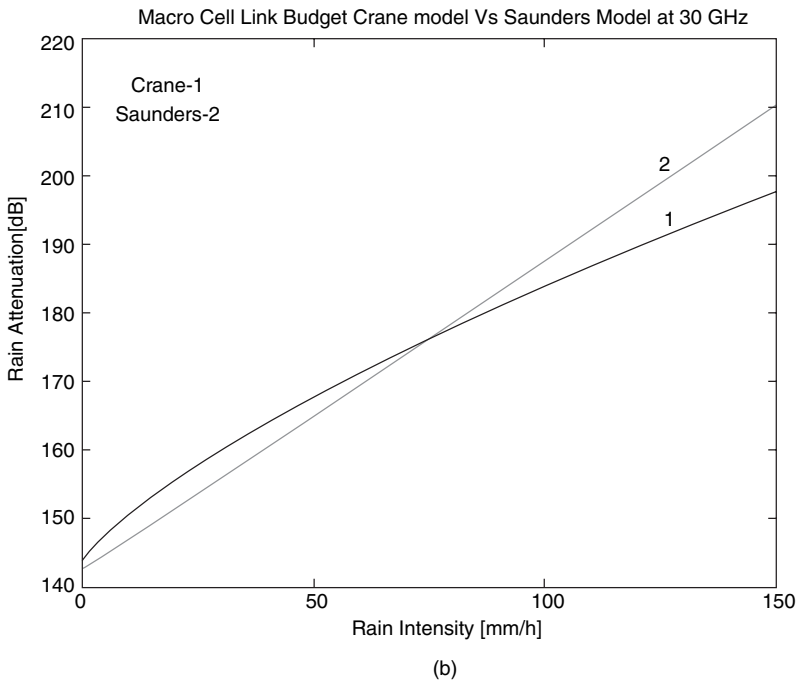
Rain Intensity [mm/h]

(b)
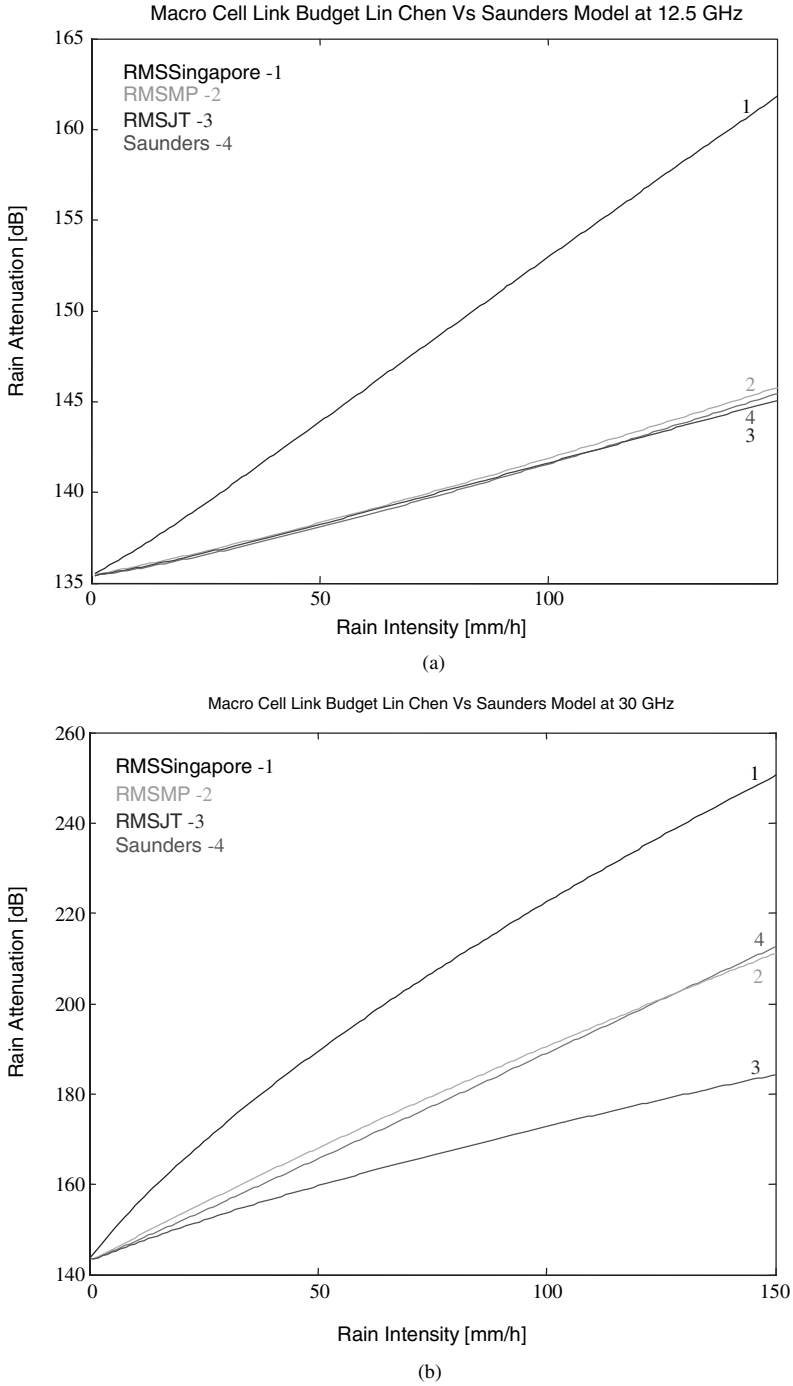
FIGURE 6.10(a,b). Path loss versus rain intensity for a macrocell at 12.5 and 30 GHz.
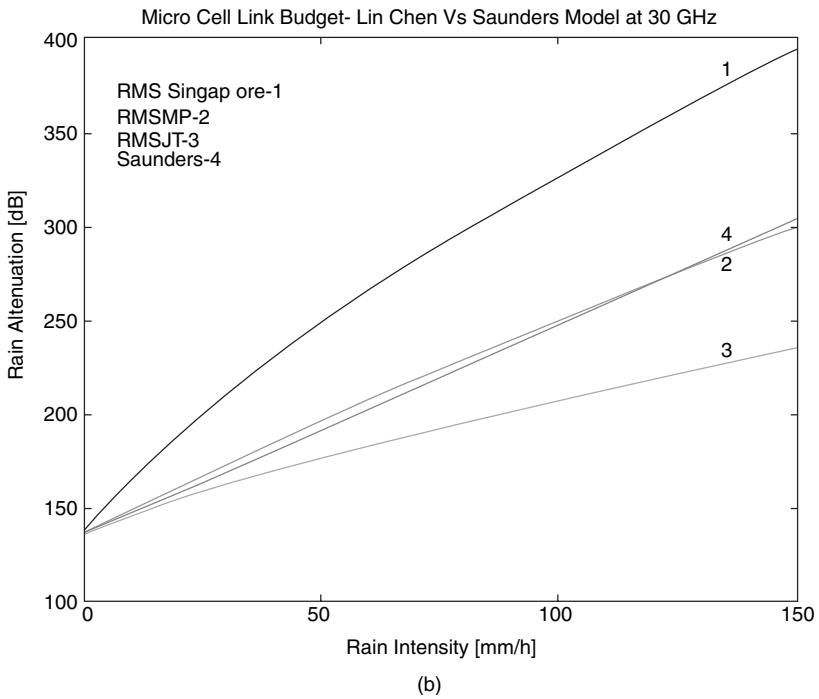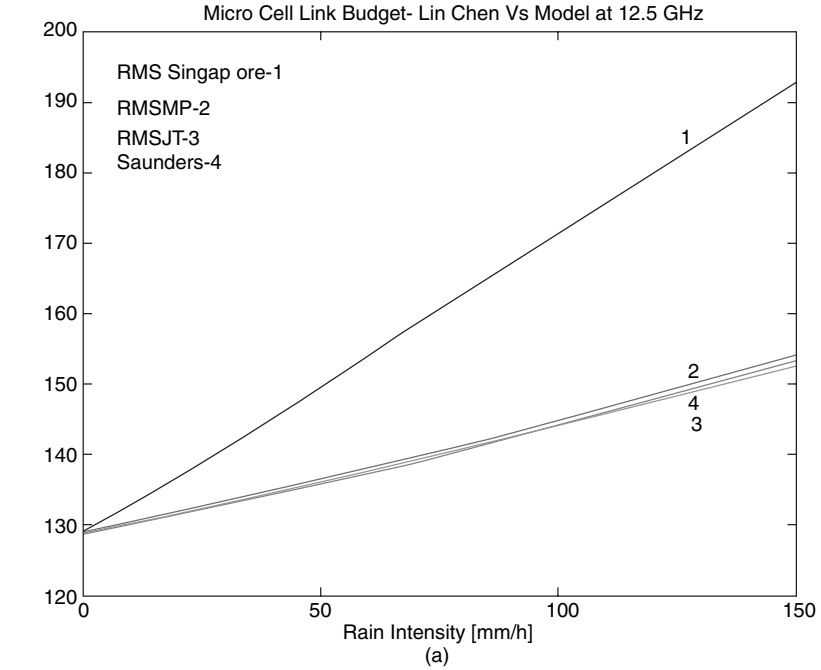
FIGURE 6.11(a,b). Path loss versus rain intensity for a microcell at 12.5 and 30 GHz.

frequencies of 12.5 and 30 GHz are shown in Figures 6.12a and 6.12b for a macrocell area ($r_R \geq 10$ km), and Figures 6.13a and 6.13b for microcell areas ($r_R \leq 2$–3 km). From the comparisons shown in Figures 6.12a and 6.13a, it follows that there is good matching between the Saunder's and the Crane model (with the average deviation of 2 dB for macrocell areas and the average deviation of 5 dB for microcell areas) for all rain intensities at 12.5 GHz. The same tendency appears in the results shown in Figures 6.12b and 6.13b, with an average deviation of 4 dB for macrocell areas and an average deviation of 7 dB for microcell areas for rain intensity in the range of 10–100 mm/h. On the other hand, there is not a good match between the Saunder's model and the Crane model, from which we got the average deviation of 10 dB for macrocell areas and the average deviation of 20 dB for microcell areas, for rain intensity in the range of 100–150 mm/h. As the rain intensity increases this difference becomes even more predominant.

There is a significant difference in rain attenuation between macro- and microcells. The path loss caused by rain attenuation reaches 270 dB, at 30 GHz, for micro cell areas versus the 200 dB attenuation that occurs in the macrocell areas. All these results are very important for designers of land-satellite link performance, because in the radio path through a microcell area containing intensive rain, there is much more signal attenuation observed than in radio paths through macrocell areas, where the areas of intensive rain cover only few percentages of the total radio path.

6.2.2. Effects of Clouds and Fog

In the cloud models described below, a distinction between *cloud cover* and *sky cover* must be explained. Sky cover is an observer's view of the cover of the sky dome, whereas cloud cover can be used to describe areas that are smaller or larger than the floor space of the sky dome.

Cloud Models. There have been several proposed mathematical formulations for the probability distribution of the sky cover. Each of them uses the variable x ranging from zero (for clear conditions) to 1.0 (for overcast conditions). Each model claims to have versatile statistical characteristics to simulate the U-shaped curves of the sky cover.

The First Cloud Cover Model. The *Beta distribution* is an early cloud model [7,36] whose density function is given by

$$f(x) = \frac{\Gamma(a+b)}{\Gamma(a)\Gamma(b)} x^{a-1}(1-x)^{b-1}; 0 \leq x \leq 1; a, b > 0. \tag{6.78a}$$

In this formula pairs of values of the two parameters (a,b) are given in some 29 regional types that cover the world, for the four midseason months, for two times of the day.
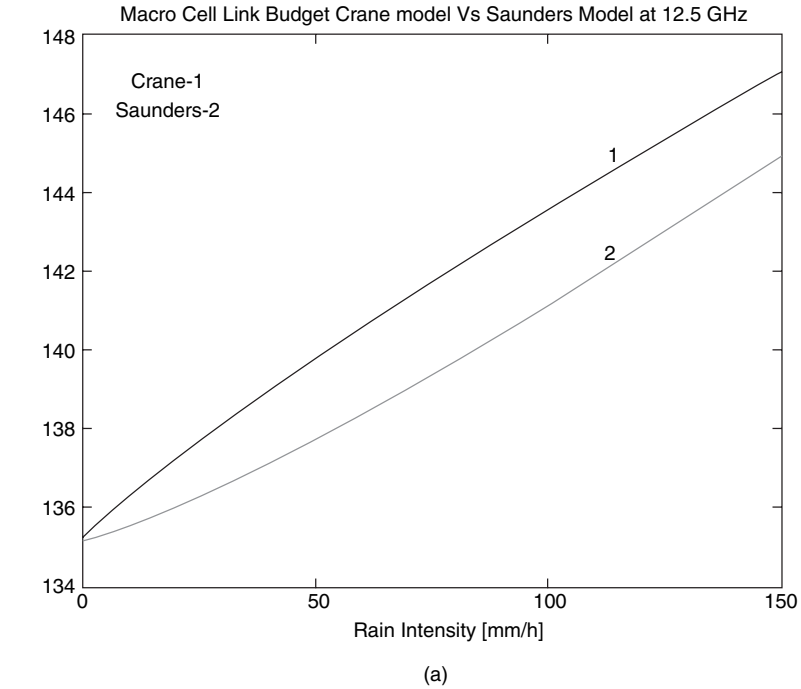
FIGURE 6.12(a,b). Path loss versus rain intensity for a macrocell at 12.5 and 30 GHz.

Micro Cell Link Budget Crane model Vs Saunders Model at 12.5 GHz

(a)

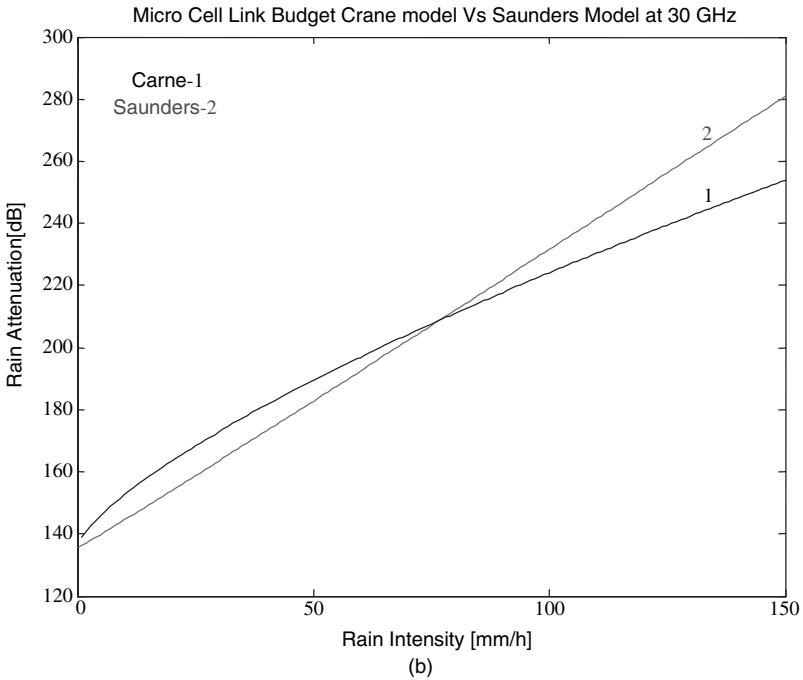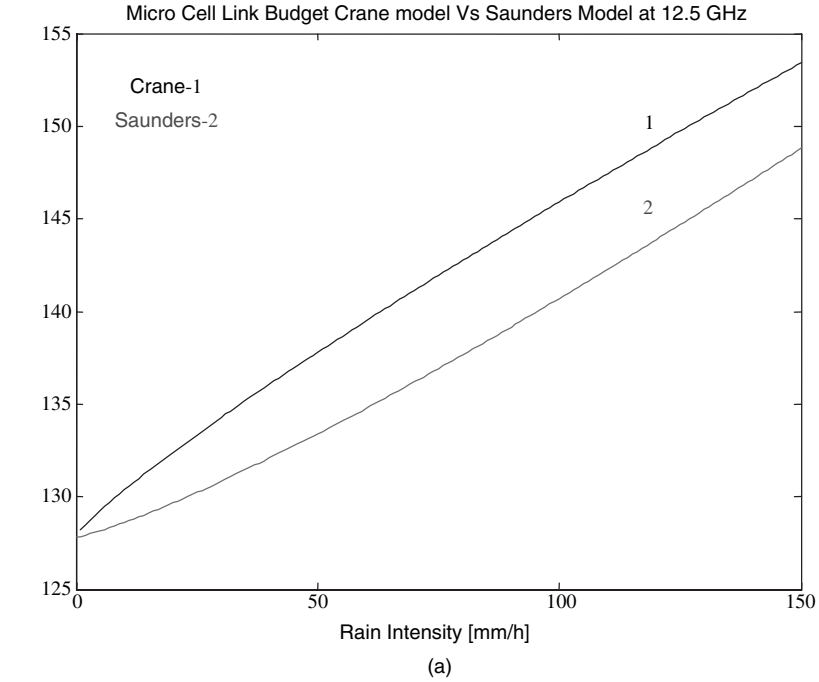Micro Cell Link Budget Crane model Vs Saunders Model at 30 GHz

(b)

FIGURE 6.13(a,b). Path loss versus rain intensity for a microcell at 12.5 and 30 GHz.

The Second Cloud Cover Model. Somerville and Bean [36] have proposed a model called the *S-distribution*, which is the cumulative probability distribution function $F(x)$ of sky cover x estimated as

$$\hat{F}(x) = 1 - (1 - x^\alpha)^\beta; \quad 0 \le x \le 1; \quad \alpha, \beta > 0. \tag{6.78b}$$

Pairs of values of the two parameters (α, β) have been determined to make the distribution $F(x)$ fit the data in the sky-cover summaries. These data have been published for 23 stations around the world, for each of eight periods of the day in each month of the year. The best pair of values for the sky cover were found to be in January at noontime, being $\alpha = 0.1468$, $\beta = 0.1721$.

The Third Cloud Cover Model. This model, which is also called the *Model B*, has been described in References [7,36]. Like the previous models, it requires two parameters for the description of the probability distribution of cloud cover. The parameters in *Model B* have physical meaning. First parameter P_0 is the median cloud cover as given in climatic summaries; it is taken to be the single-point probability of a cloud intercept when looking up from the ground. The second parameter r, known as the scale distance, is the distance between two stations whose correlation coefficient of cloud cover is 0.99.

Ceiling Cloud Model. It is one of the best models for ceiling height cumulative distributions [36]

$$\hat{F}(h) = 1 - \left\{1 + \left(\frac{h}{c}\right)^a\right\}^{-b}; \quad a, b, c > 0 \tag{6.78c}$$

where h is the ceiling height and a, b, c are parameters, determined below. Bean [36] sets the values for a, b, and c, which have been determined for eight periods of the day in each month at 23 stations around the world to make the estimated distributions, $\hat{F}(h)$, fit the data for 30 ceiling heights. The best pair of values for the sky cover were found to be in January at noontime and equal $a = 1.1678$, $b = 0.1927$ when $c = 0.305$ km.

It follows from numerous observations that in clouds and fog the drops are always smaller than 0.1 mm, and the theory for the small size scatterers is applicable [7,20–24,36]. This gives

$$\gamma_c \approx 0.438c(t)q/\lambda^2, \quad \text{[dB/km]} \tag{6.79}$$

where λ is the wavelength measured in centimeters, and q is the water content measured in gram per cubic meter. For the visibility of 600 m, 120 m, and 30 m the water content in fog or cloud is $0.032\,\text{g/m}^3$, $0.32\,\text{g/m}^3$, and $2.3\,\text{g/m}^3$, respectively. The calculations show that the attenuation, in a moderately strong fog or cloud does not exceed the attenuation due to rain with a rainfall rate of 6 mm/h. Owing to the

lack of data, a semi-heuristic approach is presented here. Specifically we assume that the thickness of the cloud layer is $w_c = 1$ km, and the lower boundary of the layer is located at the $h_c = 2$ km height. The water content of clouds has a yearly percentage of [7]

$$P(q > x) = p_c \exp(-0.56\sqrt{x} - 4.8x) \quad [\%] \tag{6.80}$$

where p_c is the probability of cloudy weather (%). Neglecting the ray bending, we have for the length of the path within the cloud layer

$$L_c = 0, \qquad h_2 \leq h_c \tag{6.81a}$$

$$L_c = \sqrt{d^2 + h_2^2}(1 - h_c/h_2), \qquad h_c < h_2 < h_c + w_c \tag{6.81b}$$

$$L_c = w_c/\sin\theta, \qquad h_2 \geq h_c + w_c \tag{6.81c}$$

where

$$\theta = \arctan(h_2/d) \tag{6.82}$$

Here h_2 is the vehicle antenna height. Although the attenuation in clouds is less than in rain, the percentage of clouds can be much more essential than that of the rain events. Thus, the additional path loss due to clouds can be estimated as 2 dB and 5 dB, for 350 km path and $h_2 = 6$ km, and for the time availability of 95% and 99%, respectively.

6.3. EFFECTS OF TROPOSPHERIC TURBULENCES ON RADIO PROPAGATION

As a result of the turbulent flows caused by the turbulent structure (sometimes called *eddies*) of the wind in the troposphere, the horizontal layers of equal refractive indeces, mainly, in it become mixed, leading to rapid refractive index variations over small distances. These are the *small-scale* variations that appear over short time intervals, and yield *rapid* refractive index variations. Let us first consider the main characteristics and parameters of atmospheric turbulence and then discuss briefly the tropospheric scintillations mentioned above, as well as the effects of multiple scattering due to the irregular structure of the troposphere.

6.3.1. Main Characteristics and Parameters of Atmospheric Turbulence

Atmospheric turbulence is a chaotic phenomenon created by the random temperature, wind magnitude variation, and direction variation in the propagation

medium. This chaotic behavior results in index-of-refraction fluctuations. The turbulence spectrum is divided into three regions by two scale sizes [42–45]

  – the outer scale of turbulence, L_0;
  – the inner scale (or micro scale) of turbulence, l_0.

These values vary according to atmospheric conditions, distance from the ground, and other factors. The inner scale l_0 is assumed to lie in the range of 1 mm to 30 mm. Near ground it is typically observed to be around 3 to 10 mm, but generally increases to several centimeters with increasing altitude h. A vertical profile for the inner scale is not known. The outer scale L_0, near ground, is usually taken to be roughly Kh, where K is a constant on the order of unity. Thus, L_0 is usually either equal to the height from the ground (when the turbulent cell is close to the ground) or in the range of 10 m to 100 m or more. Vertical profile models for the outer scale have been developed based on measurements, but different models predict very different results. Let l be the size of turbulence eddies, $k < \frac{2\pi}{\lambda}$ is a wave number, and λ is a wavelength. Then one can divide turbulences at the three regions

$$
\begin{array}{lll}
\text{Input range} & L_0 < l, & k < \dfrac{2\pi}{L_0} \\[2ex]
\text{Inertial range} & l_0 < l < L_0, & \dfrac{2\pi}{L_0} < k < \dfrac{2\pi}{l_0} \\[2ex]
\text{Dissipation range} & l < l_0, & \dfrac{2\pi}{l_0} < k
\end{array} \tag{6.83}
$$

These three regions induce strong, moderate, and weak spatial and temporal variations, respectively, of signal amplitude and phase, called in the literature *scintillations* (see paragraph below).

   Now, as the troposphere is a random medium, these variations of the index-of-refraction (or turbulences) are random by nature and can be described only (with means of stochastic processes) by the Probability Density Function (PDF) and Cumulative Distributed Function (CDF), defined in Chapters 1, or by the corresponding spectral distribution functions.

   The main goal of studying radio wave propagation through turbulent atmosphere is the identification of a tractable PDF and CDF or the corresponding spectra of the irradiance under all irradiance fluctuation conditions. Obtaining an accurate mathematical model for PDF and CDF of the randomly fading irradiance signal will enable the link planner to predict the reliability of a radio communication system operating in such an environment. In addition, it is beneficial if the free parameters of that PDF and CDF can be tied directly to atmospheric parameters.

Energy Cascade Theory of the Turbulence. The Kolmogorov energy cascade theory of turbulence is based on the division of three types of processes defined

in (6.83) by two scale sizes, inner l_0, and outer L_0. As was mentioned above, the value of L_0 and l_0 may vary widely.

In the input range of (6.83), the large-scale atmospheric characteristic such as wind forms the turbulence eddies. Here, the thermal and kinetic energy of the atmosphere is the input to the turbulent system. The process is, in general, anisotropic and varies, depending on climatic conditions.

In the inertial range of (6.83), the eddies formed in the input range are unstable and fragmented into smaller regions. These break up as well, continuing in this manner and causing energy to be distributed from the small to large turbulence wave numbers. There is very little energy loss in this process. Most cases of microwave propagation are affected predominantly by this region of the wave number spectrum [23–26].

As for the dissipation range of (6.83), here the energy in the turbulence, which was transferred through the inertial sub range, is dissipated through viscous friction by very small eddies. The Kolmogorov's cascade theory is presented schematically in Figure 6.14 according to References [44,46–48].

Turbulence Power Spectrum. Results from theoretical models of scintillation depend strongly on the assumed model for the spatial power spectrum of refractive-index fluctuations. If we ignore the outer-scale effects, which are usually not important in scintillation studies, the commonly used spectral models are all special cases of

$$\Phi_n(\kappa) = K(\alpha)C_n^2\kappa^{-\alpha-2}f(\kappa l_0) \tag{6.84}$$

where κ is the magnitude of the spatial wave number, α is a power-law index, K is a dimensionless factor, C_n^2 is the index-of-refraction structure parameter (will be described below separately because of its importance in scintillation studies) and
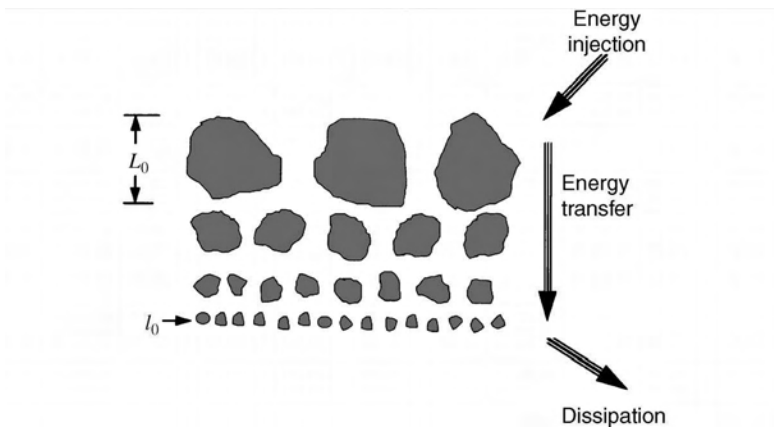
FIGURE 6.14. Kolmogorov cascade theory of turbulence.

l_0 is the inner scale (the reader can find all detailed information about such parameters in References [42–50]). The normalization factor K is set so that the index-of-refraction structure function is $C_n^2 r^\alpha$ for r larger than l_0. Kolmogorov turbulence theory predicts that α is near $5/3$, in which case K is $\sim 1/30$. The information mentioned above allows us to rewrite (6.84) in the following manner:

$$\Phi_n(\kappa) = 0.033 C_n^2 \kappa^{-11/3} f(\kappa l_0) \tag{6.85}$$

$f(\kappa l_0)$ is a factor that describes inner-scale modifications of the basic power-law form.

For example, the *Kolmogorov spectrum* in (6.85) is characterized by $f(\kappa l_0) = 1$, whereas $f(\kappa l_0) = \exp[-(\kappa l_0/5.92)^2]$ in the case of the *Tatarskii spectrum*, the latter is sometimes called the *traditional* spectrum [43,44]. However, neither of these spectrum models can be used to describe the spectrum outside the inertial range. They both show the correct behavior (in terms of fitting experimental results) only in the inertial range. The Tatarskii spectrum has been shown to be inaccurate by as much as 50% for predicting the irradiance variance for the strong-focusing regime in optical propagation experiments and by as much as 40% for weak fluctuations. A more accurate model for scintillation studies is provided by the *Hill spectrum*, or by an analytic approximation that is given by the *modified atmospheric spectrum*. Let us briefly discuss these models.

Kolmogorov Spectrum. For statistically homogeneous turbulences, the related structure function exhibits the asymptotic behavior of the form [42–50]

$$D_n(R) = \begin{cases} C_n^2 R^{2/3}, & l_0 < R < L_0 \\ C_n^2 l_0^{-4/3} R^2, & R < l_0 \end{cases} \tag{6.86}$$

where R is an eddy size.

On the basis of the above $2/3$ power-law expression, it can be deduced, and the associated power spectral density for refractive-index fluctuations can be described by the following expression:

$$\Phi_{nk}(\kappa) = 0.033 C_n^2 \kappa^{-11/3}, \qquad \frac{2\pi}{L_0} < \kappa < \frac{2\pi}{l_0} \tag{6.87}$$

This is the well-known Kolmogorov spectrum, which was calculated and shown in normalized form, $\bar{\Phi}_{nk}(\kappa) = \Phi_{nk}(\kappa)/0.033 C_n^2$, in Figure 6.15 for the *inertial* and *dissipation* ranges.

Tatarskii Spectrum. The Kolmogorov's spectrum is theoretically valid only in the inertial subrange. The use of this spectrum is justified only within that subrange or over all wave numbers if the outer scale is assumed to be infinite and the inner scale negligibly small. Other spectrum models have been proposed for calculations when inner-scale and/or outer-scale effects cannot be ignored. In order to extend the
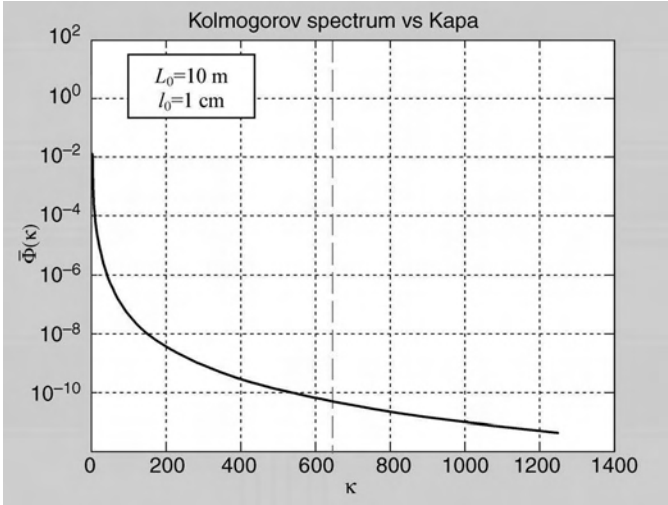
FIGURE 6.15. Kolmogorov normalized spectrum, shown for the inertial and dissipation ranges; the green vertical line indicates $\kappa = 2\pi/l_0$.

power-low spectrum (6.87) into the dissipation range (where $\kappa > 2\pi/l_0$), a truncation of the spectrum at high wave numbers is required. Tatarskii suggested doing that by modulating the Kolmogorov spectrum model (6.87) by a Gaussian function, which led to Tatarskii spectrum (or the traditional spectrum):

$$\Phi_{nk}(\kappa) = 0.033 C_n^2 \kappa^{-11/3} \exp(-\kappa^2/\kappa_m^2), \qquad \kappa > \frac{2\pi}{L_0} \qquad (6.88)$$

where $\kappa_m = \frac{5.92}{l_0}$. This is used to express the composite spectrum, in the region other than the input range. Figure 6.16 shows the Tatarskii model spectral behavior calculated and presented in the same normalized form, as in Figure 6.15. It is clearly seen from the graph how the power spectrum is "truncated" in high wave numbers relative to the Kolmogorov spectrum, specifically above $\kappa = 2\pi/l_0$. Below this value the two spectrums are almost identical.

Von Kármán Spectrum. For mathematical convenience, we may assume that the turbulence spectrum is statistically homogeneous and isotropic over all wave numbers. A spectral model that is often used in this case, one that combines the three regions defined by (6.83), is the Von Kármán spectrum:

$$\Phi_{nk}(\kappa) = 0.033 C_n^2 \left(\kappa^2 + \frac{1}{L_0^2} \right)^{-11/6} \exp(-\kappa^2/\kappa_m^2), \qquad 0 \le \kappa < \infty \qquad (6.89)$$

where $\kappa_m = \frac{5.92}{l_0}$. Note that even though the last equation describes the *entire* spectrum, its value in the input range must be considered only approximate,
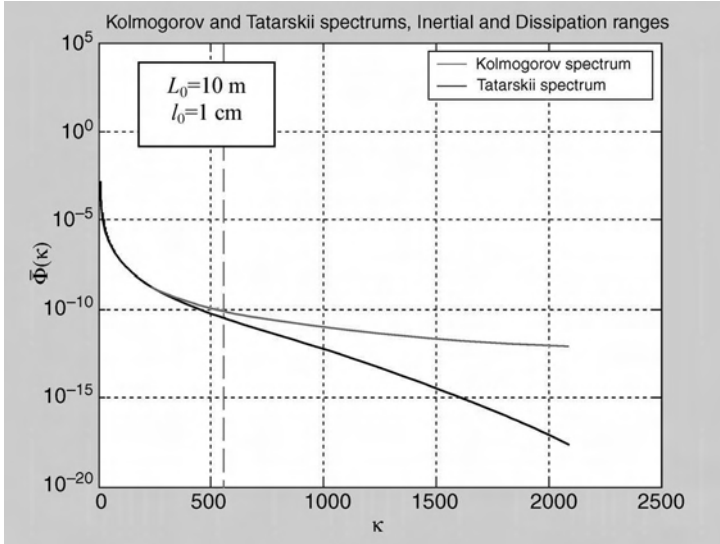
FIGURE 6.16. Tatarskii normalized spectrum, shown with Kolmogorov spectrum for inertial and dissipation range; the green vertical line indicates $\kappa = 2\pi/l_0$.

because it is generally anisotropic and depends on how the energy is introduced into the turbulence. This model, unlike the previous models, does not have a singularity at $\kappa = 0$. Therefore, the Von Kármán spectrum is almost identical to the Tatarskii spectrum except for a difference in small values of wave numbers. The Von Kármán spectrum was calculated and shown in Figure 6.17. Figure 6.18 focuses on small wave numbers to emphasize the difference between the Tatarskii and Von Kármán models in that region. It is clear that although the Tatarskii spectrum "explodes" near the origin, the Von Kármán spectrum inclination is suppressed in that region. For other regions, the two spectrums are almost identical.

Modified Atmospheric Spectrum. The last models of turbulent spectra, defined by (6.87)–(6.89), are commonly used in theoretical studies of radio wave propagation because they are relatively traceable models. Strictly speaking, however, these spectrum models have the correct behavior only in the inertial range: that is, the mathematical form that permits the use of these models outside the inertial range is based on mathematical convenience, and not because of any physical meaning. The Tatarskii spectrum has been shown to be inaccurate by as much as 50% for predicting the irradiance variance for the strong-focusing regime in optical propagation experiments and by as much as 40% for weak fluctuations. Hill (see details in References [46–48]) developed a numerical spectral model with a high wave-number rise that accurately fits the experimental data. However, as it is described in terms of a second-order differential equation that must be solved numerically, the Hill spectrum cannot be used in analytic developments. An analytic
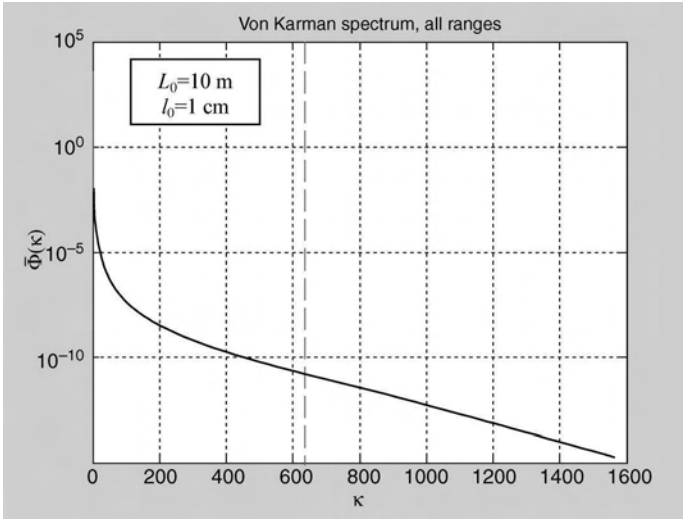
FIGURE 6.17. Von Karman normalized spectrum, shown for all ranges; the green vertical line indicates $\kappa = 2\pi/l_0$.

approximation to the Hill spectrum, that offers the same tractability as the Von Kármán model (6.89), was developed by Andrews with colleagues [46–48]. This approximation, commonly called the *modified atmospheric spectrum* (or just *modified spectrum*), is given by References [45–48], and it is valid for wave numbers in the
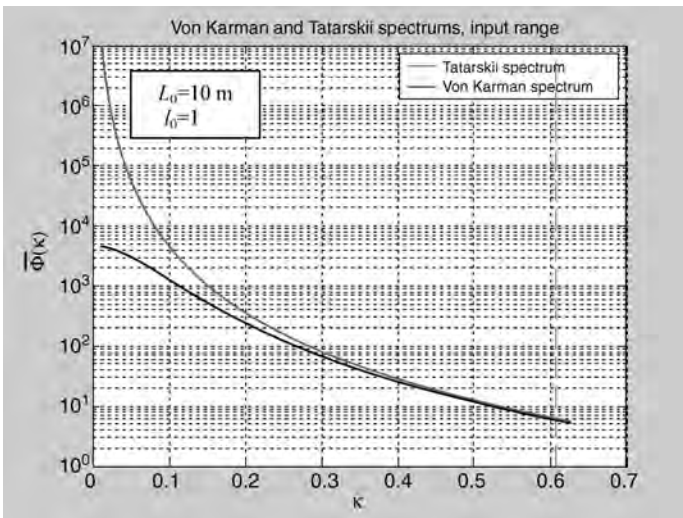
FIGURE 6.18. Comparison between Von Karman and Tatarskii normalized spectra, shown for the input range; the green vertical line indicates $\kappa = 2\pi/l_0$.
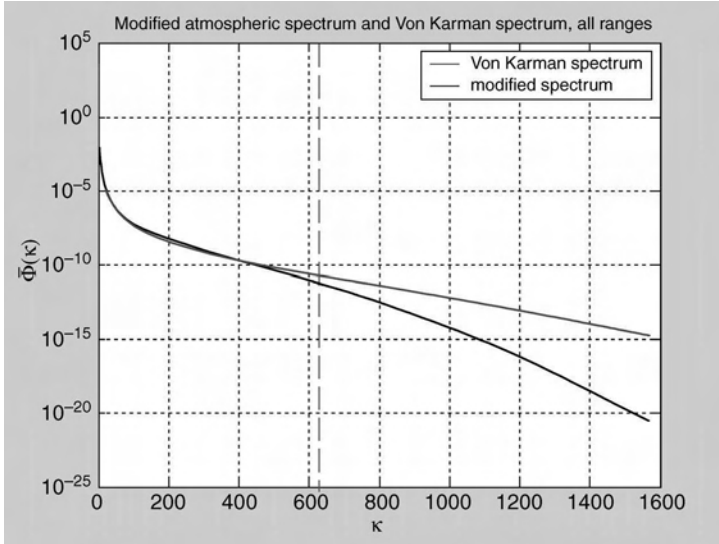
FIGURE 6.19. Comparison between the modified and Von Karman normalized spectra; the green vertical line indicates $\kappa = 2\pi/l_0$.

range of $0 \leq \kappa < \infty$:

$$\Phi_n(\kappa) = 0.033 C_n^2 [1 + 1.802(\kappa/\kappa_l) - 0.254(\kappa/\kappa_l)^{7/6}] \frac{\exp(-\kappa^2/\kappa_l^2)}{(\kappa^2 + 1/L_0^2)^{11/6}} \quad (6.90)$$

where $\kappa_l = 3.3/l_0$. Numerical comparisons of results based on the above equation and the Hill spectrum reveal differences not larger than 6% but generally within 1–2% of each other. A comparison between the normalized modified atmospheric spectrum and the Von Kármán spectrum, $\bar{\Phi}_{nk}(\kappa) = \Phi_{nk}(\kappa)/0.033 C_n^2$, can be seen in Figure 6.19. The whole modified spectrum, on a log–log scale, is shown in Figure 6.20 extracted from References [46–48]. The modified model, which is based on Hill's numerical spectral model, provides good agreement with experimental results.

The Refractive Index Structure Parameter. As was mentioned above, any turbulence in the atmosphere can be characterized by three parameters: the inner scale l_0, the outer scale L_0, and the structure parameter of refractive index fluctuation C_n^2. The refractive-index structure parameter, as the measure of the "strength" or "power" of the turbulent structure, is considered the most critical parameter along the propagation path in characterizing the effects of atmospheric turbulence. It was defined above as a refractive-index structure parameter C_n^2 (in radio propagation it is also denoted by C_ε^2, accounting relationship between the refractive index n and permittivity ε.) Values of C_n^2 near the ground, in warm climates, generally vary between 10^{-14} m$^{-2/3}$ and 10^{-12} m$^{-2/3}$. Various near-ground experiments carried out over
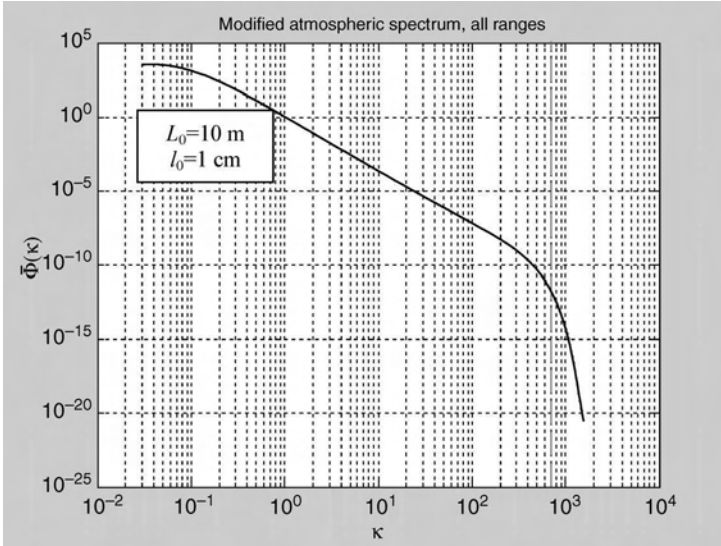
FIGURE 6.20. The modified normalized spectrum, shown for all ranges at the logarithmic f scale; the green vertical line indicates $\kappa = 2\pi/l_0$.

different daytime hours during winter time showed that with increase of altitude h, the structure parameter C_n^2 decreases to an altitude of 3 to 5 km. It then increases to some maximum near 10 km, after which it rapidly decreases with increasing altitude. Usually, to obtain relationships between the structure parameter C_n^2 and the atmospheric refractive index fluctuations δn, we assume stationary, homogeneity, and isotropism of atmospheric refractive index fluctuations. However, as was mentioned in previous sections, the refractive index n is a complicated function of various meteorological parameters. For example, for above sea atmosphere, the value of refractive index n can be presented as [42]

$$n \approx 1 + \frac{77p}{T}\left[1 + \frac{7.53 \cdot 10^3}{\lambda^2} - 7733\frac{q}{T}\right] \tag{6.91}$$

where, p is the air pressure, [mb]; T is the temperature [K]; q is a specific humidity, [g/m g/m^3]; λ is a wavelength [m]. A simple approximation of the relationship between the refractive index fluctuations and the structure parameter C_n^2 is given by [44]

$$C_n^2 \approx \frac{\langle(\delta n)^2\rangle}{x^{2/3}} \tag{6.92}$$

where x represents the distance between antennas, the transmitter, and the receiver. If so, the structure parameter C_n^2 also varies according to the variations of

meteoro-logical parameters. So, for marine atmosphere [44]

$$C_n^2 \approx \left(79 \cdot 10^{-6} \frac{p}{T^2}\right)^2 (C_T^2 + 0.113 C_{Tq} + 0.003 C_q^2) \tag{6.93}$$

where C_T^2 and C_q^2 are the air temperature and water vapor structure coefficients, respectively; C_{Tq} is the combined temperature–water vapor structure coefficient or covariance. The C_T^2 term in (6.93), which is the mean-square statistical average of the difference in temperature ΔT between two points along the radio path separated by a distance x, is given by

$$C_T^2 = \langle (\Delta T)^2 \rangle x^{2/3} \tag{6.94}$$

The structure parameter can thus be written as [42,44]:

$$C_n^2 = \left(79 \times 10^{-6} \frac{p}{T^2}\right)^2 C_T^2 \tag{6.95}$$

In daytime and near the ground surface (at the height of several meters) the value of C_n^2 can range from $10^{-16}\,\mathrm{m}^{-2/3}$ to $10^{-12}\,\mathrm{m}^{-2/3}$ with changes of magnitude in only one minute.

At the same time, the upper altitude profile of C_n^2 (for $h > 5\,\mathrm{km}$) appears to be more constant in time. There are several modes that describe the height profile of C_n^2 in the upper troposphere. We will present here the Hufnagle model [31], according to which the altitude profile of C_n^2 is

$$C_n^2(h) = 2.7 \cdot 10^{-16} \left[\exp\left(-\frac{h}{1500}\right) + 3w^2 \left(\frac{z}{10000}\right)^{10} \exp\left(-\frac{h}{1000}\right) \right] \tag{6.96}$$

where the height h is in meters, and $w = \frac{1}{15} \int_{h_1 = 5\,\mathrm{km}}^{h_2 = 20\,\mathrm{km}} v^2(z)\mathrm{d}z$ is the root mean square of the horizontal wind $v(z)$.

6.3.2. Tropospheric Scintillations

Waves traveling through tropospheric layers with rapid variations of index therefore, vary fastly and randomly in amplitude and phase. This effect is called dry tropospheric scintillation. Rain is another source of tropospheric scintillations, which are called *wet*; it leads to a wet component of scintillation, which tends to be slower than the dry effects. The scintillation is not an absorptive effect and leads to signal amplitude and phase fluctuations, that is, to the essentially unchanged mean level of the radio signal passing through the troposphere. The phase and amplitude fluctuations occur both in the space and time domains. Moreover, this phenomenon is strongly frequency-dependent: the shorter wavelengths lead to more severe fluctuations of signal amplitude and phase resulting from a given scale size. The scale size can be determined by experimentally monitoring the scintillation of a

signal on two nearby paths and by examining the cross correlation between the scintillation on those paths. If the effects are closely correlated, then the scale size is large compared with the path spacing [45].

Additional investigations have shown that the distribution of the signal fluctuations (in decibels) is approximately a Gaussian distribution, whose standard deviation is the intensity [42–45].

Scintillation Index. A wave propagating through a random medium such as the atmosphere will experience irradiance fluctuations, called scintillation, even over relatively short propagation paths. Scintillation is defined as [42–45]

$$\sigma_I^2 = \frac{\langle I^2 \rangle - \langle I \rangle^2}{\langle I \rangle^2} = \frac{\langle I^2 \rangle}{\langle I \rangle^2} - 1 \tag{6.97}$$

This is caused almost exclusively by small temperature variations in the random medium, resulting in index-of-refraction fluctuations (i.e., turbulent structures). In (6.97) the quantity I denotes irradiance or intensity of the radio wave and the angle brackets denote an ensemble average or equivalently, a long-time average. In weak fluctuation regimes, defined as those regimes for which the scintillation index is less than unity [42–45], derived expressions for the scintillation index show that it is proportional to the *Rytov variance*:

$$\sigma_1^2 = 1.23 C_n^2 k^{7/6} x^{11/6} \tag{6.98}$$

Here, as above, C_n^2 is the index-of-refraction structure parameter, k is the radio wave number, and x is the propagation path length between transmitter and receiver. The Rytov variance represents the scintillation index of an unbounded plane wave in the case of its weak fluctuations but is otherwise considered a measure of the turbulence strength when extended to strong-fluctuation regimes by increasing either C_n^2 or the path length x or both. It is shown in References [42–45] that the scintillation index increases with the increasing values of the Rytov variance until it reaches a maximum value greater than unity in the regime characterized by random focusing, because the focusing caused by large-scale inhomogeneities achieves its strongest effect. With increasing path length or inhomogeneity strength, multiple scattering weakens the focusing effect, and the fluctuations slowly begin to decrease saturating at a level for which the scintillation index approaches unity from above. Qualitatively, saturation occurs because multiple scattering causes the wave to become increasingly less coherent in the process of wave propagation through random media.

Signal Intensity Scintillations in the Turbulent Atmosphere. Early investigations concerning the propagation of unbounded plane waves and spherical waves through random media obtained results limited by weak fluctuations [45]. To explain weak-fluctuation theory, three new parameters must be introduced instead
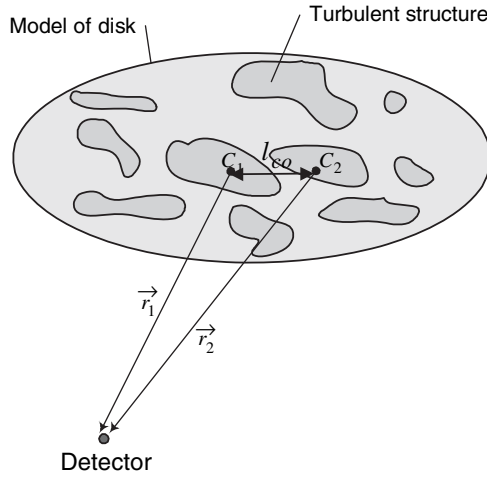
FIGURE 6.21. The coherency between two neighboring points, described by close-to-unit correlation coefficient, i.e., $0 \ll \rho(\mathbf{r}_1, \mathbf{r}_2) \leq 1$.

of the inner and outer scales of turbulences described earlier. They are (a) the coherence scale, $l_1 \equiv l_{co} \sim 1/\rho_0$, which describes the effect of coherence between two neighboring points (see Fig. 6.21); (b) the first Fresnel zone scale, $l_2 \equiv l_F \sim \sqrt{x/k}$, as was mentioned in Chapter 5, which describes the clearance of the propagation link (see Fig. 6.6a); (c) the scattering disk scale, $l_3 \sim x/\rho_0 k$, which models the turbulent structure (see Fig. 6.22).

On the basis of such definitions, Tatarskii [44] predicted that the correlation length of the irradiance fluctuations is on the order of the first Fresnel zone $l_F \approx \sqrt{L/k}$ (see Fig. 6.6(a)) . However, measurements of the irradiance covariance function under strong fluctuation conditions showed that the correlation length decreases with increasing values of the Rytov variance σ_1^2 and that a large residual correlation tail emerges at large separation distances. That is, in the strong-fluctuation regime, the spatial coherence radius ρ_0 of the wave determines the
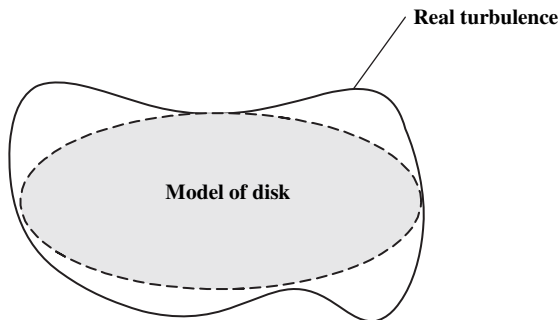
FIGURE 6.22. The area of scattering modeled by a disk.

correlation length of irradiance fluctuations, and the scattering disk characterizes the width of the residual tail: $x/\rho_0 k$. In References [46–48], the theory developed in References [43,44] was modified for strong fluctuations and showed why the smallest scales of irradiance fluctuations persist into the saturation regime. The basic qualitative arguments presented in these works are still valid. Kolmogorov theory assumes that turbulent eddies range in size from a macroscale to a microscale, forming a continuum of decreasing eddy sizes.

The largest eddy-cell size, smaller than that at which turbulent energy is injected into a region, defines an effective outer scale of turbulence L_0, which near the ground is roughly comparable with the height of the observation point above ground. An effective inner scale of turbulence l_0 is associated with the smallest cell size before energy is dissipated into heat.

We will briefly present modifications of the Rytov method obtained in References [46–48] to develop a relatively simple model for irradiance fluctuations, that is, applicable in moderate-to-strong fluctuation regimes. In References [46–48], the following basic observations and assumptions have been stated:

– atmospheric turbulence affects a propagating wave as statistically inhomogeneous structure;
– the received irradiance of a wave can be modeled as a modulation process in which small-scale (diffractive) fluctuations are multiplicatively modulated by large scale (refractive) fluctuations;
– small-scale processes and large-scale processes are statistically independent;
– the Rytov method for signal intensity scintillation is valid even into the saturation regime with the introduction of a spatial frequency filter to account properly for the loss of spatial coherence of the wave in strong-fluctuation regimes;
– the geometrical-optics method can be applied to large-scale irradiance fluctuations.

These observations and assumptions are based on recognizing that the distribution of refractive power among the turbulent eddy cells of a random medium is described by an inverse power of the physical size of the cell. Thus, the large turbulent cells act as *refractive lenses* with focal lengths typically on the order of hundreds of meters or more, creating the so-called *focusing effect* or *refractive scattering* (Fig. 6.23a). This kind of scattering is defined by the coherent component of the total signal passing the troposphere. The smallest cells have the weakest refractive power and the largest cells the strongest. As a coherent wave begins to propagate into a random atmosphere, the wave is scattered by the smallest of the turbulent cells (on the order of millimeters) creating the so-called *defocusing effect* or *diffractive scattering* (see Fig. 6.23b). This kind of scattering is defined by the incoherent component of the total signal. Thus, they act as defocusing lenses, decreasing the amplitude of the wave by a significant amount, even for short propagation distances. The diffractive scattering spreads the wave as
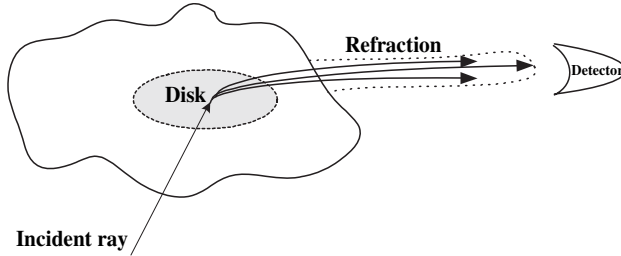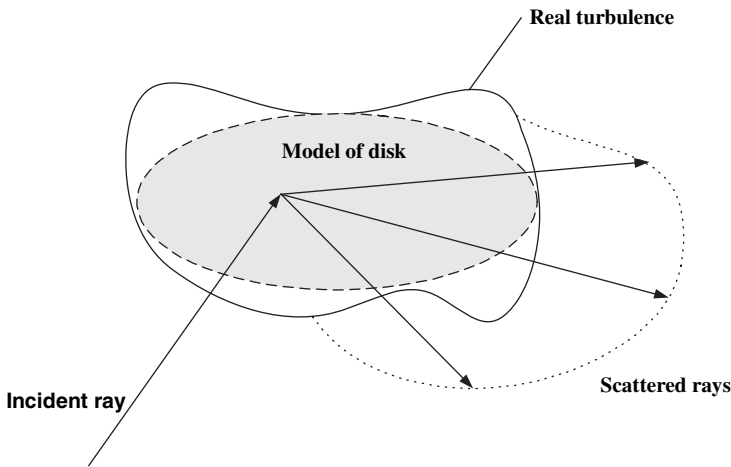
FIGURE 6.23(a). The focusing effect.

FIGURE 6.23(b). The defocusing effect.

it propagates. Refractive and diffractive scattering processes are compound mechanisms, and the total scattering process acts like a modulation of small-scale fluctuations by large-scale fluctuations. Schematically, such a situation is sketched in Figure 6.24 containing both components of the total field.

Small-scale contributions to scintillation are associated with turbulent cells smaller than the Fresnel zone $\sqrt{x/k}$ or the coherence radius ρ_0, whichever is smaller. Large-scale fluctuations in the irradiance are generated by turbulent cells larger than that of the first Fresnel zone or the scattering disk $x/k\rho_0$, whichever is larger, and can be described by the method of geometrical optics. Under strong-fluctuation conditions, spatial cells having size between those of the coherence radius and the scattering disk contribute little to scintillation. Hence, because of the loss of spatial coherence, only the very largest cells near the transmitter have focusing effect on the illumination of small diffractive cells near the receiver. Eventually, even these large cells cannot focus or defocus. When this loss of coherence happens, the illumination of the small cells is (statistically) evenly distributed and the fluctuations of the
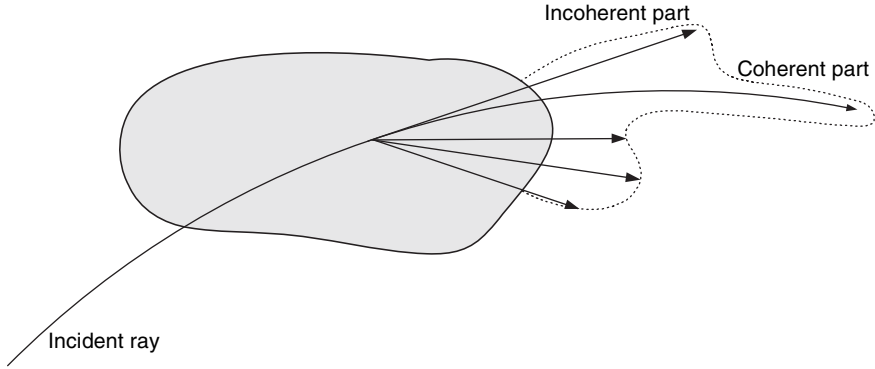
FIGURE 6.24. The total field pattern consisting of the coherent part (I_{co}) and incoherent part (I_{inc}).

propagating wave are due to random interference of a large number of diffraction scattering of the small eddy cells.

Zero-inner-scale Model for Plane Wave. For the case of $l_0 \to 0$, $L_0 \to \infty$, and $C_n^2 = const$, the plane-wave coherence radius is $\rho_0 = (1.46 C_n^2 k^2 x)^{-3/5}$, in both weak and strong fluctuation regimes, whereas the Fresnel zone $\sqrt{x/k}$ defines the correlation length in only weak irradiance fluctuations. Cell sizes smaller than the Fresnel zone cause diffractive distortions of the wave, whereas those larger than the Fresnel zone cause refractive distortions such as focus and tilt. At the onset of strong fluctuations, the coherence radius approaches the size of the Fresnel zone, and all three cell sizes are roughly equal (i.e., $l_1 \sim l_2 \sim l_3$). This happens in the vicinity of the focusing regime. For conditions of stronger fluctuations, the correlation length is defined by the spatial coherence radius ρ_0, which is now smaller than the Fresnel zone, and the scattering disk $L/k\rho_0$ is larger (i.e. $l_1 < l_2 < l_3$). Let us consider the scintillation index of a plane radio wave that has propagated a distance x through unbounded turbulent atmosphere.

(A) Weak fluctuations. Under the weak-fluctuation theory and the Rytov method, the scintillation index can be expressed in the form:

$$\sigma_I^2 = \exp(\sigma_{\ln I}^2) - 1 \cong \sigma_{\ln I}^2, \qquad \sigma_1^2 \ll 1 \tag{6.99}$$

where $\sigma_{\ln I}^2$ is the log-irradiance variance defined under the Rytov approximation by

$$\sigma_{\ln I}^2 = 8\pi^2 k^2 \int_0^L \int_0^\infty \kappa \Phi_n(\kappa) \left[1 - \cos\left(\kappa^2 \frac{z}{k}\right)\right] d\kappa \, dz = 1.06 \sigma_1^2 \int_0^1 \int_0^\infty \eta^{-11/6} (1 - \cos\eta\xi) d\eta \, d\xi \tag{6.100}$$

In the last step, we have assumed a conventional Kolmogorov spectrum and introduced the nondimensional quantities: $\eta = \frac{x\kappa^2}{k}$ and $\xi = \frac{z}{x}$. Performing the integration above, we obtain the result:

$$\sigma_I^2 \cong \sigma_1^2 = 0.847(x)^{5/6}, \qquad \sigma_1^2 \ll 1$$
$$x/k\rho_0^2 = 1.22(\sigma_1^2)^{6/5}$$

(6.101)

(B) Moderate fluctuations. At the other extreme, the asymptotic behavior of the scintillation index in the *saturation regime* is described by

$$\sigma_I^2 \cong 1 + \frac{0.86}{\sigma_1^{4/5}} = 1 + 0.919\left(\frac{k\rho_0^2}{x}\right)^{1/3}, \qquad \sigma_1^2 \gg 1$$

(6.102)

The resulting log-irradiance scintillation is

$$
\sigma_{\ln I}^2 = 8\pi^2 k^2 \int_0^L \int_0^\infty \kappa \Phi_n(\kappa) G_x(\kappa)[1 - \cos\left(\kappa^2 \frac{z}{k}\right)]\mathrm{d}\kappa\,\mathrm{d}z
$$
$$
\cong 1.06\,\sigma_1^2 \left(\frac{L}{k}\right)^{7/6} \int_0^1 \xi^2 \int_0^\infty \kappa^{4/3} \exp\left(-\frac{\kappa^2}{\kappa_x^2}\right)\mathrm{d}\eta\,\mathrm{d}\xi \cong 0.15\sigma_1^2\eta_x^{7/6}
$$

(6.103)

where $\eta_x = x\kappa_x^2/k$.

(C) Strong fluctuations. In the case of strong turbulence regime, the scintillation index for a plane wave in the absence of inner scale is given by

$$\sigma_I^2 = \exp\left[\frac{0.54\sigma_1^2}{(1 + 1.22\sigma_1^{12/5})^{7/6}} + \frac{0.509\sigma_1^2}{(1 + 0.69\sigma_1^{12/5})^{5/6}}\right] - 1, \qquad 0 \le \sigma_1^2 < \infty$$

(6.104)

An example of signal intensity scintillation index computation according to (6.104) from 1 GHz to 50 GHz versus the refractive-index structure parameter varied from 10^{-13} to 10^{-11}, for the distance $x = 10\,\mathrm{km}$ and the inner scale $l_0 = 0\,\mathrm{mm}$, is shown in Figure 6.25. It is clearly seen that the scintillation index for any $C_n^2 = const.$ (denoted, e.g., for $C_n^2 = 10^{-12}$ by the vertical line) becomes twice as strong as the frequency increases from 20 GHz to 50 GHz. This result is very important for predicting the fast fading of the signal within land–aircraft and land–satellite radio communication links passing through the turbulent troposphere and operating at frequencies in the L/X-band (i.e., more than 1 GHz).

Nonzero-inner-scale Model for Plane Wave. When inner-scale effects become important ($l_0 \ne 0$), the atmospheric power spectrum is more strictly described by a modified spectrum with high wave-number rise, that is, the traditional Tatarskii spectrum [44].
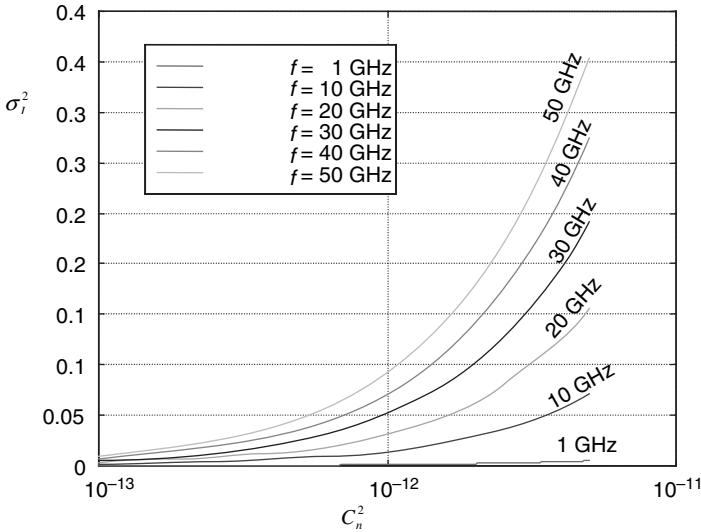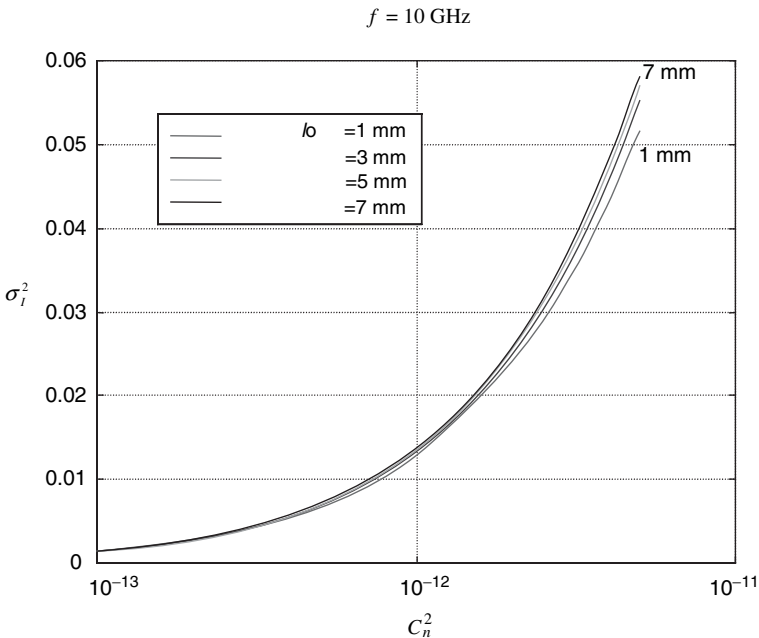
FIGURE 6.25. Index of signal intensity scintillations versus the intensity of refractive index scintillations for different frequencies from 1 GHz to 50 GHz.

Under weak irradiance fluctuations in the case of an unbounded plane wave, the scintillation index based on the modified spectrum is described for $\sigma_1^2 < 1$ by

$$\sigma_I^2(x) \cong 3.86\sigma_1^2 \left\{ (1 + Q_l^{-2})^{11/12} \left[\sin\left(\frac{11}{6}\tan^{-1}Q_l\right) + \frac{1.507}{(1 + Q_l^2)^{1/4}}\sin\left(\frac{3}{4}\tan^{-1}Q_l\right) \right.\right.$$
$$\left.\left. - \frac{0.273}{(1 + Q_l^2)^{7/24}} \times \sin\left(\frac{5}{4}\tan^{-1}Q_l\right) \right] - 3.5Q_l^{-5/6} \right\} \tag{6.105}$$

Here, $Q_l = 10.89x/kl_0^2$ is a nondimensional inner-scale parameter. Asymptotic expressions for the scintillation index in the saturation regime, which are based on the modified atmospheric spectrum, are

$$\sigma_I^2 \cong 1 + \frac{2.39}{(\sigma_{1I}^2 Q_l^{7/6})^{1/6}}, \qquad \sigma_1^2 Q_l^{7/6} \gg 100 \tag{6.106}$$

Under general conditions, the size of the inner scale l_0 relative to the Fresnel zone $\sqrt{x/k}$ is an important consideration. For example, in weak irradiance fluctuations associated with short propagation paths, the inner scale may be of similar size or larger than the width of the Fresnel zone; hence, there will be little contribution to scintillation from eddy cells smaller than the inner scale. On the contrary, over longer propagation path lengths, the inner scale can be much smaller than the Fresnel zone. In this latter situation, size of the cells is the same as the inner scale

and smaller size contributes mostly to small-scale scintillation. Large-scale scintillation is dominated by cells with size larger than x/kl_0.

Eventually, the coherence radius becomes smaller than the inner scale, and small-scale scintillation depends less and less on cell size of about the same as the inner scale in the saturation regime. Large-scale scintillation, which continues to depend on the inner scale, begins to diminish in the saturation regime, as only those cells larger than the scattering disk are strong enough to still cause focusing effects. The scintillation index for a plane wave in the presence of finite inner-scale is

$$\sigma_I^2 = \exp\left[\sigma_{\ln x}^2(l_0) + \frac{0.509\sigma_1^2}{\left(1 + 0.69\sigma_1^{12/5}\right)^{5/6}}\right] - 1 \qquad (6.107)$$

where $x/k\rho_0^2 = 1.02\sigma_1^2 Q_l^{1/6}$ is in the presence of the inner scale. Results of the scintillation index according to (6.107), versus the refractive-index parameter C_n^2 are shown in Figure 6.26a,b for $f = 10$ and $20\,\text{GHz}$, respectively. The results are

FIGURE 6.26(a). Index of signal intensity scintillations versus the intensity of refractive index scintillations for frequency of 10 GHz and for different inner scales of turbulences ranging from 1 mm to 7 mm.
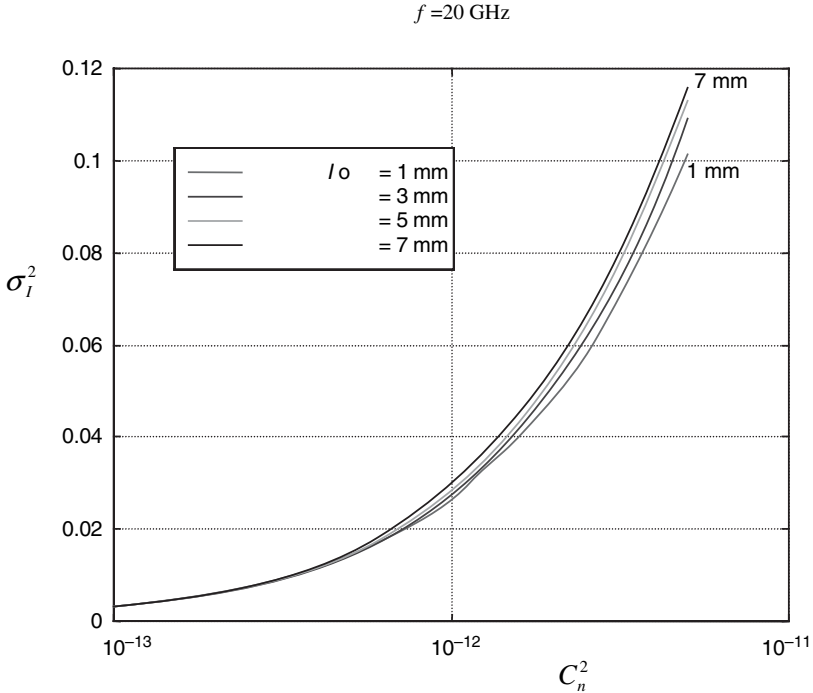
$f = 20$ GHz

FIGURE 6.26(b). The same as in Fig. 6.22(a), but for frequency of 20 GHz.

for $x = 10$ km and for the inner scale l_0 changed from 1 mm to 7 mm. It is seen that for $C_n^2 = const.$ (denoted, e.g., as $C_n^2 = 10^{-12}$ by the vertical dotted line), the scintillation index does not vary significantly with an increase of the inner scale of the initial turbulence, becoming in any way smaller than the values for the case of zero-order inner-scale model, described by (6.104). These results are summarized in Tables 6.4 and 6.5 for inner scale $l_0 = 0$ mm and 1 mm and for frequencies of 25 GHz and 50 GHz, respectively.

6.3.3. Effects of Troposheric Turbulences on Signal Fading

The fast fading of the signal at open paths is caused mainly by multipath propagation and turbulent fluctuations of the refractive index. Some very interesting ideas were proposed by Samelsohn [49,50], which are presented briefly below. As it is known,

TABLE 6.4. Scintillation Index for Radiation Frequency of 25 GHz

C_n^2				
~0.0028	~0.014	~0.027	~0.134	0 mm inner-scale
~0.0027	~0.013	~0.024	~0.091	1 mm inner-scale

TABLE 6.5. Scintillation Index for Radiated Frequency of 50 GHz

C_n^2				
~0.0093	~0.046	~0.092	~0.404	0 mm inner-scale
~0.0088	~0.038	~0.068	~0.241	1 mm inner-scale

the fluctuations of the signal intensity due to turbulence are distributed lognormally. For the Kolmogorov model, the normalized standard deviation of this distribution can be presented in terms of C_ε^2 instead of Rytov's formula (6.92) presented in terms of C_n^2:

$$\sigma^2 = 0.12 C_\varepsilon^2 k^{7/6} d^{11/6} \qquad (6.108)$$

where $k = 2\pi/\lambda$ is the wave number, and C_ε^2 is the structure constant of the turbulence averaged over the path. In the atmosphere, the structure constant C_ε^2 may vary within at least four orders of magnitude, from 10^{-15} m$^{-2/3}$ to 10^{-10} m$^{-2/3}$. As the path-averaged statistics of these variations is unknown, the margin related to this kind of fading may be estimated only heuristically. The normalized temporal correlation function was obtained in [49,50]

$$K(\tau) = \frac{1}{\sin(\pi/12)} \left[(1 + \alpha^4/4)^{11/12} \sin\left(\frac{\pi}{12} + \frac{11}{6} \arctan \frac{\alpha^2}{2} \right) - \frac{11}{6} \left(\frac{\alpha}{\sqrt{2}} \right)^{5/3} \right]$$

$$(6.109)$$

where $\alpha = \tau/\tau_0$, $\tau_0 = \frac{\sqrt{d/k}}{v}$, and v is the projection of the vehicle velocity to the plane that is perpendicular to the path. The correlation time τ_c defined as $K(\tau_c) = 0.5$, can be estimated as $\tau_c \approx 0.62\tau_0$. The spectrum of the intensity fluctuations is [49,50]

$$S(\omega) = \beta^2 w(\omega)/\omega \qquad (6.110)$$

is calculated by using the definition of the normalized spectral density

$$w(\omega) = 4\omega \int_0^\infty d\tau \cos(\omega\tau) K(\tau) \qquad (6.111)$$

which at high frequencies is given by

$$w(\Omega) = 12.0 \, \Omega^{-5/3}, \qquad \Omega \geq 5 \qquad (6.112)$$

and at low frequencies can be approximated as

$$w(\Omega) = 3.47\Omega \exp\lfloor -0.44\Omega^{\varphi(\Omega)} \rfloor, \qquad \Omega \leq 5 \qquad (6.113a)$$

TABLE 6.6. Characteristic Time and Frequency versus the Radio Path for f = 15 GHz and v = 50 m/s

Distance, km	50	100	150
τ_0, s	0.25	0.36	0.44
ω_m, Hz	6.4	4.4	3.6

where

$$\varphi(\Omega) = 1.47 - 0.054\,\Omega \qquad (6.113b)$$

and $\Omega = \tau_0\omega$ is the dimensionless frequency. The normalized density $w(\Omega)$ has the maximal value of about 2.30 at $\Omega_m \approx 1.60$, and therefore $\omega_m \approx 1.60/\tau_0$ [49,50]. The typical values for both τ_0 and ω_m are shown in Table 6.6 for the frequency 15 GHz and vehicle velocity $v = 50$ m/s, and in Table 6.7 for the frequency 13 GHz and vehicle velocity $v = 350$ m/s, calculated according to the above formulas. The phase fluctuations have normal distribution with dispersion

$$\sigma_s^2 = 0.075 C_\varepsilon^2 k^2 ds_0^{-5/3} \qquad (6.114)$$

where $s_0 \sim 2\pi/L_0$, and L_0 is the outer scale of the turbulent spectrum depending on the height which equals approximately to 10–100 m. Estimations according to References [49,50] showed that the phase fluctuations caused by turbulence are negligible under typical atmospheric conditions and even for extremely strong turbulence.

6.3.4. Radio Propagation Caused by Tropospheric Scattering

For radio paths through the troposphere, the dominant propagation mechanism is the scattering from atmospheric turbulent inhomogeneities and discontinuities in the refractive index of the atmosphere. For troposcattering propagation, the received signals are generally 50 to 100 dB below free space values and are characterized by short-term fluctuations superimposed on long-term variations. The statistical distributions are Rayleigh for the short-term variations and are lognormal for the long-term variations [51–53]. The average signal intensity of the scattered signal at the receiving antenna is given by [49,50]

$$I_s = \frac{\pi}{2} k^4 \Phi_\varepsilon(\mathbf{K}_0, \mathbf{0}) V_e / r_i^2 r_s^2 \qquad (6.115)$$

TABLE 6.7. Characteristic Time and Frequency versus the Radio Path for f = 13 GHz and v = 350 m/s

Distance, km	100	200	300
τ_0, s	0.055	0.077	0.095
ω_m, Hz	29.1	20.8	16.8

where $k = 2\pi/\lambda$ is the wave number; r_i is the distance from the transmitting antenna to the scattering volume; r_s is the distance from the scattering volume to the receiving antenna; V_e is the effective volume of scattering; $\Phi_\varepsilon(\mathbf{K}_0, \mathbf{0})$ is the spectrum of locally homogeneous turbulent permittivity fluctuations at the center of the turbulent zone; $\Phi_\varepsilon(\mathbf{K}, \mathbf{R})$ is the spectrum of locally homogeneous turbulent permittivity fluctuations at the distance $\mathbf{R}$ from its center. The permittivity fluctuations are characterized by the correlation function

$$B_\varepsilon(\mathbf{P}, \mathbf{R}) = \langle \tilde{\varepsilon}(\mathbf{R}_1)\tilde{\varepsilon}(\mathbf{R}_2) \rangle \tag{6.116}$$

where

$$\mathbf{P} = \mathbf{R}_1 - \mathbf{R}_2, \qquad \mathbf{R} = \frac{1}{2}(\mathbf{R}_1 + \mathbf{R}_2) \tag{6.117}$$

and the angular brackets determine mean ensemble averaging. The spectrum $\Phi_\varepsilon(\mathbf{K}, \mathbf{R})$ is given by the Fourier transform as

$$\Phi_\varepsilon(\mathbf{K}, \mathbf{R}) = (2\pi)^{-3} \int d\mathbf{P} \exp(-i\mathbf{K} \cdot \mathbf{P}) B_\varepsilon(\mathbf{P}, \mathbf{R}) \tag{6.118}$$

The expression for the effective scattering volume has the form [44,49,50]

$$V_e = \int d\mathbf{R} F(\mathbf{n}_i, \mathbf{n}_s) \Phi_\varepsilon(\mathbf{K}, \mathbf{R}) / \Phi_\varepsilon(\mathbf{K}_0, \mathbf{0}) \tag{6.119}$$

where

$$F(\mathbf{n}_i, \mathbf{n}_s) = |f_i(\mathbf{n}_i)f_s(\mathbf{n}_s)|^2 \tag{6.120}$$

$f_i(\mathbf{n}_i)$ and $f_s(\mathbf{n}_s)$ are the radiation patterns of the transmitting and receiving antennas, respectively. In (6.115) and (6.119), the spatial frequency vector $\mathbf{K}_0$ is defined as

$$\mathbf{K}_0 = k(\mathbf{n}_{i0} - \mathbf{n}_{s0}) \tag{6.121}$$

where the unit vectors $\mathbf{n}_{i0} = \mathbf{r}_{i0}/r_{i0}$ and $\mathbf{n}_{s0} = \mathbf{r}_{s0}/r_{s0}$ are related to the lines connecting the transmitting and receiving antennas with the center of the scattering volume.

By using (6.115) for the intensity of the scattered wave, we can calculate the power received by the antenna as

$$P_2 = F_s^2 G_2 P_1 \tag{6.122}$$

where the scattering loss, denoted by F_s^2, is given by References [44,49,50]

$$F_s^2 = \frac{\pi^2}{2} k^2 \Phi_\varepsilon(\mathbf{K}_0, \mathbf{0}) V_e / r_i^2 r_s^2 \tag{6.123}$$

There are two unknowns in (6.123). First is the spectrum $\Phi_\varepsilon(\mathbf{K}_0, \mathbf{0})$, which is proportional to the structure parameter of the turbulence and is characterized by a significant variability (see previous section). The anisotropic structure of the permittivity fluctuations can also cause rather strong variations of the received power. Second, the effective scattering volume depends essentially on the radiation patterns of both antennas. Moreover, for antennas with relatively small gain, such as those located at the air vehicle, Equation (6.119) for the effective scattering volume is no longer valid and must be corrected.

What is very important is the frequency selectivity of the channels formed by the tropospheric scattering from turbulences. As is known [30,40], for highly directive antennas, the coherence bandwidth is of the order of several megahertz. For antennas with poor directivity, the coherence bandwidth decreases significantly and may be smaller than several hundreds kilohertz. Therefore, to complete the evaluation of the link budget and frequency selectivity for the tropospheric radio paths, realistic models of the atmospheric turbulence, including anisotropic layered structures, as well as the real radiation patterns of the antennas must be taken into account.

6.4. LINK BUDGET DESIGN FOR TROPOSPHERIC COMMUNICATION LINKS

Let us summarize the above by introducing some examples of link budget calculations in decibel for the communication link between the ground-based antenna, defined by its gain G_1, and the vehicle (helicopter, aircraft, or satellite) antenna, defined by its gain G_2. We do not present these parameters because they are different for different types of antennas and can be easily computed using special formulas. In the examples presented in Tables 6.8 and 6.9, we considered different

TABLE 6.8. $f = 15$ GHz, $d = 150$ km, $h_2 = 2$ km

Time availability, %	95	99
Basic transmission loss, dB	159	159
Tx antenna gain, dB	G_1	G_1
Rx antenna gain, dB	G_2	G_2
Molecular absorption, dB	1	2
Rain attenuation, dB	0	2
Clouds and fog, dB	0	0
Fast fading (turbulence), dB	1	2
Fast fading (multipath), dB	3	5
Diffuse scattering, dB	2	4
Total, dB	$166 - G_1 - G_2$	$174 - G_1 - G_2$

TABLE 6.9. $f = 15\,GHz$, $d = 150\,km$, $h_2 = 4\,km$

Time availability, %	95	99
Basic transmission loss, dB	159	159
Tx antenna gain, dB	G_1	G_1
Rx antenna gain, dB	G_2	G_2
Molecular absorption, dB	1	2
Rain attenuation, dB	0	2
Clouds and fog, dB	2	5
Fast fading (turbulence), dB	1	2
Fast fading (multipath), dB	3	5
Diffuse scattering, dB	2	4
Total, dB	$168 - G_1 - G_2$	$179 - G_1 - G_2$

conditions of radio propagation by introducing the time availability, which varied from 95% to 99%, assuming that the existence of fast fading described by Rayleigh statistics are from 1% to 5%. In these tables we summarize all effects of hydrometeors, as well as fast fading caused by atmospheric turbulences and multipath phenomena caused by diffuse scattering.

BIBLIOGRAPHY

[1] *International Telecommunication Union, ITU-R Recommendation* pp. 453–456, "The radio refractive index: its formula and refractivity data," Geneva, 1997.

[2] *International Telecommunication Union, ITU-R Recommendation* pp. 834–2, "Effects of tropospheric refraction on radiowave propagation," Geneva, 1997.

[3] *International Telecommunication Union, ITU-R Recommendation* pp. 721–723, "Attenuation by hydrometeors, in precipitation, and other atmospheric particles," vol., Geneva, 1990.

[4] *International Telecommunication Union, ITU-R Recommendation* pp. 530–537, "Propagation data and prediction methods required to design of terrestrial line-of-sight systems," Geneva, 1997.

[5] *International Telecommunication Union, ITU-R Recommendation* pp. 676–673, "Attenuation by atmospheric gases," Geneva, 1997.

[6] *International Telecommunication Union, ITU-R Recommendation*, p. 838, "Specific attenuation model for rain for use in prediction methods," Geneva, 1992.

[7] *International Telecommunication Union, ITU-R Recommendation* pp. 840–842, "Attenuation due to clouds and fog," Geneva, 1997.

[8] *International Telecommunication Union, ITU-R Recommendation* p. 837, "Characteristics of precipitation for propagating modeling," Geneva, 1992.

[9] *International Telecommunication Union, ITU-R Recommendation* pp. 618–5, "Propagation data and prediction methods required for the design of Earth-space telecommunication systems," Geneva, 1997.

[10] Pruppacher, H. R., and R. L. Pitter, "A semi-empirical determinition of the shape of cloud and rain drops," *J Atmos. Sci.*, vol. 28, 1971, pp. 86–94.

[11] Marshall, J. S., and W. M. K. Palmer, "The distribution of raindrops below 10 GHz," *NASA Reference Publication* 1108, 1983.

[12] Joss, J., and A. Waldvogel, "Raindrops size distributions and sampling size error," *J. Atmos. Sci.*, vol. 26, 1969, pp. 566–569.

[13] McMorrow, D. J., and A. R. Davis, "Stochastic model for deriving instaneous precipitation rate distributions," *J. Applied Meteorology*, vol. 16, 1977, pp. 757–774.

[14] Crane, R. K., "Prediction of attenuation by rain," *IEEE Trans. Commun.* vol. 28, 1980, pp. 1717–1733.

[15] Li, L.-W., P.-S. Kooi, M.-S. Leong, et al., "Microwave attenuation by realistically distorted raindrops: Part II-Predictions," *IEEE Trans. Antennas Propagat.*, vol. 43, 1995, pp. 821–828.

[16] Yeo, T.-S., P.-S. Kooi, and M.-S. Leong, "A two-year measurement of rainfall attenuation of CW microwaves in Singapore," *IEEE Trans. Antennas Propagat.*, vol. 41, 1993, pp. 709–712.

[17] Lin, D. P., and H. Y. Chen, "An empirical formula for the prediction of rain attenuation in frequency range 0.6–100 GHz," *IEEE Trans. Antennas Propagat.*, vol. 50, no. 4, 2002, pp. 545–551.

[18] Laws, J. O., and D. A. Parsons, "The relation of raindrop size to intensity," *Trans. Amer. Geophys. Union*, vol. 24, 1943, pp. 452–460.

[19] Yeo, T.-S., P.-S. Kooi, M.-S. Leong, et al., "Tropical raindrop size distribution for the prediction of rain attenuation of microwaves in the 10–40 GHz band," *IEEE Trans. Antennas Propagat.*, vol. 49, no. 1, 2001, pp. 80–83.

[20] Slingo, A., "A GSM parametrization for the shortwave radiative properties of water clouds," *J. Atmos. Sci.*, vol. 46, 1989, pp. 1419–1427.

[21] Chou, M. D., "Parametrizations for cloud overlapping and shortwave single scattering properties for use in general circulation and cloud ensemble models," *J. Climate*, vol. 11, 1998, pp. 202–214.

[22] Ray, P. S., "Broadband complex refractive indices of ice and water," *Applied Optics*, vol. 11, 1972, pp. 1836–1844.

[23] Rossow, W. B., L. C. Garder, and A. A. Lacis, "Global, seasonal cloud variations from satellite radiance measurements. Part I: Sensitivity of analysis," *J. Climate*, vol. 2, 1989, pp. 419–458.

[24] Liou, K. N., *Radiation and Cloud Processes in the Atmosphere*, Oxford University Press, Oxford, England, 1992.

[25] Deirmendjian, D., *Electromagnetic Scattering on Spherical Polydispersions*, American Elsevier, New York, 1969.

[26] Nussenzveig, H. M., and W. J. Wiscombe, "Efficiency factors in Mie scattering," *Phys. Rev. Let.*, vol. 45, 1980, pp. 1490–1494.

[27] Zhang, W., "Scattering of radiowaves by melting layer of precipitation a backward and forward directions," *IEEE Trans. Anten. Propag.*, vol. 42, 1994, pp. 347–356.

[28] Zhang, W., S. I. Karhu, and E. T. Salonen, "Prediction of radiowave attenuations due to a melting layer of precipitation," *IEEE Trans. Anten. Propag.*, vol. 42, 1994, pp. 492–500.

[29] Zhang, W., J. K. Tervonen, and E. T. Salonen, "Backward and forward scattering by the melting layer composed of spheroidal hydrometeors at 5–100 GHz," *IEEE Trans. Anten. Propag.*, vol. 44, 1996, pp. 1208–1219.

[30] Saunders, S. R., *Antennas and Propagation for Wireless Communication Systems*, John Wiley & Sons, New York, 1999.

[31] Hufnagle, R. E., "Line-of-sight wave propagation though the turbulent atmosphere," *Proc. IEEE*, vol. 56, 1966, pp. 1301–1314.

[32] Brehovskih, L. M., "Reflection of plane wave from layered inhomogeneous media," *Jounal of Technical Physics*, Moscow, vol. 19, 1949, pp. 1126–1135.

[33] Blaunstein, N., "Wireless Communication Systems," chap. 12 in *Handbook of Engineering Electromagnetics*, ed. R. Bansal, Marcel Dekker, New York, 2004, pp. 417–481.

[34] Rappaport, T. S., *Wireless Communications: Principles and Practice*, IEEE Press, New York, 1996.

[35] Flock, W. L., "Propagation effects on satellite systems at frequencies below 10 GHz," *NASA Reference Publication* 1108, 1983.

[36] Bean, B. R., and E. J. Dutton, *Radio Meteorology*, Dover, New York, 1966.

[37] Crane, R. K., "A review of transhorizon propagation phenomena," *Radio Sci.*, vol. 16, 1981, pp. 649–669.

[38] Krasuk, N. P., V. L. Koblov, and V. N. Krasuk, *Effects of Troposphere and Terrain on Radar Performance*, Radio Press, Moscow, 1988.

[39] Janaswamy, R., "A curvilinear coordinate based split-step parabolic equation method for propagation predictions over terrain," *IEEE Trans. Anten. Propagat.*, vol. 46, No. 7, 1998, pp. 1089–1097.

[40] Allnutt, J. A., *Satellite-to-Ground Radiowave Propagation*, IEEE Press, New York, 1989.

[41] Blaunstein, N., *Radio Propagation in Cellular Networks*, Artech House, Boston-London, 1999.

[42] Ishimaru, A., *Wave Propagation and Scattering in Random Media*, Academic Press, New York, 1978.

[43] Rytov, S. M., Yu. A. Kravtsov, and V. I. Tatarskii, *Principles of Statistical Radiophysics*, Springer, Berlin, 1988.

[44] Tatarski, V. I., *Wave Propagation in a Turbulent Medium*, McGraw-Hill, New York, 1961.

[45] Doluhanov, M. P., *Propagation of Radio Waves*, Nauka, Moscow, 1972.

[46] Andrews, L. C., and R. L. Phillips, *Laser Propagation Through Random Media*, Society of Photo-Optical Instrumentation Engineers, Bellingham, Washington, 1998.

[47] Andrews, L. C., R. L. Phillips, C. Y. Hopen, et al., "Theory of optical scintillations," *J. Optical Society of America*, vol. 16, 1999, pp. 1417–1429.

[48] Andrews, L. C., R. L. Phillips, and C. Y. Hopen, *Laser Beam Scintillation With Applications*, The International Society for Optical Engineering (SPIE), Bellingham Washington, 2001.

[49] Samelsohn, G. M., "Effect of inhomogeneities' evolution on time correlation and power spectrum of intensity fluctuations of the wave propagating in a turbulent medium," *Sov. J. Commun. Technol. Electron.*, vol. 38, 1993, pp. 207–212.

[50] Samelsohn G. M., and B. Ya. Frezinskii, *Propagation of Millimeter and Optical Waves in a Turbulent Atmosphere*, Telecommunication University Press, St.-Petersburg, 1992.

[51] Bello, P. A., "A troposcatter channel model," *IEEE Trans. Commun.*, vol. 17, 1969, pp. 130–137.

[52] Howell, R. G., R. L. Stuckey, and J. W. Harris, "The BT Laboratories slant-pass measurement complex," *BT Tech. J.*, vol. 10, 1992, pp. 9–21.

[53] Belloul, B., S. R. Saunders, and B. G. Evans, "Prediction of scintillation intensity from sky-noise temperature in earth-satellite links," *Electronics Letter*, vol. 34, 1998, pp. 1023–1024.

Ionospheric Radio Propagation

The effects of the ionosphere on radio propagation are very important in radio communication between terrestrial antennas and air vehicles (stationary or moving) or satellites. Ionospheric radio propagation is also important in the inhomogeneous ionosphere that plays an important role in satellite-to-satellite communications. The problem of wave propagation and scattering in the ionosphere have become increasingly important in recent years: the ionosphere, atmosphere, and the Earth's background environment all play a significant role in determining the service level and quality of the land-satellite or satellite–satellite communication channel.

In recent decades, the increasing demand is observed on mobile-satellite networks designed to provide global radio coverage using constellations of low and medium Earth orbit satellites, which are now in operation. Such systems form regions, called mega cells (see definitions in References [1–3]), consisting of a group of co-channel cells, and clusters of spot beams from each satellite, which move rapidly across the Earth's surface. Signals are typically received by a moving or stationary vehicle at very high elevation angles. Only the local environmental features, ionospheric, atmospheric and terrestrial, which are very close to the concrete radio path, contribute significantly to the propagation process. Therefore, performance of predicting models of fading phenomena, slow and fast, for ionospheric communication links has the same importance as for terrestrial links (described in Chapter 5) and tropospheric links (described in Chapter 6). This is because the same propagation effects, such as multiray reflection, diffraction, and scattering of radio waves, occur in three types of over-the-Earth communication links, land, atmospheric, and ionospheric. However, as

in ionospheric links the slow fading tends to occur on similar distance scales as a fast one, they cannot therefore be easily separated, as was done for the land communication links described in Chapter 5. Unlike land communication channels, the predictions of ionospheric communication channels tend to be highly statistical in nature, because coverage across very wide areas must be included in consideration, while still accounting for the large variations due to the local environmental features. The reader can find more detailed information in References [1–3].

In Section 7.1, we briefly present information about the ionosphere as a continuous medium consisting of plasma and describe the common effects of ionospheric plasma on radio propagation, following the description of ionospheric effects in References [1–12]. Then, in Section 7.2, we discuss the effects of large-scale and small-scale ionospheric plasma inhomogeneities [13–28] and illustrate the main results of signal amplitude and phase variations, that is, the fast fading, resulting by the inhomogeneous structure of the ionosphere, on the basis of numerical computations carried out by the authors according to proposed ionospheric models [29–43]. Finally, in Section 7.3, we consider effects of inhomogeneous ionosphere on radio propagation at the long distances caused by back and forward scattering by the inhomogeneities of ionospheric plasma [44–48].

7.1. MAIN IONOSPHERIC EFFECTS ON RADIO PROPAGATION

7.1.1. Parameters and Processes Affecting Radio Propagation in the Ionosphere

The ionosphere is a region of ionized plasma (i.e., ionized gas consisting of neutral atoms and molecules on one side and charged particles, electrons and ions on the other), which surrounds the Earth at a distance ranging from 50 km to 500–600 km where it continuously extends to the magnetosphere (600–2000 km) [4,5]. The ions and electrons are created in the ionosphere by the Sun's electromagnetic radiation, solar wind, and cosmic rays that are the sources of atoms and molecules ionization. As the solar radiation penetrates deeper into the Earth's atmosphere at zenith, the ionosphere extends closest to the Earth around the equator and is more intense on the daylight side. Figure 7.1 shows the separation of the ionosphere into four distinct layers during the day: D-layer that covers 50–80 km, E-layer that covers 80–130 km, $F1$-layer and $F2$-layer, located at the altitudes of 130–250 km and above 250 km, respectively. During the nighttime these four layers are continuously transformed into the E and F layers, as the D-layer does not exist in nighttime ionosphere because of the absence of solar radiation.

The Content of the Ionosphere. For the neutral component of the ionospheric plasma, consisting in the conditions of hydrostatical equilibrium in the isothermical case, when $T_m(z) = \text{const}$, the change of neutral particle concentration can be
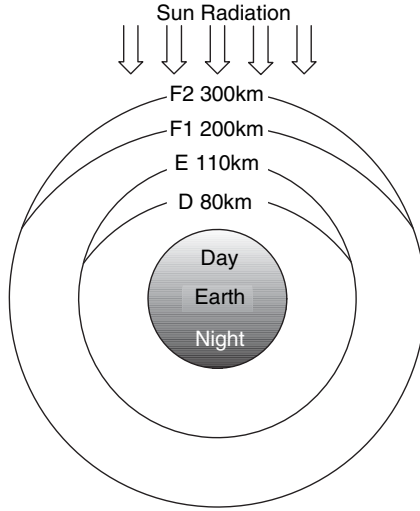
FIGURE 7.1. Presentation of ionospheric layers around the Earth.

described by the following barometric formula [4]

$$N_m = N_{m0} \exp\left\{-\frac{(z - z_0)}{H_m}\right\} \tag{7.1}$$

where N_m is the total plasma concentration; N_{m0} is the same, but for the altitude of $z = z_0$; $H_m = T_m/M_m g$ is the height of the homogeneous atmosphere; $M_m = (1/N_m)\sum_\alpha m_\alpha N_\alpha$ is the summary content of neutral particles in the higher ionosphere; α is the specification of the neutral particles; g is the acceleration of free falls; T_m is the gas temperature expressed in energetic units. Formula (7.1) is valid in the ionosphere of the Earth at altitudes of $z_e = z_0$, where $z_e \cong 1000 - 2000\,\text{km}$ (called exosphere) [4,6,7]. In such altitudes and higher, than that all particles, components of neutral atmospheric gas with specification α, leave the atmosphere as their kinetic energy exceeds the potential energy of the Earth's gravitation field and the free path length of neutral particles, λ_α, exceeds the height of the homogeneous atmosphere, H_m (see definitions above). Furthermore, in the real ionosphere the temperature of the neutral molecules and atoms T_m is increased with the height. All these factors lead to deviations from the barometric formula (7.1). As for the neutral content of the ionosphere, at altitudes less than 100 km, the atmosphere is fully presented by molecules of nitrogen N_2 and oxygen O_2. At such heights, concentration of other components of the neutral gas (He, O, H_2, NO etc.) is very small and depends on the transport process due to turbulence in the neutral atmosphere, as well as on circular and wind processes in the atmosphere (see also definitions in Chapter 6).

At altitudes of more than 100 km atmospheric turbulence is absent; the corresponding limit of $z \geq z_T \approx 100\,\text{km}$ is called the turbo pause [4,6,7]. In contrast
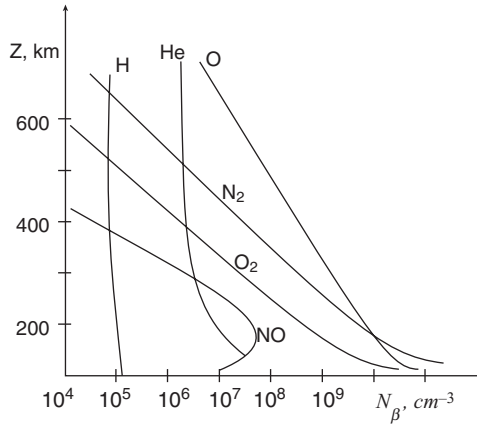
FIGURE 7.2. Height distribution of the neutral content of the ionosphere.

to the fore mentioned, here, up to $z_e \cong 1000 - 2000$ km, formula (7.1) is valid. In this range, the main components are atoms of nitrogen and oxygen created by the chemical processes of dissociations of the corresponding molecules: $N_2 \rightarrow N + N$ and $O_2 \rightarrow O + O$. At altitudes of more than 500–600 km, in magnetosphere, concentrations of helium, He, and hydrogen, H, increase quickly. Finally, at altitudes of exosphere of more than 1000–1500 km, atoms of hydrogen become predominant [4,6,7] (see Fig. 7.2, where the height distribution of all neutral components of the ionosphere is summarized).

The ion content of ionospheric plasma is changed widely depending on latitude Φ of the Earth. Thus at the middle latitudes, $|\Phi| < 55°$, it is not changed drastically, but at the high latitudes, $|\Phi| \geq 55° - 60°$, a full concentration of ions decreases rapidly with height. In the middle latitude ionosphere, at the height of the D layer, the main components of plasma are ions NO^+ and O_2^+, and at the heights of the E and F layers are ions of oxygen O^+. At altitudes of more than 300 km, plasma also contains components of He^+, H^+, N^+, N_2^+, which with the main ions mentioned above determine the total plasma content in the ionosphere. The structure of the ion content of plasma in the polar (high-latitude) ionosphere is more complicated. We do not enter deeply into this subject and refer the reader to excellent books [4,6,7].

The key parameter that has an affect on radio communications is the total electron and ions concentration N measured in free electrons number per cubic meter, because the ionospheric plasma is quasi-neutral and in each of its region, with dimensions larger than the Debye radius (definition can be found in References [5,7–10]), the concentration of electrons, N_e, is equal to the total concentration of various ions, N_i, that is, $N_e \approx N_i = N$. The variations of N with height in the ionosphere for a typical day and night is shown in Figure 7.3, extracted from References [9,10]. It must be noted that the total content of charge particles, the electrons and ions, depend on the processes that create the structure of the
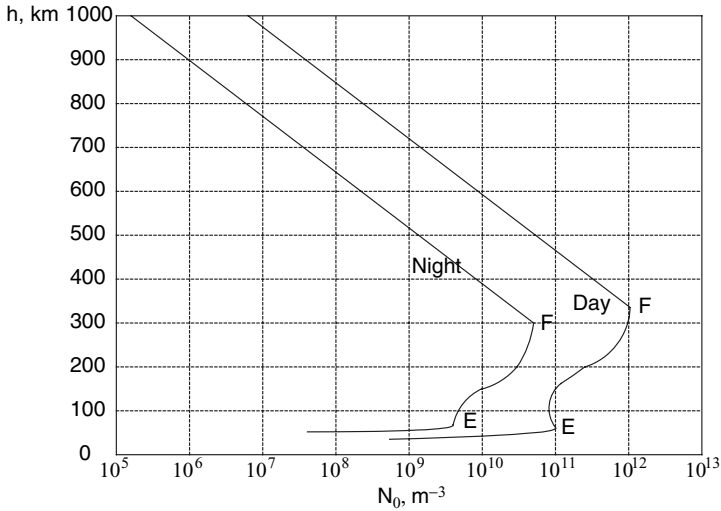
FIGURE 7.3. Ionospheric plasma density versus height for the ionosphere above the ground surface.

ionosphere such as the solar and cosmic rays radiation, wave radiation, photo-chemistry processes, which finally determine the ionization-recombination balance in the ionosphere. The degree of ionization of the ionospheric plasma is determined by the ratio of concentration of the plasma particles N and that of the neutral molecules and atoms N_m. In the lower ionosphere ($z < 100$–120 km), the degree of plasma ionization is very small ($N/N_m \sim 10^{-8} - 10^{-6}$) and increases with height h (for $h > 300$ km $N/N_m \sim 10^{-4} - 10^{-3}$). At the exospheric heights of $h > 1000$ km, the degree of ionization $N/N_m \to 1$, that is, plasma becomes fully ionized [4–10]. The temperature of electrons, T_e, and ions, T_i, strongly depends on daytime and increases with height. Thus, at lower ionospheric heights, temperature of electrons is close to temperature of ions, that is, $T_e \approx T_i$, whereas at the upper ionosphere ($z > 200$–250 km) the temperature of electrons can exceed 1.5–2 times the temperature of ions [7,9]. More detailed information about the structure and properties of the ionosphere, mid-latitude and high-latitude can be found in References [4–7].

Main Characteristics of the Ionospheric Plasma. The characteristics, which are functions of the main parameters of the plasma such as concentration, content, and temperature, are follow. They are the frequency of interactions (collisions) of charged particles with neutral molecules and atoms, between charged particles, the length of their free path between interactions, coefficients of diffusion and drift. All these characteristics determine the dynamic processes, diffusion, and drift of plasma in ambient electrical and magnetic field; they occurred in the ionosphere and were caused on formation of large-scale and small-scale plasma irregularities, which are the main ''sources'' of fading radio signals in the ionosphere. We will

not enter further into the subject presented here; more important formulas that can be used to evaluate effects of plasma inhomogeneities on radio signal amplitude and phase oscillation are described in details below. First of all, we must note that the main characteristics, which must be compared with radio wave frequency, are the frequencies of collisions of electrons and ions with neutrals and between charged particles. Approximate expressions for these characteristics are fully presented in References [4,6–10], from which the frequency of electron-neutral collisions is

$$v_{em} = 1.23 \cdot 10^{-7} N_m T_e^{5/6} \qquad (7.2)$$

where $N_m = N_{N_2} + N_{O_2}$, all other parameters are defined above. The estimation of frequency of electron–ion interactions for different ions N_i and electron temperature T_e can be done using the following approximation [4,6–10]:

$$v_{ei} = \frac{5.5 \, N_i}{T_e^{3/2}} \ln \frac{220 T_e}{(N_i)^{1/3}} \qquad (7.3)$$

Effective frequency of ion-neutral collisions can be presented as [4,6–8]

$$v_{im} = \beta_{im}^0 N_m (T_i + T_m)^{1/2} \qquad (7.4)$$

where the coefficient β_{im}^0 accounts the difference of masses of different molecules, effects of nonelastic interaction between particles, polarization, and recharge of molecules (see details in References [4,6–8]). Furthermore, to analyze the effects of ambient magnetic field on charged particles, hyromagnetic frequencies of electrons, ω_H, and ions, Ω_H, are also introduced to estimate effects of charged particles magnetization. As was investigated in References [9,10], at altitudes of the lower ionosphere ($z < 120–150$ km) $\omega_H > v_{em}$, but $\Omega_H \ll v_{im}$, that is electrons are magnetized and ions are not. Hence, the degree of magnetization of ionospheric plasma, which is defined by $\Omega_H \omega_H \gg v_{im} v_{em}$, is very small, whereas in the upper ionosphere at altitudes more than 150 km, $\omega_H \gg v_{em}$ and $\Omega_H > v_{im}$, that is, both electrons and ions, and hence, ionospheric plasma are fully magnetized.

For actual ionospheric applications in radio communications and radars, another parameter of ionization is usually used [8–12, 46–48], $p = v_{ei}/v_{em}$, instead of the earlier defined parameter N/N_m. As was mentioned in References [8,9], it can be done in spite of the fact that the ionospheric plasma has mainly low temperature (from 200 K at 80–90 km to 2500–2800 K at the 500–600 km). In such conditions the cross-sections of collisions between electrons and ions are much greater than the cross-sections of collisions of electrons with neutrals. So, the peculiarity of the real ionospheric plasma consists of the fact that even $N/N_m \ll 1$, the parameter $p = v_{ei}/v_{em}$ becomes more than the unit. Therefore, electron-ion interactions are an essential part of the transport processes in the ionospheric plasma. Figure 7.4 presents the parameter ionization p for diurnal and nocturnal middle latitude
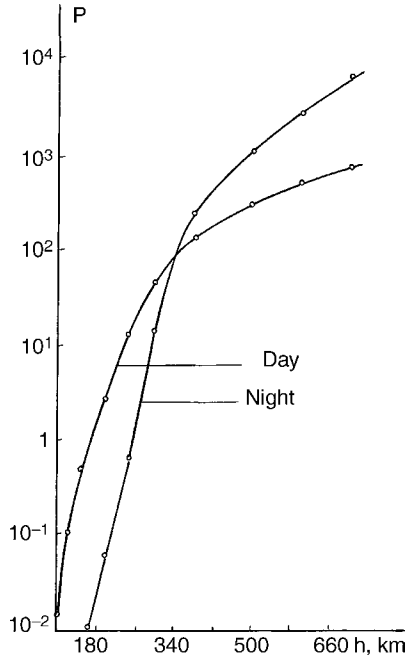
FIGURE 7.4. Parameter of plasma ionization versus height of the ionosphere above the ground surface.

ionosphere at altitudes of 90–700 km. It is clearly seen that such parameters can reach great values, though, in the ordinary sense the ionospheric plasma is weakly ionized. Another argument to use this parameter as a degree of plasma ionization, is based on the fact that at altitudes under consideration of 80–500 km, which mostly affects radio propagation, $N_m > N_e$ and $N_m > N_i$ provides the condition of stability of a full plasma pressure necessary for the transport process of diffusion and drift. Under such circumstances different disturbances of neutral molecules or atoms and their movement do not influence the diffusion of electrons and ions in the ionospheric plasma [8–10]. That is why, just as in References [8–10], we evaluated the degree of ionization of the ionospheric plasma by a parameter of ionization p shown in Figure 7.4 and presented in Table 7.1 for daily and nocturnal ionosphere. The increase in the degree of ionization in the ionosphere, observed in Figure 7.4, has a very simple physical explanation: with the increase of altitude the effective values of the collision frequencies of charged particles with neutrals fall, defined by Equations (7.3) and (7.5), whereas a frequency of electron–ion interactions increases, as defined by Equation (7.4), because with the growth of the height, the number of neutral plasma components quickly decreases, while the total number of ions in the ionosphere increases. It must be noted that beginning from $z > 500$ km (even this fact is not so important for radio communication), the growth of the parameter p decelerates with the increase in height, while the degree of plasma magnetization (as was mentioned above) is monotonically increasing with height.

TABLE 7.1. Parameter of Ionization p Altitudinal Dependence for Daily and Nocturnal Ionosphere

Heigh km	The part of day	The parameter of ionization, p	Heigh km	The part of day	The parameter of ionization, p	Heigh km	The part of day	The parameter of ionization, p
90	Day	7.5×10^{-4}	180	Day	1.78	350	Day	91.2
	Night	6.9×10^{-8}		Night	3.1×10^{-2}		Night	121.3
100	Day	1.75×10^{-2}	190	Day	2.19	400	Day	168.5
	Night	4.28×10^{-4}		Night	4.44×10^{-2}		Night	300
110	Day	7.1×10^{-2}	200	Day	2.93	450	Day	256.6
	Night	1.6×10^{-3}		Night	5.8×10^{-2}		Night	578.3
120	Day	9.35×10^{-2}	220	Day	4.72	500	Day	333
	Night	2.42×10^{-3}		Night	1.8×10^{-1}		Night	1000
130	Day	1.63×10^{-1}	240	Day	8.4	550	Day	384.5
	Night	3.92×10^{-3}		Night	4.3×10^{-1}		Night	2112
140	Day	2.8×10^{-1}	260	Day	18.1	600	Day	518.5
	Night	5.75×10^{-3}		Night	1.01		Night	243.9
150	Day	5.3×10^{-1}	280	Day	33.4	650	Day	634.2
	Night	8.37×10^{-3}		Night	2.87		Night	5001
160	Day	6.8×10^{-1}	300	Day	45	700	Day	704
	Night	1.05×10^{-2}		Night	15.5		Night	8889

Ionization-Recombination Balance in the Ionosphere. Changes of plasma components, electrons and ions (plasma is quasi-neutral, see above), in real time is determined by the equation of ionization balance

$$\frac{\partial N}{\partial t} = q_i - \alpha N^2 \tag{7.5}$$

This is actual if the processes of ionization and recombination are predominant with respect to transport processes. The latter, diffusion, thermo-diffusion and drift, are predominant beginning from 120–150 km, that is, from the *E*-layer of the ionosphere. So, Equation (7.5) is correct only in the *D*-layer and *E*-layer of the ionosphere. In (7.5) $q_i = q_{iO} + q_{iO_2} + q_{iN_2}$ is a total intensity of ionization contained from intensities for atom and molecule of oxygen, and molecule of nitrogen, α is a coefficient of dissociative recombination. This kind of recombination is predominant in the ionosphere and is described in the interaction of molecular ion M^+, with electron e^- accompanied by dissocation of molecular ion on two excited neutral atoms M^* [4–9]. For example, for molecular ion of oxygen the dissociative recombination gives [8,9]

$$O_2^+ + e^- \rightarrow O^* + O^* \tag{7.6}$$
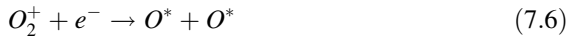
Therefore, during the process of dissociative recombination an amount of electrons, involved in this process during one second in the area of one square centimeter, can be presented as in Equation (7.5), that is, as αN^2. The coefficient of dissociative recombination can be presented as [8–10]:

$$\alpha = \alpha_1 \frac{N_{NO^+}}{N} + \alpha_2 \frac{N_{O_2^+}}{N} \tag{7.7}$$

Here, α_1 and α_2 are coefficients of dissociative recombination of ions NO^+ and O_2^+, respectively, which can be presented in the following form [8,9]:

$$\alpha_1 \approx 5 \cdot 10^{-7} \left(\frac{300}{T_e}\right)^{1.2} \tag{7.8a}$$

$$\alpha_2 \approx 2.2 \cdot 10^{-7} \left(\frac{300}{T_e}\right)^{0.7} \tag{7.8b}$$

According to (7.8), coefficients of dissociative recombination are decreased with the growth of the temperature of electrons. So, in *E*-layer and above, the concentration of electrons (i.e., plasma) is increased with the growth of their temperature. We must note that a detailed investigation of ionization–recombination balance in the ionosphere is fully described in References [1–9] and we refer the reader to these

excellent books. We will only note here that all presented formulas characterize only a local balance of ionization, because they were obtained without accounting for transport processes, which are actual and important at altitudes above the E-layer of the ionosphere. The transport processes, such as diffusion, thermo-diffusion and drift, are predominant in the F-layer of the ionosphere, determining here the maximum of plasma concentration. So, above this maximum, the transport processes are predominant where as below this maximum both processes the actual and at the lower E-layer and D-layer the recombination–ionization balance is predominant.

Transport Processes in the Ionosphere.   During the investigation of the effects of ionosphere on radio propagation, it is important to analyze transport processes in the ionosphere, diffusion, thermo-diffusion, and drift of ionospheric irregularities, large-scale and/or small-scale, connected with turbulent structure of the atmosphere at lower ionospheric altitudes [27], as well as with numerous instabilities of ionospheric plasma at the upper ionosphere [8,9]. To understand the main mechanisms of each process, it is important to compare the initial dimensions of the irregularities created in plasma and the characteristic scales of charge particles in plasma, which we briefly present following References [4–10]. Thus, according to the empirical presentation of ionospheric models [4–10], for noon ionospheric conditions and low or mode- rate solar activity, the mean free path of charged particles can be estimated as: for electrons λ_e is of about 30 cm to 10 km, for ions is about 0.5 cm to 2 km for $z = 90$–500 km. Radius of electron magnetization (called the *Larmor radius* [4–10]), ρ_{He}, is changed in the range of 1 to 5 cm, and that for ions, ρ_{Hi}, is from 0.4 m to 7.5 m at altitudes of 90–500 km. At the same time, the Debye radius, which defines the plasma quasi-neutrality (see definition above), is changed in the range of 0.5–1 cm at altitudes under consideration. The comparison of inhomogeneities of scales from several meters to several tens of kilometers, which under our consideration (see below) with above parameters allows us to state that below we can use the theory of magnetic hydrodynamics for all components of the ionospheric plasma: electrons, ions and neutral particles and estimate the influence of plasma irregularities of wide range of scales on radio propagation. This subject will be considered in the next sections.

The qualitative analysis carried out above has shown that all characteristic scales of plasma are less than the dimensions of plasma irregularities. Moreover, at altitudes beyond E-layer ($h > 160$–200 km) the transfer processes, diffusion, thermo-diffusion, and drift prevail compared with the chemical processes of ionization and recombination. Therefore, for description of transfer processes beyond altitudes of the upper E-layer, we can use a system of magneto-hydrodynamic equations for all components of the ionospheric plasma, electrons and ions, to describe the evolution of the irregular structures of ionospheric plasma of various nature. Usually, in solving the problems of dynamics of inhomogeneous ionospheric plasma at altitudes of upper E-layer and higher, the absence of the processes of ionization, attachment, detachment, and recombination is assumed, as well as the unifications between electrons and single-charge ions, and between the

ions of plasma irregularities and the ions of the background ionospheric plasma, as is usually done in References [8–10]. In this case a full system of transfer equation of plasma components (denoted by indexes $\alpha = e, i$) and neutral component (denoted by index $\alpha = m$) can be presented according to References [8–10] in the following form:

$$\frac{\partial N_\alpha}{\partial t} + \nabla \cdot \mathbf{J}_\alpha = 0 \tag{7.9a}$$

$$\frac{\partial N_m}{\partial t} + \nabla \cdot (\mathbf{U}_m N_m) = 0 \tag{7.9b}$$

$$\mathbf{j}_e = -\frac{\hat{\sigma}_e}{e}\left\{\mathbf{E} + \frac{1}{c}[\mathbf{U}_m, \mathbf{B}_0]\right\} - \hat{D}_{ee}\nabla N_e - \hat{D}_{Te}\frac{N_e}{T_e}\nabla T_e + N_e \mathbf{U}_m \tag{7.9c}$$

$$\mathbf{j}_i = \frac{\hat{\sigma}_i}{e}\left\{\mathbf{E} + \frac{1}{c}[\mathbf{U}_m, \mathbf{B}_0]\right\} - \hat{D}_{ii}\nabla N_i - \hat{D}_{Ti}\frac{N_i}{T_i}\nabla T_i + N_i \mathbf{U}_m \tag{7.9d}$$

$$MN_m\left[\frac{\partial \mathbf{U}_m}{\partial t} + (\mathbf{U}_m, \nabla)\mathbf{U}_m\right] = -\nabla(N_m T)\frac{\hat{\sigma}}{e} - \eta \mathbf{U}_m - \frac{1}{3}\eta\nabla(\nabla \mathbf{U}_m)$$
$$- m\hat{v}_{em}(N_e \mathbf{U}_m - \mathbf{j}_e) - M_i\hat{v}_{im}(N_i \mathbf{U}_m - \mathbf{j}_i) \tag{7.9e}$$

In the ionosphere, when there is any plasma irregularity, the electrical field and then the magnetic field closely related to this irregularity always arise. Therefore, Equations (7.5)–(7.6) must be completed by Maxwell's equations

$$\nabla \cdot \mathbf{E} = 4\pi e(N_i - N_e) \tag{7.10a}$$

$$\nabla \times \mathbf{E} = -\frac{\partial \mathbf{B}}{\partial t} \tag{7.10b}$$

$$\nabla \cdot \mathbf{B} = 0 \tag{7.10c}$$

$$\nabla \times \mathbf{B} = \frac{4\pi e}{c}(\mathbf{j}_i - \mathbf{j}_e) \tag{7.10d}$$

In the last Equation (7.10d) of the system, the displacement current $\frac{1}{4\pi e}\frac{\partial \mathbf{D}}{\partial t}$ is omitted from consideration, as only quasi-stationary processes for the plasma concentration and temperature are taken into account, as well as for the ambient electrical $\mathbf{E}$ and magnetic $\mathbf{B}$ fields. In Equations (7.8)–(7.10) the additional notations are introduced

$$\hat{D}_{ee} = \hat{D}_e\left(1 + \frac{T_i}{T_e}\right) - \frac{T_e}{e^2 N_e}\hat{\sigma}_e \tag{7.11a}$$

$$\hat{D}_{ii} = \hat{D}_i\left(1 + \frac{T_e}{T_i}\right) - \frac{T_i}{e^2 N_i}\hat{\sigma}_i \tag{7.11b}$$

$\hat{D}_e$, $\hat{D}_i$, $\hat{D}_{Te}$, $\hat{D}_{Ti}$ and $\hat{\sigma}_e$, $\hat{\sigma}_i$ and $\mathbf{j}_i$, $\mathbf{j}_e$ are the tensors of diffusion, thermo-diffusion, and conductivity and the current densities for electron and ion components of the plasma, respectively; $\mathbf{U}_m$ is the vector of the hydrodynamic velocity of molecules (atoms) of the atmospheric gas; η is the coefficient of viscosity; c is the speed of light; $\hat{v}_e$, $\hat{v}_i$ are the tensors of collisions of electrons and ions, respectively, with molecules and atoms of the neutral gas. As was shown in References [8–10] for ionospheric altitudes beyond 160–170 km, a degree of plasma ionization high enough ($v_{ei} \gg v_{em}$) and the charge particles, electrons and ions, are also magnetized ($\omega_H \gg v_{em}, \Omega_H \gg v_{im}$).

With satisfactions of conditions of quasi-neutrality and ambipolar diffusion of electrons and ions of the ionospheric plasma

$$N_e \approx N_i = N \tag{7.12a}$$

$$(\nabla \mathbf{j}_e = \nabla \mathbf{j}_e = \nabla \mathbf{j}) \tag{7.12b}$$

and accounting the temperature distribution of the charged particles during the ambient heating, which leads to the creation of a nonuniform distribution of the electron and ion concentration

$$\frac{\partial T_e}{\partial t} = \frac{\nabla(\hat{\kappa}_e \nabla T_e)}{N_e} + \delta_{ei} v_{ei}(T_e - T_i) - \delta_{em} v_{em}(T_e - T_m) + \frac{2}{3} \frac{Q}{N_e} \tag{7.13a}$$

$$\frac{\partial T_i}{\partial t} = \frac{\nabla(\hat{\kappa}_i \nabla T_i)}{N_e} + \delta_{ei} v_{im}(T_i - T_m) + \frac{2}{3} \frac{Q}{N_e} \tag{7.13b}$$

we finally obtain the self-matching system of three-dimensional equations of plasma transfer: diffusion, thermo-diffusion and drift.

In conditions of arbitrary degree of ionization and magnetization of the ionospheric plasma, the tensors of collisions $\hat{v}_{ei} = \hat{K}_{ei} v_{ei}$, $\hat{v}_{em} = \hat{K}_{em} v_{em}$, $\hat{v}_{im} = \hat{K}_{im} v_{im}$ can be transformed, accounting that $\hat{K}_{ei}$, $\hat{K}_{em}$, $\hat{K}_{im} \rightarrow \hat{1}$, into the simple scalar values. In this case called the *elementary theory* [8–10], in the accuracy of magnitudes of order $\gamma = \frac{m v_{em}}{M_i v_{im}} \ll 1$ (working from $h > 120$ km), we can, following References [8–10], from equations of macroscopic movement of electrons and ions

$$m N_e \hat{v}_{em} \mathbf{V}_e = -e N_e \mathbf{E} - \frac{e}{c} N_e [\mathbf{V}_e, H_0] - T_e \nabla N_e + m \hat{v}_{ei} N_e (\mathbf{V}_e - \mathbf{V}_i) \tag{7.14a}$$

$$M_i N_i \hat{v}_{im} \mathbf{V}_e = e N_i \mathbf{E} - \frac{e}{c} N_i [\mathbf{V}_i, H_0] - T_i \nabla N_i + M_i \hat{v}_{ei} N_i (\mathbf{V}_i - \mathbf{V}_e) \tag{7.14b}$$

obtain the components of tensors of diffusion, thermo-diffusion and conductivity, which in the case of nonisothermal plasma ($T_e \neq T_i$) can be written in the

following form:

$$D_{e\parallel} = \frac{T_e(1 + T_i/T_e)(1 + \gamma p)}{mv_{em}(1 + p)}, \quad D_{i\parallel} = \frac{T_i(1 + T_e/T_i)(1 + 2p)}{M_i v_{im}(1 + p)},$$

$$D_{e\perp} = \frac{T_e(1 + T_i/T_e)}{mv_{em}A}\left[(1 + p)(1 + 2\gamma p) + Q_H^2(1 + 2p)\right],$$

$$D_{i\perp} = \frac{T_i(1 + T_e/T_i)}{M_i v_{im}A}\left[(1 + p)(1 + 2p) + q_H^2(1 + 2\gamma p)\right],$$

$$D_{e\wedge} = \frac{T_e(1 + T_i/T_e)q_H}{mv_{em}A}(1 + Q_H^2 + 3\gamma p),$$

$$D_{i\wedge} = \frac{T_i(1 + T_e/T_i)Q_H}{M_i v_{im}A}(1 + q_H^2 + p/\gamma),$$

$$A = (1 + p)^2 + q_H^2(1 + 2\gamma p + Q_H^2)$$

$$D_{Te\parallel} = \frac{T_e(1 + \gamma p)}{mv_{em}(1 + p)}, \quad D_{Ti\parallel} = \frac{T_i}{M_i v_{im}},$$

$$D_{Te\perp} = \frac{T_e\left[(1 + p)(1 + Q_H^2) + \gamma p^2\right]}{mv_{em}B}, \quad D_{Ti\perp} = \frac{T_i\left[p^2 + (1 + \gamma p)(q_H^2 + 2p)\right]}{M_i v_{im}B},$$

$$D_{Te\wedge} = -\frac{T_e q_H\left[(1 + Q_H^2) + 2\gamma p\right]}{mv_{em}B}, \quad D_{Ti\wedge} = \frac{T_i Q_H\left[\gamma(q_H^2 + 2p)\right]}{M_i v_{im}B},$$

$$B = p^2 + (q_H^2 + 2p)(1 + Q_H^2 + 2\gamma p)$$

$$\sigma_{e\parallel} = \frac{e^2 N_e}{mv_{em}(1 + p)}, \quad \sigma_{i\parallel} = \frac{e^2 N_i}{M_i v_{im}(1 + p)},$$

$$\sigma_{e\perp} = \frac{e^2 N_e}{mv_{em}A}(1 + Q_H^2 + p), \quad \sigma_{i\perp} = \frac{e^2 N_i}{M_i v_{im}A}(1 + q_H^2 + p/\gamma),$$

$$\sigma_{e\wedge} = -\frac{e^2 N_e q_H}{mv_{em}A}(1 + Q_H^2 + \gamma p), \quad \sigma_{i\wedge} = -\frac{e^2 N_i Q_H}{M_i v_{im}A}(1 + q_H^2 + p/\gamma),$$

$$\kappa_{e\parallel} = \frac{N_e T_e}{mv_{em}(1 + p)}, \quad \kappa_{i\parallel} = \frac{N_i T_i}{M_i v_{im}(1 + v_{ii}/v_{im})},$$

$$\kappa_{e\perp} = \frac{N_e T_e}{mv_{em}}\frac{(1 + p)}{\left[q_H^2 + (1 + p)^2\right]}, \quad \kappa_{i\perp} = \frac{N_i T_i}{M_i v_{im}}\frac{(1 + v_{ii}/v_{im})}{\left[Q_H^2 + 1 + (1 + v_{ii}/v_{im})^2\right]}$$

$$\kappa_{e\wedge} = \frac{N_e T_e}{mv_{em}}\frac{q_H}{\left[q_H^2 + (1 + p)^2\right]}, \quad \kappa_{i\wedge} = \frac{N_i T_i}{M_i v_{im}}\frac{Q_H}{\left[Q_H^2 + 1 + (1 + v_{ii}/v_{im})^2\right]}$$

Here, in (7.9) $[\mathbf{V}_\alpha, \mathbf{H}_0]$ is the cross-product of two vectors $\mathbf{V}_\alpha$ and $\mathbf{H}_0$ for electrons ($\alpha = e$) and ions ($\alpha = i$); in (7.12)–(7.14) parameters $\sigma_{\alpha\parallel}$, $D_{\alpha\parallel}$ and $D_{T\alpha\parallel}$, $\sigma_{\alpha\perp}$, $D_{\alpha\perp}$

and $D_{T\alpha\perp}$, $\sigma_{\alpha\wedge}$, $D_{\alpha\wedge}$ and $D_{T\alpha\wedge}$ are the longitudinal, perpendicular (Pedersen) and crossing (Halls) components of coefficients of conductivity, diffusion, and thermo-diffusion, respectively, relative to the electrical and magnetic fields, accounting that $\mathbf{E} \perp \mathbf{H}$ and $\mathbf{E} = \mathbf{E}_0 + \mathbf{E}_p$ is a full electrical field in the ionosphere, where $\mathbf{E}_0$ is the ambient electric field and $\mathbf{E}_p = -\nabla\varphi$ is the intrinsic potential field of polarization (sometimes called the *ambipolar field*), where φ is the potential of this field.

In the Equations (7.13a)–(7.13b) $\delta_{ei} \approx 2m/M_i$, $\delta_{em} \approx 10^{-3}$, $\delta_{im} \approx 1$ are, respectively, the fractions of energy lost by electrons in collisions with ions and neutrals and also by ions in collisions with neutrals; an external source of heating is associated with high-energy photoelectrons forming in the ionosphere in the process of ionization of the neutral component by solar ultra-violet radiation. As was shown in References [21–26], the real coefficients of diffusion are changed with altitude of the ionosphere nonmonotonically. Thus, for $D_{e\parallel}$ and $D_{i\perp}$ the wide maxima are observed at the 200 km and 150 km, respectively; for $D_{e\perp}$ the wide minimum is observed at altitudes of 200–250 km and the maximum at altitude of about 300 km. As for the coefficient of ion diffusion along the magnetic field, $D_{i\parallel}$, it grows monotonically with increase of ionospheric altitudes.

Additional evaluations carried out in References [21–26] have shown that components of the tensor of conductivity, $\sigma_{e\perp}$, $\sigma_{i\perp}$, $\sigma_{i\parallel}$ and $\sigma_{e\parallel}$, have the maxima at altitudes of 100, 150, 250 and 300 km, respectively. The same tendency of nonmonotonically height dependence with local maxima was observed for other transport coefficients [21–26]. Hence, apart from the macro-scale regular distribution of plasma in the ionosphere, there occur the naturally created nonregular distributions of plasma concentration, the so-called macroscale plasma irregularities, having dimensions from hundreds of kilometers (large-scale disturbances) to tens and few meters (small-scale disturbances), evolution of which can be described by the self-matching system of diffusion, thermo-diffusion, and drift (7.8)–(7.10). At the same time, the peculiarities of the processes of relaxation of such plasma irregularities are determined by the coefficients of transfer of electron and ion components of inhomogeneous plasma according to (7.11)–(7.14).

So, during the analysis of the processes of formation and evolution of plasma inhomogeneities in the ionosphere and their influence on radio propagation, it is necessary to account the whole spectrum of physical–chemical processes which form both large-scale regular and small-scale irregular structures in the ionospheric plasma, the effects of which we will investigate in the following section.

7.1.2. Main Effects of Radio Propagation Through the Ionosphere

Now we will discuss the common effects of the ionosphere as a continuous plasma layered medium.

Refraction. The plasma content of the ionosphere changes the effective refractive index encountered by radio waves transmitted from the Earth, changing their direction by increasing wave velocity. Depending on special conditions, which are
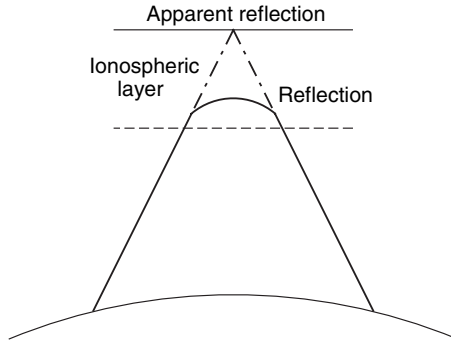
FIGURE 7.5. The reflection phenomenon in the ionosphere.

determined by wave frequency, elevation angle of ground-based or air-based vehicle antenna, and electron/ion content, the radio wave may fail to escape from the Earth and may appear to be reflected back to the Earth. This process is actually refraction (see Fig. 7.5). The same effects are found in Chapter 6 for the troposphere as a gaseous quasi-homogeneous continuum. The refractive index n_r of an ordinary radio wave depends on both N and the wave frequency f according to References [1–3,7,11]

$$n_r^2 = 1 - \frac{f_c^2}{f^2}$$ (7.15)

where f_c is the critical frequency of plasma at the given height, given by [1–3,7,11]:

$$f_c = 8.9788\sqrt{N}\,[\text{Hz}]$$ (7.16)

Apparent reflection from the ionosphere back to the Earth, as shown in Figure 7.5 extracted from References [1–3], can occur whenever the wave frequency is below this critical frequency f_c, from which follows the ''working'' frequencies for satellite communications must be above this critical frequency f_c. The greatest critical frequency usually observed in the real ionosphere does not exceed 12 MHz. This is the other extreme of an overall atmospheric ''window'' which is bound at the high-frequency end by atmospheric absorption at hundreds of gigahertz, as is shown in Chapter 6. A number of ionospheric effects for radio waves with frequencies above 12 MHz, which are very important in land-satellite communications, will be considered briefly according to the corresponding references [1–3,7].

Faraday Rotation. A linearly polarized wave rotates during its passage through the ionosphere because of the combined effects of the free electrons and the Earth's magnetic field. This phenomenon is called Faraday rotation. The angle associated

with this rotation depends on the frequency and the total number of electrons encountered along the radio path, according to References [1–3,7]

$$\phi = \frac{2.36 \cdot 10^{20}}{f^2} \langle B \rangle N_{\Sigma} \qquad (7.17)$$

where f is in hertz and $\langle B \rangle = \mu \langle H \rangle$ is the average induction of magnetic field of the Earth (called *geomagnetic* [8–12,44–46]) at the ionospheric altitudes with a typical value $\langle B \rangle = 7 \cdot 10^{-21}$ Wb $\cdot m^{-2}$ and $\langle H \rangle$ is the average strength of the magnetic field. Here we use average values of the magnetic field, as many satellite and rocket observations of this parameter of the ionosphere have shown that it varies randomly with daytime, latitude, and longitude of the Earth [4–7,9,10]. The parameter N_{Σ} in Equation (7.11) is the total number of electrons contained in a column of cross-sectional area 1m^2 and a length equal to the path length, that is, the total electron content, N_{Σ} [1–3,7]

$$N_{\text{tot}} = \int_{0}^{r_T} N dr \quad [\text{electrons} \cdot \text{m}^{-2}] \qquad (7.18)$$

The total electron content for a zenith path varies over the range to electrons per square meter, with the peak taking place during the daytime.

   If linearly polarized waves are used, extra path loss will result, due to depolarization consequence is that, between the satellite antennas and ground-based or air-based antennas there is a polarization mismatch. There are some ways to minimize this extra path loss. In fact, as was discussed in References [1–3,7,11], by use of circular polarized waves one can exclude the depolarization effect. Moreover, one can vary physically or electronically the receiving antenna polarization or align the antennas to compensate for an average value of the rotation, provided that the resulting mismatch loss is acceptable. All details about such methods can be found by the reader in References [1–3,7,11].

Absorption of Radio Waves. In the absence of the local inhomogeneities of the ionospheric plasma, the radio wave passing through the ionosphere as a homogeneous plasma continuum, is absorbed due to pair interactions between electron and ion components of plasma. In such a situation, the intensity of radio wave is determined as [7,11,46]

$$I = I_0 \exp\left\{ -2\frac{\omega}{c} \int \kappa ds \right\} \qquad (7.19)$$

where I_0 is the intensity of the incident radio wave, κ is the coefficient of absorption, ω is the angular frequency of the incident wave, $\omega = 2\pi f$, c is the velocity of light in free space, $c = 3 \cdot 10^8 \text{m/s}$, and integration in Equation (7.13) occurs along the wave trajectory s.

For weakly magnetized plasma, when $\omega \gg \omega_{He}$ (ω_{He} is the hydro-frequency of plasma electrons), and for high radiation frequencies, when $\omega \gg \omega_{pe}$ (ω_{pe} is the plasma frequency, $\omega_{pe} = (e^2 N / \varepsilon_0 m_e)^{1/2}$, e and m_e are the charge and mass of electron, respectively, and ε_0 is the average dielectric parameter of the ambient ionospheric plasma), the coefficient of absorption can be presented in the following form:

$$\kappa = \frac{1}{2} \frac{\omega_{pe}^2 (\nu_{em} + \nu_{ei})}{\omega[\omega^2 + (\nu_{em} + \nu_{ei})^2]} \tag{7.20}$$

Here, ν_{em} and ν_{ei} are the frequencies of interactions of plasma electrons with neutral molecules and atoms, and with ions, respectively, defined in References [8–10]. To estimate losses due to absorption, that is, the part of energy of radio wave that is absorbed in the quasi-regular layers of the ionosphere, from D to F, a special value of absorption in decibels (dB) is usually introduced [7–12]

$$A_\omega = 10 \log \frac{I_0}{I} \approx \frac{4.3}{c} \int \frac{\omega_{pe}^2 (\nu_{em} + \nu_{ei})}{[\omega^2 + (\nu_{em} + \nu_{ei})^2]} \, ds \tag{7.21}$$

The expected value of absorption at the ionospheric radio links is estimated usually by using the measured radiometric absorption along radio traces at the fixed frequency and by experimental knowledge of frequency dependence of absorption determined by (7.15). We do not enter into details on how to measure these parameters and address the reader to special literature [8–10].

Group Delay. Due to the effect of refraction of the radio wave passing through the ionosphere, the resulting phase difference between waves expected in LOS direction and that observed really in refracted direction is a function of the corresponding shift in physical path length, Δr (in m) [1–3]:

$$\Delta r = \frac{40.3}{f^2} N_\Sigma \tag{7.22}$$

The shift in physical path length leads to a corresponding time delay, τ (in sec) [1–3]

$$\tau = \frac{\Delta r}{c} = \frac{40.3}{cf^2} N_\Sigma \tag{7.23}$$

We can use this formula as a definition of the time delay of radio waves passing through the quasi-homogeneous ionospheric plasma.

Dispersion. As follows from (7.23), the time delay of waves arriving at the receiver is frequency dependent. Thus, the dispersion properties of radio waves passing

through a homogeneous plasma layer can be determined by a derivative of the time delay τ over the frequency (in s/Hz), or according to (7.23) [1–3],

$$\frac{d\tau}{df} = -\frac{80.6}{cf^3} N_\Sigma \tag{7.24}$$

For the purpose of satellite communication, using knowledge of radio channel bandwidth Δf, one can obtain the differential time delay as [1–3]

$$\Delta\tau = \frac{d\tau}{df}\Delta f = -\frac{80.6}{cf^3}\Delta f \cdot N_\Sigma \tag{7.25}$$

This parameter describes the delay-spread of the signal total intensity due to the effect of refraction of radio wave in the quasi-homogeneous layered ionosphere.

Ionospheric Scintillation. There is a wind presented in the ionosphere, just as in the troposphere considered in Chapter 6, which causes rapid variations in the local electron density, particularly close to sunset. These density variations cause changes in the refraction of the radio wave in the Earth–satellite channel and hence of changes in signal levels. Portions of the ionosphere then act like lenses, cause focusing, defocusing, and divergence of the wave and hence lead to signal level variations, that is, the signal scintillation (see Section 7.2).

To summarize the main propagation effects through the ionosphere as a plasma continuum we must follow the results presented above. As follows from the literature [1–3], for frequencies beyond the range of 20 to 50 GHz, which are usually used for construction of Earth–satellite communication links, the effects of Faraday rotation are negligible (about a dozen of degrees), the propagation delay is very small (a dozen nanoseconds), and the radio frequency dispersion is very weak (a dozen picoseconds per one megahertz), so we can withdraw them from computations. As for attenuation, signal amplitude, and phase scintillations (i.e. fading), these effects are strongly dependent on nonregular features of the ionosphere, usually called inhomogeneities or irregularities [1–12]. Accumulative effects of which created inhomogeneous structure of the ionosphere, consisting of nonregular and sporadic layers. This will be a subject of further discussions.

7.2. EFFECTS OF THE INHOMOGENEOUS IONOSPHERE ON RADIO PROPAGATION

Let us now introduce the reader to some very important "thin" effects on radio propagation that occur in the ionospheric inhomogeneous plasma medium consisting of different kinds of irregularities in a wide range of scales: from small to large [7–12].

The ionosphere varies randomly in time and space such that the amplitude and phase of propagating waves may similarly fluctuate randomly in these domains. The

inhomogeneity of the ionosphere is an important factor in determining VHF/X-band wave propagation conditions (see References [1–3,7,11,12]). As a result, interest in satellite communications has stimulated investigations of ionospheric properties, in particular, the analysis of the spatial–temporal distribution of ionospheric irregularities [8–10].

Many experiments are carried out using ground facilities (radars and ionosondes) [13–20]. The methods of active modification of the ionosphere [21–27] and direct satellite measurements [28,29] show that in the normal ionosphere there exists a wide spectrum of irregular inhomogeneities, which cause a number of radio physical effects, such as interference, scattering, diffraction, and refraction of radio waves passing through the ionosphere, variations of the incident angles of reflected waves, the "multirays effect," and so on [30–37]. When waves are propagated through an irregular medium, small-angle scattering causes what is known as scintillation. We must note that the same phenomenon was found in the troposphere (see Section 6.3). All these effects result in amplitude and phase fluctuations of radio signals near the ground surface, change in the duration and shape of radio waves, and finally a decrease in the signal-to-noise ratio (SNR or S/N).

The influence of inhomogeneities with various scales (large-scale and small-scale) on the effectiveness of the satellite-terrestrial communication will be discussed in Sections 7.2.1 to 7.2.3. It should be emphasized that because of the nature of the problem, it is necessary to employ various approximations to obtain useful results and therefore approximation techniques applicable to a variety of different plasma inhomogeneities are presented.

7.2.1. Propagation Effects of Large-Scale Inhomogeneities

In a spherical-symmetric homogeneous ionosphere, radio waves propagate in a plane of a *great circle* [1–7]. In the presence of large-scale inhomogeneities (with the horizontal scale L larger than the radius of the first Fresnel zone $d_F = (\lambda R)^{1/2}$, where λ is the wavelength and R is the distance from the ground facilities to the inhomogeneous area of the ionosphere, $L \gg d_F$) the radio waves can change their direction from this plane.

Main Equations. The wave equation (3.142), introduced in Chapter 3 for the description of radio wave propagation in an isotropic medium, such as plasma, written in Cartesian coordinate system with the origin in the center of the Earth and for the radiation frequency exceeding plasma hydromantic frequency, $\omega_0 \gg \omega_{He}$, can be reduced to the following form:

$$\Delta E + k_0^2 \varepsilon E = 0 \qquad (7.26)$$

where E is the component of electric field of the radio wave along the radius-vector **r**, $k_0 = 2\pi/\lambda$, $\varepsilon = \varepsilon(\mathbf{r})$ is the complex relative dielectric permittivity of the ionospheric plasma, $R = |\mathbf{r}|$, ω_0 is the wave frequency, ω_{He} is the electron hydro frequency, and c is the speed of light. Neglecting absorption and taking the case

when the frequency ω_0 is more than the plasma frequency ω_{pe} the dielectric permittivity can be presented as

$$\varepsilon = 1 - \frac{\omega_{pe}^2}{\omega_0^2} \tag{7.27}$$

Clearly the plasma frequency is a function of the spatial coordinates. Let us present the field E as [7,11,12]

$$E = E(\mathbf{r}) \exp[i\Phi(\mathbf{r})] \tag{7.28}$$

where E is the amplitude and $\Phi(\mathbf{r})$ is the phase of the radio wave. The wave vector is

$$\mathbf{k} = \nabla\Phi(\mathbf{r}) \tag{7.29}$$

For small variations of the amplitude at distances comparable with the wave length, from (7.26)–(7.29) one obtains

$$k^2 = k_0^2 \varepsilon(\mathbf{r}) \tag{7.30}$$

Method of Characteristics. After differentiating Equation (7.30) and knowing the relationship $\nabla\mathbf{k} = \nabla\nabla\Phi(\mathbf{r}) = 0$, the equation for the wave vector $\mathbf{k}$ was found to be [11,12]

$$(\mathbf{k}\,\nabla\,\mathbf{k}) = (1/2)k_0\nabla\varepsilon(\mathbf{r}) \tag{7.31}$$

The solution of Equation (7.31) can be defined using the method of characteristics used in References [11,12]. This method transforms (7.31) into a characteristic equation, which in the spherical coordinate system $\{r, \theta, \varphi\}$ can be presented for all the components of wave vector $\mathbf{k} = \{k_r, k_\varphi, k_\theta\}$ as

$$\frac{dr}{k_r} = r\frac{d\theta}{k_\theta} = r\sin\theta\frac{d\varphi}{k_\varphi} = \frac{dk_r}{\dfrac{k_0^2}{2r^2}\dfrac{\partial(r^2\varepsilon)}{\partial r} - \dfrac{k_r^2}{r}} = \frac{dk_\theta}{\dfrac{k_0^2\cos\theta}{r} - \dfrac{k_0^2}{2r}\dfrac{\partial\varepsilon}{\partial\theta} - \dfrac{k_r k_\theta}{r}}$$
$$= \frac{dk_\varphi}{\dfrac{k_0^2}{2r\sin\theta}\dfrac{\partial\varepsilon}{\partial\varphi} - \dfrac{k_\theta k_\varphi}{r}\cot\theta - \dfrac{k_r k_\varphi}{r}} \tag{7.32}$$

From expression (7.32) it follows that

$$\frac{\partial r}{\partial\varphi} = \frac{rk_r}{k_\theta}, \qquad \frac{\partial\varphi}{\partial\theta} = \sin\theta\frac{k_\varphi}{k_\theta} \tag{7.33}$$

After a differentiation of (7.32) over the θ, we finally get

$$\frac{\partial^2 \varphi}{\partial \theta^2} + 2 \cot \theta \frac{\partial \varphi}{\partial \theta} + \frac{1}{2} \sin 2\theta \left(\frac{\partial \varphi}{\partial \theta} \right)^3 = \frac{k_0^2}{2k_0^2 \sin^2 \theta} \frac{\partial \varepsilon}{\partial \varphi} - \frac{1}{2} k_0^2 \frac{\partial \varphi}{\partial \theta} \frac{\partial \varepsilon}{\partial \theta} \qquad (7.34)$$

If inhomogeneities do not exist, that is, $\partial \varepsilon / \partial \varphi = \partial \varepsilon / \partial \theta = 0$, then from (7.34) the integral becomes

$$\tan \theta \sin(\varphi - \varphi_0) = C_0 \qquad (7.35)$$

where φ_0 and C_0 are the integration constants obtained. Equation (7.35) for the selected C_0 and φ_0 describes a circle with its center at the origin of the coordinate system. Hence in References [11,12] a rule followed that is: *In the homogeneously-layered ionosphere (independent of θ and φ) the ray trajectory lies in the plane of a great circle*.

However, in the presence of large-scale irregularities the derivative $d\varphi / d\theta = 0$, but $d\varepsilon / d\theta \ll 1$. This enables terms proportional to $(d\varphi / d\theta)^3$ and $(d\varphi / d\theta)(\partial \varepsilon / \partial \theta)$ to be neglected. Thus the ray trajectory in a weak inhomogeneous plasma is defined by the equation:

$$\frac{\partial^2 \varphi}{\partial \theta^2} + 2 \cot \theta \frac{\partial \varphi}{\partial \theta} = \frac{1}{2} \sin^2 \theta \frac{\partial \varepsilon}{\partial \varphi} \qquad (7.36)$$

As was shown in References [11,12], analyzing Equation (7.36), it results that: *the existence of large-scale inhomogeneities causes the ray trajectory to deviate from the plane of the great circle*.

The same effect, defined as refraction in the troposphere, is discussed in Section 6.2.

The Curved Smooth Screen Model. The problem of multi-mode reflection from ionospheric layers can be resolved by using (7.31). However, there exists a simpler method based on the model of a curved smooth screen moving with respect to the observer. This model is correct if $\omega_{pe} \gg \omega_0$, where ω_{pe} is a critical frequency of plasma for each ionospheric layer, and $L \gg d_F$. The geometric optic approximation is applied in this method. The simplest model of a curved mirror is the smooth screen with a sinusoidal shape, which moves with a constant speed without changing shape. Let us consider a rectangular coordinate system $\{x, y, z\}$ with z-axis in the vertical direction and the base on the ground surface. The receiver and transmitter are at the origin of the system, the altitude z is a function of time t and coordinate $x, z = z(x, t)$, as is shown in Figure 7.6, according to References [11,12]. The coordinates of the reflected points are defined from the following condition:

$$Z(X, t) \frac{\partial Z(X, t)}{\partial X} = -X \qquad (7.37)$$
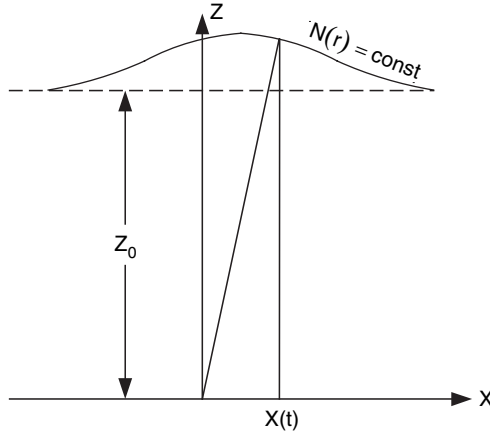
FIGURE 7.6. Modeling of the ionospheric layer by a sinusoidal layer.

If ionospheric inhomogeneities have the shape of a running wave with amplitude δ, wavelength Λ, and period T, then

$$Z(X,t) = Z_0[1 + \delta \sin 2\pi(X/\Lambda - t/T)] \tag{7.38}$$

and from (7.37) it follows that

$$(2\pi Z_0^2 \delta/\Lambda) \cos 2\pi(X/\Lambda - t/T)[1 + \delta \sin 2\pi(X/\Lambda - t/T)] = -X \tag{7.39}$$

Here, Z_0 is the average height of the reflected level. For relatively small oscillations of the reflected level ($\delta \ll 1$) ordinates X of the reflected points are found from the solution of the transcendental equation [11,12]

$$(2\pi Z_0^2 \delta/\Lambda) \cos 2\pi(X/\Lambda - t/T) = -X \tag{7.40}$$

From (7.40), it follows that the number of solutions depend on the position of the screen and on the amplitude δ. As was shown in References [11,12], the solution is unique if

$$2\pi Z_0^2 \delta/\Lambda < 1 \tag{7.41}$$

Inequality in (7.41) represents the condition of a single ray reflection from the smooth surface. If the condition for (7.41) is not valid, there are several rays forming the interference picture at the receiving point.

From formulas (7.37) and (7.38) we can calculate the incident angle θ' of the radio wave at the receiving point

$$\cot \theta' = X/Z = (2\pi Z_0 \delta/\Lambda) \cos 2\pi(X/\Lambda - t/T) \tag{7.42}$$

The maximum ray reflection from the vertical axis, which is a half width of the angle spectrum γ, equals

$$\gamma = 2\pi Z_0 \delta / \Lambda \tag{7.43}$$

Analysis of (7.40) presented in References [11,12] has shown that even very small oscillations of the height of equal plasma density level lead to the multimode reflection of radio signals, to the growth of the angular spectrum width of waves, and to interference.

Amplitude and Phase of Reflected Waves. If A_0 is the amplitude of the signal reflected from the level of equal plasma density, then the amplitude A of a radio wave reflected from the smooth surface at the point X is [11,12]

$$A(X,t) = \frac{A_0}{(1 - Z_0/\rho)} \tag{7.44a}$$

where $\rho = [1 + (dZ/dX)^2]^{3/2}/(d^2Z/dX^2)$ is the radius of curvature of the screen at the point (X, Z). Relationship (7.44a) describes the focusing and defocusing effects of reflected radio waves caused by large-scale inhomogeneities. The phase at the receiving point is

$$\Phi(X,t) = 2\omega R/c + \pi/4 \tag{7.44b}$$

where R is the optical path length from the reflector to the receiving point, factor $\pi/4$ corresponds to the change of wave phase when reflection from the ionosphere takes place. When oblique propagation of radio waves takes place for large distances the ray is reflected from an ionospheric surface of about ten thousand square kilometers. Such a surface contains many inhomogeneities, with about 20–100 km scales, on which radio wave scattering takes place. In the geometrical-optics approximation, the wave scattering on the ionospheric density fluctuations is the same as the scattering on the rough surface. If now the radio wave falls on the bottom boundary of the ionosphere under the angle θ_0, then the angle $\theta = \theta(X, Y, Z)$ will be changed according to Snell's law

$$[\varepsilon(X, Y, Z)]^{1/2} \sin \theta(X, Y, Z) = \sin \theta_0 \tag{7.45}$$

during the field penetration to the upper altitudes. At the turning point $Z = Z_m(X, Y)$, the angle $\theta = \pi/2$ and reflection takes place. The height of a turning point is defined as a minimum root $Z = Z_m$ of Equation [11,12]

$$1 - \varepsilon(X, Y, Z) = \cos^2 \theta_0 \tag{7.46a}$$

If $N_0(Z)$ is an average concentration in the ionospheric level and $N_1(Z)$ is a disturbed density caused by the plasma inhomogeneities, then the left part of (7.46a) can be rewritten as

$$1 - \varepsilon(X, Y, Z) = 1 - \widetilde{\varepsilon}_0 - \widetilde{\varepsilon}_1 \tag{7.46b}$$

where

$$\widetilde{\varepsilon}_0 = e^2 N_0(Z) / m_e \omega^2 \varepsilon_0 \tag{7.47a}$$

and

$$\widetilde{\varepsilon}_1 = e^2 N_1(Z) / m_e \omega^2 \varepsilon_0 \tag{7.47b}$$

In the absence of inhomogeneities, the height of the reflection point (turning point) Z_{0m} is a function of coordinates X and Y, and the thickness of the reflected layer is defined from vertical oscillations of equal electron density level (from mean square deviation of the turning point from the height Z_{0m}). Thus, even weak large-scale inhomogeneities also increase the thickness of the reflecting layer. The radio wave trajectory due to horizontal changes of the screen height has a complex oscillatory character.

If the frequency of the ionospheric layer is f_0, radio wave reflection can occur for frequencies $f > f_0$ cosec θ_0 and radio wave penetration for frequencies $f < f_0$ cosec θ_0. The first condition shows the possibility of radio wave communication for frequencies more than the maximum useful frequency. The second condition shows the possibility to reflect and scatter radio waves with frequencies $f < f_0$ cosec θ_0.

Radio Waves with Frequency $\omega > \omega_{pe}$. Now some effects of large-scale inhomogeneities for radio waves with frequency $\omega > \omega_{pe}$ are presented, where ω_{pe} is a plasma frequency of the ionospheric layer defined above.

Let us suppose, as in References [11,12], that the wave propagates vertically down and passes through the layer with an inhomogeneous density. After passing the layer at the height Z_0 the phase Φ of the wave will be a function of the horizontal coordinate X (see Fig. 7.7, according to References [11,12]).

$$\Phi(X_1) = \frac{\omega}{c} R(X_1) \tag{7.48}$$

It can be seen that inhomogeneities are stretched along the Y-axis and N_1 does not depend on Y. For radio frequencies with $\omega > \omega_{pe}$, $\varepsilon_0 \sim 1$ and

$$R(X_1) \sim \frac{e^2}{m_e \omega^2 \varepsilon_0} N_1(X_1) \tag{7.49}$$
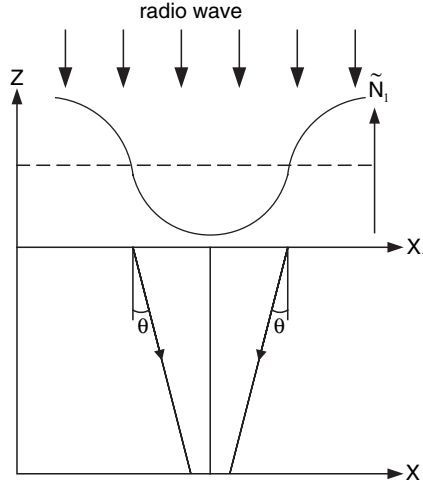
FIGURE 7.7. Penetration of radio waves through the sinusoidal ionospheric layer.

where

$$N_1(X_1) = \int N_1(X_1, Z)\mathrm{d}z \tag{7.50}$$

A ray passing through the layer at the point X_1 changes its trajectory from the vertical axis by the angle θ

$$\theta = \frac{c}{\omega}\frac{\partial \Phi}{\partial X_1} = \frac{\partial R_1}{\partial X_1} \tag{7.51}$$

and comes to the Earth's surface at the point

$$X = X_1 + Z_0 \tan \theta \tag{7.52}$$

If the wave amplitude at the height Z_0 is equal to $A(Z_0)$, then from the law of energy conservation in the ray tube with scale $\mathrm{d}X$, it follows that

$$|A(Z_0)|^2 \mathrm{d}X_1 = |A(Z = 0)|^2 \mathrm{d}X \tag{7.53}$$

From Equations (7.52) and (7.53) the wave amplitude at the Earth's surface is found to be

$$|A(Z = 0)| = |A(Z_0)|\left|\frac{\mathrm{d}X_1}{\mathrm{d}X}\right|^{1/2} = \frac{|A(Z_0)|}{\left|1 + Z_0\dfrac{\mathrm{d}^2 R_1}{\mathrm{d}X^2}\right|} \tag{7.54}$$

If $d^2R_1/dX^2 > 0$, then $A(0) < A(Z_0)$, there is a *defocusing* effect; whereas, when $d^2R_1 dX^2 < 0$, then $A(0) > A(Z_0)$ there is a *focusing* effect. The same effects occur in the troposphere (see Chapter 6). The phase of the wave passing through the layer in the point X_1 and reaching the point X on the Earth's surface (Fig. 7.7) is

$$\Phi(X, X_1) = \Phi_0 + \frac{\omega}{c} Z_0 [\sec \theta(X_1) - 1] \tag{7.55}$$

where Φ_0 is the wave phase in the absence of inhomogeneities. The rays come from different points to the point X on the layer boundary. The difference of ray phases between the points X_1 and X_1' observed at the point X of the Earth's surface is [11,12]

$$\Delta\Phi = \Phi(X, X_1) - \Phi(X, X_1') = \frac{\omega}{c} Z_0 \left[\sec\theta(X_1) - \sec\theta(X_1') \right] \tag{7.56}$$

If rays coming to the point X at the Earth's surface have the phase difference $\Delta\Phi \geq \pi/2$, the essential interference picture is recorded. Calculations show that inhomogeneities in the ionospheric F-region ($Z = 200$–300 km) cause an interference pattern for waves with frequency $f < 40$ MHz and only for the relative changes of ionospheric plasma density $N_1/\widetilde{N}_0 > 0.002$. Where, according to Reference [11], $\widetilde{N}_0 = \int_{Z_0}^{\infty} N_0 dZ$ is the plasma electrons content in the whole layer of the ionosphere. Thus, the large-scale inhomogeneities exist when the horizontal scale of the irregularity is larger than the width d_F of the first Fresnel zone. The phenomena of large-scale inhomogeneities are important for different and varied ranges of radio wave frequencies during which radio waves are reflected from the ionospheric layer with large-scale inhomogeneities. When radio waves are reflected from the ionospheric layer with large-scale inhomogeneities, a number of radio physical effects occur:

- *deviation of the radio wave's direction from a great circle plane.*
- *increase of the vertical size of the layer forming the reflected signal.*
- *the change of propagation of the radio wave to "multimode."*
- *the complication of pattern and additional modulation of radio wave amplitude, due to the arrival of several rays to the receiving point with different phases.*

7.2.2. Propagation Effects of Small-Scale Inhomogeneities

Radio wave diffraction effects due to small-scale inhomogeneities that are usually contained in the ionospheric E- and F-layer are now examined. The influence of small-scale inhomogeneities results mainly in phenomena like diffraction and scattering.

Perturbation Method. For inhomogeneities with a characteristic scale of $l \ll d_F$, (where, as above, $d_F = (\lambda R)^{1/2}$ and l represents the scale of inhomogeneity), and

with $l < \lambda$, the geometrical optic approximation is not valid, and we must use the method of disturbance (perturbation) for Equation (7.26), as it is described in Sections 3.2–3.4 (see Chapter 3). As before, the dielectric permeability ε in (7.26) is presented as a sum of $\widetilde{\varepsilon}_0 + \widetilde{\varepsilon}_1$, where $\widetilde{\varepsilon}_0$ and $\widetilde{\varepsilon}_1$ can be defined from (7.47a) and (7.47b), respectively. Below, we will summarize briefly the general results mentioned in Chapter 3 and also in References [11,12], and then will present the additional results obtained in References [29–41] as well as by the authors of this book with the computational examples of the effects.

The height $Z = Z_0$ is the height for which reflection takes place ($\widetilde{\varepsilon}_0 = 0$). For the heights $Z_0 - D < Z < Z_0$ a model of a linear layer with thickness D can be used. As a result, the dielectric permittivity can be rewritten in the following form [11,12]:

$$\widetilde{\varepsilon}_0(Z) = -\frac{Z - Z_0'}{D} \tag{7.57}$$

The field change E, in the horizontal homogeneous layer of the ionosphere with ε_0 defined from (7.57) and for the normal wave incidence on the layer, can be described by the equation [11,12]

$$\frac{\partial^2 E}{\partial Z^2} - \left[k_0^2 \frac{Z - Z_0'}{D} \right] E = 0 \tag{7.58}$$

This equation has an exact solution, which can be expressed by the Airy functions U and V

$$U(-\tau) = \frac{1}{\pi^{1/2}} \int\limits_0^{+\infty} \sin\left(x^3/3 - x\tau\right) dx \tag{7.59a}$$

$$V(-\tau) = \frac{1}{\pi^{1/2}} \int\limits_0^{+\infty} \cos\left(x^3/3 - x\tau\right) dx \tag{7.59b}$$

where $\tau = k_0^{2/3} Z/D^{1/3}$.

Small-scale inhomogeneities have a weak influence on wave propagation. If small-scale inhomogeneities of plasma density exist in the ionospheric layer, then the field changes are described by the equation

$$\Delta E + k_0(\widetilde{\varepsilon}_0 + \widetilde{\varepsilon}_1)E = 0 \tag{7.60}$$

which is solved by the method of perturbations, that is, the Airy function $V(-\tau)$ can be assumed as a standard function for a strict solution of (7.60), which is described in the following form:

$$E = E_0 \exp\{ik_0 g\} V(-k_0^{2/3}\Phi) \tag{7.61}$$

where E_0 is the amplitude of the incident wave on the boundary of the layer; g and Φ are the logarithm of wave amplitude and the wave phase, respectively. By putting expression (7.61) in (7.60), the following system is obtained

$$2\nabla g\nabla\Phi + k_0^{-1}\nabla^2\Phi = 0$$

$$-k_0^{-1}\Delta g + (\nabla g)^2 - \Phi(\nabla\Phi)^2 + \widetilde{\varepsilon}_0 + \widetilde{\varepsilon}_1 = 0$$

(7.62)

Let us suppose that k_0^{-1} and ε_1 are small, and present functions g and ψ as perturbation sums (see perturbation method description in Sections 3.2 and 3.4)

$$g = g_0 + g_1 + \cdots, \qquad \Phi = \Phi_0 + \Phi_1 + \cdots$$

(7.63)

Then for the first and second order approximation of (7.62) the wave phase can be given as [11,12]

$$\Phi_0 = 2k_0X_0 = 2k_0 \int_Z^{Z_0'} (\widetilde{\varepsilon}_0)^{1/2}dZ$$

(7.64a)

$$\Phi_1 = 2k_0X_1 = 2k_0 \int_Z^{Z_0'} \widetilde{\varepsilon}_1/(\widetilde{\varepsilon}_0)^{1/2}dZ$$

(7.64b)

Parameter Φ_0 defines the phase of a nonperturbed wave and Φ_1 defines the disturbance of phase in the ionospheric layer with small-scale inhomogeneities. The function g_1 in expansion (7.63) can be expressed as [11,12]

$$g_1 = (1/2k_0)\ln[|E(Z)|/E_0] = -(1/2k_0)\int_Z^{Z_0'} [\Delta_\perp X_1/(\widetilde{\varepsilon}_0)^{1/2}]dZ$$

(7.65)

and it describes the changes of the signal level in the process of scattering, and

$$\Delta_\perp = \frac{\partial^2}{\partial X^2} + \frac{\partial^2}{\partial Y^2}.$$

The Cross-correlation Function of Phase Disturbances. Using expressions (7.63)–(7.64) we can find the cross-correlation function of phase disturbance Φ_1

of the radio wave reflected from the layer with thickness D

$$
\Gamma_\Phi(\xi, \eta) = k_0 \int_{Z_0'-D}^{Z'} dZ_1 \int_{Z_0'-D}^{Z_0'} dZ_2 \, \langle \tilde{\varepsilon}_1(X_1, Y_1, Z_1) \tilde{\varepsilon}_1(X_2, Y_2, Z_2) \rangle
$$

$$
(7.66a)
$$

$$
= 2k_0^2 \int_0^D \Gamma_\varepsilon(\xi, \eta, \zeta) d\zeta \int_{Z_0'-D-\zeta/2}^{Z_0'-\zeta/2} D/[(Z - Z_0') - \zeta^2/4] dZ
$$

where $\xi = X_1 - X_2, \eta = Y_1 - Y_2, \zeta = Z_1 - Z_2$. The second integral in formula (7.66a) equals

$$
\int_{Z_0'-D-\zeta/2}^{Z_0'-\zeta/2} D/[(Z - Z_0') - \zeta^2/4] dZ = D\{\ln[D - \zeta/2 + (D^2 - \zeta^2/4)^{1/2} - \ln(\zeta/2)\}
$$

$$
\approx D \ln(4D/\zeta) \qquad\qquad (7.66b)
$$

For the following calculations, as in References, [21–27], we consider that the shape of the inhomogeneities of plasma density $\delta N \equiv N_1 < N_0$, distributed according to the Gaussian law inside inhomogeneous ionospheric layer at the height Z_0, as

$$
\Gamma_\varepsilon(\xi, \eta, \varsigma) = \Gamma_\varepsilon(\xi, \eta) \exp\left\{\frac{\varsigma^2}{l^2}\right\} \qquad\qquad (7.67)
$$

where l is the characteristic scale of $|N_1|^2$ changing along the Z-axis. If

$$
\Gamma_\varepsilon(0, 0, 0) = \langle \tilde{\varepsilon}_1^2 \rangle = \frac{\omega_{pe}^4}{\omega^4} \left\langle \left| \frac{N_1}{N_0} \right|^2 \right\rangle \qquad\qquad (7.68)
$$

does not depend on Z, then the maximum of the cross-correlation function of the phase fluctuations is

$$
\Gamma_\Phi(0, 0) = \langle \Phi_1^2 \rangle = \pi^{1/2} k_0^2 lD \langle \tilde{\varepsilon}_1^2 \rangle \ln\left(\frac{8D}{l} + \frac{C}{2}\right) \qquad\qquad (7.69)
$$

where C is the Euler constant [11]. Expression (7.69) takes into account that $\langle N_1^2 \rangle$ is the same for all altitudes of the ionosphere. If relative fluctuations of plasma density

$\langle |N_1/N_0|^2 \rangle$ depend on the height, then

$$\langle \tilde{\varepsilon}_1^2 \rangle = (1 - \tilde{\varepsilon}_0)^2 \left\langle \left| \frac{N_1}{N_0} \right|^2 \right\rangle \tag{7.70}$$

is the function of Z. In this case

$$\langle \Phi_1^2 \rangle = \pi^{1/2} k_0^2 l D \left\langle \left| \frac{N_1}{N_0} \right|^2 \right\rangle \ln\left(\frac{8D}{l} + C - \frac{3}{2} \right) \tag{7.71}$$

From formula (7.71) it is seen that the main contribution to the phase fluctuations of the radio wave are determined by the inhomogeneities placed near the reflected level Z_0', where $\tilde{\varepsilon}_0 \sim 0$. If the following form of spectrum of plasma density fluctuations $U_N(K)$ or of dielectric permeability fluctuations $U_\varepsilon(K)$ is used, then

$$U_N(K) \sim U_\varepsilon(K) = M_\varepsilon [1 + (K_X^2 + K_Y^2 + K_Z^2) L_0^2 / 4\pi^2]^{-p/2} \tag{7.72}$$

where L_0 is an external (outer) scale of inhomogeneities and M_ε is determined by the condition $\langle \tilde{\varepsilon}_1^2 \rangle = \int U_\varepsilon(K) dK_X \, dK_Y \, dK_Z$, then the correlation function of phase fluctuations can be presented as

$$\Gamma_\Phi(\xi, \eta) = 2k_0^2 D M_\varepsilon \int\limits_{Z_0' - D}^{Z_0'} dK_X \, dK_Y \, dK_Z \int\limits_{Z_0' - D - \zeta/2}^{Z_0' - \zeta/2} dZ \exp\{i(\xi K_X + \eta K_Y + \zeta K_Z)\}$$

$$\times \left\{ [1 + (K_X^2 + K_Y^2 + K_Z^2) L_0^2 / 4\pi^2]^{-p/2} / Z - Z_0' - \zeta^2/4^{1/2} \right\} \tag{7.73}$$

In Reference [23] it was pointed out that the formula (7.73) could not be analytically integrated. Moreover, for the case $L_0 \ll D$ calculations of the spectrum of phase fluctuations Φ_1 have shown that spectrum U_{Φ_1} does not reproduce spectrum U_N.

The Thin Screen (Kirchhoff) Approximation. Now, using the formulas presented above, the question of phase and amplitude fluctuations for the case of low-orbit satellite communication can be investigated in more detail, using the thin screen approximation method [33,40–41] presented schematically in Fig. 7.8. Let us suppose that the satellite trajectory and the receiving point on the Earth's surface are in the magnetic meridian plane. To simplify the problem, it is assumed that geometric field lines are vertical at point O on the Earth's surface (see Fig. 7.9). The z-axis is directed along the magnetic field lines and the x-axis lies in the meridian plane. The case $\omega_0 \gg \omega_{pe}$, a real case in satellite mobile communication, is now discussed. Due to diffraction and scattering effects at the small-scale inhomogeneities, radio waves from a satellite located at point P have a stochastic modulation of phase after passing through the ionospheric layer having thickness L.

For the case of waves from VHF to X-band, that is, for $\lambda \ll l$, where l is the scale of inhomogeneity that is from a few meters up to a few centimeters and for weak
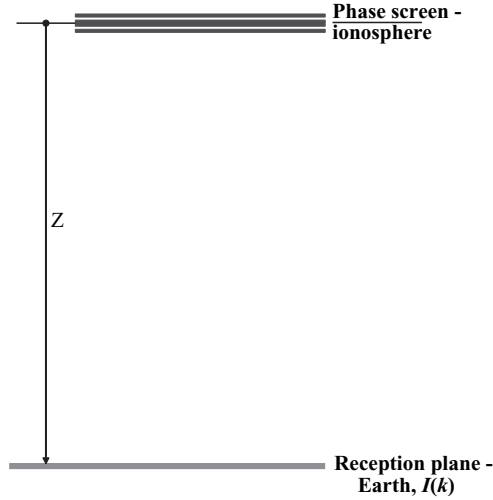
FIGURE 7.8. The 1D phase changing screen model.

inhomogeneities ($\langle \Phi_1^2 \rangle \ll 1$), the angle of scattering of radio waves $\Phi_s \sim (\lambda/l)\langle \Phi_1^2 \rangle$ is small. In the coordinate system $\{x', y', z'\}$ with the z'-axis directed along the ray OP, the phase fluctuations Φ_1 on the bottom boundary of the layer are (Fig. 7.9)

$$\Phi_1(x', y') = k_0 L \sec i \int_{Z_a}^{Z_a + L \sec i} \varepsilon((x', y', z') \mathrm{d}z' \qquad (7.74)$$
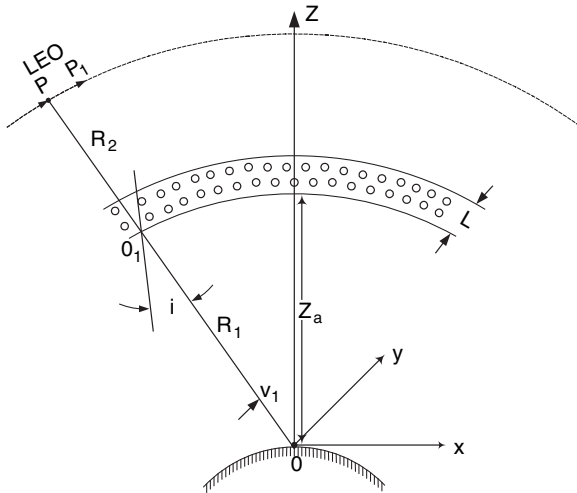
FIGURE 7.9. Geometry of a link LEO-satellite communication with the terminal antenna placed at the Earth's surface.

Then a cross-correlation function Γ_Φ can be presented as

$$\Gamma_\Phi(\xi,'\eta') = k_0^2 L \sec i \int\limits_{-L \sec i}^{L \sec i} \Gamma_\varepsilon(\xi',\eta',\zeta')d\zeta' \qquad (7.75)$$

where $\xi' = x_1' - x_2', \eta' = y_1' - y_2', \zeta' = z_1' - z_2'$. Using Kirchoff's diffraction formulas, we can calculate the wave field strength at the receiving point following Reference [33]

$$E_r = iE_0 \frac{\exp[-ik_0(R_1 + R_2)]}{\lambda R_1 R_2} \int \exp\{i\Phi_1(x',y')\} \exp\left\{-i\pi\frac{x'^2 + y'^2}{\lambda\widetilde{R}}\right\} dx'dy' \quad (7.76)$$

where E_0 is the amplitude of wave at a transmitting point P, $\widetilde{R} = R_1 R_2/(R_1 + R_2)$.

If Φ_1 is distributed according to $\langle\exp(i\Phi_1)\rangle = \exp(-\langle\Phi_1^2\rangle/2)$, we can obtain the average field $\langle|E_r|\rangle$ at the receiving point

$$\langle|E_r|\rangle = \frac{E_0}{R}\exp\left(-\frac{\langle\Phi_1^2\rangle}{2}\right) \qquad (7.77)$$

The average field is attenuated because part of the wave energy is transformed into the noncoherent component of the field. When the satellite moves from point P to point P_1 with coordinates $\{x', y', z'\}$ and $R' = R_1' + R_2'$ (Fig. 7.9), the received field equals

$$E_r = iE_0 \frac{\exp[-ik_0(R_1' + R_2')]}{\lambda R_1 R_2} \int \exp\{i\Phi_1(x'',y'')\}$$

$$\times \exp\left\{-i\pi\frac{\left[\left(x'' - \frac{R_2}{\widetilde{R}}x_1'\right)^2 + y'^2\right]}{\lambda\widetilde{R}}\right\} dx''dy'' \qquad (7.78)$$

Here the difference between R and R' is taken into account only in phase multiplication. Thus the cross-correlation function of the received field can be presented as

$$\Gamma_E = \langle|(E_r - \langle E_r\rangle)(E_{r1} - \langle E_{r1}\rangle)|\rangle = \frac{E_0^2}{R^2}\left\{\frac{1}{\lambda^2\widetilde{R}^2}\int \langle\exp[i\Phi_1(x',y') - i\Phi_1(x'',y'')]\rangle\right.$$

$$\times \exp\left[-\frac{i\pi}{\lambda\widetilde{R}}\left(x'^2 - \left(x'' - \frac{R_2}{\widetilde{R}}x_1'\right)^2 + y'^2 - y''^2\right)\right] dx'dy'dx''dy'' - \exp\left(-\langle\Phi_1^2\rangle\right)\right\}$$

$$(7.79)$$

Using the relationship $\rho_{\Phi 1}(\xi', \eta') = \Gamma_{\Phi 1}/\langle \Phi_1^2 \rangle$, we can calculate the cross-correlation function of the wave field [36,37]

$$\Gamma_{\mathrm{E}} = \frac{E_0^2}{R^2} \left\{ \exp\left[-\langle \Phi_1^2 \rangle \left(1 - \rho_{\Phi 1}\left(\frac{R_1}{R} x_1' \right) \right) \right] - \exp(-\langle \Phi_1^2 \rangle) \right\} \tag{7.80}$$

The parameter $R_1 x_1'/R = x_0'$ is the coordinate of ray OP along the x-axis at height Z_0 (Fig. 7.9). It can be found from the speed V_0 of point O when the satellite moves as

$$x_0' = |V_0| t \tag{7.81}$$

Here, a coherent function that gives us the correlation function of the field in a specific plane is defined. By using this function it is possible to obtain later the intensity of field fluctuations, $I(r)$.

Spectrum of Amplitude Fluctuations. Expression (7.80) enables the relationship between the cross-correlation function of phase fluctuations on the bottom boundary of the ionospheric layer and the correlation function of signal amplitude fluctuations, Γ_{E}. The latter can be found for weak phase fluctuations ($\langle \Phi_1^2 \rangle < 1$) as

$$\Gamma_{\mathrm{E}} = \frac{E_0^2}{R^2} \langle \Phi_1^2 \rangle \rho_{\Phi 1}(x_0') \tag{7.82}$$

The time fluctuations of the field amplitude are found from the spatial phase fluctuations on the bottom boundary of the ionospheric layer with small-scale inhomogeneities. Taking into account relationship (7.82), we obtain

$$\Gamma_{\mathrm{E}}(\xi, \eta) = (E_0^2/R^2) k_0^2 L \sec i \int_{-L \sec i}^{L \sec i} \Gamma_\varepsilon(x_0', \zeta') \mathrm{d}\zeta' \tag{7.83}$$

The Fourier transform of Equation (7.83) gives the spectrum of amplitude oscillations

$$\mathrm{U_g}(f) \sim \int \mathrm{U}_\varepsilon(K_{x'}, K_{y'}, K_{z'}) \mathrm{d}K_{y'} \tag{7.84}$$

Now, at point O, the angle i_1 is the angle between the magnetic field and ray OP (see Fig. 7.9). In the coordinate system $\{x_0, \zeta\}$, with the ζ-axis along the geomagnetic field and with the base at point O, there are two cases

(1) For the case $i_1 = 0$ when the ray is parallel to the magnetic field $\mathbf{B}_0$ lines, the disturbance of plasma density is averaged and the field correlation function Γ_{E} is determined [36,37] by the scales of the inhomogeneities perpendicular to $\mathbf{B}_0$.

(2) In the other critical case when $i_1 = 90°$, the density oscillations are averaged in the direction transverse to the magnetic field and the spectrum Γ_E is expressed from the spectrum of the scales of the inhomogeneities elongated along $\mathbf{B}_0$.

One should note that expressions (7.74) and (7.77) were obtained for the small-scale inhomogeneities ($l \ll d_F$). In real cases of satellite experiments a wide spectrum of scales are observed — from centimeters up to kilometers. For a more general two-dimensional (2D) case, the spectrum of plasma density $U_N(K)$ of inhomogeneities was calculated by Shkarofsky [38]. At the same time the spectrum of amplitude scintillations, measured in satellite experiments, shows that for the spatial frequencies $L_0^{-1} \ll K_\perp \ll l_0^{-1}$ the spectrum of plasma density $U_N(K)$ can be presented in a simpler manner in one-dimensional (1D) case as [38]

$$U_N(K_\perp) = \frac{\langle N_1^2 \rangle \Gamma\left(\frac{p-1}{2}\right)}{\pi \Gamma\left(\frac{p-2}{2}\right)} \frac{K_0^{p-2}}{(K_0^2 + K_\perp^2)^{(p-2)/2}} \approx K_\perp^{1-p} \tag{7.85}$$

where $l_0, L_0 = 2\pi/K_0$ are the inner and outer scale of inhomogeneities, respectively; $K_\perp = 2\pi/l_\perp$ is the scale of inhomogeneity perpendicular to the geomagnetic field $\mathbf{B}_0$, and $\Gamma(w)$ is the gamma-function.

It was also obtained from satellite experiments that in the direction parallel to $\mathbf{B}_0$ for the longitudinal scales $l_\parallel > d_F$, the spectrum of inhomogeneities $U_N(K_\parallel)$ is Gaussian:

$$U_N(K_\parallel) \sim \exp\left\{ -K_\parallel^2 l_\parallel^2 \right\} \tag{7.86}$$

The transformation from spectrum (7.85) to spectrum (7.86) was observed in satellite experiments at the angles i_1' between the radio ray and the geomagnetic field $\mathbf{B}_0$:

$$i_1' \sim \tan^{-1}\left(\frac{l_\perp}{l_\parallel}\right) \tag{7.87}$$

In many experiments it was shown that ionospheric inhomogeneities of the F-region, which give radio scintillations, are stretched along the geomagnetic field ($(l_\perp/l_\parallel \ll 1)$ and the angle i_1 has a value of only several degrees. Thus, the spectrum of field amplitude fluctuations is determined by the spectrum of transversal scales of inhomogeneities.

It should also be noted that for the metric and decimetric wave band the case $l_0 \ll d_F \ll l_\perp$ occurs and more general formulas than (7.85)–(7.86), such as (7.72), must be used. But analytical calculation for the more general case of anisotropic inhomogeneities and of oblique incidence of radio waves on the ionospheric layer is a very complicated mathematical problem. The analytical result was obtained only

for the case when the wave was incident on the ionospheric layer perpendicular to its surface and when the magnetic field lines were also perpendicular to the ionosphere surface. In this case, one can present the spectra of signal logarithmic amplitude g, $U_g(\mathbf{K}_\perp)$, and signal phase S_1, $U_{S_1}(\mathbf{K}_\perp)$, fluctuations as

$$U_{S_1}(\mathbf{K}_\perp) = k_0^2 L U_\varepsilon(\mathbf{K}_\perp) \cos^2\left(\frac{K_\perp^2 d_F^2}{2}\right) \qquad (7.88a)$$

$$U_g(\mathbf{K}_\perp) = k_0^2 L U_\varepsilon(\mathbf{K}_\perp) \sin^2\left(\frac{K_\perp^2 d_F^2}{2}\right) \qquad (7.88b)$$

Expressions (7.88) show that for a wide spectrum of inhomogeneities the amplitude and phase spectra are determined by the spectra $U_\varepsilon(\mathbf{K}_\perp)$ of inhomogeneities and by "filter" functions $\cos^2(K_\perp^2 d_F^2/2)$ and $\sin^2(K_\perp^2 d_F^2/2)$.

The Scintillation Index. In an observation of the fading of radio signals passing the ionosphere, usually used a scintillation index [29–41], which is denoted by σ_I^2, in the same manner as in Chapter 6, because it also determines the "strength or "power" of inhomogeneities (how they are strong) inside the ionospheric layer, and therefore can be defined by formula (6.97) from Section 6.3.2 as the dispersion of the radio wave intensity I fluctuations. We will rewrite this formula for our future discussions:

$$\sigma_I^2 = \frac{\langle I^2 \rangle - \langle I \rangle^2}{\langle I \rangle^2} \equiv \frac{\langle I^2 \rangle}{\langle I \rangle^2} - 1 \qquad (7.89)$$

For weak scintillations this index was obtained in References [29,39–41]

$$\sigma_I^2 = 4\langle g^2 \rangle = 4 \int U_g(K_\perp) dK_x dK_y \qquad (7.90)$$

Here again, g is the logarithm for the amplitude of the radio signal. The above mentioned allows us to conclude that it the small-scale inhomogeneities exist, then two conditions are followed (see also Section 6.3):

– The inhomogeneity scale, l, is smaller than the first Fresnel zone, d_F.
– l is larger than the wavelength λ.

The influence of small-scale inhomogeneities was mainly manifested in phenomena like diffraction and scattering [29–41]. However, the effect of small-scale inhomogeneities on wave propagation in the ionosphere is not well recognized. Although a lot of literature exists about large-scale inhomogeneities, the role of small-scale inhomogeneities seems to be less well understood. As the spectrum of small-scale inhomogeneities gives more complicated effects, in the next section we will focus mainly on the effects of these phenomena, will analyze them according to

the results obtained in References [29–41] and will generalize some theoretical results. Calculations of phase fluctuations $\left[\left\langle \Phi_1^2 \right\rangle\right]^{1/2}$ on the bottom boundary of the ionospheric layer with inhomogeneities for various radio frequencies and for different plasma density fluctuations $[\langle N_1^2/N_0^2 \rangle]^{1/2}$ will be given in section 7.3.3. The one-dimensional spectra of plasma density disturbances $U_N(K_x) \sim K_x^{-p+2}$ for various extinction parameters in exponent, $p' = p - 2$, will also be given. Furthermore, the index of scintillation σ_I^2 as a function of phase fluctuations $\left[\left\langle \Phi_1^2 \right\rangle\right]^{1/2}$ and of parameter p' will be analyzed, because it characterizes the power of ionospheric inhomogeneities and is defined as dispersion of the radio wave intensity variations.

7.2.3. Scattering Phenomena Caused by Small-Scale Inhomogeneities

As was mentioned in the previous section, when radio waves are propagated through an irregular ionosphere, small-angle scattering causes what is known as scintillation of signal strength or intensity. In such phenomena, a distinction can be drawn between diffractive scattering from small-scale irregularities and refractive scattering from large-scale irregularities. The same phenomena are observed in troposphere, caused by large-scale and small-scale turbulent gaseous structures (see Section 6.3). We put the same question as was done in the previous chapter on how we can separate these effects as well as the inhomogeneities that caused them. For a given location in the medium of terminal antennas, the transmitter and receiver, a Fresnel scale, d_F, is the parameter which can give the corresponding separation. According to the definition above, it depends on the wavelength and the coordinate locations of the source and the observer. In such an assumption, diffractive scattering is caused by irregularities whose scale is less than the Fresnel scale. Diffractive scattering of electromagnetic waves by a scintillation medium is described in References [34,41]. Refractive scattering involves irregularities whose scale is greater than the local Fresnel scale [31].

In order to present the effect of refractive and diffractive scattering, the thin phase changing screen model (see Fig. 7.8) of the scintillation medium was introduced by Booker [31,34,41]. Such a model replaces weak multiple scattering by strong single scattering in a way that enables us to understand the relation between "diffractive" and "refractive" scattering in scintillation phenomena.

Main Parameters of the Problem. The phase changing screen model has the following characteristic parameters:

a) phase changing screen representing the ionospheric *F*-region. As tropospheric gaseous turbulent structures (see Section 6.3), the ionospheric plasma inhomogeneities are characterized by the following parameters:

  – mean square fluctuation of phase $[(\Delta\Phi)^2] \equiv \left\langle \Phi_1^2 \right\rangle$;
  – outer scale L_0;
  – inner scale l_0.

b) reception plane representing the surface of the Earth (see Fig. 7.8).

The spectrum of intensity fluctuation is created and obtained in the reception plane. At the same time, to determine physical processes that accompany radio wave propagation through the inhomogeneous ionosphere we must compare the outer scale of irregular ionospheric region with the Fresnel scale defined as $d_F = (\lambda Z/2\pi)^{1/2}$, where Z is the distance from the screen to the reception plane and λ is the wavelength. In References [31,34,41] it was assumed that the RMS fluctuation of phase $\left[\langle \Phi_1^2 \rangle\right]^{1/2}$ is large compared with one radian. Moreover, in 1D-case of ionospheric layer presented in Figure 7.8, as follows from (7.73), the power spectrum of phase fluctuations $S(k)$ is proportional to k^{-p}, when $k \gg (1/L_0)$ and p is referred to as the *spectral index*.

For a practical scintillation medium, the latter parameter p is defined as the spectral index that is observed in any measurements of phase fluctuations along a straight line. For the ionosphere, it is also the spectral index that is observed when the source is at the satellite moving above the ionosphere in a straight line. Usually, in literature, the spectral index p is determined as one integer greater than that observed when measurements of the average refractive index $\langle n \rangle$ are made along a straight line in the medium with scintillations, that is, $p = \langle n \rangle + 1$ [29–41].

At the same time, the spectral index p is one integer less than that obtained by analyzing fluctuations of phase made over an area rather than along a line. Observed values of the spectral index p range from about 2 to 4, with values between about 2.5 and 3.5 being most common [31,34–37,41]. The smaller values of p are found when the scintillation phenomenon is strong.

Let us also define the expression $[(\Delta\Phi)^2]S(k)$ as the power spectrum of phase fluctuations, where $[(\Delta\Phi)^2]$ is the mean square fluctuation of phase, and $S(k)$ is the phase spectra. The corresponding autocorrelation function $\rho(x)$ is obtained by inverse Fourier transformation of $S(k)$ (see Section 7.2.2). Tables 7.2 to 7.3 present the values of $S(k)$ and the corresponding autocorrelation functions $\rho(x)$ obtained in Reference [41].

Now, to differentiate the effects of "refractive" scattering from large-scale irregularities and "diffraction" scattering from small-scale irregularities and to analyse the significant roles in the physical processes, in addition to the earlier introduced outer scale L_0, the inner scale l_0, and the Fresnel scale d_F, additional parameters following References [31,34,35] were introduced. They are: the lenses scale l_L, the focal scale l_F, and the peak scale l_P.

The *lens scale*, l_L, is defined as the size of the inhomogeneity in the phase changing screen [31,34,41]. An array of optical foci is produced in a plane parallel to the screen at distance Z. These foci lie in the reception plane at a distance Z if

$$Z = \frac{l_L^2}{(\lambda/(2\pi))[2(\Delta\Phi)^2]^{1/2}} \tag{7.91a}$$

from which we get

$$l_L = \left(\frac{\lambda Z}{2\pi}\right)^{1/2}[2(\Delta\Phi)^2]^{1/4} \tag{7.91b}$$

TABLE 7.2. [41]: Phase spectra $S(k)$ per unit mean square fluctuation of phase together with the corresponding autocorrelation function $\rho(x)$ (inner scale l_0 is zero relative to outer scale L_0)

p	$S(k)$	$\rho(x)$
2	$\dfrac{4L_0}{1+k^2L_0^2}$	$\exp\left(-\dfrac{x}{L_0}\right)$
3	$\dfrac{2\pi L_0}{(1+k^2L_0^2)^{3/2}}$	$\dfrac{x}{L_0}K_1\left(\dfrac{x}{L_0}\right)$
4	$\dfrac{8L_0}{(1+k^2L_0^2)^2}$	$\left(1+\dfrac{x}{L_0}\right)\exp\left(-\dfrac{x}{L_0}\right)$
5	$\dfrac{3\pi L_0}{(1+k^2L_0^2)^{5/2}}$	$\dfrac{x}{L_0}\left[K_1\left(\dfrac{x}{L_0}\right)+\dfrac{1}{2}\dfrac{x}{L_0}K_0\left(\dfrac{x}{L_0}\right)\right]$

Lens action occurs in the screen, producing focal action in the reception plane. As follows from (7.88), the lens scale l_L can be defined through the Fresnel scale

$$l_L = d_F[2(\Delta\Phi)^2]^{1/4} \tag{7.92}$$

TABLE 7.3(a). [41]: Autocorrelation function for an outer scale L_0 and an inner scale l_0

P'	$\rho(X)$
2	$\dfrac{\exp\left(-\dfrac{(x^2+l_0^2)^{1/2}}{L_0}\right)}{\exp\left(-\dfrac{l_0}{L_0}\right)}$
3	$\dfrac{\dfrac{(x^2+l_0^2)^{1/2}}{L_0}K_1\left(\dfrac{(x^2+l_0^2)^{1/2}}{L_0}\right)}{\dfrac{l_0}{L_0}K_1\left(\dfrac{l_0}{L_0}\right)}$
4	$\dfrac{\left(1+\dfrac{(x^2+l_0^2)^{1/2}}{L_0}\right)\exp\left(-\dfrac{(x^2+l_0^2)^{1/2}}{L_0}\right)}{\left(1+\dfrac{l_0}{L_0}\right)\exp\left(-\dfrac{l_0}{L_0}\right)}$
5	$\dfrac{\dfrac{(x^2+l_0^2)^{1/2}}{L_0}\left[K_1\left(\dfrac{(x^2+l_0^2)^{1/2}}{L_0}\right)+\dfrac{1}{2}\dfrac{(x^2+l_0^2)^{1/2}}{L_0}K_0\left(\dfrac{(x^2+l_0^2)^{1/2}}{L_0}\right)\right]}{\dfrac{l_0}{L_0}\left[K_1\left(\dfrac{l_0}{L_0}\right)+\dfrac{1}{2}\dfrac{l_0}{L_0}K_0\left(\dfrac{l_0}{L_0}\right)\right]}$

TABLE 7.3(b). [41]: Phase spectra per unit mean square fluctuation of phase for an outer scale L_0 and an inner scale l_0

P'	$S(k)$
2	$4l_0\, exp\left(\dfrac{l_0}{L_0}\right)\dfrac{K_l\left(\frac{l_0}{L_0}(1+K^2L_0^2)^{1/2}\right)}{(1+k^2L_0^2)^{1/2}}$
3	$\dfrac{2\pi l_0^2}{L_0 K_l\left(\frac{l_0}{L_0}\right)}\,\dfrac{1+\left(\frac{l_0}{L_0}(1+k^2L_0^2)^{1/2}\right)}{\left(\frac{l_0}{L_0}(1+k^2L_0^2)^{1/2}\right)^3}\,exp\left(-\frac{l_0}{L_0}(1+k^2L_0^2)^{1/2}\right)$
4	$\dfrac{8l_0^4}{L_0^3\left(1+\frac{l_0}{L_0}\right)\exp\left(-\frac{l_0}{L_0}\right)}\,\dfrac{K_1\left(\frac{l_0}{L_0}(1+k^2L_0^2)^{1/2}\right)+\frac{1}{2}\left(\frac{l_0}{L_0}(1+k^2L_0^2)^{1/2}\right)K_0\left(\frac{l_0}{L_0}(1+k^2L_0^2)^{1/2}\right)}{\left(\frac{l_0}{L_0}(1+k^2L_0^2)^{1/2}\right)^3}$
5	$\dfrac{3\pi d_0^4}{L_0^3\left(K_l\left(\frac{l_0}{L_0}\right)+\frac{l_0}{L_0}K_0\left(\frac{l_0}{L_0}\right)\right)}\,\dfrac{1+\left(\frac{l_0}{L_0}(l+k^2L_0^2)^{1/2}\right)+\frac{1}{3}\left(\frac{l_0}{L_0}(1+K^2L_0^2)^{1/2}\right)^2}{\left(\frac{l_0}{L_0}(1+k^2L_0^2)^{1/2}\right)^5}\,exp\left(-\frac{l_0}{L_0}(1+k^2L_0^2)^{1/2}\right)$

Hence, the irregularities with a scale of l_L defined by (7.91b)–(7.92) give a focusing effect of a radio wave passing the ionosphere at the Earth's surface. Therefore in Reference [41] this scale was defined as a lens scale.

The *focal scale*, l_F, is defined as the width of the average focal spots at the reception plane by the scattering of radio waves from the medium- and large-scale ionospheric irregularities. It determines fluctuations of radio signal amplitude at the Earth's surface after such a scattering. The focal scale, which varies with the spectral index, is associated with the arrival at the reception plane of an angular spectrum of waves that are approximately co phased within an angle of about $\pm\lambda/(2\pi l_F)$ of the norm. It is determined as [31,34,41]

$$l_F = l_L[2(\Delta\Phi)^2]^{1/2} \tag{7.93}$$

It is seen from (7.93) that for a given scale in the screen, the larger the mean square fluctuation of phase, the closer is the focal plane to the screen and the sharper are the foci.

The *peak scale*, l_P, represents the peak in the intensity spectrum $I(k)$, such that the angular spatial frequency $K = l_P^{-1}$ gives the low frequency edge of the peak in the intensity spectrum in the reception plane. When "refractive" scattering dominates, the reciprocals of the scales l_P and l_F give the lower and upper roll-off angular spatial frequencies K for the intensity spectrum in the reception plane,

TABLE 7.4. [31,41]: The focal scale l_F and the peak scale l_P for large L_0/d_F and $(\Delta\Phi)^2$

	Spectral Index p'				
	2.5	3.0	3.5	4.0	4.5
l_F	$\dfrac{L_O}{\left[2\overline{(\Delta\Phi)^2}\right]^{2/3}}$	$\dfrac{L_O}{\left[2\overline{(\Delta\Phi)^2}\,ln\overline{(\Delta\Phi)^2}\right]^{1/2}}$	$\dfrac{L_O}{\left[4\overline{(\Delta\Phi)^2}\right]^{1/2}}$	$\dfrac{L_O}{\left[2\overline{(\Delta\Phi)^2}\right]^{1/2}}$	$\dfrac{L_O}{\left[\overline{(\Delta\Phi)^2}\right]^{1/2}}$
l_P	$\dfrac{d_F^2}{L_O}\left[2\overline{(\Delta\Phi)^2}\right]^{2/3}$	$\dfrac{d_F^2}{L_O}\left[\overline{(\Delta\Phi)^2}\,ln\overline{(\Delta\Phi)^2}\right]^{1/2}$	$\dfrac{d_F^2}{L_O}\left[4\overline{(\Delta\Phi)^2}\right]^{1/2}$	$\dfrac{d_F^2}{L_O}\left[2\overline{(\Delta\Phi)^2}\right]^{1/2}$	$\dfrac{d_F^2}{L_O}\left[\overline{(\Delta\Phi)^2}\right]^{1/2}$

whether this is a focal plane or not. The intensity spectrum therefore extends roughly from the angular spatial frequency $K = l_P^{-1}$ to the angular spatial frequency $K = l_F^{-1}$. The focal scale and the peak scale have a geometric mean equal to the Fresnel scale

$$l_P = d_F^2/l_F \tag{7.94}$$

Table 7.4 represents the focal scale and the peak scale obtained in Reference [31] for polynomial spectrum of irregularities with $p' = 2$–5, as a function of the outer scale L_0 and the mean square fluctuation of phase $(\Delta\Phi)^2$, for $(\Delta\Phi)^2 > 1$. As follows from results presented in Table 7.4, for $(\Delta\Phi)^2 > 1$ spectrum of amplitude fluctuations of radio signals within a range of spatial frequencies, $l_F^{-1} < K < l_0^{-1}$, is determined by "diffractive" scattering from small-scale irregularities and can describe the corresponding spectrum of ionospheric inhomogeneities. At the same time, at frequencies $K < l_F^{-1}$ the scattering is related with scattering from medium and large inhomogeneities with dimensions $l > d_F$, that is, it describes the focusing properties of the ionospheric plasma. Therefore, determination of the spectrum of ionospheric inhomogeneities using measurements of amplitude fluctuations can be done only when $l_F \gg l_0$.

What does it mean in a practical point of view for satellite communications? Results obtained above show that the effects of "diffractive" scattering occur mostly for medium- and small-scale irregularities because they become significant for high frequencies beyond the UHF/X-band, where, as have been shown earlier, effects of large-scale irregularities are not so actual. Moreover, large-scale irregularities cause the "refractive" scattering (such a definition was introduced in References [31,34,41]). This effect was described earlier in Section 7.2.2. In Reference [41] it was shown that the "refractive" scattering at large-scale inhomogeneities is predominant with respect to "diffraction" scattering from small-scale inhomogeneities, if $l_F < l_0$, which means it is actual only for waves of HF/VHF-frequency-band. This effect is also stronger if the power spectrum parameter p' is higher (see Table 7.4). The same effect is observed with an increase of signal phase fluctuations. Thus, for $(\Delta\Phi)^2 \equiv \langle\Phi_1^2\rangle \geq 10^3$, the spectrum of amplitude variations, $U_g(K)$ defined by (7.88b) for all p', is determined by the "refractive" scattering, which gives the so-called focusing effects.

Signal Intensity Fluctuations. Using the selected appropriate autocorrelation function $\rho(x)$ (from Tables 7.2 and 7.3), two functions are formulated that each depend on x and k. The first is $f(x,k)$, which is obtained by substituting $\rho(x)$ into the following equation:

$$f(x,k) = 2\rho(x) - \rho(x - kd_F^2) - \rho(x + kd_F^2) \tag{7.95}$$

The second function is $g(x,k)$, which is obtained by substituting $f(x,k)$ into the following equation:

$$g(x,k) = \exp\left\{-[(\Delta\Phi)^2][f(0,k) - f(x,k)]\right\} - \exp\left\{-[(\Delta\Phi)^2]f(0,k)\right\} \tag{7.96}$$

The intensity spectrum in the reception plane is then [34,41]

$$I(k) = 4\int_0^\infty g(x,k)\cos(kx)dx \tag{7.97}$$

Using now the formula (7.97), we can obtain the square of the scintillation index, σ_I

$$\sigma_I = \frac{1}{2\pi}\int_0^\infty I(k)dk \tag{7.98}$$

For weak scattering $((\Delta\Phi)^2 = 10^{-1}, 1)$ the general expression for the spectrum of signal intensity fluctuation (7.97) can be reduced to [41]

$$I(k) = 4\langle(\Delta\Phi)^2\rangle S(k)\sin^2\left(\frac{1}{2}k^2 d_F^2\right) \tag{7.99}$$

where $S(k)$ has the value shown in Table 7.3 if the concrete inner scale l_0 was taken into account and in Table 7.2 if $l_0 = 0$.

We mentioned that the Fresnel oscillation associated with the $\sin^2(0.5k^2 d_F^2)$ term in the equation is depicted for the main lobe and the first side lobe. For the remaining lobes only the average value is considered (corresponding to replacement of $\sin^2(0.5k^2 d_F^2)$ by 0.5). For spectral index of $p' = 2$, and using Table 7.2, a substitute of $S(k) = 4L_0/(1 + k^2 L_0^2)$ leads to the following equation for $I(k)$

$$I(k) = 16\langle(\Delta\Phi)^2\rangle\frac{L_0}{1 + k^2 L_0^2}\sin^2\left(\frac{1}{2}k^2 d_F^2\right) \tag{7.100a}$$

The same substitute of $S(k)$ for $p' = 3$ leads to an intensity fluctuation of

$$I(k) = 8\pi\langle(\Delta\Phi)^2\rangle\frac{L_0}{(1 + k^2 L_0^2)^{3/2}}\sin^2\left(\frac{1}{2}k^2 d_F^2\right) \tag{7.100b}$$

Finally, for $p' = 4$ we get

$$I(k) = 32\langle(\Delta\Phi)^2\rangle \frac{L_0}{(1 + k^2L_0^2)^2} \sin^2\left(\frac{1}{2}k^2d_F^2\right) \qquad (7.100c)$$

Therefore, substituting in (7.98) for different $I(k)$ from (7.100) leads to the following equations for σ_I:
  – for $p' = 2$

$$\sigma_I^2 = \frac{2\sqrt{2}}{\sqrt{\pi}L_0} d_F\langle(\Delta\Phi)^2\rangle \qquad (7.101a)$$

  – for $p' = 3$

$$\sigma_I^2 = \frac{\pi}{2L_0^2} d_F^2\langle(\Delta\Phi)^2\rangle \qquad (7.101b)$$

  – for $p' = 4$

$$\sigma_I^2 = \frac{8\sqrt{2}}{3\sqrt{\pi}L_0^3} d_F^3\langle(\Delta\Phi)^2\rangle \qquad (7.101c)$$

Computation of intensity spectrum have been performed in accordance with Equations (7.97)–(7.98) for strong fluctuations and formulas (7.100)–(7.101) for weak fluctuations for an outer scale $L_0 = 10d_F$ and inner scale $L_i = 10^{-2}d_F$ and for the spectral index $p' = 3, 4, 5$. Figures 7.10–7.12 represent the scintillation index calculated numerically according to (7.100)–(7.101) for weak signals and according to (7.97)–(7.98) for strong signal phase fluctuations, respectively, versus square mean deviations of signal phase for various parameters of 1D-spectrum $p' = p - 2$ and different scales of ionospheric irregularities, respectively. It is seen from Fig. 7.11 that for $p' = 2$ the scintillation index with an increase of phase fluctuations limits to the unit. For higher spectral index ($p' > 2$) σ_I exceeds the unit, which explain the focusing properties of the ionospheric layer consisting of various irregularities for strong variations of signal phase after passing the ionosphere.

Signal Phase Fluctuations. We once again model the ionospheric F-region as a slab of ionization of mean ionization density N with a uniform mean square fractional fluctuation of ionization density $(\Delta N/N)^2$ (see Fig. 7.8) with the thickness D and the outer scale L_0. We suppose that on the Earth's plane we receive radiation of wavelength λ from a distant point source at zenith angle χ.

In our computations, to illustrate results obtained in References [34,41], we shall take the outer scale equal to the scale height H of the F-region, and we shall also take the thickness of the F-region to be H. In such notations, the mean square fluctuation of signal phase experienced on passage through the F-region may
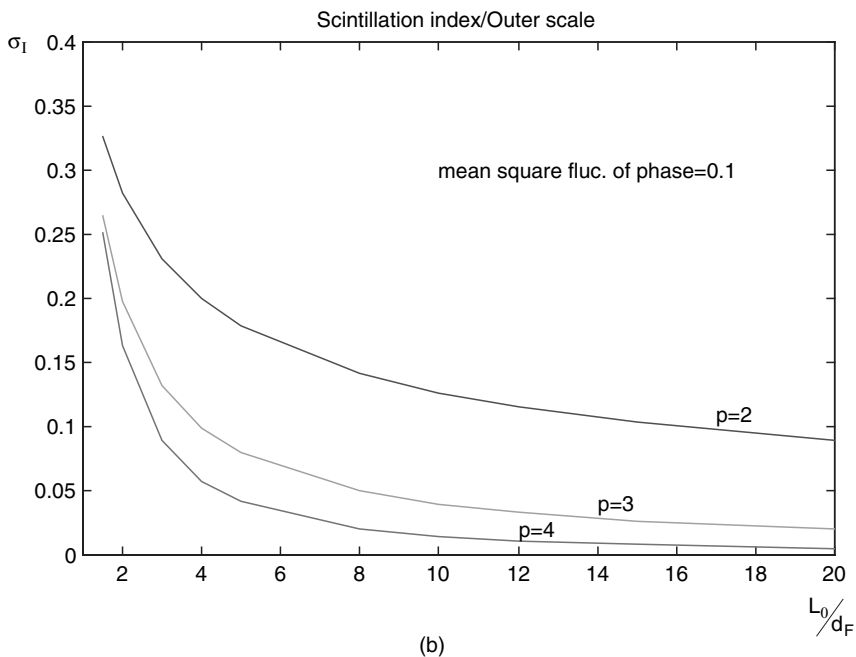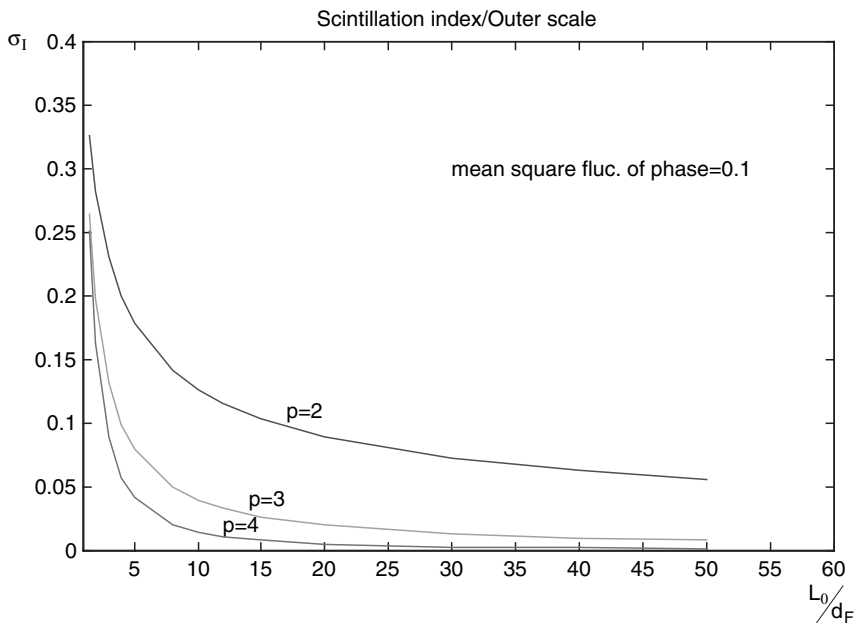
FIGURE 7.10. (a) Illustration for various values of the spectral index; the scintillation index σ_I, as a function of the normalized outer scale L_0; $1.5d_F \leq L_0 \leq 50d_F$; $\langle (\Delta\Phi)^2 \rangle = 0.1$. (b) Illustration for various values of the spectral index; the scintillation index σ_I, as a function of the normalized outer scale L_0; $1.5d_F \leq L_0 \leq 20d_F$; $\langle (\Delta\Phi)^2 \rangle = 0.1$.
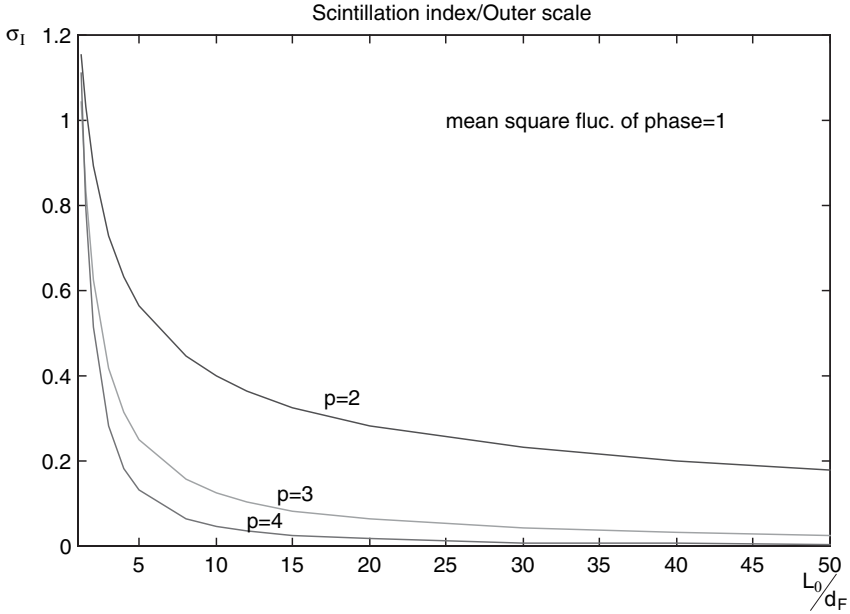
(a)
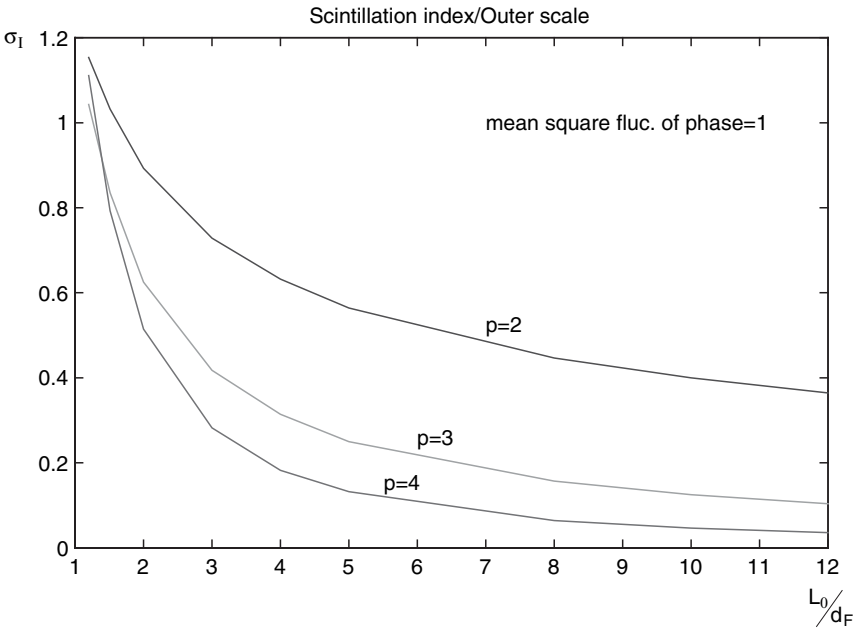
(b)

FIGURE 7.11. (a) Illustration for various values of the spectral index; the scintillation index σ_I, as a function of the normalized outer scale L_0; $1.2d_F \leq L_0 \leq 50d_F$; $\langle (\Delta\Phi)^2 \rangle = 1$. (b) Illustration for various values of the spectral index; the scintillation index σ_I, as a function of the normalized outer scale L_0; $1.2d_F \leq L_0 \leq 20d_F$; $\langle (\Delta\Phi)^2 \rangle = 1$.
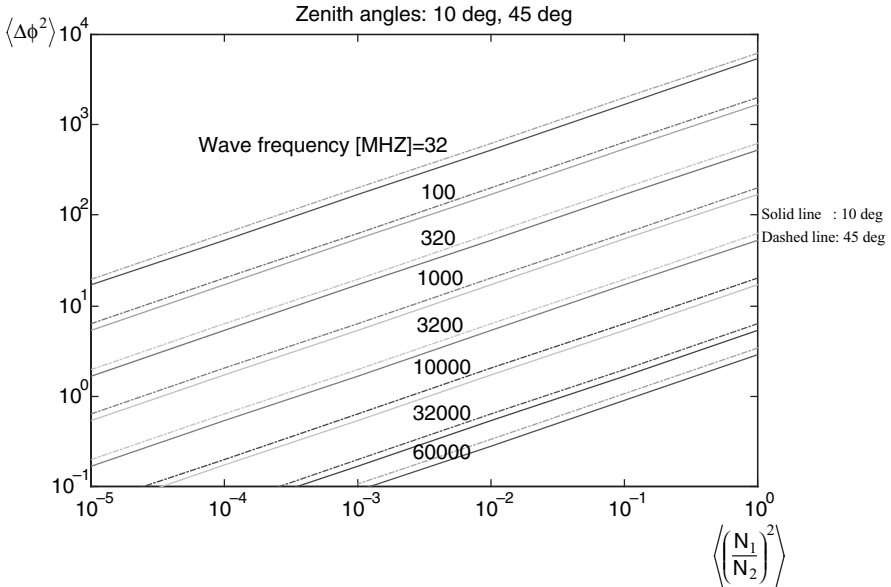
(a)
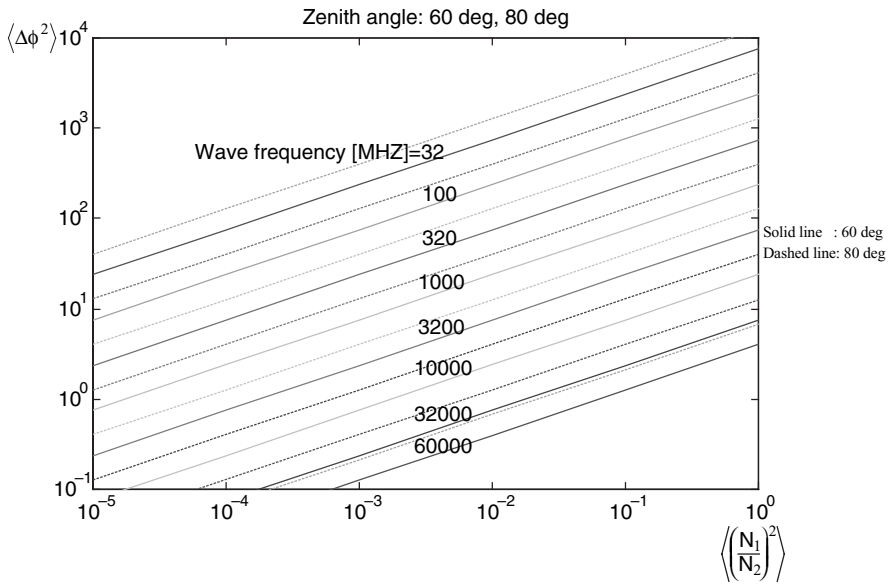
(b)

FIGURE 7.12. (a) The RMS fluctuations of phase versus the fractional fluctuations of ionization density for different frequencies at zenith angles of $10°, 45°$. The outer scale is equal to a layer thickness of $L = 10$ km. Mean ionization density is 10^{12} m^{-3}. (b) The RMS fluctuations of phase versus the fractional fluctuations of ionization density for different frequencies at zenith angles of $60°, 80°$. The outer scale is equal to a layer thickness of $L = 10$ km. Mean ionization density is 10^{12} m^{-3}.

then be taken as

$$\langle (\Delta\Phi)^2 \rangle \equiv \langle \Phi_1^2 \rangle = 4r_e^2 N^2 \left\langle \left(\frac{N_1}{N_0}\right)^2 \right\rangle \lambda^2 H^2 \sec\chi \qquad (7.102)$$

Here all parameters are defined above; r_e is the radius of the electron. For numerical computations we take $H = 100\,\text{km}$ and $N_0 = 10^{12}\,\text{m}^{-3}$. The curves in Figures 7.12a,b present the RMS fluctuation of a phase as a function of the RMS fractional fluctuation of ionization density for a series of frequencies running from 32 MHz to 60 GHz. The figures illustrate the ionospheric propagation of various wave frequencies at zenith angles of 10, 45, 60, 80 degrees, respectively. Both axes, vertical and horizontal, are plotted logarithmically.

We can see that for a given frequency, an increase of ionization density causes an increase in phase fluctuations. Furthermore, for a given ionization density, when we use high frequencies for the satellite communication channel (from UHF to X-band and higher), we can see a decrease in phase fluctuations to values appropriate for weak scattering. Finally, for a given ionization density, when the zenith angle χ becomes larger, the effect of phase fluctuations becomes stronger. In fact, for a zenith angle of $60°$, the phase fluctuation experienced in the passage of a 32 MHz wave through the F-region with a fractional ionization density $\left\langle \left(\frac{N_1}{N_0}\right)^2 \right\rangle$ of 10^{-2} is about 750 radians. But when the zenith angle is $80°$, and for the same frequency and ionization density, we obtain phase fluctuations of ~ 1270 radians. In order to obtain 750 radians, we need the ionization density $\left\langle \left(\frac{N_1}{N_0}\right)^2 \right\rangle$ to be $\sim 3.5 \times 10^{-3}\,\text{m}^{-3}$.

To understand the role of satellite position with respect to the observer at the Earth's plane, additional analysis of the RMS fluctuation of a phase as a function of the zenith angle was done and is shown for a series of frequencies running from 32 MHz to 60 GHz in Figures 7.13a,b. The figures illustrate the ionospheric propagation of various wave frequencies at ionization densities of 100%, 80%, 30%, and 1%. Again, both the vertical and horizontal axes are plotted logarithmically. As we mentioned earlier, in the following figures we can see that for a given frequency, an increase of zenith angle causes an increase in phase fluctuations. Furthermore, for a given zenith angle, when we use high frequencies for the communication channel (more than 1 GHz), we can see a decrease in phase fluctuations to values appropriate for weak scattering. The same features, as in Figures 7.12, are clearly seen from illustrations of Figures 7.13a,b.

Frequency Dependence of Signal Intensity Fluctuation Spectrum. Above, we evaluated the expressions of the spectrum of the signal intensity fluctuations defined by (7.97). On the basis of this expression, we present in Figures 7.10–7.11 the normalized intensity fluctuation as a function of the wave frequency, for various values of the spectral index, p'.

It was shown that for a given spectral index, the behavior of the intensity is an exponential type. Furthermore, for a given frequency, when the spectral index

(a)

(b)
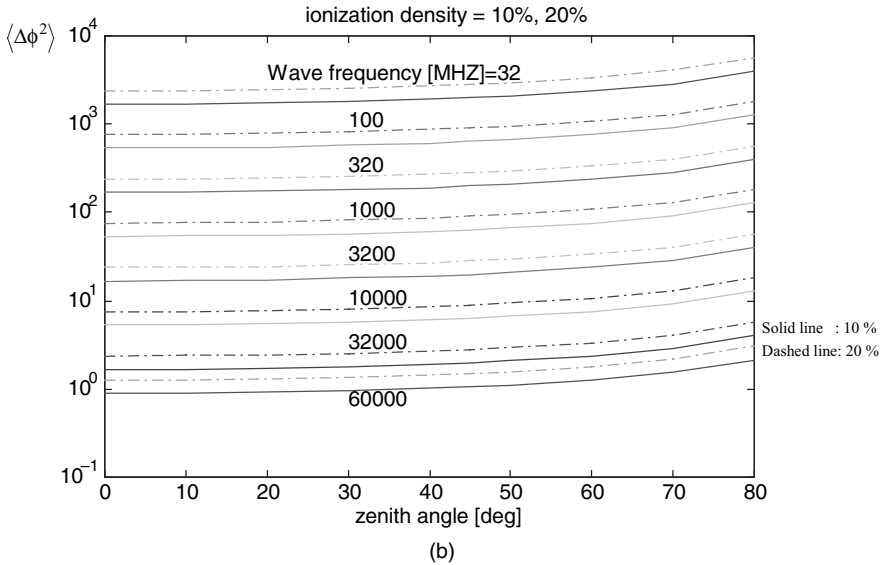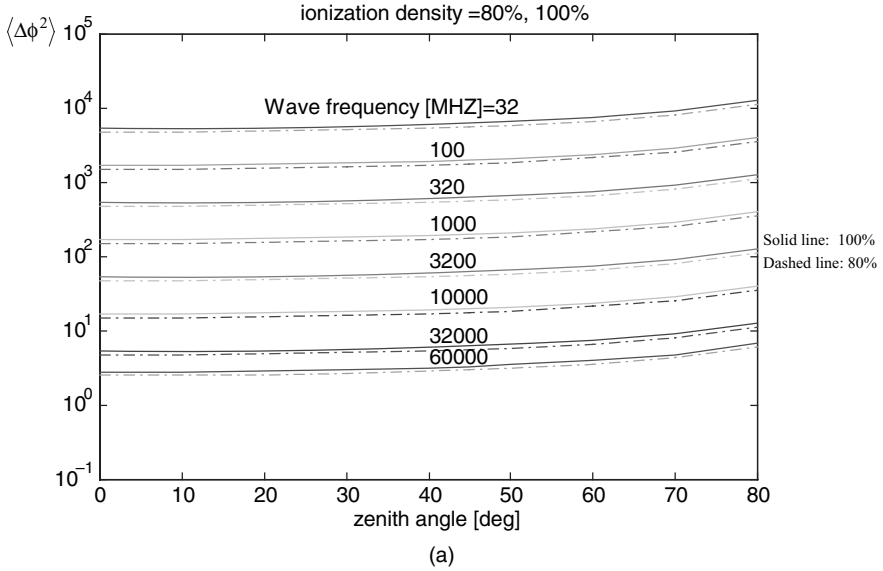
FIGURE 7.13. (a) The RMS fluctuations of phase versus the zenith angle for different frequencies at ionization densities of 80% and 100%. The outer scale is equal to a layer thickness of $L = 10\,\text{km}$. Mean ionization density is $10^{12}\,\text{m}^{-3}$. (b) The RMS fluctuations of phase versus the zenith angle for different frequencies at ionization densities of 10% and 20%. The outer scale is equal to a layer thickness of $L = 10\,\text{km}$. Mean ionization density is $10^{12}\,\text{m}^{-3}$.
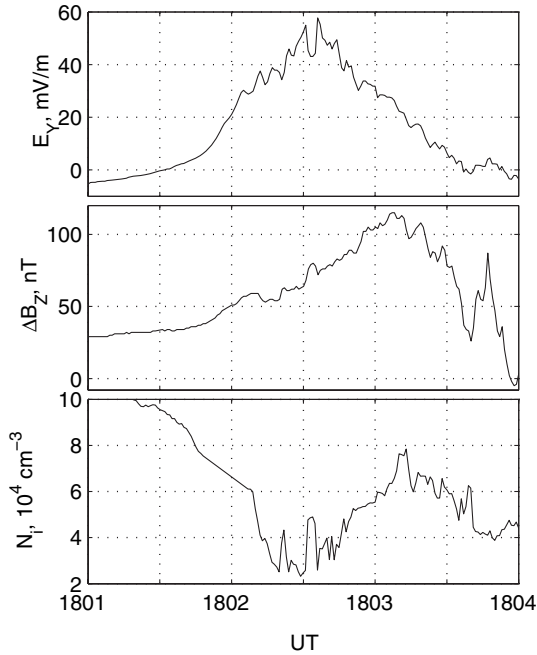
FIGURE 7.14. Deviations of the ambient electrical (top graph) and magnetic (middle graph) fields. The ionospheric plasma content during magnetic storms is presented for short-term period of 3 minutes (denoted along the horizontal axis).

increases, an increase in the intensity fluctuations is observed. Finally, for a given frequency, when phase fluctuation becomes larger, the effect of the signal intensity fluctuations becomes stronger.

To verify the proposed approach of how to estimate effects of ionosphere on signal fading in land-satellite communication links regarding GPS applications, special numerical computations were performed to investigate the role of magnetic storms that usually occurred in the ionosphere due to solar activity, its influence on the magnetosphere and changes to magnetosphere-ionosphere coupling, on ionospheric plasma perturbations [42,43] (see also literature referred therein). As was found experimentally, the plasma density due to a magnetic storm falls at 100% and higher. For example, in Figure 7.14 extracted from Reference [43], the changes of ambient electric field (top graph), magnetic field (middle graph), and ionospheric plasma content (bottom graph) are presented during magnetic storms registered by satellites in special measurements, described in Reference [42]. It is clearly seen that during the storm (the magnetic field strength is maximum) the ionospheric plasma content was decreased significantly (more than twice). The decrease of plasma content leads to the creation of strong plasma irregulaties caused by the corresponding strong deviations of signal phase and amplitude, that is, the intensive signal scintillations at the receiver. As was mentioned above, this effect depends on radiated frequency.

To show this effect we performed a numerical virtual experiment in the ionosphere above the USA territory. The following results are measurements carried out in Reference [42] for low, mid, and high latitudes of the ionosphere, which we refer in our experiment as the south of the USA, mid latitude of the USA, and Alaska. We compared for these three regions a random mean square (RMS) of signal intensity fluctuations as a function of normalized mean density of ionospheric plasma ($10^{12}\,\text{m}^{-3}$), for the usually used frequencies of 10, 32, and 60 GHz, and for the spectral index of p corresponding to each case of the perturbed region. Thus, for the perturbed south ionosphere of the USA it was taken from the ionospheric data equal $p' = 2$, for the perturbed mid latitude ionosphere equal $p' = 3$, and for the perturbed polar ionosphere above Alaska equal $p' = 4$. To understand the effects of a satellite zenith angle to the ground based antenna, we changed it from 10 degrees to 80 degrees, modeling the case of low-elevation-orbit (LEO) satellite (see definitions in Chapter 14). The outer scale (thickness) of ionospheric layer was chosen to be constant, equal to 100 km and the ionospheric height was chosen to be 200 km. Results of computations are shown in Figures 7.15a,c–7.17a,c for the three regions of disturbed ionosphere corresponding to the south of USA, mid-latitude region of USA, and the polar ionospheric region above Alaska, for a zenith angle of 10, 45 and 80 degrees, respectively. From presented illustrations, it is clearly seen that the effects of plasma disturbances on signal intensity phase fluctuations become stronger with the decrease of radiated frequency and the increase of zenith angle. It is obvious that in the polar ionosphere the effect of magnetic storm on signal scintillations is more significant compared with that for the mid latitude ionosphere and, of course, for the ionosphere above the south regions of USA. Again, these effects strongly depend on the radiated frequency within the land-satellite communication link and the zenith angle of satellite with respect to ground based facilities.

Let us now summarize some important results obtained above concerning the effects of the small-scale inhomogeneities of the ionospheric plasma on radio wave propagation. Here, on the basis of the original works [29–41], we analyzed the field intensity and phase fluctuations by the use of the perturbation method. We examined and analyzed the fluctuation of the phase as a function of the ionization density for different zenith angles (from the source). Then we analyzed the fluctuation of phase as a function of the zenith angles for different ionization densities of plasma irregularities. Using the perturbation method, we briefly introduced an analysis of intensity fluctuation in the frequency domain. We have answered questions on how the plasma irregularities of wide range dimensions affect radio propagation in land-satellite communication channel, and in what frequency band their effects are more actual. Finally, we get that the accumulation of the analysis are:

  – for a given frequency band, an increase of ionization density of ionospheric irregularities (''power'') causes an increase in signal phase fluctuations. Furthermore, for a given ionization density, using high frequencies for the satellite communication channel (more than UHF-band), a decrease in phase and amplitude fluctuations to values appropriate for weak scattering
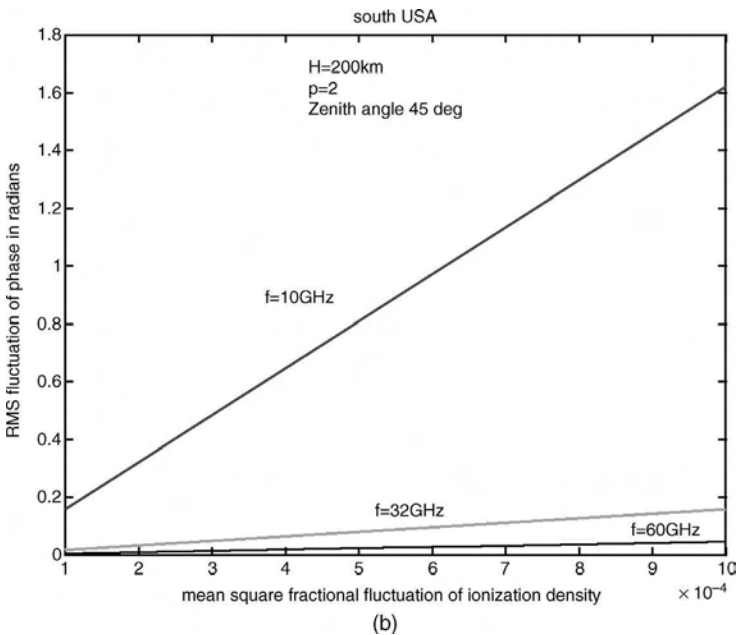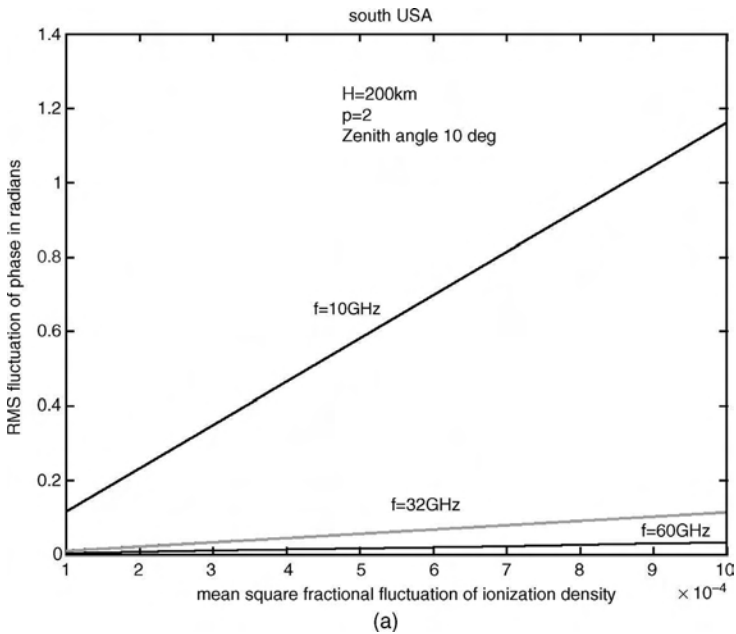
FIGURE 7.15 (a) RMS of signal intensity phase fluctuations (in radians) versus mean square fractional fluctuations of plasma density (normalized by the mean ionization density of $10^{12}\,\text{m}^{-3}$) for frequencies of 10, 32 and 60 GHz, for a spectral index of $p' = 2$ (corresponded to perturbed ionosphere above the south of USA) and zenith angle of $10°$. The outer scale (thickness) of ionospheric layer is $100\,\text{km}$ and the ionospheric height is $200\,\text{km}$. (b) The same as in Fig. 7.15a, but for a satellite zenith angle of $45°$. (c) The same as in Fig. 7.15a, but for a satellite zenith angle of $80°$.

south USA
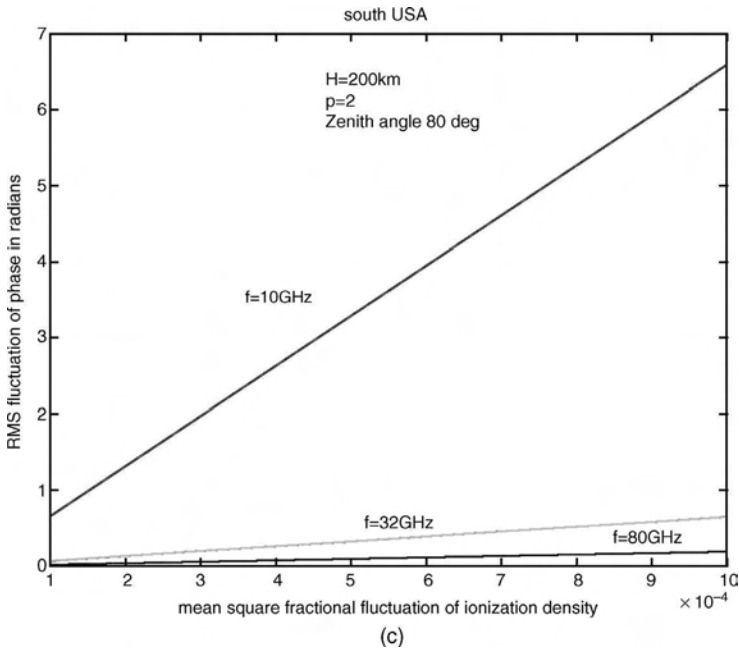
FIGURE 7.15. (*Continued*)
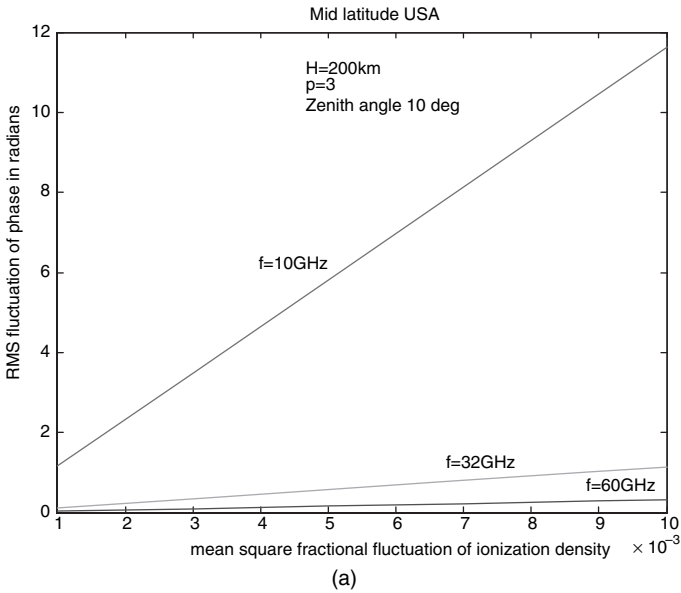
FIGURE 7.16. (a) RMS of signal intensity phase fluctuations (in radians) versus mean square fractional fluctuations of plasma density (normalized by the mean ionization density of $10^{12}\,\mathrm{m^{-3}}$) for frequencies of 10, 32 and 60 GHz, for a spectral index of $p' = 3$ (corresponded to perturbed mid latitude ionosphere above USA) and zenith angle of $10°$. The outer scale (thickness) of ionospheric layer is 100 km, the ionospheric height is 200 km. (b) The same as in Fig. 7.16a, but for satellite zenith angle of $45°$. (c) The same as in Fig. 7.16a, but for satellite zenith angle of $80°$.

(b)

(c)
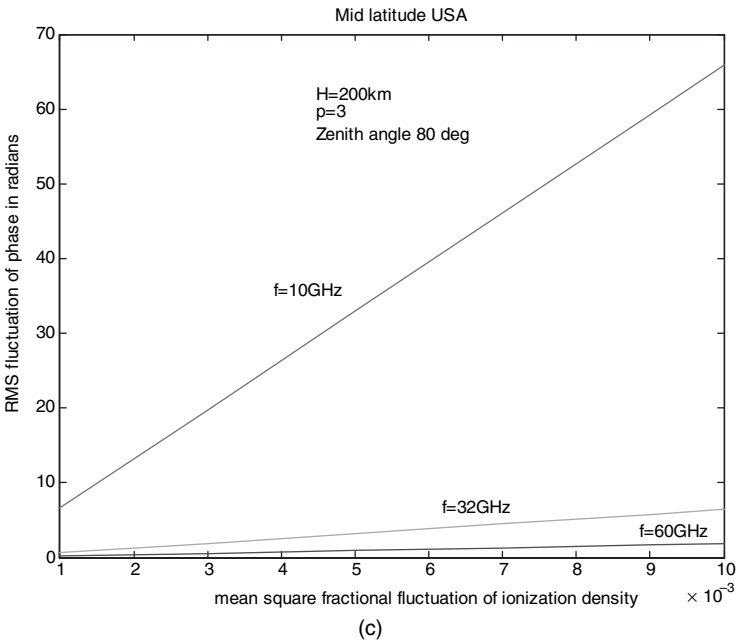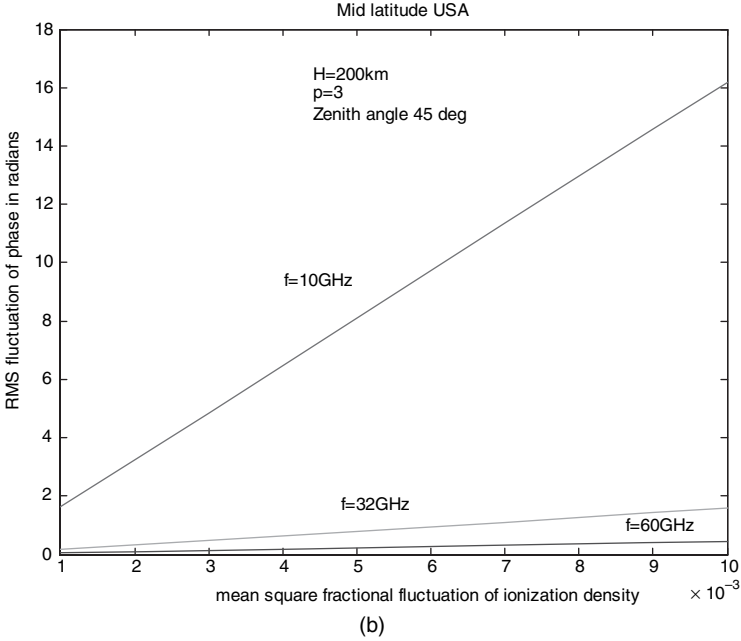
FIGURE 7.16. (*Continued*)
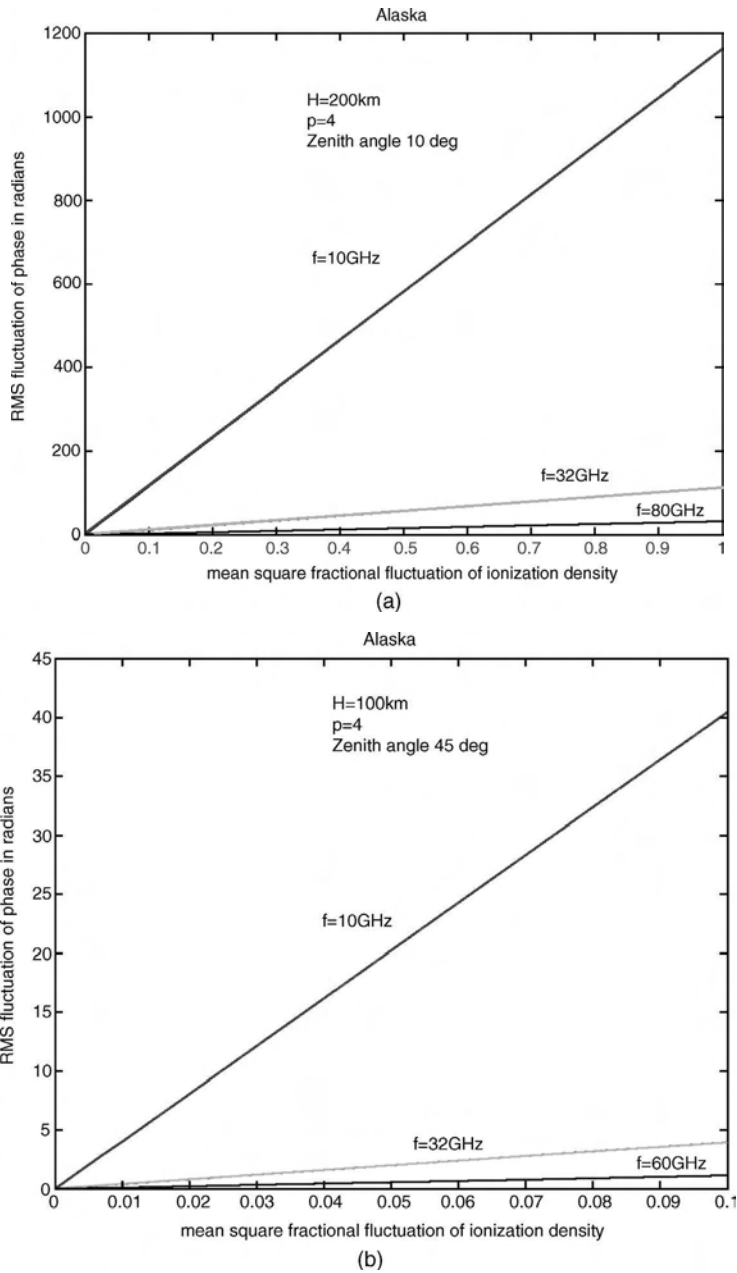
FIGURE 7.17 (a) RMS of signal intensity phase fluctuations (in radians) versus mean square fractional fluctuations of plasma density for frequencies of 10, 32 and 60 GHz, for a spectral index $p' = 4$ (corresponded to perturbed polar ionosphere above Alaska) and for satellite zenith angle of $10°$. The outer scale (i.e., thickness) of ionospheric layer is 100 km, and the ionospheric height is 200 km. The mean ionization density is $10^{12}\,\mathrm{m^{-3}}$, on which the horizontal axis is normalized. (b) The same as in Fig. 7.17a, but for a satellite zenith angle of $45°$. (c) The same as in Fig. 7.17a, but for a satellite zenith angle of $80°$.

Alaska

H=100km
p=4
Zenith angle 80 deg

f=10GHz

f=32GHz

f=60GHz

RMS fluctuation of phase in radians

mean square fractional fluctuation of ionization density

(c)
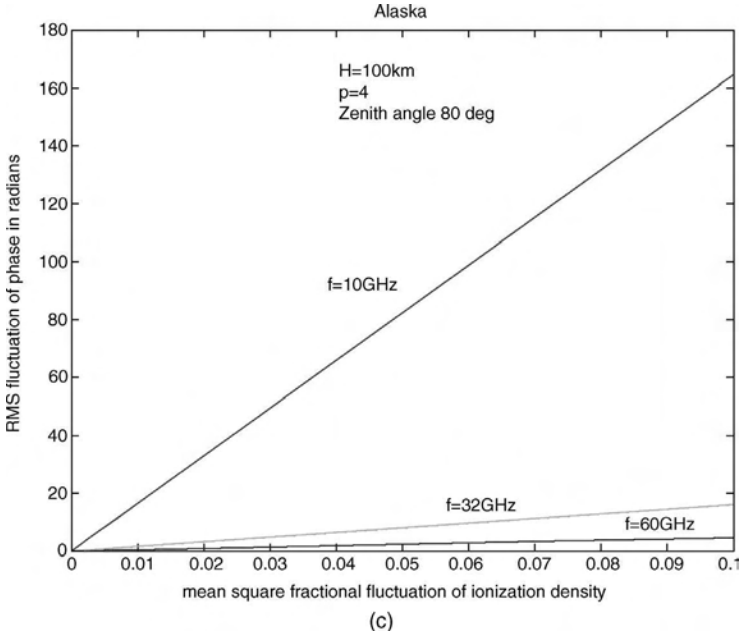
FIGURE 7.17. (*Continued*)

from ionospheric irregularities is observed. Finally, for a given ionization density, when the zenith angle χ became larger, the effect of signal phase and amplitude fluctuations became stronger.

- the analysis of field intensity by use of the perturbation method, as well as the scintillation index was done for various values of the spectral index. In addition, a distinction was made between weak scattering, $\sim \langle (\Delta \Phi)^2 \rangle = 10^{-1}, 1$, and strong scattering, $\sim \langle (\Delta \Phi)^2 \rangle = 100$, namely;

- For a given frequency, an increase in the spectral index causes an increase in the intensity fluctuations.

- For a given frequency, an increase in phase fluctuation, causes an increase in the intensity of fluctuations.

- The behavior of the spectrum of signal intensity fluctuations in the frequency domain is of exponential type.

7.3. BACK AND FORWARD SCATTERING OF RADIO WAVES BY SMALL-SCALE IONOSPHERIC INHOMOGENEITIES

In previous sections we considered effects of large- and small-scale ionospheric inhomogeneities on radio propagation through the ionosphere mostly for the

purpose of land satellite communication problems. As was shown in References [44–49], scattering at large angles, up to 180°, occurs at the male-scale inhomogeneities oriented along the ambient geomagnetic field. This effect is actually for HF/VHF-band radio propagation ($1\,\text{MHz} < f < 100\,\text{MHz}$), for which all characteristic scales of plasma inhomogeneities are at the same order or smaller than the wavelength, that is $l \leq \lambda$. In other words, this effect is actual for over-horizon radar applications due to reflections from the ionosphere, or for long-range radio propagation due to scattering in the inhomogeneous ionosphere. All these effects are very actual for an investigation of radar echoes caused by back and forward scattering from small-scale ionospheric inhomogeneities [44,45] and for creation of HF/VHF-radio wave communication channels due to forward scattering from small-scale magnetic field oriented nonisotropic ionospheric inhomogeneities (called the H_E-irregularities [46–48]).

7.3.1. Effects of Back and Forward Scattering

The theory of back scattering of radio waves by nonisotropic ionospheric irregularities was created by Booker [44,45] for the purpose of radiolocation and radar applications, which we briefly present below. The geometry of the problem is presented in Figure 7.18. The coordinate system is located at the point O inside the scattering volume V consisting of small-scale nonisotropic inhomogeneities. Let us consider that the transmitter is located at the point P_1 and the receiver is at the point P_2. Thus the field of the radio wave, E_0, in the point O_1 from the transmitter with
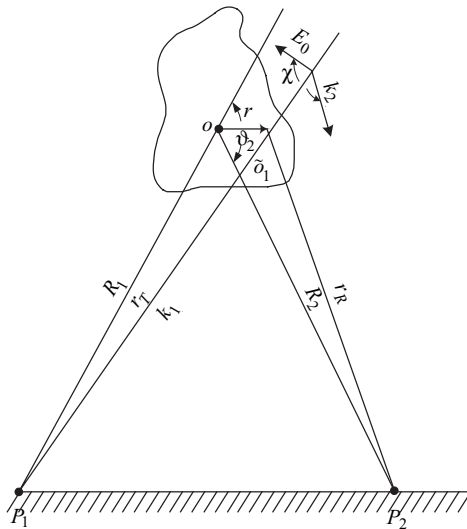
FIGURE 7.18. The radio path of back and forward scattering by the ionospheric volume consisting of small-scale plasma inhomogeneities.

isotropic antenna and power $\widetilde{W}$ can be presented as [44,45]

$$E_0 = \left(\frac{Z\widetilde{W}}{2\pi}\right)^{1/2}\frac{e^{ik\mathbf{r}_T}}{r_T} \tag{7.103}$$

where Z is the impedance of the environment. Due to small-scale fluctuations of plasma permittivity $\widetilde{\varepsilon}_1$ in the ionosphere within the volume of scattering defined by (7.70), an additional electrical momentum, described by the vector Hertz $\Pi = \varepsilon_1\mathbf{E}_0$, is created. Finally, the scattering wave arrives at the point P_2 of the receiver after scattering from the elementary volume dv within the total volume V, which covers point O and O_1. This field can be presented in the following form [44,45]:

$$dE = \frac{k_0^2\sin\chi}{4\pi}|\Pi|\frac{\exp\{-ik_2(R_2 - r)\}}{|R_2 - \mathbf{r}|}dv \tag{7.104}$$

where χ is the angle between the vector of the electric field $\mathbf{E}_0$ and the wave vector $\mathbf{k}_2$ of the scattered wave (see Fig. 7.18). Then the cumulative scattering effect from the total volume V can be presented as

$$E = \frac{k_0^2\sin\chi}{4\pi}\left(\frac{Z\widetilde{W}}{2\pi}\right)^{1/2}\int\widetilde{\varepsilon}_1(\mathbf{r})\frac{\exp\{i(\mathbf{k}_1\mathbf{r}_T - \mathbf{k}_2\mathbf{r}_R\}}{r_T r_R}dv \tag{7.105}$$

All geometrical parameters are shown in Figure 7.18. Finally, the intensity of the scattered signal at the receiver has the following form [44,45]:

$$I = \langle|E|^2\rangle = \frac{k_0^4\sin^2\chi}{32\pi^3}Z\widetilde{W}\int\langle\widetilde{\varepsilon}_1(\mathbf{r})\widetilde{\varepsilon}_1(\mathbf{r}')\rangle\frac{e^{\left\{i(\mathbf{k}_1\mathbf{r}_T - \mathbf{k}_2\mathbf{r}_R - \mathbf{k}'_1\mathbf{r}'_T + \mathbf{k}'_2\mathbf{r}'_R)\right\}}}{\mathbf{r}_T\mathbf{r}_R\mathbf{r}'_T\mathbf{r}'_R}dv\,dv' \tag{7.106}$$

As was shown in Section 7.2.2, for the statistically homogeneous distribution of fluctuations of plasma density within the volume V,

$$\langle\widetilde{\varepsilon}_1(\mathbf{r})\widetilde{\varepsilon}_1(\mathbf{r}')\rangle = \int U_{\widetilde{\varepsilon}}(\mathbf{K})e^{-i\mathbf{K}\mathbf{r}''}d\mathbf{K} \tag{7.107}$$

where $\mathbf{r}'' = \mathbf{r} - \mathbf{r}'$. We can simplify the integrand in formula (7.106) following References [44,45] by saying that the maximum linear dimension of the volume V, denoted by L, is smaller than the distances R_1 and R_2 between the scattered volume and the transmitter and receiver, respectively, but it is larger than the characteristic scales of plasma density fluctuations introduced in Section 7.2.2. In such assumptions, the expression for the field intensity can be presented as

$$I = I_0\frac{k_0^4\sin^2\chi}{R_2^2}VU_{\widetilde{\varepsilon}}(\mathbf{k}_1 - \mathbf{k}_2) \tag{7.108}$$

where I_0 is the field intensity within the volume of scattering V.

Let us now introduce the specific area of scattering (also called in the literature, the radar cross section), $\widetilde{\sigma}(\vartheta_2, \chi, k_0)$, as a wave power scattered by the unit element of the volume V inside the unit spatial angle for the wave with an unit energy incident at this volume.

$$\widetilde{\sigma}(\vartheta_2, \chi, k_0) = \frac{k_0^4 \sin^2 \chi}{4\pi^2} U_{\widetilde{\varepsilon}}(\mathbf{k}_1 - \mathbf{k}_2) \tag{7.109}$$

For the case of *forward scattering* with given angle ϑ_2 (see Fig. 7.18), the absolute value of the difference $\mathbf{k}_1 - \mathbf{k}_2$ equals

$$|\mathbf{k}_1 - \mathbf{k}_2| = k_0(1 - \cos \vartheta_2) \tag{7.110}$$

For the case of *back scattering*, when the transmitter and receiver are at the same point, that is, $\vartheta_2 = \pi$, we have $|\mathbf{k}_1 - \mathbf{k}_2| = 2k_0$. Furthermore, because $k_0^4 = \omega^4/c^4$ and, as was shown in previous sections, $\langle \widetilde{\varepsilon}_1^2 \rangle = \frac{\omega_{p0}^4}{\omega^4} \langle |\frac{N_1}{N_0}|^2 \rangle$, the coefficient in (7.109) before $U_{\widetilde{\varepsilon}}(\mathbf{k}_1 - \mathbf{k}_2)$ does not depend on the frequency of the radio wave. The frequency dependence of the radar cross section $\widetilde{\sigma}(\vartheta_2, \chi, k_0)$ is determined by the normalized spectrum of plasma density fluctuations, that is by $U_{\widetilde{\varepsilon}}(\mathbf{k}_1 - \mathbf{k}_2)/\langle \widetilde{\varepsilon}_1^2 \rangle$.

For Gaussian distribution of plasma inhomogeneities, as was shown above, the correlation coefficient in the Cartesian coordinate system with z-axis oriented along the geomagnetic field lines are equal

$$\rho_{\widetilde{\varepsilon}}(x, y, z) = \exp\left\{ -\frac{x^2 + y^2}{l_\perp^2} - \frac{z^2}{l_\parallel^2} \right\} \tag{7.111}$$

In this case, the normalized spectrum of plasma density fluctuations equals [44–46]

$$U_{\widetilde{\varepsilon}}(\mathbf{k}_1 - \mathbf{k}_2)/\langle \widetilde{\varepsilon}_1^2 \rangle = l_\perp^2 l_\parallel (2\pi)^{3/2} \exp\left\{ -2k_0^2(l_\perp^2 + l_\parallel^2 \sin^2 \psi) \right\} \tag{7.112}$$

where $\psi = \pi/2 - \beta$, β is the angle between the geomagnetic field lines and the direction of scattered wave (determined by $\mathbf{k}_2$). For the spectral function of the form (7.112), the frequency dependence of the radar cross section from the nonisotropy small-scale inhomogeneities is

$$\widetilde{\sigma}(f) \sim \exp\left(-f^2/f_{p0}^2 \right) \tag{7.113}$$

where f_{p0} is the plasma frequency.

In Reference [46], the exponential linear frequency dependence $\widetilde{\sigma}(f) \sim \exp(-f/f_{p0})$ has been obtained experimentally, which can be obtained if instead of Gaussian distribution (7.111), the polynomial distribution of $\widetilde{\varepsilon}_1$ is used

$$\rho_{\tilde{\varepsilon}}(x, y, z) \sim \left\{ \frac{1}{2\pi} + \alpha_1^2 x^2 + \alpha_2^2 y^2 + \alpha_3^2 z^2 \right\}^{-2} \qquad (7.114)$$

where α_i, $i = 1, 2, 3$, are the coefficients of anisotropy of plasma inhomogeneities along the corresponding coordinate axes.

7.3.2. Power of H_E–Scatter Signals

In References [46–48] the effective area of forward scattering by isotropic inhomogeneities of the ionospheric E-layer, which is oriented along the geomagnetic field, has been derived for determining the power of the quasi-continuous and burst-like signals scattered from such plasma irregularities. Caused by the scattering from these inhomogeneities, radio signals can propagate within the land-ionospheric communication channel at long distances. It was shown both theoretically and experimentally, that such plasma anisotropic inhomogeneities have a double nature. First the nature, is created by meteor trails and the second by different kinds of instabilities in plasma, called H_E–inhomogeneities [46–48], caused by the chaotic motions of the atmospheric wind streams, gradients of ambient temperature, and pressure.

Therefore, two kinds of scattered signals are usually observed. One, having a burst-like form due to scattering by meteor trails and the second, a quasi-continuous form due to scattering by H_E–inhomogeneities. Furthermore, as the processes of diffusion and drift in ambient electric and magnetic fields are usually predominant in the ionosphere, the same as in the troposphere, striation of large-scale plasma turbulences (called irregularities) on an ensemble of small-scale turbulences is constantly observed [47,48]. These irregularities are usually oriented along the geomagnetic field lines generating an area with anisotropic plasma density disturbances strongly aligned along the geomagnetic field. Investigations of such kinds of scattering of metric waves ($f = 44 – 74$ MHz), carried out both theoretically and experimentally, have shown that at the altitudes of E- and F-layer of the middle latitude ionosphere, the average longitudinal (along the magnetic field) scales of field-aligned plasma irregularities, responsible for these types of scattering, range from a few meters to hundreds of meters and their transverse scales (across to the magnetic field) range from tenths of a meter to a few meters. These inhomogeneities allow us to send HF/VHF-signals at long distances due to scattering from the inhomogeneous ionosphere. Let us now describe the main features of such forward scattering that covers scattering angles up to 180°.

Cross-section of Forward Scattering. We rewrite (7.109) to present the effective area of scattering in the spatial wavelength domain through the unit vectors of
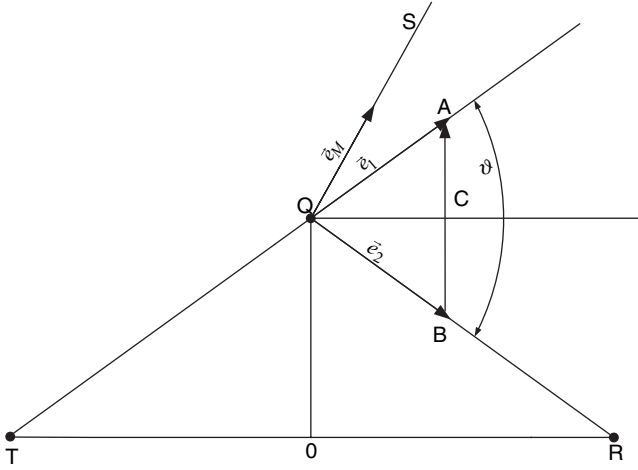
FIGURE 7.19. Geometry of forward scattering.

incident and scattered waves instead of the corresponding angles

$$\tilde{\sigma} = \left\langle \left| \frac{\tilde{\varepsilon}_1}{\varepsilon_0} \right|^2 \right\rangle \frac{\pi^2 \sin^2 \chi}{\lambda^4} F_{\tilde{\varepsilon}}[k_0(l_2 - l_1), k_0(m_2 - m_1), k_0(n_2 - n_1)] \qquad (7.115)$$

Here $F_{\tilde{\varepsilon}}$ is the Fourier transform of the space correlation function $U_{\tilde{\varepsilon}}$ of the dielectric permittivity; $\mathbf{e}_1(l_1, m_1, n_1)$ is the unit vector of the incident wave; $\mathbf{e}_2(l_2, m_2, n_2)$ is the unit vector of the scattered wave; all other parameters are described above in Section 7.3.1. A geometry of the problem is shown in Figure 7.19, where TQ is the incident ray, OR is the reflected ray, and QS is the direction of an inhomogeneity, that is, $\mathbf{e}_M$ is the unit vector describing the orientation of the inhomogeneity with respect to the direction of the incident ray; and QC is the projection of the inhomogeneity onto a reference plane. Here, we also assume that the z-axis coincides with the direction of the inhomogeneity and suppose that QS forms an angle of $90° + \psi$ (in the case of specular reflection $\psi = 0$). According to investigations carried out in References [44–48] it was found that the autocorrelation function of signal-level fading has a Gaussian form in most cases. This suggests that the normalized space correlation function of the permittivity fluctuations within the scattering medium, $U_{\tilde{\varepsilon}}$, is also Gaussian and its Fourier transform can be presented in the following form:

$$F_{\tilde{\varepsilon}}[k_0(l_2 - l_1), k_0(m_2 - m_1), k_0(n_2 - n_1)] = (2\pi)^{3/2} abc$$
$$\times \exp\left\{ -\frac{k_0^2}{2} [a^2(l_2 - l_1)^2 + b^2(m_2 - m_1)^2 + c^2(n_2 - n_1)^2] \right\} \qquad (7.116)$$

where a, b, and c are the correlation scales of the fluctuations of the dielectric permittivity along the corresponding coordinate axes. From geometry shown in Figures 7.18 and 7.19 we get

$$
\begin{aligned}
|AB| &\equiv [(l_2 - l_1)^2 + (m_2 - m_1)^2 + (n_2 - n_1)^2]^{1/2} \\
&= 2 \sin \frac{\vartheta}{2} (n_2 - n_1)^2 = 4 \sin^2 \frac{\vartheta}{2} \sin^2 \psi
\end{aligned}
\tag{7.117}
$$

Assuming that the inhomogeneity is symmetric with respect to the longitudinal axis QS (along z-axis), we set $a = b = l_\perp$ and $c = l_\parallel$, where $l_\perp$ is the transverse and $l_\parallel$ is the longitudinal correlation scales of the fluctuations of the plasma density (or plasma permittivity). For the small angles ψ, that is, for the quasi-specular scattering, and for strong anisotropy of inhomogeneities ($l_\parallel \gg l_\perp$) from (7.115)–(7.117) we get

$$
\widetilde{\sigma} = (2\pi)^{3/2} \frac{\pi^2 \sin^2 \chi}{\lambda_N^4} \left\langle \left(\frac{N_1}{N_0} \right)^2 \right\rangle l_\parallel l_\perp^2 \exp \left\{ -\frac{8\pi^2}{\lambda^2} l_\perp^2 \sin^2 \frac{\vartheta}{2} \right\} \exp \left\{ -\frac{8\pi^2}{\lambda^2} l_\parallel^2 \psi^2 \sin^2 \frac{\vartheta}{2} \right\}
\tag{7.118}
$$

Here λ_N is the plasma wavelength; the above formula was obtained keeping in mind that $\left\langle \left| \frac{\tilde{\varepsilon}_1}{\tilde{\varepsilon}} \right|^2 \right\rangle = 1 - \left(\frac{\lambda}{\lambda_N} \right)^4$ for an ionized medium and that $\left\langle \left| \frac{\tilde{\varepsilon}_1}{\tilde{\varepsilon}} \right|^2 \right\rangle = \left(\frac{\lambda}{\lambda_N} \right)^4 \left\langle \left(\frac{N_1}{N_0} \right)^2 \right\rangle$; N_1 is the density of the plasma disturbances with respect to the ambient ionospheric plasma density N_0.

The Power of The Scattered Signal. The power of the forward scattered signal at the receiving antenna input can be determined by the following formula [44–46]

$$
P_R = P_T \frac{\lambda^2}{(4\pi)^2} \int_V \frac{G_T G_R \widetilde{\sigma} dv}{r_T^2 r_R^2}
\tag{7.119}
$$

where G_T and G_R are the transmitting and receiving antenna gain factors, respectively. For sufficiently long radio paths, when the working volume of scattering is not too large with respect to radio path, that is, $V^{1/3} \ll r_T, r_R$, the product $r_T^2 r_R^2$ can be replaced by r^4. Where r is the distance from the receiver and transmitter along the straight line TOR (see Fig. 7.19), so that

$$
P_R = P_T \frac{\lambda^2}{(4\pi)^2 r^4} \int_V G_T G_R \widetilde{\sigma} dv
\tag{7.120}
$$

The power of *quasi-continuous scattered signals* can be determined by numerical integration of (7.120) where $\widetilde{\sigma}$ is determined from (7.118). Here, we note that the

factor $l_\perp^2 \exp\left\{-\frac{8\pi^2}{\lambda^2} l_\perp^2 \sin^2 \frac{\vartheta}{2}\right\}$ has a maximum for $l_\perp^{\mathrm{opt}} = \lambda/[2\sqrt{2}\pi \sin(\vartheta/2)]$. As this factor decreases fairly sharply for values $l_\perp$ other than $l_\perp^{\mathrm{opt}}$, we can assume that those inhomogeneities are mainly involved in the scattering process for which $l_\perp = l_\perp^{\mathrm{opt}}$. In this case, factor $\exp\left\{-\frac{8\pi^2}{\lambda^2} l_\perp^2 \sin^2 \frac{\vartheta}{2}\right\} = \exp(-1)$. Taking the foregoing into account and introducing notation $\alpha = l_\parallel/\lambda$, we finally get the power of scattered quasi-continuous H_E-signals

$$P_R = P_T \frac{\alpha\lambda^2}{32e(2\pi)^{1/2}r^4} \left\langle \left(\frac{N_1}{N_0}\right)^2 \right\rangle \int_V \frac{G_T G_R \sin^2 \chi}{\sin^2(\vartheta/2)} \exp\left\{-8\pi^2\alpha^2\psi^2 \sin^2 \frac{\vartheta}{2}\right\} dv$$

(7.121)

For the practical use of this formula, one must determine the parameters ϑ, χ and ψ at the center of each element of volume of scattering using the geometry and geophysical parameters of the radio trace and allow for the gain factors of the transmitting and receiving antennas for the corresponding directions. This procedure for the concrete middle-latitude radio trace is fully described in Reference [46]. We do not enter into details of the problem presented in Figure 7.20. To limit the working volume in the numerical integration, it is convenient to plot the isolines of the quantity of angle $\gamma = \psi \sin(\vartheta/2)$ given in Figure 7.20, at the left side of each isoline. The numbers in decibel at the right side of each isoline in Figure 7.20 indicate the decrease of the power received due to the exponential factor $\exp\{-8\pi^2\alpha^2\gamma^2\}$. Here, the first number is for $\alpha = l_\parallel/\lambda = \sqrt{10} \approx 3.16$, the second is for $\alpha = 10$. We can see that for $\alpha = 3.16$ integration can be confined to within the volume of scattering between the isolines $\gamma = \pm 3°$ and for $\alpha = 10$ between the lines
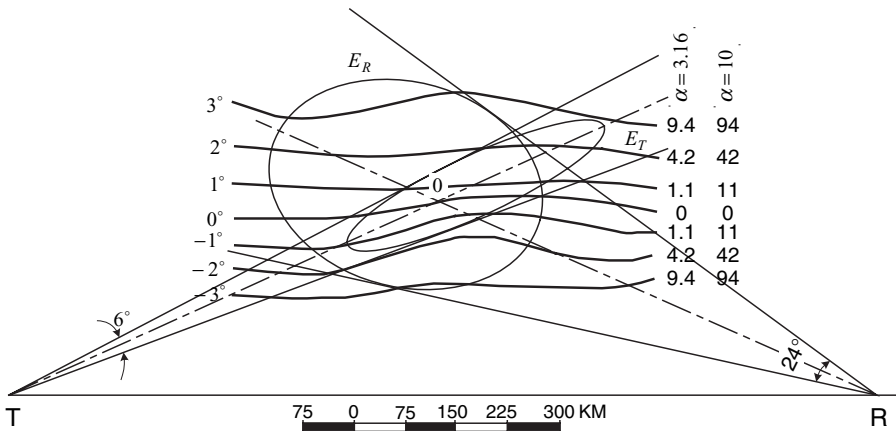
FIGURE 7.20. The active zone of forward scattering defined by the intersection of the transmitting and receiving antenna patterns.

$\gamma = \pm 1°$, because beyond this region the exponential factor gives a decrease in the level of more than $10\,\text{dB}$. Figure 7.20 also shows the limitation of the working scattered volume due to the spatial antenna radiation patterns. The ellipses E_T and E_R represent the intersection of the antenna diagrams by the horizontal plane plotted at the center of the active scattering zone at the height of about $100\,\text{km}$ above the Earth's surface. From the corresponding experiments carried out at the middle-latitude radio traces, it follows that the height of H_E signals is ranged between 100 and $110\,\text{km}$. We can assume that the effective height of the working volume at the vertical plane is about $5\,\text{km}$ and therefore, can be regarded as a cylindrical body aligned along the geomagnetic field lines.

The same derivations can be done for the *burst-like signals*, which are most likely of meter origin. In this case, in formula (7.121) one should confine oneself to a volume ΔV_F, where half of the Fresnel zone forms

$$\Delta V_F = S \cdot \sqrt{\frac{\lambda r_T r_R}{(r_T + r_R)(1 - \cos^2 \beta \sin^2 \Phi}} \tag{7.122}$$

Here, S is the effective area of scattering (cross section) of an inhomogeneity; β is the angle between the direction of the inhomogeneity and the TQR-plane; and 2Φ is the angle TQR (see Fig. 7.19). As the cross section S, it is reasonable to take the area of the circle whose diameter equals the radius of the cross-correlation $l_\perp^{opt}$. Considering that

$$N_0 = \frac{f_N^2}{80.8} = \frac{9 \cdot 10^{16}}{80.8 \lambda_N^2}$$

one can represent the factor $\left\langle \left(\frac{N_1}{N_0}\right)^2 \right\rangle / \lambda_N^4$ in the form $8 \cdot 10^{-31} \langle N_1^2 \rangle$. With allowance for the foregoing, formula (7.121) takes the form:

$$P_R = 37.7 \cdot 10^{-34} P_T \frac{\alpha \lambda^5 \langle N_1^2 \rangle}{32 e (2\pi)^{1/2} r^4} \frac{G_T G_R \sin^2 \chi}{\sin^2(\vartheta/2)} \exp\{-8\pi^2 \alpha^2 \gamma^2\} \Delta V_F \tag{7.123}$$

This formula is more general with respect to the known power formula for radio wave reflection from under dense meteor trails [50]. Experiments carried out during the seventies [46] have shown a good agreement of experimental data with theoretical predictions based on formula (7.123). Particularly, a good agreement was obtained for $\alpha = 300$, that is, for $l_\| = 300\lambda$, which for frequencies changed from 44 to $74\,\text{MHz}$ approximately gives the width of the half Fresnel zone.

Hence, it can be concluded that the statistical character of quasi-continuous and burst-like signals are properly described by the theory of forward scattering on local plasma inhomogeneities described above.

BIBLIOGRAPHY

[1] Evans, B. G., *Satellite Communication Systems*, IEE, London, 1999.

[2] Pattan, B., *Satellite-Based Cellular Communications*, McGraw-Hill, NY, 1998.

[3] Saunders, S. R., *Antennas and Propagation for Wireless Communication Systems*, J. Wiley & Sons, New York, 1999.

[4] Ratcliffe, J. A., *Physics of the Upper Atmosphere*, Academic Press, New York, 1960.

[5] Ginzburg, V. L., *Propagation of Electromagnetic Waves in Plasma*, "Science," Moscow, 1964.

[6] Ratcliffe, J. A., *Introduction in Physics of Ionosphere and Magnetosphere*, Academic Press, New York, 1973.

[7] Alpert, Ya. L., *Propagation of Electromagnetic Waves and Ionosphere*, "Science," Moscow, 1972.

[8] Gurevich, A. V., and A. B. Shvartzburg, *Non-linear Theory of Radiowave Propagation in the Ionosphere*, "Science," Moscow, 1973.

[9] Philipp, N. D., N. Sh. Blaunstein, L. M. Erukhimov, et al., *Modern Methods of Investigation of Dynamic Processes in the Ionosphere*, "Shtiintsa," Kishinev, Moldova, 1991.

[10] Philipp, N. D., V. N. Oraevsky, N. Sh. Blaunstein, et al., *Evolution of Artificial Plasma Inhomogeneities in the Earth's Ionosphere*, "Shtiintsa," Kishinev, Moldova, 1986.

[11] Gurevich, A. V., and E. E. Tsedilina, *Extremely-Long-Range Propagation of Short Waves*, "Science," Moscow, 1979.

[12] Gel'berg, M. G., *Inhomogeneities of High-Latitude Ionosphere*, "Science," Novosibirsk, USSR, 1986.

[13] Banks, P., "Collision frequencies and energy transfer," *Planet. Space Sci.*, vol. 14, 1969, pp. 1085–1122.

[14] Belikovich, V. V., E. A. Benediktov, M. A. Itkina, et al., "Frequency dependence of anomalous absorption of cosmic radio radiation in the ionosphere in areas of polar cups," *Geomagn. and Aeronomy*, vol. 9, 1969, pp. 485–490.

[15] Taubenheim, J., and V. Hense, "The contribution of the ionospheric region to cosmic noise absorption," *Annales Geophys.*, vol. 22, 1966, pp. 320–322.

[16] Mehta, N. C., and N. D. D'Angelo, "Cosmic noise absorption by E-region plasma waves," *J. Geophys. Res.*, vol. 85, 1980, pp. 1779–1782.

[17] Titheridge, J. E., "The diffraction of satellite signals by isolated ionospheric irregularities," *J. Atmosph. Terrest. Phys.*, vol. 33. 1974, pp. 47–69.

[18] Leadabrand, R. L., A. G. Larson, and J. C. Hodges, "Preliminary results on the wavelength dependence and aspect sensitivity of radar echoes between 50 and 3000 MHz," *J. Geophys. Res.*, vol. 72, 1967, pp. 3877–3887.

[19] Reinisch, B. W., and X. Huang, "Automatic calculation of electron density profiles from digital ionograms, 3, Processing of bottomside ionograms," *Radio Sci.*, vol. 18, 1983, pp. 477–492.

[20] Huang, X., and B. W. Reinisch, "Vertical electron content from ionograms in real time," *Radio Sci.*, vol. 36, no. 2, 2001, pp. 335–342.

[21] Blaunstein, N. Sh., and Ye.Ye. Tsedilina, "Spreading of strongly elongated inhomogeneities in the upper ionosphere," *Geomagn. and Aeronomy*, vol. 24, no. 3, 1984, pp. 340–344.

[22] Blaunstein, N. Sh., and Ye.Ye. Tsedilina, "Effects of the initial dimensions on the nature of the diffusion spreading of inhomogeneities in a quasi-uniform ionosphere," *Geomagn. and Aeronomy*, vol. 25, no. 1, 1985, pp. 39–44.

[23] Blaunstein, N., "Diffusion spreading of middle-latitude ionospheric plasma irregularities," *Annales Geophysicae*, vol. 13, 1995, pp. 617–626.

[24] Blaunstein, N., "The character of drift spreading of artificial plasma clouds in the middle-latitude ionosphere," *J. Geophys. Res.*, vol. 101, 1996, pp. 2321–2331.

[25] Blaunstein, N., "Changes of the electron concentration profile during local heating of the ionospheric plasma," *J. Atmosph. Terr. Phys.*, vol. 58, no. 12, 1996, pp. 1345–1354.

[26] Blaunstein, N., "Evolution of a stratified plasma structure induced by local heating of the ionosphere." *J. Atmos. and Terr. Phys.*, vol. 59, no. 3, 1997, pp. 351–361.

[27] Belikovich V. V., E. A. Benediktov, A. V. Tolmacheva, et al., *Ionospheric Research by Means of Artificial Periodic Irregularities*, Copernicus, GmbH, Katlenburg-Lindau, Germany, 2002.

[28] Reinisch, B. W., D. M. Haines, K. Bibl, et al., "The radio plasma imager investigation on the image spacecraft," *Space Sci. Rev.*, vol. 91, 2000, pp. 319–359.

[29] Wernik, A. W., and C. H. Liu, "Application of refractive scintillation theory to ionospheric irregularities stadies," *Artificial Satellites*, vol. 10, 1975, pp. 37–58.

[30] Erukhimov, L. M., and V. A. Rizhkov, "Study of focusing ionospheric irregularities by methods of radio-astronomy at frequencies of 13–54 MHz," *Geomagn. and Aeronomy*, vol. 5, 1971, pp. 693–697.

[31] Crain, C. M., H. G. Booker, and S. A. Fergusson, "Use of refractive scattering to explain SHF scintillations," *Radio Sci.*, vol. 14, 1974, pp. 125–134.

[32] Briggs, B. H., and I. A. Parkin, "On variation of radio star and satellite scintillations with zenith angle," *J. Atmos. Terrest. Phys.*, vol. 25, 1963, pp. 339–365.

[33] Ga'lit, T. A., V. D. Gusev, L. M. Erukhimov, et al., "About the spectrum of phase fluctuations during sounding of the ionosphere," *Radiophysics*, Izv. Vuzov, vol. 26, 1983, pp. 795–801.

[34] Booker, H. G., S. A. Rateliffe, and D. H. Shinn, "Diffraction from an irregular screen with applications to ionospheric problems," *Philos. Trans. Royal Soc. London*, Ser. A, vol. 242, 1950, pp. 579–607.

[35] Chernov, L. A., *Radiowave Propagation in Medium with Random Irregularities*, Academy of Science, Moscow, 1958.

[36] Alimov, A. A., and L. M. Erukhimov, "About distribution of fluctuations of the shortwave signals," *Radiophysics*, Izv. Vuzov, vol. 16, 1973, pp. 1540–1551.

[37] Erukhimov, L. M., G. P. Komrakov, and V. L. Frolov, "About the spectrum of the artificial small-scale ionospheric turbulence," *Geomagnetism and Aeronomy*, vol. 20, 1980, pp. 1112–1114.

[38] Shkarovsky, I. P., "Generalized turbulence space-correlation and wave-number spectrum function pairs," *Can. J. Phys.*, vol. 46, 1968, pp. 524–528.

[39] Rino, C. L., and E. J. Fremouw, "The angle dependence of single scattered wavefields," *J. Atmos. Terrestr. Phys.*, vol. 39, 1977, pp. 859–868.

[40] Booker, H. G., "Application of refractive scintillation theory to radio transmission through the ionosphere and the solar wind and to reflection from a rough ocean," *J. Atmos. Terrestr. Phys.*, vol. 43, 1981, pp. 1215–1233.

[41] Booker, H. G., and A. G. Majidi, "Theory of refractive scattering in scintillation phenomena," *J. Atmos. Terrestr. Phys.*, vol. 43, 1981, pp. 1199–1214.

[42] Burke, W. J., A Rubin, N. Maynard, et al., "Ionospheric disturbances observed by DMSP at mid to low latitudes during magnetic storm in June 4–6, 1991," *J. Geophys. Res.*, vol. 105, no. 18, 2000, pp. 391–398.

[43] Mishin, E. V., J. Foster, A. Potekhin, et al., "Global ULF disturbances during a stormtime substorm on 25 December 1998," *J. Geophys. Res.*, vol. 107, 2002, pp. 1486–1990.

[44] Booker, H. G., and W. E. Gordon, "A theory of radio scattering in the ionosphere," *Proc. IRE*, vol. 38, 1950, pp. 400–412.

[45] Booker, H. G., "A theory of scattering by non-isotropic irregularities with applications to radar reflection from the Aurora," *J. Atmos. Terr. Phys.*, vol. 8, 1956, pp. 204–221.

[46] Philipp, N. D., "Power of H_E-scatter signals," *Radiophysics,* vol. 22, No. 4, 1979, pp. 407–411.

[47] Philipp, N. D., and N. Sh. Blaunstein, "Effect of the geomagnetic field on the diffusion of ionospheric inhomogeneities," *Geomagnetism and Aeronomy*, vol. 18, 1978, pp. 423–427.

[48] Philipp, N. D., and N. Sh. Blaunstein, "Drift of ionospheric inhomogeneities in the presence of the geomagnetic field," *Radiophysics*, Izv. Vuzov, vol. 18, 1978, pp. 1409–1417.

[49] Leadabrand, R. L., A. G. Larson, and J. C. Hodges, "Preliminary results on the wavelength dependence and aspect sensitivity of radar echoes between 50 and 3000 MHz," *J. Geophys. Res.*, vol. 72, 1967, pp. 3877–3887.

[50] Dolukhanov, M. P., *Distant Microwave Propagation*, Svyaz'izdat, USSR, 1962.

CHAPTER EIGHT

Indoor Radio Propagation

Indoor use of wireless systems poses one of the biggest design challenges, as indoor radio propagation is essentially a Black Art. Personal communications systems (PCS), wireless local area networks (WLANs), wireless private branch exchanger (WPBXs), and Home Phoneline Network Alliance (HomePNA, IEEE 802.11x, etc.) are the services that are being deployed in indoor areas on an increasing scale. The latter application of indoor wireless networks is proving to have a large market as it will be integrated to the emerging Digital Subscriber WLAN technologies. The Present deployment of WLAN services is reaching out to offices, schools, hospitals, and factories. The increasing demand for indoor radio applications, such as wireless LAN, "Smart house", and so on, develops a need to design and analyze those systems wisely and efficiently. An important consideration in successful implementation of the PCS is indoor radio communication. In the design process of those systems, the designer is required to place the picocell antennas (at ranges not more than 100 m) in a way that will provide an optimal coverage of the building area [1–4]. Indoor radio communication covers a wide variety of situations ranging from communication with individuals walking in residential or office buildings, supermarkets or shopping malls, to fixed stations sending messages to robots in motion in assembly lines and factory environments of the future. The indoor radio propagation modeling efforts can be divided in two categories. In the first category, transmission occurs between a unit located outside a building and a unit inside [5–7]. Expansion of current cellular mobile services to indoor application of the two types of services has been the main thrust behind most of the measurements in this category.

In the second category the transmitter and the receiver are located inside the building [8–11]. Establishment of specialized indoor communication systems has motivated most of the researchers in this category. Although the impulse response

approach is compatible with both, it has been mainly used for measurements and modeling effort reported in the second category.

There is a large variety of different models developed in recent decades to describe the propagation of signals in indoor environments [12–23]. Their ability to predict the behavior of signals in indoor communication channels is crucial, and the confusion and lack of correlation between these models diminish their usefulness. The thorough understanding of these models and their unification to a more applicable one will allow a better behavioral prediction and better capabilities in the design of indoor communication networks. The indoor radio propagation environment is very complex and has many specific features and characteristics [1,3,4]. Adding all these variables together produces a very complex problem that has to be dealt with efficiently and elegantly. Every indoor communication system, as well as wireless outdoor system (see Chapter 1), has a different structure and requirements due to their various applications. Therefore, giving an accurate answer to each indoor communication system using the same models is complex. Path loss is difficult to calculate for an indoor environment. Because of the variety of physical barriers and materials within the indoor structure, the signal does not predictably lose energy. Walls, ceilings and other obstacles usually block the path between receiver and transmitter. Depending on the building construction and layout, the signal usually propagates along corridors and into other open areas. In some cases, transmitted signals may have a direct path (Line-of-Site, LOS) to the receiver. LOS examples of indoor spaces are warehouses, factory floors, auditoriums, and enclosed stadiums. In most cases the signal path is obstructed (NLOS). Finally, those who are involved in the wireless discipline whether as a designer or as a user, must be aware of the different construction materials used for the interior and exterior walls, and of the location of a building for the best position of WLAN radio equipment. For optimal performance, the user should also consider work activities. Ultimately, the WLAN user needs to understand the relationship between indoor propagation effects and how WLAN performance is affected.

The indoor and the outdoor channels are similar in their basic features: they both experience multipath dispersions caused by a large number of reflectors and scatterers. As illustrated further in this book, they can be described using the same mathematical models. However, there are also major differences, which we want to describe here briefly.

The conventional outdoor mobile channel (with an elevated base antenna and low-level mobile antennas) is stationary in time and nonstationary in space. The temporal stationary picture is observed due to the fact that the signal dispersion is usually caused by large fixed objects (such as buildings). In comparison, the effects caused by people and vehicles in motion are negligible. The indoor channel, on the contrary, is stationary neither in space nor in time. Temporal variations in the indoor channel statistics are due to the motion of people and equipment around the low-level portable antennas.

The indoor channel is characterized by higher path losses and sharper changes in the mean signal level, as compared to the mobile channel [3,24,25]. Furthermore, applicability of a simple negative-exponent distance-dependent path loss model,

well established for the outdoor channels (see Chapter 5), is not universally accepted for the indoor channel. Rapid motion and high velocities, typical of mobile users, are absent in an indoor environment. The Doppler shift effects, that is the frequency-selective *fast fading* effects (see Chapter 1), in the indoor channel are therefore negligible.

Maximum excess delay for the mobile channel is typically several microseconds if only the local environment of the mobile is considered, and more than 100 μs without distant reflectors, and 10–20 μs with distant reflectors. The indoor channel, on the contrary, is characterized by excess delays of less than 1 μs and an rms delay spread in the range of several tens to several hundreds of nanoseconds (most often less than 100 ns [3,26]).

As a result, for the same level of inter-symbol interference (ISI), transmission rates can be much higher, and the bit-error-rate (BER) can be much lower in indoor environments [27]. Also, the relatively large outdoor mobile transceivers are powered by the vehicle's battery with an antenna located away from the mobile user. This is in contrast with lightweight portables normally operated close to the user's body. As a result, much higher transmitted powers are feasible in a mobile environment.

Finally, the indoor radio channel differs from the outdoor mobile or personal radio channel in two principal aspects: the distances covered, which are much smaller, and the variability of the environment, which is much greater for smaller transmitter–receiver separation distances.

8.1. MAIN PROPAGATION PROCESSES AND CHARACTERISTICS

The propagated electromagnetic signal in the indoor environment can undergo three primary physical mechanisms. These are reflection, diffraction, and scattering. The following definitions assume small signal wavelength, large distances (relative to wavelength), and sharp edges.

Reflection occurs when the radio wave impinges on an obstacle whose dimensions are considerably larger than the wavelength of the incident wave. A reflected wave can either decrease or increase the signal level at the reception point. Reflections occur from the ground surface and from buildings and walls. In practice, not only metallic materials but also dielectrics (or electrical insulators) cause reflections. Other materials will reflect part of the incident energy and transmit the rest. The exact amount of transmission and reflection is also dependent on the angle of incidence, material thickness, and dielectric properties. The actual signal levels reflected from insulators depends, in a very complicated way, on many characteristics such as geometry, different materials' characteristics, and so on. Major contributors to reflection are walls, floors, ceilings, and furniture.

Diffraction occurs when direct visibility between the transmitter and the receiver can be obstructed by sharp obstacles (edges, wedges, etc.), the dimensions of which are considerably larger than the signal wavelength. The secondary waves resulting from the obstructing surface are present throughout the space and even behind the obstacle, giving rise to a bending of waves around the obstacle, even when a LOS

path does not exist between the transmitter and receiver. At high frequencies of UHF/X-bands, diffraction, like reflection, depends on the geometry of the object as well as on the amplitude, phase, and polarization of the incident wave at the point of diffraction. It is a deterministic process where the cumulative effect of rays arriving at the receiver can be described by the Fresnel integrals introduced in Chapter 4.

Scattering occurs when the medium through which the wave travels contains the obstacles whose dimensions are smaller than or comparable to the wavelength and where the number of obstacles per unit volume is large. Scattered waves are produced by rough surfaces, small objects, or by other irregularities in the channel. The nature of this phenomenon is not similar to the reflection and diffraction because radio waves are scattered in a greater number of directions with random phase and amplitude deviations, and at the receiver a random cumulative effect is observed. From all the above mentioned effects, scattering is most difficult to predict.

Multipath Phenomena. Figure 8.1 shows how a transmitted radio wave, in the indoor environment, reaches the receiving antenna in more than one path. The phenomena of reflection, diffraction, and scattering give rise to additional radio propagation paths beyond the direct "line-of-sight" (LOS) path between the radio transmitter and receiver. It is clear that in the indoor propagation situation it is very difficult to design an "RF friendly" building that is free from multipath reflections, diffraction around sharp corners, or scattering from wall, ceiling, or floor surfaces. To describe all these phenomena, the following characteristics of the channel, the same as for outdoor propagation, are usually used, for example, the attenuation or *path loss*, the *fast* and *slow fading* described in detail in Chapter 1. Regarding the indoor testing, fading effects are also caused by human activities inside buildings and are usually defined as slow variations of the total signal. Sometimes oscillating
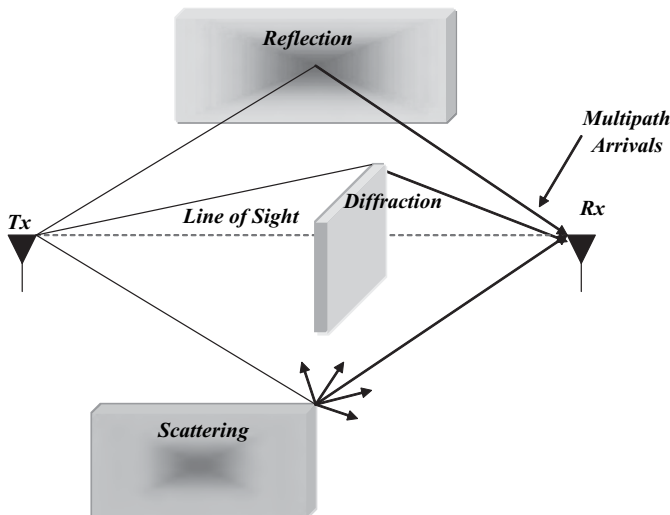
FIGURE 8.1. Multipath effects.

metal-bladed fans can cause rapid fading effects, which can be described using multipath time delay spreading. As the signal can take many paths before reaching the receiver antenna, the signals will experience different arrival times. Thus, a spreading in time (as well as frequency) can occur. Typical values for indoor spreading are less than 100 ns. Different arrival times ultimately create further degradation of the signal.

At the same time, the indoor radio channel differs from the traditional outdoor radio channel in two aspects: the distances covered, which are much smaller, and the variability of the environment, which is much greater for a much smaller range of T–R separation distance. It has been observed that propagation within buildings is strongly influenced by specific features such as the construction materials of the building and the building type. As explained previously, indoor radio propagation is dominated by reflection, diffraction, and scattering. However, the conditions are much more variable than in outdoor environments. For example, signal levels vary greatly depending on whether the interior doors are open or closed inside a building. The place where antennas are mounted also impacts large-scale propagation. Antennas mounted at the desk level in a partitioned office receive vastly different signals than those mounted on the ceiling. Also, the smaller propagation distances make it more difficult to insure far-field radiation for all receiver locations and all types of antennas. One of the main reason for indoor signal losses is the partitions. Partitions losses can be divided into two kinds:

(1) *Partition losses at the same floor.* Buildings have a wide variety of partitions and obstacles, which form the internal and external structure. Houses typically use a wood frame partition with plastic board to form internal walls and have also wood or nonreinforced concrete between floors. Office buildings, on the contrary, often have large open areas (open plane), which are constructed by using moveable office partitions so that the space may be reconfigured easily, and use metal-reinforced concrete between floors. Partitions that are formed as part of the building structure are called hard partitions, and partitions that may be moved and which do not span to the ceiling are called soft partitions. Partitions vary widely in their physical and electrical characteristics, making it difficult to apply general models to specific indoor installation.

(2) *Partition losses between floors.* The losses between floors of a building are determined by its external dimensions and wall material, as well as by the type of construction used to create the floors and the external surroundings. Even the number of windows in a building and the presence of tinting (with attenuated radio energy) can impact losses between floors.

8.2. MODELING OF LOSS CHARACTERISTICS IN VARIOUS INDOOR ENVIRONMENTS

This section outlines models for path loss within buildings. As mentioned earlier, there is not a single theoretical model for path loss and fading effects prediction in

indoor communications. What we have is that for each separate situation (i.e., propagation along the corridor, inside the room, between floors and walls), a corresponding model is employed. Here we focus the reader's attention to the most widely used propagation models in today's practical applications.

8.2.1. Numerical Ray-Tracing UTD Model

Ray tracing and the unified theory of diffraction (UTD) have been used successfully in predicting the behavior of indoor communication channels [1,28–30]. Here we present an accurate UTD model for the analysis of complex indoor radio environments in which microwave WLAN systems operate. The model employs a heuristic UTD diffraction coefficient capable of taking into account not only the effects of building walls, floors, and corners but also the presence of metallic and penetrable furniture. A numerical tool based on an enhanced 3D beam-tracing algorithm, which includes diffraction phenomena, has been developed to compute the field distribution with a high degree of accuracy, providing description of the scattered field and a physical insight into the mechanisms responsible for the multipath phenomenon. The numerical results show that the electromagnetic field distribution and the channel performance are significantly influenced by the diffraction processes arising from the presence of furniture.

The Field Prediction. The electromagnetic field is represented in terms of diffracted and ray-optical fields. The various elements of the environment are modeled as junctions of thin flat multi-layered lossy or lossless structures. The geometric optics (GO) field is computed by means of reflection **R** and transmission **T** matrices, whereas the diffracted field is evaluated by means of a suitable UTD heuristics diffraction coefficient **D**. The adopted diffraction coefficient accurately models the field interaction with furniture edges and junctions between thin flat plates of different materials so that all significant field processes, which take place in the indoor environment, are rigorously modeled. As in indoor environments the field contributions arising from double diffraction are small [1,28–30], only a single diffraction process is considered in this model. According to the high-frequency approximation, the radio source is modeled using its vector-effective height to describe the gain pattern and the polarization properties. The field prediction procedure described above is outlined in Figure 8.2 [30]. The structure that is illuminated by an incident electric field E^i can be modeled by a thin flat penetrable plate located near a partially reflecting plane. To simplify the graphical representation, only the rays that have experienced up to two interactions are taken into account.

With reference to the field processes shown in Figure 8.2, the electric field at the observation point r_7 is given by the sum of the following contributions [30]:

a) direct ray-field

$$E_a(r_7) = E^i(r_7); \tag{8.1}$$
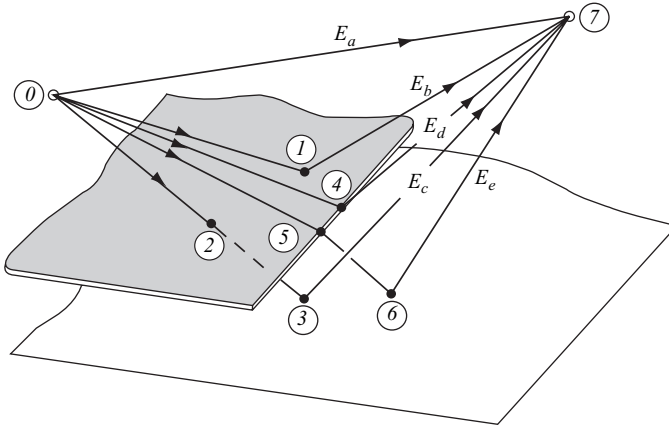
FIGURE 8.2. A structure illuminated by an incident electric field; points 0 and 7 indicate the source and the observation points, respectively [30].

b) reflected ray-field

$$E_b(r_7) = R_1 \cdot E^i(r_1) \frac{S_{01}}{S_{01} + S_{17}} e^{-jks_{17}}; \tag{8.2}$$

c) transmitted and reflected ray-field

$$E_c(r_7) = R_3 \cdot T_2 \cdot E^i(r_2) \frac{S_{02}}{S_{02} + S_{23} + S_{37}} e^{-jk(s_{23}+s_{37})}; \tag{8.3}$$

d) diffracted ray-field

$$E_d(r_7) = D_4 \cdot E^i(r_4) \sqrt{\frac{S_{04}}{S_{47}(S_{04} + S_{47})}} e^{-jks_{47}}; \quad \text{and} \tag{8.4}$$

e) diffracted and reflected ray-field

$$E_e(r_7) = R_6 D_5 E^i(r_5) \sqrt{\frac{S_{05}}{(S_{56} + S_{67})(S_{05} + S_{56} + S_{67})}} e^{-jk(s_{56}+s_{67})} \tag{8.5}$$

where k is the wave number and S_{ij} is the optical length between the points r_i and r_j.

Let us now use the broadcast beam-tracing algorithm [30] used for the computation of the electromagnetic field and the characteristics of the radio channel. The broadcast technique has a computation burden that does not strongly depend on the number of surfaces describing the environment, and it is particularly efficient when the number of the field computation points is large.
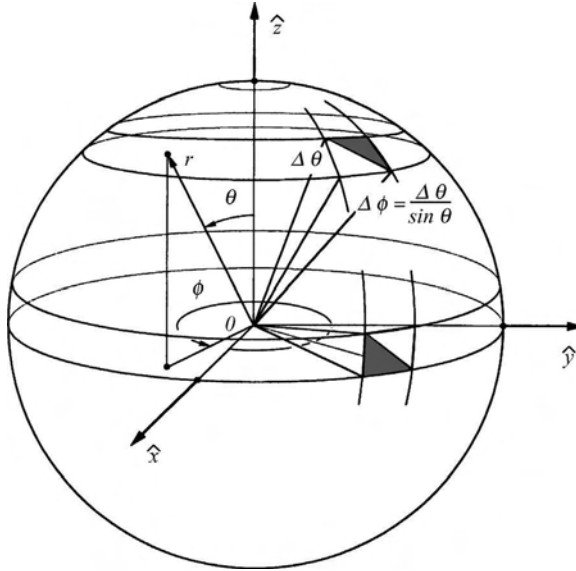
FIGURE 8.3(a). Beams emanating from the antenna towards all directions [30].

The Beam-Tracing Algorithm. This numerical algorithm consists of two parts. The *first*, determines the ray optical paths, while the *second* evaluates the electromagnetic field distribution. The field radiated from the antenna is modeled by means of beams shooting from the antenna location towards all space directions, independently of the observation point (see Fig. 8.3a [30]). During the propagation, the beam can impinge, totally or partially, on a surface describing the environment (see Fig. 8.3b, extracted from Reference [30]), it can capture the observation point,
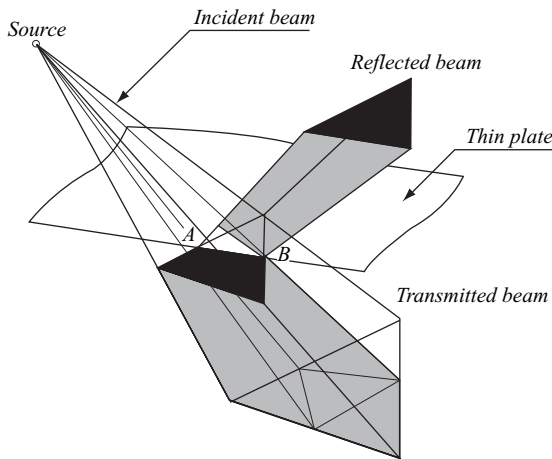
FIGURE 8.3(b). The beam impinges on a surface [30].
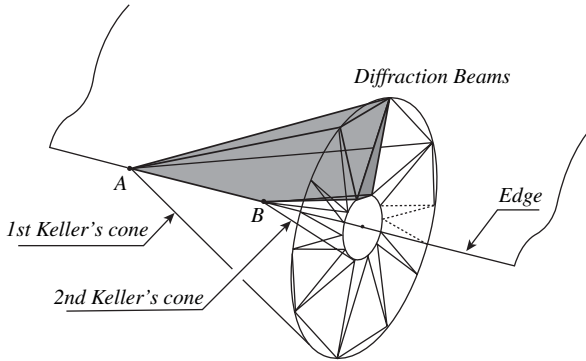
FIGURE 8.3(c). Division of the diffracted ray tube [30].

or finally it may not intercept any of the environment elements. In the first case, using Snell's law, the transmitted and the reflected beams are evaluated. If the beam partially impinges on the surface, it is splitted in new beams in a way that they totally intercept, or not, the surface under construction. Then, the ray optical paths of the diffracted field are determined. To this end, a subdivision of the diffracted ray tube, identified by the two Keller's cones whose tips coincide with the extremes of the segment excited by the incident ray beam, is performed (see Fig. 8.3c [30]). If the beam does not intercept any obstructions, it does not produce any secondary beams, and, consequently, it is removed from the field computation procedure.

The same happens when the beam has a cross section less than a definite size area, or it carries a field amplitude less than a specific threshold, or, finally, it exceeds a maximum number of permissible bounces. For each observation point lighted by the beam, the exact ray path is computed by means of the image method. In this way, the computation technique does not suffer either from multipath count error or from the error generated by the field approximation based on the computation of the beam median ray. In the second part of the beam-tracing algorithm, the GO and diffracted fields are evaluated using the reflection, transmission, and diffraction matrices at the points where the incident field impinges. In the numerical procedure, only the edge diffraction processes excited by the GO field have been taken into account.

To increase the numerical accuracy of the computation, one can take into account the GO field contribution that has experienced up to five reflections/transmissions. The diffracted field arising from any scattering object is considered to be excited either by the line-of-sight GO field or by the GO contributions that have experienced up to three reflections/transmissions. Finally, the diffracted field contribution is taken into account whether it reaches the observation point directly or after three reflections/transmissions processes. The complete analysis is carried out in References [1,28–30], and on the basis of experimental data and numerical results of the UTD ray model, it has been shown that the presence of furniture in the LOS region gives rise to greater field diffusion and additional attenuation of the received signal. This effect decreases efficiency of the channel performance in wireless

indoor communication systems. In particular, it has been observed that the field diffusion due to the edges of penetrable objects introduces an additional attenuation of the echoes of the radio signal with respect to the empty environment. Because of its numerical accuracy and limited computational requirements, the UTD ray-tracing model can be successfully employed to estimate the channel performance and the total field distribution (radio coverage) directly during the design phase of indoor wireless communication.

8.2.2. Physical Waveguide Model of Radio Propagation Along the Corridor

This model is an analytic model of radio wave propagation along an impedance corridor as a waveguide. This model, which differs from other models [14,18], allows us to analyze the electromagnetic field distribution inside a building corridor to obtain an expression for the attenuation (extinction) length and the path loss.

The Geometry of the Problem. Below we briefly present the guiding effects of the corridor on the basis of same theoretical approach that was followed for the outdoor street scene [2], that is, we model the corridor by a two-dimensional impedance parallel waveguide (Fig. 8.4).

As $d \gg \lambda$, where d is the corridor's width and λ is the wavelength, we can use the approximation of geometrical theory of diffraction (GTD). This approximation is valid as long as the first Fresnel zone $\sim(\lambda x)^{1/2}$ equals or does not exceed the width of corridor d. In this case, $x \leq 30$–50 m, $\lambda = 3$–10 cm (L/X-band); $d = 2$–3 m; $(\lambda x)^{1/2} \leq d$. The electrical properties of walls are defined by the surface impedance $Z_{TE} \sim \varepsilon^{-1/2}, \varepsilon = \varepsilon_0 - j(4\pi\sigma/\omega)$, where ε is the dielectric permittivity of the wall's surface, ε_0 is the dielectric constant of the vacuum, σ is the conductivity, and $\omega = 2\pi f$ is the angular frequency of the radiated wave.

We consider the 2D problem of wave reflection without taking into account the reflection from the corridor's floor and ceiling because the corridor's height H and the position of the transmitter/receiver $h = 2$–3 m are usually larger values than λ. Let us also assume, according to the geometry presented in Figure 8.4, that a vertical electric dipole is placed at the point $(0, w, h)$ at the (y, z) plane, as it is shown in Figure 8.5.

To convert the problem to a 2D case, we must consider the dipole oriented along the y-axis, that is, the horizontal dipole with respect to the (x, y) plane, which
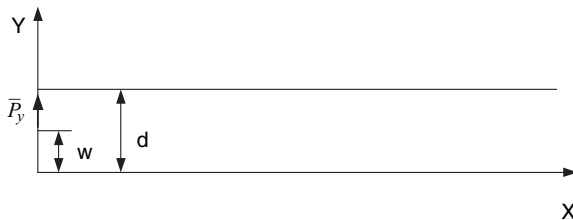
FIGURE 8.4. The corridor waveguide model; a view from the top.
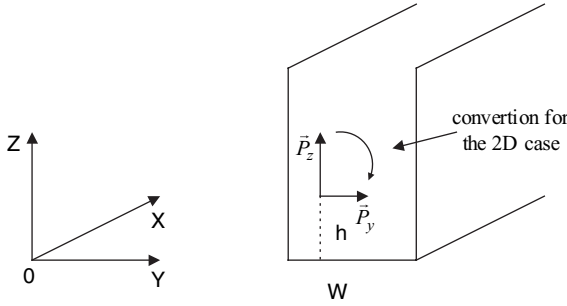
FIGURE 8.5. The corridor in the 2D case.

corresponds to the well-known electromagnetic field equation described by the Hertzian potential vector $\Pi_y^i(x, y)$ [2]:

$$\nabla^2\Pi_y^i(x, y) - k^2\Pi_y^i(x, y) = -\frac{4\pi i}{\omega}\mathbf{p}_y\delta(x)\delta(y - w) \tag{8.6}$$

The solution of such an equation can be presented using the Green's function [2]:

$$\Pi_y^i(x, y) = \frac{i}{\omega}\mathbf{p}_y\frac{e^{ik\rho}}{\rho} \tag{8.7}$$

Here, $\mathbf{p}_y$ is the electric momentum of a point horizontal electric dipole, $\rho = \sqrt{x^2 + y^2}$ is the distance from the source.

Total Field in 2D Unbroken Impedance Waveguide. The reflected field in an unbroken waveguide can be determined according to Reference [2] as the sum of reflected modes replaced by the image sources (as shown in Fig. 8.6).

The straight computations made according to Reference [2] give the normal mode expression inside the impedance wave guide (called the *discrete spectrum* of the total field):

$$\Pi_n(x, y) = D_1 e^{i\rho_n^{(0)}x}\exp\left\{-\frac{|\ln|R_n||}{\rho_n^{(0)}d}\left(\frac{\pi n}{d}\right)x\right\} \tag{8.8}$$

where

$$\rho_n^{(0)} = \sqrt{k^2 - K_n^2} = \sqrt{k^2 - \left(\frac{n\pi}{d}\right)^2}$$

and $R_n = \frac{K_n - kZ_{EM}}{K_n + kZ_{EM}}$; $D_1 = \frac{2DR_n}{i\rho_n^{(0)}d}$; $K_n = \frac{n\pi}{d}$ is the wave number of normal modes of number n that propagate along the waveguide with width d, $k = \frac{2\pi}{\lambda}$, D is the parameter of electrical dipole including its momentum $\mathbf{p}$ [2].
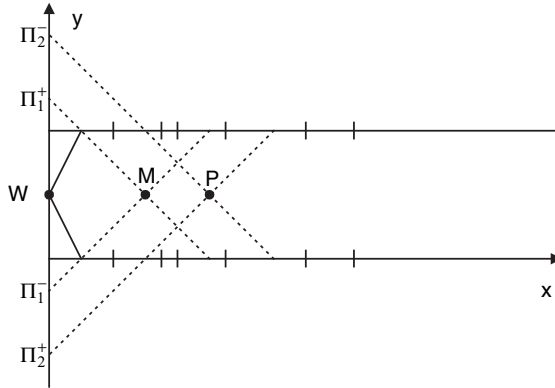
FIGURE 8.6. The waveguide modes created by the corresponding image sources.

Following Reference [2], we can also present the continuous spectrum of the total field for $x/d \gg 1$ as:

$$\Pi_c \approx \sqrt{2}De^{i\left(\frac{3\pi}{4}\right)} \frac{1 - |R_n|}{1 + |R_n|} \frac{e^{ikx}}{x} \tag{8.9}$$

For the case of a perfectly conductive waveguide, when $|R_n| = 1$, $Z_{EM} = 0$, we obtain that $\Pi_c = 0$, that is, in the case of the ideal conductive waveguide, the continuous part Π_c of the total field vanishes, and only the discrete spectrum of the normal waves propagates along the ideal waveguide without attenuation according to (8.8). Finally, the intensity of the total field can be approximately obtained as

$$I \approx \lfloor (\Pi_n + \Pi_c) \cdot (\Pi_n + \Pi_c)^* \rfloor$$

where $(\Pi_n + \Pi_c)^*$ is the complex conjugate of $(\Pi_n + \Pi_c)$. The path loss of the radio wave can be derived as [2]

$$L \approx 32.1 - 20\log_{10}|R_n| - 20\log_{10}\left[\frac{1 - [R_n]^2}{1 + |R_n|^2}\right]$$

$$+ 17.8\log_{10}x + 8.6\left\{-[\ln|R_n|]\left(\frac{\pi n}{d}\right)\frac{x}{\rho_n^{(0)}d}\right\} \tag{8.10}$$

where x is the distance between two terminals, receiver and transmitter, along the corridor.

Analysis of the Waveguide Corridor Model. Let us present some examples of simulation of the total path loss L in decibels (dB) according to (8.10) versus
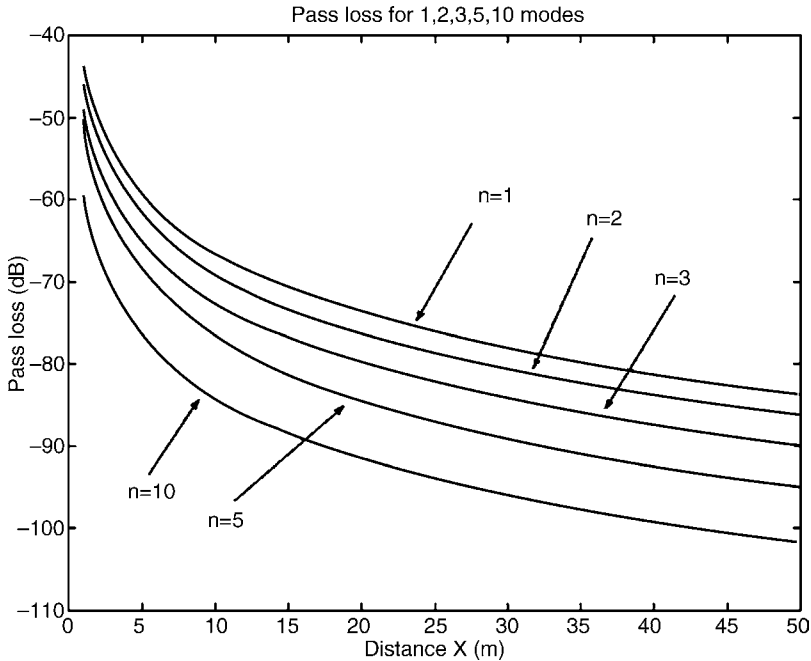
FIGURE 8.7(a). Path loss for $n = 10$ wave modes versus distance from the transmitter.

distance between the transmitter and receiver. For our numerical computation, we considered the following parameters: the width of the corridor $d = 3$ m, the conductivity of walls $\sigma = 0.0133\,\text{S/m}$, and the signal frequency $f = 900\,\text{MHz}$ [33]. The results of these path loss computations, according to (8.10), are shown in Figure 8.7a for the guiding modes with the number n varying from 1 to 10. For $n > 3$, the effect of these modes is negligible at ranges beyond 20 m, and we just have to subtract the attenuation from the first two main modes of the original signal power in order to get the total power of a signal (in decibels) for each distance d between the transmitter and the receiver located along the corridor waveguide. This effect was also shown in Reference [2], where it was experimentally obtained that only one to two main modes are important in the range of ten and more meters from the transmitter. Therefore in Figure 8.7b, we present the total filed attenuation, as a sum of the first two waveguide modes, that fully describes the total path loss inside the corridor as a guiding structure versus the distance from the transmitter. We will compare this theoretical prediction of the path loss with the real experiment carried out in Reference [33] along the corridor.

8.2.3. Physical Model of Radio Propagation Between Floors and Walls

Bertoni et al. [1,21,22] developed a theoretical model, based on the geometrical theory of diffraction (GTD), which explains the propagation between a transmitter and a
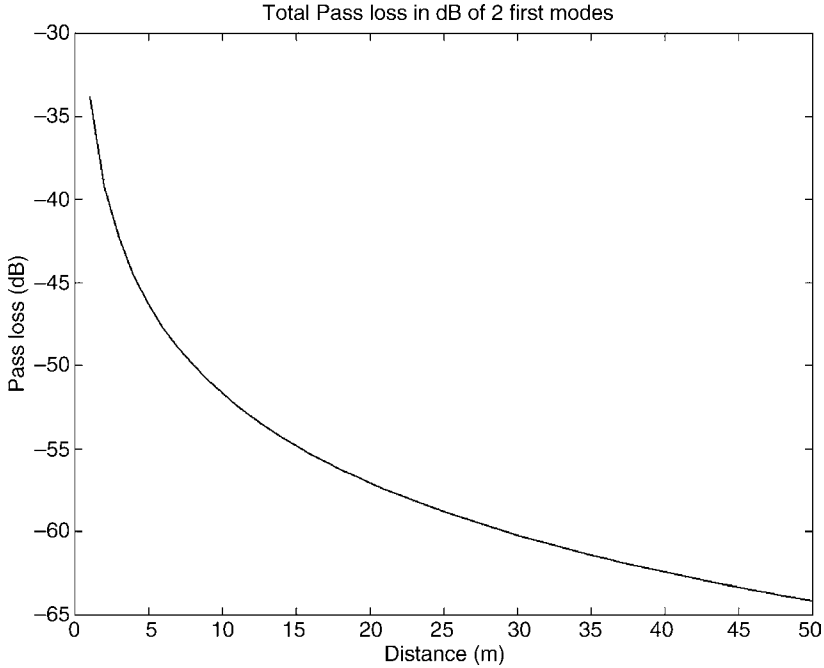
FIGURE 8.7(b). Path loss for the first modes versus distance from the transmitter.

receiver located on different floors of a building. Depending on the structure of the building and the location of the antennas, either direct ray propagation through floors or diffraction outside the building will determine the propagation characteristics and the range dependence of the signal. There are two paths over which propagation can take place:

(1) Paths that involve transmission through the floors;

(2) Paths having segments outside the building and involving diffraction at window frames.

The paths through the floors include the direct ray, the multiple-reflected rays, and the rays that are transmitted through semitransparent walls and floors. These rays are contained entirely within the building perimeter. The diffracted ray paths involve transmission outside the building through windows and diffraction into paths that run alongside the face of the building and then reenter through another window at a different floor. For propagation of the direct ray through semitrans-parent floors, as indicated by path T in Figure 8.8, extracted according to Reference [1], the electromagnetic field strength in general reaching a receiving site is given by [21,22]

$$|\mathbf{E}|^2 = \frac{Z_0 P_e}{4\pi L^2} \prod_m T^2_{\text{floor},m} \prod_n T^2_{\text{wall},n} \tag{8.11}$$
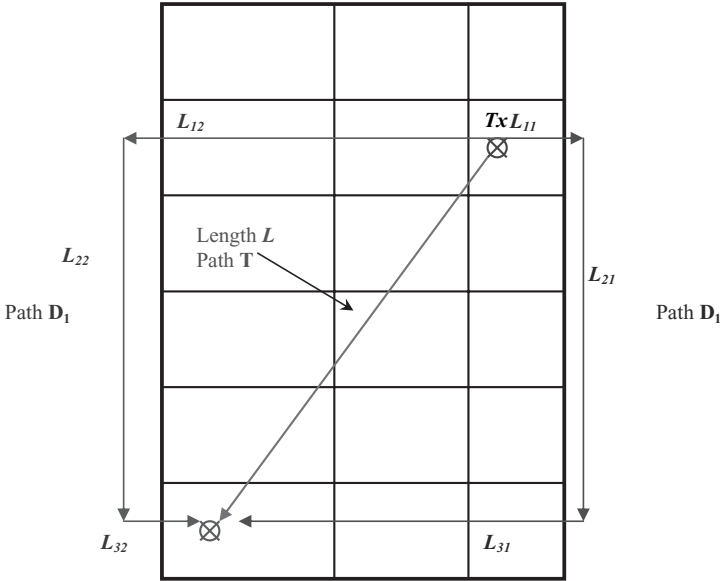
FIGURE 8.8. The Bertoni's model.

Here, $Z_0 = 120\,\pi\,\Omega = 377\,\Omega$ is the free-space wave impedance, P_e is the effective transmitted power and L is the direct distance between the transmitter (Tx) and the receiver (Rx) antennas. T_{floor} and T_{wall} are the loss coefficients of each floor and wall, respectively, passed by the direct ray. Such a direct ray, passing through three floors and two interior walls, is indicated in Figure 8.8. If one knows the reflection coefficient Γ of each wall and floor, then we can calculate T_{floor} or T_{wall} as [21,22]

$$T = \sqrt{X(1 - |\Gamma|^2)} \tag{8.12}$$

where X is a constant, obtained from the concrete experiment. The signal can also reach other floors via paths that involve diffraction. Referring to paths D_1 and D_2 in Figure 8.8 (in general denoted as D_i), the field reaching the receiver via one such diffracted path is given by [21,22]

$$|\mathbf{E}|^2 = \frac{Z_0 P_e}{4\pi} \frac{\prod_i D^2(\alpha_i) \prod_j T_{\text{glass},j}^2 \prod_k T_{\text{wall},k}^2}{\prod_m \sum_n L_{nm}} \tag{8.13}$$

where L_{nm} is the length of D_i diffracted path. In the geometry of the concrete experiment carried out in the hotel schematically presented in Figure 8.8 according

to References [21,22]; L_{nm} is the length of D_1 and D_2 where $\prod_m \sum_n L_{nm} = (L_{11} + L_{21} + L_{31})(L_{12} + L_{22} + L_{32})$; $T_{\text{glass}(m)}$ and $T_{\text{wall}(n)}$ are the transmission coefficients through glass and through interior walls crossed by path segments. In (8.13), $D(\alpha_i)$ is the diffraction coefficient for a propagating ray bending through angle α_i.

Depending on the construction of the building and its window frames, different choices may be made for the diffraction coefficient. For simplicity in investigating the relative strength of the total field associated with the direct ray and the diffracted ray, the coefficient for an absorbing wedge, obtained by Keller's diffraction theory [1] was used:

$$D(\alpha_i) = \frac{1}{2\pi k}\left[\frac{1}{2\pi + \alpha_i} - \frac{1}{\alpha_i}\right] \tag{8.14}$$

where $k = 2\pi/\lambda$ is the wave number. Thus, when propagation takes place through the floors, the signal will decrease rapidly with the number of floors separating the transmitter and the receiver.

On the contrary, if propagation occurs via diffracted paths, the signal will be small even for separation by a single floor but will decrease a bit slower with increased separation. For testing the model, an experiment was made according to Figure 8.8, in the frequency of 852 MHz, where according to presented geometry the angle $\alpha_i = \pi/2$. Measurements have shown that in each floor the attenuation was about 12–13 dB. From various experiments the coefficients for the walls, windows, and floors are

$$T'_{\text{wall}} = 2.2\,\text{dB}; \quad T'_{\text{glass}} = 0.25\,\text{dB}; \quad T'_{\text{floor}} = 13.0\,\text{dB} \tag{8.15}$$

The total received power in decibels at the Rx position can be calculated according to (8.11) for the direct path through floors and walls as

$$P_{r_{\text{Direct}}} = 10\log_{10}\lambda^2|E|^2_{\text{direct}}/(Z_0 \cdot 4\pi) \quad [\text{dB}] \tag{8.16}$$

where $P_{r_{\text{Direct}}}$ is the power gain from direct propagation wave; $|E|^2$ is calculated according to (8.11), and $\lambda = \frac{c}{f}$ is the wavelength; $Z_0 = 120\pi[\text{ohm}]$ is the impedance in free space, and according to (8.13)

$$P_{r_{\text{Diff}}} = 10\log_{10}\lambda^2|E|^2_{\text{diff}}/(Z_0 \cdot 4\pi) \quad [\text{dB}] \tag{8.17}$$

where $P_{r_{\text{Diff}}}$ is the power gain from diffracted propagation wave and $|E|^2$ is calculated according to (8.13).

Then the total received power will be

$$P_{r_{\text{total}}} = P_{r_{\text{Direct}}} + P_{r_{\text{Diff}}} \quad [\text{dB}] \tag{8.18}$$

Additional numerical analysis of Bertoni's model and comparison with numerous experiments carried out by other researchers (see Section 8.3 below) have shown that despite the fact that this model offers very precise physical calculations that are suitable for different kinds of buildings, the attenuation effects due to shadowing caused by diffraction from internal obstructions are not taken into consideration. This type of attenuation must be accounted for, because it can decrease the total strength of radio signal that reaches the receiver by 10 dB to 15 dB. However, the shadow effect is actual only at the upper floors, that is, when the difference between antenna locations is more than two to three floors.

Also another difficulty with the implementation of Bertoni's model is that it requires a priori knowledge of the precise building architecture and the establishment of various propagation paths, which by all means is a very difficult task to achieve. The estimation of path loss through walls and floors, according to (8.11), is more precise compared to other existing empirical models (see formulas (8.19) and (8.20) below). Therefore we will use (8.11) in future link budget design of indoor communication links, taking into account shadow effects caused by the internal obstructions located within the radio path between the two terminal antennas, following Reference [33] or the receipt proposed in Chapter 5 for link budget design.

8.2.4. Empirical Models

Such models are based mostly on numerous experiments carried out in various indoor environments as the best-fit prediction to the corresponding measured data. We start with a very simple model that modifies the well-known dual-slope model, usually used in outdoor environments (so-called "two-ray" model, see Chapter 5), and then we introduce the most applicable empirical model that is currently used for loss characteristics prediction in indoor communication links.

Modified Dual-Slope Model. The challenging problem in applying the well-known dual-slope models from the outdoor environment to the indoor environment is that we need to account for the wall and floor factors. In Reference [31], to characterize indoor path loss a fixed path loss exponent $\gamma = 2$, just as in free space (see Chapter 5), was used, plus additional attenuation factors (in decibels) per floor, α_f, and per wall, α_w, timing on the number of floors, N_f, and walls, N_w, respectively, that is,

$$L = L_0 + 20 \log r + N_f \alpha_f + N_w \alpha_w \tag{8.19}$$

where r is the straight-line distance between the terminal antennas and L_0 is a free-space path loss at the referenced range of 1 m.

As no values for the wall and floor factors were reported in Reference [31], an improved model was developed, which is called the ITU-R model [32]. According to this dual-slope approach, only the floor loss is accounted for explicitly. The loss between points located at the same floor is accounted by changing the path loss

TABLE 8.1. Path Loss Exponent γ for the ITU-R Model [32]

| Frequency [GHz] | Residential | Environment | |
		Office	Commercial
0.9	–	3.3	2.0
1.2–1.3	–	3.2	2.2
1.8–2.0	2.8	3.0	2.2
4.0	–	2.8	2.2

exponent γ. The frequency effect is accounted in the same manner as in free space (see Chapter 5), producing the following total path loss (in decibels):

$$L = 10\gamma \log r + 20 \log f + L_f(N_f) - 28 \tag{8.20}$$

where γ is shown in Table 8.1 [32], and $L_f(N_f)$ is the floor attenuation factor, which varies with the number of penetrated floors N_f, as shown in Table 8.2 [32].

Rappaport's Path Loss Prediction Model. Rappaport and his associates [3,11,13,20] made a lot of experiments in various indoor environments in different locations and sites. The main goal of these experiments was to achieve unique parameters of attenuation and loss prediction on different kind of multifloored buildings.

Distance-Dependent Path Loss Model. In References [3,20] it was assumed that the mean path loss $\bar{L}$ is an exponential function of distance d with the power n:

$$\bar{L}(d) \propto \left(\frac{d}{d_0}\right)^{\gamma} \tag{8.21}$$

where $\bar{L}(d)$ is the mean path loss; γ is the mean path loss exponent that indicates how fast path the loss increases with distance; d_0 is a reference distance, usually chosen equal to 1 m in indoor communication links; and d is the transmitter–receiver separation distance. Absolute mean path loss, in decibels, is defined as the path loss

TABLE 8.2. Floor Attenuation Factor $L_f(N_f)$ in dB for the ITU-R Model [32]

| Frequency [GHz] | Residential | Environment | |
		Office	Commercial
0.9		9(1 floor)	
	–	19 (2 floors)	–
		24 (3 floors)	
1.8–2.0	$4N_f$	$15 + 4(N_f - 1)$	$6 + 3(N_f - 1)$

from the transmitter to the reference distance d_0, plus the additional path loss [3], that is,

$$\bar{L}(d) = L(d_0) + 10\,\gamma\log\left(\frac{d}{d_0}\right) \quad \text{[dB]} \tag{8.22}$$

For these data, $L(d_0)$ is the reference path loss due to free-space propagation from the transmitter to a 1 m reference distance, and calculated by

$$L(d_0) = 20\log\left(\frac{4\pi d_0}{\lambda}\right) \quad \text{[dB]} \tag{8.23}$$

This empirical model takes into account the effects of shadowing by introducing in (8.22) a term X_σ, which describes the statistical character of slow fading within the indoor link and, as a random variable, satisfies the lognormal distribution with a standard deviation of σ in decibels (see definitions in Chapter 1). Then the total path loss within building equals, in decibels, [3]:

$$L(d) = L(d_0) + 10\,\gamma\log\left(\frac{d}{d_0}\right) + X_\sigma \quad \text{[dB]} \tag{8.24}$$

For this model, the exponent γ and standard deviation σ were determined as parameters that are functions of building type, building wing, and number of floors between *Tx* and *Rx*. Thus, a model to predict the path loss for a given environment is given by [3]

$$L(d) = \bar{L}(d) + X_\sigma \quad \text{[dB]} \tag{8.25}$$

where X_σ is a zero mean lognormally distributed random variable with standard deviation σ and accounts for attenuation due to diffraction from the environment. Table 8.3 [3] summarizes the mean path loss exponent γ, standard deviation σ about the mean $\bar{L}$ for different indoor environments, and the number of measurement locations used to compute the statistics for each building. From Table 8.3, it can be seen that the parameters for path loss prediction for all antenna locations are $\gamma = 3.14$ and $\sigma = 16.3$ dB. This large value of σ is typical for data collected from different building types and indicates that only 68% of actual measurements will be within ± 16.3 dB of the predicted mean path loss. As stated in References [3,20], these parameters may be used in modeling the first-order prediction of mean signal strength when only the *Tx–Rx* separation is known but not specifics about the building. In multifloored environments, (8.22) is used to describe the mean path loss as a function of distance. Equation (8.22) emphasizes that the mean path loss exponent is a function of the number of floors between *Tx* and *Rx*. The values of γ (*multifloor*) are given in Table 8.3 for use in (8.22), and this equation can be rewritten as [3]

$$\bar{L}(d) = L(d_0) + 10\,\gamma(\text{multifloor})\log\left(\frac{d}{d_0}\right) \tag{8.26}$$

TABLE 8.3. Path Loss Exponent and Standard Deviation for Various Types of Buildings Based on Measurements at a Carrier Frequency of 914 MHz

Place	γ	σ [dB]	Number of Locations
All Buildings			
All Locations	3.14	16.3	634
Same Floor	2.76	12.9	501
Through One Floor	4.19	5.1	73
Through Two Floors	5.04	6.5	30
Through Three Floors	5.22	6.7	30
Grocery Store	1.81	5.2	89
Retail Store	2.18	8.7	137
Office Building 1:			
Entire Building	3.54	12.8	320
Same Floor	3.27	11.2	238
West Wing 5th Floor	2.68	8.1	104
Central Wing 5th Floor	4.01	4.3	118
West Wing 4th Floor	3.18	4.4	120
Office Building 2:			
Entire Building	4.33	13.3	100
Same Floor	3.25	5.2	37

Floor Attenuation Factor (FAF). In (8.26), γ (multifloor) is a function of the number of floors between *Tx* and *Rx*. Alternatively, a constant floor attenuation factor FAF (in decibels), which is a function of the number of floors and building type, was added in References [3,20] to the mean path loss predicted by (8.22), which uses the "same floor" path loss exponent for a particular building type:

$$\bar{L}(d) = L(d_0) + 10\,\gamma(\text{same floor}) \log\left(\frac{d}{d_0}\right) + \text{FAF} \quad [\text{dB}] \qquad (8.27)$$

where d is in meters, and $L(d_0)$ is the free space path loss determined by (8.23). Table 8.4 [3] gives the floor attenuation factors FAF (in decibels) and the standard deviation σ (in decibels) between the measured and predicted path loss and the number of discrete measurement locations used to compute the statistics.

Soft Partition and Concrete Wall Attenuation Factor. The above formulas include the effects of *Tx–Rx* separation, building type and the number of floors between the *Tx* and *Rx,* and the first step for including site information to improve propagation predictions. There are often obstructions between the transmitter and receiver even when the terminals are on the same floor.

   The model considers the path loss effects of *soft partition* and *concrete walls* between the *Tx* and *Rx*. The model assumes that path loss increases with distance as

TABLE 8.4. Average Floor Attenuation Factor in dB for One, Two, Three and Four Floors in [3] Two Office Buildings

Building	FAF	σ	Number of Locations
Office Building 1:			
Through One Floor	12.9	7.0	52
Through Two Floors	18.7	2.8	9
Through Three Floors	24.4	1.7	9
Through Four Floors	27.0	1.5	9
Office Building 2:			
Through One Floor	16.2	2.9	21
Through Two Floors	27.5	5.4	21
Through Three Floors	31.6	7.2	21

in free space ($\gamma = 2$), as long as there are no obstructions between the *Tx* and *Rx*. Then, attenuation factors for each soft partition and concrete walls that lie directly between *Tx* and *Rx* are included. Let *p* be the number of soft partitions, and *q* is the number of concrete walls in the direct path between *Tx* and *Rx*. The mean path loss predicted by this model is

$$\bar{L}(d) = 20 \log_{10}\left(\frac{4\pi d}{\lambda}\right) + p \cdot \text{AF(soft partition)} + q \cdot \text{AF(concrete wall)} \quad \text{[dB]}$$

(8.28)

where AF(soft partition) is the attenuation factor per soft partition, and AF(concrete wall) is the attenuation factor per concrete wall. Typical values for AF are 1.4 dB for soft partition and 2.4 dB for concrete wall.

Numerical Simulations of Rappaport's Model. To compare different approaches described by formulas (8.26) and (8.27), let us introduce some typical parameters obtained experimentally by Rappaport et al., as presented in Table 8.3 and 8.4. Thus, for simulation purposes we used the following parameters: $f = 915$ MHz ($\lambda = 0.32$ m); γ for the same floor $= 3.27$; $\gamma = 4.19$ for the 1st floor; $\gamma = 5$ for the 2nd floor; $\gamma = 5.22$ for the 3rd floor; $\gamma = 5.35$ for the 4th floor; $\gamma = 5.45$ for the 5th floor; FAF for the 1st floor $= 12.9$ dB; FAF for the 2nd floor $= 18.7$ dB; FAF for the 3rd floor $= 24.4$ dB; FAF for the 4th floor $= 26$ dB; FAF for the 5th floor $= 27$ dB.

In Figure 8.9, the path loss versus the number of floors is presented according to (8.26) with γ(multifloor), and in Figure 8.10 it is according to the FAF model (8.27) with γ(same floor). From Figure 8.9, the attenuation of radio wave penetrating through the first three floors increases linearly and then according to the square root curve dependence, which is in a good agreement with Bertoni's model, taking into account the diffraction path loss described by formula (8.23).
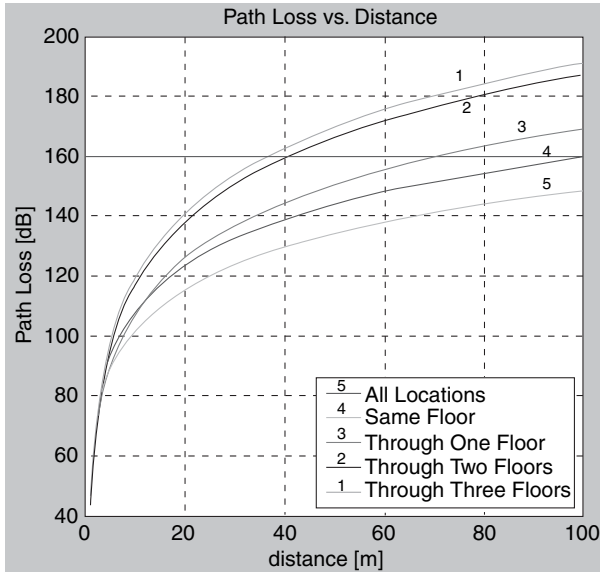
FIGURE 8.9. Path loss versus distance from the transmitter for various scenarios inside a building.
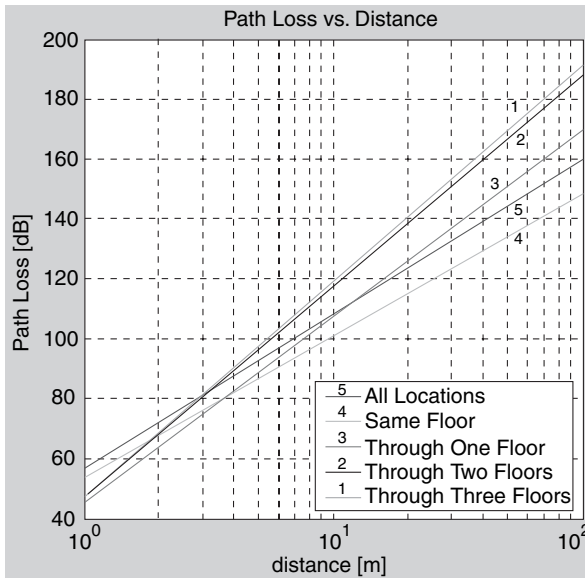
FIGURE 8.10. Path loss versus distance from the transmitter for various scenarios inside a building.

Additional analysis of Rappaport's model has shown that there are some difficulties in using this model in practical situations for indoor environments. Rappaport's model relies heavily on experimental data to determine the required parameters that can be used for modeling purposes.

Let us now compare two approaches, Bertoni's and Rappaport's, through the prism of experimental data. Rappaport's model is based on experimental factors (FAF and γ), and it does not provide the radio wave propagation characteristic, such as the attenuation inside buildings in the case when the transmitter and the receiver are located at different floors.

Bertoni's model states that when there is a several-floor separation between the terminal antennas, the additional loss occurs due to the diffraction path through the frames of the windows according to (8.13). The slow fading effect, called shadowing (see definitions in Chapter 1), can easily be represented in Bertoni's model as the additional effect of the wave field that comes from the diffraction paths. In the Rappaport model, the shadowing effect is accounted by the FAF factor and by the path loss exponent γ. Obviously, the slow fading factor must be added to Rappaport's model during the measurement phase, where parameters FAF and γ are usually determined. In general, Rappaport's model is suitable for buildings with a low number of floors (up to 4–5). The results are very similar to Bertoni's model in the lower floors when radio propagation mostly occurs through the direct path as described by (8.11). When taller buildings are tested, Bertoni's model is a more appropriate model to use. In the following paragraph we indicate additional improvements to Bertoni's model by accounting for the shadow effects.

Suggested Model. As mentioned above, the models that predict link budgets for the indoor environment are complex, sometimes using parameters without any physical meaning and explanation. Here we suggest a model, proposed in Reference [33], for the radio propagation between floors that takes into consideration the physical media and parameters of the total path loss obtained from experiments. In general, the suggested model will follow the formula:

$$L_{\text{total}} = \bar{L} + X_\sigma \quad [\text{dB}] \tag{8.29}$$

which is similar to (8.25) as shown in the Rappaport's model, but now $\bar{L}$ is the loss achieved from a direct propagated ray with NLOS features, and X_σ is a zero mean lognormally distributed random variable with standard deviation σ in decibels and accounts for attenuation from diffracted propagated waves. The parameter X_σ can be easily obtained from experiments made in different building environments, and $\bar{L}$ must be calculated according to the direct NLOS attenuation described by (8.11) following Bertoni's model. In other words, model (8.29) is a combination of Bertoni's physical model of direct propagation through floors (8.11) and Rappaport's empirical model by estimating the parameter X_σ from the approach presented in Chapter 5 for link budget design or from experimental data. The suggested path loss model is based on two essential aspects. First, it uses Bertoni's prediction to obtain the received power signal along the radio path of rays

TABLE 8.5. Technical Specifications of the System

Transmission Method	Spreading in spectrum and skipping in frequency
Frequency Spectrum	2.4–2.4835 GHz
Brooding Time	32, 64, 128 ms
Transmission Power	Up to 100 mV (20 dBm)
Sensitivity	
@1 Mbps	−81 dBm
@2 Mbps	−75 dBm
@3 Mbps	−67 dBm
Antenna Division	2 Antenna

penetrating through floors and described by (8.11), and secondly, it uses Rappaport's statistical measured σ and the method of fade margin estimation according to the procedure of link budget design described in Chapter 5 (see also Reference [33]).

8.3. LINK BUDGET DESIGN VERIFICATION BY EXPERIMENTAL DATA

In order to investigate the accuracy of the well-known models and the suggested above models of radio propagation along the corridor (8.10) and between floors and walls as described by (8.29) with help of (8.11) and (8.16) for the average path loss evaluation, we carried out some special experiments within several four-storied buildings.

Path Loss Along the Corridor.   The system consists of two main parts: the first is a wireless accesses point (BreezeCom AP10) connected to a power supply, and the second is a laptop with a wireless LAN card (BreezeCom SA-PCR). The laptop was located on a portable surface in order to separate it from the floor. Table 8.5 presents several important technical specifications of the system. The signal was measured at different locations 10 times in term of 2 to 3 min. This assures that local interferences such as electrostatic waves, cellular communication, and moving objects can be eliminated. In the building used for measurement, there was a 51 m corridor with glass and metal doors at the edges. The transmitting and receiving stations were placed on a portable laptop surface. The transmitting access points were placed in the beginning and in the middle of the corridor. The results are presented in Figure 8.11, from which it follows that with an increase in distance between the transmitter and receiver (more than 20–25 m), the saturation of the effect of attenuation is observed. There are few spikes that are probably caused by the variance in the architecture characteristics of the walls and by some local obstructions such as people walking along corridor and interference from the additional cellular communication networks. Comparison of these results with those obtained, theoretically, using the corridor waveguide model, are presented in
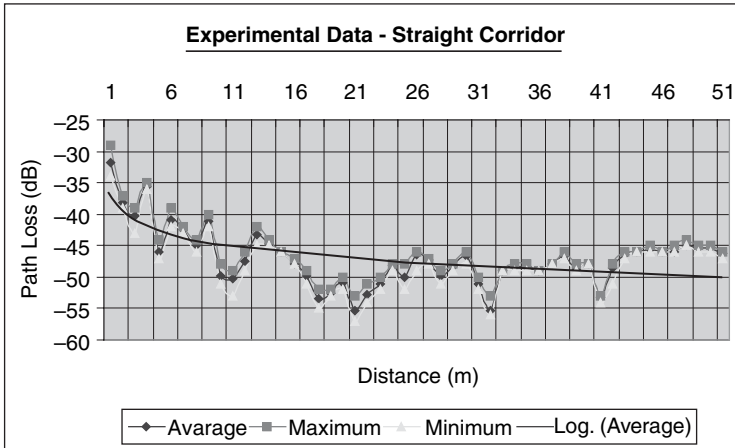
FIGURE 8.11. Comparison of experimental data measured along the corridor and theoretical prediction according to the corridor waveguide model (continuous curve).

Figure 8.11 by the continuous curve. It is clearly seen that the mean difference between the theoretical prediction and experimental data does not exceed 2–3 dB at the beginning of the corridor, becomes 4–5 dB in the middle sites, and reaches maximum difference of 9.794 dB at the end of the corridor, where an intersection with another crossing corridor exists. So, the corridor waveguide model is a good predictor of radio coverage inside the straight corridor except for some intersections with other crossing corridors within the tested building.

Link Budget for Indoor Links between the Floors and Walls. All experiments have been carried out in different campuses of Ben-Gurion University, Israel, each of which is a typical three-floor university campus, comprising long hallways and contiguous enclosed classrooms with windows. All outside and inside walls are made of concrete. There are large windows along the corridors (north wing) and inside every classroom (south wing). Each classroom is furnished with chairs and tables having the same size and height and made of metal and wood. During the experiments, all windows were closed in each floor (both along the corridor and inside each classroom). The receiver (*Rx*) and the transmitter (*Tx*) were separated with obstructions between them, that is, having both NLOS and LOS conditions. The transmitter was located in a fixed position on the first floor. The receiver was moved from one location to another within the measurement area from the third floor to the second floor. On the basis of numerous experimental data and measurement analysis, a preliminary suggestion was done that the proposed model, L_{total} [dB] $= \bar{L}$[dB] $+ X_\sigma$[dB], which is based on the combination of Bertoni's formula of direct penetration through floors and walls (8.11) and the additional attenuation X_σ, which accounts the *lognormal* shadowing effects caused by internal structures and obstructions, predicts the path loss measurements with the smallest deviation
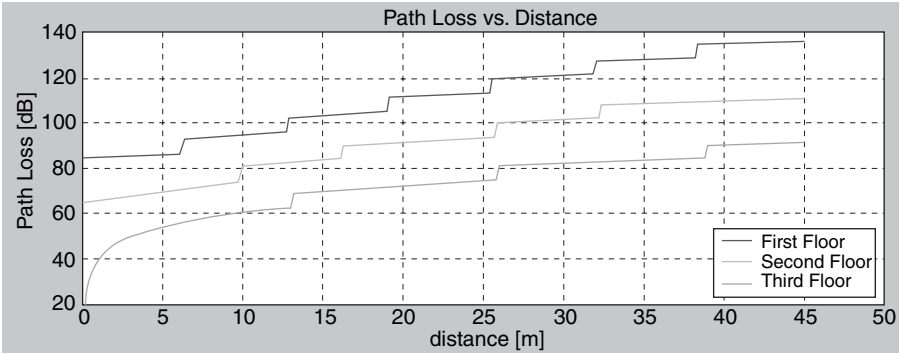
FIGURE 8.12. Path loss versus distance for various scenarios inside a building, computed according to Bertoni's model.

from experiment results (see Figs. 8.12–8.13). According to receipt described in Chapter 5 or in Reference [33], the probability for shadowing in the selected area can also be found. Figure 8.12 presents the simulation according to Bertoni's model (8.18) for conditions of the experiment described above and the same simulation according to the suggested model (8.29) shown by Figure 8.13.

Below we present the distinct difference between the suggested model for predicting path loss between floors (8.29) and Bertoni's path loss prediction model (8.18), which takes into account diffraction by window corners for the receiver at the third floor (Fig. 8.14) and then for the receiver at the second floor (Fig. 8.15).

From Figure 8.14a–b, the suggested model achieved better agreement with measurements, with an average error of 4.76 dB, than with Bertoni's model where the average error exceeds 10 dB. On the third floor where Rx was located, the shadowing term was evaluated to be $X_\sigma = 12.9$ dB. On the second floor (see Fig. 8.15a–b), again, the suggested model achieved better results with error of
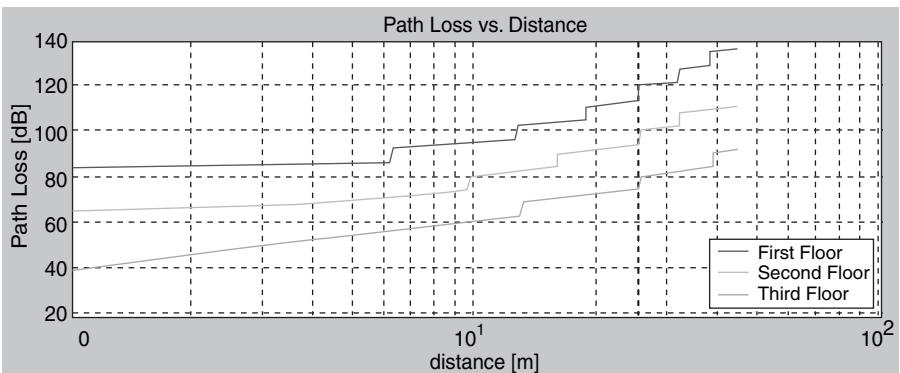
FIGURE 8.13. Path loss versus distance for various scenarios inside a building, computed according to suggested model.
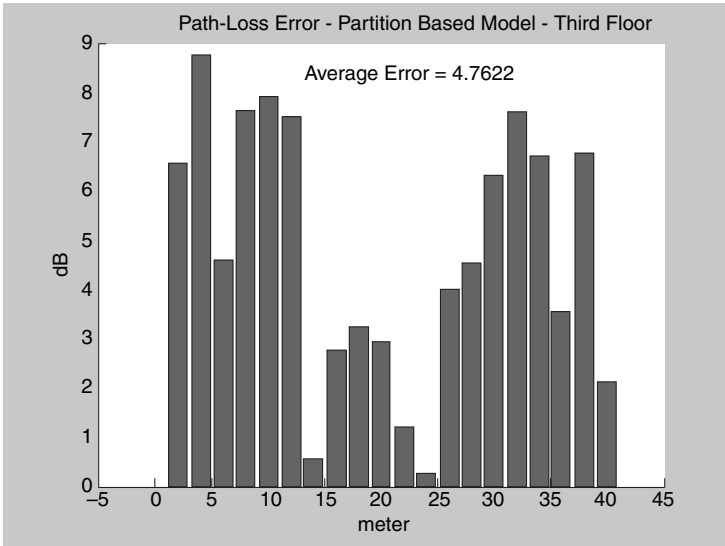
FIGURE 8.14(a). Error of suggested model compared to measurements.

8.00 dB compared to 9.58 dB obtained from Bertoni's model. On the second floor the term of shadowing was $X_\sigma = 8.1$ dB. In computations and comparison with Bertoni's model, the wall attenuation factor of 4 dB (for concrete wall) and the floor attenuation factor of 13 dB (for mixed concrete walls) were accounted [33].
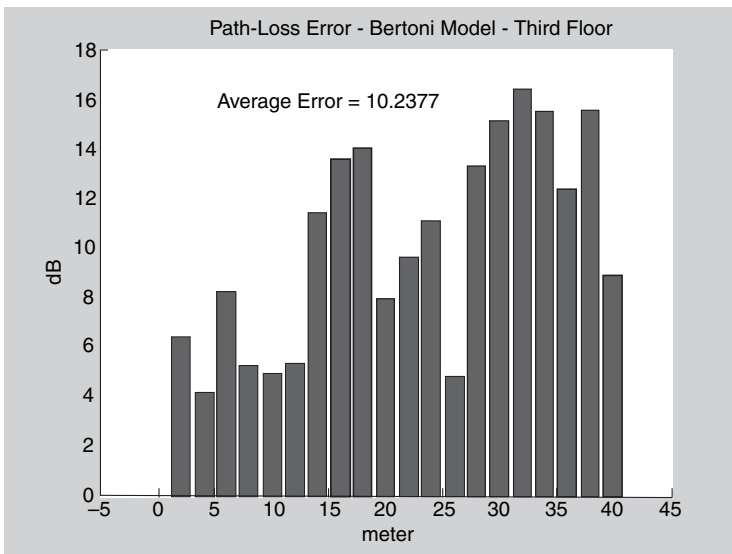
FIGURE 8.14(b). Error of Bertoni's simulation compared to measurements.
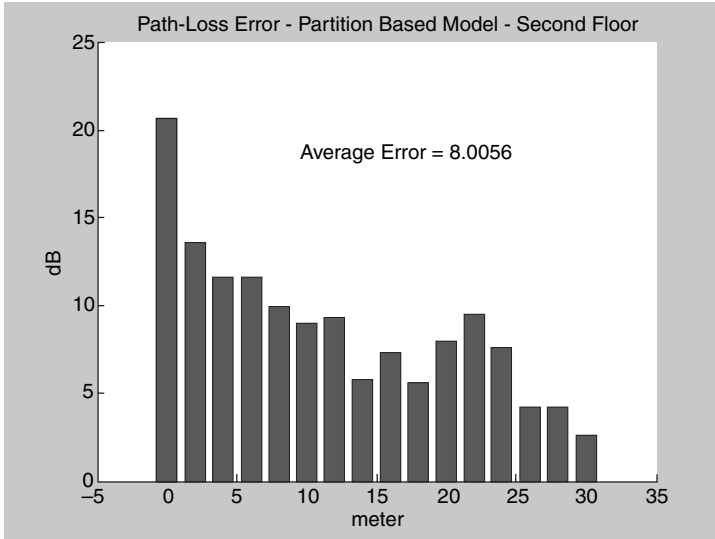
FIGURE 8.15(a). Error of suggested model compared to measurements.

The cumulative effect of deviation from the theoretical prediction, based on Equation (8.29) and measured data, for different three-story buildings is shown in Figure 8.16.

According to these results, we can conclude that the suggested model is very simple in terms of calculation and that it takes into account the slow fading
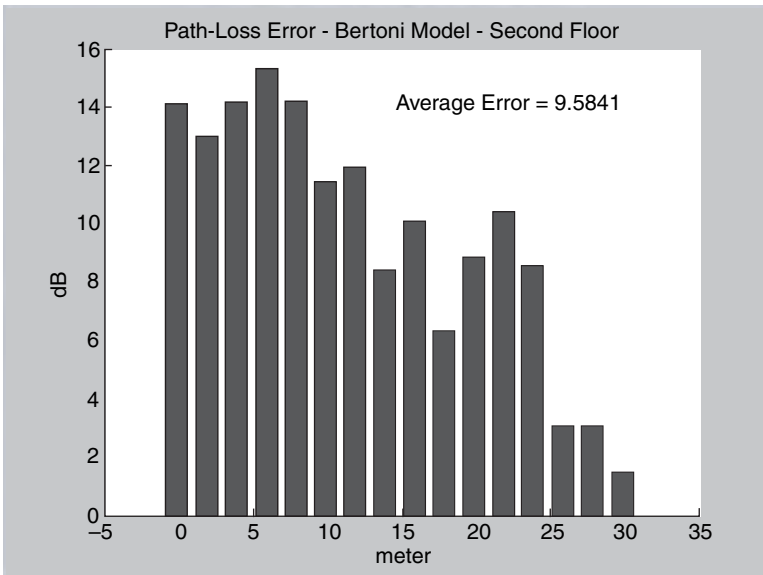
FIGURE 8.15(b). Error of Bertoni's simulation compared to measurements.
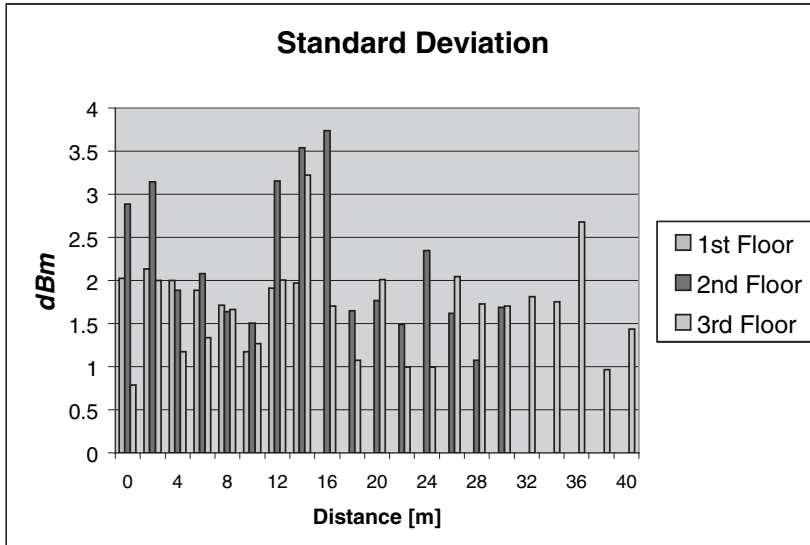
FIGURE 8.16. Standard deviation obtained from the statistical analysis of all scenarios.

(statistical approach) that other models omit. At the same time, the proposed model and the corresponding simulation results do not take into account objects such as furniture, people, and their movements. Therefore, some deviation error between simulation and actual link test results should be expected. Again, we can state that there is not one single, general enough model that takes into account all features and processes that occur within an indoor environment.

Finally, we present some experimental results in the form of a straight-line model as a best fit to the measured data to follow the same procedure used in outdoor communication links (see Chapter 5). Thus, in Figures 8.17–8.19, the total path loss versus distance, according to experimental data, are shown for the third, second, and first floors, respectively. The path loss exponent γ for each floor has been obtained from the approximate equations of straight lines. In Figure 8.17, both antennas are at the same, third, floor, that is, in LOS conditions. As was found for the LOS conditions, between the transmitter and receiver, the attenuation parameter equals $\gamma = 2.18$. For the receiver located at the second floor, that is, one floor below the transmitter, we found (see Fig. 8.18) that $\gamma = 3.45$. Finally, for the receiver located on the first floor having two floors difference with the transmitter location, the attenuation parameter is $\gamma = 4.51$ as a best fit to, the experimental data (see Fig. 8.19).

These results are very close to those obtained by Rappaport in his numerous experiments for different kinds of buildings (see Table 8.3), thus we can summarize that the suggested model (8.29) can be successfully used for prediction of the total path loss inside buildings for different antenna positions and different floors if we take into account Bertoni's formulas strictly (8.11) and (8.16) for the direct path loss
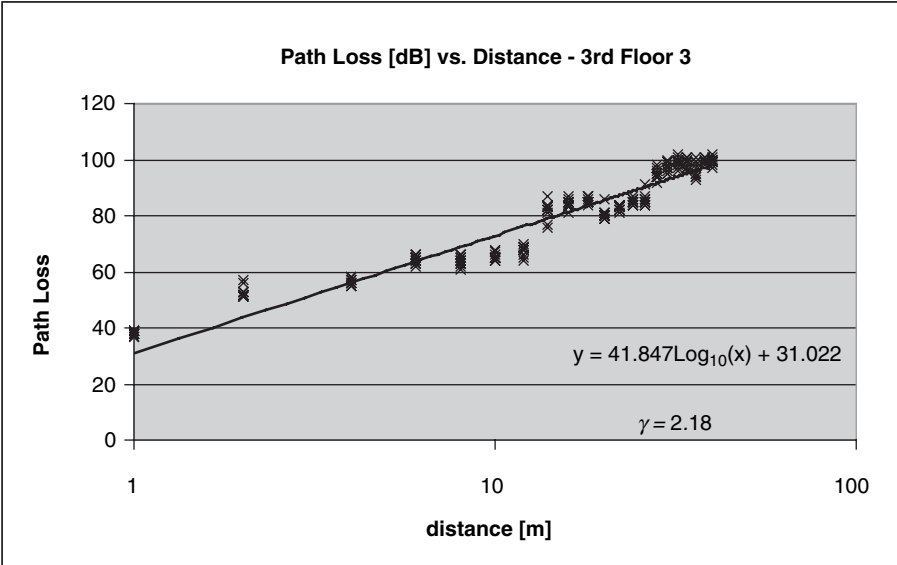
FIGURE 8.17. Best fit obtained for an experiment carried out at the same third floor.
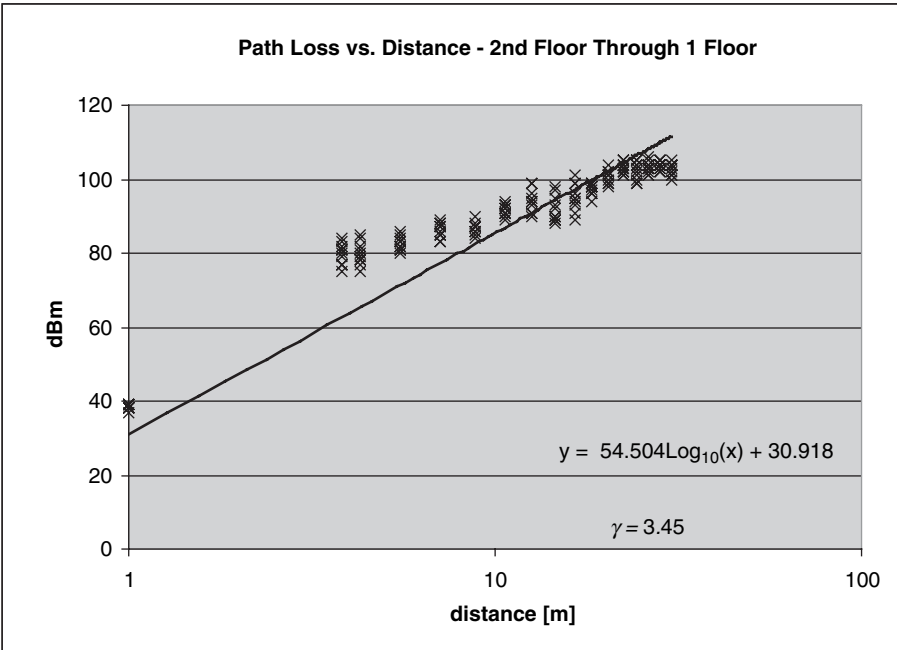
FIGURE 8.18. Best fit obtained for an experiment carried out through one floor between antennas.
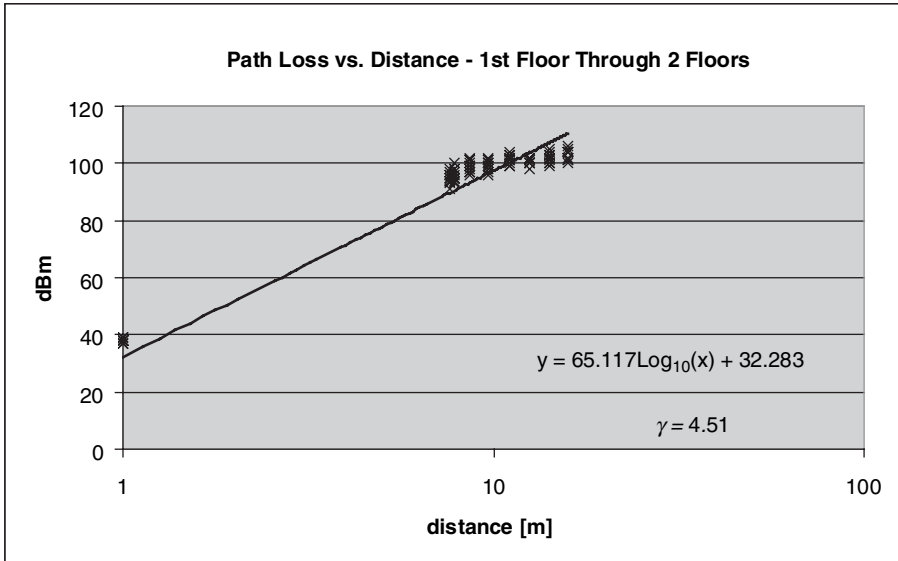
FIGURE 8.19. Best fit obtained for an experiment carried out through two floors between antennas.

between floors and walls and the shadow margin, which can be obtained either from experimental data or by using the method of shadow effect estimation described in Chapter 5 for link budget design.

BIBLIOGRAPHY

[1] Bertoni, H. L., *Radio Propagation for Modern Wireless Systems*, Prentice Hall PTR, New Jersey, 2000.

[2] Blaunstein, N., *Radio Propagation in Cellular Networks*, Artech House, London, 2000.

[3] Rappaport T. S., *Wireless Communications*, Prentice Hall PTR, New York, 1996.

[4] Saunders, S. R., *Antennas and Propagation for Wireless Communication Systems*, John Wiley & Sons, New York, 1999.

[5] Cox, D. C., R. R. Murray, and A. W. Norris, "Measurements of 800 MHz radio transmission into buildings with metallic walls," *AT&T Bell Lab. Tech. J.*, vol. 62, 1983, pp. 2695–2717.

[6] Davidson, A., and C. Hill, "Measurement of building penetration into medium building at 900 and 1500 MHz," *IEEE Trans. Veh. Technol.,* vol. 46, 1997, pp. 161–167.

[7] Turkmani, A. M. D., and A. F. de Toledo, "Modeling of radio transmission into and within multistory buildings at 900, 1800, and 2300 MHz," *IEE Proc.–1*, vol. 40, 1993, pp. 462–470.

[8] Alexander, S. E., "Radio propagation within buildings at 900 MHz," *Electronics Letters*, vol. 18, no. 21, 1982, pp. 913–914.

[9] Hashemi, H., "The indoor radio propagation channel," *Proc. IEEE*, vol. 81, no. 7, 1993, pp. 943–968.

[10] Lemieux, J. F., M. Tanany, and H. M. Hafez, "Experimental evaluation of space/frequency/polarization diversity in the indoor wireless channel," *IEEE Trans. Veh. Technol.*, vol. 40, no. 3, 1991, pp. 569–574.

[11] Rappaport, T. S., "Characterization of UHF multipath radio channels in factory buildings," *IEEE Trans. Antennas Propagat.*, vol. 37, no. 8, 1989, pp. 1058–1069.

[12] Devasirvatham, D. M., M. J. Krain, and T. S. Rappaport, "Radio propagation measurements at 850 MHz, 1.7 GHz, and 4.0 GHz inside two dissimilar office buildings," *Electronics Letters*, vol. 26, no. 7, 1990, pp. 445–447.

[13] Rappaport, T. S., and D. A. Hawbaker, "Wide-band microwave propagation parameters using cellular and linear polarized antennas for indoor wireless channels," *IEEE Trans. on Communications*, vol. 40, no. 2, 1992, pp. 231–242.

[14] Tarng, J. H., W. R. Chang, and B. J. Hsu, "Three-dimensional modeling of 900 MHz and 2.44 GHz radio propagation in corridors," *IEEE Trans. Veh. Technol.*, vol. 46, 1997, pp. 519–526.

[15] Gibson, T. B., and D. C. Jenn, "Prediction and measurements of wall intersection loss," *IEEE Trans. Antennas Propagat.*, vol. 47, 1999, pp. 55–57.

[16] Lafortune, J. F., and M. Lecours, "Measurement and modeling of propagation losses in a building at 900 MHz," *IEEE Trans. Veh. Technol.*, vol. 39, 1990, pp. 101–108.

[17] Arnod, H. W., R. R. Murray, and D. C. Cox, "815 MHz radio attenuation measured within two commercial buildings," *IEEE Trans. Antennas Propagat.*, vol. 37, 1989, pp. 1335–1339.

[18] Whitman, G. M., K. S. Kim, and E. Niver, "A theoretical model for radio signal attenuation inside buildings," *IEEE Trans. Veh. Technol.*, vol. 44, 1995, pp. 621–629.

[19] Seidel, S. Y., and T. S. Rappaport, "Site-specific propagation prediction for wireless in-building personal communication system design," *IEEE Trans. Veh. Technol.*, vol. 43, 1994, pp. 879–891.

[20] Seidel, S. Y., and T. S. Rappaport, "914 MHz path loss prediction models for indoor wireless communication in multifloored buildings," *IEEE Trans. Antennas Propagat.*, vol. 40, no. 2, 1992, pp. 207–217.

[21] Honcharenko, W., H. L. Bertoni, J. Dailing, et al., "Mechanisms governing UHF propagation on single floors in modern office buildings," *IEEE Trans. Veh. Technol.*, vol. 41, no. 4, 1992, pp. 496–504.

[22] Honcharenko, W., H. L. Bertoni, and J. Dailing, "Mechanisms governing propagation between different floors in buildings," *IEEE Trans. Antennas Propagat.*, vol. 41, no. 6, 1993, pp. 787–790.

[23] Dersch, U., and E. Zollinger, "Propagation mechanisms in microcell and indoor environments," *IEEE Trans. Veh. Technol.*, vol. 43, 1994, pp. 1058–1066.

[24] Clarke, R. H., "A statistical theory of mobile-radio reception," *Bell Systems Technical Journal*, vol. 47, 1968, pp. 957–1000.

[25] Rappaport, T. S., S. Y. Seidel, and K. Takamizawa, "Statistical channel impulse response models for factory and open plan building communication system design," *IEEE Trans. on Communications*, vol. 39, no. 5, 1991, pp. 794–805.

[26] Devasirvatham, D. M. J., "Time delay spread and signal level measurements of 850 MHz radio waves in building environments," *IEEE Trans. Antennas Propagat.*, vol. 34, no. 2, 1986, pp. 1300–1305.

[27] Rappaport, T. S., and V. Fung, ''Simulation of bit error performance of FSK, BPSK, and $\pi/4-$DQPSK in flat fading indoor radio channels using measurement-based channel model,'' *IEEE Trans. Veh. Technol.,* vol. 40, no. 4, 1991, pp. 731–739.

[28] Kanatas, A. G., I. D. Kountouris, G. B. Kostraras, et al., ''A UTD propagation model in urban microcellular environments,'' *IEEE Trans. Veh. Technol.,* vol. 46, no. 2, 1997, pp. 185–193.

[29] Katedra, M. F., J. Perez, F. S. de Adana, et al., ''Efficient ray-tracing techniques for three-dimensional analyses of propagation in mobile communications: application to piicocell and microcell scenarios,'' *IEEE Antennas Propagat. Magazine*, vol. 40, no. 2, 1998, pp. 15–28.

[30] Kim, S. C., B. J. Guarino, Jr. T. M. Willis III, et al., ''Radio propagation measurements and prediction using three dimensional ray tracing in urban environments at 908 MHz and 1.9 GHz,'' *IEEE Trans. Veh. Technol.,* vol. 48, 1999, pp. 931–946.

[31] Keenan, J. M., and A. J. Motley, ''Radio coverage in buildings,'' *BT Tech. J.*, vol. 8, no. 1, 1990, pp. 19–24.

[32] International Telecommunication Union, *ITU-R Recommendation P. 1238*: ''Propagation data and prediction models for the planning of indoor communication systems and local area networks in the frequency range 900 MHz to 100 GHz,'' Geneva, 1997.

[33] Yarkoni, N., and N. Blaunstein, ''Prediction of propagation characteristics in indoor radio communication environments,'' *J. Progress In Electromagnetic Research*, PIER 59, 2006, pp. 151–174.

Adaptive Antennas for Wireless Networks

As was mentioned in previous chapters, the main problem in mobile or stationary wireless communications, satellite and aircraft communications (megacell), outdoor (macrocell and microcell), and indoor communications (picocell), is the additional noise factor (to the white or additive noise). This noise has two aspects to it: (a) the multiplicative noise caused by multipath propagation fading, delay spread, and Doppler spread (see definitions in Chapter 1), and (b) the co-channel interference noise caused by interactions of information sent by different users located in the area of service and involved in the multiple access communication occurred in real time during servicing. Both of these physical phenomena degrade the grade-of-service (GOS), the quality of service (QOS), the capacity of the information data stream and, finally, the efficiency of wireless communication networks.

Several methods have been developed during the last two-three decades to eliminate these kinds of noise factors. These methods are based on filtering [1–5], signal processing [6–12], and the so-called adaptive or smart antenna systems [13–22]. The term ''smart antenna'' reflects the antenna's ability to adapt to the communication channel environment in which it operates. Because both terms ''adaptive antennas'' and ''smart antennas'' are interchangeable, from now on we will be using the term ''adaptive antennas'' as it is based on analog and digital beamforming technology [24–30]. Adaptive antennas are not only used in cellular communications, but also in many other applications such as aircraft and satellite communications, radars, and remote sensing [31–37]. The increasing demands on the operational efficiency of various wireless communication networks put a lot of

technical and mathematical questions not only on how to eliminate noise within a channel, but also on how to increase the capacity of the information data stream inside a channel. One has to account for limitations in the bandwidth of the existing communication networks, and increase the bit rate with small bit-error-rate (BER), the parameters that determine the quality of service. According to Shannon's formula, channel capacity linearly increases with allocating new frequencies to the service or with spreading the existing bandwidth. The latter is a very complicated problem, and with a logarithmical increase of its signal-to-noise ratio (SNR), it includes additive (white) noise, multiplicative noise, and noise caused by co-channel interference in cellular networks.

From previous discussions, to predict the noise factors in environments with strong ''clutter'' and hard obstructive (NLOS) conditions is a very complicated task. During the last four decades, designers have proposed new strategies where they combined adaptive antennas with advanced signal processing to obtain effective filtering systems that can simultaneously operate in the space, time, and frequency domains. Using such interdisciplinary mathematical and technical tools, a lot of other problems in wireless communications have been effectively solved. Here, we only point out the problems connected with multiple access communications, which deal with simultaneous service of numerous subscribers and occurs in frequency, time, code, and space domain. These multiple access communications are the frequency division multiple access (FDMA), time division multiple access (TDMA), code division multiple access (CDMA), and space division multiple access (SDMA). The use of adaptive antennas can essentially improve the grade-of-service (GOS), eliminate the influence of co-channel interference by increasing the carrier-to-interference ratio (C/I) and, finally, to determine with great accuracy the position of the desired subscriber, which must be serviced by a system. However, as will be discussed later, in urban environments, a wide spread antenna pattern in both azimuth and elevation domains, is observed, caused by the random distribution of buildings both in the horizontal and vertical planes. Therefore, it is very complicated to use more directive or adaptive antennas for urban communication links. These problems are difficult to solve without knowledge, not only of the signal strength or power distribution in the space domain, that is, along the radio path between the terminal antennas, but also of the signal distribution in the separate and joint angle-of-arrival (AOA), azimuth and elevation, time-of-arrival (TOA) or delay-spread (DS) domains. All these aspects will be briefly presented in the next section. Next, we start with the architecture of adaptive antennas for different array configurations (linear, circular, and planar).

9.1. ANTENNA ARRAYS

The definition of ''adaptive or smart'' antenna has been used in [13] to describe self-phasing antenna systems, which reradiate a radio signal in the direction from which it was received. Figure 9.1 shows the architecture of two arrays used in a communication system. The receiver array consists of N elements and the receiver

MIMO Communication Network
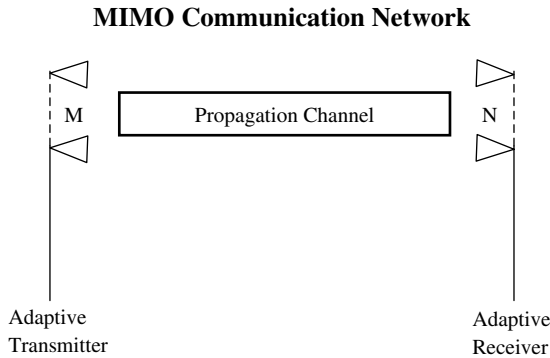
FIGURE 9.1. The MIMO channel.

has M elements. Such multichannel system in literature is called the multiple-input-multiple-output (MIMO) wireless channel [38].

> The concept of using antenna arrays and innovative signal processing is not new to the radar and aerospace technology. Until recent years, cost effectiveness has prevented their use in commercial systems. The advent of very fast and low-cost digital signal processors have begun to make adaptive antennas very smart and practical for cellular land- or satellite-mobile communication systems. This trend is only the beginning and the use of smart antennas is going to accelerate in the future. Main hurdles to overcome are the costs and the technological issues relating to the manufacturing of a multi-antenna system.

Before we start explaining the principles of adaptive arrays and their operation, we proceed with a review of some of the basics of antenna arrays.

9.1.1. Antenna Array Terminology

As was shown in Chapter 2, antennas in general may be classified as isotropic, omni-directional, and directional. For antenna array there are some additional terms that must be introduced such as array factor, phased arrays, steerable beams, and so on. [12–14,39–44]. A *phased array antenna* uses an array of antennas, called "elements" that combine their signals to achieve a more directive radiation pattern in some direction than others. The direction where the maximum gain would appear is controlled by adjusting the phase of the individual elements. So, in the direction where maximum gain occurs, the signals from the elements are added *in-phase* and that is the reason why an array is used to achieve more gain than a single antenna element.

An *adaptive array antenna*

> utilizes sophisticated signal processing algorithms to continuously distinguish between desired signals, multipath, and interfering signals as well as calculate their directions of arrival. The adaptive approach continuously updates its beam pattern based on changes in both the desired and interfering signal locations. The ability to smoothly track users with main lobes and interferers with nulls guarantees that the link budget is constantly maximized.
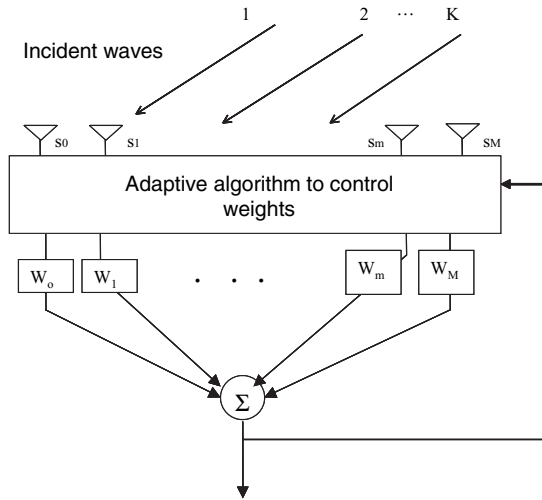
FIGURE 9.2. Typical adaptive antenna. Several signals S's are impinging on the antenna elements. W's are the weights that each signal is multiplied by before the summation point.

A block-scheme of the typical adaptive antenna is shown in Figure 9.2. The signals received by the elements of the antenna are weighted and combined to maximize the signal-to-interference ratio [18]. A typical adaptive antenna array is shown in Figure 9.2.

The Array Factor. A plot of the array response as a function of angle is commonly referred to as the array pattern, beam pattern or power pattern. To characterize this pattern, a new parameter called the *array factor* and denoted by $F(\varphi, \theta)$, is defined. It represents the far-field radiation pattern of an array of isotropic radiating elements in the θ and ϕ angles. The process of combining signals from different elements is known as *beamforming*. We will discuss several beamforming technologies later in this chapter.

Steering Process. For a given array, the main beam can be pointed in different directions by mechanically moving the array. This process is known as *mechanical steering*. In contrast, *electronic steering* uses the inherent delay of signals arriving at each element of the array before combining them. For narrow-band signals in Figure 9.3, phase shifters are used to change the phase of signals before combining them at the output of the antenna where they arrive with their own time delay $\tau_m(\theta)$ [42].

The steering locations, which result in maximum power, yield the direction-of-arrival (DOA) estimates, that is, the steering vector contains the responses of all elements of the array to a narrow-band source of unit power. Because the response of the array is different in different directions, a steering vector is associated with each directional source. The correlation between them depends upon the array geometry [40]. Because each component of the steering vector denotes the phase delay caused by the spatial position of the corresponding element of the array, this vector is also called the *space vector* or *array response vector*. In multipath situations in wireless communication channel, the space vector denotes the response of the array to all
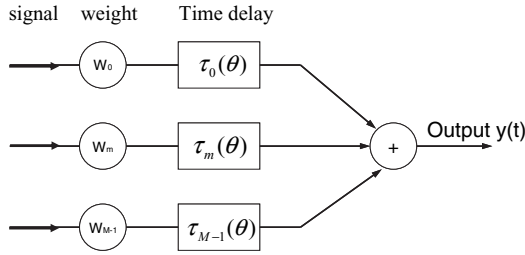
FIGURE 9.3. Summation of arriving signals with different time delays.

signals arising from the source [41,43,44]. The array response is steered by forming a linear combination of the element outputs, as will be shown mathematically later.

The Pattern of the Antenna Array. In an antenna array, if the distance between the elements-sensors is larger than the wavelength of radiation, several main lobes will be formed in the visible space. Conversely, if the element spacing is less than a wavelength, and all signals from elements are summed without any delay (see Fig. 9.2), then the produced array output signal will have a symmetric pattern about $\theta = 0°$ (see Fig. 9.4a). On the contrary, if in this case the output of each element is
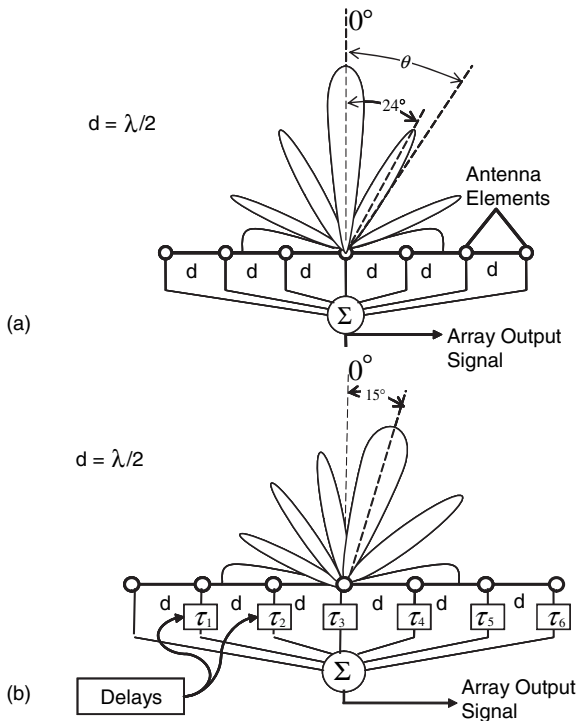
FIGURE 9.4. Antenna array (a) All signals arrive without any delay: the main beam is oriented normally to the sensors' line; (b) each signal is delayed by its own delay that gives a shift in the main beam by 15 degrees. (Source [14]: Reprinted with permission © 1967 IEEE)

delayed in time before being summed (see Fig. 9.3), the resulting directivity pattern will have its main lobe displaced at an angle ψ defined as

$$\sin \psi = \frac{\lambda \tau f}{d} = \frac{c\tau}{d} \qquad (9.1)$$

where d is the spacing between antenna array elements, $c = \lambda/T = \lambda f$ is the signal propagation velocity, and τ is the time-delay difference between neighboring-element outputs. Figure 9.4b shows the direction of the main beam and nulls for an array with $\theta = 24°$, $d = \lambda/2$, $\tau = 0.12941/f$, and $\psi = \sin^{-1}(2\tau f) = 15°$.

9.1.2. Architecture of the Antenna Array

Next we discuss the most common geometrical configurations used in adaptive array antennas.

Linear Array. Let us consider a receiving antenna with a linear array of $M - 1$ elements from the origin, which is uniformly spaced along the horizontal axis as shown in Figure 9.5 [24]. Let the spacing between elements be denoted by d. At each element input there is a complex signal given by $U_m = A_m e^{j\beta_m}$ (i.e., the signal input at the element m with amplitude A_m and phase $\beta_m = m\alpha$, $m = 0, 1, 2, \ldots$, $M - 1$). Here, α is the constant phase difference between two adjacent elements.

We also assume that at the origin, the phase of the arriving ray is equal to zero, and the differential distance of two rays at points $m + 1$ and m is $\Delta d = md \sin \theta$. Then the array factor can be determined as [24]:

$$F(\theta) = U_0 + U_1 e^{jkd \sin \theta} + U_2 e^{j2kd \sin \theta} + \ldots$$

$$= \sum_{m=0}^{M-1} U_m e^{jmkd \sin \theta} = \sum_{m=0}^{M-1} A_m e^{j(mkd \sin \theta + m\alpha)} \qquad (9.2)$$
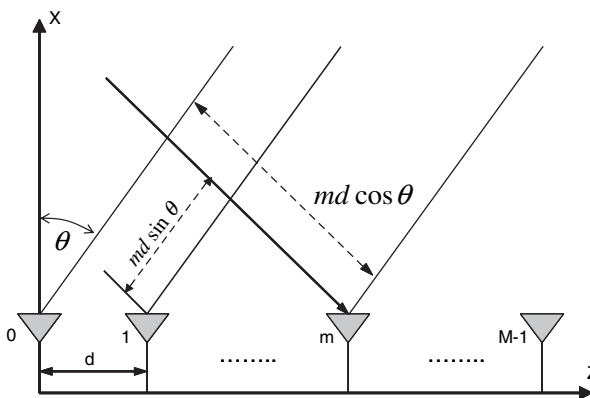
FIGURE 9.5. Linear antenna array to obtain the path difference between two neighboring elements.
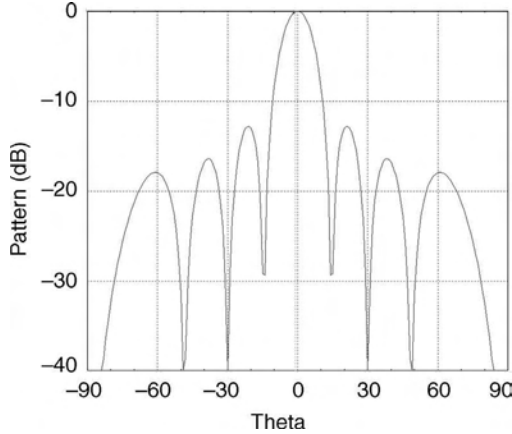
FIGURE 9.6. Field pattern of an 8-element adaptive array antenna.

or in terms of vectors and an inner product:

$$F(\theta) = \mathbf{U}^T \mathbf{u} \tag{9.3}$$

where

$$\mathbf{U} = [U_0 \, U_1 \ldots U_{M-1}]^T \tag{9.4}$$

is the array propagation vector that contains information about the angle-of-arrival (AOA) of the signal. Also,

$$\mathbf{u} = [1 \, e^{jkd \sin \theta} \, e^{j2kd \sin \theta} \ldots e^{j(M-1)kd \sin \theta}]^T \tag{9.5}$$

is the weigh vector with the corresponding component for each element of the array. If now $\alpha = -kd \sin \theta_0$, a maximum response of $F(\theta)$ will result at the angle θ_0, that is, the antenna beam pattern will be steered towards the wave source. Figure 9.6 shows the radiation pattern for an eight-element linear array with λ spacing between elements.

Circular Array. The same situation can be said for a circular array of equally distributed $M - 1$ elements placed on a circle of radius R, as shown in Figure 9.7.

Here, we introduce the azimuth angle for each element m, $\varphi_m = 2m\pi/M$. The relative phase β_m at each element m with respect to the center of the array is

$$\beta_m = -kR \cos(\varphi - \varphi_m) \sin \theta \tag{9.6}$$

Again, for a main beam directed at angles θ_0 and φ_0 in space, the phase of the complex signal $U_m = A_m e^{j\alpha_m}$ for the element m equals

$$\alpha_m = kR \cos(\varphi_0 - \varphi_m) \sin \theta_0 \tag{9.7}$$
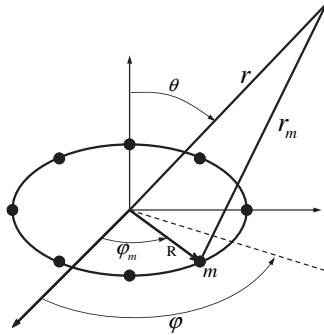
FIGURE 9.7. Geometry of a circular antenna array.

In this case, the array factor for the circular antenna can be presented in the following form:

$$F(\varphi, \theta) = \sum_{m=0}^{M-1} A_m \, e^{j[\alpha_m - kR\cos(\varphi - \varphi_m)\sin\theta]} \tag{9.8}$$

Figure 9.8 shows the radiation pattern for an adaptive circular array of radius 0.8λ. The array factor $G(\varphi, \theta)$ can be found as

$$G(\varphi, \theta) = f(\varphi, \theta) \cdot F(\varphi, \theta) \tag{9.9}$$

where $f(\varphi, \theta)$ is the element factor. This equation is usually called the *principle of pattern multiplication*, which allows us to determine the array factor of more
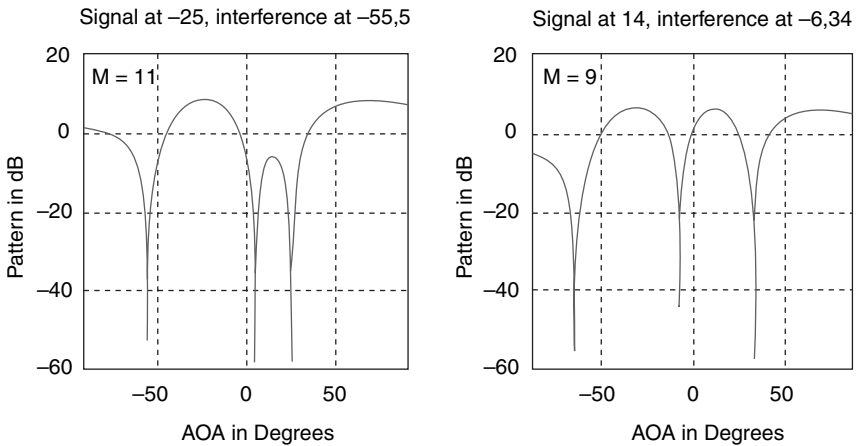
FIGURE 9.8. Radiated pattern for an adaptive circular array radius 0.8λ. The desired signal to be tracked and the interference signals are shown in degrees at the top.
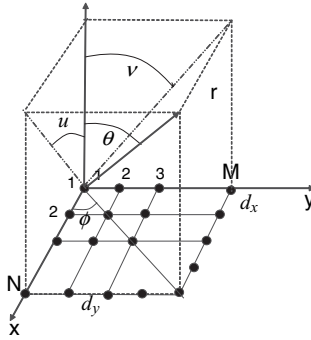
FIGURE 9.9. Geometry of a planar antenna array.

complicated arrays as a composition of simple subarrays, and account for their mutual dependence.

Planar Array. An example of the planar array is shown in Figure 9.9 as a combination of two linear arrays, one is with $M - 1$ elements and the second is with $N - 1$ elements. Then, according to (9.2), the array factor for the first M-element array with the complex signal at the element m of $U_m = A_m e^{jm\alpha}$, $m = 0, 1, 2, \ldots, M - 1$, is given as

$$F_1(u) = \sum_{m=0}^{M-1} A_m \, e^{j(mkd_x \sin u + m\alpha)} \tag{9.10}$$

where $u = \sin\theta \cos\varphi$. The array factor for the N-element array with the complex weight at the element n of $U_n = A_n e^{jn\beta}$, $n = 0, 1, 2, \ldots, N-1$, is given as [24]:

$$F_2(v) = \sum_{n=0}^{N-1} A_n \, e^{j(mkd_y \sin v + n\beta)} \tag{9.11}$$

where $v = \sin\theta \sin\varphi$. According to the principle of pattern multiplication, the overall array factor for the rectangular array is then given by

$$F = F_1(u) \cdot F_2(v) \tag{9.12}$$

The same procedure can be used for the more complicated antenna structures such as the hexagon planar array and so on.

9.2. BEAMFORMING TECHNIQUES

The term beamforming relates to the capability of the antenna array to focus energy along a specific direction in space [18,19,21,24]. Thus, in multiple access

communications, a desired user must be serviced in "clutter" conditions. In this case, "clutter" means the existence of other users located in the area of service. Beamforming allows the antenna to focus energy only towards a desired user and nulls in the undesired directions. For this reason, beamforming is often referred to as spatial filtering. Spatial filtering or beamforming was the first approach to carry out space-time processing of data sampled at antenna arrays [12].

The conventional (Bartlett) beamformer was the first to emerge during the Second War [45]. It is a natural extension of the classical Fourier-based spectral analysis for spatial-temporal sampled data. Later, adaptive beamformers [46–49] and classical time-delay estimation techniques [49] were applied to enhance the ability to resolve signal sources that are closely spaced. From a statistical point of view, the classical techniques can be seen as spatial extensions of the spectral Wiener (or *matched*) filtering method [50]. However, the conventional beamforming approach has some fundamental limitations connected to the physical size of the aperture or the array, to the available data collection time, and to signal-to-noise ratio (SNR). For more details the reader is referred to [8,21,51,52]. Next, we present some aspects of *analog* and *digital* beamforming.

9.2.1. Analog Beamforming

An analog beamforming system usually consists of devices that change the phase and power of the signal emanating from its output. Figure 9.10 shows an example for creating only one beam at the output of the RF beamformer [24]. Such simple, one-beam antenna array systems can be constructed by using microwave waveguides, microstrip structures, transmission lines, and printed microwave circuits.

Multiple-beam beamforming systems are more complex systems whose operational characteristics are based mathematically on the beamforming matrix, with the Butler matrix being the most known matrix [53]. In a beamforming matrix, an array of hybrid junctions and fixed-phase shifters are used to achieve the desired results. As an example, a Butler-beamforming matrix for a four-element antenna
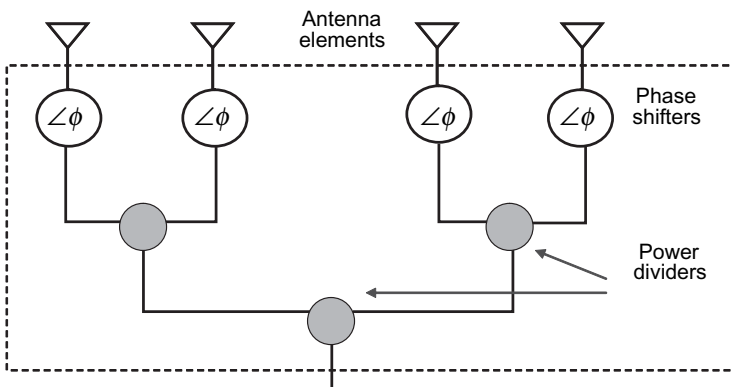
FIGURE 9.10. A simple beamformer.
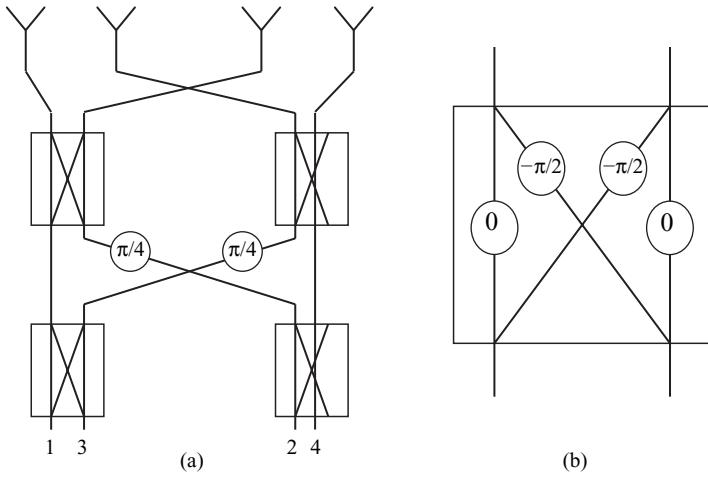
FIGURE 9.11. (a) A Butler beamforming matrix for a four-element antenna array, and (b) Its phasing scheme.

array is shown in Figure 9.11a. This matrix uses two 45° fixed-phase shifters and four 90° phase-lag hybrid junctions with the corresponding computation links. (see Fig. 9.11b).

By tracing the signal from the four ports to the array elements, one can verify that the relative phase distribution at the antenna aperture corresponds to the individual ports of the four-port Butler matrix, computed as shown in Figure 9.12 [24,53]. An
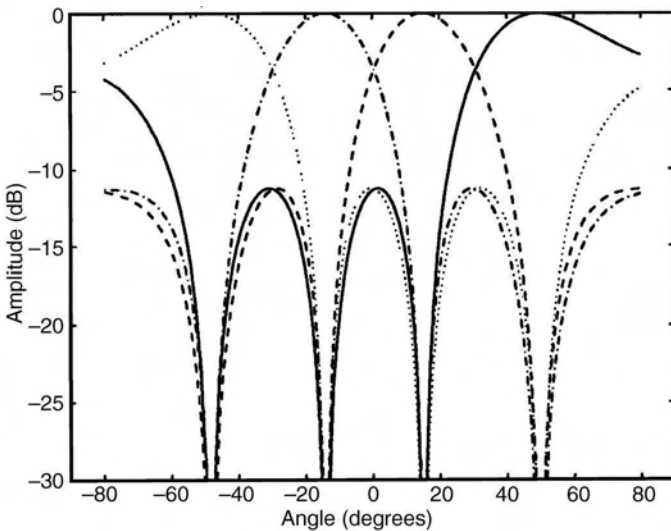
FIGURE 9.12. Computation of the antenna pattern corresponding to the beamformerin Fig. 9.11. (Source [24]: Litva, J and T. Lo, Artech House, 1996)

example of an array antenna pattern with elements spaced at $\lambda/2$ is shown in Figure 9.12. Although, these four beams are overlapping and they are mutually orthogonal.

Here, we must note that the Butler matrix was developed before the fast Fourier transform (FFT) and that they are both completely equivalent. One (the Butler matrix) is used for analog beamforming, and the other (FFT) is for digital beamforming [19,21,24,51–53].

Conventional Beamforming is a simple beamformer, sometimes known as the delay-and-sum beamformer, with all it weights of equal amplitude.

As was mentioned previously, the phases of the elements are selected to steer the main beam of the array in a particular direction (φ_0, θ_0), known as the look direction. The system must be able to adapt its pattern to have lobes at $M-1$ places. This ability is known as a degree of freedom of the array. For an equally spaced linear array this feature is similar to an $M-1$ degree polynomial of $M-1$ adjustable coefficients, with the first coefficients having the value of unity [see formula (9.5)]. The concept of a delay beamformer or phase delay is shown in Figure 9.13 [42].

Here, due to the delay of each arriving ray at an array element with respect to its neighboring element, a corresponding shift in phase occurs with the amplitude weights remaining fixed as the beam is steered. As mentioned before, this type of array is commonly known as a *phased array*.

Null-Steering Beamformer is used to place nulls in the radiation pattern in specified directions. Usually, the nulls are placed in the directions of interfering signals or mobile users. In the earliest schemes [54–57], this was achieved by estimating the signal arrived from a known direction by steering a conventional beam in the direction of the desired source and then subtracting the output from each element in this case the beam output $y(t)$ is presented by a sum of the signals x_m, $m = 0, 1, \ldots, M-1$, received from a given direction, defined by the angle θ, by
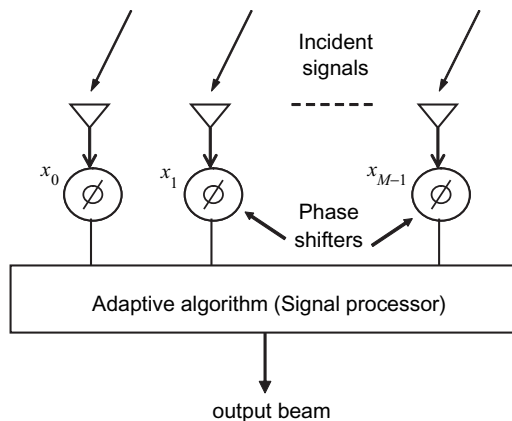
FIGURE 9.13. A beamformer with phase shifters.

each of the M elements. Each element has its own weight coefficient w_m and time delay of arrival $\tau_m(\theta)$. The output of the antenna is expressed as

$$y(t, \theta) = \sum_{m=0}^{M-1} w_m x_m[t - \tau_m(\theta)] \qquad (9.13)$$

By adjusting these weights, one can shape the beams. This process is very effective for canceling strong interference between subscribers.

Frequency-Domain Beamforming. Here, by using the direct and inverse fast Fourier transform (FFT), the broadband signals from each element of the array are transformed into the frequency domain and then each frequency bin is processed by a narrowband processor structure (see details in References [58–60]). The weighted signals from all elements are summed to produce an output at each bin (see Fig. 9.14). The weights are selected by independently minimizing the mean output power at each frequency bin subject to steering-direction constraints. Thus, the weight required for each frequency bin are selected independently, and this selection may be performed in parallel, leading to a faster weight update. Various aspects of frequency-domain beamforming are reported in References [58–60] and other references.

   Multiple Beamforming is used to generate several beams simultaneously. These beams can be fixed in certain directions or adaptive with nulls steerable in desirable directions. This can be achieved using very complex networks of phase shifters.

   In *beam-space processing* [61–63], the beamformers can distribute the signal energy to all the formed beams. One of the problems with multiple-beam beamformers is that as the number of beams is increased, the SNR of channels being carried by the individual beam decreases. This is due to additional noise introduced from the additional number of radio frequency (RF) and intermediate frequency (IF) components that must be used to increase the beamformer capacity.
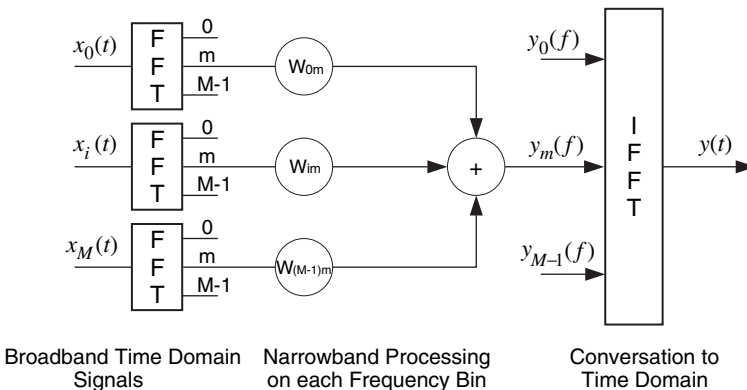
FIGURE 9.14. Summation of weights. (Source [14]: Reprinted with permission © 1967 IEEE)

9.2.2. Digital Beamforming

Earlier ideas to use digital beamforming come from foundations in sonar [27] and radar systems [31] as a bridge between antenna technology and digital technology. Using digital techniques, it is possible to capture RF information in the form of digital streams. Digital beamforming is based on the conversion of the incident RF signal at each antenna element into two streams of binary complex baseband signals representing an in-phase component (I) and a 90° phase shifted or quadrature component (Q). In digital beamforming technique, the weighted signals from each element are sampled and stored, and beams are formed summing the appropriate samples [64–70]. Despite the fact that digital beamforming does not have the same direct physical meaning as analog beamforming, the same process of adaptive beamformer is used by weighting digital signals and presenting the total beam by the same array factor (9.8).

Next, a simple algorithm of beamforming without any phase delays will be introduced.

Element-Space Beamforming. A simple structure that can be used for such beamforming is shown in Figure 9.15 [14,42]. It is the same as the one sketched in Figure 9.2, but here we introduce notations that correspond to digital processing jargon.

The output $y_n(\theta)$ at a discrete time $t = nT$ is given by a linear combination of the binary data at M sensors (also known as the *array snapshot* at the nth instant of time given by Reference [42]). We define a *snapshot* as one simultaneous sampling of all array element signals.

$$y_n(\theta) = \sum_{m=0}^{M-1} w_m^* x_m(n) \tag{9.14}$$

or in inner vector form [42]:

$$y_n(\theta) = \mathbf{w}^H \cdot \mathbf{x}(n) \tag{9.15}$$

where the sampling time T was omitted to simplify our discussions. Here, x_m is the signal from m^{th} element of the array, w_m^* is the weight applied to x_m, sign "*"
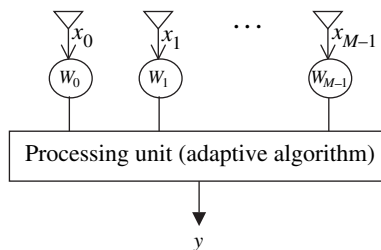
FIGURE 9.15. A simple digital beamformer.
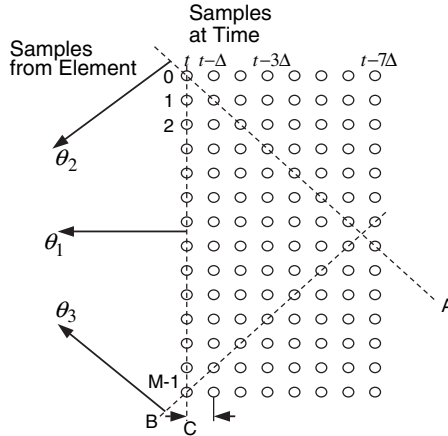
FIGURE 9.16. Obtaining the desired direction using a linear array of sensors. (Source [42]: Reprinted with permission © 1997 IEEE)

represents a complex conjugate, and the superscript H represents the Hermitian transpose. To relate these notations to the analog beamforming, we assume that $x_m(n) = U_m$ and $w_m^* = e^{-jmkd\sin\theta}$. Then the total output signal $y(t)$ is equal to $F(\theta)$ from (9.2), that is, $y_n(\theta) = F(\theta)$. In such a manner, (9.14) describes the process that is referred to as the *element-space beamforming*, where the binary data signals x_m are directly multiplied by a set of weights to form a beam in any desired angle.

To consider the delayed adaptive beamforming using delays, we need to use Equation (9.13) and represent each delay as an integer multiple of the sampling interval Δ. The process is shown in Figure 9.16 for a linear array of uniformly spaced elements, where it is desired that a beam is formed in the specific direction θ_2 [42].

The time delay along θ_2 is

$$\tau_m(\theta_2) = m\Delta, \quad m = 0, 1, \ldots, M-1 \tag{9.16}$$

Thus, the signal from the mth element needs to be delayed by $m\Delta$ seconds. This may be accomplished by selecting the samples for summing, as shown in Figure 9.16 by the line marked with symbol A. Similarly, a beam may be steered in a direction θ_3 by summing the samples connected by the line marked with symbol B in Figure 9.16, where the signals from the mth element need to be delayed by $(M-1-m)\Delta$ seconds. At the same time, the beam formed in direction θ_1, by summing the samples connected by the line marked with symbol C, does not require any delay. So, using such a process we can only form beams in those directions that require delays equal to some integer multiple of the sampling interval, that is, correspond to (9.16). The number of discrete directions where a beam can be pointed exactly increases with increased sampling. This leads to the formation of additional beams. For more information on how to form multiple beams simultaneously and
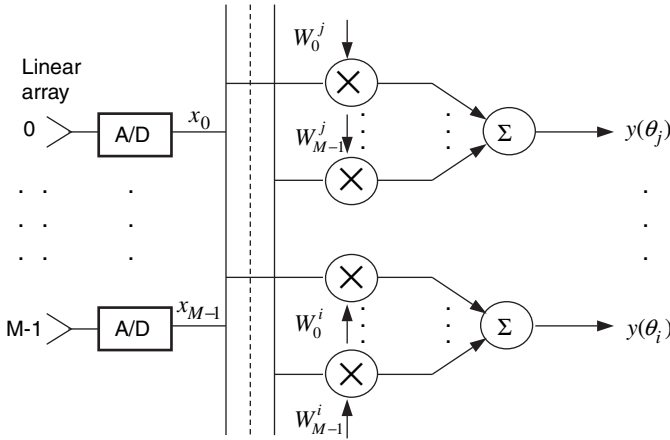
FIGURE 9.17. A simple beamformer without time delays.

synchronize the digital beamforming process, the reader is referred to work reported in References [26,66–71].

An example of a simple beamformer that generates an arbitrary number of simultaneous beams from M antenna elements is shown in Figure 9.17. Each beamformer creates an independent beam by applying independent weights to the array signals, that is, [29]:

$$y(\theta_i) = \sum_{m=0}^{M-1} w_m^{i*} x_m \tag{9.17}$$

where $y(\theta_i)$ is the output of the beamformer, x_m is a sample from the mth array element, and w_m^i are the weights for forming beam at angle θ_i. By selecting appropriate weight vectors, we can implement beam steering, adaptive nulling, and beam shaping.

Space Beamforming. Instead of directly weighting the outputs from the array elements, they can be processed first by a multiple-beam beamformer to form a suite of orthogonal beams. The output of each beam is then weighted and combined to produce a desired output. This process is often referred to as space beamforming. The required multiple beamformer usually produces orthogonal beams namely, the beamformer that can be implemented by using the fast Fourier transformation (FFT). Thus, an M-element linear array with M overlapped orthogonal beams can be used to give [29]

$$v(\theta_m) = \sum_{m=0}^{M-1} x_m \, e^{-j2\pi m\theta_m/(M-1)}, \quad m = 0, 1, 2, \ldots, M-1 \tag{9.18}$$
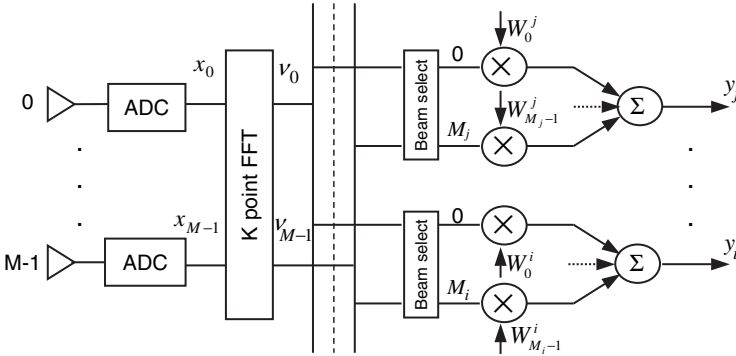
FIGURE 9.18. An FFT-based beamformer. (Source [29]: Reprinted with permission © 1998 IEEE)

where $\theta_m = \sin^{-1}[m\lambda/(M-1)d]$. Because of the fixed discrete nature of $v(\theta_m)$, the individual beam control requires the following steps:

a) Interpolation between beams in order to precise-steer the resultant beam precisely;

b) Linear combination of the output beams to synthesize a shaped beam or a low sidelobe pattern;

c) Linear combination of a selected set of beams to create nulls in the direction of the interfering sources.

Thus for space beamforming, a set of beam-space combiners to generate weighted outputs is required. In Figure 9.18 in the weighted FFT-based beam former, the digital signal streams from the antenna elements are fed to the FFT processor, which generates M simultaneous orthogonal beams.

The role of the beam select function in Figure 9.18 is to choose a subset of these orthogonal beams that are to be weighted to form a desired signal. For example, the ith desired output may happen to be the combination of the weighted m^{th} and $(m+2)$th beams, that is,

$$y_i = w_1^i v(\theta_m) + w_2^i v(\theta_{m+2}) = \sum_{m=0}^{M_i-1} w_m^i v(\theta_{i(m)}) \qquad (9.19)$$

where $i(m)$ is the selected beam index (i.e., $i(1) = m$ and $i(2) = m+2$) and $(M_i - 1)$ is the number of orthogonal beams that is required to form the ith desired beam.

Two-Dimensional Beamforming. Digital beamforming technologies for mobile-satellite communications are usually based on two-dimensional planar antenna arrays [72,73]. As was shown in Section 9.1, all algorithms, techniques, and methods

for linear antenna arrays can be easily and naturally extended to two-dimensional planar arrays. Thus, for a $M \times K$ rectangular planar array, the output of the beamformer at the discrete time $t_n = n$, $y_n(\theta, \varphi)$, is given by [72,73]

$$y_n(\theta, \varphi) = \sum_{k=0}^{K-1} \sum_{m=0}^{M-1} w_{k,m}^* x_{k,m}(n) \qquad (9.20)$$

or in the standard matrix form through inner product

$$y_n(\theta, \varphi) = \mathbf{w}^H \mathbf{x}(n) \qquad (9.21)$$

where the weight matrix is

$$\mathbf{w} = (w_{0,0}, \quad w_{1,0}, \ldots, \quad w_{K-1,0}, \quad w_{0,1}, \ldots, \quad w_{K-1,M-1})^T \qquad (9.22)$$

and the output signal matrix at each element of the planar array is

$$\mathbf{x}(n) = [x_{0,0}(n), \quad x_{1,0}(n), \ldots, \quad x_{K-1,0}(n), \quad x_{0,1}(n), \ldots, \quad x_{K-1,M-1}(n)]^T \qquad (9.23)$$

In a similar way, the output of the beamformer at time n can be constructed for any planar array.

Adaptive Beamforming. Adaptive beamforming has been a subject of considerable interest for more than three decades, traditionally starting as other types of beamforming to be employed in sonar and radar applications. There are numerous technical papers and articles on the basic concept, special technologies, and applications of adaptive beamforming, from which more general are [9,14,16,19,29,74–80].

Adaptive beamforming started with the invention of the intermediate frequency *side lobe canceller* (SLC), reported in References [13,15]. This was the first adaptive antenna system that was capable of nulling interference signals automatically at the antenna ouput. His antenna array had a typical configuration of nondelayed beamformer presented in Figure 9.4a, but with one significant difference: it contained one high-gain main-beam "dish" antenna (with weight w_0) surrounded by a linear array of several low-gain antenna sensors (with weights $w_m, m = 1, 2, \ldots, M - 1$).

Applebaum [47] developed a theoretical concept, commonly known as the Howells-Applebaum algorithm, on how to control the weights of the adaptive beamformer. The main goal of this algorithm was to maximize the SNR at the array output. For the analog SLC multibeam antenna loop, Applebaum expressed a differential adaptive processing equation given by

$$T \frac{dw_i}{dt} + w_i = G \left\{ K_i - x_i^*(t) \sum_{m=0}^{M-1} w_m x_m(t) \right\} \qquad (9.24)$$

From this equation, one can obtain the weights in a matrix form by using

$$\mathbf{w} = \mu \mathbf{R}^{-1} \mathbf{K} \tag{9.25}$$

where $\mathbf{R}$ is the $M \times M$ covariance matrix $\mathbf{R} = E[\mathbf{x}(t)\mathbf{x}^H(t)]$ which is formed from the expected values of the array signal correlation. In (9.24), w_i, $i = 0,1, \ldots, M-1$, is the ith weight at the ith element output, $x_i(t)$ is a signal from the ith antenna element, K_i is the component of cross-correlation matrix $\mathbf{K}$ of $x_i(t)$ with the output of the main high-gain antenna channel (with weight w_0). T is the smoothing filter time constant, and G is the amplifier gain. A positive scalar μ (called the gradient step size) controls the convergence characteristic of the algorithm, that is, how fast and how close the estimated weights approach the optimal weights.

A different beamforming technique was proposed by Capon [46]. This approach leads to an adaptive beamformer with a minimum-variance distortionless response (MVDR), also known in literature as the maximum likelihood method (MLM), because it maximizes the likelihood function of the input signal vector.

Then, Reed with coworkers showed that fast adaptivity is achieved by using the *sample-matrix inversion* (SMI) technique [57]. This algorithm is more convenient when fast convergence response is required in a SLC configuration [19,57,79]. Sometimes it is better to use an *orthogonal lattice filter adaptive network*, often referred to as the Gram-Schmidt algorithm. According to this algorithm, each weight w_{im} represents the adaptive coefficient obtained from a one-stage Gram-Schmidt orthogonal filter and can be expressed through the nth time-sampled voltage $V_{\text{im}}(n)$ of a set of N signal data samples from the ith input as [21,22,79]

$$|w_{\text{im}}| = \frac{\displaystyle\sum_{n=1}^{N} V_i^*(n) V_m(n)}{\displaystyle\sum_{n=1}^{N} V_i^*(n) V_i(n)} \tag{9.26}$$

Using this technique, the adaptive weights can be computed directly. A comparison of the convergence speed performance obtained by the Gram-Schmidt algorithm and that obtained by Howells-Applebaum algorithm made in Reference [22], has shown that the first one converses in about 30 snapshot data samples, whereas the second one achieves a signal at the level of 14 dB above the receiver noise after 180 snapshots.

The SMI algorithm can be sped up by using the direct inversion of the covariance matrix $\mathbf{R}$ in (9.25). If the desired and the interference signals are known a priori, then the covariance matrix could be evaluated and the optimal solution for the weights could be computed using (9.25). As in most cases the signals are not known, they can be generated as a set of "pseudo" signals $\widetilde{x}_m(t)$ that closely represent the real signals. A general adaptive beamforming scheme is considered in Figure 9.19 below [19,24,79].

The choice of the weight vector $\mathbf{w}$ is based on the statistics of the signal vector $\mathbf{x}(t)$ received at the array. Basically, the objective is to optimize the beamforming
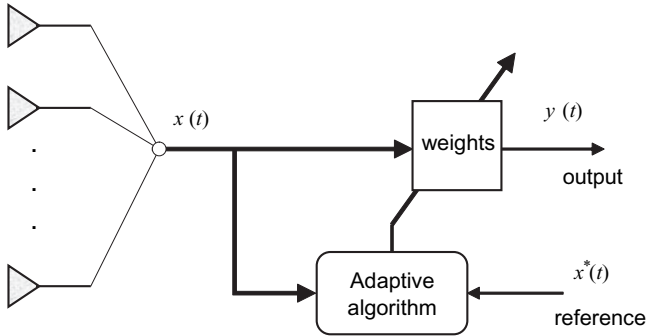
FIGURE 9.19. General adaptive beamforming.

response according to a prescribed criterion of the adaptive processor operation, so that the output $y(t)$ will contain minimum contribution from noise and interference. In such a situation, the adaptive processor must continually update the weight vector to meet a new requirement imposed by the varying conditions of the signal environment. Therefore, instead of the real covariance matrix $\mathbf{R}$, the adaptive processor "deals" with the approximate covariance matrix $\widetilde{\mathbf{R}} = E[\widetilde{\mathbf{x}}^*(t)\mathbf{x}(t)]$, and (9.25) becomes the Wiener-Holf equation, which is also called the optimum Wiener solution [57]

$$\mathbf{w}_{\text{opt}} = \mu \mathbf{R}^{-1}\widetilde{\mathbf{R}} \tag{9.27}$$

In this algorithm the weight vector is updated without a priori information and it leads to estimates of $\mathbf{R}$ and $\widetilde{\mathbf{R}}$ in a finite observation interval. These estimates are then used in (9.27) to obtain the desired weight vector. The error, due to these estimates, can be viewed as the least squares formulation of the problem. So, the weight vector derived using the SMI method can be defined as the least squares solution.

Another algorithm, the *Least Squares* or *LMS algorithm*, was developed by Widrow and his colleagues [10,14]. Because of its simplicity, the LMS algorithm is the most commonly used adaptive algorithm for continuous adaptation and it is capable of achieving satisfactory performance under the right set of conditions. The LMS algorithm was further developed with the introduction of constrains [76,77] that are used to ensure that the desired signals are not filtered out against the unwanted signals.

The LMS algorithm is based on the optimization method that recursively computes and updates the weight vector. It is clear that the process of successive corrections of the weight vector leads to the estimation of the mean-square error (MSE), which finally allows to obtain an optimum value for the weight vector. According to the optimization method [81], the weight vector is updated at time $n + 1$ using the following relation:

$$\mathbf{w}(n + 1) = \mathbf{w}(n) + \mu[\widetilde{\mathbf{R}} - \mathbf{R}\mathbf{w}(n)] \tag{9.28}$$
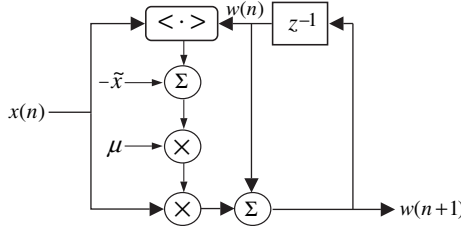
FIGURE 9.20. Schematical presentation of LMS algorithm.

As in the previous algorithms, a prior knowledge of both $\mathbf{R}$ and the approximate $\widetilde{\mathbf{R}}$ is not possible. Again, their instantaneous estimates are used through the error matrix

$$\mathbf{E} = \mathbf{R}\mathbf{w}_{\mathrm{opt}} - \widetilde{\mathbf{R}} \tag{9.29}$$

Then the estimated weights can be updated as

$$\hat{\mathbf{w}}(n+1) = \hat{\mathbf{w}}(n) + \mu\mathbf{x}(n)\mathbf{E}(n)] \tag{9.30}$$

The gain constant μ controls the convergence characteristics of the random vector sequence $\mathbf{w}(n)$. This is a continuously adaptive approach that works well when the signal environment is statistically stationary. A signal-flow scheme representing the LMS algorithm is shown in Figure 9.20 [81].

It is clear that such an algorithm is very simple and therefore successfully used in sonar, radar, and communication applications [82–90].

However, its convergence characteristics depend strongly on the eigenvalues of the covariance matrix $\mathbf{R}$, which has a tendency to change widely with a change in the signal environment. When this occurs, convergence can be very slow. Furthermore, unlike the Applebaum's maximum SNR algorithm and the LMS algorithm, which may suffer from slow convergence, the performance of the SMI algorithm is more preferable in this situation because it is independent of the value of the eigenvalue spread.

Despite the fact that the Applebaum's maximum SNR algorithm and Widrow's LMS error algorithm were discovered independently and were developed using different approaches, they are basically similar. For stationary signals, both algorithms converge to the optimum Wiener solution [78].

Let us now present a simple example of an adaptive antenna processing for steering and modifying an array's beam in order to "work" only with a desired signal and to show how the complex weight coefficients are obtained to suppress the interfering signals. Consider a base station with a simple array of two antennas separated by a distance of $d = \lambda/2$, as shown in Figure 9.21. For simplicity, let us assume that the desired signal arrives from the first mobile user at $\theta_1 = 0°$ and the interfering signal arrives from the second mobile user at $\theta_2 = \pi/6$. Both signals send their information at the same frequency f. The first desired signal, $s_w = a_w\,e^{j2\pi ft}$, arrives at the first and second elements with the same phase. The output y_w for the
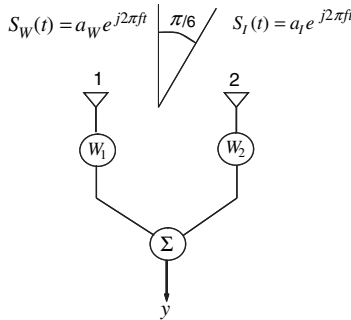
FIGURE 9.21. An adaptive array of two elements.

wanted signal is a linear combination of the two corresponding weight coefficients, w_1 at the first element antenna and w_2 at the second element antenna, that is,

$$y_w = a_w \, e^{j2\pi ft}(w_1 + w_2) \tag{9.31}$$

At the same time, the interfering signal $s_I(t) = a_I \, e^{j2\pi ft}$ arrives at the first and second element antenna with a phase shift of $\phi = kd \sin(\pi/6) = 2\pi(\lambda/2)(1/2)/\lambda = \pi/2$. Thus, the array output for the interfering signal at the two elements equals [24]

$$y_I = a_I \, e^{j2\pi ft}w_1 + a_I \, e^{j(2\pi ft + \pi/2)}w_2 \tag{9.32}$$

To make sure that at the output of the array there is a desired signal, we must satisfy

$$\begin{cases} \text{Re}[w_1] + \text{Re}[w_2] = 1 \\ \text{Im}[w_1] + \text{Im}[w_2] = 0 \end{cases} \tag{9.33}$$

At the same time, to minimize the effect of the interfering signal leaving the desired signal unaffected, one must state that the array output for the interference response must be zero or as follows from (9.32)

$$\begin{cases} \text{Re}[w_1] + \text{Re}[jw_2] = 0 \\ \text{Im}[w_1] + \text{Im}[jw_2] = 0 \end{cases} \tag{9.34}$$

Expressions (9.33) and (9.34) are then solved simultaneously to give us

$$\begin{cases} w_1 = 1/2 - j(1/2) \\ w_2 = 1/2 + j(1/2) \end{cases} \tag{9.35}$$

With these weights, the array of two element antennas will accept the desired signal while simultaneously eliminating the interfering signal. Of course, in this simple example we assumed prior knowledge of the direction of arrivals for the

interfering and desired signals, frequency, and so on. Nevertheless, this example demonstrates that a system consisting of an array of antenna elements, which is configured with complex weights, provides countless possibilities for realizing array system objectives.

9.3 ADAPTIVE ANTENNA FOR WIRELESS COMMUNICATION APPLICATIONS

The demand for mobile and fixed wireless communication continues to grow, making subscriber capacity and reliability of wireless systems a critical issue. Efficient temporal processing, such as advanced source coding, channel coding, modulation, equalization, and detection techniques, can help alleviate this problem. However, more dramatic improvements may be achieved by exploiting the spatial dimension using a smart antenna system and multiple access techniques.

Multiple access refers to the simultaneous coverage of numerous users by manipulating the transmission and reception process of signals in time, frequency, code, and space domains. In time division multiple access (TDMA), each user located in the area of service obtains or transmits information in a certain period of time called a *time slot*. In frequency division multiple access (FDMA), the frequency bandwidth is divided into segments, which are then portioned among different users located in certain service area. In code division multiple access (CDMA), each user obtains a unique random sequence of bits, that is, a unique code, generated by a generator of special random sequences. The information waveform is spread after modulation by this code over the entire frequency bandwidth, which is allocated to all users serviced by the network. The receiver uses the same code to detect the signal with information corresponding only to the desired user by rejecting other users (having other codes) and noises (multiplicative, additive, and due to interference) that exist in the communication channel. In cellular communications, there is another access called space division multiple accesses (SDMA), which is usually used by a division of each cell in sectors using directed antennas to serve each user located in the corresponding sector. The latest form of SDMA usually employs adaptive antenna arrays based on digital beamforming technology [19,24–31]. Here, we will consider the applications of adaptive antennas in different networks on the basis of these four types of multiple access communication [91–96]. Let us first start with the applications of adaptive antenna in terrestrial communications.

9.3.1. Adaptive Antennas for Outdoor Wireless Communications

The important aim in using adaptive antenna arrays is to reject the multiplicative noise caused by multipath fading, slow or fast, to decrease the time-delay effect occurred because of the multipath phenomena, and finally to eliminate the co-channel interference that occurs between subscribers allocated in the same frequency band (in CDMA) or that share the same time frame [75]. To overcome
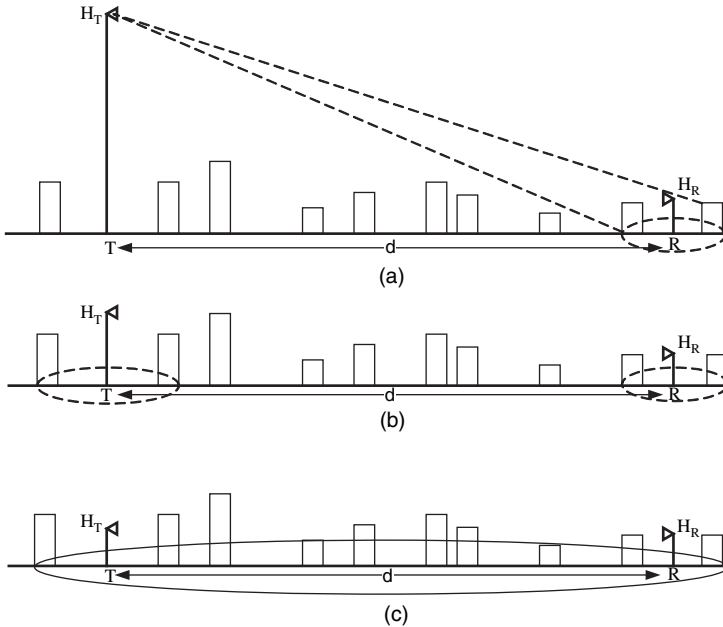
FIGURE 9.22. Three typical antenna positions with respect to rooftops level.

these impairments, an array technology consisting of multiple input and multiple output (MIMO) channel is usually used (see Fig. 9.1). Using M antenna elements, a significant increase of antenna gain is achieved plus a diversity gain against multipath fading, which depends on the correlation of the fading among the antenna elements. To provide a low correlation (i.e., diversity gain) between elements, there are several basic ways that can be considered: *spatial*, *polarization*, *time*, *frequency*, and *angle diversity* [23,75].

For spatial diversity, the antenna elements are separated far enough for low fading correlation among them. The required separation depends on the obstructions surrounding the antenna such as buildings, trees, hills, and so on. There are three typical situations in the urban environment scene: when the base station (BS) antenna is higher than the overlay profile of the buildings (Fig. 9.22a); the BS antenna is at the same level as the height of the buildings (Fig. 9.22b); and when the BS antenna is lower than the overlay profile of the buildings (Fig. 9.22c). Depending on the number of obstructions (scatterers) surrounding the terminal antennas, the angle-of-arrival of the total signal at the receiver will spread dramatically. Thus, for the BS antenna sketched in Figure 9.22a, when only few obstructions surround the user antenna, the angular spread may be only few degrees [75], whereas for the situation in urban areas sketched in Figure 9.22b, the angular spread can exceed ten and more degrees. In these situations, a horizontal separation of antenna elements of 10–20 wavelengths is required. In the third situation shown in Figure 9.22c, the angular spread can reach up to $360°$ and the antenna element spacing only of a
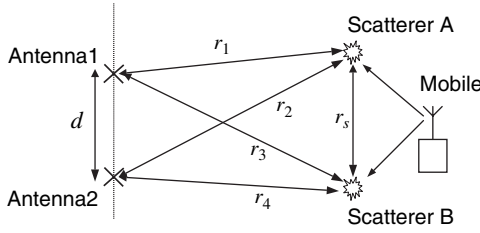
FIGURE 9.23. Spatial diversity estimation.

quarter wavelength is sufficient (these phenomena will be considered more in detail in the next chapter).

A simpler way to obtain spatial diversity is to use two antennas separated by a distance d in space, as shown in Figure 9.23 [94]. The multipath fading is due to waves from two scatterers, A and B, separated by distance r_s, which is much smaller than the distance between antennas and the scatterers, so both antennas view the scatterer from the same direction. In such assumptions, we can present the phase difference between waves incident on the antennas in the following form: $\phi = -kd\sin\theta$.

Figure 9.24 shows the path from a single scatterer at an angle θ to the broadside direction in the horizontal plane (for the horizontal antenna spacing). Assuming now that the amplitude after scattering is the same for both antennas, we get [94]

$$s_1 = a\cdot e^{j2\pi ft} \quad\text{and}\quad s_2 = a\cdot e^{j(2\pi ft+\phi)} \tag{9.36}$$

For the large number of scatterers N, these expressions can be generalized as

$$s_1 = \sum_{i=1}^{N} a_i\, e^{j2\pi ft} \quad\text{and}\quad s_2 = \sum_{i=1}^{N} a_i\, e^{j(2\pi ft+\phi_i)} \tag{9.37}$$
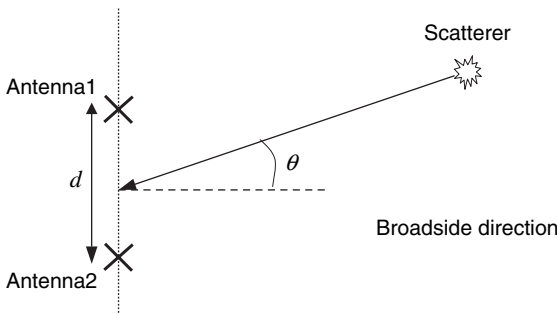
FIGURE 9.24. A single scatterer for the antenna elements separated by a distance d.

where a_i are the amplitudes associated with each of the scatterers. The correlation between these two signals, assuming that amplitudes from each of the scatterers are uncorrelated, is given by

$$\rho_{12}(d) = \int_0^{2\pi} p(\theta)\, e^{jkd\sin\theta} d\theta \tag{9.38}$$

where $p(\theta)$ is the PDF function of the random variable θ. This expression can be used for a wide range of situations, provided a reasonable distribution for $p(\theta)$ can be found. Note that (9.38) is a Fourier transform relationship between $p(\theta)$ and $\rho_{12}(d)$. So, there is an inverse relationship between the widths of these two functions: A narrow angular distribution after multiple scattering will produce a slow decrease in the correlation with antenna spacing, which finally will limit the usefulness of space diversity. Conversely, an environment with significant scatterers, around the antenna with a wide angular distribution, will produce a decrease in the correlation with antenna element spacing. In this situation, if d goes to zero, the correlation between the antenna elements will be higher. In many cases of *mobile-to-mobile* (*MO-MO*) communication (Fig. 9.22c), the angular distribution of the signal after multiple scattering from obstructions can be described by a uniform PDF over $[0, 2\pi]$ with $p(\theta) = 1/2\pi$. In this case from (9.38) we get, according to Reference [94], a solution in terms of the modified Bessel function of zero order

$$\rho(d) = J_0\left(\frac{2\pi d}{\lambda}\right) \tag{9.39}$$

From Figure 9.22, for the *base-station-to-mobile* (*BS-MO*) communication, the angular distribution of scattering at the base station may be very different from that of the low mobile antenna. In the case of Figures 9.22a and 9.22b, with scatterers present at distance r from the base station on a ring centered around the mobile station with radius, we use instead of (9.39), the following expression [96]

$$\rho(d) = J_0\left(\frac{2\pi d}{\lambda}\frac{r_s}{r}\cos\theta\right) J_0\left(\frac{\pi d}{\lambda}\left(\frac{r_s}{r}\right)^2 \sqrt{1 - \frac{3}{4}\sin^2\theta}\right) \tag{9.40}$$

where θ is the scattering angle directed from the base station to the ring of scatterers.

Comparison between (9.39) obtained for the case of MO-MO communications and (9.40) obtained for the case of BS-MO communications shows that in the second case the spacing d between antenna elements required is much greater than that in the mobile to mobile case.

If a more compact antenna structure is used (i.e., small spacing between elements), the vertical space diversity becomes essential, as two neighboring antenna elements can be packaged together into a single vertical structure. Now, if we assume that all waves after scattering arrive at the horizontal plane, we have $p(\theta) = \delta(\theta)$, that is, the Delta-function angular spread distribution. In this case, the

signals will be perfectly correlated for all separations between antenna elements. However, in more realistic conditions where waves arrive with some moderate spreading relative to the horizontal plane, the angular spread PDF can be presented according to Reference [97] as

$$
\rho(d) = \begin{cases} \dfrac{\pi}{4|\theta_m|} \cos \dfrac{\pi\theta}{2\theta_m}, & |\theta| \leq |\theta_m| \leq \dfrac{\pi}{2} \\ 0, & elsewhere \end{cases}
\tag{9.41}
$$

where θ_m is half of the vertical angular spread.

We notice that expression (9.40) gives more conservative correlation values with respect to (9.41), as it does not include the vertical spreading of the angle-of-arrival. This is essential when we want to calculate the effect of vertical antenna element spacing, which nevertheless requires even larger spacing than the horizontal case [98].

Despite the required large spacing of antenna elements, horizontal space diversity is very commonly applied in cellular base stations to allow compensation for the low transmit power obtained from handheld portables compared to the base stations. Vertical spacing is rarely used [23,91–93,96–98]. This is because of the large spacing required to obtain low cross-correlation and because the different heights of the antennas within an array can lead to significant differences in path loss for each antenna, which degrades the diversity effect. The example shown in Figure 9.22a is more related to macrocell environments that have very narrow angular spread, whereas those in Figures 9.22b and 9.22c are related to microcell environments, where the angular spread is larger.

For polarization diversity, both horizontal and vertical polarization is used. These orthogonal polarizations have low correlation, and the antenna elements can have small spacing, creating a small profile for the total antenna. This effect has been found experimentally in Reference [99] and it was shown that these two components are almost uncorrelated, so, a pair of cross-polarized antennas can provide diversity with no spacing between them. However, polarization diversity only doubles the diversity of any antenna, and for high base station antennas, the horizontal polarization can be 6–10 dB weaker than the vertical polarization, which reduces the diversity gain [78]. Under the assumption that the vertical and horizontal components of the signal field are independently Rayleigh-distributed (i.e., we now consider the Rayleigh fading communication channel), the correlation coefficient can be presented in the following form [99]:

$$
\rho = \frac{\tan^2 \alpha \cos^2 \beta - \Gamma}{\tan^2 \alpha \cos^2 \beta + \Gamma}
\tag{9.42}
$$

where the cross-polar ratio Γ is defined as the ratio between the mean powers from the horizontally, E_H, and vertically, E_V, polarized signal strengths

$$
\Gamma = \frac{\langle |E_H|^2 \rangle}{\langle |E_V|^2 \rangle}
\tag{9.43}
$$

Here, the fields are received by antennas inclined at an angle α with respect to the vertical axis, and the mobile is situated at an angle β with respect to the antenna bore sight.

In References [100,101], a new method to improve the performance of polarization diversity was proposed by using a mixed scheme where the antenna array elements were used simultaneously for both spatial and polarization diversity. In this case the multiplicative correlation coefficient is approximately a product

$$\rho \approx \rho(\alpha) \cdot \rho(d, h) \tag{9.44}$$

Equation (9.44) describes the pure polarization diversity with co-located antenna elements polarized at an angle α with respect to the vertical axis, $\rho(\alpha)$, and the correlation described for co-polarized antenna elements having a horizontal spacing d and vertical spacing h, $\rho(d, h)$. The correlation coefficient obtained from (9.44) can therefore be smaller than that obtained from polarization diversity or spatial diversity alone.

Time diversity can be obtained by transmitting the same signal multiple times, spaced apart in time sufficiently that the channel fading will be not correlated. From (9.39) we have the same result that can be produced by the autocorrelation function of the fading signal at a single antenna between two moments in time when the mobile antenna is in motion. This is, except with the time delay, introduced by the antenna motion reinterpreted as a horizontal antenna spacing by putting the time delay as $\tau = d/v$, where d is the antenna spacing, and v is the mobile velocity. However, the time diversity is rarely used in practice of wireless communications as the retransmission of information reduces the system capacity and introduces a transmission delay. Usually, this principle is applied to improve efficiency in coded modulation schemes, which apply interleaving to spread errors across fades, allowing better potential for error correction [23,75].

In wideband channels, *frequency diversity* is used when two frequency components spaced wider than the coherent bandwidth experience uncorrelated fading. As in time diversity, the simple retransmission of information on two frequencies is not so efficient. Usually, the principle of frequency diversity is implicitly employed in some forms of equalizers [23,75].

For *angle diversity*, adjacent narrow beams are used. The total antenna profile is small, and the adjacent beams could have received signal levels more than 10 dB weaker than the strongest beam, resulting in small diversity gain [75].

Due to low fading correlation among antenna elements, diversity gain is typically achieved in current *base stations* by using either *selection diversity*, where selection of the antenna element (sensor) with the highest signal power is made, or *maximal radio combining*, where the procedure of beamforming (weighting and combining the received signal to maximize the SNR) is performed. This provides additional gain on the *uplink* (or *reverse link*, from mobile antenna to base station) to compensate for the higher transmit power of the base station on the *downlink* (or *direct link*, from base station to mobile antenna). Typically, only a single transmiter and receiver antenna is used on the downlink.

The *formation of multiple beams* by multiple antennas at the base station is performed to cover the whole cell size. For instance, three beams with bandwidth of $120°$ each or six beams with a bandwidth of $60°$ each may be formed for the multiple beam pattern creation. Then, each beam is treated as a separate cell (as is done in the process of splitting cells on sectors, see References [91–95]), and the frequency assignment to each user may be performed in a usual manner. Mobile users are handed to the next beam (sector) as they leave the area covered by the current beam, as is done in a normal handoff process when users cross the cell boundary [91–95].

Such multiple beams can be created by the so-called switched-beam system (SBS) [13] consisting of: a beamformer, which forms the multiple nonadaptive beams; a sniffer, which determines the beam that has the best signal-to-interference-noise ratio (SINR); and a switch, which is used to select the best one or two beams for the receiver. The main advantage of SBS is the improvement in cell radio coverage on the reverse link due to the array gain and improved voice quality due to reduced interference between users who occupy the same segments in frequency or time domains. As the performed beams are narrower than the regular sector beamwidth, reduction of the interference power is obtained when the desired signal and the interfered signals are separated in angle and fall into different beams. This SINR improvement offers better information quality (digital or voice) and therefore improves capacity of data stream and spectrum efficiency of the network (see Chapter 12).

The performance of SBS depends on a number of factors, including angle-of-arrival and time delay spreading (see Chapters 10 and 13) caused by multipath fading, interference, and the antenna array topology. Performance gain in SBS comes from array gain, diversity gain, reduced interference, and trunking efficiency [13]. The array gain is given by M (in dB) or by $10\log M$, where M is a number of input antenna elements (see Fig. 9.2). The element spacing determines the degree of decorrelation of the signal across the antenna array. Therefore, for a $\lambda/2$-spacing in an M-element antenna, the diversity gain of 5 dB is preserved for the land macrocells (with radius more than 2–3 km) [91–95]. There are other system loss factors, which must be accounted, such as cusping loss, mismatch loss, beam-selection loss, and path diversity loss [13]. Cusping loss occurs because of the 2 to 3 dB cusp between beams. Mismatch loss refers to the use of planar beamforming in the presence of potentially nonplanar wavefronts due to local scatterers surrounding the antenna array. Beam-selection loss occurs in the presence of interference when, during signal fades, another beam containing mainly interference may be selected for processing at the receiver.

The formation of *adaptive beams* is based on adaptive beamforming, which forms independent (uncorrelated) beams at the base station. The array is used to find the location of each user, stationary or mobile, and then beams are formed to cover different groups of subscribers. As above, each beam can be considered as a co-channel cell, and thus may be able to use the same frequency, time or code, as the case may be arranged. A typical setup involving different beams covering different moving or stationary users is shown in Figure 9.25.
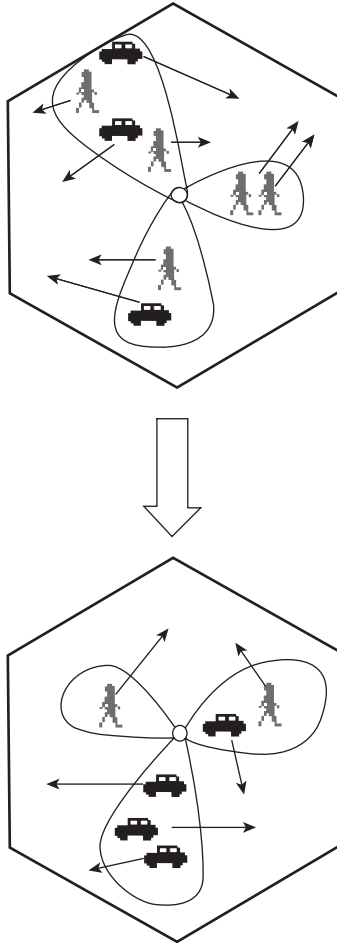
FIGURE 9.25. Typical setup for a cell of service.

In Figure 9.26a, a fixed number of beams with a fixed shape cover the whole cell, whereas in Figure 9.26b, the beams are shaped to cover the traffic following any changes that may occur in traffic conditions. As the users move, the different beams cover different clusters of users, offering the benefit of transmission of energy towards the desired users. Each mobile may be covered by a separate beam if the number of elements is large enough. Using a beam to follow the desired mobile, one can reduce the handoff problem [103,105].

Now, let us examine the gain of the array in different urban conditions as sketched in Figure 9.22. In the first case, one of the antennas (usually, the base station antenna) is located above the rooftops (Fig. 9.22a). In this case, only obstructions located in the vicinity of the mobile vehicle must be taken into account. Let the gain of the M-element array at the base station be G_1, and the gain of the N-element array
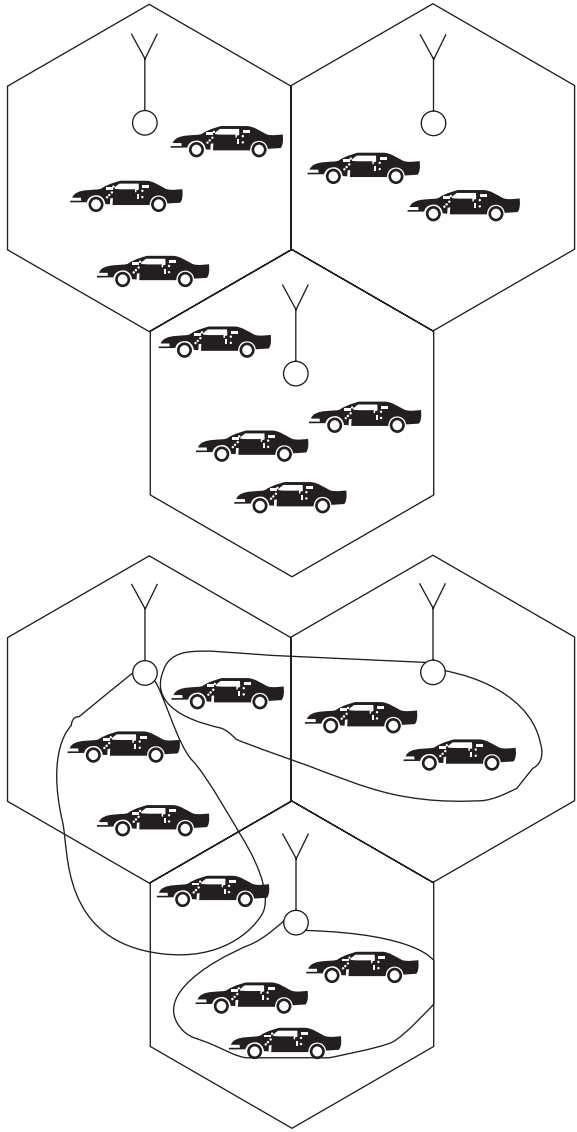
FIGURE 9.26. Using an adaptive antenna in cellular networks.

antenna at the mobile be G_2. Then, the link gain G_L, is given by $G_L = MN$, with a diversity gain order of MN [106–108]. From a range extension point of view the situation is close to the LOS conditions.

In the second case, when the base station antenna is near the rooftop of the buildings (Fig. 9.22b), scattering is observed around both terminal antennas. In this case, the two clusters of scatterers are widely spaced, so that they look like ''point

sources." This means that each antenna plus its immediate surrounding can be accounted as one effective antenna, and these two effective antennas are in the far field of each other. In this assumption $G_L = MN$ with a diversity order of NM [106–108]. In a MIMO connection (see Fig. 9.1) this is called a keyhole situation, as there is only one channel.

In the third case, both the terminal antennas are below the rooftop of the buildings (Fig. 9.22c). In this case, both the antennas are not independent and to obtain the weight parameters of the two antennas is a very complicated analytical problem. According to References [106–108], the asymptotic result for large values of M and N gives $G_L = (\sqrt{M} + \sqrt{N})^2$ with a diversity order of MN. If N is small and M is large, the gain approaches M. Even in this worst-case scenario we can increase the accuracy of multi-user detection and service because the gain for the desired user will be close to M (for $M \gg N$), but all other users will, on average, have a gain of unity. If M is sufficiently high, this will give a good protection against multi-user interference in multiple access performance, namely, for *SDMA*.

Problems with Using Adaptive Antennas for Outdoor Communication. Unfortunately, by using directive antennas or adaptive antennas we cannot cancel the effects of environment, mostly in urban areas, where even from the beginning the narrow antenna beam significantly spreads in the azimuth and elevation domains after passing through a couple of building rows, as it is shown in Figure 9.27. This means that the multipath component (i.e., the incoherent part of the total signal spectrum) prevails over the coherent part. Finally, in the azimuth domain we have a wide spread of signal power distribution instead of a narrow one (see the right side of Fig. 9.27).
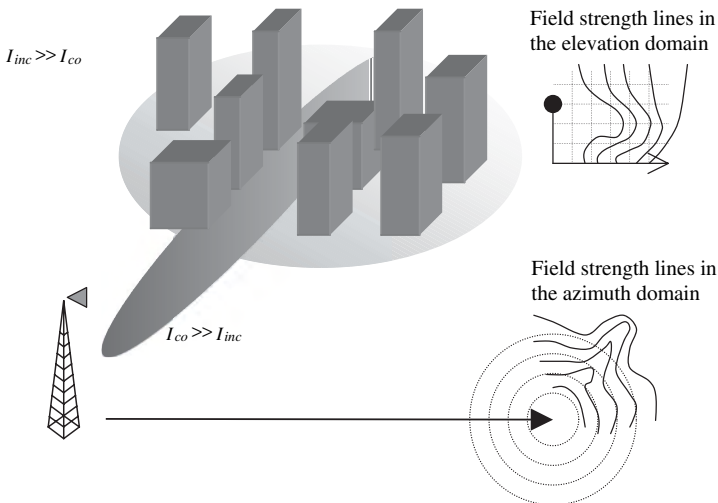
FIGURE 9.27. Effect of built-up area on a narrow-beam adaptive antenna pattern.
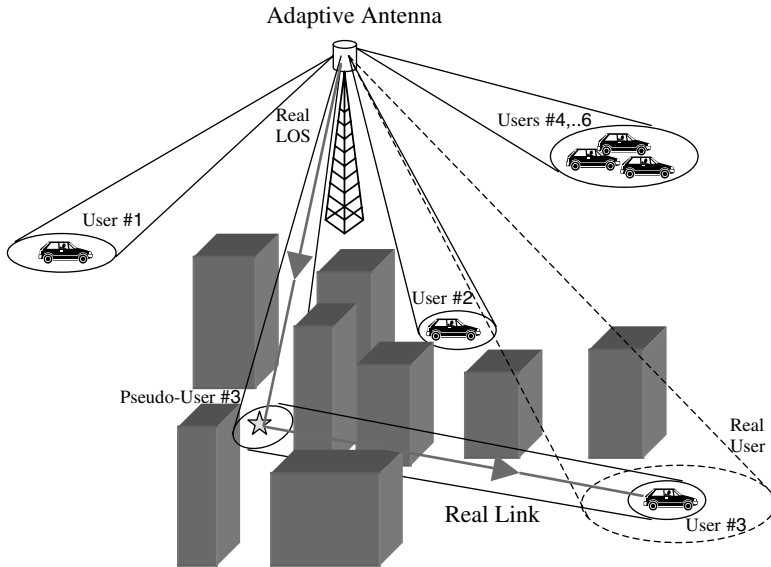
FIGURE 9.28. Street ''masking'' effect for servicing user #3 by an adaptive antenna.

In a typical urban case, the guiding effect along the streets is predominant and the desired signal will arrive to the base station antenna from directions different from the line-of-sight (LOS) direction shown in Figure 9.28 for user #3. We will discuss ways to resolve this and many other problems in land communication channels by using smart antennas in Chapters 10 and 13.

9.3.2. Adaptive Antennas for Indoor Wireless Communications

There are some differences between the outdoor land-mobile and land-stationary systems and indoor systems. In indoor communications, users are usually moving on foot and use hand-held portables. This results in different fading rates (negligible Doppler shift, and fading does not depend strongly on frequency, see Chapter 1). The fading rate for the indoor network is much slower than that for the outdoor network (called *flat fading*), implying that optimal combining could be implemented with the use of adaptive techniques [109–111]. The angle-spread problem in the two cases is different as well. Thus, the angular spread of signal arrival at the receiving antenna for base station antennas in indoor systems is typically isotropic 360° [112,113]. The problem of delay spread is also different for the two cases [114–116]. For land outdoor communication channels, the signals generally arrive in delayed clusters due to multiple reflections and multiple diffractions from large obstructions such as hills, trees, and buildings. For indoor communications, there exist a large number of local small obstructions inside a building, which scatter and reflect rays, creating a multipath fading at the receiver. This causes the impulse response of the indoor radio channel to appear like a series of pulses [111]. The use of adaptive antennas to
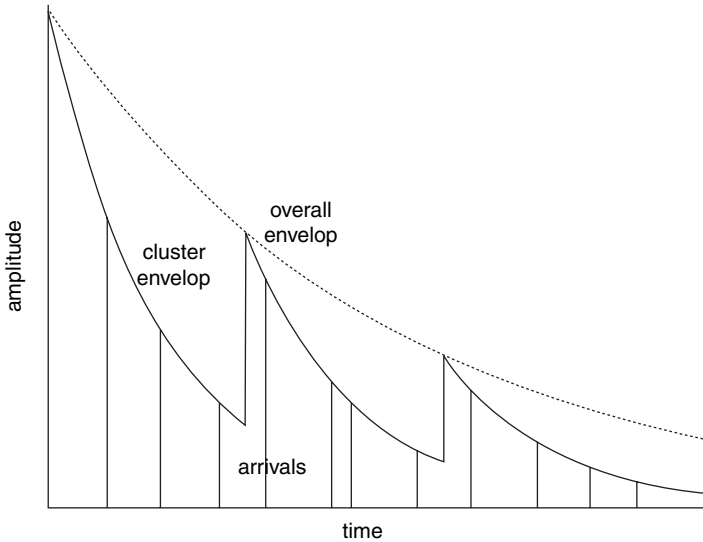
FIGURE 9.29. Cluster effect in time domain obtained in indoor communication channels according to [117].

improve such channels is discussed in References [114,115]. The theoretical basis for the angle-of-arrival and delay spread signal distribution, observed experimentally [113,115], is given in References [116,117]. It was shown both experimentally and theoretically that the arrivals come in one or two large groups within a 200 ns observation window, where in each cluster an additional attenuation is observed (see Fig. 9.29 according to Reference [117]). Within each cluster the arrivals are also delayed with time. In Figure 9.29, a mean envelope of a channel of three clusters is shown. The time-of-arrival distribution corresponds to different Poisson processes [113–117].

The first process describes the arrival time of clusters defined by the cluster arrival decay time constant Γ (which varies from 30 to 80 ns) and by the cluster arrival rate A (where 1/A is changed from 16 to 300 ns) [116,117]

$$p(T_i|T_{i-1}) = A\,e^{-A(T_i - T_{i-1})} \tag{9.45a}$$

where T_i describes the first arrival of each cluster with number i.

The second Poisson process models the arrival time of rays within each cluster defined by the ray arrival decay time constant γ (which varies from 20 to 80 ns) and by the ray arrival rate α (where 1/α is changed from 5 to 7 ns)

$$p(\tau_{ij}|\tau_{(i-1)j}) = \alpha\,e^{-\alpha(T_{ij} - T_{(i-1)j})} \tag{9.45b}$$

τ_{ij} is the inter-ray arrival time, dependent on the time of the first arrival in the cluster.

At the same time, the angles-of-arrival, θ, distribution is better fitted by a zero-mean Laplacian process [116,117]

$$p(\theta) = \frac{1}{\sqrt{2}\sigma} e^{-\left|\frac{\sqrt{2}\theta}{\sigma}\right|} \qquad (9.46)$$

As was shown in [116,117], Equation (9.46) is valid only for low elevation antennas, with the standard deviation varying from $\sigma = 21.5°$ to $\sigma = 25.5°$. In Chapter 10 we present a detailed analysis of angle-of-arrival and time delay distributions both in outdoor and indoor communication channels.

9.3.3. Adaptive Antennas for Satellite-Mobile Communications

Let us now consider the use of adaptive antenna arrays in satellite communications. In such systems, the mobiles directly communicate with the satellite. In the direct communication link, multiple antenna elements may be utilized on the mobile as well as on a satellite.

Array on a Satellite. It can be assembled on board of a satellite and can provide communication in a number of ways. For instance, different frequencies may be allocated to beams covering different areas such that each area acts as a cell (called in literature *megacell* [23,94], see also Chapter 14). This allows frequency reuse similar to land communication cellular networks [23,91,92,94]. However, there is a difference between the two systems: the mobile-satellite system generates beams covering different cells rather than having different base stations for different cells as it was done in land communication systems. The antenna array system mounted on board of the satellite provides beam generation, which can be done using different possible scenarios.

A simple method is to utilize beams of fixed shape and size to cover the area of service, allowing normal handoff as the mobile pass from one cell to another or as the beams move in low-orbit satellites covering different areas (see details in Reference [118]). In various European Space Agency (ESA) projects for the European geostationary satellite systems, the frequency scanning systems have been combined with phased array antennas [35,118] assembled in a feed network to control the beam coverage area. A typical system consists of a high-gain large reflector antenna, along with an array of feed elements, placed in the focal plane of the reflector in a particular geometry to generate a limited number of fixed-shape spot beams. A particular beam is selected by choosing a combination of feed elements. The steering of beams is achieved by controlling the phases of signals prior to the feed elements. The capability of the system to generate multiple spot beams with independent power control and frequency use makes it attractive for mobile communications. The frequency scanning system considered in References [35,118] uses an array of active antennas to provide a high-gain beam with the capability to steer it at any user location using frequency-dependent inter-element phase shift. The same array is used for the transmitting as well as for the receiving
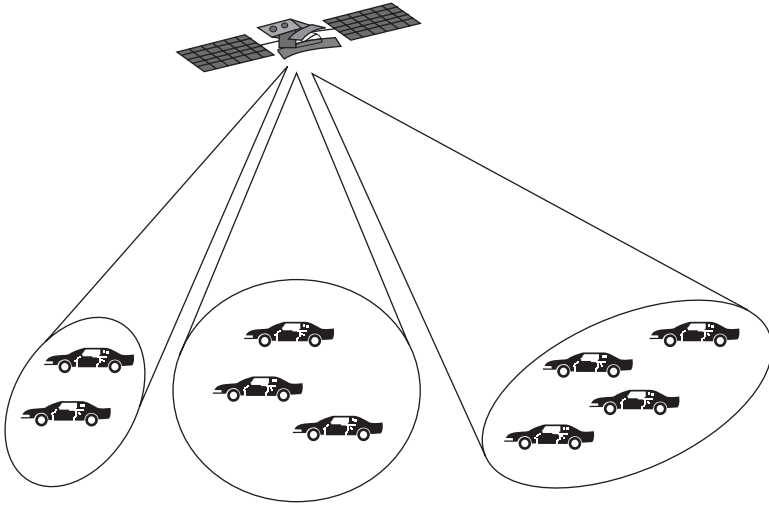
FIGURE 9.30. Coverage of different service areas using satellite antenna beams.

modes. The frequency scanning system operates as a conventional multispot system in terms of capacity and required power per channel, but requires a complex beamforming network and mobile terminal location procedure. Such a system, which uses fixed-shape beams, does not require any knowledge of the traffic conditions.

In contrast, a system generating spot beams of varying shapes and sizes (called *dynamic beams*) depends on the traffic conditions dictated by the positions of mobiles, as shown in Figure 9.30.

To generate an arbitrarily shaped beam to be pointed at a desired location, the system architecture requires an advanced beamforming network with independent beam-steering capability [39]. These systems have been implemented in recent system developments including the GLOBALSTAR [119] and IRIDIUM [120] systems (see also chapter 14).

Separate Beams for Each Mobile. The possibility of using separate beams for each mobile was investigated in Reference [37]. A satellite acts as a relay station between mobiles and the base station, with communication between the base station and the satellite being at a different frequency than that between mobiles and the satellite. Service in such a manner allows each mobile to be tracked and the beam is pointed towards the desired mobile, with nulls in the directions to other mobiles operating at the same frequency. Different frequencies are used to communicate with the mobiles in close vicinity to the desired one. So, this system is similar to CDMA and TDMA operational systems [91–96]. We note that the direction-finding and beamforming algorithms in this case operate in an environment different than those operating for the land BS-MO communication systems. Because of the distance involved between the satellite and the mobiles, the signals arriving from the mobiles

appear more like point sources, which is not the case for the signals arriving at the base station in land communication because of the spreading of signals caused by reflections and scattering in the vicinity of mobiles.

Arrays on Mobile. When an array of antennas is mounted on a mobile to communicate directly with a satellite, the beam steering toward the satellite can be performed using simple phase shifters [121]. As the direction of the satellite with respect to the mobile varies, tracking of the satellite and adjusting of the direction of the beam is required so that the main beam points towards the satellite.

In the German TV-SAT 2 system [36], which uses multiple antennas, electronic steering was not utilized. Instead, it employs four sets of fixed beams, formed separately and switched on depending on the orientation of the mobile relative to the geostationary satellite used. The system was shown to be useful for large vehicles, such as buses and trains. At the same time, separate array elements are suggested in Reference [122] which alternately placed side by side in a planar configuration for transmit and receive mode using digital beamforming techniques for tracking two satellites in multi-satellite system base on low-orbit satellites.

Test results on the characteristics and the suitability of a spherical antenna array mounted on an aircraft employing digital beamforming to communicate directly with a satellite were reported in Reference [123]. An experimental development of a four-element antenna array to receive signal from the INMARSAT II F-4 geostationary satellite with a fixed position receiver show that a significant improvement in link reliability can be produced using an adaptive array at a handheld mobile compared to omni-antenna [124].

9.4. NETWORK PERFORMANCE IMPROVEMENT USING AN ANTENNA ARRAY

An antenna array is able to improve the performance of wireless communication systems by providing the capability to reduce co-channel interferences, multipath fading, and delay spread, and therefore, results in a better quality of services (QOS), such as reduced bit-error rate (BER) and outage probability. Furthermore, its capability to form multiple beams that can be exploited to serve many users in parallel, results in an increased spectral efficiency of the system. The possibility also exists to handle traffic conditions by adapting beam shapes and reducing the handoff rate, which results in increased trunking efficiency. A number of studies have been reported in the literature covering all these aspects [125–150]. Some of them are briefly mentioned in this section.

9.4.1. Reduction in Multipath Phenomena

A key issue for adaptive array antennas in wireless communication systems is their performance in multipath versus line-of-sight (LOS) environments. First of all, let us consider what happens when adaptive arrays are operating in LOS conditions. As

shown in Section 9.2, in a LOS channel an adaptive array can be used to enhance signal reception in a desired direction and to place nulls in the direction of interference. Under these conditions, with the number of antennas much greater than a number of arriving signal multipath components (usually called *rays*), it is easy to express the array response in terms of a small number of angles-of-arrival, rather than the received signal phase at each antenna element. Techniques that exploit this fact for improved performance include the MUSIC and ESPRIT algorithms [125], which determine the direction-of-arrival (DOA) of the rays. Thus, such an array of M elements (called in technical literature *sensors*) can form up to $M - 1$ nulls to cancel up to $M - 1$ interferers caused by multipath components arriving at the receiver. As was shown in Reference [126], such angular domain methods can be also useful in some situations with near-LOS, such as at mobile radio base stations in flat rural environments with many (in Reference [126] it was eight) high elevated antennas.

However, in *clutter conditions* with multipath, the signals arrive from each user via multiple paths and angles-of-arrival due to multiple scattering, reflection and diffraction phenomena. Thus, it becomes impossible to form an antenna pattern with a beam in the direction of each arriving path of the desired signal and nulls in the directions of all interfering signals, as the number of required nulls would be much greater than the number of antenna elements. Furthermore, to provide diversity gain, the elements at the base station can be spaced many wavelengths apart, which results in many grating lobes (as shown in Fig. 9.12). However, no matter how many paths each signal covers, the result is a given phase and amplitude at each antenna for each signal. Thus, there is an array response for each signal, and the performance of the array depends on the number of signals, not the number of paths, so one can do the analysis in the signal space domain rather than the angular domain. This holds true as long as the delay spread is small. If not, then the delayed versions of the signals must be considered as separate signals. Hence, an adaptive array can null $M - 1$ interferes due to multipath independent of the environment, it is either LOS or clutter with multipath. It was also mentioned in Reference [38] that an important feature of adaptive arrays in multipath conditions is their ability to cancel interferers independent of the angle-of-arrival (AOA). Thus, it is not sufficient if the interferer is a few meters from the desired mobile or at several kilometers from the base station. In LOS conditions, the separation of such closely spaced signals is not possible. In a multipath environment, obstructions around antennas act as a huge reflection antenna, with the actual antennas acting as feeds, which permit the receiving array to separate the signals. If the receiving antennas are spaced far enough apart such that beams that are smaller than the angular spread can be formed, then the signals from two closely spaced antennas can usually be separated using adaptive combining techniques. They are the combination of spatial diversity of the array and channel coding [128–130], using a combined mode of diversity combining with interference canceling [131,132] or using the same diversity combining with adaptive equalization [133–136]. As was shown experimentally in Reference [127], the number of signals that can be separated increases with the number of receive antennas of the array. The same features were observed for the angular spread and for the density of the multipath reflections within the angular spread.

9.4.2. Reduction in Delay Spread

As mentioned in Chapter 1, delay spread is caused by multipath propagation due to multiple scattering, diffraction, and reflection from obstructions surrounding the transmitter and the receiver. In this case, the desired signal arriving from different directions gets delayed due to different travel radio paths involved. An antenna array with the capability to form beams and nulls in certain directions is able to cancel some of these delayed arrivals. There are two ways to achieve this:

a) the *first way* occurs in the transmit mode when an antenna array focuses energy in the required direction, and finally reduces multipath components causing a reduction in the delay spread;

b) the *second way* occurs in the receive mode when an antenna array provides compensation in multipath fading by (1) diversity combining, (2) adding the signals belonging to different clusters of signals after compensating for delays, and (3) canceling delayed signals arriving from directions other than that of the main signal.

Let us briefly present some of these techniques [102,114,141,144–156].

Use of Diversity Combining. Diversity combining achieves a reduction in fading by increasing the signal level based upon the level of signal strength at different antennas [102,139,141], whereas in multipath cancellation methods, it is achieved by adjusting the beam pattern to accommodate nulls in the direction of late arrivals assumed to be interferences. For the latter case, a beam is pointed in the direction of the direct path or a path along which a major component of the signal arrives, causing a reduction in the energy received from other directions and thus reducing the components of multipath signal coming at the receiver. Techniques on how to identify a LOS component from a group of received multipath signals have been discussed in Reference [142].

Combining Delayed Arrivals. This technique is based on the organization of clusters of signals identically delayed within each cluster. This occurs because a radio wave originating from a source arrives at a distinct point in clusters after getting scattered and reflected from obstructions along the radio path. This occurs in the urban scene with large buildings or hills where delayed arrivals are well separated [143], as well as in indoor communications [116,117]. We can use these clustered signals constructively by grouping them as per their delays compared to a signal available from the shortest path. Individual paths of these delayed signals may be resolved by exploiting their spatial or temporal structure (as shown in Fig. 9.26 in the time domain).

The resolution of paths using temporal structures depends upon the bandwidth of the signal compared to the coherence bandwidth of the channel, and it increases as this bandwidth increases. In a CDMA system, the paths may be resolved provided their relative delays are more than the chip period [144–147]. When these paths are

well separated spatially, an antenna array may be used. This can be done, for example, by determining their directions. Spatial diversity combining similar to that used in RAKE, a receiver, (see details in Reference [148]) may also be employed to combine signals arriving in multipath.

The signals in each cluster may be separated by using specific information present in each signal, such as the frame identification number or the use of a known symbol in each frame utilized in a TDMA system (see details in Reference [149]).

Nulling Delayed Arrivals.   It was found that by using an adaptive antenna array, an essential reduction in delay spread is possible. Similar conclusions were obtained in Reference [150] using an experimental array of four elements mounted on a vehicle. It was shown that the array with the corresponding processing is able to null the delayed arrival in a time-division multiplexed channel. In channels where frequency-selective fading occurs, that is where signals with different frequencies fade differently, a frequency-hopping (FH) system may also be used for eliminating degradation of signals due to fading. For information about differences between direct-sequence spread spectrum (DS-SS) systems and frequency-hopping systems, the reader is referred to References [23,91–94]. Applications of adaptive arrays in FH-communication systems are described in References [151–154] and for DS-SS-communication system the reader can check References [155,156].

9.4.3. Reduction in Angular Spread

Angular spreading occurs when a transmitted signal gets scattered or reflected in the vicinity of the source and the receiver and a signal arrives at the receiver within range of angles. This range, called an *angular spread*, depends on the situation in the environment and on the antenna locations with respect to building rooftops. Thus, the conditions of land macrocell base-station-mobile (BS-MO) communication are close to that shown in Figure 9.22a, where the base station antenna is normally high enough from the ground surface and the mobile antenna is close to the ground. In this case, the angular spread occurs only in the vicinity of the mobile. Here, a signal arrives at the base station with an angular distribution depending on the range from the two terminals and the density of obstructions surrounding the mobile antenna. Thus, the range of angle spreading becomes smaller as the distance between the mobile and the base station increases. Experimental results indicate that the angular spreading of about $3°$ results for a distance of 1 km between terminals [157]. In Reference [158], it was shown that the angle-of-arrival (AOA) distribution of the signal is statistically related to the path delay spread. Angular spread causes space-selective fading, which means that the signal amplitude depends on the spatial location of the antenna. Space-selective fading is characterized by the coherence distance [23,91–94]; the larger the angular spread, the shorter the coherence distance. The latter represents the maximum spatial separation for which the channel responses at two antennas remain strongly correlated. Selection of the distribution function, however, does not appear to be critical as long as the spread is small around the main direction [157–161].

For the cases shown in Figures 9.22b and 9.22c, which usually occur in microcell environments for BS-MO-communications or for MO-MO-communications, the angular spread may become wide enough (up to 45°–60°) to decrease the efficiency of the adaptive antenna. Thus, a dispersion of the radio environment results in the distortion of the antenna side-lobe levels at the base station [162], as well as in an increase in the correlation of fading at different antenna elements of the array [132].

The problem of fading correlations is studied in Reference [163]. It was shown that by deriving the relationships between AOA, beamwidth, and correlation of fading, larger element spacing is required to reduce the correlation, especially when the AOA is parallel to the array. A correlation coefficient of fading, between the various antenna elements, greater than 0.8 can cause signals at all elements to fade away simultaneously [164]. A detailed investigation of the effect of fading correlation on the performance of the adaptive arrays to combat fading was done in Reference [132]. It was shown that a correlation up to 0.5 causes little degradation of the antenna efficiency, but a higher correlation decreases its performance significantly. However, the array is able to suppress interferences as independent fading is not required for interference suppression [132]. The aspect of AOA distribution as well as delay spread distribution for different land communication links will be analyzed in detail in the Chapters 10 and 13.

9.4.4. Range Increase

In typical land macrocell communication links with high base station antenna and low mobile antenna (see Figs. 9.22a and 9.22b), when angular spread is small enough, a MIMO system consisting of M and N-element antenna arrays at both ends of the link gives a link gain of $G_L = MN$ with a diversity gain equal *to NM* (see Section 9.3). It means that both the physical M-element adaptive array and a multibeam (phased array) antenna provide an MN-fold increase in antenna gain. Even if only one antenna (either base station or mobile) is in the form of an array with M elements, the increase will be in $G_L = M$ times. In the case of low elevation antennas shown in Figure 9.22c, the link gain is $G_L = (\sqrt{M} + \sqrt{N})^2$ with a diversity gain of NM. If N is small and M is large, the gain will approach M.

This capability of adaptive or multibeam antennas to increase the range of a communication link by the factor $G_L^{1/\gamma}$ is used to reduce the number of base stations required to cover a given area by a factor of $G_L^{2/\gamma}$, where γ is the propagation-loss exponent. From Chapter 5, γ is set to be somewhere between 2 and 5. The physical adaptive array antenna also provides diversity gain, and for a given array size with spatial diversity, the diversity gain increases with angular spread and the fading correlation decreases, thus providing a greater range for the radio link. For the multibeam (phased array) antenna, however, the diversity gain is limited, as angular diversity provides only a small diversity gain. Another disadvantage of the multibeam antenna is that the antenna gain is limited by the angular spread. That is, the antenna cannot provide additional antenna gain when the beamwidth is less than the angular spread because smaller beamwidths exclude signal energy outside the beam.

With an angular spread of $\alpha_0 = 20°$ for a 10-element adaptive antenna, the range can be increased by a factor of 2 (with respect to the single element), whereas for the same 10-beam multibeam antenna, the increase is about 1.7 [165]. This difference increases with any increase in the number of adaptive antenna elements or beams in a multibeam antenna. For example, for 30-element antenna with an angular spread of $\alpha_0 = 20°$, the range increase is 2.5 times that of a single regular antenna, whereas for the same angular spread and number of beams, the range increase of the multibeam antenna will be by a factor of 1.7. Note that these results are valid only for the uplink, where the mobile user transmits information and the base station receives it [165]. For the downlink, as the downlink frequency is different from the uplink frequency [for FDMA, GSM (combination of FDMA and TDMA), IS-95, and IS-136 systems], the same adaptive array techniques cannot be used for transmission by the base station and reception by the mobile antenna. Here, the multibeam antenna can be used more effectively, but to achieve diversity gain, transmit diversity must be used or the handset vehicle must have multiple antennas [166]. Although these techniques may provide less gain on the downlink than on the uplink, this may be compensated for by the higher transmit power of the base station as compared to the handset vehicle.

The results obtained in Reference [165] are valid for the uplink and for systems close to TDMA or its combinations with FDMA. In CDMA systems, the RAKE receiver provides three-time diversity, and different beams can be used for each output of the RAKE receiver. So, in CDMA the multibeam antenna gives the same range increase as the adaptive array antenna. As multibeam antennas require less complexity (with respect to weight and tracking), the multibeam antenna is preferable for CDMA systems, whereas an adaptive array antenna may be preferable for TDMA or GSM systems, particularly in environments with large angular spreads.

9.4.5. Reduction in Co-Channel Interference and Outage Probability

In this section we will briefly consider the integration of an idealized adaptive antenna array into an existing cellular network and will compare it with the conventional omnidirectional base-station antenna following the well-known hexagonal cell topology, all details of which the reader can find in References [91–94,167].

Let the cluster size be given in terms of the number of cells N_C, which uses different frequencies compared to the *wanted* cell (i.e., the cell under service). This number (N_C) is related to the co-channel reuse factor $Q = D/R_{cell}$ by References [103,167]:

$$N_C = Q^2/3 \tag{9.47}$$

where R_{cell} is the radius of a cell and D is the reuse distance, which defines a range between cells allocated by the same frequency band. There is a limited number of N_C cells that are possible in a hexagonal cellular network [103,167], that is, $N_C = 3, 4, 7, 9, 12, \ldots$
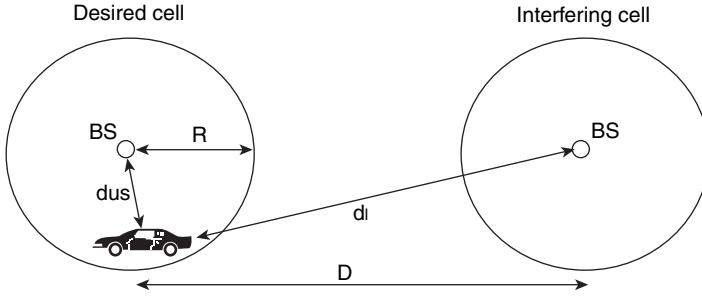
FIGURE 9.31. Co-channel interference between a desired and an interfering cell.

Co-channel interference will occur when the ratio of the received (e.g., wanted) signal envelope, S, to the interfering signal envelope, I, is less than some protection ratio p_r (a threshold), that is [168],

$$\frac{S}{I} \le p_r \tag{9.48}$$

Now we consider only one co-channel cell as an i part of a cellular network, as shown in Figure 9.31. Assume that only propagation-loss effects are proportional to distances d_{MS} and d_I between the desired mobile subscriber and each of the desired and interfering BS, respectively. Then,

$$\frac{S}{I} = \frac{d_I^\gamma}{d_{MS}^\gamma} \le p_r \tag{9.49}$$

where γ is the loss exponent. So, for a given protection we get [168–169]

$$\frac{d_I}{d_{MS}} \le (p_r)^{1/\gamma} \tag{9.50}$$

In the case when the desired user lies along a straight line between two base stations (the worst case for a user), the co-channel reuse ratio is

$$Q = D/R_{cell} = 1 + d_I/d_{MS} = 1 + p_r^{1/\gamma} \tag{9.51}$$

For a given protection ratio and modulation scheme, this expression defines the minimum spacing between co-channel cells in order to avoid interference. For six co-channel cells interferers (Fig. 9.32), which lie only in the first tier of co-channel cells, we have instead of (9.49), the following expression [103]:

$$\frac{S}{I} = \frac{d_{MS}^{-\gamma}}{6d_I^{-\gamma}} \le p_r \tag{9.52}$$
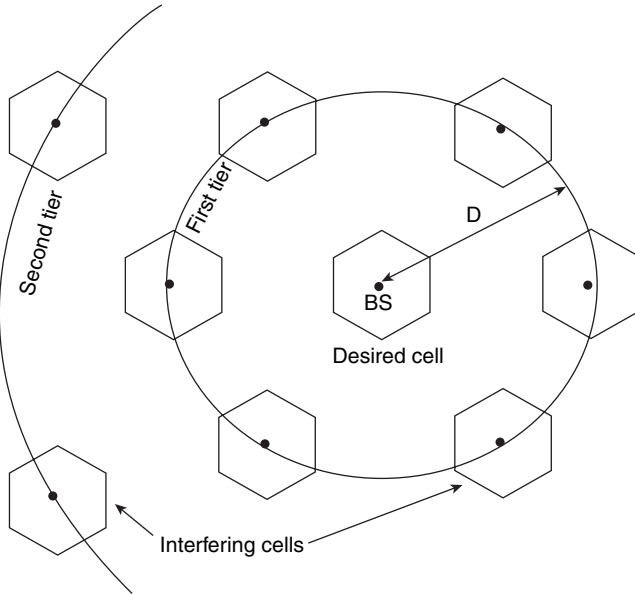
FIGURE 9.32. Scheme of how to eliminate the co-channel interference between neighboring cells operating at the same frequency band.

The co-channel reuse factor can be expressed as [167]

$$Q = D/R_{cell} = [6(S/I)]^{1/\gamma} \qquad (9.53)$$

To see how these parameters influence the co-channel interference occurrence, let us define some other parameters of the network. First, we assume that all users are uniformly distributed per cell with a blocking probability of service P_{bl} constant for all cells. Blocking probability is measured, by the number of users/calls that cannot be served during the period of service. The parameter A (in *Erlangs*) defines the traffic intensity offered, where *Erlang* is a measure of traffic intensity defining the quantity of traffic on a channel or group of channels (users) per unit time. Then the actual traffic carried is equal to $A(1 - P_{bl})$ *Erlangs*, and the so-called *outgoing channel usage efficiency* or *loading factor* becomes [169]

$$\eta = A(1 - P_{bl})/n_c \qquad (9.54)$$

where n_c is the total number of channels allocated per cell.

We now assume that instead of an omnidirectional base-station antenna we have an adaptive one, which generates M ideal beams with a bandwidth of $2\pi/M$, and a gain equal to that of omniantenna. Each adaptive beam will only carry the channels that are assigned to the mobiles within its coverage area. So, any mobile or group of mobiles can be tracked by using adaptive base-station antennas, as sketched in Figure 9.26.

As the occurrence of co-channel interference between subscribers is a statistical problem, instead of the *probability of co-channel interference*, η, we use the *outage probability*, $P(S \leq I \cdot p_r)$. This probability determines the frequency of failing to obtain satisfactory reception at the mobile in the presence of interference. For identical cells, having equal probability of call blocking, there will be in average $n_c\eta$ active channels in each cell. Then, for the omnidirectional base-station antenna, assuming the desired mobile is already allocated a channel, the probability of that channel being active in an interfering cell is the required outage probability, given by

$$P(S \leq I \cdot p_r) = \frac{number\_of\_active\_channels}{total\_number\_of\_channels} = \frac{\eta n_c}{n_c} \equiv \eta \qquad (9.55)$$

Hence, when the desired mobile is in the region of co-channel interference for the omniterminal antennas, the outage probability is identical to the probability of co-channel interference.

For adaptive antennas with M beams per base-station, we have $n_c\eta/M$ channels per beam with a uniform distribution of subscribers. Here, a desired mobile is always covered by at least one beam from the co-channel cell. Then, the outage probability is equal to the probability that one of the channels in the aligned beam is the corresponding active co-channel (i.e., the channel that has been allocated to the desired mobile). Thus, this probability equals

$$P(S \leq I \cdot p_r) = \frac{number\_of\_channels\_per\_beam}{total\_number\_of\_channels} = \frac{\eta n_c/M}{n_c} \equiv \frac{\eta}{M} \qquad (9.56)$$

Thus, the co-channel interference decreases with an increase in the number of antenna elements in the adaptive array or the number of beams in the multibeam antenna.

Now using a simple geometry presented in Figure 9.31, it can be shown, that for the six co-channel cells in the first tier, the outage probability at the regions of interference equals

$$P(S \leq I \cdot p_r) = \left(\frac{\eta}{M}\right)^6 \qquad (9.57)$$

that is, it decreases M^{-6} times with an increase of M. This means that there are six beams aligned onto the desired mobile at any time, and the outage probability within the region of interference is defined by the probability that the active co-channel is in each of these beams. For more details the reader is referred to References [103,170–172]. It is the spatial filtering capabilities of adaptive antennas that reduce co-channel interference.

In general, an adaptive array requires some information about the desired signal, such as the direction of its source, a reference signal, or a signal that is correlated with the desired signal. In situations where the precise direction of the signal is

known, interference cancellation may be achieved by solving a constrained beamforming problem [39] or by using a reference signal [155,173].

Despite the fact that the multibeam antenna is less effective than the adaptive antenna in reducing interference in TDMA systems, for the downlink, multibeam antennas can be used at the base station in combination with adaptive arrays on the uplink. The problem is even worse in GSM or IS-136 systems, because the handsets require a continuous downlink. Therefore, the same beam pattern must be used for all users in a channel, which further reduces the effectiveness of multibeam antenna against interference.

In CDMA systems the users' capacity or loading factor and the outage probability depend on the spreading gain and the corresponding number of equal-power co-channel interferers. Here, the multibeam antenna with M beams also reduces the number of interferers per one beam by a factor of M, increasing the user capacity M-fold. At the same time, for CDMA systems, the adaptive arrays can provide only limited additional interference suppression, because the number of interferers is generally much greater than the number of antenna elements in an array. Furthermore, as multibeam antennas are less complex than adaptive arrays and their beams need to be switched at least every few seconds and tracking 178 Hz fading signals in adaptive arrays [75], multibeam antennas are generally preferred in CDMA systems.

We also note here that interference is typically worse on the uplink than on the downlink for two reasons. First, it is possible that the signal from an interfering mobile is stronger than that from the desired mobile at the base station (i.e., on the uplink), whereas at the mobile, as a receiver, the signal from an interfering base station (i.e., on downlink) does not matter as the mobile chooses the base station with the strongest signal. Second, base stations are typically more uniformly spaced than the mobiles and are located constantly near the center of each cell. Hence, more interference suppression on the uplink than on the downlink may be desirable.

9.4.6. Increase in Spectrum Efficiency and Decrease of BER by Using Smart Antennas

Spectrum efficiency refers to the amount of traffic a given system with certain spectrum allocation could handle [39]. An increase in the number of users of a wireless communication system, mobile or personal, causes the spectrum efficiency to increase. This measure allows us to compare the quality of service of different cellular systems [168].

According to Reference [105], we can determine this measure, denoted by E, as the spectrum utilization through the number of channels/users per bandwidth in Megahertz and per square kilometer, that is,

$$E = \frac{B_T/B_w}{B_T(N_C A_c)} = \frac{1}{B_w N_C A_c} \tag{9.58}$$

Here, B_T is the total available bandwidth of the system; B_w is a channel spectral spacing, but in Megahertz, N_C is the number of cells per cluster, and A_c is the cell

area in square kilometer. To perform a simple comparison between an omniantenna and an adaptive antenna array, we assume that an identical modulation scheme is employed in both cases. As $E \sim N_C^{-1}$, the relative spectrum efficiency can be expressed as [103,105]

$$\frac{E_{\text{adapt}}}{E_{\text{omni}}} = \frac{N_{C_{\text{omni}}}}{N_{C_{\text{adapt}}}} \tag{9.59}$$

where N_C can be expressed as a function of the protection ratio p_r and the fading parameter z_d, as

$$N_C = \frac{1}{3}\left[1 + \sqrt{10^{(z_d+p_r)/20}}\right]^2 \tag{9.60}$$

Many other studies have shown that the use of adaptive antennas can essentially increase the spectrum efficiency by increasing user capacity [174–179]. An array can also create additional channels by forming multiple beams without any extra spectrum allocation, which results in potentially extra users and thus increases the spectrum efficiency.

Using SDMA techniques, we can efficiently serve many mobile users using only two frequencies [178]. The multipath Raleigh fading channel gives a fundamental limit on the maximum data rate and the spectral capacity of a multiple beam antenna system [179]. It was shown in References [179,180] that using an antenna array in a base station, in the uplink to locate the positions of the mobile users in a cell, and then transmitting in a multiplexed manner toward different clusters of mobiles, the spectrum efficiency increases and it depends on the number of elements in the array.

Base-station antenna arrays used for CDMA systems, for example, at an outage probability of 0.01, can increase the system capacity from 31, for a single antenna system, to 115 for a five-element array and to 155 for an array of seven elements [181,182]. Also, an antenna array at the base station for TDMA system can increase the reuse factor by three, if dynamic channel assignment is utilized (see details in References [180,183,185]). The same base-station array of L elements may lead up to an L-fold capacity improvement in an indoor-mobile communication systems by allowing many users to share the same channels [184,186–190]. In Reference [191], using an LMS algorithm, it was found that for an omnidirectional antenna the probability of bit error (BER) is given by [191]

$$P_{\text{eOM}} = Q\left(\sqrt{\frac{3G}{U(1+8\beta)-1}}\right) \tag{9.61}$$

Whereas, for an antenna array we get

$$P_{\text{eMULT}} = Q\left(\sqrt{\frac{3GD}{U(1+8\beta)-1}}\right) \tag{9.62}$$

Here $Q(X)$ is the standard Q-function defined in Chapter 1, x, G is the processing gain of the CDMA system, $\beta = 0.05513$, and D is the directivity of the beam of the multibeam antenna system. A comparison of the BER performance of the systems using other than LMS algorithms [149,190,192] has shown that the maximum entropy method [190] and the spatial discrete Fourier transform method [192] provide better BER performance than the LMS algorithm.

Finally, we note that there are some other performance improvements that can be obtained by using an antenna array, such as an increase in transmission efficiency, reduction in handoff rate and in cross talks, improvement of dynamic channel assignment, cost-effective implementation, complexity reduction, and network implication. All these are aspects beyond the subject of this book and are well described in existing literature [161–163,178,180,193–196].

SUMMARY

Smart antenna systems are usually categorized as either switched beam or adaptive array systems. Although both systems attempt to increase gain in the direction of the user, only the adaptive array system offers optimal gain while simultaneously identifying, tracking, and minimizing interfering signals.

The traditional switched beam method is considered as an extension of the current cellular sectorization scheme in which a typical sectorized cell site is composed of three 120° macrosectors. The switched beam approach further subdivides the macrosectors into several microsectors. The adaptive antennas take a very different approach. By adjusting to an RF environment as it changes, adaptive antenna technology can dynamically alter the signal patterns to optimize the performance of the wireless system. Usually, in the transmit mode, the adaptive array focuses energy in the required direction, which helps to reduce multipath reflections and the delay spread. In the receive mode, however, the array provides compensation in multipath fading by adding the signals emanating from other clusters after compensating for delays, as well as by canceling delayed signals emanating from directions other than that of the desired signal.

BIBLIOGRAPHY

[1] Glaser, E. M., "Signal detection by adaptive filters," *IEEE Trans. Inform. Theory*, vol. IT-7, no. 1, 1961, pp. 87–98.

[2] Davisson, L. D., "A theory of adaptive filters," *IEEE Trans. Inform. Theory*, vol. IT-12, no. 1, 1966, pp. 97–102.

[3] Griffits, L. J., "A comparison of multidimensional Weiner and maximum-likelihood filters for antenna arrays'', *Proc. IEEE*, vol. 55, 1967, pp. 2045–2057.

[4] Goode, B. B., "Synthesis of a nonlinear Bayer detector for Gaussian signal and noise fields using Wiener filters," *IEEE Trans. Information Theory*, vol. IT-13, 1967, pp. 116–118.

[5]   Burg, J. P., ''Three-dimensional filtering with an array of sesmometers,'' *Geophysics*, vol. 29, 1964, pp. 693–713.

[6]   Haykin, S., ed., *Array Signal Processing*, Prentice-Hall, Englewood Cliffs, New Jersey, 1985.

[7]   Stuber, G. L., ''*Principles of Mobile Communication*,'' Kluwer Academic Publishers, 1996.

[8]   Proakis, J. G., *Digital Communication*, McGraw Hill, New York, NY, 2001.

[9]   Steele, R., *Mobile Radio Communications*, IEEE Press, New York, 1992.

[10] Rappaport, T, S., ''*Wireless Communications Principles and Practice*,'' Prentice Hall, New York, NY, 1996.

[11] Farina, A., *Antenna-Based Signal Processing Techniques for Radar Systems*, Artech House, Norwood, Massachusetts, 1992.

[12] Krim, H., and M. Viberg, ''Two decades of array signal processing research,'' *IEEE Signal Processing Magazine*, no. 1, 1996, pp. 67–94.

[13] Paulraj, A. J., and C. B. Papadias, ''Space-time processing for wireless communications,'' *IEEE Personal Communications*, vol. 14, no. 5, 1997, pp. 49–83.

[14] Widrow, B., P. E. Mantey, L. J. Griffits, et al., ''Adaptive antenna systems,'' *Proc. IEEE*, vol. 55, no. 12, 1967, pp. 2143–2159.

[15] ''Special Issue on Active and Adaptive Antennas,'' *IEEE Trans. Antennas Propagat.*, March 1964; vol. AP-24, no. 3, September 1976.

[16] Gabriel, W. F., ''Adaptive arrays-an introduction,'' *Proc. IEEE*, vol. 64, no. 2, 1976, pp. 239–272.

[17] Gabriel, W. F., ''Spectral analysis and adaptive array super resolution techniques,'' *Proc. IEEE*, vol. 68, no. 6, 1980, pp. 654–666.

[18] Monzingo, R. A., and T. W. Miller, *Introduction to Adaptive Arrays*, Wiley and Sons, New York, 1980.

[19] Hudson, J. E., *Adaptive Array Principles*, Peter Peregrinus, New York, 1981.

[20] ''Special Issue on Adaptive Processing Antenna Systems,'' *IEEE Trans. Antennas Propagat.*, vol. AP-34, March 1986.

[21] Compton, R. T., Jr., *Adaptive Antennas: Concepts and Performance*, Prentice-Hall, Englewood Cliffs, New Jersey, 1988.

[22] Gabriel, W. F., ''Adaptive processing array systems,'' *Proc. IEEE*, vol. 80, no. 1, 1992, pp. 152–162.

[23] Barret, M., and R. Arnott, ''Adaptive antennas for mobile communications,'' *Electron. Communic. Eng. J.*, vol. 6, no. 2, 1994, pp. 203–214.

[24] Litva, J., and T. Lo, *Digital Beamforming in Wireless Communications*, Artech House, 1996.

[25] Pridham, R. G., and R. A. Mucci, ''A novel approach to digital beamforming,'' *J. Acoust. Soc. Amer.*, vol. 63, 1978, pp. 425–434.

[26] Pridham, R. G., and R. A. Mucci, ''Digital interpolation beamforming for low-pass and bandpass signals,'' *Proc. IEEE*, vol. 67, no. 5, 1979, pp. 904–919.

[27] Curtis, T. E., ''Digital beamforming for sonar system,'' *IEE Proc. Pt. F*, vol. 127, no. 2, 1980, pp. 257–265.

[28] Mucci, R. A., ''A comparison of efficient beamforming algorithms,'' *IEEE Trans. Acoust., Speech, Signal Processing*, vol. ASSP-32, no. 3, 1984, pp. 548–558.

[29] Van Veen, B. D., and K. M. Buckley, "Beamforming: A versatile approach to spatial filtering," *IEEE Trans. Acoustics, Speech and Signal Processing Magazine*, vol. 5, no. 1, 1988, pp. 4–24.

[30] Gocler, H. G., and H. Eyssele, "A digital FDM-demultiplexer for beamforming environment," *Space Communic.*, vol. 10, no. 2, 1992, pp. 197–205.

[31] Barton, P., "Digital beamforming for radar," *IEE Proc. Pt. F*, vol. 127, no. 1, 1980, pp. 266–277.

[32] Sakagami, S., S. Aoyama, K. Kuboi, et al., "Vehicle position estimates by multibeam antennas in multipath environments," *IEEE Trans. Veh. Technol.*, vol. 41, no. 1, 1992, pp. 63–68.

[33] Wu, W. W., E. F. Miller, W. L. Prichard, et al., "Mobile satellite communications," *Proc. IEEE*, vol. 82, 1994, pp. 1431–1448.

[34] Horton, C. R., and K. Abend, "Adaptive array antenna for satellite cellular and direct broadcast communications," *Proc. 3rd Int. Mobile Satellite Conf.*, Pasadena, California, 1993, pp. 47–52.

[35] Cornacchini, C., R. Crescimbeni, A. D'ippolito, et al., "A comparative analysis of frequency scanning and multispot beam satellite systems for mobile communication," *Int. J. Satellite Communic.*, vol. 13, no. 1, 1995, pp. 84–104.

[36] Schrewe, H. J., "An adaptive antenna array for mobile reception of DBS-satellites," *Proc. 44th Veh. Technol. Conf.*, Stockholm, Sweden, 1994, pp. 1494–1497.

[37] Gebauer, T., and H. G. Gockler, "Channel-individual beamforming for mobile satellite communications," *IEEE J. Select. Areas Communic.*, vol. 13, no. 3, 1995, pp. 439–448.

[38] Rappaport, T. S., ed., *Smart Antennas*, IEEE Press, Piscaraway, New Jersey, 1998.

[39] Ioannides, P., and C. Balanis, "Uniform Circular Arrays for Smart Antennas," *IEEE Antennas and Propagat. Magazine*, vol. 47, no. 4, 2005, pp. 192–206.

[40] Tsoulos, G. V., and G. E. Athanasiadou, "On the application of adaptive antennas to microcellular environments: radio channel characteristics and system performance," *IEEE Trans. Vehicular Techn.*, vol. 51, 2002, pp. 1–16.

[41] Naguib, A. F., A. Paulraj, and T. Kailath, "Capacity improvement with base-station antenna arrays in cellular CDMA," *IEEE Trans. Veh. Technol.*, vol. 43, 1994, pp. 691–698.

[42] Godava, L. C., "Applications of antenna arrays to mobile communications, Part II: Beam-Forming and Direction-of-Arrival Considerations," *Proc. IEEE*, vol. 85, no. 8, 1997, pp. 1195–1245.

[43] Anderson, S., M. Millnert, M. Viberg, et al., "An adaptive array for mobile communication systems," *IEEE Trans. Veh. Technol.*, vol. 40, no. 2, 1991, pp. 230–236.

[44] Vaugham, R. G., and N. L. Scott, "Closely spaced monopoles for mobile communications," *Radio Sci.*, vol. 28, 1993, pp. 1259–1266.

[45] Barlett, M. S., "Smoothing periodograms from time series with continuous spectra," *Nature*, vol. 161, 1948, pp. 686–687.

[46] Capon, J., " High-resolution frequency-wavenumber spectrum analysis," *Proc. IEEE*, vol. 57, no. 8, 1969, pp. 1408–1418.

[47] Applebaum, S. P., "Adaptive arrays," *IEEE Trans. Antennas Propagat.*, vol. 24, no. 9, 1976, pp. 585–598.

[48] Lacoss, R. T., "Data adaptive spectral analysis method," *Geophysics*, vol. 36, 1971, pp. 661–675.

[49] "Special Issue of Spectra From Various Techniques," *IEEE Trans. Acoustics, Speech and Signal Processing*, vol. ASSP-29, no. 3, 1981.

[50] Wiener, N., *Extrapolation, Interpolation and Smoothing of Stationary Time Series*, MIT Press, Cambridge, Massachusetts, 1949.

[51] Haykin, S., J. Litva, and T. J. Shepherd, eds., *Radar Array Processing*, Springer-Verlag, Berlin, 1993.

[52] Johnson, D. H., and D. E. Dudgeon, *Array Signal Processing Concepts and Techniques*, Prentice-Hall, Englewood Cliffs, New Jersey, 1993.

[53] Butler, J. L., "Digital matrix, and intermediate frequency scanning," in *Microwave Scanning Arrays*, ed. R. C. Hansen, Academic Press, New York, 1966.

[54] Anderson, V. C., "DICANNE, a realizable adaptive process," *J. Acoust. Soc. Amer.*, vol. 45, 1969, pp. 398–405.

[55] Anderson, V. C., and P. Rudnick, "Rejection of a coherent arrival at an array," *J. Acoust. Soc. Amer.*, vol. 45, 1969, pp. 406–410.

[56] Brennan, L. E., and I. S. Reed, "Theory of adaptive radar," *IEEE Trans. Aerosp. Electron. Syst.*, vol. AES-9, 1973, pp. 237–252.

[57] Reed, I. S., J. D. Mallett, and L. E. Brennan, "Rapid convergence rate in adaptive arrays," *IEEE Trans. Aerosp. Electron. Syst.*, vol. AES-10, 1974, pp. 853–863.

[58] Weber, M. E., and R. Heisler, "A frequency-domain beamforming algorithm for wideband, coherent signal processing," *J. Acoust. Soc. Amer.*, vol. 76, 1984, pp. 1132–1144.

[59] Florian, S., and N. J. Bershad, "A weighted normalized frequency domain LMS adaptive algorithm," *IEEE Trans. Acoust., Speech, Signal Processing*, vol. 36, 1988, pp. 1002–1007.

[60] Zhu, J. X., and H. Wang, "Adaptive beamforming for correlated signal and interference: A frequency domain smoothing approach," *IEEE Trans. Acoust., Speech, Signal Processing*, vol. 38, 1990, pp. 193–195.

[61] Klemm, R., "Suppression of jammers by multiple beam signal processing," in *Proc. IEEE Int. Radar Conf.*, Sendai, Japan, 1975, pp. 176–180.

[62] El Zooghby A., C. G. Christodoulou, and M. Georgiopoulos, "Neural Network-based Adaptive Beamforming for one and two Dimensional Antenna Arrays," *IEEE Trans. Antennas Propagat.*, vol. 46, 1998, pp. 1891–1893.

[63] El Zooghby A., C. G. Christodoulou, and M. Georgiopoulos, "A Neural Network-based Smart Antenna for Multiple Source Tracking," *IEEE Trans. Antennas Propagat.*, vol. 48, 1999, pp. 768–776.

[64] Anderson, V. C., "Digital array phasing," *J. Acoust. Soc. Amer.*, vol. 32, 1960, pp. 867–870.

[65] Rudnick, P., "Digital beamforming in the frequency domain," *J. Acoust. Soc. Amer.*, vol. 46, 1969, pp. 1089–1095.

[66] Dudgeon, D. E., "Fundamentals of digital array processing," *Proc. IEEE*, vol. 65, 1977, pp. 898–904.

[67] Pridham, R. G., and R. A. Mucci, "A novel approach to digital beamforming," *J. Acoust. Soc. Amer.*, vol. 63, 1978, pp. 425–434.

[68] Mucci, R. A., "A comparison of efficient beamforming algorithms," *IEEE Trans. Acoust., Speech, Signal Processing*, vol. ASSP-32, 1984, pp. 548–558.

[69] Fan, H., E. I. El-Masry, and W. K. Jenkins, "Resolution enhancement of digital beamforming," *IEEE Trans. Acoust., Speech, Signal Processing*, vol. ASSP-32, 1984, pp. 1041–1052.

[70] Mohamed, N. J., "Two-dimensional beamforming with non-sinusoidal signals," *IEEE Trans. Electromag. Compat.,* vol. EMC-29, 1987, pp. 303–313.

[71] Maranda, B., "Efficient digital beamforming in the frequency domain," *J. Acoust. Soc. Amer.*, vol. 86, 1989, pp. 1813–1819.

[72] Chujo, W., and K. Yasukawa, "Design study of digital beamforming antenna applicable to mobile satellite communications," *IEEE Antennas and Propagation Symp. Dig.*, Dallas, Texas, 1990, pp. 400–403.

[73] Gebauer, T., and H. G. Gockler, "Channel-individual adaptive beamforming for mobile satellite communications," *IEEE J. Select. Areas Communic.*, vol. 13, no. 3, 1995, pp. 439–448.

[74] Steyskal, H., "Digital beamforming antenna, an introduction," *Microwave J.*, no. 1, 1987, pp. 107–124.

[75] Winters, J. H., "Smart antennas for wireless systems," *IEEE Personal Communic.*, vol. 1, no. 1, 1998, pp. 23–27.

[76] Griffiths, L. J., "A simple adaptive algorithm for real-time processing in antenna array," *Proc. IEEE*, vol. 57, 1969, pp. 64–78.

[77] Frost III, O. L., "An algorithm for lineary constrained adaptive array processing," *Proc. IEEE*, vol. 60, 1972, pp. 926–935.

[78] Brook, L. W., and I. S. Reed, "Equivalence of the likelihood ratio processor, the maximum signal-to-noise ratio filter, and the Wiener filter," *IEEE Trans. Aerosp. Electron. Syst.*, vol. 8, 1972, pp. 690–692.

[79] Monzingo, R. A., and T. W. Miller, *Introduction in Adaptive Array*, John Wiley & Sons, New York, 1980.

[80] Haykin, S., *Adaptive Filter Theory*, Prentice Hall, Englewood Cliffs, New Jersey, 1991.

[81] Murray, W., ed., *Numerical Methods for Unconstrained Optimization*, Academic Press, New York, 1972.

[82] Horowitz, L. H., and K. D. Senne, "Performance advantage of complex LMS for controlling narrow-band adaptive arrays," *IEEE Trans. Circuits Syst.*, vol. CAS-28, 1981, pp. 562–576.

[83] Iltis, R. A., and L. B. Milstein, "Approximate statistical analysis of the Widrow LMS algorithm with application to narrow-band interference rejection," *IEEE Trans. Communic.*, vol. COM.-33, no. 1, 1985, pp. 121–130.

[84] Feuer, A., and E. Weinstein, "Convergence analysis of LMS filters with uncorrelated Gaussian data," *IEEE Trans. Acoust., Speech, Signal Processing*, vol. ASSP-33, 1985, pp. 222–229.

[85] Gardner, W. A., "Comments on convergence analysis of LMS filters with uncorrelated data," *IEEE Trans. Acoust., Speech, Signal Processing*, vol. ASSP-34, 1986, pp. 378–379.

[86] Clarkson, P. M., and P. R. White, "Simplified analysis of the LMS adaptive filter using a transfer function approximation," *IEEE Trans. Acoust., Speech, Signal Processing*, vol. ASSP-35, 1987, pp. 987–993.

[87] Boland, F. B., and J. B. Foley, "Stochastic convergence of the LMS algorithm in adaptive systems," *J. Signal Processing*, vol. 13, 1987, pp. 339–352.

[88] Foley, J. B., and F. M. Boland, "A note on the convergence analysis of LMS adaptive filters with Gaussian data," *IEEE Trans. Acoust., Speech, Signal Processing*, vol. 36, 1988, pp. 1087–1089.

[89] Jaggi, S., and A. B. Martinez, "Upper and lower bounds of the misadjustment in the LMS algorithm," *IEEE Trans. Acoust., Speech, Signal Processing*, vol. 38, 1990, pp. 164–166.

[90] Solo, V., "The error variance of LMS with time-varying weights," *IEEE Trans. Signal Processing*, vol. 40, 1992, pp. 803–813.

[91] Jung, P., Z. Zvonar, and K. Kammerlander, eds., *GSM: Evolution Towards 3rd Generation*, Kluwer Academic Publishers, 1998.

[92] Rappaport, *Wireless Communications: Principles and Practice*, Prentice Hall, Englewood Cliffs, New Jersey, 1996.

[93] Prasad, R., *CDMA for Wireless Personal Communications*, Artech House, Boston-London, 1996.

[94] Saunders, S. R., *Antennas and Propagation for Wireless Communication Systems*, John Wiley & Sons, New York, 1999.

[95] Blaunstein, N., and J. B. Andersen, *Multipath Phenomena in Cellular Networks*, Artech House, Boston-London, 2002.

[96] Jakes, W. C., ed., *Microwave Mobile Communications*, IEEE Press, New York, 1994.

[97] Parsons, J. D., and A. M. D. Turkmani, "Characterization of mobile radio signals," *IEE Proc. I*, vol. 138, no. 6, 1991, pp. 549–556.

[98] Turkmani, A. M. D., A. A. Arowojolu, P. A. Jefford, et al., "An experimental evaluation of the performance of two-branch space and polarization diversity schemes at 1800 MHz," *IEEE Trans. Veh. Technol.*, vol. 44, no. 3, 1995, pp. 318–326.

[99] Kozono, S., T. Tsurahara, and M. Sakamoto, "Base station polarization diversity reception for mobile radio," *IEEE Trans. Veh. Technol.*, vol. 33, 1984, pp. 301–306.

[100] Vaughan, R. G., "Polarisation diversity in mobile communications," *IEEE Trans. Veh. Technol.*, vol. 39, no. 2, 1990, pp. 177–186.

[101] Eggers, P. C. F., J. Toftgard, and A. M. Oprea, "Antenna systems for base station diversity in urban small and micro cells," *IEEE J. Select. Areas Communic.*, vol. 11, no. 7, 1993, pp. 1046–1057.

[102] Mizuno, M., and T. Ohgane, "Application of adaptive array antennas to radio communications," *Electron. Communic. Japan*, vol. 77, no. 1, 1994, pp. 48–59.

[103] Swales, S. C., M. A. Beach, D. J. Edwards, et al., "The performance enhancement of multi-beam adaptive base-station antennas for cellular land mobile radio systems," *IEEE Trans. Veh. Technol.*, vol. 39, 1990, pp. 56–67.

[104] Anderson, S., M. Millnert, M. Viberg, et al., "An adaptive array for mobile communication systems," *IEEE Trans. Veh. Technol.*, vol. 40, no. 2, 1991, pp. 230–236.

[105] Swales, S. C., M. A. Beach, D. J. Edwards, et al., "The realization of a multi-beam adaptive base-station antenna for cellular land mobile radio systems," *Proc. of IEEE Veh. Technol. Conf.*, San Francisco, California, 1989, pp. 341–348.

[106] Andersen, J. B., "Antenna arrays in mobile communications," *IEEE Antenna Propagat. Magazine*, vol. 42, no. 2, 2000, pp. 12–16.

[107] Andersen, J. B., "Array gain and capacity for known random channels with multiple element arrays at both ends," *IEEE J. Select. Areas in Communic.*, vol. 18, no. 11, 2000, pp. 2172–2178.

[108] Andersen, J. B., ''Role of antennas and propagation for the wireless systems beyond 2000,'' *J. Wireless Personal Communic.*, vol. 17, 2001, pp. 303–310.

[109] Winters, J. H., ''Optimum combining in digital mobile radio with co-channel interference,'' *IEEE J. Select. Areas Communic.*, vol. SAC-2, 1984, pp. 528–539.

[110] Winters, J. H., ''Optimum combining for indoor radio systems with multiple users,'' *IEEE Trans. Communic.*, vol. COM-35, 1987, pp. 1222–1230.

[111] Hashemi, H., ''The indoor radio propagation channels,'' *Proc. IEEE*, vol. 81, 1993, pp. 943–968.

[112] Lo, T., and J. Litva, ''Angles of arrival in indoor multipath,'' *Electronics Letters*, vol. 28, no. 18, 1992, pp. 1687–1689.

[113] Wang, Jian-Guo, A. S. Mohan, and T. A. Aubrey, ''Angles-of-arrival of multipath signals in indoor environments,'' in *IEEE Veh. Technol. Int. Conf.*, 1996, pp. 155–159.

[114] Passerini, C., M. Missiroli, G. Riva, et al., ''Adaptive antenna arrays for reducing the delay spread in indoor radio channels,'' *Ins. Elect. Eng. Electron. Lett.*, vol. 32, 1996, pp. 280–281.

[115] Litva, J., A. Chaforian, and V. Kezys, ''High-resolution measurements of AOA and time-delay for characterizing indoor propagation environments,'' in *IEEE Anten. Propagat. Soc. Int. Symp.*, 1996 Digest, IEEE, vol. 2, 1996, pp. 1490–1493.

[116] Adel, A., M. Saleh, and R. A. Valenzula, ''Statistical model for indoor multipath propagation,'' *IEEE J. Select. Areas Communic.*, vol. SAC-5, 1987, pp. 128–133.

[117] Spencer, Q., M. Rice, B. Jeffs, et al., ''Indoor wideband time/angle of arrival multipath propagation results,'' in *IEEE Veh. Technol. Conf.*, Phoenix, Arizona, 1997, pp. 1415–1419.

[118] Russo, P., A. D'ippolito, M. Ruggieri, et al., ''A frequency scanning satellite system for land mobile communications,'' *Int. J. Satell. Communic.*, vol. 11, 1993, pp. 87–103.

[119] Hirshfield, E., ''The Globalstar system,'' *Appl. Microwave Wireless*, no. 4, 1995, pp. 26–41.

[120] Schuss, J. J., J. Upton, B. Muers, et al., ''The IRIDIUM main mission antenna concepts,'' in *Proc. IEEE Int. Symp. Phased Array Systems Technol.*, Boston, Massachusetts, 1996, pp. 411–415.

[121] Bodnar, D. G., B. K. Rainer, and Y. Rahmatsamii, ''A novel array antenna for MSAT applications,'' *IEEE Trans. Veh. Technol.*, vol. 38, no. 1, 1989, pp. 86–94.

[122] Suzuki, R., Y. Matsumoto, R. Miura, et al., ''Mobile TDM/TDMA system with active array antenna,'' in *Proc. IEEE Global Telecommun. Conf*, Houston, Texas, 1991, pp. 1569–1573.

[123] Ohmori, S., Y. Hase, H. Wakana, et al., ''Experiments on aeronautical satellite communications using ETS-V satellite,'' *IEEE Trans. Aerosp. Electron. Syst.*, vol. 28, 1992, pp. 788–796.

[124] Allnutt, R. M., T. Pratt, and A. Dissanayake, ''A study in small scale antenna diversity as a means of reducing effects of satellite motion induced multipath fading for handheld satellite communication systems,'' in *Proc. IEEE, 9th Int. Conf. Antennas Propagat.*, Eindhoven, The Netherlands, 1995, pp. 135–139.

[125] Roy, R. H., ''ESPRIT, Estimation of signal parameters via rotation invariance techniques,'' *Ph.D. thesis*, Stanford University, California, August 1987.

[126] Thomson, J. S., P. M. Grant, and B. Mulgrew, ''Smart antenna array for CDMA system,'' *IEEE Person. Communic.*, vol. 3, no. 5, 1996, pp. 16–25.

[127] Foschini, G. J., "Layered space-time architecture for wireless communication in a fading environment when using multi-element antennas," *Bell Labs Technol. J.*, vol. 1, no. 1, 1996, pp. 41–59.

[128] Despins, C. L. B., D. D. Falconer, and S. A. Mahmoud, "Compound strategies of coding, equalization and space diversity for wideband TDMA indoor wireless channels," *IEEE Trans. Veh. Technol.*, vol. 41, no. 3, 1992, pp. 369–379.

[129] Despins, C. L. B., D. D. Falconer, and S. A. Mahmoud, "Coding and optimum baseband combining for wideband TDMA indoor wireless channels," *Canadian J. Elect. Comput. Eng.*, vol. 16, no. 1, 1991, pp. 53–62.

[130] Chang, L. F., and P. J. Porter, "Performance comparison of antenna diversity and slow frequency hopping for the TDMA portable radio channel," *IEEE Trans. Veh. Technol.*, vol. 38, no. 2, 1989, pp. 222–229.

[131] Winters, J. H., J. Salz, and R. D. Gitlin, "The impact of antenna diversity on the capacity of wireless communication systems," *IEEE Trans. Communic.*, vol. 42, 1994, pp. 1740–1751.

[132] Salz, J., and J. H. Winters, "Effect of fading correlation on adaptive arrays in digital mobile radio," *IEEE Trans. Veh. Technol.*, vol. 43, 1994, pp. 1049–1057.

[133] Balaban, P., and J. Salz, "Optimum diversity combining and equalization in digital data transmission with application to cellular mobile radio-Part I: Theoretical considerations," *IEEE Trans. Communic.*, vol. 40, 1992, pp. 885–894.

[134] Balaban, P., and J. Salz, "Optimum diversity combining and equalization in digital data transmission with application to cellular mobile radio-Part II: Numerical results," *IEEE Trans. Communic.*, vol. 40, 1992, pp. 895–907.

[135] Proakis, J. G., "Adaptive equalization for TDMA digital mobile radio," *IEEE Trans. Veh. Technol.*, vol. 40, no. 3, 1991, pp. 333–341.

[136] Ishii, N., and R. Kohno, "Spatial and temporal equalization based on an adaptive tapped-delay-line array antenna," *IEICE Trans. Communicat.*, vol. E78-B, 1995, pp. 1162–1169.

[137] Barroso, V. A. N., M. J. Rendas, and J. P. Gomes, "Impact of array processing techniques on the design of mobile communication systems," in *Proc. IEEE 7th Mediterranean Electrotechnic. Conf.*, Antalya, Turkey, 1994, pp. 1291–1294.

[138] Fernandez, J., I. R. Corden, and M. Barrett, "Adaptive array algorithms for optimal combining in digital mobile communication systems," in *Proc. IEEE of Int. Conf. Antennas Propagat.*, Edinburgh, Scotland, 1993, pp. 983–986.

[139] Abu-Dyya, A. A., and N. C. Beaulieu, "Outage probability of diverse cellular systems with co-channel interference in Nakagami fading," *IEEE Trans. Veh. Technol.*, vol. 41, no. 3, 1992, pp. 343–355.

[140] Goldburg, M, and R. Roy, "The impacts of SDMA on PCS system design," in *Proc. IEEE Int. Conf. Personal Communic.*, San Diego, California, 1994, pp. 242–246.

[141] Ohgane, T., T. Shimura, N. Matsuzawa, et al., "An implementation of a CMA adaptive array for high speed GMSK transmission in mobile communications," *IEEE Trans. Veh. Technol.*, vol. 42, no. 2, 1993, pp. 282–288.

[142] Klukas, R. W., and M. Fattouche, "Radio signal direction finding in the urban radio environment," in *Proc. Nat. Tech. Meeting Institute Navigation*, San Francisco, California, 1993, pp. 151–160.

[143] Morrison, G, M. Fattouche, and D. Tholl, ''Parametric modeling and spectral estimation of indoor radio propagation data,'' in *Proc. Wireless 1992*, T. R. Labs, Calgary, Alberta, Canada, 1992, pp. 112–119.

[144] Naguib, A. F., and A. Paulraj, ''Performance of CDMA cellular networks with base-station antenna arrays,'' in *Proc. IEEE Int. Zurich Seminar Communic.*, Zurich, Switzerland, 1994, pp. 87–100.

[145] Turin, G. L., ''Introduction to spread-spectrum antimultipath techniques and their application to urban digital radio,'' *Proc. IEEE*, vol. 68, 1980, pp. 328–353.

[146] Lehnert, J. S., and M. B. Pursely, ''Multipath diversity reception of spread spectrum multiple access communications,'' *IEEE Trans. Communic.*, vol. COM-35, 1987, pp. 1189–1198.

[147] Turin, G., ''The effect of multipath and fading on the performance of direct sequence CDMA systems,'' *IEEE J. Select. Areas Communic.*, vol. 2, 1984, pp. 597–603.

[148] Price, R., and P. E. Green, ''A communication technique for multipath channels,'' *Proc. IRE*, vol. 46, 1958, pp. 555–570.

[149] Choi, S., and T. K. Sarkar, ''Adaptive antenna array utilizing the conjugate gradient method for multipath mobile communication,'' *Signal Process.*, vol. 29, 1992, pp. 319–333.

[150] Ohgane, T., N. Matsuzawa, T. Shimura, et al., ''BER performance of CMA adaptive array for high-speed GMSK mobile communication-A description of measurements in central Tokyo,'' *IEEE Trans. Veh. Technol.*, vol. 42, no. 4, 1993, pp. 484–490.

[151] Choi, S., T. K. Sarkar, and S. S. Lee, ''Design of two-dimension Tseng window and its application to antenna array for the detection of AM signal in the presence of strong jammers in mobile communication,'' *Signal Processing*, vol. 34, 1993, pp. 297–310.

[152] Torrieri, D. J., and K. Bakhru, ''An anticipative adaptive array for frequency-hopping communication,'' *IEEE Trans. Aerosp. Electron. Syst.*, vol. 24, 1988, pp. 449–456.

[153] Bakhru, K., and D. J. Torrieri, ''The maximum algorithm for adaptive array and frequency-hopping communications,'' *IEEE Trans. Antennas Propagat.*, vol. AP-32, 1984, pp. 919–927.

[154] Torrieri, D. J., and K. Bakhru, ''Frequency compensation in an adaptive antenna system for frequency-hopping communication,'' *IEEE Trans. Aerosp. Electron. Syst.*, vol. AES-23, 1987, pp. 448–467.

[155] Compton, R. T. Jr., ''An adaptive array in a spread-spectrum communication system,'' *Proc. IEEE*, vol. 66, 1978, pp. 289–298.

[156] Dlugos, D. M., and R. A. Scholtz, ''Acquisition of spread spectrum signals by an adaptive array,'' *IEEE Trans. Acoust., Speech, Signal Processing*, vol. 37, 1989, pp. 1253–1270.

[157] Trump, T., and B. Ottersten, ''Estimation of nominal direction of arrival and angular spread using an array of sensors,'' *Signal Process.*, vol. 50, no. 1, 1996, pp. 57–69.

[158] Dasilva, J. S., B. Liu, and B. A. Fernandez, ''European mobile communications on the move,'' *IEEE Communic. Magazine*, vol. 34, no. 1, 1996, pp. 60–69.

[159] Zettemberg, P., and B. Ottersten, ''The spectrum efficiency of a base station antenna array system for spatially selective transmission,'' *IEEE Trans. Veh. Technol.*, vol. 44, 1995, pp. 651–660.

[160] Yamada, Y, K. Kagoshima, and K. Tsunekawa, ''Diversity antennas for base and mobile situation in land mobile communication systems,'' *IEICE Trans.*, vol. E74, 1991, pp. 3202–3209.

[161] Adachi, F., M. T. Feeney, A. G. Williamson, et al., ''Cross correlation between the envelopes of 900 MHz signals received at a mobile radio base station site,'' *Proc. IEE*, vol. 133, Pt. F, 1986, pp. 506–512.

[162] Eggers, P. C. F., ''Angular dispersive mobile radio environments sensed by highly directive base station antennas,'' in *Proc. IEEE Int. Symp. Personal Indoor Mobile Radio Communic.*, Toronto, Canada, 1995, pp. 522–526.

[163] Lee, W. C. Y., ''Effects of correlation between two mobile radio base station antennas,'' *IEEE Trans. Communic.*, vol. COM-21, 1973, pp. 1214–1224.

[164] Jakes, W. C. Jr., ed., *Microwave Mobile Communications*, Wiley and Sons, New York, 1974.

[165] Winters, J. H., and M. J. Gans, ''The range increase of adaptive versus phased arrays in mobile radio systems,'' *Proc. 28th Asilomar Conf. Signals, Systems and Comput.*, Pacific Grove, California, 1994, pp. 109–115.

[166] Seshadri, N., and J. H. Winters, ''Two signaling schemes for improving the error performance of frequency-division-duplex (FDD) transmission systems using transmitted antenna diversity,'' *Int. J. Wireless Information Networks*, no. 1, 1994, pp. 103–109.

[167] Blaunstein, N., *Radio Propagation in Cellular Networks*, Artech House, Boston-London, 1999.

[168] Hammuda, H., J. P. McGeehan, and A. Bateman, ''Spectral efficiency of cellular land mobile radio system,'' in *Proc. 38th IEEE Veh. Technol. Conf.*, Philadelphia, Pennsylvania, 1988, pp. 616–622.

[169] Gosling, W., ''Protection ratio and economy of spectrum use in land mobile radio,'' *Proc. IEE*, vol. 127, pt. F, 1980, pp. 174–178.

[170] Daikoku, K., and H. Ohdate, ''Optimum channel reuse in cellular land mobile radio system,'' *IEEE Trans. Veh. Technol.*, vol. VT-32, no. 2, 1983, pp. 217–224.

[171] French, R. C., ''The effects of fading and shadowing on reuse in mobile radio,'' *IEEE Trans.Veh. Technol.*, vol. VT-28, no. 1, 1979, pp. 171–182.

[172] Muammar, R., and S. Gupta, ''Co-channel interference in high capacity mobile radio systems,'' *IEEE Trans. Communic.*, vol. COM-30, 1982, pp. 1973–1978.

[173] Windram, M. D., L. Brunt, and E. J. Wilson, ''Adaptive antennas for UHF broadcast reception,'' *Proc. IEE*, vol. 127, Pt. F, 1980, pp. 249–256.

[174] Raith, K., and J. Uddenfeldt, ''Capacity of digital cellular TDMA systems,'' *IEEE Trans. Veh. Technol.*, vol. 40, no. 2, 1991, pp. 323–332.

[175] Gilhousen, K. S., I. M. Jacobs, R. Padovani, et al., ''On the capacity of cellular CDMA system,'' *IEEE Trans. Veh. Technol.*, vol. 40, no. 2, 1991, pp. 303–312.

[176] Sivanand, S., ''On adaptive arrays in mobile communication,'' in *Proc. IEEE Nat. Telesystems Conf.*, Atlanta, Georgia, 1993, pp. 55–58.

[177] Balaban, P., and J. Salz, ''Dual diversity combining and equalization in digital cellular mobile radio,'' *IEEE Trans. Veh. Technol.*, vol. 40, no. 2, 1991, pp. 342–354.

[178] Tangemann, M., and R. Rheinschmitt, ''Comparison of upgrade techniques for mobile communication systems,'' in *Proc. IEEE Int. Conf. Communications*, New Orleans, Louisiana, 1994, pp. 201–205.

[179] Winters, J. H., ''On the capacity of radio communication systems with diversity in Rayleigh fading environment,'' *IEEE J. Select. Areas Communic.*, vol. SAC-5, 1987, pp. 871–878.

[180] Lopez, A. R., "Performance predictions for cellular switched beam intelligent antenna systems," *IEEE Communic. Magazine*, vol. 34, no. 1, 1996, pp. 152–154.

[181] Suard, B., A. F. Naguib, G. Xu, et al., "Performance of CDMA mobile communication systems using antenna arrays," in *Proc. IEEE Int. Conf. Acoust., Speech, Signal Processing*, Minneapolis, Minnesota, 1993, pp. 153–156.

[182] Wang, Y., and J. R. Cruz, "Adaptive antenna arrays for the reverse link of CDMA cellular communication systems," *IEEE Lett.*, vol. 30, 1994, pp. 1017–1018.

[183] Winters, J. H., "Signal acquisition and tracking with adaptive arrays in the digital mobile radio system IS-54 with flat fading," *IEEE Trans. Veh. Technol.*, vol. 42, no. 3, 1993, pp. 377–384.

[184] Winters, J. H., "Optimum combining in digital mobile radio with co-channel interference," *IEEE J. Select. Areas Communic.*, vol. SAC-2, 1984, pp. 528–539.

[185] Ohgane, T., "Characteristics of CMA adaptive array for selective fading compensation in digital land mobile radio communications," *Electron. Communic. Japan*, vol. 74, 1991, pp. 43–53.

[186] Beach, M. A., P. Guemas, and A. R. Nix, "Capacity and service extension for wireless networks using adaptive antennas," *Electron. Letters*, vol. 30, 1994, pp. 1813–1814.

[187] Beach, M. A., H. Xue, R. Davies, et al., "Adaptive antennas for third generation systems," in *Proc. IEE Colloquium Mobile Communications Toward Year 2000*, London, The United Kingdom, 1994, pp. 10/1–10/6.

[188] Kawala, P., and U. H. Sheikh, "Adaptive multiple-beam array for wireless communications," in *Proc. IEE 8th Int. Conf. Antennas Propagation*, Edinburgh, Scotland, 1993, pp. 970–974.

[189] Ganz, M. W., and R. T. Compton, Jr., "Protection of PSK communication systems with adaptive arrays," *IEEE Trans. Aerosp. Electron. Syst.*, vol. AES-23, 1987, pp. 528–536.

[190] Nagatsuka, M., N. Ishii, R. Kohno, et al., "Adaptive array antenna based on spatial spectrum estimation using maximum entropy method," *IEICE Trans. Communic.*, vol. E77-B, 1994, pp. 624–633.

[191] Liberti, J. C., and T. S. Rappaport, "Analytical results for reverse channel performance improvements in CDMA cellular communication systems employing adaptive antennas," *In Proc. Globcom'93*, Houston, Texas, 1993, pp. 42–47.

[192] Yim, C., R. Kohno, and H. Imai, "Adaptive array antenna based on estimation of arrival angles using DFT on spatial domain," *Electron. Communic. Japan*, vol. 76, 1993, pp. 96–108.

[193] Harbin, S. A., and B. K. Rainer, "Low-power wireless mobile communication system," in *Proc. IEEE 44th Vehicular Technology Conf.*, vol. 1, Stockholm, Sweden, 1994, pp. 673–676.

[194] Wirth, P. E., "Teletraffic implications of database architectures in mobile and personal communications," *IEEE Communic. Magazine*, vol. 33, no. 1, 1995, pp. 54–59.

[195] Jabbari, B., G. Colombo, A. Nakajima, et al., "Network issues for wireless communications," *IEEE Communic. Magazine*, vol. 33, no. 1, 1995, pp. 88–98.

[196] Ivancic, W. D., M. J. Shalkhauser, and J. A. Quintana, "A network architecture for a geostationary communication satellite," *IEEE Communic. Magazine*, vol. 32, no. 1, 1994, pp. 72–84.

Prediction of Signal Distribution in Space, Time and Frequency Domains in Radio Channels for Adaptive Antenna Applications

Multipath phenomena limit performance of wireless communication systems by introducing fast fading due to frequency spread in narrowband systems and by causing intersymbol interference in wideband systems due to time delay spread. Finally, a strong multiplicative noise occurs in all kinds of wireless links becoming a great problem in land communications [1–30]. As was mentioned in Chapter 9, to mitigate the effects of multiplicative noise and the noise due to interference between users in multiple access communication, the directional, sectorial, and adaptive antennas (array or multibeam) are used in one or both ends of the channel, which was defined in Chapter 9 as a MIMO channel. Using the adaptive antenna together with the corresponding processing algorithms operating in the space, time, and frequency domains (see details in Chapter 9), allows the channel to radiate the desired energy in the desired direction or to cancel the undesirable energy from the undesirable direction (see Fig. 9.21). The same method is used to minimize effect of multipath fading.

However, the operational ability of all kinds of antennas, and mostly of adaptive antennas strongly depends on the degree of accuracy to predict propagation characteristics of the actual channel. These types of propagation models, which are a priori, used to predict the angular, time, and frequency distribution of the multipath components of the total signal arriving at the receiver, are the main sources of the

multipath interference [31–48]. As was mentioned in Chapter 5, realistic channel models are used for performance evaluation of different adaptive antenna solutions and for the estimation of the obtainable capacity gain. In other words, to design effectively different kinds of wireless networks with optimal user and frequency allocation and cellular planning, we need realistic spatial and temporal channel models combined with high-resolution precise experiments. The latter are required for ''parameterization and validation'' of such channel models [10]. Despite the importance of these aspects, a limited number of high-resolution spatial and temporal experiments are available (see Reference [3] and references therein), and only few of them use three-dimensional (3D) measurements accounting not only for angle-of-arrival (AOA) and time-of-arrival (TOA) but also for elevation-of-arrival (EOA) distributions of the multipath components within the communication channel [5–10]. The same situation also occurs with theoretical prediction of these characteristics; only few models, simple or more complicated, exist, which can describe the mutual AOA and TOA distributions of the total signal, and at the same time, may account different situations in the corresponding environment [46–58]. Namely, in the urban scene a predicting model must account for various built-up parameters, such as height, density, and real street orientation of a building as well as position of the antenna with respect to the overlay profile of the building (see Fig. 9.22a–c).

Furthermore, as was mentioned in Section 9.3, system gain is another important issue that has a high priority in cellular network performance. Especially, because the base station (BS) output power is not limited, the *downlink* gain is not a subject of discussion; the system gain aspect in the *uplink* is the main problem. Increasing the system gain is found to be efficient by using an uplink diversity technique. As was mentioned in Chapter 9, different types of diversity systems exist: spatial, temporal, and polarization. But the common feature related to each of them is the correlation factor between branches that defines the potential of diversity gain. Particularly, low correlation increases the utilization of the diversity gain potential. The analysis of parameters, which influence the correlation, is based on an understanding of signal AOA and TOA distribution, which are based on the corresponding theoretical models. Figure 10.1 shows the main concept of spatial diversity technique described by Saunders [48]. As discussed in Chapter 9, the main idea was to combine two faded signals received by two different antennas separated in space. Here, different propagation situations influence the correlation factor in various manner. Thus the requirement proposed by diversity designers is the ability to analyze and to simulate a potential for the diversity gain as a function of main environmental propagation parameters, such as AOA, TOA (called also the *delay spread* (DS)), and EOA signal distributions. As can be summarized, the detailed understanding of radio propagation phenomena is a keystone for the development and performance assessment of different communication systems, stationary or mobile.

Below, we briefly present more realistic models on the basis of experimental and theoretical investigations of the propagation problem. We start with the simple and achieve those which are more complicated but predictable regarding corresponding experiments. Then, we present the reader with some useful recommendations on
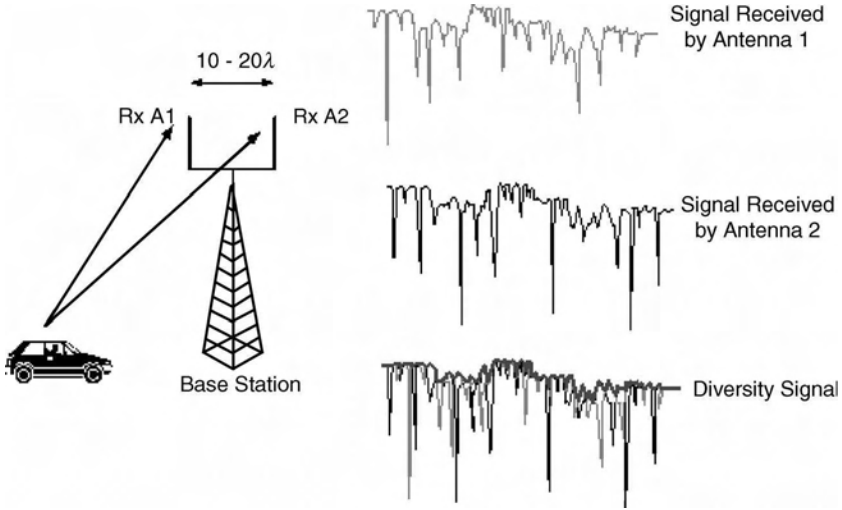
FIGURE 10.1. Explanation of spatial diversity follow discussions ch [48].

how to predict a signal power in spatial (AOA and EOA) and temporal (TOA or DS) domains based on modified stochastic approach proposed in References [55–63] and verify its accuracy comparing it with well-known ray tracing model and with the experiments carried in different European cities. Using this approach, we will present in Chapter 13 some virtual numerical experiments with adaptive antenna for the specific urban scenarios to show how the parameters of the antenna affect the signal power distribution in the space and time domains. These aspects are very actual for the localization of any desired subscriber in the area of service.

10.1. PREDICTING MODELS FOR INDOOR COMMUNICATION CHANNELS

The increasing use of adaptive antennas in radio indoor communications demands an intensive study of the indoor propagation environments, including offices, buildings, warehouses, factories, hospitals, apartments and so forth Reference [21,22]. Temporal data on indoor propagation have been collected and analyzed [21,22], from which a new statistical time-domain model for indoor propagation has been created [21]. Here, experiments have been carried out at 1.5 GHz modulated by a set of 10 ns (nanosecond) pulses with 600 ns repetition period (see Fig. 10.2, according to Reference [21,22]) in a two-story office building. The transmitter was fixed in the hallway near the center of the first floor of the building with the antenna located at a height of 2 m. The receiver, with the same antenna height, was moved to collect measurements in the hallway and in several rooms of the same floor. Figure 10.2 shows one of the examples of four measured pulse responses in different locations of the receiving antenna within a building. In Figure 10.2a, two clearly separated clusters of arriving rays covering a 200 ns time span are shown.
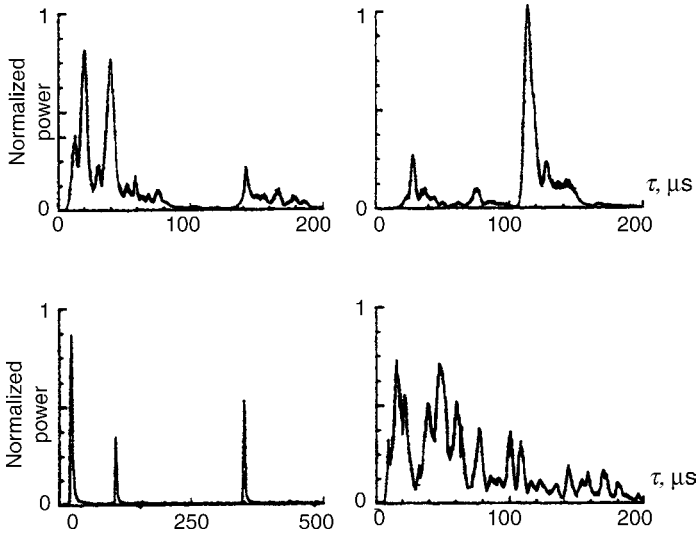
FIGURE 10.2. Normalized power versus time delay spread. (Source [22]: Reprinted with permission © 1997 IEEE)

Figure 10.2b shows a 100 ns delayed echo signal that is much stronger than the first arriving rays. A strong narrow echo signal that is delayed by about 325 ns, which was the largest delay of the relevant echo observed during this set of experiments, is represented in Figure 10.2c. Figure 10.2d corresponds to measurements done when both transmitter and receiver were on the second floor of the building, with the receiver located in clutter conditions due to many obstructions surrounding it.

Therefore, the high density of the rays arriving at the receiver, as multiple components of the total signal caused by the multipath fading, over the entire 200 ns time axis is noticed. Results of the whole set of experiments showed that the maximum observed delay spread within the building is about 100–200 ns, the measured root mean square (*rms*) delay spread from 25 ns to 50 ns within the rooms, and with occasional delays of more than 300 ns within hallways. In obstructive non-line-of-sight (NLOS) conditions, the signal attenuation was proportional to inverse distance-power law with exponent between three and four, which is in agreement with other results obtained within buildings [29,30] and corresponds to those discussed in Chapter 9. Very similar results of time delay spread, but using higher carrier frequency of 7 GHz, were observed [22], according to which a block-scheme of the experimental setup is shown in Figure 10.3. Especially, arrival multipath components tend to come in clusters, with the strongest cluster arriving first, and the strongest arrivals in each cluster also arriving first, as shown in Figure 9.29. As the delay time increases, the power of the clusters and the arrivals within the clusters tend to decay in amplitude until they disappear into the noise floor. Furthermore, as was observed in Reference [22], arrivals corresponding to the same cluster tend to be close in angles, whereas the clusters themselves tend to come at any angle. So, the first important result that the AOA distribution in an indoor multipath environment is not uniformly distributed was
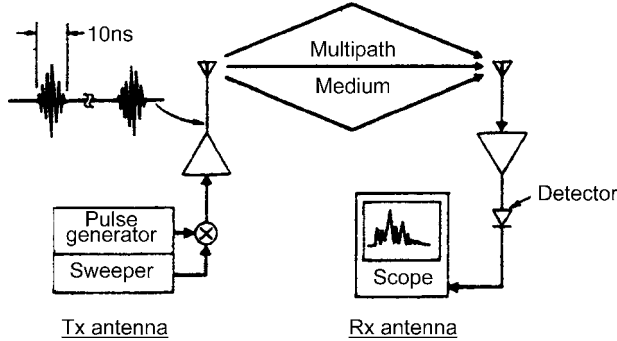
FIGURE 10.3. Experiment, described in Reference [22], for indoor communication. (Reprinted with permission © 1997 IEEE)

observed experimentally in Reference [22]. Using results of experiments and the corresponding statistics obtained there, a simple statistical model was proposed in Reference [23], which can accurately model the observed phenomena by two Poisson laws for the AOA of clusters and the AOA of rays in each cluster as follows from formulas (9.45a) and (9.45b), respectively.

However, most measurement carried out until very recently, dealt with time domain data, and did not include any data on the AOA distribution in indoor communication links. As was mentioned in the previous chapter, knowledge of the AOA associated with a multipath arrival is important because of increasing use of multiple antenna systems with different kinds of antenna diversity, namely, the use of phased array beam forming [25], diversity combining or adaptive array processing (see the corresponding references in Chapter 9) to mitigate the effects of multipath fading and multiple user servicing. In the latter case, for multiple access communications, the adaptive antenna systems have the potential to allow multiple subscribers to simultaneously use the same frequency band, making efficient utilization of the system bandwidth. In order to predict the performance of such access, knowledge of both time and angle of each arrival in a multipath and multiple interference channel is needed. Some works have begun recently to address the AOA signal distribution in indoor communication channels, and the first of them, using the statistical approach proposed by References [23,24], has found that the AOA distribution of the multipath components of the total signal arriving at the receiver can be accurately described by the Laplacian law [18,22] (see formula (9.46) presented in the previous chapter). In Reference [25], it was found that multipath arrivals tend to occur at various angles indoors. In Reference [26], a data acquisition system was used (which is similar to that of Reference [18,22]) to collect narrowband AOA data and wideband TOA data, but this was done separately without accounting for their joint distribution by measuring simultaneously signal features in the angle and time domains. In Reference [27], the authors used a rectangular antenna array to estimate both elevation and azimuth (or angle-of-arrival, AOA) for major multipaths, but without accounting for the corresponding time-of-arrival of each multipath component of the total signal. Authors in Reference [28] used a rectangular adaptive array to make simultaneous

measurements of angle- and time-of-arrival, similar to what was done in References [18,22]. However, as was mentioned in References [30–31], the experiment carried out in Reference [28] was not extensive enough to make any conclusions about the propagation channel.

To satisfy the recent increasing demand on communication speed and ubiquity for the wireless local area networks (WLANs), wireless private branch exchanger (WPBXs), home phoneline network alliance (HomePNA), as well for Internet and data network applications, new theoretical approaches and more precise experiments were carried out [32–41]. We will discuss only a few of them, which in our opinion give a realistic physical description of the channel. First of all, this is the research started in References [18,22,23], and then continued and completed in Reference [36]. A new statistical model for site-specific radio propagation as a combination of geometrical optics ray tracing description of the propagation phenomena and probabilistic description of processes occurred within a channel may be accounted. This model was proved by high-resolution measurements carried out at 1 GHz in indoor environments, both in the azimuth and time domain. However, all researchers have reported only the fact that the Laplacian angle distribution and Gaussian time distribution are a good match to the experimentally observed multipath components AOA and TOA distributions, without any satisfactory physical explanation as to why these distributions were chosen in favor of the others except that they fit the measured data well. Only in Reference [32], a new statistical wideband spatio-temporal channel model for WLAN system operated at 5 GHz frequency band, a phenomenological qualitative explanation of the effects was done. The authors have divided the situations inside the indoor communication channel into three typical types: line-of-sight (LOS) conditions between terminal antennas, obstructive line-of-sight (OLOS) conditions, in which both direct visibility and multiple reflection and scattering from obstruction occur, and non-line-of-sight (NLOS) conditions. As shown in Reference [32] the a priori assumption concerning the independence between the propagation phenomena in the temporal and spatial domains [18,21–23] is appropriate only under NLOS and OLOS scenarios. In LOS scenarios in indoor environments they must be investigated jointly due to dependency that exists between the spatial-temporal domains.

As was shown in Reference [32], a two-dimensional (2D) joint distribution of AOA–TOA of the signal power can be expressed as a product of marginal AOA and TOA distributions, where the AOA power spectrum is described for NLOS, OLOS, and LOS scenarios by the Laplacian law for clusters, and for arrivals in each cluster by the same Laplacian law for LOS scenario only and by uniformly distributed function over the range of $[0, \ 2\pi]$ for OLOS and NLOS scenarios [32], that is,

$$P_{clust}(\phi) \propto \frac{1}{\sqrt{2}\sigma_\phi} \exp\left\{-\sqrt{2}\frac{|\phi|}{\sigma_\phi}\right\} \tag{10.1a}$$

$$\begin{cases} P_{arrive}(\phi) \propto \dfrac{1}{\sqrt{2}\sigma_\varphi} \exp\left\{-\sqrt{2}\dfrac{|\varphi|}{\sigma_\varphi}\right\}, & \text{LOS} \\[4mm] P_{arrive}(\varphi) \propto \dfrac{1}{2\pi}, & \text{OLOS and NLOS} \end{cases} \tag{10.1b}$$

and TOA spectrum is described by the decayed exponential function for all three scenarios and for clusters and each arrival in clusters [32],

$$\begin{cases} P_{arrive}(\mathrm{T}) \propto \dfrac{1}{\sigma_{\mathrm{T}}} \exp\left\{ -\dfrac{\mathrm{T}}{\sigma_{\mathrm{T}}} \right\} \\[2mm] P_{arrive}(\tau) \propto \dfrac{1}{\sigma_{\tau}} \exp\left\{ -\dfrac{\tau}{\sigma_{\tau}} \right\} \end{cases} \qquad (10.2)$$

Here T and τ are the time-of-arrival, ϕ and φ are the angle-of-arrival, σ_T and σ_τ are the *rms* delay spread, and σ_ϕ and σ_φ are the angle spread for clusters and for each arrival component in clusters, respectively. Furthermore, in Reference [32] the physical concept based on local and distances scatterers effects, and the corresponding geometry based on distribution and density of scatterers surrounding both the terminal antennas, TX and RX (see Fig. 10.4), was proposed to explain a Laplacian shape of clusters AOA distribution at the receiver RX. As depicted in Figure 10.4, according to Reference [32], the RX is surrounded by many local scatterers in its vicinity, reflections from which give rise to a wide spread of AOA in OLOS or NLOS conditions, as shown, according to Reference [32], in Figure 10.5a. Conversely, distance scatterers are located much further away from the RX and reflected paths arriving at the RX are firstly from one particular direction through a much narrower angular spread. If we now assume, following Reference [32], that there are same number of scatterers at both ends of the radio path and each of the scatterers gives rise to the same number of paths, the higher density of paths will be observed at one particular direction (usually a direct vision path) and lower densities at other directions. This effect leads also to a Laplacian distribution with higher occupancies at the center and lower occupancies at the larger angular values, results
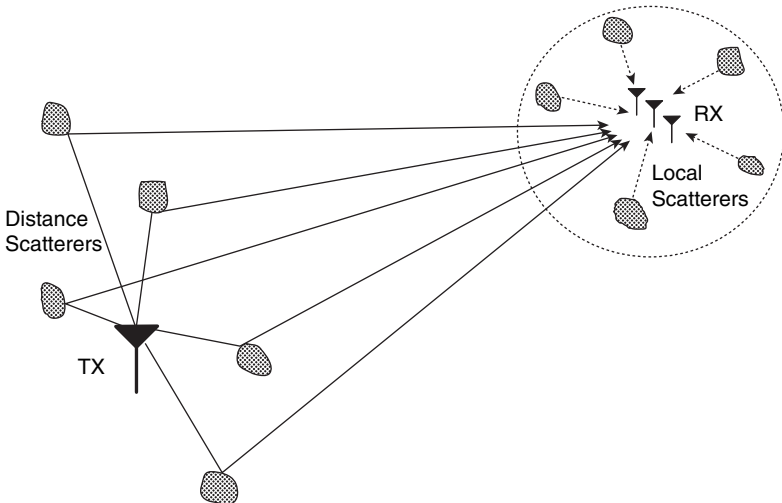
FIGURE 10.4. Geometry of obstructions around the transmitting and receiving antennas.
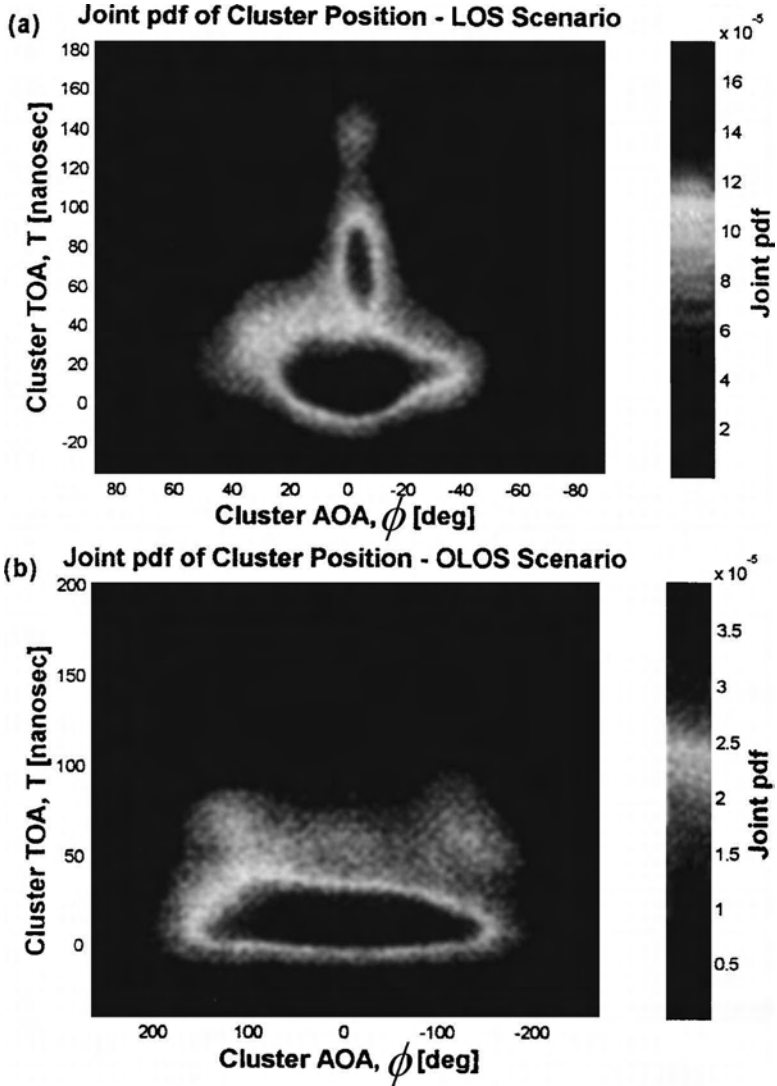
FIGURE 10.5. Joint AOA–TOA distribution obtained during experiments carried in [32]. (Reprinted with permission © 2003 IEEE)

obtained experimentally and shown for LOS conditions in Figure 10.5b, following Reference [32].

The same Laplacian AOA distribution was obtained in Reference [41] by using the elliptical scattering model based on uniformly distributed scatterers in the elliptical regions surrounding the transmitter and the receiver antennas (see Fig. 10.4), and the same obtained in [15,42] for indoor and outdoor communication channels based on geometrical LOS model in the presence of multipath phenomena.

All researchers, however, on the basis of qualitative phenomenological description of the problem without strict account for real obstruction density around antennas, studied the spatial distribution of obstructions, depending on antenna height with respect to building heights, and other features of the built-up terrain. All these features are accounted in the corresponding stochastic multiparametric model developed for outdoor communication channels and can be also converted for indoor communications (see below).

10.2. PREDICTING MODELS FOR OUTDOOR COMMUNICATION CHANNELS

More realistic models for prediction of propagation characteristics in outdoor environments have been developed in References [42–47] based on the unified theory of diffraction (UTD) and ray launching or ray tracing methods using a 3D building data. Here, the terrain can be also taken into account for portions of rays that can go around buildings.

VPL Model. A more general model is described in Reference [46] based on the vertical plane launch (VPL) method. The VPL technique is capable in determining the 3-D ray paths that travel between a transmitter and a receiver influenced by multiple reflections and diffractions. The VPL algorithm uses geographic vector data of buildings and the terrains that are available with a high level of accuracy. Finally, the vertical trajectory of each ray can be calculated analytically determining each ray path in three dimensions. To obtain this 3D picture, both the plane of rays reflected from walls and the vertical plane of rays diffracted from rooftops were taken into account [47]. The temporal and spatial impulse power response of the channel is written in the form [46]:

$$P(\tau, \varphi) = \sum_{m=1}^{M} |A_m|^2 \delta(\tau - \tau_m) \delta(\varphi - \varphi_m) \qquad (10.3)$$

where M is the number of rays arriving at the base station, A_m is the complex amplitude of the mth ray, and τ_m and φ_m are the time delay and the angle-of-arrival of the mth ray respectively. The VPL tool gives the delay, the direction, and the amplitude of each ray propagated between the base station and a mobile. Finally, this tool can also be used to define the delay spread (DS) and the azimuth spread (AS) (i.e., angle-of-arrival spread). More specially, using VPL and the power response definition of (10.3), the DS and AS can be derived as [46]:

$$DS = \sqrt{\frac{\sum |A_m|^2 (\tau_m - \bar{\tau})^2}{\sum |A_m|^2}} \qquad (10.4)$$

$$AS = \frac{180}{\pi} \sqrt{1 - |\bar{v}|^2} \qquad (10.5)$$

where $\bar{\upsilon}$ is the mean vector of direction of arrival and $\bar{\tau}$ is the average delay of the rays arriving from the mobile.

Using Monte-Carlo simulations, based on this site-specific 3D ray tracing code, the *rms* delay spread and the mean time delay have been computed in Reference [46] and compared with experiments carried out at 900 MHz in various built-up areas of Seoul, (Korea), Munich (Germany), and Rosslyn, Virginia (United States). It was shown, both numerically and experimentally, that the delay spread (DS) is different for different built-up areas and depends on the buildings' overlay profile and the statistical distribution of buildings over the terrain. At the same time, the simulation results showed that the cumulative distribution function (CDF) for delay spread is not so sensitive to the building distribution statistics compared to the CDF of azimuth spread (AS). In most cases the azimuth spread was very sensitive to the distribution of building heights and to antenna location with respect to the surrounding buildings. Thus, decreasing the BS antenna height from ∼80 m (i.e., 5 m above the rooftops) to ∼39 m (i.e., when 80% of the buildings are higher than BS) leads to an increase of the median DS from 0.13 to 0.18 μsec, which is not significant, whereas the median AS is increased from 7° to 18°, that is, significantly, approximately a 2.5 factor.

2D Statistical Model of AOA Distribution. A new statistical 2D model taking in account multiple scattering from the obstructions surrounding the terminal antenna was proposed in References [49–51]. This model was a way to find AOA power spectrum distribution for low-resolution antennas.

Figure 10.6 describes a particular situation, where a large number of rays are scattered from a finite area in space and arriving at the antenna. Here, the spatial derivative of the total phase along the array axis is taken as a measure of the sine of the apparent angle-of-arrival (AOA). The PDF and power spectrum of the AOA were determined from the sine of the angle distribution. It is assumed [49–51] that the antenna beamwidth is much larger than an apparent direction of arrival θ, therefore the scattering area can be considered as a point source. A large number of
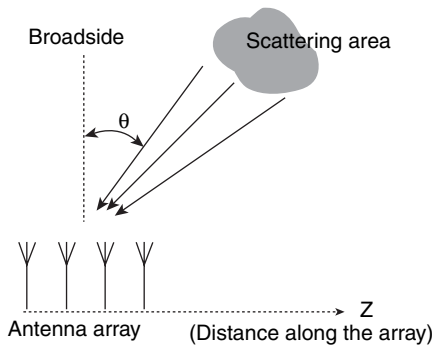
FIGURE 10.6. Scattered rays impinging on the antenna array. (Source [51]: Reprinted with permission © 2002 IEEE)

rays emanating from finite region in space are impinging on the antenna, which has a beamwidth larger than the extent of this region. We also assume that the array depends only on distance z and that the maximum occurs when $\sin \theta = 1$. When the antenna is mechanically rotated or electronically scanned, the total signal at the receiver will be in a form of a weighted sum of all incident rays. The sum will be dependent on the direction of scan and it will vary randomly due to the random amplitudes and phases of the incident rays. For one given position of the transmitter there will be one apparent direction of arrival, but when the transmitter has moved to a new position (or the receiver has moved to a new position) the phases of the incident rays will be changed, and the result is a new apparent direction of arrival. If the signal plane wave is incident on the array from direction θ measured from broadside (see Fig. 10.6), then the common form of the accepted field E can be defined as [49–51]:

$$E = \exp\{jkz \sin \theta\} \tag{10.6}$$

where k is the wave number, and $\varphi = kz \sin \theta$ is the phase that varies linearly with z.

The phase gradient distribution obtained in Reference [49–51] allows, after simple derivations, to accept the desired θ distribution on the basis of phase gradient statistics and to obtain the power spectrum in u-domain:

$$\langle |H|^2 | u \rangle = \frac{s^2}{(u - \bar{u})^2 + s^2} \tag{10.6}$$

where $u = sin\theta$ and $\bar{u}$ and $\overline{u^2}$ are the first and second moments of the average power distribution measured in AOA-space; s is a measure of angular spread:

$$s^2 = \overline{u^2} - \bar{u}^2 \tag{10.7}$$

For a small array, the variation of the phase is close to linear; thus the knowledge of the statistics of the phase gradient is the same knowledge of the distribution of $\sin \theta$, from which we can derive the statistics of θ. For small-angle results, substituting θ instead of $\sin \theta$ in (10.6) gives good results for small angles θ, when $\sin \theta$ limits to the angle θ defined in *radians* [22,23]. Figure 10.7 shows the agreement with results of measurement provided in References [22,23] for a single-element antenna ($N = 1$) and proves the theoretically derived fact that an apparent direction of arrival is actually the instantaneous azimuth direction of signal maximum power [49–51].

Unfortunately, the presented model gives only signal power distribution in the AOA domain. Moreover, this model does not describe the actual situation in the urban scene, because the distribution of power (10.6) does not take into account the actual distribution and density of obstructions around the transmitter and the
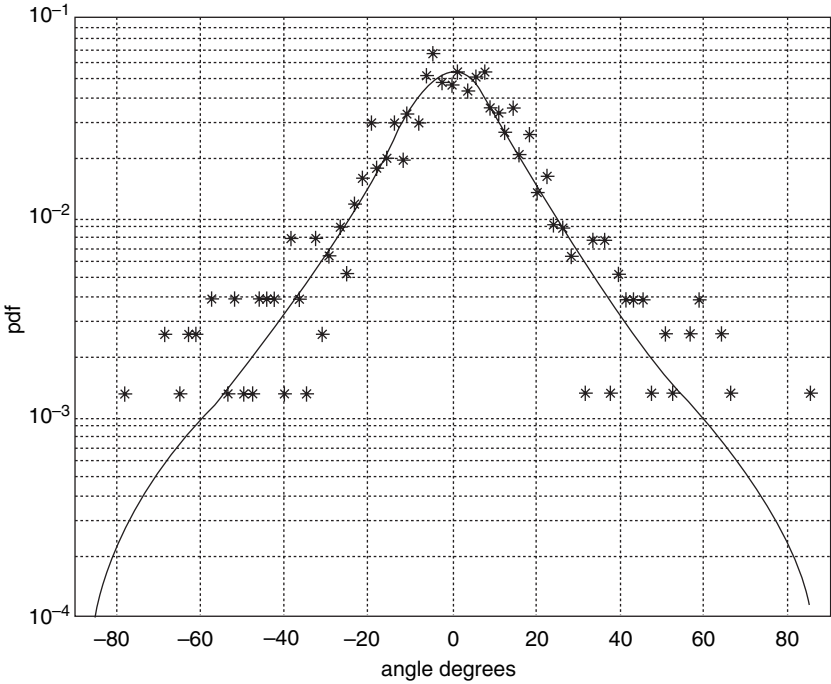
FIGURE 10.7. Distribution of angle-of-arrival obtained in Reference [22,23] compared with computations made for s = 0.3 in Reference [51].

receiver, as well as their positions and heights with respect to the overlay profile of the obstructions.

2D Statistical Approach of AOA and TOA Distribution Prediction. A 2D statistical approach has been proposed in References [4,14,52–54], which is a measurement-based multipath approach of signal angle-of-arrival (or azimuth) (AOA) and delay spread (DS) distribution prediction. This model describes the probability density function (*PDF*) of azimuth and time delay separately, and jointly as well. Moreover, according to this model, different root second central moments must be derived for different area types, so such prediction method becomes inconvenient for predicting propagation characteristics in mixing areas making this concept just like a simple first-order approach for complicated propagation environments. This concept was proposed by References [4,14,52–54], based on the statistical representation of the mobile radio channel. The signal model takes into account a multipath propagation, which can cause several replicas of the transmitted signal at the receiver. The azimuth-delay spread function in these cases, as [4]

$$h(\varphi, \tau) = \sum_{i=1}^{L} \alpha_l \delta(\varphi - \varphi_l, \tau - \tau_l) \tag{10.8}$$

where L is the number of impinging waves from different directions φ_l and with different time delay τ_l, each of them with a complex amplitude α_l. Derivation of the azimuth spread (AS) and delay spread (DS) in Reference [4] is based on the definition of AS and DS as a root second central moment σ_{AS} and σ_{DS} of the azimuth power spectrum $P_{AS}(\varphi)$, and the delay power spectrum $P_{DS}(\tau)$, respectively. Here, $P_{AS}(\varphi)$ and $P_{DS}(\tau)$ are determined as [4,54]

$$P_{AS}(\varphi) = \int P(\varphi, \tau)d\tau \tag{10.9}$$

$$P_{DS}(\tau) = \int P(\varphi, \tau)d\varphi \tag{10.10}$$

and $P(\varphi, \tau)$ is a power azimuth-delay spectrum and according to References is [4,54] defined as

$$P(\varphi, \tau) \propto E\{|\alpha|^2|\varphi, \tau\}f(\varphi, \tau) \tag{10.11}$$

where $E\{|\alpha|^2|\varphi, \tau\}$ is the expected power of the waves conditioned on their azimuth and delay, and $f(\varphi, \tau)$ is a joint probability density function. It was proved in References [4,54] that the azimuth and delay spread distributions are independent, that is,

$$f(\varphi, \tau) = f(\varphi)f(\tau) \tag{10.12}$$

This fact will be used below to obtain a joint PDF for modified stochastic multi-parametric model. Probability density functions $f(\varphi)$ and $f(\tau)$ were derived empirically through the prism of the numerous experiments described in References [4,52–54]. It was found that a Gaussian PDF matches the $f(\varphi)$, and an exponential decaying function is the best fit to the $f(\tau)$. Thus, $f(\varphi)$ and $f(\tau)$ were described as [4,54]

$$f(\varphi) = \frac{1}{\sqrt{2\pi}\sigma_\varphi}\exp\left\{-\frac{\varphi^2}{2\sigma_\varphi^2}\right\} \tag{10.13}$$

$$f(\tau) = \frac{1}{\sigma_\tau}\exp\left\{-\frac{\tau}{\sigma_\tau}\right\} \tag{10.14}$$

where σ_τ and σ_φ are standard deviations of time delay and azimuth distribution, respectively. Different environments were investigated in References [4,52–54]. The probability density function (PDF) of the azimuth and delays were estimated from data measured for different environments. The probability distribution of the model parameters was extracted from experimental data collected during extensive
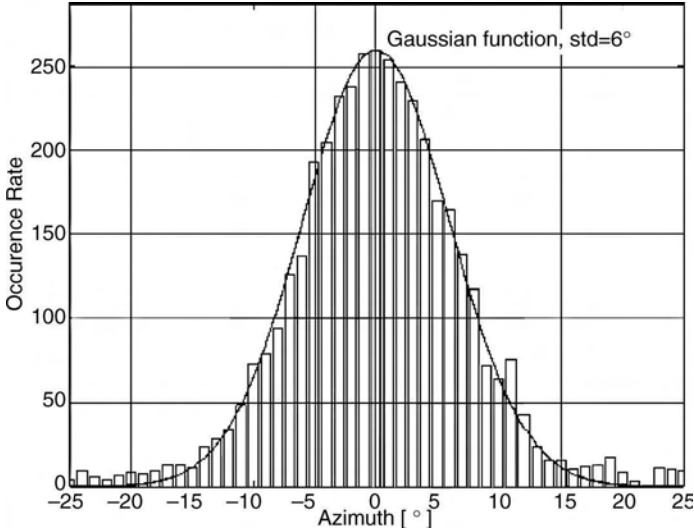
FIGURE 10.8. Histogram of the estimated azimuth with antenna located 12 m above the rooftop level obtained in [4,54]. (Reprinted with permission © 2000, 2002 IEEE)

measurement campaigns in the cities of Aarhus and Aalborg in Denmark, and Stockholm in Sweden. The investigated environments are characterized as macrocellular urban typical (UT) and bad urban (BU) areas. The stochastic model was entirely described by the joint probability distribution of its random parameters. The random variables $(\alpha_l, \tau_l, \varphi_l)$ were assumed to be independent and identically distributed for each wave (with number L). Local realization of the delay azimuth spread function was obtained by combining L waves with random amplitudes, delays, and azimuths.

Figure 10.8 shows a histogram of the power azimuth spread obtained experimentally in the cities of Aarhus and Stockholm according to the References [4,54]. The standard deviation estimated from this experimentally obtained histogram equals $\bar{\sigma} = 6$. The solid curve in Figure 10.8 is a Gaussian function predicted theoretically according to formula (10.13) with the same $\sigma = 6$ like an estimated $\bar{\sigma}$. This Gaussian function provides a best fit for all results. It was also shown both experimentally and theoretically [4,52–54] that the power azimuth spread is increased 40 to 50% when the BS antenna height is decreased 12 m below the rooftop level. From Figure 10.8, the incoming power is highly concentrated around 0° even though the measurement results were obtained in NLOS conditions. At the same time, Figure 10.9 shows a histogram of the PDS obtained experimentally in Aarhus and Stockholm for the power delay spectrum (DS) versus time delay according to References [4,54]. One can see that the exponential function, plotted according to the (10.14), fits well to the histogram. The results presented above relate to the particular urban environment called typical urban (TU), implying uniform density of buildings. Other PDF plot, for bad urban (BU)
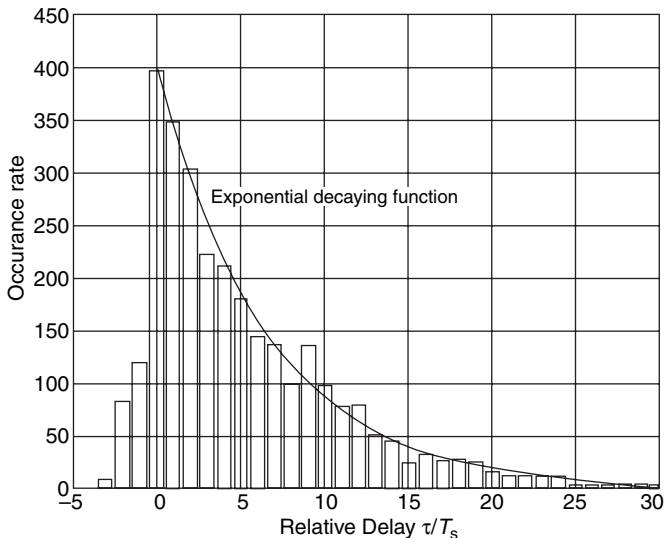
FIGURE 10.9. Relative delay τ/T histogram [4,54]. (Reprinted with permission © 2000, 2002 IEEE)

environment, was also proposed in References [4,54]. In the case of BU channel, the dispersion in the radio channel looks completely different. For the mixture of open area and densely built-up zones the accepted result for time delay distribution is presented in Figure 10.10 [4]. Obviously, the distribution of received signal depends
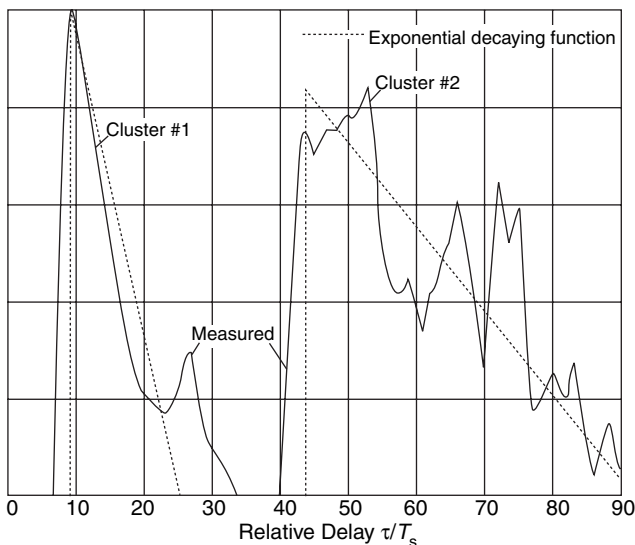
FIGURE 10.10. Relative delay τ/T_s for mixed environment [4,54]. (Reprinted with permission © 2000, 2002 IEEE)

significantly on the types of clusters created along radio paths from the TX to the RX antennas. The authors in References [4,54] describe this time the delay distribution by a two-cluster model, as was done by References [22,23] for indoor environments. The suggestion is to consider the power azimuth-delay spectrum as

$$P(\varphi, \tau) = \sum_{k=1}^{2} P_k(\varphi, \tau) \tag{10.15}$$

where $P_k(\varphi, \tau)$ represents the contribution from each cluster. Situations with more than two clusters may also be described as in (10.15) by summarizing all contributions from all clusters. The disadvantage of the proposed method is the absence of the area dependent unique parameter in the model that adapts the result according to the type of the environment.

Experimental-Based Model. In References [6–10], another approach, which introduces urban propagation mechanism based on high-resolution 3D radio channel measurements, was proposed. This approach analyses the propagation using comprehensive classification of different types of wave propagation in urban scene. This classification defines three propagation classes: Street-guided propagation as a first class (denoted "Class1"), direct propagation (over the rooftops) as a second class (denoted "Class 2"), and scattering from obstructions (reflection from high-rise objects) as a third class (denoted "Class 3"). To define the corresponding channel models, three different series of measurements were carried out in an urban environment. The first case corresponds to situations when the receiving base station antenna is below the rooftop; the second and the third one correspond to situations near the rooftop level and above the rooftop level, respectively. All measurements have been done in the downtown of Helsinki (Finland). A typical experimental site with both terminal antennas located below the rooftop level is presented in Figure 10.11 [9,10]. The resultant joint azimuth-delay spread distribution is shown in Figure 10.12 [9,10]. Figures 10.11 and 10.12 represent the situation when the transmitter (mobile) antenna is at the height of 1.5 m, that is, at the normal street level with NLOS and the receiver (BS) antenna is *below the rooftops*. Obviously a significant number of rays propagates within the street waveguide because of multiple reflections from walls of buildings that lie along the streets. Another arrival mechanism, but not so dominant, is the scattering from the high-rise object (such as the Theatre Tower denoted in Fig. 10.11). From the measurement results, presented in Figure 10.12, more than 80 to 90% of rays arrive at the receiver from two streets. These rays get affected by the guiding effects of the streets, that is, by the multiple reflection from buildings located along the streets. Thus, propagation "Class 1" and "Class 3" are dominant in this urban area according to the urban radio channel propagation classification made in References [9,10]. Class 1 (street-guided propagation) dominates with over 90% of the total power for cases when the receiver (BS) antenna is below or at the same level of the rooftops.
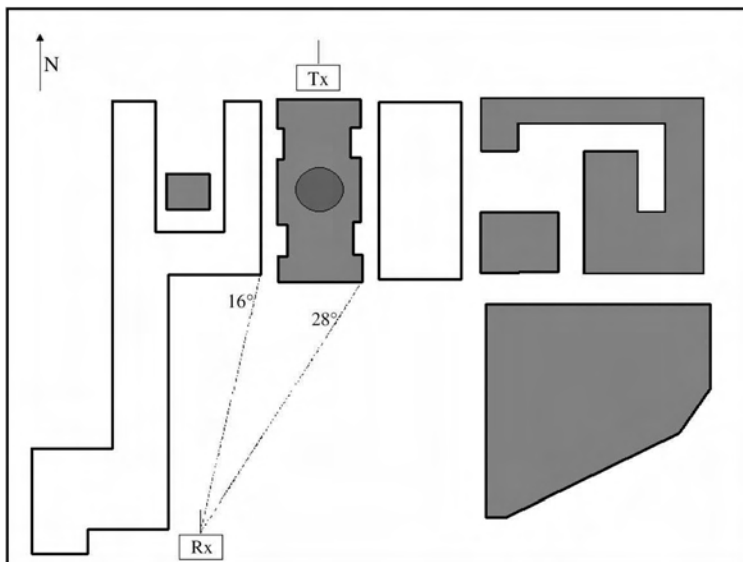
FIGURE 10.11. A typical experimental site in Helsinki [9,10]. (Reprinted with permission © 2002 IEEE)

Another experiment, when the RX antenna is *at the rooftop level* as shown in Figure 10.13, has been carried out under the following conditions: There is no traffic on the streets, the TX antenna kit is at the street ground level (with height of 2 m), and the RX antenna is at the rooftop level (with height of 27 m). Moreover, the 3 dB beamwidth of the TX antenna is of 70° the azimuth and elevation directions. Finally,
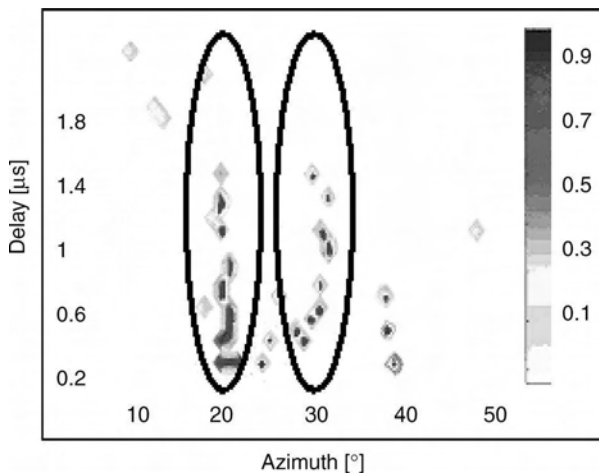
FIGURE 10.12. PDF of joint AOA–TOA distribution measured in References [9,10]. (Reprinted with permission © 2002 IEEE)
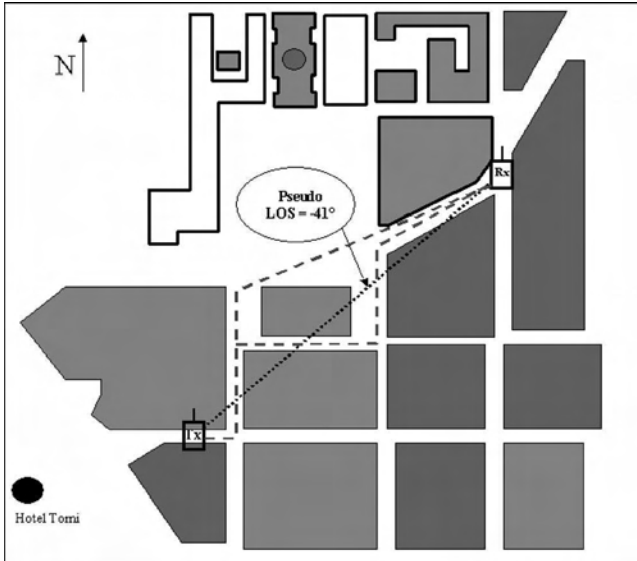
FIGURE 10.13. A microcell urban environment extracted from References [9,10]. (Reprinted with permission © 2002 IEEE)

the RX antenna is omnidirectional in the azimuth and with 87° in the elevation domain. A wideband (100 MHz) channel sounder has been used with the carrier frequency of 2.154 GHz. And no LOS between the TX and RX antennas. A pseudo-LOS distance was set at about 420 m. One wide street is placed at $\varphi = -30°$ from the main lobe of the RX antenna (RX is mounted at 270 degree from the North direction). Figure 10.14 shows the results image of the postprocessed measured data for the area shown in Figure 10.13. It is clear that Class 2 and Class 3 are starting to be significant (25%), but not dominant, for cases where the BS antenna is at the same level or above the average height of rooftops.

Generally speaking, the approach proposed in References [9,10] has demonstrated the strong dependence between the built-up profile seen from the base station and the propagation mechanisms in the corresponding urban areas. It proves that accurate prediction based on advanced simulation tool, incorporating a building geographic database, is needed to achieve network planning. Unfortunately, all the above mentioned theoretical models cannot account for all the built-up terrain features as far as overlay profile, density of buildings and their positions and heights with respect to both terminal antennas. As shown in References [55–62], the multiparametric stochastic approach can account for specific features of different urban areas and for various positions of the terminal antennas. This approach can be used as an actual predictor of AOA and DS signal distribution for various specific situations in the urban communication channel.

2D and 3D Stochastic Multiparametric Models. The realistic statistical 2D and 3D models, which take into account the terrain features, such as the height profile
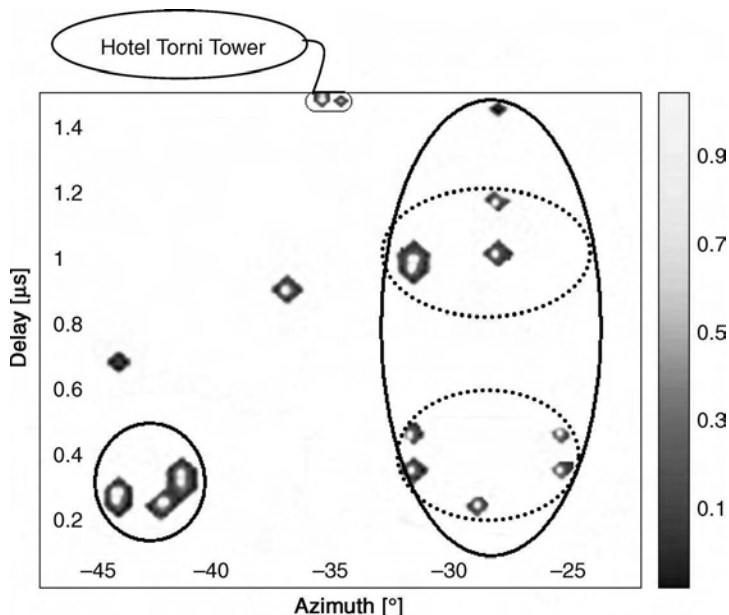
FIGURE 10.14. Measurement results in AOA–TOA plane [9,10]. (Reprinted with permission © 2002 IEEE)

of buildings, their density, and reflection properties, were created in References [55–61]. From Chapter 5, the propagation channel for UHF/X-band waves, in the built-up environment, according to these stochastic models, can be modeled by an array of randomly distributed buildings and/or natural obstacles placed on a rough terrain. The law of distribution of the obstacles is assumed to be a Poisson law and the city's relief is described by introducing the special probability functions. Using the proposed statistical multiparametric model of wave propagation in such an urban channel, the field intensity attenuation can be examined and the single and multiple scattering effects pointed out, taking into account the diffraction from the roofs of the buildings depending on the position of the receiver and transmitter antennas on the rough terrain. Using the unified stochastic approach proposed above, we employ probability theory to directly evaluate the statistical parameters of the channel and deterministic theory to obtain the correlation between the signal spectral characteristics and parameters of an urban propagation channel.

Thus, the power spectrum of a signal in the azimuth domain can be presented at the receiving antenna in the following form [56]:

$$W(\varphi) = \frac{\Gamma \lambda \ell_v \bar{h}}{16\pi^2 [\lambda^2 + (2\pi\ell_v\gamma_0\bar{h})^2] d^3} \{f_1(\varphi) + f_2(\varphi)\} \qquad (10.16)$$

where:

$$f_1(\varphi) = \frac{2z_1^2(\gamma_0 d)^2}{(z_2 + \bar{h})} \frac{\varsigma'(1 - \cos\varphi)}{\bar{h}} \frac{\exp\left[-\gamma_0 d\left(\dfrac{\bar{h}}{z_2} + \dfrac{\varsigma'}{2}\dfrac{(1 + \cos\varphi)}{\left[1 + \dfrac{\gamma_0 d}{2}\left(1 + \dfrac{\bar{h}}{z_2}\right)(1 - \cos\varphi)\right]}\right)\right]}{\left[1 + \dfrac{\gamma_0 d}{2}\left(1 + \dfrac{\bar{h}}{z_2}\right)(1 - \cos\varphi)\right]}$$

(10.17)

$$f_2(\varphi) = \frac{2\bar{h}(\gamma_0 d)}{(z_2 + \bar{h})}\left[1 + \left(\frac{\bar{h}}{z_2}\right)\frac{1 + (k\ell_v \gamma_0 d)^2}{1 + (\gamma_0 \varsigma' d)^2}\right]$$

$$\times \frac{\exp\left[-\gamma_0 d\left(\dfrac{\bar{h}}{z_2} + \dfrac{\varsigma'}{2}\dfrac{(1 + \cos\varphi)}{\left[1 + \dfrac{\gamma_0 d}{2}\left(1 + \dfrac{\bar{h}}{z_2}\right)(1 - \cos\varphi)\right]}\right)\right]}{\left[1 + \dfrac{\gamma_0 d}{2}\left(1 + \dfrac{\bar{h}}{z_2}\right)(1 - \cos\varphi)\right]}$$

(10.18)

Γ is the reflection coefficient from the building surface, ℓ_v is height or width of the segments of the building (window, balcony etc), λ is a wavelength, z_1 is the height of the MS and z_2 is the height of the BS, φ is the angle-of-arrival (i.e., azimuth), $\bar{h}$ is an average height of the building, and d is distance between receiver and transmitter. Also

$$\gamma_0 = 2\langle L\rangle v/\pi$$

(10.19)

where v is the building density (per 1 km^2), $\langle L\rangle$ is the average length of buildings (screens), γ_0 is the density of the contours of the buildings in the horizontal plane $z = 0$. Here, we will not take into account the overlay profile of the buildings, because this terrain feature is not very important for azimuth, time delay, and frequency distribution of the signal power, that is, for 2D stochastic model [55]. Here also a new parameter $\varsigma' = \frac{[(\lambda d/4\pi^3) + (z_2 - \bar{h})^2]^{1/2}}{z_2}$ is introduced [56,57], which accounts for the process of diffraction from buildings, instead of the $\varsigma = \frac{z_2 - \bar{h}}{z_2}$, used in Reference [55], which did not take into consideration any diffraction phenomena.

The expression in (10.16) consists of two main terms f_1 and f_2 (the same as two terms μ_1 and μ_2 in joint PDF (5.163) of space–time distribution of scattered waves, analyzed in Chapter 5). Each of them relates to a different propagation phenomenon. The term f_1 is the significant term that describes the influence of the scattering area located at the proximity of MS. The term f_2 describes the general effect of rare scatterers that are distributed uniformly in areas surrounding the BS and MS. The influence of different scatterers for the three typical cases, depending on the BS antenna height, is sketched in Figure 9.22. When both antennas are lower than the height of the buildings (see Fig. 9.22c), then both components, f_2 and f_1, are actual. From formulas (10.16)–(10.18) follows that, if the base station antenna height

increases up to $z_2 = \bar{h}$ (see Fig. 9.22b), then $\varsigma' = \sqrt{(\lambda d/4\pi^3)}/z_2 \ll 1$ and $f_1(\varphi) \to 0$, $f_2(\varphi)_{z_2=h} > f_1(\varphi)_{z_2=h}$. In the case of $z_2 = \bar{h}$, f_1 is close to zero, and it means that all scatterers located in the far zone from the MS, near the BS, will influence the spreading of the total signal at the BS. With an increase in the height of the BS antenna, that is, $z_2 > \bar{h}$, the influence of buildings surrounding the MS on the total signal distribution will be more significant, and f_1 becomes larger than f_2, describing the effect of scatterers located close to the MS (see Fig. 9.22a). When the BS antenna is above the rooftop level (Fig. 9.22a), the spectrum distribution in the azimuth domain $W(\varphi)$ depends only on the position and the distribution of scatterers (obstructions) close to MS. Influence of scatterers (buildings) in the proximity of MS on the signal received at the MS is increased and it contributes more than the scatterers surrounding the BS (Fig. 9.22b) and than those located far from the MS.

The signal power spectrum distribution in time delay domain can be obtained in the same manner [56]:

$$W(\tau) = \frac{\Gamma}{8\pi^2 d^2} \frac{k\ell_v\gamma_0\bar{h}}{1+(k\ell_v\gamma_0\bar{h})^2} \left\{ (1-\varsigma') \left[1 + (1-\varsigma')^2 \frac{1+(k\ell_v\gamma_0\bar{h})^2}{1+(\varsigma'\gamma_0\bar{h})^2} \right] f_1(\tau) + \frac{\varsigma'}{(1-\varsigma')} f_2(\tau) \right\}$$

(10.20)

where

$$f_1(\tau) = \frac{(\gamma_0 d)^2 \sqrt{\tau^2-1}}{4\tau^2} \exp\left\{ -\gamma_0\tau \frac{(2-\varsigma')}{2} d \right\} I_0\left(\frac{\gamma_0\varsigma'd}{2} \right) \qquad (10.21a)$$

$$f_2(\tau) = \frac{\gamma_0 d}{2} \exp\left\{ -\frac{\gamma_0\tau d}{2} \right\} \left[\exp\left\{ -\frac{\gamma_0\tau d}{2} \right\} + \frac{\sqrt{\tau-1}}{\sqrt{\tau+1}} I_0\left(\frac{\gamma_0 d}{2} \right) \right] \qquad (10.21b)$$

Here, we introduce the relationships between $\tilde{r}, r, d$, and relative time τ of signal arrival (i.e., with respect to that of LOS component),

$$\tau = \frac{(r+\tilde{r})}{d}, \quad r(\tau, \varphi) = \frac{d(\tau^2-1)}{2(\tau-\cos\varphi)}, \quad \tilde{r}(\tau, \varphi) = \frac{d(\tau^2-2\tau\cos\varphi+1)}{2(\tau-\cos\varphi)} \quad (10.22)$$

where $\tilde{r} = (d^2 + r^2 - 2rd\cos\varphi)^{1/2}$, $\bar{h}$ is an average building height, and φ is azimuth.

In the time delay plane, the same properties of the signal power spectrum, as was done for the azimuth plane, can be obtained. Thus, in the case of $z_2 \leq \bar{h}$,

$$\frac{\varsigma'}{(1-\varsigma')} f_2(\tau) \gg \left[1 + \frac{1+(k\ell_v\gamma_0\bar{h})^2}{1+(\varsigma'\gamma_0\bar{h})^2} \right] f_1(\tau) \qquad (10.23a)$$

and the distribution of scatterers far from the BS antenna, that is, close to the MS antenna (see Fig. 9.22a), does not influence on a power spectrum $W(\tau)$ in the time

delay domain. Then, with a height increase of the receiver antenna (when $z_2 > \bar{h}$, $\varsigma' > 1$), the main contribution follows from the first term with $f_1(\tau)$ that really describes the influence of the neighboring area around the MS. In this case, condition (10.23a) must be rewritten as

$$\frac{\varsigma'}{(1-\varsigma')} f_2(\tau) \ll \left[1 + \frac{1 + (k\ell_v \gamma_0 \bar{h})^2}{1 + (\varsigma' \gamma_0 \bar{h})^2} \right] f_1(\tau) \qquad (10.23b)$$

We also note that the function $f_2(\tau)$ does not depend on parameter ς', that is, on the receiving antenna's height with respect to the rooftops. Therefore, for $\varsigma' > 0.3$ the form of the power spectrum versus time delay becomes practically constant value.

So, the proposed 3D stochastic model based on the general formulas (10.16)–(10.22), gives more realistic description of the propagation phenomena with respect to 2D model obtained in Reference [55] (see results of comparison between theoretical prediction and experimental data described in References [57,58]). Generally speaking, the 3D model [56,57] covers the 2D model [55] in the case where base station antenna is located near or above the building profile height, and where the effects of diffraction from rooftops are more realistic. When the BS antenna is smaller than the building profile height, both the models, the 2D and 3D can be used, but the latter gives more precise results. Moreover, this model can be used to describe street effects found in high-sensitive experiments carried out in Helsinki and described in References [9,10]. The results of these experiments were presented in Figures 10.12 and 10.14. This "guide" effects were defined in References [9,10] as a "Class 1" of propagation phenomenon. We now will prove this statement by combining the stochastic and waveguide models, which were briefly described in Chapter 5 and more in detail in References [62,63].

3D Stochastic Model Accounting Straight Crossing-Street Grid. There are two distributions of particular interest here. The *first* distribution is $\mu(r, \varphi)$ and it gives distribution of multiple scattered waves in the AOA and TOA domains, that is, it describes the general spatial distribution of scatterers. A joint (spatial–temporal) distribution of waves $\mu(\mathbf{r}, \varphi)$ can be arranged as a joint angle-of-arrival (AOA) and time-of-arrival (TOA) distribution, $\mu(\tau, \varphi)$, which for $\gamma_0 r \gg 1$ and in the case of $z_1 < \bar{h} < z_2$ can be presented as follows [56,62,63]:

$$\mu(\tau,\varphi) = \mu_1 + \mu_2 = 0.5v\sin^2(\alpha/2)\left\{ \gamma_0\bar{h}\frac{d^2(\tau^3 - \tau)}{2(\tau - \cos\varphi)} \right\} f_1(\tau,\varphi)$$
$$+ 0.5v\sin^2(\alpha/2)\left\{ (z_2 - \bar{h})\frac{d(\tau^2 - 2\tau\cos\varphi + 1)}{2(\tau - \cos\varphi)} f_2(\tau,\varphi) \right\} \qquad (10.24a)$$

For the case of $z_1 < \bar{h}$, and $z_2 < \bar{h}$ formula (10.24a) can be reduced as [56,62,63]:

$$\mu(\tau,\varphi) = 0.5v\gamma_0\sin^2(\alpha/2)\tau d\exp\{-\gamma_0\tau d\} \qquad (10.24b)$$

Here

$$f_1(\tau, \varphi) = \exp\left[-\gamma_0 \left(\frac{d\tau^2(z_2 + \bar{h}) - 2d\tau z_2 \cos\varphi + d(z_2 - \bar{h})}{2z_2(\tau - \cos\varphi)}\right)\right]\Big/ z_2 \quad (10.25a)$$

$$f_2(\tau, \varphi) = \exp\left[-\gamma_0 \frac{d(\tau^2 - 2\tau\cos\varphi + 1)}{2(\tau - \cos\varphi)}\right]\Big/ \bar{h} \quad (10.25b)$$

where, as before, φ is the angle of multipath components of the total field in the horizontal plane (i.e., azimuth) arriving at the receiver after multiple scattering from the buildings surrounding both the transmitter and the receiver, and α is the angle between lines to the receiver and to the transmitter. All other parameters are defined the same way as in formulas (10.16)–(10.18). Here, we only change the BS station antenna height from z_1 to z_2 to obtain the same results as before. The above expression consists of two main terms μ_1 and μ_2. Each one relates to a different propagation phenomenon depending on situation with BS antenna height with respect to overlay profile of the buildings (see Fig. 9.22, Chapter 9). In fact, because $\mu(\tau, \varphi)$ is a normalized signal power distribution in the AOA and TOA plane, its main terms μ_1 and μ_2 give the same effects as f_1 and f_2 in (10.16) and in (10.20), with a change in the BS antenna height, as was shown in Figure 9.22.

The *second* distribution function is $\mu(r)_{wg}$ that describes a probability of the wave mode existence caused by a multislit street waveguide at distance r from the transmitter. The PDF, $\mu(r)_{wg}$, is shown in Figure 10.15. We assume that the angle φ
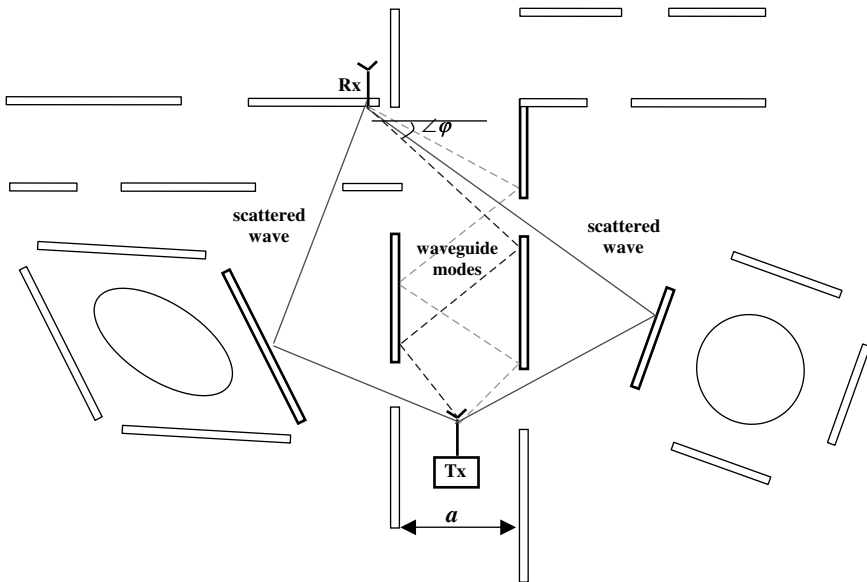
FIGURE 10.15. 2D model of the street waveguide effects and scattering caused by a spatial random building distribution.

takes discrete values with a resolution of degrees. Finally, we get according to References [62,63]

$$\mu(r, \varphi)_{wg} = \exp\left[-2\frac{|\ln \chi|}{a'(\varphi)}r\right] \tag{10.26}$$

Here, $\chi = \frac{\langle L \rangle}{\langle L \rangle + \langle l \rangle}$ is a brokenness parameter, a is the street width, $\langle L \rangle$ and $\langle l \rangle$ are the average length of screens (nontransparent buildings lining the street) and slits (gaps between buildings and intersections of streets), r is the BS–MS distance. The definitions of $a'(\varphi)$ will be presented below. Let us examine the correlation between $\mu(r, \varphi)$ and $\mu(r, \varphi)_{wg}$. These two functions are strongly independent, because they describe two different physical phenomena. The first, $\mu(r, \varphi)$ relates to the random distribution of buildings, as scatterers that are placed around both terminal antennas, and the second, $\mu(r, \varphi)_{wg}$, relates to the scatterers that lie along the streets and mainly contribute to the guiding effect (see Fig. 10.15). Then the completed form of the joint AOA and TOA distribution of scatters can be written as

$$\mu_f = \mu(r, \varphi)\mu(r, \varphi)_{wg} \tag{10.27}$$

Substituting the appropriate function for $\mu(r, \varphi)$ and $\mu(r, \varphi)_{wg}$, we can rewrite (10.27) in the extended form by accepting the density function of all single scatterers as a function of φ and τ [62,63]

$$\mu_f(\tau, \varphi) = 0.5\gamma_0 v \sin^2(\alpha/2)\tau d \exp\{-\gamma_0\tau d\} \exp\left[-2\frac{|\ln \chi|}{a'(\varphi)}\frac{d(\tau^2 - 1)}{2(\tau - \cos \varphi)}\right] \tag{10.28}$$

Equation (10.28) is valid for the typical urban situation when both, the receiver and transmitter, are placed below the rooftop level. Here $a' = \sqrt{\frac{4a^4}{\lambda^2 n^2} + a^2}$, where a is the street width and n is the number of reflections from walls (number of waveguide modes). For $a > \lambda$, we have that $a' = \frac{2a^2}{\lambda n}$. For distances far from the source, only the main waveguide mode (with $n = 1$) propagates without any attenuation within the street waveguide, as shown in references [58,62]. This result was accounted in References [58,62] during numerical simulation of (10.26) and in comparison with experimental data obtained in built-up areas with straight crossing grid-plan streets (as Manhattan street-grid).

We define the discrete spectrum of the total signal power within a broken waveguide taking into account the geometry presented in Figure 10.15, as [62,63]

$$W_{wg}(\tau, \varphi) = W_0 \frac{2(\tau - \cos \varphi)}{d(\tau^2 - 1)} \exp\left[-2\frac{|\ln \chi|}{a'(\varphi)}\frac{d(\tau^2 - 1)}{2(\tau - \cos \varphi)}\right] \tag{10.29}$$

where W_0 is a signal power of the antenna in the direction of direct visibility (LOS component). Now to find the total signal power distribution, in time and azimuth domains, and to account for guiding street effects, we need to combine formulas (10.29), (10.16), and (10.20). That leads to

$$W_{\text{fin}}(\varphi, \tau) = W(\varphi)W(\tau)W(\varphi, \tau)_{wg} \tag{10.30}$$

to determine the joint 2D distribution in the angle-of-arrival (AOA) and time delay (TD) domains, respectively.

10.3. EXPERIMENTAL VERIFICATION OF SIGNAL POWER DISTRIBUTION IN AZIMUTH, ELEVATION, AND TIME DELAY DOMAINS

Let us now verify a general stochastic model introduced as a combination of regular and non regular distribution of buildings and streets in the city, using the experimental data obtained during the measurement campaign carried out in different urban environments.

AOA–TOA Measurement Results Affected by Antenna Pattern. In experiments carried out in the downtown Helsinki [9,10], a wide band single-channel sounder with RF-switch has been used to perform spatial channel measure. Built-up environment around the experimental area is shown in Figure 10.11 for the cases when the BS antenna is *below than building rooftops*. The receiving antenna is installed on the rooftop level (left low corner on the map). The transmitting antenna is placed in such a way that there is no LOS between the receiver and the transmitter (TX11 position in Fig. 10.11). Parameters of built-up terrain have been calculated on the basis of detailed maps shown in Figure 10.11. The results of simulation based on a new model described by general formula (10.28) are shown in Figure 10.16. They repeat
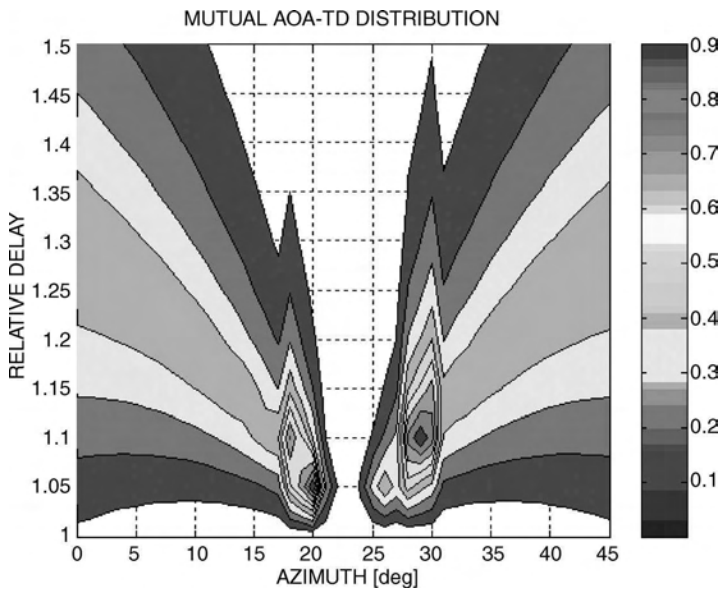
FIGURE 10.16. Simulation results of the multiparametric model that takes into consideration the guiding street effects: The antenna is below the rooftop level.
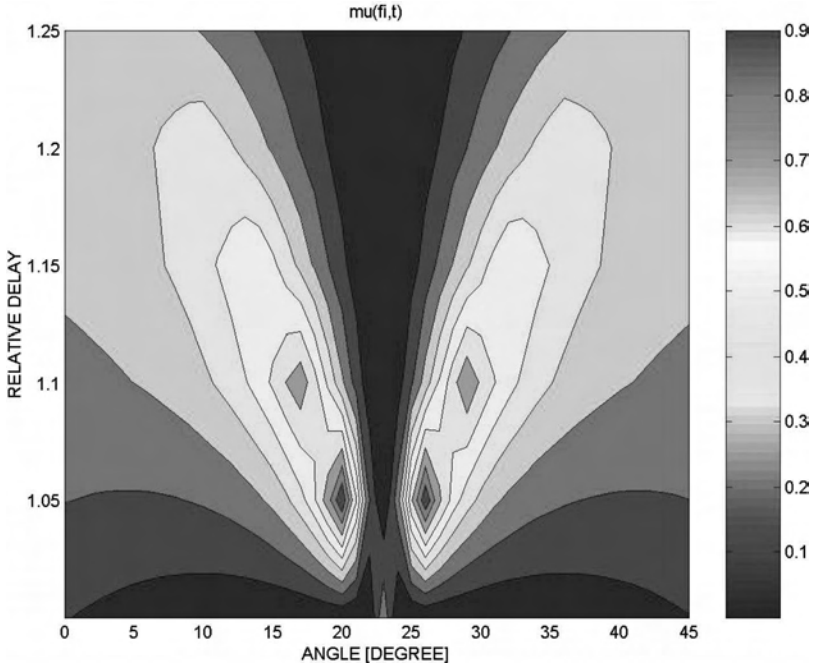
FIGURE 10.17. Simulation results of the multiparametric model only.

the results of measurements of area shown in Figure 10.11, which are presented in Figure 10.12. The guiding effect of two streets shown in Figure 10.12 is clearly seen from both measured data and results of computations. A model strictly predicts the maximum and the distribution of signal AOA as well as TOA distributions. At the same time, results obtained according to pure stochastic model, described by (10.24) (see Fig. 10.17), are not in the precise agreement with the measured data seen in Figure 10.12.

The same results were obtained by the computation of joint signal power spectrum distribution in the AOA–TD plane, defined by (10.30), where combination of pure stochastic and pure waveguide models were taken into account. The results of numerical simulation for the experimental site depicted in Figure 10.11 are shown in Figure 10.18a and Figure 10.18b for 2D-case and 3D-case, respectively. The illustrations of numerical computations, presented by these figures also showed that the influence of scatterers surrounding LOS direction is more significant (see Fig. 10.11) on the received field distribution than the direct LOS arrivals (called *pseudo-LOS* components). Nevertheless, all Figures, 10.16 and 10.18a,b, show that despite the fact that the dominant number of rays (more than 80%) arrive with the guiding effect of streets, there are number of arrivals (about 15–20%), which are coming from different directions with symmetry to the pseudo-LOS azimuth. In addition, the maximal number of arrivals has minimal time delay and is coming closest to the pseudo-LOS direction street canyons. This result is clearly understood
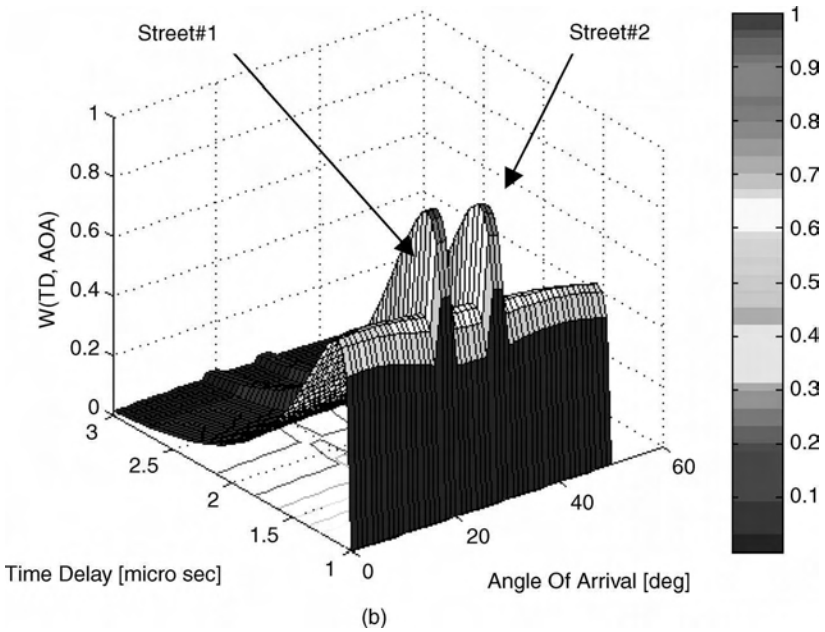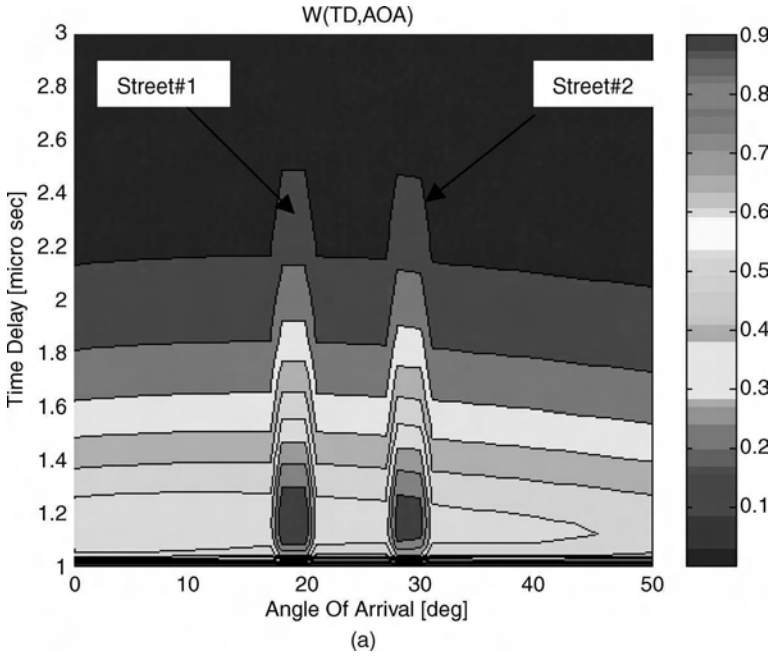
FIGURE 10.18. The simulated power spectrum, $W(\tau, \varphi)$, (a) in 2D (b) and 3D planes.
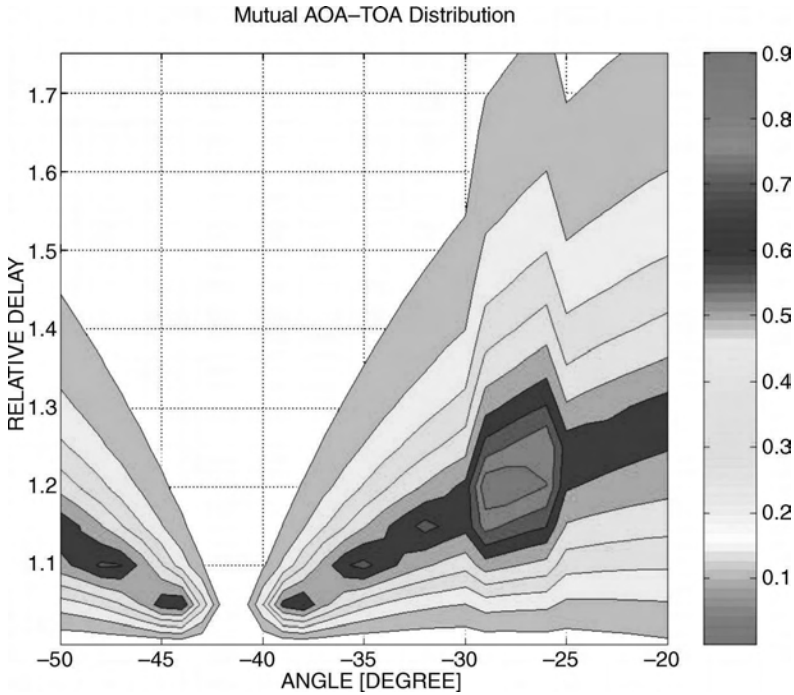
FIGURE 10.19. Simulation results: The antenna is at the rooftop level.

through the analysis of formulas (10.28) and (10.30) for the cases where TX and RX antennas are below the rooftop level.

Let us now describe the second experiment depicted in Figure 10.13, where a BS antenna is located *at the same level as the rooftops*. Figure 10.19 shows the result image of simulations of joint PDF of AOA–TOA distribution according to formula (10.28) for the case of the experiment presented in Figure 10.13. Figures 10.20a and 10.20b show results of computations of joint AOA–TOA signal power spectrum distribution according to formula (10.30) for 2D-plane and 3D-plane, respectively. Once again, a good agreement between measured data presented by Figure 10.14 and simulation results is observed. It was also obtained on the basis of results of simulation, that the number of scatterers, influencing on the number of arrivals from TX direction, exponentially reduces with increase of azimuth and time delay. This result was obtained experimentally in References [1,4,8,9–11,20] without any satisfactory theoretical explanation of the influence of urban street orientation on the results of field distribution at the receiver.

At the same time, we must note here that the proposed modified stochastic model described by (10.28) and (10.30), presented only in the azimuth plane, cannot show properly two groups of arrivals as in Figure 10.14, which are characterized by common azimuth range from $-25°$ to $-30°$ and different time delay (see
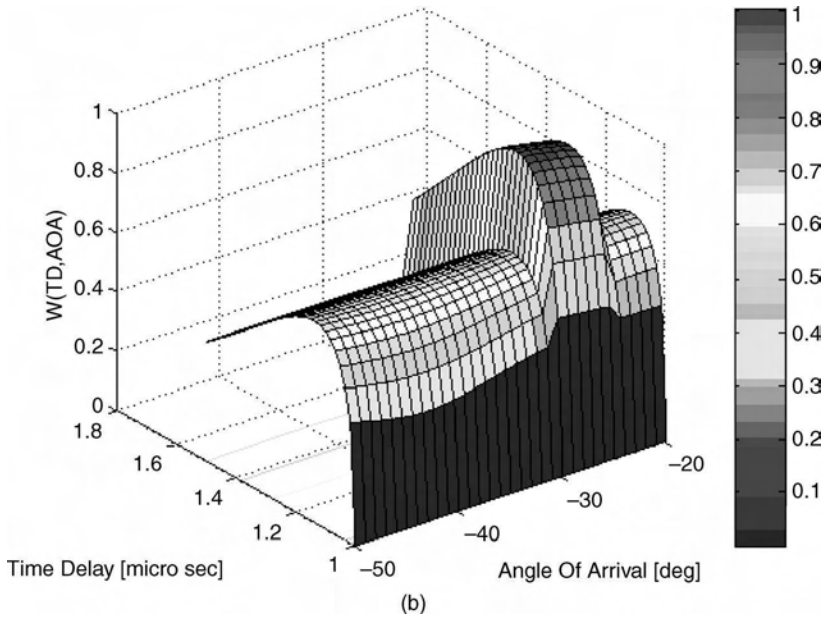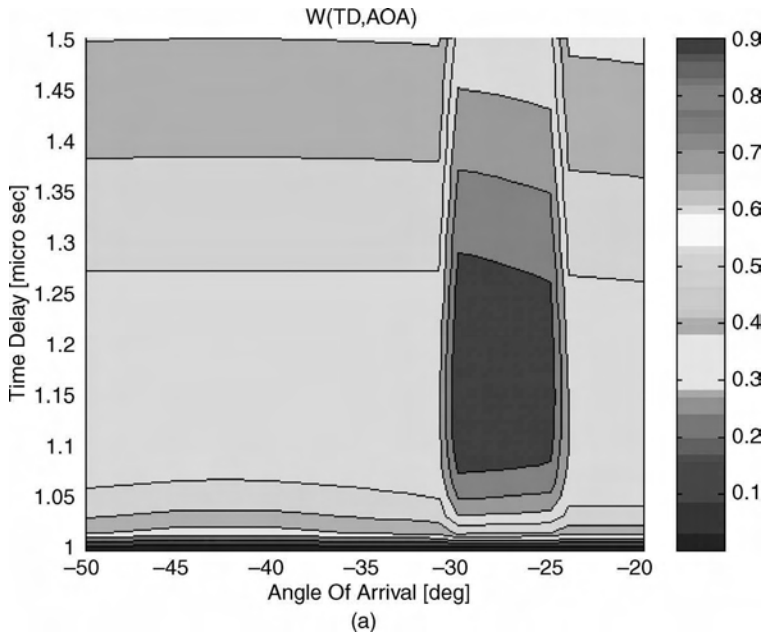
FIGURE 10.20. The simulated power spectrum, $W(\tau, \varphi)$, (a) in 2D (b) and 3D planes.

* The model does not describe sharp fluctuation at elevation domain
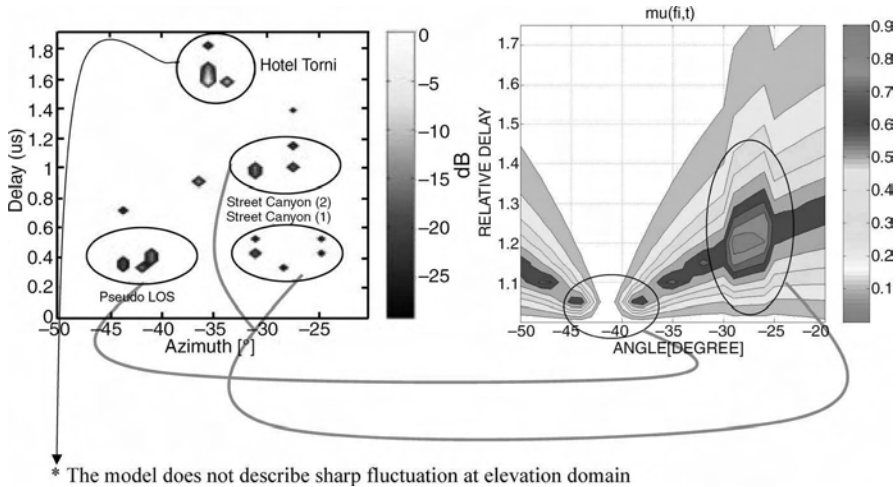
FIGURE 10.21. Comparison with experiments in References [9,10].

comparison theory with experiment shown in Fig. 10.21). Each of the two groups describes different ray travel distance, when all arrivals in the group have the same route. Our model takes in to account consolidation of arrivals across the waveguides, assuming straight-crossing-street-grid plan. The urban scene, presented in Figure 10.13, does not support our basic assumption completely, and that is the reason for the differences mentioned above. Using only azimuth plane, the proposed model cannot describe sharp fluctuations at elevation domain. Owing to this reason, we cannot see matching for the arrivals from the high tower (Hotel Torni), which is measured in [9,10] and presented in Figure 10.21. The reason is due to our basic assumption that the building height distribution is homogenous between h_1 and h_2, which are the minimum and maximum building heights in the area of investigation. Therefore we start now to investigate signal distribution in the elevation plane, following results obtained in References [61–63].

AOA–EOA Measurement Results Affected by Antenna Pattern. When we consider a smart antenna, it is important to understand that we deal with a directional, and not with omnidirectional or isotropic antenna radiation pattern. Scanning the literature, we have found that the well-known von Mises probability density function (PDF) satisfies our requirements to describe the behavior of the directional antenna. Von Mises introduced this PDF in 1918 to study the deviations of measured atomic weights [64,65]. Recently, this distribution was introduced for statistical modeling and analysis of angular variables [62,63]. We analyzed all antenna directivity and tilt effects by assuming a priori omnidirectional antenna pattern in the angle-of-arrival (AOA) or domain azimuth and a variable antenna pattern, according to von Mises distribution, in the elevation-of-arrival (EOA) domain.

Let the variable θ represent the elevation angle and β represent antenna tilt ($\beta < 0$ corresponds to the direction of tilt downward, $\beta > 0$ is for the direction of tilt
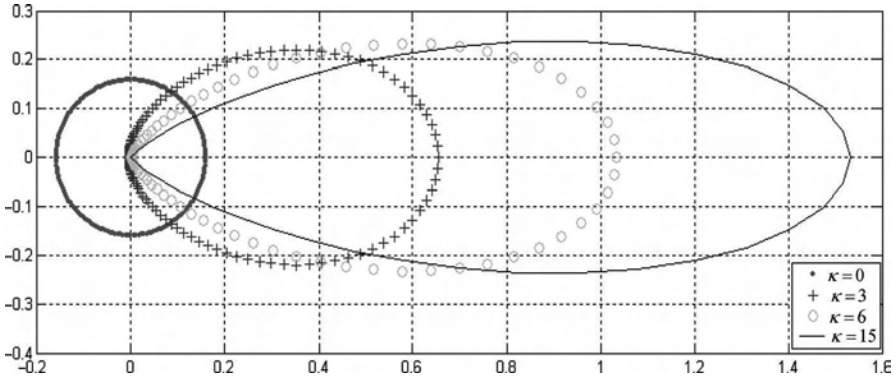
FIGURE 10.22. The von Mises PDF for different antenna directivities.

upward). The von Mises distribution is defined as [63–65]

$$p(\theta) = \frac{1}{2\pi I_0(\kappa)} \exp[\kappa \cos(\theta - \beta)] \tag{10.31}$$

where $I_0(\kappa)$ is the zero-order modified Bessel function, and κ can be regarded as an antenna directivity parameter. Particularly, the antenna directivity κ is one of the basic antenna parameters, and it was defined in Chapter 2. This general idea of antenna pattern introduced by von Mises PDF, is presented in Figure 10.22. The solid thick line relates to the omnidirectional isotropic pattern in the vertical domain with $\kappa = 0$ value; the $(+)$, (o) and the thin solid lines relates to $\kappa = 3$, $\kappa = 6$ and $\kappa = 15$ values, respectively.

It is obvious that various antenna patterns influence, in different manner, the AOA and TOA signal distribution at the receiver. To reflect this influence let us examine the PDF, $p(\theta)$, from (10.31) and the PDF, $\mu_{fin}(\tau, \varphi)$, from (10.28). These two distributions are independent, as was shown in References [62,63], therefore their product can be written as

$$\mu_{total}(\tau, \varphi, \theta) = \mu_{fin}(\tau, \varphi) \cdot p(\theta) \tag{10.32}$$

The obtained formula (10.32) is a general description of the adaptive antenna pattern in both the vertical and horizontal planes and fully present the AOA, EOA and TOA distribution of signal affected by the array of obstructions surrounding the BS–MS terminal antennas.

The corresponding signal intensity distribution in the EOA domain can be easily obtained taking into account the same derivation algorithm as was done for AOA and TOA domains, accounting for their mutual independency. Following the same procedure of derivation mentioned in References [56,63], we get

$$W(\theta) = \frac{W_0}{2\pi I_0(\kappa)} \exp[\kappa \cos(\theta - \beta)] \tag{10.33}$$
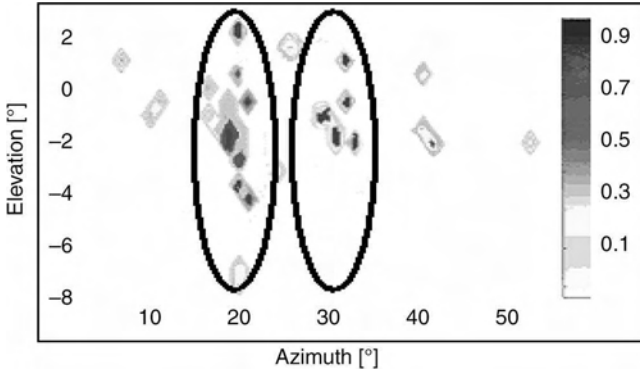
FIGURE 10.23. Measurement results: The antenna is below the rooftop level (AOA–EOA).

where, as above, W_0 is the signal power of the isotropic antenna in LOS conditions. Formula (10.33), combined with (10.16) or with (10.20), describes the joint signal power spectrum in AOA–EOA and EOA–TD plane, respectively.

The results of joint AOA–EOA distribution measured in the urban scene, depicted in Figure 10.11, are presented in Figure 10.23. It was measured that the arrivals were coming homogeneously over elevation angles of $-4°$ to $+2°$ with concentration of rays near the street canyons caused by guiding effect. Figure 10.24 shows results of simulation of the general PDF (10.31) and Figures 10.25a and 10.25b show results
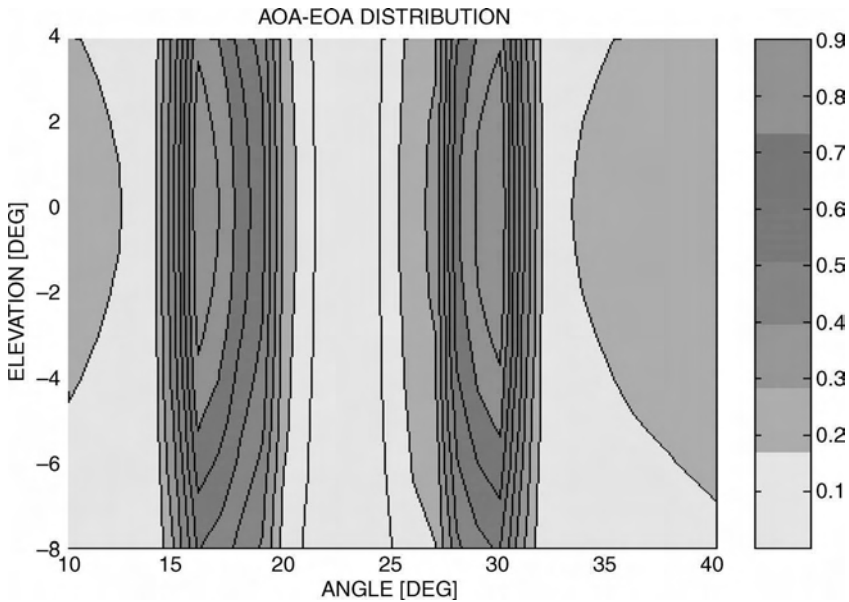
FIGURE 10.24. Simulation results of the joint PDF of AOA–EOA distribution.
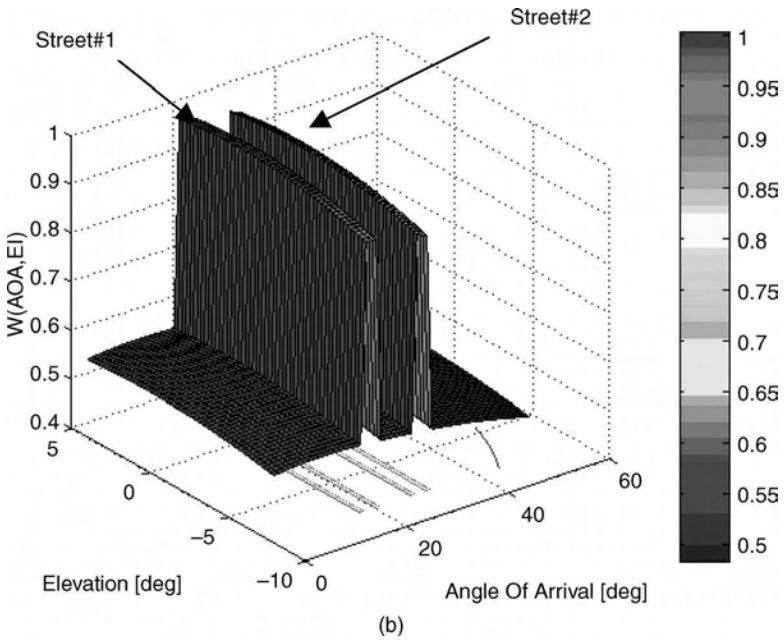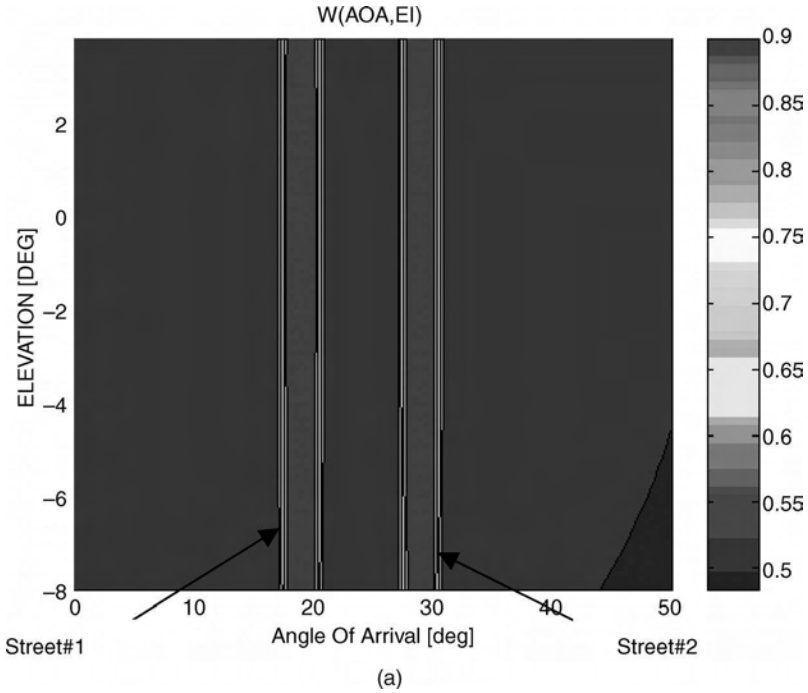
FIGURE 10.25. The simulated power spectrum, $W(\theta, \varphi)$, (a) in 2D (b) and 3D planes.

of simulation of the total signal power spectrum, as combination of (10.33) and (10.16), in the AOA–EOA plane for the urban experiment scenario depicted in Figure 10.11.

As above for AOA–TOA joint distribution, here we also obtained an agreement between measurement and simulation results in the AOA–EOA plane. Simulation results as well as experimental data show the guiding effect from two parallel streets presented in Figures 10.11 and 10.12. Furthermore, they show that the maximum number of arrivals is concentrated around zero elevation angles. This result explains the over-rooftop-propagation effect observed during experiments (see Fig. 10.23 and [9,10]). It means that the buildings, which are placed in close proximity to the receiver (RX), define the elevation angles-of-arrival at the RX antenna. In addition, a significant number of arrivals spread around elevation angle of zero, when there is the guiding effect at the azimuth domain. This result explains the multiple reflections of rays passing through the street canyon. So, we can fully explain the guiding effect of streets and concentration of rays near the elevation angles of zero by using a modified stochastic approach which combines the two models, the multiparametric and waveguide, by using corresponding combinations of formulas (10.16), (10.20), (10.28), (10.30), and (10.33), depending on what plane, azimuth, elevation or time delay we need to investigate.

Better results of measurements of joint AOA–EOA distributions were obtained in the experimental site, where antenna was located at the rooftop level (see Fig. 10.13). Thus, results of measurements of joint AOA–EOA signal power distribution are shown in Figure 10.26. The corresponding simulations of joint PDF of AOA–EOA distribution and those for normalized signal power (to signal power
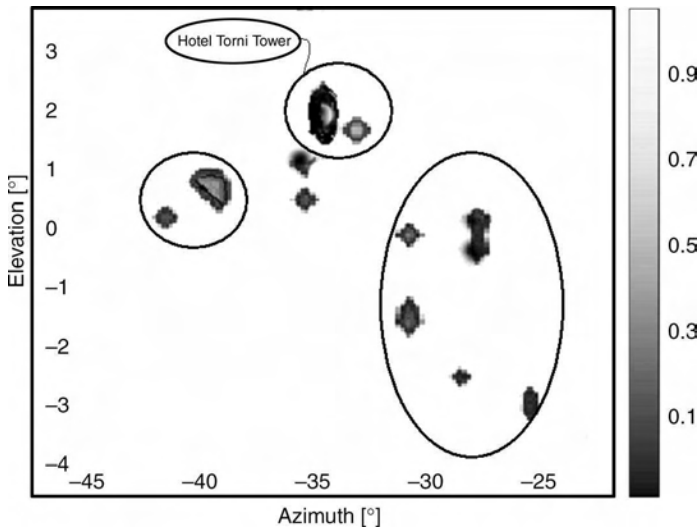
FIGURE 10.26. Measurement data in the AOA–EOA plane [9,10]. (Reprinted with permission © 2002 IEEE
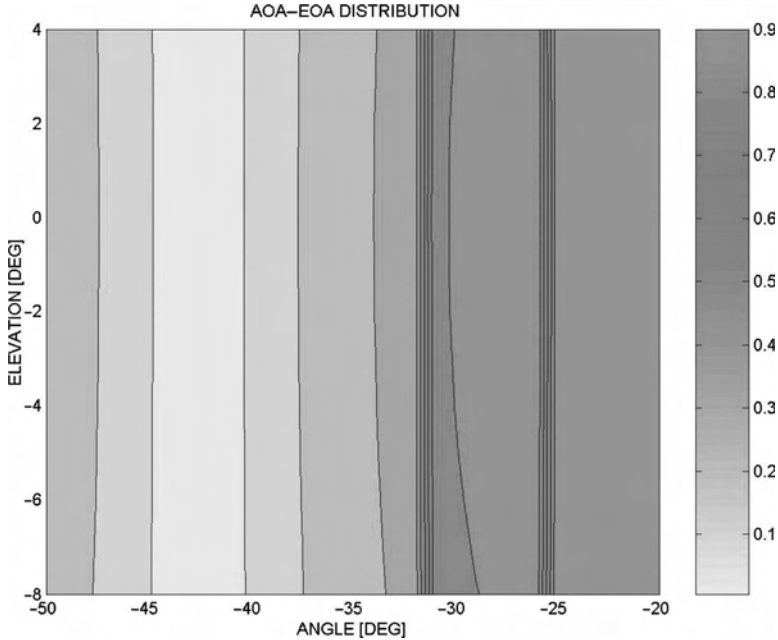
FIGURE 10.27. Joint PDF distribution in AOA–EOA plane.

along LOS direction) are presented in Figure 10.27, and Figures 10.28a (2D-case) and 10.28b (3D-case), respectively. These results explain the over-rooftop propagation (in our examples RX antenna is at the rooftop level) experimentally observed in References [9,10]. It means that the light of the buildings, which are placed in the closest receiver area, define the elevation angles of the arrival at the RX antenna. In addition, a significant number of arrivals spread around the elevation angle of zero are observed, when there is the guiding effect in the azimuth domain. The guiding effect may be explained by the multiple reflections of rays passing through the street canyon, as observed in References [9,10]. It is clearly seen from Figures 10.28a and 10.28b that the main signal energy arrives at the receiver after diffraction caused by the right-side buildings (with respect to TX), localized at the azimuth range of $-20°-30°$ (for the range of elevation angles of $0°\pm10°$). These results are in good agreement with measurements [9,10], according to which the effects of diffraction from the building blocks located in the right side (from TX) are predominant. The distance between these buildings is about 350–400 meters from RX2 that corresponds to time delay spread of 1.2–1.3 µs. These buildings are located $-25°-30°$ from the location of the transmitter in the azimuth plane (see Fig. 10.13).

Comparison with Ray Tracing Model. Let us now analyze and compare the theoretical approach proposed above with the results of the VPL ray-tracing algorithm
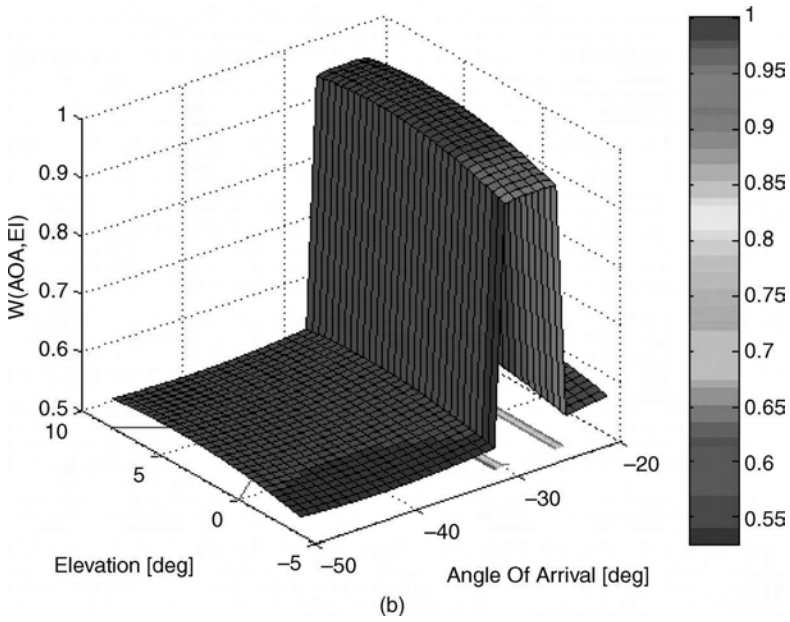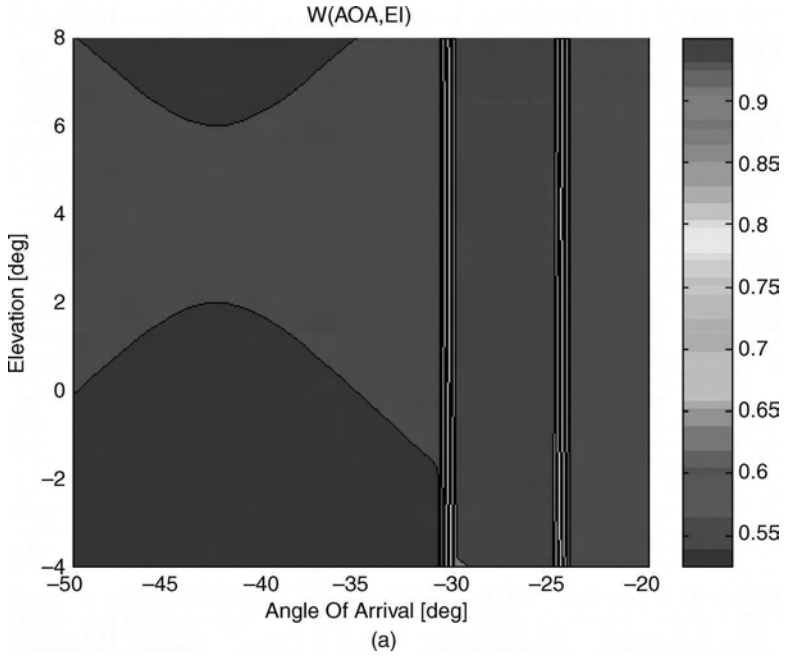
FIGURE 10.28. The simulated power spectrum, $W(\theta, \varphi)$, (a) in 2D (b) and 3D plane.
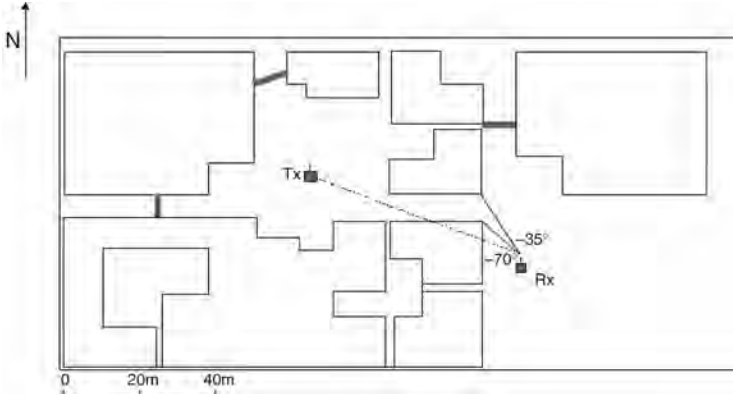
FIGURE 10.29. Aalborg University as a microcell environment. (Source [67]: Reprinted with permission © 2001 IEEE)

[46,66], which were compared with AOA measurements made at Aalborg University, Denmark [67]. We also compare our results with those from the Reference [67]. Let us introduce an urban scene in Figure 10.29 according to Reference [67]. The area comprises of several buildings connected by glass-covered bridges and walkways. The buildings are two-story high, about 8 m. The TX antenna is omnidirectional in the azimuth plane and it is located 4 m above the ground. The RX antenna has 3-dB beamwidth in both polarizations and it is located on the ground level. There is no LOS between the TX and RX antennas. The TX–RX distance is about 100 m. The measurements were made using 80-MHz wide band channel sounder at a carrier frequency of 1.845 GHz. The following parameters, extracted from Figure 10.29, describe the urban scene. The parameters $\gamma_0 = 3$, $v = 50$, $\lambda = 0.16$, $\chi = 0.5$, and $d = 0.1$ define the results of the stochastic model (10.16)–(10.30) simulation presented in Figure 10.30 compared against the measurement results [67], and against the VPL model prediction [46,66]. There is a good fit between the measured the VPL predicted and the proposed model simulated results. However, the stochastic model shows better agreement achieved in the azimuth range of 0° to 40°, where VPL prediction results differ from the measured data. Thus, the difference between measurements and VPL-model prediction can achieve in this range of upto 30%, whereas the stochastic model predicts with accuracy 95% the experimental data. Comparing the VPL model, the stochastic model simulation, and the measured data results, we have found that the stochastic model gives better prediction over the entire range of the considered points (from −80° to +80°). The mean error, with respect to the measured data, equals 0.16 for our model simulation and 0.3 for the results based on VPL technique, that is, our model in these ranges is twice as precise.

Next we present some important simulation results that define the joint distribution of AOA and TOA at the receiver. We analyze the distribution using the results presented separately for AOA in References [9,10], and using the built-up terrain data presented in Reference [67]. In Figure 10.31, from the concentration of rays near the direction of the two streets, which are placed between −40° and 0°,
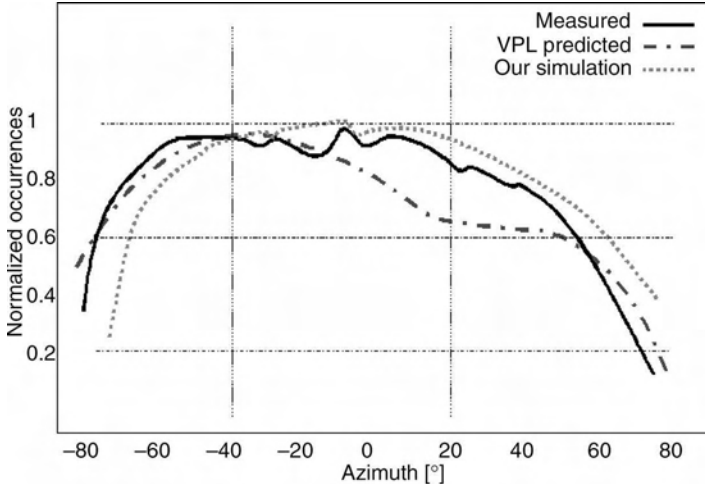
FIGURE 10.30. VPL model and measured data compared to the stochastic model prediction.

according to the map shown in Figure 10.29, we can see the existence of a strong street guide effect. This effect plays a significant role for the case where both the TX and RX antennas are below the rooftop level (as was mentioned in References [9,10], more than 80% of rays arriving at the receiver antenna are generated by the guiding effect of straight streets). It is also interesting to note that there are ray
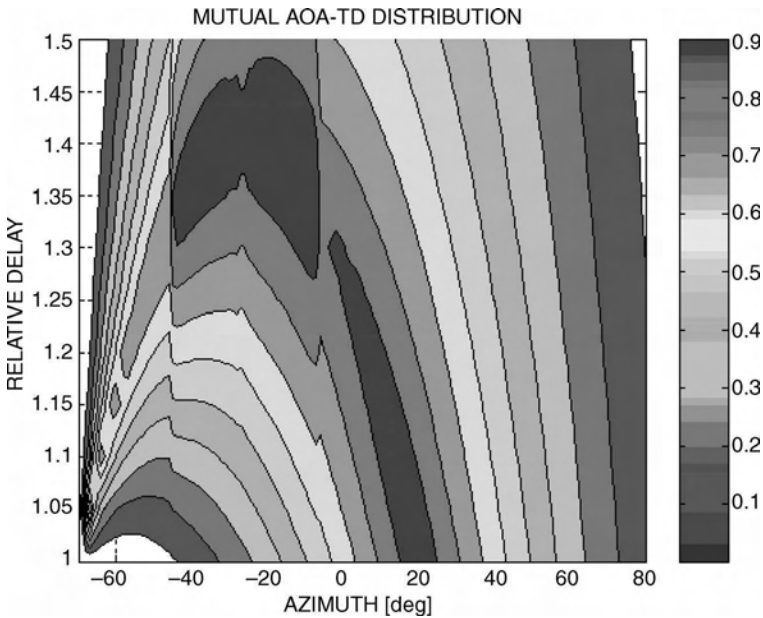
FIGURE 10.31. Joint AOA–TOA distribution for Aalborg University experimental site.

arrivals on the azimuth of $-70°$ (pseudo-LOS direction), and these arrivals have the normalized energy (compared with free space) of about 0.9. Apparently, these pseudo-LOS arrivals present over rooftop diffracted components with low time delay and narrow angular dispersion, but they do not contribute significantly to the RX received power, as shown in Figure 10.29.

This fact states again that all specific features of the built-up terrain and situations with antennas are important and can change significantly the spatial and temporal characteristics of the signal arriving at the antenna. These effects are very important for predicting effective operational characteristics of smart wireless systems (using adaptive antennas).

Azimuth-Distance Signal Dependence. Let us now analyze the behavior of expressions (10.28)–(10.33), obtained by the proposed stochastic approach, using the conclusions of experiments from References [4,9,10,46,67–69]. It was shown in Reference [68,69] that the azimuth spread depends on the distance between the TX and RX antenna in a specific manner. We show here a similar dependence described by (10.28). In References [46,67–69], the angular spread is reduced when the distance is increased for certain situations.

We analyzed two cases to confirm the empirical results obtained in References [68,69]. In the first case, which is shown in Figure 10.32, there is no street guide effect because the street plan grid does not have a rectangular form. In the second case shown in Figure 10.33 there is a straight-cross street grid. The pseudo-LOS azimuth between TX–RX antennas is about 23°. Different lines depict different distances between them. A curve denoted by "*" is for the distance 0.2 km. The "o"
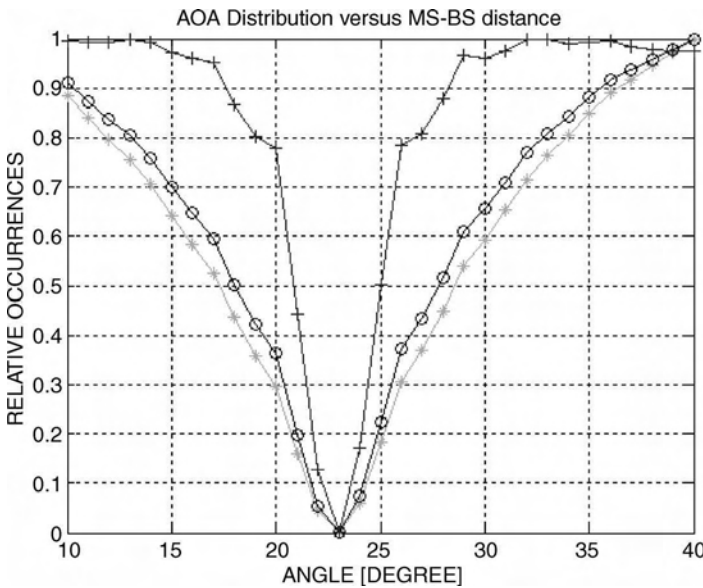
FIGURE 10.32. AOA distribution versus BS–MS distance without the street guide effect.
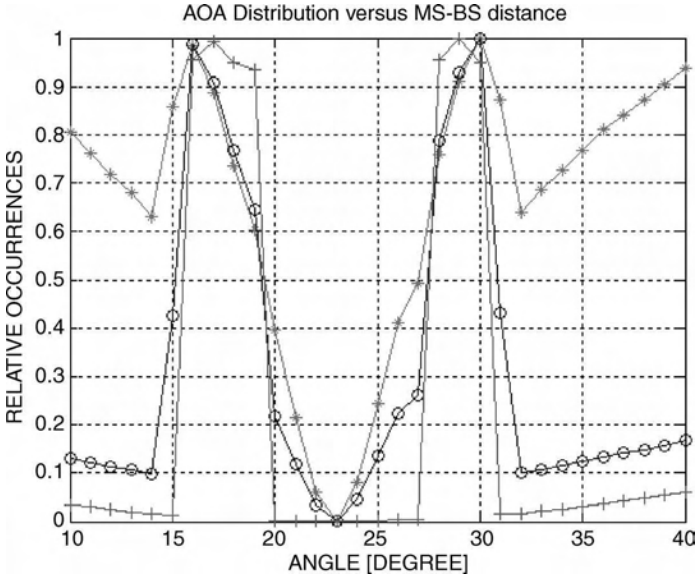
FIGURE 10.33. AOA distribution depends on BS–MS distance with the street guide effect.

line is for 0.6 km, and the "+" line is for the 2 km distance between the antennas. Here, only the distance parameter is varied in equations (10.28)–(10.33) to investigate its influence. Other parameters have typical values for urban scene

$$\gamma_0 = 4\text{km}^{-1} \quad (v = 120 \text{ buildings per km}^2 \text{ and } \bar{\rho} = 250\,\text{m}), \quad \lambda = 0.13\,\text{m}, \quad \text{and}$$
$$\chi = 0.5$$

Figures 10.32 and 10.33 show that the angular spread is decreased with an increase in separation distance between the antennas. Figure 10.33 shows an interesting phenomenon: As the distance between the MS and BS antennas increases, the street guide effect becomes more dominant. It is intuitively obvious, when the MS is far enough from the BS, that the probability of arrival of multiple reflected rays across randomly distributed scatterers is low. The same results were observed in Helsinki [9,10] for the urban scene with a grid-street plan.

10.4. SIGNAL POWER SPECTRA DISTRIBUTION IN FREQUENCY SHIFT DOMAIN

Now we will talk about the spectral characteristics of the received (or transmitted) signal in order to describe the Doppler spectrum for the moving subscriber (MS) antennas in various built-up areas.

10.4.1. Spatial Signal Distribution

Let us, first of all, consider the spectral properties of the signal strength spatial variations. We can present the spectral function $\widetilde{W}(q, \varphi_0)$ for two typical situations

in the urban scene regarding the elevations of the two terminal antennas with respect to the average height of the buildings.

For the *first case*, when the transmitter/receiver is placed *at rooftops level or below it*, that is, $z_1 \leq \bar{h}$ we get [55,61]

$$\widetilde{W}(X, \varphi_0) = \frac{2sh\chi(ch\chi - X\cos\varphi_0)}{k[1 - X^2]^{1/2}[(ch\chi - X\cos\varphi_0)^2 - (1 - X^2)\sin^2\varphi_0]} \tag{10.34}$$

where $X = \frac{q}{k}$, $X \in (-1, 1)$; q is the spatial wave vector, $k = \frac{2\pi}{\lambda}$; $sh\chi$ and $ch\chi$ denote hyperbolic sine and cosine, respectively, and the parameter χ accounts the density of the buildings and the range between the antennas

$$\chi = \ln\left[\left(1 + \frac{1}{\gamma_0 d}\right) - \left(\left(1 + \frac{1}{\gamma_0 d}\right)^2 - 1\right)^{1/2}\right] \tag{10.35}$$

The dependence of $\widetilde{W}(X, \varphi_0)/\widetilde{W}(0, \varphi_0)$ as a function of the normalized parameter X for $\varphi_0 = \frac{\pi}{2}, \frac{\pi}{3}, \frac{\pi}{4}, \frac{\pi}{6}$ (curves 1, 2, 3, 4, respectively) for $\gamma_0 d = 10$ (built-up area with high density of buildings around the receiver and transmitter, or the terminals are placed far from each other) is presented in figure 10.34a. The non symmetrical spectrum $\widetilde{W}(X, \varphi_0)$ is observed for the orientation angle φ_0 deviations from $\frac{\pi}{2}$ (φ_0 is the angle between the scatterer and radio path between terminal antennas). This phenomenon can be understood if we again return to the results of the analysis presented previously, where the PDF and the signal power angle-of-arrival distributions are unified and symmetrical relative to the wave path, which is directed strictly to the transmitter. If we consider that the position of a segment of the scatterer relative to radio path is not fixed and that it can be oriented with equal probability anywhere in space, that is, the angle φ_0 is the angle regularly distributed within the angle interval $[0, 2\pi]$, we immediately obtain the same case that is described in References [55,61]. According to these expressions, we get

$$\langle \widetilde{W}(X) \rangle = \frac{2}{X[1 - X^2]^{1/2}} \tag{10.36}$$

From this formula it follows that the spectrum of spatial frequencies for the case of $z_1 \leq \bar{h}$ does not depend on the range d between the BS and MS antennas and on the building contours density γ_0 at the plane $z = 0$. This result also follows from the dependence of $\langle \widetilde{W}(X) \rangle / \langle \widetilde{W}(0) \rangle$ shown in Figure 10.34b.

In the *second case*, when the transmitter/receiver is above the level of rooftop, that is, $z_1 > \bar{h}$, an increase of the illumination area ($\bar{\rho}$-area) surrounding the receiver/transmitter is observed. In this case the signal spectrum of normalized spatial frequencies $\left(X = \frac{q}{k} \in \{-1, 1\}\right)$ can be determined as

$$\langle \widetilde{W}(X) \rangle = \frac{2(1 - X\cos\varphi_0)}{X[1 - X^2]^{1/2}} \tag{10.37}$$
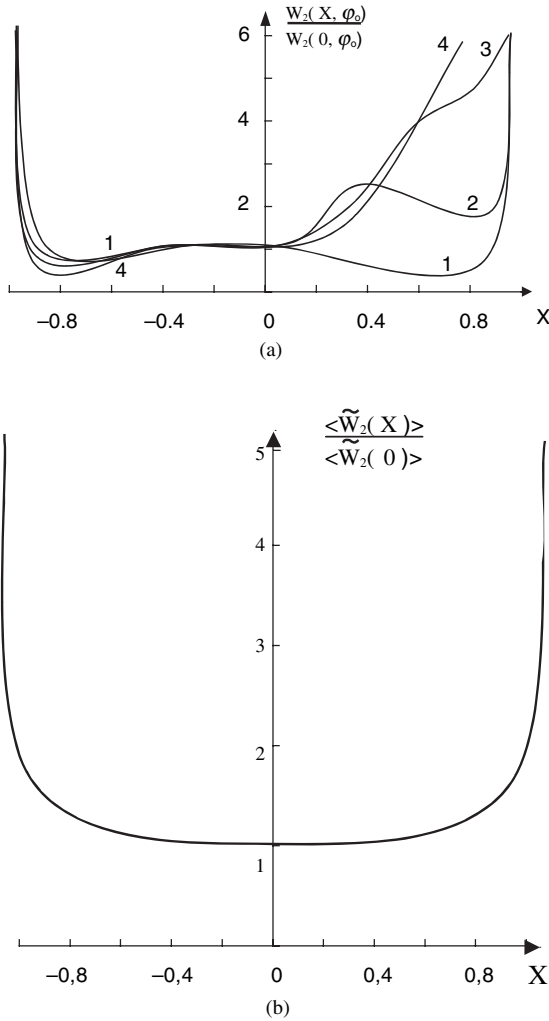
FIGURE 10.34. The dependence $\tilde{W}(X, \varphi_0)/\tilde{W}(0, \varphi_0)$ as a function of the normalized parameter X (a) for $\varphi_0 = \frac{\pi}{2}, \frac{\pi}{3}, \frac{\pi}{4}, \frac{\pi}{6}$ (curves 1, 2, 3, 4) for $\gamma_0 d = 10$. (b) The same dependence of $\langle \tilde{W}(X) \rangle / \langle \tilde{W}(0) \rangle$, but for φ_0 is regularly distributed from 0 to 2π. BS antenna is at the same level or below the rooftops.

In Figure 10.35, the dependence $\widetilde{W}(X, \varphi_0)/\tilde{W}(0, \varphi_0)$ as a function of normalized parameter X for $\varphi_0 = \frac{\pi}{2}, \frac{\pi}{3}, \frac{\pi}{4}, \frac{\pi}{6}$ (curves 1, 2, 3, 4, respectively) for $\gamma_0 d = 10$ is shown. The deformation of the classical U-shape (shown in Fig. 10.346) is observed.

10.4.2. Signal Power Distribution in Doppler Shift Domain

In built-up areas, the spatial distribution of signal strength fully determines the properties of temporal signal distribution obtained at the receiver. As indicated
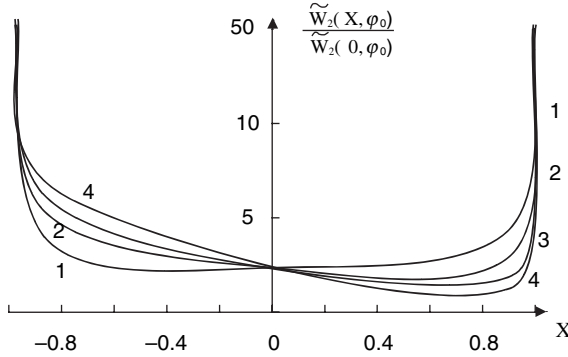
FIGURE 10.35. The same dependence $\widetilde{W}(X, \varphi_0)/\widetilde{W}(0, \varphi_0)$, as in Figure 10.34a, but calculated for the limited interval $q \in [-k, k]$. BS antenna is higher than the rooftops.

in References [55,61], the energy spectrum of the signal temporal deviations, which are created by the interference of waves arriving at the receiver, relates to the spectrum of spatial variations of signal strength through the following relationship [55,61]

$$\widetilde{W}_\tau(\tau, \varphi_0) = \frac{1}{v} \widetilde{W}\left(\frac{\omega}{v}, \varphi_0\right) \qquad (10.38)$$

Using this relation between the signal spectra in the space and time domains, we can examine their distribution in various built-up areas with randomly distributed buildings.

Let us consider two typical situations in the urban scene. For the *first case* the stationary transmitter/receiver antenna is *at the roofs level*, that is, $z_1 \leq \bar{h}$. In this case one can obtain the following expression for the spectral function of signal temporal fluctuations [55,61]:

$$\widetilde{W}_\tau(\omega, \varphi_0) = \frac{2 \cdot sh\chi \cdot \omega_d}{\sqrt{\omega_d^2 - \omega^2}} \frac{(\omega_d \cdot ch\chi - \omega \cdot \cos \varphi_0)}{[(\omega_d \cdot ch\chi - \omega \cdot \cos \varphi_0)^2 - (\omega_d^2 - \omega^2) \sin^2 \varphi_0]} \qquad (10.39)$$

where, $\omega_d = kv = \frac{v}{c}\omega_0 = 2\pi f_m, f_m$ is the maximal Doppler frequency; $\omega_0 = 2\pi f_0, f_0$ is the radiation frequency of the moving transmitter with speed v; c is the speed of light.

The frequency dependence of power spectrum described by expression (10.39) is the same as the one presented in Figure 10.34, which is very complicated and depends on several of the built-up terrain factors, such as the parameter χ, the direction of moving vehicles (on φ_0) and their speed v (on $\omega_d \propto v/\lambda$).

For the *second case*, when the antenna height is *higher than the rooftops* of buildings, that is, $z_1 > \bar{h}$, and $\gamma_0 d \geq 10$, we obtain [57,61]

$$\widetilde{W}_\tau(\omega, \varphi_0) \approx \frac{2(\omega_d - \omega \cdot \cos \varphi_0)}{\omega_d \sqrt{\omega_d^2 - \omega^2}} \tag{10.40}$$

The power spectrum, in the frequency domain, in this case can be presented by the function

$$\widetilde{W}_\tau(\omega, \varphi_0) \approx \left[\left(\omega_0 \frac{v}{c} \right)^2 - \omega^2 \right]^{-1/2} \tag{10.41}$$

which is close to the classical Clark's "U-shaped" Doppler spectrum distribution described in Reference [18].

The effect of asymmetry that follows from (10.34) or (10.39) depends on the angle φ_0 and the influence of the built-up terrain, accounted by the parameter χ. We notice that the same asymmetry was obtained in Reference [64] by the statistical multiray model described by Ricean statistics (see definition in Chapter 1). However, this model cannot explain the influence of terrain features, of the antenna elevation compared to the buildings surrounding it, that is, the effects which follow from the unified stochastic approach described above. In fact, based on the above approach, it can be easily shown that the obstructive effects of buildings for the particular trajectory of the MS antenna movements sharply decrease the area surrounding this antenna in which the reflections are formed [61]. Moreover, due to the screening effect of nontransparent buildings, as the scatterers, discussed earlier in Chapter 5, there is a gap along the radio path between the receiver and the transmitter when this radio path intersects the buildings, giving screening effects to the receiver. As a consequence, the angle distribution of reflection points significantly differs from the uniform distribution. In the case where the base station antenna height is at the same level as the rooftop, $z_1 \leq \bar{h}$, we obtain the PDF in the following form [55,61]:

$$w(\varphi) = \frac{\sqrt{1 + 2\gamma_0 d}}{2\pi\{1 + \gamma_0 d[1 - \cos(\varphi - \varphi_0)]\}} \tag{10.42}$$

where all parameters are defined above in this chapter.

With the increase of base station antenna height to be above the built-up layer, the density $w(\varphi)$ for $z_1 > \bar{h}, \widetilde{\varsigma} = (z_1 - \bar{h})/z_1 > 0.2$ can be presented as [55,61]

$$w(\varphi) = \frac{1 - \cos(\varphi - \varphi_0)}{2\pi} \tag{10.43}$$

We see that this PDF does not depend on the parameters of the built-up area. In both cases of a base station antenna location compared to the roof of the buildings, the power spectra as function of ω_{dn} will differ from distributions (10.41), obtaining the asymmetry form with the same maximum at the boundaries of the frequency band $[-\omega_d, +\omega_d]$.

BIBLIOGRAPHY

[1] Paulraj, A., and C. Papadias, ''Space-time processing for wireless communications,'' *IEEE Signal Processing Magazine*, vol. 14, no. 1, 1997, pp. 49–83.

[2] Ertel, R. B., P. Cardieri, K. W. Sowerby, T. S. Rappaport, and J. H. Reed, ''Overview of spatial channel models for antenna array communications systems,'' *IEEE Personal Communic.*, vol. 5, no. 1, 1998, pp. 10–22.

[3] Martin, U., J. Fuhl, I. Gaspard, et al., ''Model scenarios for direction-selective adaptive antennas in cellular communication systems-scanning the literature,'' *Wireless Personal Communic.*, vol. 11, no. 1, 1999, pp. 109–129.

[4] Pedersen, K., P. Mogensen, and B. Fleury, ''A stochastic model of the temporal and azimuthal dispersion seen at the base station in outdoor propagation environments,'' *IEEE Trans. Veh. Technol.*, vol. 49, no. 2, 2000, pp. 437–447.

[5] Fuhl, J., J. P. Rossi, and E. Bonek, ''High resolution 3-D direction-of-arrival determination for urban mobile radio,'' *IEEE Trans. Antennas Propagat.*, vol. 44, no. 4, 1997, pp. 672–682.

[6] Kuchar, A., J. P. Rossi, and E. Bonek, ''Directional macro-cell channel characterization from urban measurements,'' *IEEE Trans. Antennas Propagat.*, vol. 48, no. 1, 2000, pp. 137–146.

[7] Kalliola, K., H. Laitenen, L. Vaskelainen, and P. Vainikainen, ''Real-time 3D spatial-temporal dual-polarized measurement of wideband radio channel at mobile station,'' *IEEE Trans. Instrum. Measurements*, vol. 49, no. 3, 2000, pp. 439–448.

[8] Kalliola, K., and P. Vainikainen, ''Characterization system for radio channel of adaptive array antennas,'' in *Proc. Int. Symp. Personal Indoor Mobile Radio Conf. (PIRMC'97)*, Helsinki, Finland, 1997, pp. 95–99.

[9] Laurila, J., K. Kalliola, M. Toeltsch, et al., ''Wide-band 3-D characterization of mobile radio channels in urban environment,'' *IEEE Trans. Antennas Propagat.*, vol. 50, no. 2, 2002, pp. 233–243.

[10] Toeltsch, M., J. Laurila, K. Kalliola, et al., ''Statistical characterization of urban spatial radio channels,'' *IEEE J. Select. Areas Communic.*, vol. 20, no. 3, 2002, pp. 539–549.

[11] Libetri, J. C., and T. S. Rappaport, *Smart Antennas for Wireless Communications*, Prentice-Hall, Englewood Cliffs, NJ, 1999.

[12] Martin. U, ''Spatio-temporal radio channel characteristics in urban macrocells,'' in *Proc. IEE Radar, Sonar Navigation*, vol. 145, no. 1, 1998, pp. 42–49.

[13] Pedersen, K., P. E. Mogensen, and B. Fleury, ''Dual-polarized model of outdoor propagation environments for adaptive antennas,'' in *Proc. IEEE Veh. Technol. Conf. (VTC'99)*, Houston, TX, 1999, pp. 990–995.

[14] Pedersen, K., P. E. Mogensen, and B. Fleury, ''Power azimuth spectrum in outdoor environments,'' *IEE Electron. Letters*, vol. 33., 1997, pp. 1583–1584.

[15] Liberti, J. C., and T. S. Rappaport, ''A geometrical based model for line-of-sight multipath radio channels,'' in *Proc. of Veh. Technol. Conf.,* Atlanta, GA, 1996, pp. 844–848.

[16] Fuhl, J., A. F. Molisch, and E. Bonek, ''Unified channel model for mobile radio systems with smart antennas,'' *IEE Proc. Radar, Sonar Navigation*, vol. 145, no. 1, 1998, pp. 32–41.

[17] Petrus, P., J. H. Reed, and T. S. Rappaport, ''Geometrically based statistical channel model for macrocellular mobile environments,'' in *Proc. of IEEE Global Telecommunic.*, London, UK, 1996, pp. 1197–1201.

[18] Clarke, R. H., "A statistical theory of mobile-radio reception," *Bell Syst. Technol. J.*, vol. 47, no. 6, 1968, pp. 957–1000.

[19] Petrus, P., J. H. Reed, and T. S. Rappaport, "Effects of directional antennas at the base station on the Doppler spectrum," *IEEE Communic. Letters*, vol. 1, no. 2, 1997, pp. 40–42.

[20] Aulin, T., "A modified model for the fading signal at a mobile radio channel," *IEEE Trans. Veh. Technol.*, vol. 28, no. 3, 1979, pp. 182–203.

[21] Saleh, A. A. M., and R. A. Valenzula, "A statistical model for indoor multipath propagation," *IEEE J. Select. Areas Communic.*, vol. 5, no. 2, 1987, pp. 128–137.

[22] Spencer, Q., M. Rice, B. Jeffs, and M. Jensen, "Indoor wideband time/angle of arrival multipath propagation results," in *Proc. of IEEE Vehicular Technology Conf.*, 1997, pp. 1410–1414.

[23] Spencer, Q., M. Rice, B. Jeffs, and M. Jensen, "Astatistical model for angle of arrival in indoor multipath propagation," in *Proc. of IEEE Vehicular Technology Conf.*, 1997, pp. 1415–1419.

[24] Turin, G. L., et al., "A statistical model of urban multipath propagation," *IEEE Trans. Veh. Technol.*, vol. 21, no. 1, 1972, pp. 1–9.

[25] Lo, T., and J. Litva, "Angles of arrival of indoor multipath," *Electron. Letters*, vol. 28, no. 18, 1992, pp. 1687–1689.

[26] Guerin, S., "Indoor waveband and narrowband propagation measurements around 60.5 GHz in an empty and furnished room," in *Proc. of IEEE Veh. Technol. Conf.*, IEEE, 1996, pp. 160–164.

[27] Wang, J.-G., A. S. Mohan, and T. A. Aubrey, "Angles-of-arrival of multipath signals in indoor environments," in *Proc. of IEEE Veh. Technol. Conf.*, IEEE, 1996, pp. 155–159.

[28] Litva, J., A. Ghaforian, and V. Kezys, "High-resolution measurements of aoa and time-delay for characterizing indoor propagation environments," in *IEEE Antennas and Propagation Society International Symposium 1996 Digest*, IEEE. vol. 2, 1996, pp. 1490–1493.

[29] Devasirvatham, D., C. Banerjee, M. Krain, et al., "Multi-frequency radiowave propagation measurements in the portable radio environment," in *Proc. IEEE ICC'90*, 1990, pp. 1334–1340.

[30] Molkdar, D., "Review on radio propagation into and within buildings," in *Proc. IEE – H*, vol. 138, 1991, pp. 61–73.

[31] Keenan, J., and A. Motley, "Radio coverage in buildings," *British Telecom Technol. J.*, vol. 8, 1990, pp. 19–24.

[32] Chong, C.-C., C.-M. Tan, D. I. Laurenson, et al., "A new statistical wideband spatio-temporal model for 5-GHz band WLAN systems," *IEEE J. Select. Areas Communic.*, vol. 2, no. 2, 2003, pp. 139–150.

[33] Hassan-Ali, M., and K. Pahlavan, "A new statistical model forsite-specific indoor radio propagation prediction based on geometric optic and geometric probability," *IEEE Trans. Wireless Communic.*, vol. 1, no. 1, 2002, pp. 112–124.

[34] Fortune, S., D. Gay, B. Kernighan, et al., "WISE design of indoor wireless systems: Practical computation and optimization," *IEEE Comput. Sci. Eng.*, vol. 2, no. 1, 1995, pp. 58–69.

[35] Hassan-Ali, M., and K. Pahlavan, "Site-specific wideband and narrowband modeling of indoor radio channel using ray-tracing," in *PMIRC'98*, Boston, MA, 1998, pp. 134–137.

[36] Valenzula, R., O. Landron, and D. Jacob, "Estimating local mean signal strength of indoor multipath propagation," *IEEE Trans. Veh. Tech.* vol. 46, 1997, pp. 203–212.

[37] McKown, J., and R. Hamilton, "Ray tracing as a design tool for radio networks," *IEEE Network Magazine*, no. 1, 1991, pp. 27–30.

[38] Fortune, S., "Algorithms for the prediction of indoor radio propagation," *http://cm.bell-labs.com/cm/cs/who/sjf/pubs.html*, 1998.

[39] Dietert, J. E., and B. Rembold, "Stochastic channel model for outdoor applications based on raytrace simulations," in *Proc. of Millennium Conf. Antennas and Propagat. (AP2000)*, Davos, Switzerland, 2000.

[40] Chong C.-C., D. I. Laurenson, and S. McLaughlin, "Statistical characterization of the 5.2 GHz wideband directional indoor propagation channels with clustering and correlation properties," in *Proc. IEEE Vehicular Technol. Conf.* (*VTC 2002-Fall*), Vancouver, BC, Canada, vol. 1., 2002, pp. 629–633.

[41] Ertel, R. B., and J. H. Reed, "Angle and time of arrival statistics for circular and elliptical scattering models," *IEEE J. Select. Areas Communic.*, vol. 17, 1999, pp. 1829–1840.

[42] Constantinou, C. C., and L. C. Ong, "Urban radio propagation: A 3-D path-integral wave analysis," *IEEE Trans. Antennas Propagat.*, vol. 46, no. 2, 1998, pp. 266–270.

[43] Kanatas, A. G., I. D. Kountouris, G. B. Kostraras, et al., "A UTD propagation model in urban microcellular environments," *IEEE Trans. Veh. Technol.*, vol. 46, no. 1, 1997, pp. 185–193.

[44] Erceg, V., S. J. Fortune, G. Ling et al., "Comparisons of a computer-based propagation prediction tool with experiment data collected in urban microcellular environments," *IEEE J. Select. Areas Communic.*, vol. 15, 1997, pp. 677–684.

[45] Kim, S. C., B. J. Guarino, Jr., T. M. Willis III, et al., "Radio propagation measurements and prediction using three dimensional ray tracing in urban environments at 908 MHz and 1.9 GHz," *IEEE Trans. Veh. Technol.*, vol. 48, 1999, pp. 931–946.

[46] Liang, G., and H. L. Bertoni, "A new approach to 3-D ray tracing for propagation prediction in cities," *IEEE Trans Antennas Propagat.*, vol. 46, 1998, pp. 853–863.

[47] Kurner, T., D. J. Cichon, and W. Wiesbeck, "Concepts and results for 3D digital terrain-based wave propagation models: An overview," *IEEE J. Select. Areas Communic.*, vol. 11, 1993, pp. 1002–1012.

[48] Saunders, S. R., *Antennas and Propagation for Wireless Communication Systems*, J. Wiley & Sons, New York, 1999.

[49] Andersen, J. B., S. L. Lauritzen, and C. Thommesen, "Distribution of phase derivatives in mobile communications," in *Proc. IEE H*, vol. 137, 1990, pp. 197–201.

[50] Andersen, J. B., and I. Z. Kovacs, "Power distributions revisited," *COST-273*, Guildford, Jan. 2002, pp. 183–189.

[51] Andersen, J. B., and K. I. Pedersen, "Angle-of-arrival statistics for low resolution antennas," *IEEE Trans. Antennas Propagat.*, vol. 50, no. 3, 2002, pp. 391–395.

[52] Pedersen, K. I., P. E. Mogensen, and B. Fleury, "Spatial channel characteristics in outdoor environments and their impact on BS antenna system performance," in *Proc. Int. Conf. On Vehicular Technologies*, VTC'98, Ottawa, Canada, May 1998, pp. 719–723.

[53] Pedersen, K. I., P. E. Mogensen, B. Fleury, et al., "Analysis of time, azimuth and Doppler dispersion in outdoor radio channels," in *Proc. ACTS Mobile Communication Summit'97*, Aalborg, Denmark, 1997, pp. 308–313.

[54] Algans, A., K. I. Pedersen, and P. E. Mogensen, "Experimental analysis of the joint statistical properties of azimuth spread, delay spread, and shadow fading," IEEE *J. Select. Areas Communic.*, vol. 20, no. 3, 2002, pp. 523–531.

[55] Ponomarev, G. A., A. N. Kulikov, and E. D. Telpukhovsky, *Propagation of Ultra – Short Waves in Urban Environments,* Tomsk, Rasko, USSR, 1991.

[56] Blaunstein, N., "Distribution of angle–of–arrival and delay from array of building placed on rough terrain for various elevation of base station antenna," *Journal of Communic. and Networks,* vol. 2, no. 4, 2000, pp. 305–316.

[57] Blaunstein, N., *Wireless Communication Systems*, Ch. 12 in *Handbook of Engineering Electromagnetics*, Ed. R. Bansal, New Jersey: Marcel Dekker, 2004.

[58] Blaunstein, N., "Prediction of cellular characteristics for various urban environments," *IEEE Antennas and Propogat. Magazine,* vol. 41, no. 6, 2000, pp. 135–145.

[59] Blaunstein, N., D. Katz, D. Censor, et al., "Prediction of loss characteristics in built-up areas with various buildings' overlay profiles," *IEEE Anten. Propagat. Magazine*, vol. 43, no. 6, 2001, pp. 181–191.

[60] Blaunstein, N., and Y. Ben-Shimol, "Frequency dependence of path loss characteristics and link budget design for various terrestrial communication links," *IEEE Trans. on Antennas and Propagat.*, vol. 52, no. 10, 2004, pp. 2719–2729.

[61] Blaunstein, N. and Y. Ben-Shimol, "Spectral properties of signal fading and Doppler spectra distribution in urban communication mobile links," *Wireless Communic. and Mobile Computing*, vol. 6, no. 1, 2006.

[62] Blaunstein, N., and E. Tsalolihin, "Signal distribution in the azimuth, elevation and time delay domains in urban radio communication links," *IEEE Antennas and Propagation Magazine*, vol. 46, no. 5, 2004, pp. 101–109.

[63] Blaunstein, N., M. Toeltsch, C. Christodoulou, et al., "Azimuth, elevation and time delay distribution in urban wireless communication channels," *Antennas and Propagat, Magazine*, vol. 48, no. 2, 2006, pp. 160–167.

[64] Abdi, A., J. Barger, and M. Kaveh, "A parametric model for distribution of the angle of arrival and the associated cor. fun. and power spectrum at the MS," *IEEE Trans. Veh. Technol.,* vol. 51, no. 3, 2002, pp. 425–434.

[65] Jenison, R., and K. Fissell, "A comparison of the von Mises and Gaussian basis function for approximating spherical acoustic scatter," *IEEE Trans. Neural Networks*, vol. 6, no. 5, 1995, pp. 1284–1287.

[66] Bertoni, H., *Radio Propagation for Modern Wireless Systems*, Prentice Hall, New Jersey, 2000.

[67] Kloch, C., G. Liang, J. B. Andersen, et al., "Comparison of measured and predicted time dispersion and direction of arrival for multipath in a small cell environment," *IEEE Trans. Antennas Prop*agat, vol. 49, no. 9, 2001, pp. 867–876.

[68] Pedersen, K. I., P. Mogensen, and B. H. Fleury, "A stochastic model of the temporal and azimuthal dispersion seen at the base station in outdoor propagation environments," *IEEE Trans. Antennas Propagat.*, vol. 49, 2000, pp. 437–447.

[69] Pedersen, K. I., P. Mogensen, and B. H. Fleury, "Experimental analysis of the joint statistical properties of azimuth spread, delay spread, and shadow fading," *IEEE J. Select. Areas Communic.*, vol. 20, no. 3, 2002, pp. 523–531.

Multipath Fading Phenomena in Land Wireless Links

For all cellular radio communication networks, land, atmospheric, and ionospheric, the process of transmitting information must be accompanied by the knowledge of the parameters of both the transmitting and receiving terminal antennas at the ends of the radio link. It is also important to have some knowledge of the statistical parameters of the channel and their correlations in the space, time, and frequency domains, in order to evaluate the performance of the radio system considered. As was mentioned in Chapter 1, the important statistical characteristics that must be predicted is path loss, slow and fast fading, which allow radio network designers to predict strict link budgets, and to obtain the full radio coverage of areas of service, that is, to create radio maps of service areas.

In order to avoid measuring channel statistics for all operating environments and network designs, we proposed in Chapters 5 and 10 a unified stochastic approach for multipath radio channel description based on real physical phenomena, such as multiple reflections, diffraction, and scattering from various nontransparent obstructions (trees, hills, houses, buildings) located at the terrain. All of them produced the relevant effects when compared to measurements reported in the literature for specific rural, forested, mixed residential, suburban, and urban environments.

In Section 11.1, we compare the theoretical prediction of the loss characteristics in the space domain with experiments carried out in various land environments. Here, we also focus our attention on estimating the accuracy of the statistical description of the built-up terrain, on radio signal spatial attenuation and its frequency dependence. Furthermore, we analyze the advantages and limitations of

the proposed stochastic approach concerning mostly urban environments with very complicated built-up terrain configurations. Section 11.2 presents theoretical and experimental analysis of slow and fast fading based on the unified algorithm estimating these phenomena in various communication links taking into consideration both the classical methods and the unified stochastic multiparametric model. In Section 11.3, the role of Rician K-factor in multipath phenomena differentiation is briefly described. Section 11.4 deals with radio coverage and radio map constructions accounting for terrain features and overlay profile effects of the buildings, that is, the 3D configuration of built-up terrain. These terrain features have not been utilized until now in physical analysis of the problem of radio propagation in various land communication links.

First, we start our analysis with a prediction of propagation characteristics of the land radio channel via the proposed stochastic approach and the corresponding experiments carried out for various scenarios occurring in the different built-up areas.

11.1. PREDICTION OF LOSS CHARACTERISTICS FOR LAND RADIO LINKS

As was mentioned in Chapter 5, the proposed 3D multiparametric model is the stochastic approach that combines a statistical description of the terrain and overlay profile of the buildings with a description of the signal strength and average intensity based on the theoretical description of wave propagation phenomena in random media (see Chapters 3 and 4). Here, specific features of the land communication channels based on multiple reflections, diffraction, and scattering are described, caused by various obstructions as well as accounting for their vertical and horizontal reflection characteristics (see Chapter 5).

It should be pointed out that using the multiparametric stochastic approach, we cannot give exact, point-to-point description of signal strength surrounding each individual obstruction, which can be easily obtained by the use of ray tracing approaches [1–4]. In the stochastic approach, we strive to express some average properties of obstructions that take into account scattering (or *diffuse reflections*) from the rough wall surfaces and diffraction mechanisms from building rooftops and corners along the propagation paths. With all advantages of the proposed physical–statistical method to describe the terrain relief and overlay profile of the buildings as well as the average signal intensity or path loss, it is clear that it cannot explain some extreme cases of receiver antennas positioned within deep shadow regions surrounded by tall buildings. For such cases, the strict 2D-multiple diffraction and ''knife-edge'' models, mentioned in Chapter 4 (see also References [2,5–13]), are better predictors of the local signal strength. As will be shown in Section 11.2, in some experimental sites where antennas were located well within the shadow zone caused by nearby buildings, the median error and standard deviations between theoretical predictions and measured data are significant, (around 15–20 dB). Therefore, the validity and accuracy of the multiparametric stochastic approach will be established via experimental data.

11.1.1. Statistical Distribution of Buildings in Urban Environments

In Chapter 5, by introducing the stochastic approach, we have assumed that the number of rays N, which arrive at the receiver during time t after multiple diffuse reflections by randomly distributed buildings lining the streets or on the terrain, can be described by the Poisson distribution described in Chapter 5 (see also References [14–21]). An array of buildings (nontransparent scatterers) was presented there as an "ordinary and simple flow of positive virtual pulses," where each pulse represents the real building location at the terrain. Such mathematical description of an array of buildings randomly distributed around both terminal antennas allowed us, in Chapter 5, to determine a probability of direct visibility between antennas and other statistical functions. Finally, we used them to derive the average field intensity as a superposition of coherent and incoherent components of the total signal average intensity. Poisson's law strictly describes the real situation of building distribution in the urban environment with randomly distributed buildings as nontransparent screens. To verify this law for real situations in the urban scene, statistical analysis of topographic maps of built-up areas that correspond to the experimental sites mentioned in References [15–28] was carried out. This procedure was based on the following algorithm. If the randomly distributed buildings create a flow of randomly distributed positive virtual pulses placed at the smooth plane, then the distribution of such pulses of amount m, at the limit segment d, along the radio path must be described according to Poisson's law by the following probability function

$$P_d(m) = \frac{(\mu)^m}{m!} \exp\{-\mu\} \tag{11.1}$$

where the mean number of positive virtual pulses, μ, within the segment d can be presented in the following form [14,21]:

$$\mu = \int_0^l \gamma_0(\mathbf{r}_{1\perp} + \mathbf{q}_\perp l)\mathrm{d}l, \qquad l \in (0, d] \tag{11.2}$$

As defined in Chapter 5, $\mathbf{r}_{1\perp}$ is the projection of the vector to the transmitter at the ground plane $z = 0$ (see Fig. 5.15, Chapter 5); $\mathbf{q}_\perp = (\mathbf{r}_{2\perp} - \mathbf{r}_{1\perp})/d$ is a unit vector at the ground plane $z = 0$; $d = |\mathbf{r}_{2\perp} - \mathbf{r}_{1\perp}|$, where $\mathbf{r}_{2\perp}$ is the projection of the vector to the receiver at the ground plane $z = 0$; parameter γ_0 determines the density of the building contours at the plane $z = 0$ and was defined by (5.59) in Chapter 5. To obtain the real form of probability function $P_d(m)$, we must use the following computational procedure based on the statistical analysis of topographic maps from the tested built-up areas and compare it with Poisson's distribution (11.1). We have analyzed topographic maps of experimental sites where continuous measurements have been carried out, for example, in Stockholm (Sweden), Arhus, Aalborg, and Copenhagen (Denmark), Lisbon (Portugal), Helsinki (Finland), Jerusalem, Ramat-Gan, Beer-Sheva, and Tel-Aviv (Israel). We have used only similar areas
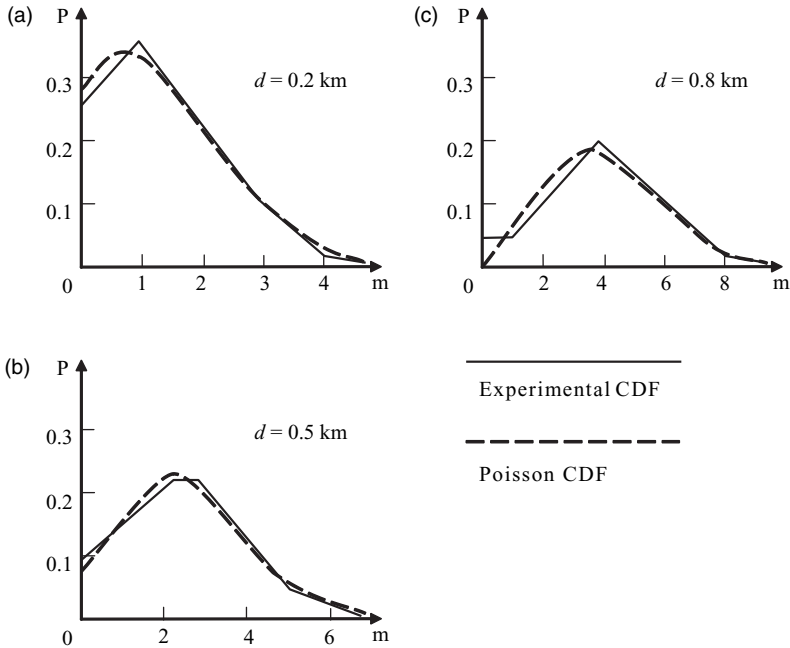
FIGURE 11.1. The building distribution above shows the terrain for each tested radio path: 200 m, 500 m and 800 m, respectively. Continuous curves describe statistical data; dashed curves describe the actual Poisson distributions according to eqn. (11.1).

with the quasi-homogeneous building density of 80–100 buildings per square kilometer, the average building length of 70–100 m, and the amount of building floors varied from 5 to 15. Finally, all open areas consisting of parks and gardens were eliminated from consideration. Using topographic maps of experimental sites mentioned above, a set of virtual radio paths for each position of the base station antenna (or the radio port) were constructed around it from 0° up to 360° with the step of 5°. Thus, for radio paths with ranges $d \in (0, 200 \text{ m})$, a number of crossings (outcomes) with buildings along each radio path for all experimental sites were 920, for radio paths with ranges $d \in (200 \text{ m}, 500 \text{ m})$, this amount was 550, and for radio paths with ranges $d \in (500 \text{ m}, 1000 \text{ m})$ it was 360. We summarized these statistics in Figures 11.1a–c by the corresponding continuous curves for each range: 200 m, 500 m, and 800 m, respectively. Then using these statistics and the parameters of each topographic map of the concrete experimental site, the mean value μ was estimated and used for the calculation of the actual Poisson's distribution (11.1). Results of these calculations are presented in Figures 11.1a–c by dashed curves.

Here, as in Chapter 5, we consider an ordinary and simple flow of scatterers, that is each single ray scattered as independent without crossing other rays or other scatterers. Notice that only rays with the level of −10 dB below the maximum were
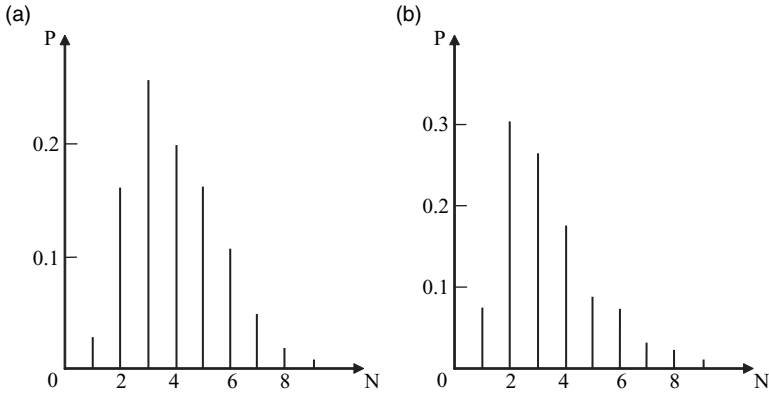
FIGURE 11.2. Probability laws of rays' number for links: (a) from 300 m to 500 m and (b) from 800 m to 1.5 km.

taken into account in our statistical analysis. Moreover, for four similar experimental sites of Beer-Sheba, Tel-Aviv, Ramat-Gan, and Jerusalem, the topographic maps were described more in detail compared to other experimental sites. A statistical analysis of the number of waves N arriving at the receiver for each concrete radio path, which corresponds to the number of scatterers, was carried out. Figures 11.2a and b show the distribution of rays after multiple scattering. Poisson's law can explain the statistical distribution for about 70% of rays that vary from 300 to 500 m (Fig. 11.2a), and for about 90% of rays that vary from 800 m to 1.5 km (Fig. 11.2b).

Simultaneously, the same statistical analysis from the experimental sites mentioned above, was carried out to verify situations of direct visibility between antennas along each radio path. The results of this statistical analysis are depicted by points in Figure 11.3 in a logarithmic scale versus the range between the real base station and virtual subscriber placed at a range d from this station.

Using formula (5.68) from Chapter 5, which describes the probability of direct visibility, and rewriting it in the following form

$$P_d(0) = \exp(-\gamma_o d) \tag{11.3}$$

where for each experimental site and for the concrete range d the parameter γ_o was estimated, we finally calculated the probability function presented in Figure 11.3 by the dashed curve.

From the results of the statistical analysis of the topographic map of various built-up areas and those calculated using formulas (11.1) and (11.3), a significant deviation from Poisson's law is observed, specifically for radio links with ranges between the antennas that are less than 50–100 m. Beyond these ranges (important for micro and macrocell planning) these deviations are negligible.
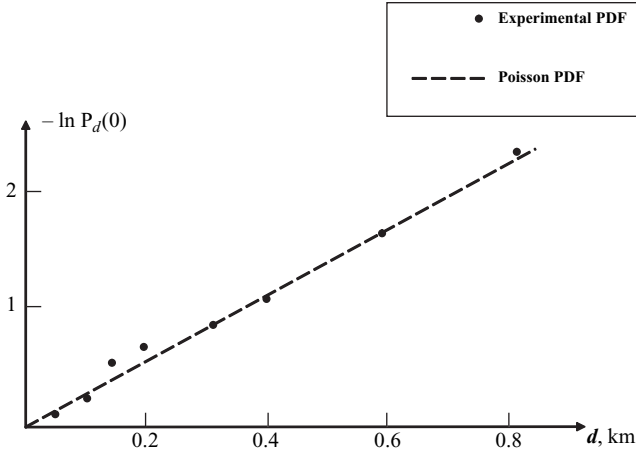
FIGURE 11.3. Results of the statistical analysis of direct visibility versus range d between base station and each virtual subscriber; points correspond to the statistical experiment and the dashed curve is obtained according using eqn. (11.3).

11.1.2. Influence of Terrain Features on Loss Characteristics

The accuracy of the theoretical prediction depends on the range of the variance of each parameter that describes the terrain features. Thus, in rural forested, mixed residential, and urban areas, the variations of the tree and building densities, the average height and reflection properties significantly affect the signal path loss. Therefore, it is very important to estimate all these parameters accurately.

Let $\bar{\Theta}$ be a vector of the set of parameters we are using to describe the terrain features

$$\bar{\Theta} = \{\Gamma, \gamma_0, l_h, l_v, \delta_1, \delta_2\} \tag{11.4}$$

and $\Delta\bar{\Theta}$ be the vector of errors in each of those parameters. Here, $\delta_1 = (\bar{h} - z_1)$ and $\delta_2 = (z_2 - \bar{h})$. All parameters of the terrain are defined in Chapters 5 and 10. Now, let Θ_i denote one of these parameters, and $\Delta\Theta_i$ be an error in that parameter. It is clear that an error in the path loss introduced by the ith parameter, where other five parameters are constant, can be written in the following form:

$$\Delta L_i = \frac{\partial L}{\partial \Theta_i} \Delta\Theta_i \tag{11.5}$$

The following expressions for the total path loss immediately have come from (11.5) that

$$\frac{\partial L}{\partial \Theta_i} = -\frac{10}{\ln 10} 10^{\frac{L}{10}} \frac{\partial(\langle I \rangle_{\text{co}} + \langle I \rangle_{\text{inc}})}{\partial \Theta_i} \tag{11.6}$$

Let us now analyze the variations of the total path loss according to (11.6) for the mixed residential areas with vegetation, according to (5.49)–(5.50), and for the urban areas, according to (5.94) to (5.97). In this case we get

$$\frac{\partial \langle I \rangle}{\partial \Theta_1} \equiv \frac{\partial \langle I \rangle}{\partial \Gamma} = \frac{1}{\Gamma} \langle I \rangle \tag{11.7}$$

$$\frac{\partial \langle I \rangle}{\partial \Theta_2} \equiv \frac{\partial \langle I \rangle}{\partial \gamma_0} = -\gamma_0 \langle I_{co} \rangle - 2\gamma_0 \langle I_{inc} \rangle [K_1 + K_2] \tag{11.8}$$

$$\frac{\partial \langle I \rangle}{\partial \Theta_3} \equiv \frac{\partial \langle I \rangle}{\partial l_h} \equiv \frac{\partial \langle I_{inc} \rangle}{\partial l_h} = \langle I_{inc} \rangle K_3 \tag{11.9}$$

$$\frac{\partial \langle I \rangle}{\partial \Theta_4} \equiv \frac{\partial \langle I \rangle}{\partial l_v} \equiv \frac{\partial \langle I_{inc} \rangle}{\partial l_v} = \langle I_{inc} \rangle K_4 \tag{11.10}$$

$$\frac{\partial \langle I \rangle}{\partial \Theta_5} \equiv \frac{\partial \langle I \rangle}{\partial \delta_1} = \langle I_{inc} \rangle K_5 + \langle I_{co} \rangle K_6 \tag{11.11}$$

$$\frac{\partial \langle I \rangle}{\partial \Theta_6} \equiv \frac{\partial \langle I \rangle}{\partial \delta_2} \equiv \frac{\partial \langle I_{inc} \rangle}{\partial \delta_2} = \langle I_{inc} \rangle K_7 \tag{11.12}$$

Here,

$$
\begin{aligned}
&K_1 = \frac{(2\pi \ell_h)^2}{\lambda^2 + [2\pi \ell_h \bar{L} \gamma_0]^2}, \qquad K_2 = \frac{[2\pi \ell_v (\bar{h} - z_1)]^2}{\lambda^2 + [2\pi \ell_v \gamma_0 (\bar{h} - z_1)]^2} \\
&K_3 = \frac{1}{l_h} - \frac{8\pi^2 \gamma_0^2}{\lambda^2 + [2\pi \ell_h \bar{L} \gamma_0]^2}, \qquad K_4 = \frac{1}{l_v} - \frac{8\pi^2 \gamma_0^2 (\bar{h} - z_1)^2}{\lambda^2 + [2\pi \ell_v \gamma_0 (\bar{h} - z_1)]^2} \\
&K_5 = -\frac{4\pi^2 \gamma_0^2 l_v^2}{\lambda^2 + [2\pi \ell_h \gamma_0 (\bar{h} - z_1)]^2}, \qquad K_6 = -\frac{\gamma_0 d}{z_2 - z_1} \\
&K_7 = \frac{(z_2 - \bar{h})}{[(\lambda d / 4\pi^3)^2 + (z_2 - \bar{h})^2]}
\end{aligned}
\tag{11.13}
$$

Without loss of generality, we replaced the profile function $F(z_1, z_2)$, in the above formula, with its simple approximation $(z_2 - \bar{h})$ valid for quasi-homogeneous distribution of building height, that is when parameter of building profile $n = 1$ (see details in Chapter 5.) As seen by computations of the above formulas, deviations of the terrain and antenna location parameters over the range of $\pm(30\%–50\%)$ lead to deviations of the average path loss in the wide range, mostly due to variations of the parameter of building contour densities γ_0. These variations of path loss can reach $\pm(7.0–15.0)$ dB. Hence, the analysis presented above shows that having full information about the tested area and conditions of the experiment one can precisely predict loss characteristics in the area of service.

In the following section we will estimate the influence of the built-up relief and terrain features on the frequency dependence of the total signal intensity within various kinds of land communication channels.

11.1.3. Frequency Dependence of Signal Intensity in Various Built-Up Areas

It was shown in References [29–35] that the total field attenuation increases in built-up areas with a decrease in wavelength. Other researchers have obtained the same conclusions later [10–14,36]. Such dependence given in energy units can be presented in the following form [10–14,29–36]:

$$\langle I_{total} \rangle \sim f^{-p} \tag{11.14}$$

The loss factor, p, varies from 0.2 to 2.5 with an increase in frequency from 100 MHz to 3 GHz at radio ranges that do not exceed 8–10 km. Beyond this range, a weak frequency dependence of signal strength loss is observed experimentally [29–32].

Now, let us present the frequency dependence of the signal intensity for various kinds of terrains, mixed residential and urban, taking into account the detailed information about the spatial distribution of buildings and natural obstructions (hills, trees, vegetation etc.).

Results of signal frequency dependence (11.14) obtained from numerous experiments can be explained using results of the theoretical prediction of the total field frequency dependence described by (5.63) for the grid-street scene, by (5.59) and (5.60) for mixed residential, and (5.94) to (5.99) for suburban and urban areas.

In fact, for urban and suburban areas, we consider in (5.94) that $\lambda^2 < (2\pi l_v \gamma_0 (\bar{h} - z_1))^2$, then

$$\langle I_{inc1} \rangle \sim \lambda^{3/2}(\sim f^{-3/2}), \quad \text{if} \quad (\lambda d/4\pi^3) > (z_2 - \bar{h})^2 \tag{11.15a}$$

and

$$\langle I_{inc1} \rangle \sim \lambda^1(\sim f^{-1}), \quad \text{if} \quad (\lambda d/4\pi^3) < (z_2 - \bar{h})^2 \tag{11.15b}$$

In the case, when we deal with (5.96)

$$\langle I_{inc2} \rangle \sim \lambda^4(\sim f^{-4}), \quad \text{if} \quad (\lambda d/4\pi^3) > (z_2 - \bar{h})^2 \tag{11.16a}$$

and

$$\langle I_{inc2} \rangle \sim \lambda^3(\sim f^{-3}), \quad \text{if} \quad (\lambda d/4\pi^3) < (z_2 - \bar{h})^2 \tag{11.16b}$$

Depending on the relationship between $\langle I_{inc1} \rangle$ and $\langle I_{inc2} \rangle$, the total field intensity is changed with frequency as

$$\langle I_{total} \rangle \sim f^{-1} - f^{-4} \tag{11.17}$$

If now in (5.94) $\lambda^2 > (2\pi l_v \gamma_0 (\bar{h} - z_1))^2$, then

$$\langle I_{inc1} \rangle \sim \lambda^{-1/2} (\sim f^{1/2}), \quad \text{if} \quad (\lambda d/4\pi^3) > (z_2 - \bar{h})^2 \tag{11.18a}$$

and

$$\langle I_{inc1} \rangle \sim \lambda^{-1} (\sim f^{1}), \quad \text{if} \quad (\lambda d/4\pi^3) < (z_2 - \bar{h})^2 \tag{11.18b}$$

In the case of (5.96), then

$$\langle I_{inc2} \rangle \sim \lambda^{0} (\sim f^{0}), \quad \text{if} \quad (\lambda d/4\pi^3) > (z_2 - \bar{h})^2 \tag{11.19a}$$

and

$$\langle I_{inc2} \rangle \sim \lambda^{-1} (\sim f^{1}), \quad \text{if} \quad (\lambda d/4\pi^3) < (z_2 - \bar{h})^2 \tag{11.19b}$$

Again, comparing $\langle I_{inc1} \rangle$ and $\langle I_{inc2} \rangle$, we get for the total field intensity the following frequency dependence:

$$\langle I_{total} \rangle \sim f^0 - f^1 \tag{11.20}$$

From (11.17) and (11.20), we can see that the average signal intensity frequency dependence is not constant and depends on the situation in the urban scene.

For mixed residential areas mostly close to rural environments, if we consider now in (5.59) that $\lambda^2 < [2\pi \ell_h \bar{L} \gamma_0]^2$, that is also $\lambda^2 < (2\pi l_v \gamma_0 (\bar{h} - z_1))^2$, then

$$\langle I_{inc1} \rangle \sim \lambda^{5/2} (\sim f^{-5/2}), \quad \text{if} \quad (\lambda d/4\pi^3) > (z_2 - \bar{h})^2 \tag{11.21a}$$

and

$$\langle I_{inc1} \rangle \sim \lambda^{2} (\sim f^{-2}), \quad \text{if} \quad (\lambda d/4\pi^3) < (z_2 - \bar{h})^2 \tag{11.21b}$$

Here, comparing (11.21a) and (11.21b), we get

$$\langle I_{total} \rangle \sim f^{-2} - f^{-5/2} \tag{11.22}$$

If now in (5.59), $\lambda^2 > (2\pi l_v \gamma_0 (\bar{h} - z_1))^2$, that is also $\lambda^2 > [2\pi \ell_h \bar{L} \gamma_0]^2$, then

$$\langle I_{inc1} \rangle \sim \lambda^{-3/2} (\sim f^{3/2}), \quad \text{if} \quad (\lambda d/4\pi^3) > (z_2 - \bar{h})^2 \tag{11.23a}$$

and

$$\langle I_{inc1} \rangle \sim \lambda^{-2} (\sim f^{2}), \quad \text{if} \quad (\lambda d/4\pi^3) < (z_2 - \bar{h})^2 \tag{11.23b}$$

Again, comparing (11.23a) and (11.23b), we finally get

$$\langle I_{total} \rangle \sim f^{3/2} - f^2 \tag{11.24}$$

From (11.22) and (11.24), the average signal intensity is also not constant and depends on the terrain parameters in the mixed residential area.

From the above formulas, it is clear that the frequency dependence of the total average signal intensity is changed from $\lambda^{-0.5} - \lambda^{-1.5}$ ($f^{0.5} - f^{1.5}$) for the low part of the HF-frequency band, and to $\lambda^{0.5} - \lambda^{1.5}$ ($f^{-0.5} - f^{-1.5}$) for the higher part of VHF/UHF-band with continuous transaction through $\sim \lambda^0$ (no dependence) around $f = 70$–90 MHz. This dependence can vary widely depending on the propagation scenario that occurred in the built-up environment, the building density, the average height of the building layer with respect to both terminal antennas, the building average length, the distance between antennas, and so on.

Figure 11.4 shows an example where the field loss relative to that in free space is presented versus the radiated frequency for the antenna heights of $z_1 = 2$ m and $z_2 = 90$ m, and for the ranges between antennas of $d = 0.5, 1.0, 2.0, 5.0, 10.0$ km. The continuous curves are a result of calculations according to formulas (5.94) to (5.98) taking into account the various situations in the urban areas, described in
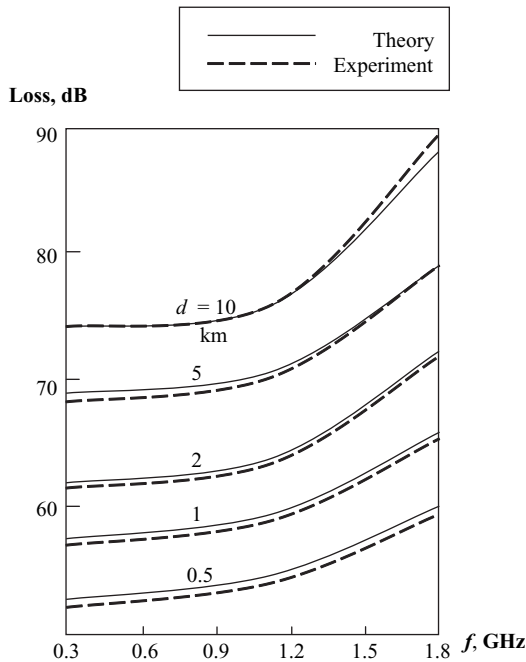
FIGURE 11.4. Relative signal loss versus radiated frequency for $z_1 = 2$ m, $z_2 = 90$ m, and for $d = 0.5, 1.0, 2.0, 5.0$, and 10.0 km.

References [15–27]. The dashed curves are the results of measurements of the median signal power obtained for each corresponding experiment described in References [29–35]. The results of theoretical prediction are close to those obtained by the corresponding measurements. Moreover, the frequency dependency of the signal loss, obtained analytically for various land environments, cover all results of this dependence obtained experimentally that allows designers of the land wireless networks to predict various situations in radio communication links for each subscriber located within the area of service.

11.1.4. Radio Pattern Around a Building—Comparison Theory and Experiment

In Chapter 5, it was shown theoretically, the importance of understanding the radio field pattern around a building in order to determine the influence of an array of buildings on the total path loss. Now, let us verify these theoretical results with special experiments carried out in some urban environments. The tested environment was a typical small urban region with two to four-floor buildings with approximately uniform heights of $h_b = 8$–$15\,$m (see details in References [15]). The base station omnidirectional transmitter antenna was at a height $h_T = 7\,$m; the mobile had an omnidirectional antenna at a height $h_R = 2.5\,$m, that is, lower than the rooftop level. In the experiment [15] the spatial field intensity distribution at the frequency $f_0 = 930\,$MHz $(\lambda = 0.3\,$m) surrounding the isolated four-floor brick building was measured. The geometry of the experiment is shown in Figure 11.5. The omnidirectional transmitted antenna with vertical polarization was placed at points P and Q. The point Q was placed centrally between the edges of the building.

Its distance to the front building wall was of about 110 m. The point P was placed at a distance of 90 m from the point Q parallel to the front wall (see Fig. 11.5). In
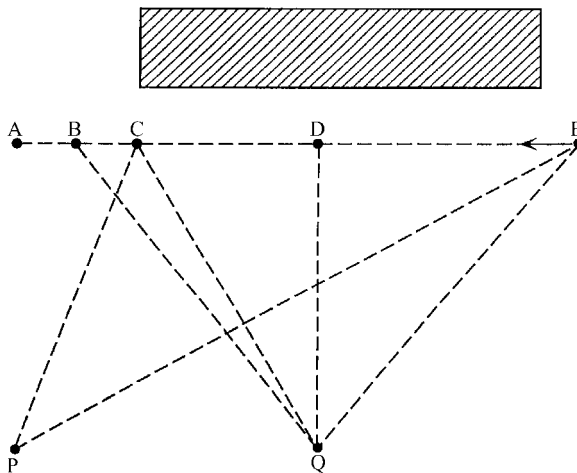
FIGURE 11.5. Experiment according to [15].
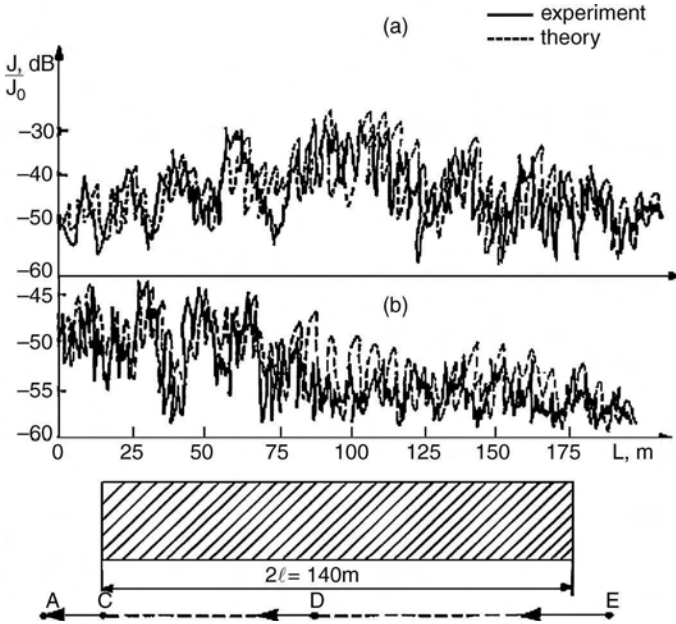
FIGURE 11.6. Normalized signal intensity distribution along a building; continuous curve is measured data and dashed curve is for computed data.

these experiments, the radio port moved along the line EA at a distance of about 30 m from the front wall. The results of these experiments are shown in Figure 11.6a (transmitter at point Q) and Figure 11.6b (transmitter at point P) by the continuous curves. As expected, the direct and reflected waves from the front wall determine a well expressed interference pattern of the resulting field with periodical spatial oscillations of the measured signals (with a period of about several meters) along line CA. The results of the measurements are shown in Figure 11.6a–b for the resulting wave strength plotted relative to the amplitude of the direct wave measured at point D. Measurements also showed that the average level of the reflected signal was 10 dB lower than the corresponding signal from the direct source. The sharp changes in the amplitude of the reflected waves, when the receiver moves along line BD, can be associated with the scattering effects from the building wall contours (windows, balconies).

In the computations related to the real experiment, described in Figure 11.5, the observation point moved parallel to the front building wall along the line AE. For computations we used $2l = 200\,\lambda$, $2h = 30\,\lambda$, $2d = 50\,\lambda$ with $\lambda = 0.3$ m. The spatial step of observation in the calculations was chosen to be 1 m. The modulus of the reflection coefficient was chosen to be for a moderate subsoil medium, $|R_g| = 0.7$–0.8, and for brick walls, $|R_w| = 0.3$–0.5, respectively. The coefficient of diffraction from the brick corners was chosen to be $|D| = 0.4$–0.5 according to estimations carried out in Reference [15]. The dotted curve in Figure 11.6a presents the results of

calculations for a source placed at point Q; the dotted curve in Figure 11.6b presents results for a source placed at point P (see Fig. 11.5).

These experimental and theoretical predictions, presented in Figure 11.6 by the continuous and dotted curves, respectively, allow us to create a qualitative picture of the field pattern around the building with very complicated oscillations of the wave strength in the "light" zones and with very fast attenuation in the total field amplitude when the observer passes along the building. Moreover, the numerical and experimental results give a satisfactory explanation of the field intensity oscillations using the interference phenomena of direct and reflected rays from walls and the ground surface and the rays diffracted from the building contours.

11.1.5. Verification of the Stochastic Approach via Numerous Experiments

Here, we focus our attention on estimating the accuracy of the proposed stochastic approach by verifying the results of the theoretical prediction against numerous measurements carried out in different land communication links, mixed residential, urban, and suburban areas.

Path Loss in Mixed Residential Areas. The measurements were taken in three locations in Poland: Lipniki, Koscierzyna, and Tarczyn [23,26]. These are typical rural neighborhoods, with one or two story houses surrounded by vegetation. The frequency used was 3.5 GHz. The measurements were made with a transmitter antenna, at h_T, of 40 m and 80 m, above the average tree and building heights whereas the height of the receiver antenna, h_R, was between 3 to 15 m. Between 5 to 8 points were measured in each of the locations (see References [23,26]).

The average parameters of the obstructions were estimated in the following manner. For the reflection coefficient, Γ, we used the average value measured for the brick walls and wooden surfaces of trees, that is 0.3–0.4. As for the correlation scales, ℓ_h and ℓ_v, for trees they are of the order of tens of centimeters, whereas for one–two floor houses they are of the order of 1–1.5 meter. In the case of uniformly distributed obstructions, we took ℓ_h and ℓ_v to be between 0.5 and 1 m in our calculations. The same procedure was used in obtaining the minimum, average, and maximum obstruction contours density, γ_0. Thus, using the topographical map of the mixed area we divided it into regions of 1 km^2 area each and in each region we estimated the density of the obstructions. In regions with pure vegetation, the parameter γ_0 varies from $\gamma_0 = 0.01 \, \text{km}^{-1}$ to $\gamma_0 = 0.1 \, \text{km}^{-1}$. In regions where buildings are predominant, it ranges between $\gamma_0 = 1 \, \text{km}^{-1}$ to $\gamma_0 = 3 \, \text{km}^{-1}$ (see References [23,26]). Finally we obtained that the average parameter of obstruction density over the terrain varies between $\gamma_0 = 0.1 \, \text{km}^{-1}$ to $\gamma_0 = 1 \, \text{km}^{-1}$. These values were used below in the numerical computations of path loss based on formulas (5.59) and (5.60), and in formulas (5.42), (5.48) to (5.50).

In Figures 11.7 and 11.8, the path loss (in dB) is presented as a function of the receiver antenna height calculated according to formulas (5.59) and (5.60) for the case of single scattering with diffraction (denoted by circles) and formulas (5.48) to
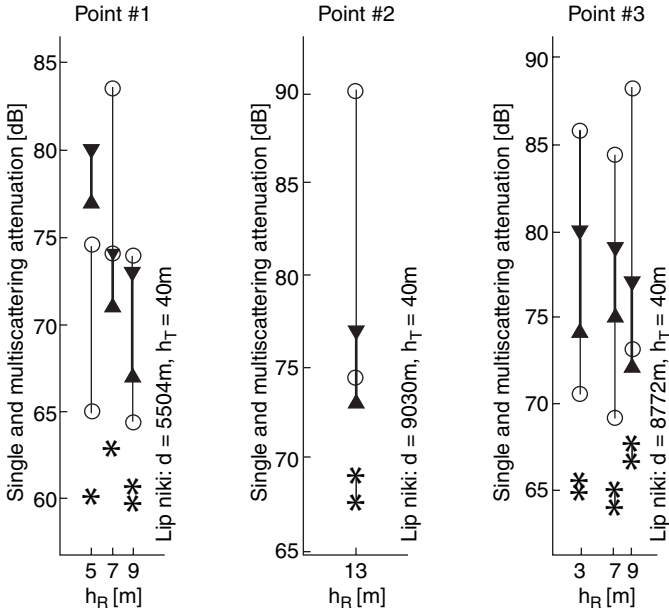
FIGURE 11.7(a). Average field attenuation versus receiver height for a transmitter height of 40 m. Wide thick segments represent experimental data. Circles and asterisks "*" represent calculations according to (5.59)–(5.60) and (5.48)–(5.50), respectively.
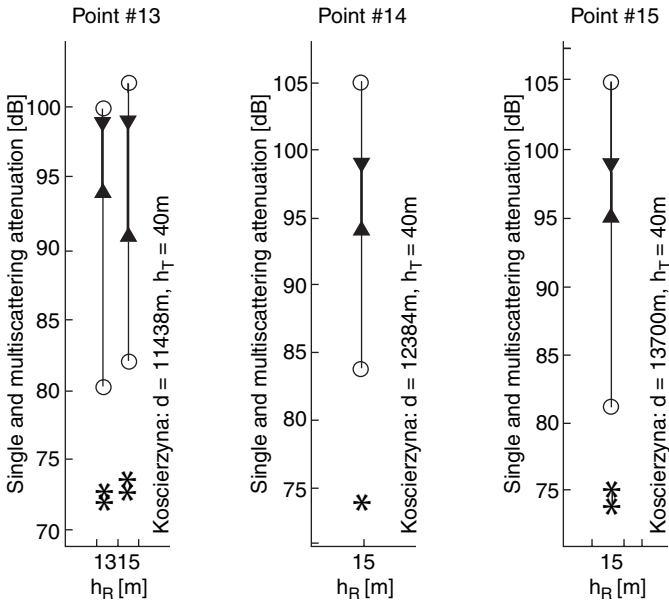
FIGURE 11.7(b). The same, as in Fig. 11.7a, but for the other experimental site.
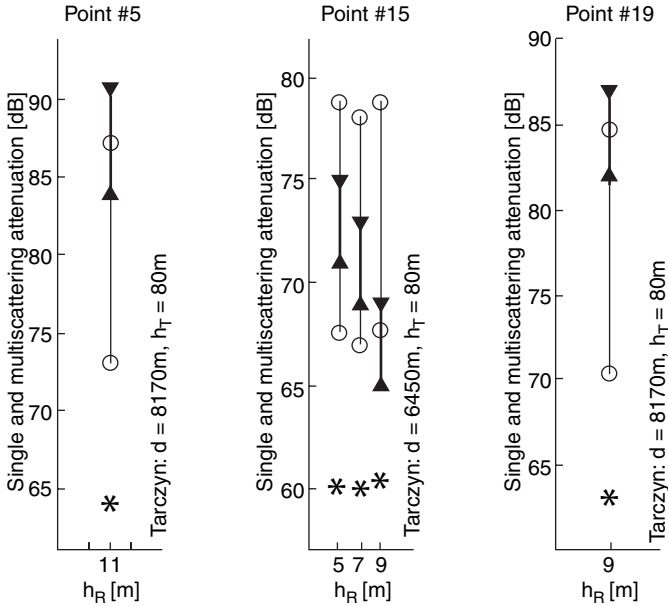
FIGURE 11.8(a). The same, as in Fig. 11.7a, but for another experimental site and for a transmitter antenna height of 80 m.
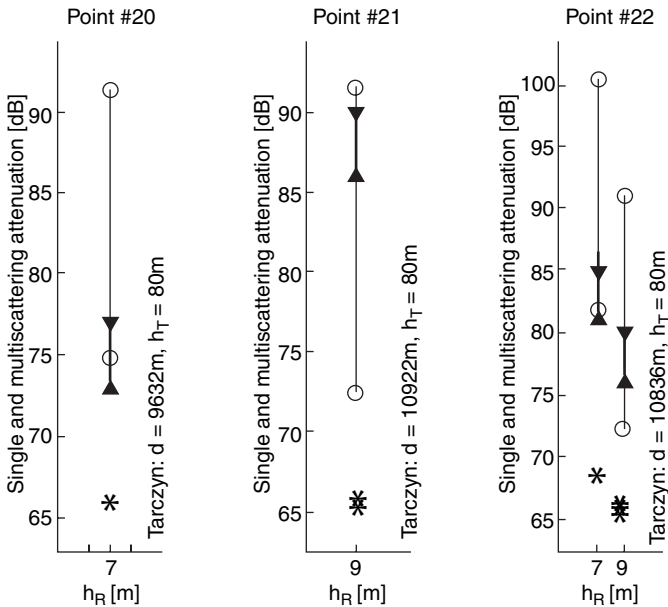
FIGURE 11.8(b). The same, as in Fig. 11.7b, but for the other experimental site and for a transmitter antenna height of 80 m.

(5.50), (5.42) for the case of multiple scattering without diffraction (denoted by asterisks "*"). The experimental data is presented here by a thick line which connects the minimum and maximum measured values. We also connected the circles and asterisks by thin lines spanning the range between possible results from the minimum value (the bottom circle calculated for $\gamma_0 = 0.1\,\mathrm{km}^{-1}$) and the maximum value (the top circle calculated for $\gamma_0 = 1\,\mathrm{km}^{-1}$).

In these figures the distance d between the transmitting and receiving antennas, as well as the base station antenna height, h_T, are given in meters. Thus, for points 1–3 the measured data are close to those obtained numerically. The deviation between the calculated and measured values does not exceed 2–5 dB (see Fig. 11.7a, the Lipniki experimental site).

On the other hand, results of calculations made by using a model that does not take diffraction into account gives a much larger deviation from the experimental data, about 8–10 dB (for points 1–3).

The same behavior can be observed at the other sites, as presented in Figure 11.7b (for the Koscierzyna experimental site) and Figure 11.8a,b (for the Tarczyn experimental site), respectively.

From the above illustrations, one can see that the difference between the theoretical model without diffraction effects and the experimental data can exceed 25–30 dB. At the same time, the model that includes diffraction from the rooftops and corners of the houses can predict the signal intensity attenuation with an accuracy equivalent to that of measurements. The deviation between them does not exceed 2–5 dB, an effect which depends on the density of the houses surrounding both terminal antennas, as well as on the height of the antennas.

Path Loss in Urban and Suburban Areas. In each experiment carried out in Israel, Sweden, and Portugal, the stand-alone radio port unit (RPU) plays the role of the transmitter. The fixed access unit (FAU) was used as the receiver, which during the experiment was moved from point to point. According to the FAU specification, its measurement accuracy in all experiments does not exceed 3–4 dB. The investigated built-up terrain was different: in Stockholm it was characterized as quasi-smooth whereas in Jerusalem and Lisbon it was characterized as hilly.

Experiments in Jerusalem. We will start by examining the experiments in Jerusalem according to References [19,20]. The notion of the medium urban area is relevant to Jerusalem's propagation conditions. Two or three samples were taken at each experimental point along the vehicle route and the average values based on these measurements have been found. To determine RSSI values from the above expressions of average intensity of the field, we have to multiply the sum of (5.94) through (5.98) by the term $\sim\lambda^2$ according to References [19,20], which finally gives us (5.99). The major problem is the non flat terrain profile of Jerusalem (i.e., the existence of substantial height differences between relatively close points in the area). In this situation, the accuracy of the theoretical prediction is reduced. In addition, the complex terrain can affect the distance of direct visibility and this influence, which is the diffraction phenomena, has to be taken into consideration. To overcome these
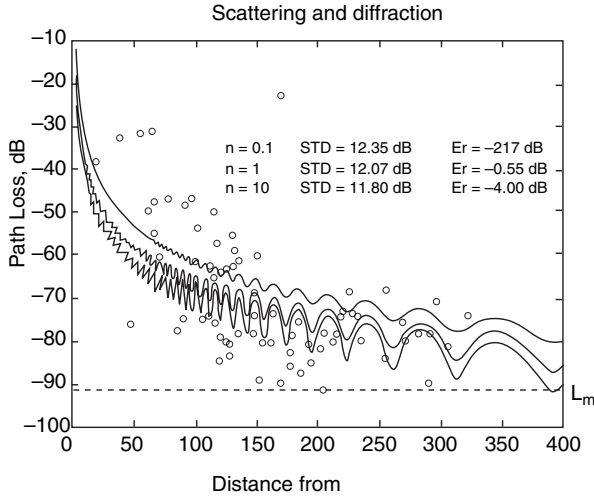
FIGURE 11.9. Numerical calculation results of the average total field according to (5.94)–(5.98) and (5.99) (continuous curves) for $n = 0.1$, 1 and 10; the measurements are denoted by circles.

difficulties, we took into account the ground height to determine the actual FAU height as a function of its location. We added the ground height to the building height as well and then determined the average building height.

From the topographical map, we found that we can approximate the different built-up layer profiles obtained for each experimental site by the polynomial functions (5.73) with parameter n lying between 0.1 and 10. From the topographical map of Jerusalem's experimental site, we obtained the following parameters of the built-up terrain: the building density $v = 103.9 \, \text{km}^{-2}$, the average building length $\bar{L} = 18 \, \text{m}$, and the average building height (not including the local ground height) $h = 8.3 \, \text{m}$. All the local ground heights were determined by using the global positioning system (GPS). The measurements were made at 930 MHz bandwidth using the transmitting antenna with a height $z_2 = 42 \, \text{m}$ [19,20]. The results of numerical calculations are presented in Figure 11.9 by oscillating curves for $n = 1$ (uniform built-up terrain), $n = 0.1$, and $n = 10$ (nonuniform built-up terrain with a predominant number of small and tall buildings, respectively).

In Figure 11.9, the measurement results denoted by circles are compared with the multiple scattering and diffraction model according to formulas (5.94) to (5.99). The indicated number pair is the standard deviation value (STD) and the following prediction error (Err) between two points sets (theory and measurements). We can define them as follows [19,20]:

$$\text{Err}_{\text{model}} = R_i - r_i, \qquad [\text{dB}] \tag{11.25}$$

$$\langle \text{Err}_{\text{model}} \rangle = \frac{1}{N} \sum_{i=1}^{N} (R_i - r_i), \qquad [\text{dB}] \tag{11.26}$$

$$\text{STD}_{\text{model}} = \sqrt{\langle (\text{Err}_{\text{model}} - \langle \text{Err}_{\text{model}} \rangle)^2 \rangle}, \qquad [\text{dB}] \tag{11.27}$$

Here, N is the set dimension and R_i and r_i are the theoretically obtained and measured path loss values.

From Figure 11.9, the poorer convergence between the theoretical prediction and experimental data can be improved by at least 3–7 dB by taking into account the real built-up layer relief. In fact, as was shown above, depending on the parameter n, from (5.73) and both antenna evaluations, this can be improved up to 5–15 dB. Thus, for the conditions of the experimental site in Jerusalem and of both antennas (see References [19,20]), we have the following: for $n = 0.1$, the additional excess loss is of -5–7 dB; for $n = 1$, it is 10–12 dB; and for $n = 10$, it is 15–17 dB. These results cover all experimental measurements. Taking into account these factors in the proposed parametric model, one can give the same and more accurate predictions of loss characteristics within a channel than Hata's small-medium model [17]. In fact, the comparison between the experimental results obtained in Jerusalem (denoted, as in Fig. 11.9, by circles) and the calculations according to Hata's small-medium model (denoted by the curve) is presented in Figure 11.10. In this case, the value of the standard deviation is at the same level as that obtained by using the parametric model, but the absolute value of mean error is higher with respect to the parametric model.

We have physically clear relations between the parameters of environment, terrain profile, both antennas elevations and the loss characteristics of the signal within the urban communication channel. Moreover, the multiparametric model is relatively simple and it does not need to be calibrated every time. What was missing in these experiments was that we had no real profile for the built-up terrain in Jerusalem [19,20]. On the contrary, in the other experimental city sites, the actual terrain relief and the building layer profile (the concrete parameter n) have been used to compare the experimental data with our theoretical prediction.
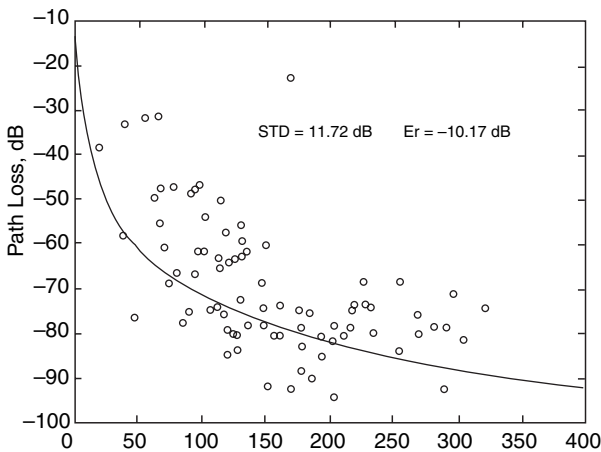
FIGURE 11.10. The same as in Fig. 11.9, but for comparison with the Hata model (continuous curve).
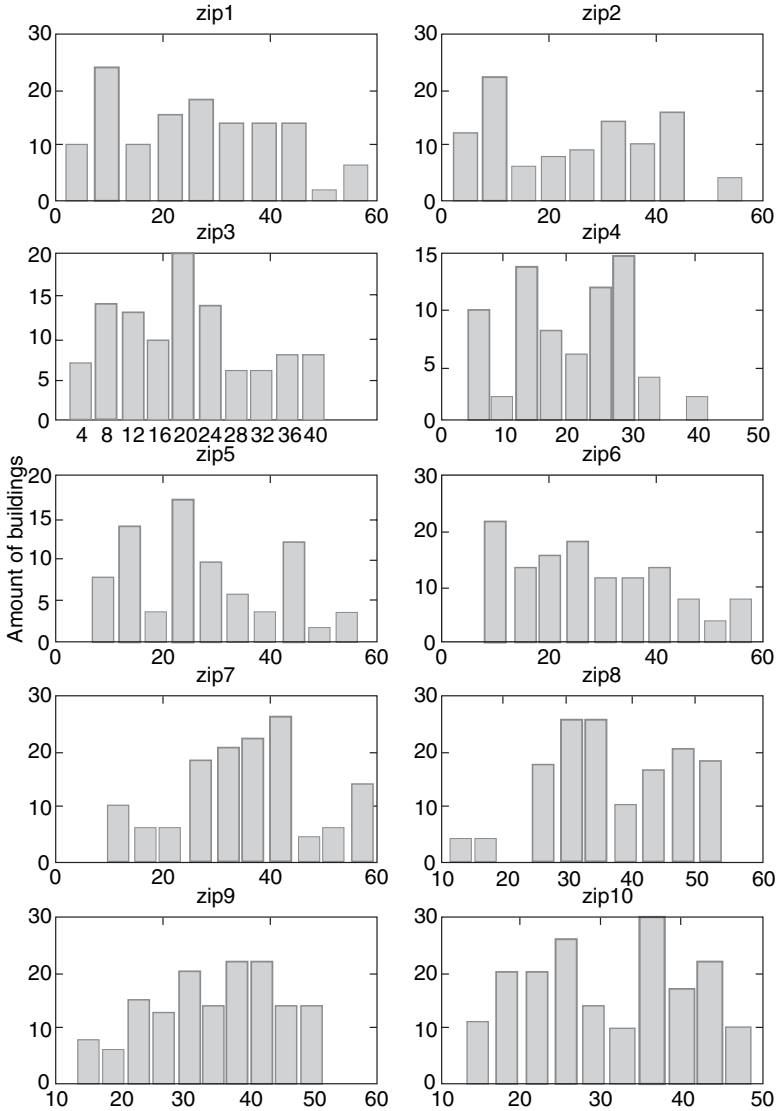
FIGURE 11.11(a). Distribution of buildings along each radio path.

Experiments in Stockholm. As was mentioned in References [37,38], the built-up area of the experimental site can be characterized as high, dense, or obstructed. According to the topographical map of the experimental site [37,38], the height of the buildings distribution versus the number of buildings along the radio path from BS to each vehicle's position was estimated and presented in Figure 11.11a. From this, the probability density function $P_h(z)$ was obtained along each route of the moving vehicle from the base station to the path-end denoted as zip1 to zip10
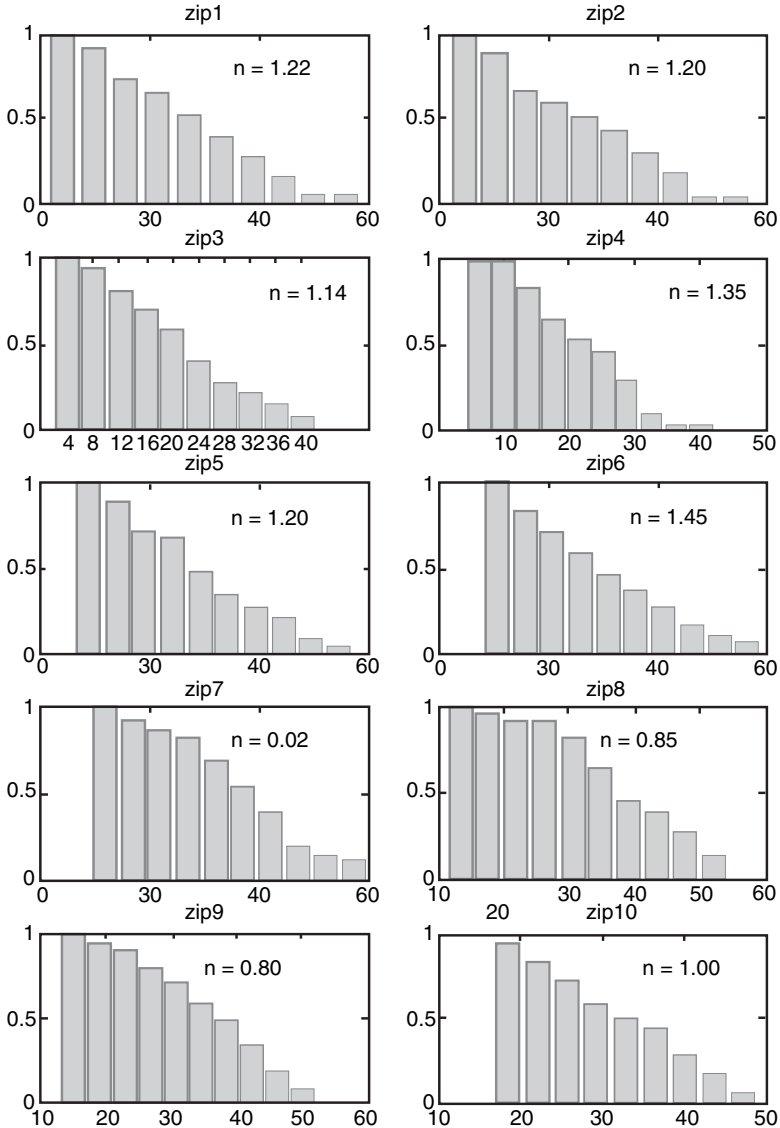
FIGURE 11.11(b). The corresponding CCDF of buildings' profile distribution.

(see Fig. 11.11b). According to the experimental data and topographical map of the site described in References [37,38], the building contour density parameter, γ_0, was estimated by using (5.32) or (5.69) as about $8-12 \, km^{-1}$ with the mean value of $10 \, km^{-1}$. The built-up profile parameter n is estimated from (5.73). Each individual vehicle path is presented in Figure 11.11b and is changed from 0.65 (for the vehicle end position denoted as zip8) to 1.48 (for point zip6). All experiments were carried out at the carrier frequency of 1.8 GHz.
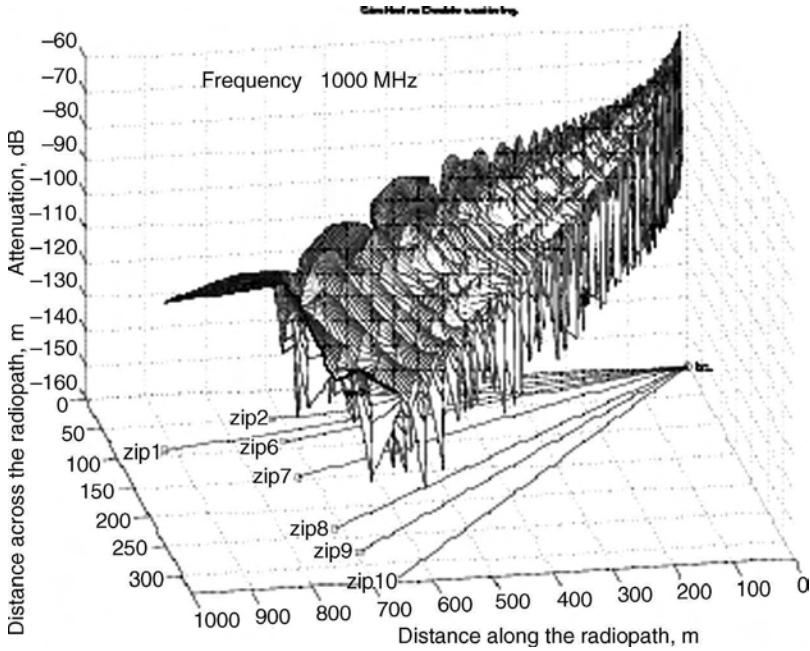
FIGURE 11.12. The average field intensity attenuation along and across each radio path.

The numerical simulation results for the total field intensity attenuation, according to the proposed multiparametric model, are presented as a 3D picture in Figure 11.12. The comparison between theoretical predictions, using formulas (5.94) to (5.99) and the corresponding experimental data, shows that the mean error and the standard deviation do not exceed 6 dB (Err = 5.2 dB, STD = 5.6 dB). We must note that close results were also obtained in other cities with different terrain profiles (see [19–21]).

Experiments in Lisbon. To understand and assess the accuracy of the present stochastic approach, and to find its limits for predicting path loss characteristics, specific experiments were carried out in Lisbon (Portugal) [24,25]. As mentioned in References [24,25], the Lisbon terrain profile is hilly with various densities of buildings and vegetation surrounding the base station antenna, which was 93 m high. Two typical examples of these profiles in various experimental sites (identified by numbers at the top of the figure) are presented in Figures 11.13a–11.13b. In the experiments, the receiver antenna was mounted on a crane and changed its height from a line-of-sight (LOS) position down to a position behind the building in NLOS conditions, when the signal amplitude was reduced to the noise level. The clearance between terminals, the transmitter, and receiver is shown in each figure by introducing the first Fresnel zone, as an ellipse, clearly showing the extent of obstruction within such an elliptical cross section. By reducing the receiver antenna height,
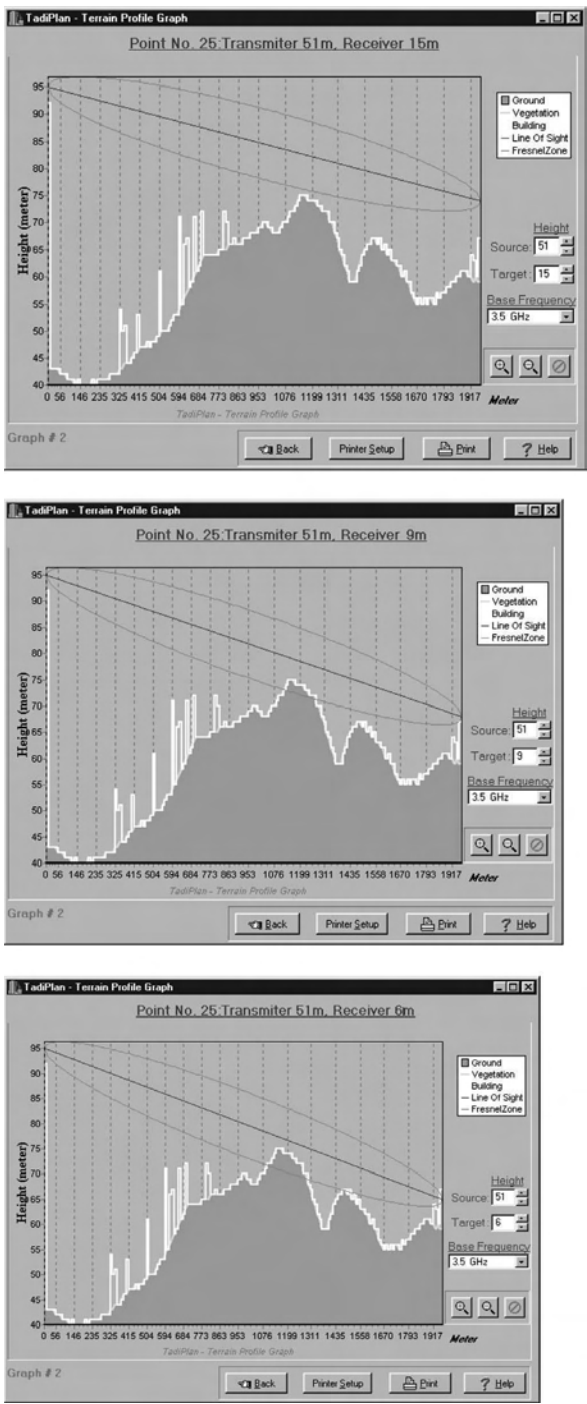
FIGURE 11.13(a). Typical examples of profiles of various experimental sites identified as #25.
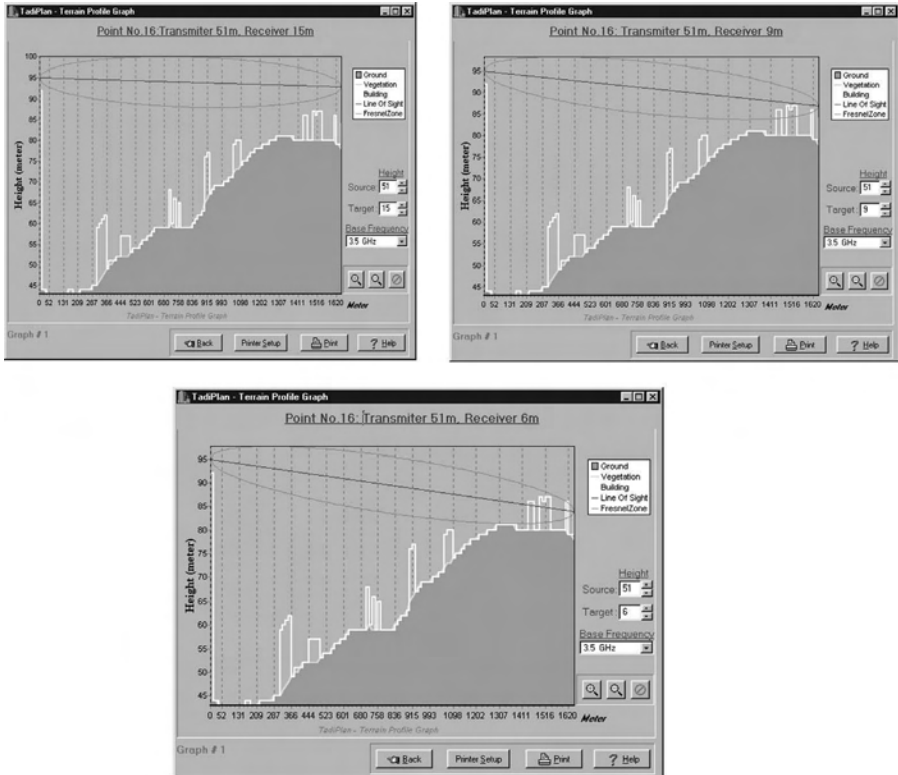
FIGURE 11.13(b). The same as in Fig. 11.13a, but for experimental site #16.

we continuously move from conditions of full clearance (LOS) to NLOS conditions, that is, from fully illuminated paths to shadow zones due to the obstructing building.

Figures 11.14a to 11.14c show a comparison of the measured and theoretically predicted path loss in some experimental points in Lisbon. Each figure shows the following:

- The measured path loss, denoted by a thick line bar connecting the minimum and maximum loss measured at that point.
- The results of the model described in Chapter 5 using (5.98) and (5.99) with (5.94), (5.96), and (5.97) with the values of the parameters taken from a topographic map of Lisbon city. These results are depicted by asterisks, connected by a thin line indicating the results for high, medium, and low values of the obstacle density v in km^{-2}.
- The results of various "knife-edge" models, described in Reference [17], indicated by circles. For the sites point #44 and #51, we used a single diffraction model according to Lee's approximate formulas (see Chapter 5). For points #4, #25 and #41, we used a double diffraction model based on the
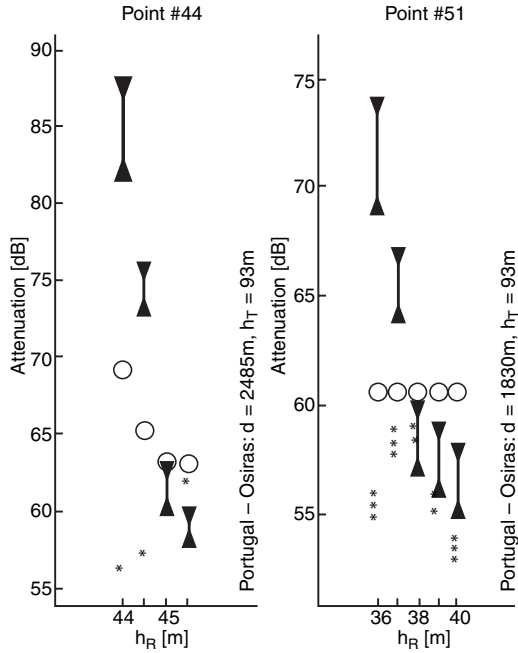
FIGURE 11.14(a). Signal intensity decay versus vehicle antenna height; the experimental data are denoted by segments; the theoretical prediction according to (5.94)–(5.99) and the 2-D "knife-edge" (Lee's) model are denoted by segments, asterisks "*" and circles, respectively.
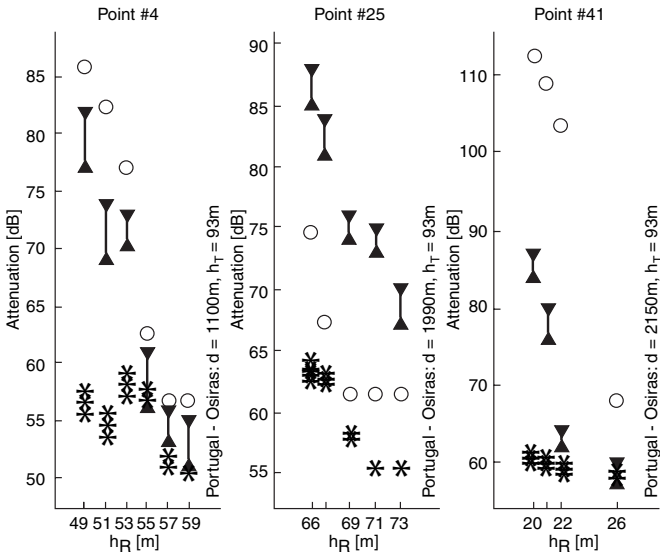
FIGURE 11.14(b). The same as in Fig. 11.14a, except the circles indicate results of calculations by using the double diffraction "knife-edge" model.
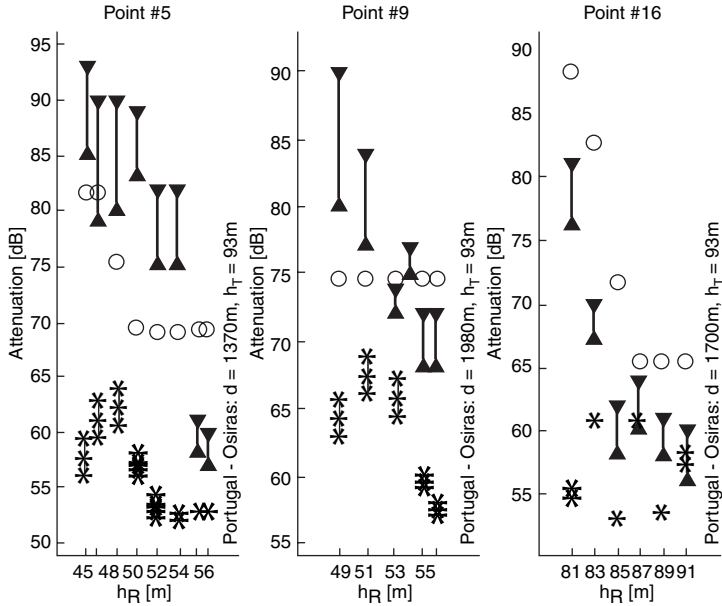
FIGURE 11.14(c). The same as in Fig. 11.14a, but circles indicate results of calculations by use of three-time diffraction "knife-edge" model.

same formulas, and finally for points #5, #9 and #16 we used the triple diffraction model based on the empirical approach described in Reference [17] based on the same Lee's "knife-edge" model.

From all the figures presented, it is clear that the performance of the present stochastic model (with accuracy of 1–3 dB) is satisfactory as long as the receiver antenna height does not decrease to the extent that it is placed in the local shadow zone in the vicinity of high obstructing buildings. In such regions, the knife-edge diffraction models are better predictors for the signal attenuation.

11.1.6. Advantages and Limitations of 3D Stochasic MultiParametric Approach

First, let us consider the advantages of the proposed stochastic model. As was mentioned in References [19–25], the proposed 3D multiparametric model is the stochastic approach that combines the statistical description of the terrain and the built-up overlay with a description of the signal intensity according to (5.94) to (5.99), taking into account the effects of various obstructions according to their vertical and horizontal geometrical parameter distributions.

Figure 11.15a is a 2D cross-sectional view of a 3D urban relief profile, with buildings indicated by black blocks. The positions of the antennas are shown as well. The purpose of Figure 11.15 is to explain the physical motivation for the definition of
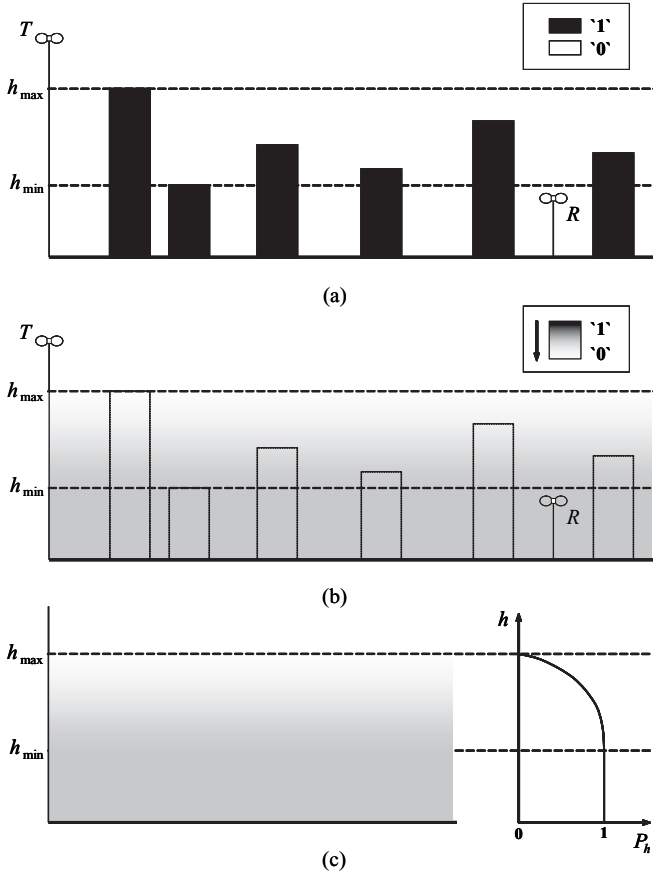
FIGURE 11.15. (a) the 2-D built-up profile of city relief; the black blocks correspond to sign "1" and the gaps between them correspond to sign "0", (b) the 3D-case taking into account "side looking" effects, and (c) the 3D-distribution of $P_h(z)$ inside the building layer.

$P_h(z)$. We are interested in the probability of a full clearance between antennas, connected with strong signal intensity. The less electromagnetic radiation is obstructed, that is fewer high buildings encountered, the higher this probability will be. Note that we do not describe the "local" deterministic expected signal strength for the individual receiving antenna position within the urban communication channel. We strive to express some average properties that will take into account specular reflection from building tops and diffraction mechanism, along the propagation route. Evidently this stochastic approach must be proved via experimental data.

In Figure 11.15a, we put the "1" value in areas of location of the buildings (black pixels) and "0" value elsewhere. The averaging on horizontal "slices" will produce a grey scale appearance (Fig. 11.15b). Below h_{min} we obtain the darkest grey, and above h_{max} we have only white. Finally, the correspondence of this description to $P_h(z)$ is shown in Figure 11.15c.

The present averaging method can be carried out over an area of urban scene, as it is done on the corresponding 2D cross section shown in Figure 11.15a. Although a 2D model ignores "side-looking" effects, such as horizontal specular reflections and diffraction mechanisms, a 3D approach accounts for these effects very well. Furthermore, the shape of CCDF, $P_h(z)$, distribution inside the overlay of the buildings, depicted in Figure 11.15c at the right side of the picture depends on the relief parameter n. Thus, the height profile function $P_h(z)$ describes a wide range of city building profiles: from one-level height close to h_1 (for $n \gg 1$) or to h_2 (for $n \ll 1$) to various levels of buildings heights h_i, including a quasi-homogeneous distribution of h_i with equal probability from h_1 to h_2, when $n = 1$, for which the average building height equals $\bar{h} = (h_1 + h_2)/2$, where $h_1 = h_{min}$, $h_2 = h_{max}$.

Hence, the proposed multiparametric stochastic model is a 3D model that uses data for terrain and building's overlay geometries to calculate the pertinent complementary cumulative distribution function (CCDF). As was mentioned in Chapter 5, this CCDF determines the probability of an event for each observer located in the built-up layer. This is a general approach that takes into account the terrain input parameters, such as the height distribution of the buildings, their density, and spatial distribution over the ground surface.

At the same time, the principal limit of the proposed stochastic model was found during its evaluation. Thus, it was found that the *critical boundary*, beyond which one can use only 2D deterministic multiple diffraction or empirical "knife-edge" models, depends mainly on the angle-of-arrival distribution depicted in Figure 11.16.
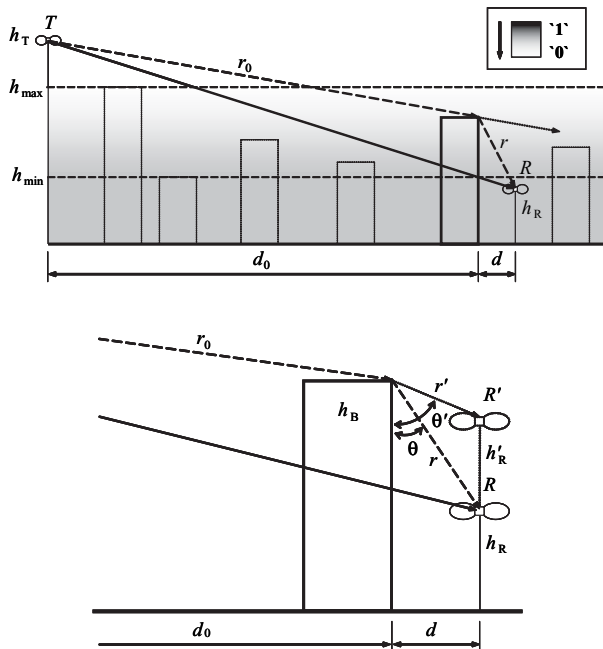
FIGURE 11.16. Geometry shadowing from a building's roof.

Using our knowledge about signal power distribution as a function of the angle-of-arrival, described in Chapter 10 following References [22,26], we can estimate the range of critical angles between the ray arriving from the base station and the top of specific buildings. In Figure 11.16, the choice of the geometry is shown, for which the angle $\theta = \tan^{-1}[d/(h_B - h_R)]$ is defined. In the case where the random distribution of the angles of diffraction occur from roofs of the randomly distributed buildings, one can determine, following the geometry presented in this figure, the virtual angle $\theta' = \tan^{-1}[d/(h_B - h_R - h'_R)]$. Beyond this boundary of *critical angles*, we cannot use the proposed statistical approach and must account for additional shadowing effects.

11.2. LINK BUDGET DESIGN FOR VARIOUS LAND ENVIRONMENTS

The main goal of this analysis is to predict, according to the existing stochastic approach and the corresponding statistical distributions (Gaussian, Rayleigh, and Rician), a set of relevant parameters of signal power budget design in RF wireless networks, for different kinds of terrestrial environments: rural forested, mixed residential, and urban.

11.2.1. Existing Methods of Link Budget Design

First, we determine the various parameters of a communication link budget according to well known concepts [39–42], and then we derive all parameters for the same link budget following the multiparametric stochastic approach and also on the classical statistical presentation of fading phenomena. According to References [39–42], the link power budget, that is the *total path loss* inside the communication link, consists of three main terms that satisfy three independent statistical processes (see Chapter 1).

There are three independent characteristics of the signal power decay: the *median path loss* or the mean signal power decay along the radio path, $\bar{L}$, the *slow fading* or the characteristic of shadowing, L_{SF}, and the characteristic of *fast fading*, L_{FF}, which yield:

$$L_{Link} = \bar{L} + L_{SF} + L_{FF} \tag{11.28}$$

As was shown in References [39–42], these characteristics in general vary as a function of propagation range between terminal antennas, operating frequency, spatial distribution of natural and man-made obstructions surrounding these antennas, vehicle speed, and antenna height with respect to obstructions, and so forth.

First, we describe a well known approximate concept of link budget estimation that is based on numerous experimental data obtained for various terrestrial communication links [40]. According to this concept, the expected median signal power at the moving station (MS) must be derived. This is also used for determining
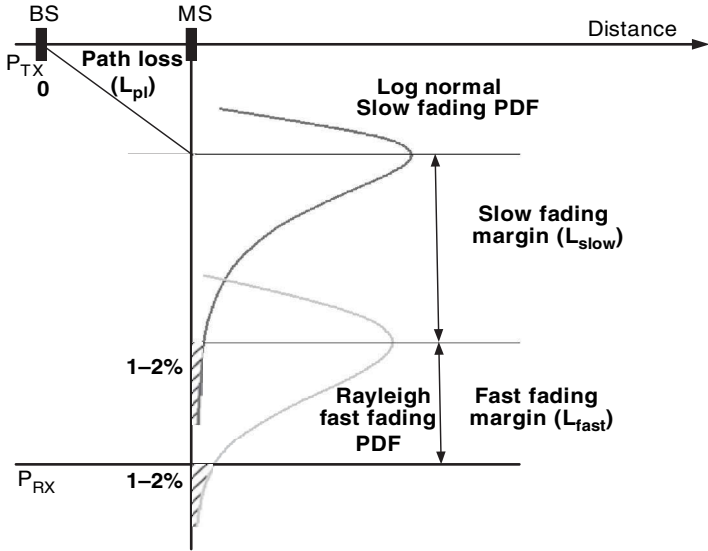
FIGURE 11.17. Path loss, slow and fast fading margins for Gaussian and Rayleigh PDFs. (Source: [40]. Reprinted with permission © 1995 IEEE)

the radio coverage of a specific base station (BS) and the interference tolerance for the purpose of cellular map construction. Usually, when designing the network power budget and the coverage area pattern, the slow and fast fading phenomena are taken into account, as schematically demonstrated in Figure 11.17 by introducing a shadow fading margin $L_{SF} = 2\sigma_{Sh}$ and a fast fading margin L_{FF}, as functions of the range between BS and MS (σ_{Sh} is the standard deviation of shadowing [40].) In other words, a shadow fading margin, which is usually predicted to be the 1–2% part of the lognormal PDF, and a fast fading margin, which is typically predicted to be the 1–2% part of the Rayleigh or Rician PDF, may be taken into account simultaneously or separately in a link budget design depending on the propagation situation. This situation is often referred to as ''fading margin overload'' resulting in a very low-level received signal almost entirely covered in noise. The probability of such worst cases determines the event of how rapidly the signal level drops below the receiver's *noise floor level* (NFL). The probability of such an event was predicted in Reference [40] as a sum of the individual margin overload probabilities, the slow and the fast, when the error probability is close to 0.5, since the received signal is at the NFL. According to the three-step scenario, illustrated in Figure 11.17, the following practical algorithm of power budget design is proposed.

First Step. Estimation of median path loss by using the well-known Hata-model [6,40] and deployment of a correction factor corresponding to the local antenna elevation, deduced from measurements, for example,

$$\bar{L} = L_{LOS} + L_{NLOS} \tag{11.29}$$
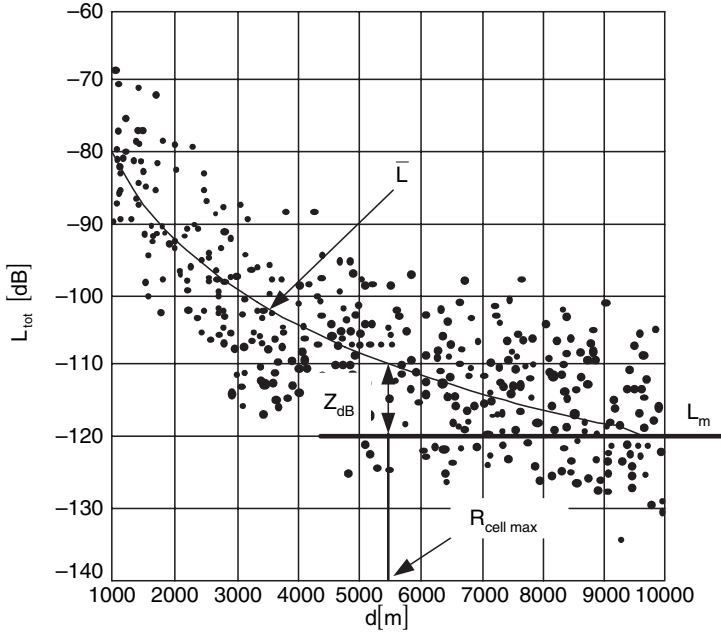
FIGURE 11.18. Median path loss and slow fading margin with respect to experimental data versus distance d from the transmitter in m. (Source [41]: Reprinted with permission of John Wiley & Sons)

Second Step. Estimation of slow fade margin, using the characteristic slow fading variance of typically 6 to 9 dB [40], and assuming lognormal slow fading PDF with a 1–2% slow fading margin overload probability (see Fig. 11.17). In this case, one has a slow fading margin of $L_{SF} = 2\sigma_{Sh} = 10\text{–}15$ dB.

Third Step. Assuming the Rician fast fading PDF, as a more general PDF for multipath channel prediction, with the Rician parameter $K = 5\text{–}10$ [40] and a fast fading margin overload probability of 1% (see Fig. 11.17), one has a fast fading margin of $L_{FF} = 5\text{–}7$ dB.

Another concept that still uses the same statistical approach for obtaining the slow and fast fade margins was proposed in Reference [41]. According to the proposed concept, the effect of slow fading or shadowing can be described as a difference between the median path loss and the maximum acceptable path loss, L_m. The median path loss can be predicted by any standard propagation model (see, for example, References [2,6,21,39,40]), which is depicted in Figure 11.18 by the continuous curve according to Reference [41].

The parameter L_m relates to the noise floor figure (NFL) of the concrete communication system. To obtain the shadow fade margin, one needs information on the PDF of the slow fading, which is defined in References [39–42] as a Gaussian process with a zero-mean Gaussian variable σ_{SF} and with a standard

deviation of shadowing σ_L. Its PDF was described in Chapter 1, we rewrite it using a definition as

$$PDF(x) = \frac{1}{\sigma_L\sqrt{2\pi}}\exp\left\{-\frac{\sigma_{SF}^2}{2\sigma_L^2}\right\} \tag{11.30}$$

Then the corresponding term of shadowing Equation (11.28) in dB for link budget design equals: $L_{SF} = 10\log\sigma_{SF} \equiv \sigma_{SF}[dB]$. Now we can, as in References [40–42], introduce an error function to obtain the so-called *complementary cumulative distribution function*, CCDF $\equiv Q(t) \equiv 1 - CDF(t)$, which describes the probability that the shadowing increases the median path loss by at least Z dB (Fig. 11.18)

$$Q(t) \equiv \Pr(\sigma_{SF} > Z) = \frac{1}{\sqrt{2\pi}}\int\limits_{x=t}^{\infty}\exp\left\{-\frac{x^2}{2}\right\}dx \tag{11.31}$$

where $t = Z/\sigma_L$. The CCDF is depicted in Figure 11.19 following References [39,40] versus the normalized parameter t. In this approach it was assumed a priori that either a maximum acceptable path loss of the system compared to noise floor level is known, or the concrete percentage of successful communication at the fringe of coverage of test area is known. In both cases the margin level Z can be obtained and, finally, for the concrete range of test area, the slow fading margin. To explain to the reader how to use the results of calculations according to References [40,41] that are presented in Figure 11.18 and Figure 11.19, let us first explain an example illustrated in Figure 11.18.
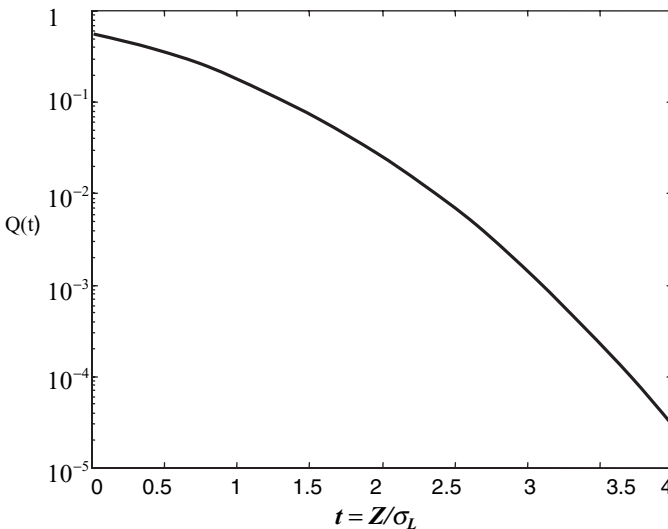
FIGURE 11.19. Gaussian CCDF versus the relative shadowing parameter normalized by the standard deviation of slow fading.

For the case where the maximum acceptable path loss of the system is $L_m = 120\,\text{dB}$ and the median path loss at the range of the test area (or cell) is $\bar{L} = 110\,\text{dB}$, the maximum fading margin is $z = 10\,\text{dB}$ at the range $r = 5.5\,\text{km}$. On the contrary, when the range of service and the maximum acceptable path loss are unknown, but the percentage of the successful coverage for each individual subscriber location inside the test side, as well as the standard deviation of slow fading are known, one can use the CCDF depicted in Figure 11.19. Now, if one considers the radio coverage of the area of service of about 90%, then we can find the value t for which the path loss is less than the maximum accepted path loss, L_m. It means that there is a probability of 90% to locate any user in the area of service. Thus, the shadowing effect (the worst case) can be found in the following manner: $\text{CCDF} \equiv Q(t) = 100\% - 90\% = 10\%$ or $Q(t) = 10^{-1}$. From Figure 11.19 this occurs for $t = 1.28155$. Moreover, if the standard deviation of shadowing is also known, for example, $\sigma_L[dB] = 8\,\text{dB}$, we get that

$$L_{\text{SF}} = Z[\text{dB}] = t\sigma_L = 1.28155 \cdot 8 = 10.2524\,\text{dB}$$

that is the same result as was estimated when the range of the test area and L_m were a priori known. Finally, if all parameters of shadowing and the system are known, one can easily obtain from Figure 11.19 the maximum range of the test area where full coverage is possible, using results shown in Figure 11.18.

Using the concept described in References [41,42], one can also estimate the *fast fade margin*, L_{FF}, using well-known Rician PDF distribution of such parameter (see also definitions introduced in Chapter 1.) We will rewrite it using new notations as

$$\text{PDF}(L_{\text{FF}}) = \frac{2L_{\text{FF}}}{(\text{rms})^2}\exp\left\{-\frac{L_{\text{FF}}^2}{(\text{rms})^2}\right\} \cdot \exp(-K) \cdot J_0\left(\frac{2L_{\text{FF}}}{\text{rms}}\sqrt{K}\right) \qquad (11.32)$$

where, as in References [40–42], $rms = \sqrt{2} \cdot \sigma_F$, σ_F is the standard deviation of fast fading, K is the ratio of LOS component (deterministic part of the total signal) and NLOS component (random part of the total signal). Then the last term in the equation of the link budget (11.28) can be defined as $L_{\text{FF}} = 10\log\sigma_{\text{FF}} \equiv \sigma_{\text{FF}[\text{dB}]}$. When parameters rms and K a priori are known, one can use the results presented in Figure 11.20 to find L_{FF}.

Now, if, for example, $K = 10$ and the fast fading probability equals 10^{-3}, it means the probability of the event that there exists fast fading between subscribers equals 0.1%, or that there are about 99.9% cases of successful communication links. If so, we have, from the curve depicted in Figure 11.20, that for $K = 10$ we get $w = -10\log(L_{\text{FF}}/rms) = -L_{\text{FF}[\text{dB}]} + rms_{[\text{dB}]} = -7\,\text{dB}$, that is, the fast fade margin L_{FF} is 7 dB below the rms. If rms is known, for example [41,42] $rms = 5\,\text{dB}$, then $L_{\text{FF}} = 5 + 7 = 12\,\text{dB}$. According to the scenario of how to obtain the link power budget proposed in References [41,42], one has two variants of link-budget design prediction.
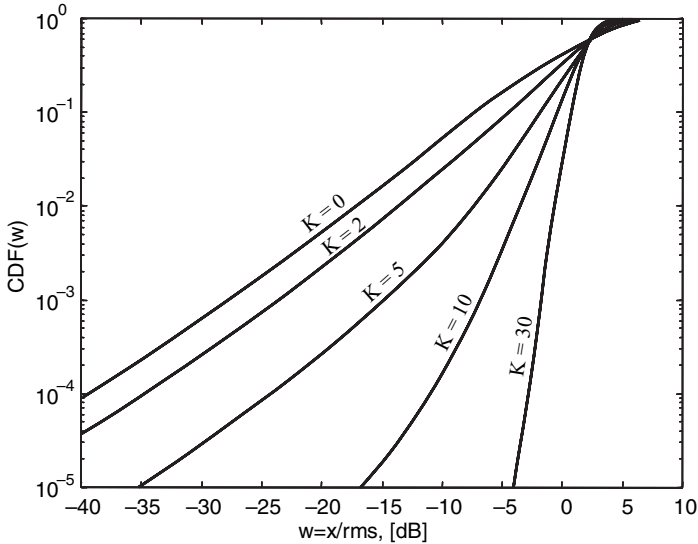
FIGURE 11.20. Rician CDF versus relative strength of the signal.

First Variant. Estimation of the *slow fade margin*, Z, deriving the median path loss, $\bar{L}$, by using well known propagation models [39–42], and using the maximum acceptable path loss, L_m, as well as the range between concrete terminal antennas, the knowledge of which is done for the performed wireless system. Estimation of the fast fade margin can be done, if the standard deviation and the Rician parameter K are known for the concrete propagation channel and wireless system.

Second Variant. Estimation of the slow fade margin, Z, and the range between concrete terminal antennas using derivation of the median path loss, $\bar{L}$, through well known propagation models [39–42], and using the standard deviation of slow fading, σ_L, as well as the percentage of the success communication for the concrete wireless system performed. In this case, using Figure 11.19 and the known value of σ_L, one can easily obtain the slow fade margin $L_{SF} \equiv Z = t\sigma_L$. As for the fast fade margin, L_{FF}, it can be obtained when the standard deviation of fast fading, σ_F, or *rms*, as well as the probability of the successful communication (that is, the CDF) are known for the concrete wireless communication channels by using the results from Figures 11.18–11.20.

11.2.2. Link Budget Design Based on the Stochastic Approach

Both approaches presented above need a priori information about the situation inside the propagation channel, that is, about the features of propagation environment and about the concrete wireless system. This means that designers of wireless networks need full information of the ''success'' (in percentages) of communication between subscribers and radio coverage of the area of service, as well as characteristics of the system, such as the standard deviation of slow- and fast-fading signal, the maximum

acceptable path loss or noise floor level, and so forth. As was mentioned above, to have all these characteristics one must obtain experimentally all features of the communication channel (environment) and have full information about the concrete wireless system. This way is unrealistic, because all these characteristics are not predictable simultaneously: either the concrete communication system parameters are known and designers need to carry out test experiments to find the characteristic features of the channel (environment), or conversely, having information about the terrain features, designers predict future wireless system for effective service of subscribers.

In the following section we propose an approach developed in Reference [27], which is based on information absout the propagation characteristics of the channel obtained either by measurements or by using information obtained from topographic maps. In other words, we propose an approach, which is based on the stochastic models described above for rural mixed residential and built-up terrain.

At the same time we have some information about the wireless networks. Namely, about parameters of the base station and the vehicle antennas, as well as about the noise floor level (NFL) or *maximum accepted path loss* of the wireless system. We will present our approach for link budget design in the form of a prediction algorithm.

First Step. At this step, we obtain the standard deviation of slow fading, σ_L, as a logarithm of ratio between the signal intensity with and without diffraction phenomena, which gives the main influence on shadowing from building contours: in the case of a single diffraction

$$\sigma_L = 10 \log \frac{[(\lambda d/4\pi^3) + (z_2 - \bar{h})^2]^{1/2}}{(z_2 - \bar{h})} \qquad (11.33)$$

in the case of multiple diffraction

$$\sigma_L = 10 \log \frac{\langle I_1 \rangle + \langle I_2 \rangle}{\langle I_3 \rangle} \qquad (11.34)$$

where $\langle I_1 \rangle$ is described by (5.94) and $\langle I_2 \rangle$ by (5.96) for urban and suburban environments. The term $\langle I_3 \rangle$ is described by the following expression:

$$\langle I_3 \rangle = \frac{\Gamma \lambda l_v}{8\pi \{\lambda^2 + [2\pi l_v \gamma_0 (\bar{h} - z_1)]^2\} d^3} (z_2 - \bar{h}) \qquad (11.35)$$

Finally, this allows us to obtain the fade margin using two options described in References [40,41]:

– according to Reference [40] because of the shadowing effect from building roofs and corners:

$$\sigma_{SF} = 2\sigma_L \quad \text{and} \quad L_{SF} = 10 \log \sigma_{SF} \qquad (11.36)$$

– according to Reference [41] using information about the maximum acceptable loss within the system or NFL, for the concrete range of test area, $d = constant$, we immediately obtain this value as $L_{SF} = L_m - \bar{L}$, where $\bar{L}$ is defined by (5.98)–(5.99) for each concrete terrain environment. In this case, obtaining σ_L and then, $t = \sigma_{SF}/\sigma_L$, we finally (by using Figure 11.19) can figure out (in percentages) how successful the communication link will be, without obtaining any shadowing effects.

Second Step. To obtain information about the *fast fading margin*, L_{FF}, we need, first of all, the knowledge of the Rician parameter K as a ratio of coherent (LOS component) and incoherent (multipath component without diffraction) parts of the total signal intensity [27], that is,

$$K = \frac{\langle I_{co} \rangle}{\langle I_{inc} \rangle} \tag{11.37}$$

Here, for the mixed residential rural areas, $\langle I_{inc} \rangle$ and $\langle I_{co} \rangle$ are described by expressions (5.59) and (5.60). For urban and suburban areas they are described by (5.94) or (5.96) and (5.97), respectively. At the same time, we obtained above (for each terrain type) the rms of the total signal intensity, $rms = \sqrt{\langle I_{total} \rangle}$, using for each case the corresponding formulas (5.98). Finally, we use, instead of the method proposed by Reference [27] and presented above with help of CDF(x) depicted in Figure 11.20, the corresponding formula for Rician distribution, which allows us to obtain σ_{FF} or L_{FF} using well-known equation:

$$L_{FF} = 10\log \sigma_{FF} = 10\log \left\{ \int_0^\infty x^2 \text{PDF}(x) dx - \left(\int_0^\infty x\text{PDF}(x)dx \right)^2 \right\} \text{ dB} \tag{11.38}$$

where x is the random amplitude of the received signal. Using (11.38) we get [27]

$$\sigma_{FF} = [2 \cdot (rms)^2 \cdot e^{-K}] \cdot \left[\frac{1}{2} \cdot e^K \int_0^\infty y^3 \cdot e^{-y^2} \cdot I_0(2 \cdot \sqrt{K} \cdot y) \cdot dy \right. $$
$$\left. - \left(\int_0^\infty y^2 \cdot e^{-y^2} \cdot I_0(2 \cdot \sqrt{K} \cdot y) \cdot dy \right)^2 \right]^{1/2} \tag{11.39}$$

Now, the knowledge of corresponding *rms*, the ratio L_{FF}/rms, and K for the concrete range between subscribers or between base station and subscribers allows us to obtain the outage probability function CDF(L_{FF}/rms). Conversely, if CDF(L_{FF}/rms) is known, using result of *rms* and K derivations, as well as the corresponding Rician

CDF(w) distribution, depicted in Figure 11.20 according to References [41,42] versus the normalized magnitude of the fast fading, $w = L_{FF}/rms$, we can obtain the fast fade margin L_{FF}.

Finally, taking L_{FF} either from (11.39) or from Figure 11.20, and σ_L according to (11.33)–(11.35) and relations $\sigma_{SF} = 2\sigma_L$ ($L_{SF} = 10\log\sigma_{SF}$) [27,41,42], we get the total power budget (in decibels) for the actual communication link design. Moreover, we simultaneously can strictly predict the percentages of the fast fading effects (via CDF(L_{FF}/rms), see above) for the real situation within the urban communication channel.

11.2.3. Experimental Verification of the Link Budget

To account for the long-term (e.g., slow) fading effects, the proposed stochastic approach and the corresponding formulas (11.34)–(11.36) are used to increase the accuracy of the proposed model by taking into account the shadowing effects from building roofs for low antenna elevation. As was shown in experiments in Lisbon, this can significantly change results of the theoretical prediction of path loss for antennas that can be arranged deeply within the built-up layer. In this case, we need to estimate the additional signal attenuation due to shadowing and introduce in a link-budget equation not only the mean value of path loss but also the effects of slow fading, described by formulas (11.30)–(11.31). Returning to Figure 11.16, we analyze the situation that occurs when the antenna is located at the height that corresponds to the angles greater than θ'. The procedure that estimates long-term (slow) fading phenomena for the propagation link budget design, using existing methods, is described above in Section 11.2.2. Taking into account the additional fading effects, using formulas (11.34) to (11.36), for the median path loss obtained for tested area of Lisbon by using formulas (5.94) to (5.99), we can significantly correct the results of total path loss prediction using the following formula:

$$L_{total} = 10\log\lfloor\lambda^2(\langle I_{co}\rangle + \langle I_{inc}\rangle)\rfloor + 10\log\sigma_{SF} \qquad (11.40)$$

For comparison with the experimental results presented in Figures 11.14(a)–(c), we selected only the worst-case scenarios (i.e., with shadowing), where the difference between theoretical prediction and measurements exceeds 20–25 dB. These sites are presented in Figures 11.21(a),(b) where again segments that describe the experimental data with asterisks correspond to theoretical calculations of mean pass loss according to (5.94) to (5.99).

Using the more general formula (11.40) for link budget design with the effects of slow fading, we get the results depicted by diamonds in Figures 11.21(a),(b). By inspection of these figures, it is seen that the additional excess attenuation, which we now add to the stochastic model, yields a better agreement with the experimental data for five of the six tested points. The discrepancy of about 20–30 dB for these five points is reduced to about 3–5 dB, and the standard deviation does not exceed 5–6 dB.
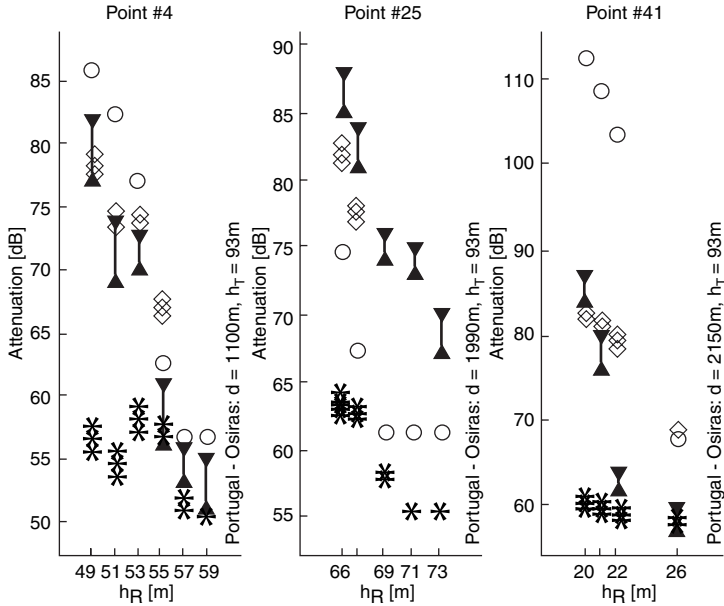
FIGURE 11.21(a). Comparison of experimental data with theoretical prediction taking into account shadowing (denoted by diamonds); The other notations are the same as in Fig. 11.14.
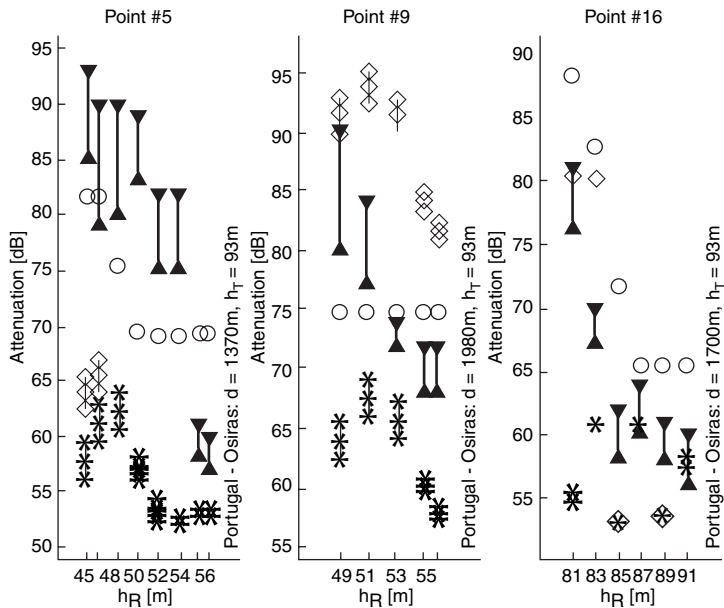
FIGURE 11.21(b). The same, as in Fig. 11.21a, but for other experimental sites.

11.2.4. Experimental Verification of Slow and Fast Fading

During the Seventies and Eighties of the last century, some pioneer experimental and theoretical investigations of spatial-temporal variations of signal strength or power in various built-up environments have been carried out. It was shown that the propagation process within the urban communication link is usually locally stationary in the time domain [14,35,40,44–49]. The spatial variations of the signal passing such a channel have a double nature, the large-scale and the small-scale [40,44,49], which in Chapter 1 we defined as slow and fast fading, respectively, according to the well-known standard.

Experimental Verification of Slow Fading. As was shown by numerous experimental observations of spatial and temporal fluctuations of radio signals in urban communication links, slow fading is observed mostly for higher elevated BS antenna and lower elevated MS antennas compared to roofs of the buildings and are caused by the shadowing effects of buildings surrounding both terminal antennas. Finally, deep "shadow" zones in communications are created along the radio path in NLOS (clutter) conditions between each BS and MS antenna located within the area of service. A summary of experimental results, obtained in different cities of Israel, was presented in terms of the cross-correlation function of signal amplitude $D_i(d) = \langle [E_i(\mathbf{r}_1) - E_i(\mathbf{r}_2)] \rangle$ for three components of the field strength ($E_1 = E_x$, $E_2 = E_y$, $E_3 = E_z$). These components were analyzed by measuring along the radio paths between the terminal antenna located at the point $\mathbf{r}_2$ and that at the point $\mathbf{r}_1$, that is versus $d = |\mathbf{r}_2 - \mathbf{r}_1|$. The result of this statistical analysis, shown in Figure 11.22, is direct evidence of the existence of such long-scale random variations of signal strength level along the radio path d.

   These spatial signal variations have been obtained after signal processing of the average signal amplitudes (about 3800 magnitudes of signal strength has been investigated) with the scale of averaging ~ 8–10 wavelengths at the frequency band from 80 to 400 MHz to exclude effects of fast fading due to random interference between multipath field components.

   As can be seen from Figure 11.22, there are two sharp maxima which correspond to two scales of signal spatial variations, $L_1 = 15$–20 m and $L_2 = 80$–100 m, respectively. As was shown experimentally [14,44–49], the first scale can be related to the average length of gaps between buildings. It determines the so-called "light zones" observed within these gaps.

   The second scale, according to References [14,44–49], can be related to the large "dark" zones, which follow the "illuminated" zones, and can be explained only by the diffraction from buildings located along and across the radio path. Other experimental investigations carried out during the 1980s and the beginning of the 1990s proved this principal result, which describes a nature of slow signal fading in urban communication links. In other words, all referred experimental works have shown that the effect of shadowing is a realistic cause for long-term variations of signal strength (or power) after its averaging with "window scale" exceeding several wavelengths during the statistical processing. Moreover, as was obtained
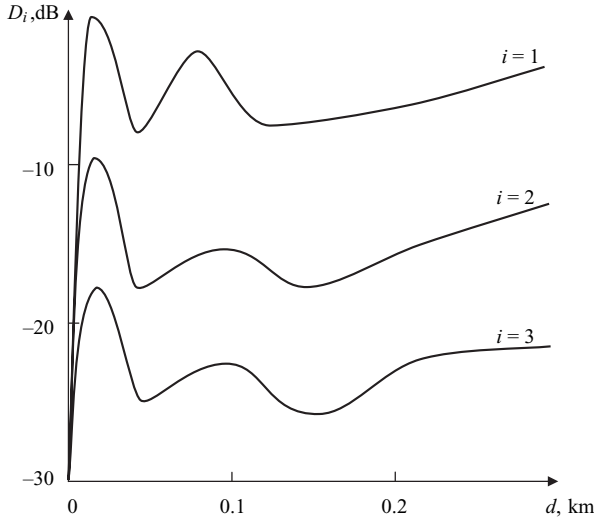
FIGURE 11.22. Statistical analysis of long-scale slow fading along the radio path d for three components of the electromagnetic field ($i = 1, 2, 3$).

both theoretically and experimentally [46–60], the statistical distribution of slow signal variations, measured in decibels (dB), is very close to lognormal distribution. As for this phenomenon, we described it in detail in Chapter 1 and also in this section using corresponding analytical presentation of the slow fading.

Experimental Verification of Rayleigh and Rician Laws for Fast Fading. As in Reference [14], we based on Rician statistical distribution, because, as was mentioned in Chapter 1, the latter distribution is more general and covers the Rayleigh fast fading statistics. Therefore, it can be successfully used for the analysis of signal fast fading both for close and for open fixed radio links. At the same time, first Clarke [61] and Aulin [62], and later Ali Abdi with colleagues [63], have used Rayleigh statistics in their analysis of fast fading. To understand the accuracy of each distribution of fast fading phenomenon in built-up environments, we have carried out several experiments in various urban and suburban areas [15–27,44–49]. About 3800 magnitudes of signal strength were collected, and then divided into three separate groups depending on the type of radio path and antenna elevations with respect to roofs of the buildings. The *first group* of signal outputs was measured at radio links with the obstructive conditions for the low elevated terminal antennas where there is no line-of-sight (NLOS) between the terminal antennas. The *second group* of signal outputs was obtained for radio links where both LOS and NLOS conditions were observed between the terminal antennas. In this case, one antenna (usually the base station antenna) was higher than rooftops. The *third group* was obtained for radio links where only LOS conditions for radio signal were observed. Thus, the measured output samples for the first group were differentiating as satisfying Rayleigh statistics, (about 800 from 1200 measured points). The measured
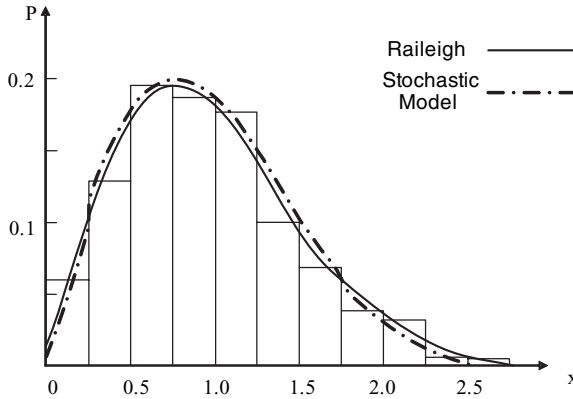
FIGURE 11.23(a). Distribution of signal strength amplitude $r(t)$ versus the normalized parameter $x = r(t)/rms$; the histogram corresponds to experiments and the curve describes the Rayleigh distribution.

output points for the second and the third groups were combined together, approximately 1000 points from 1200 samples for the second group, and 800–900 from 1300 samples points for the third group. The reason for not using all the samples will be explained below.

Statistical analysis of the first group of outputs, which is approximately 1200 magnitudes of signal strength, is presented as a histogram in Figure 11.23(a), versus the normalized parameter $x = r(t)/rms$. Where $r(t)$ is the local magnitude of signal envelope, the parameter *rms* was defined in Chapter 1.
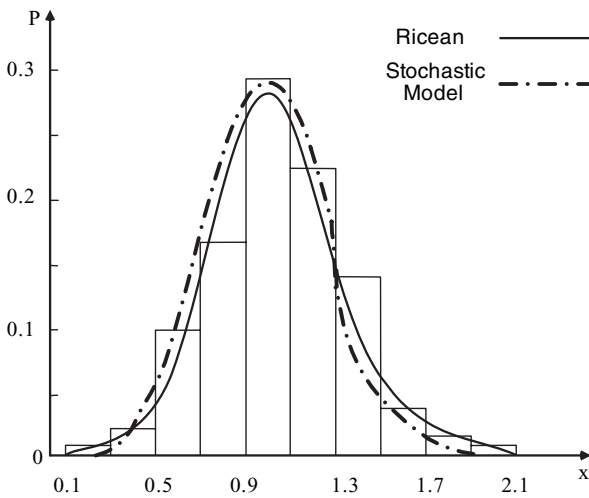
FIGURE 11.23(b). Distribution of signal strength amplitude $r(t)$ versus the normalized parameter $x = r(t)/rms$; the histogram corresponds to the experiments and the curve describes the Rician distribution.

This histogram was constructed using approximately 800 points along the radio path at ranges from 200 m to 1.5 km between the terminal antennas. The corresponding continuous curve presented in Figure 11.23(a) was derived from the Rayleigh distribution (see Chapter 1) with all parameters obtained from resulting statistical analysis of measured points. This shows agreement between the experimentally obtained distribution of signal strength presented and the theoretical prediction presented by Rayleigh's law described the worst (NLOS) situation occurs in wireless communication link. The measured output points for the second and the third groups were combined together (approximately 1300 points for the second group and 700–800 points for the third group). Their statistical analysis is presented in the histogram in Figure 11.23 as a function of the normalized signal strength $x = r(t)/rms$.

The continuous curve in the figure describes calculations of the Rician distribution (see Chapter 1) of fast signal variations obtained by using the information about *rms* and *K* from statistical analysis of experimental data. As it is seen, a good explanation of experimental data was obtained by using the Rician's law. Results of the statistical analysis of numerous experiments and theoretical prediction, both presented in Figure 11.23, allow us to conclude that the Rayleigh statistics can be used during analysis of closed urban communication links for low elevated mobile terminal antennas. That is, for a case of NLOS conditions in mobile communication. At the same time, the Rician law strictly describes fast fading effects for combined NLOS (close areas) and LOS (open areas) conditions where one of the antenna is higher than the rooftops.

Description of Multipath Effects by Use of Stochastic Approach. Now, we will explain why all the experimental samples obtained in the statistics were not used. As was mentioned above, about 30–35% of more than 3800 measurement points cannot be described by the Rayleigh–Rician statistics. Thus, in the first group only about 800 from the 1200 measured points could be analyzed by using the Rayleigh statistics description. The same situation occurred with the second group where only about 1000 points of the 1200 satisfy the Rayleigh law. Finally, from the third group only about 800–900 of the 1300 points could be analyzed by using Rician statistics. In all the points, which are not described by the well-known Rayleigh–Rician statistics, we observe deeper signal strength fast variations.

In order to explain the mechanism of deep signal strength variations, we have used the unified stochastic approach [14–21], taking into account the multiple reflection and scattering effects from buildings and other obstructions randomly distributed on the terrain according to Poisson's law. Such a model allows us to take into account the strength of the total field at the receiver because of the additive effect of one-time to *n*-time scattered waves with independent strengths. As was obtained in References [14–21], in the zones close to the BS antenna ($d < 1$ km) the single scattered waves are predominant, whereas far from the BS antenna ($d > 2$ km) the two- and three-times scattered waves prevail. However, the field strength of the *n*-reflected waves exponentially attenuates with distance. Therefore, for microcell communication channels with ranges less than 2–3 km, only single- and two-time scattered waves must be taken into account; this phenomenon was also

mentioned in Chapter 5. Moreover, the strengths of these waves are normally distributed with the zero-mean value and dispersion σ_1^2 (for single scattered waves) and σ_2^2 (for two-time scattered waves) and depend strongly on the characteristic features of the terrain. The main features are the density of the building v per kilometer square, the average length of the buildings (or width, depending on the orientation to antenna direction) $\bar{L}$, and the contours density of the buildings γ_0, defined by (5.69). The average wave number also depends on the distance from the BS antenna d. Thus, following formulas (5.88) and (5.89) in Chapter 5, we get:

– for the average number of single scattered waves

$$\bar{N}_1 = \frac{\pi v d^2}{4} K_2(\gamma_0 d) \tag{11.41}$$

– for the average number of double scattered waves

$$\bar{N}_2 = 9(\pi v d^2)^2 \left[\frac{K_4(\gamma_0 d)}{8!} + \sqrt{\frac{2}{\pi \gamma_0 d}} \frac{K_{7/2}(\gamma_0 d)}{7!} \right] \tag{11.42}$$

where $K_n(\gamma_0 d)$ is the MacDonald's function of n-order.

The probability of receiving single and double scattered waves at the MS antenna was computed according to the following formula [14]:

$$P_i = 1 - \exp(-\bar{N}_i), i = 1, 2 \tag{11.43}$$

Following the above mentioned, we took into account in our computations of formula (11.44) for cumulative distribution function, (cdf) the effects of independent single (the first term) and double (the second term) scattering, as well as their mutual influences on each other (the third term), that is

$$
\begin{aligned}
\text{cdf}(r) = &\frac{P_1(1 - P_2)}{P_0} \frac{r}{\sigma_1^2} \exp\left\{ -\frac{r^2}{2\sigma_1^2} \right\} + \frac{P_2(1 - P_1)}{P_0} \frac{r}{\sigma_2^2} \exp\left\{ -\frac{r^2}{2\sigma_2^2} \right\} \\
&+ \frac{P_1 P_2}{P_0} \frac{r}{(\sigma_1^2 + \sigma_2^2)} \exp\left\{ -\frac{r^2}{2(\sigma_1^2 + \sigma_2^2)} \right\}
\end{aligned}
\tag{11.44}
$$

where $P_0 = 1 - (1 - P_1)(1 - P_2) = 1 - \exp[-(\bar{N}_1 + \bar{N}_2)]$ is the probability of direct visibility (i.e., of LOS). In Figure 11.24, the corresponding histogram shows the cumulative distribution of signal strengths of the "anomalous" 1000–1100 samples together with the cdf (the continuous curve) computed according to (11.44), taking into account the same experimental data as was done earlier for the Rayleigh and Rician statistics evaluation.

We have analyzed this more general distribution as a function of the normalized random signal strength envelope $x = r/\sqrt{\sigma_1^2 + \sigma_2^2}$ using the probabilities P_1 and P_2.
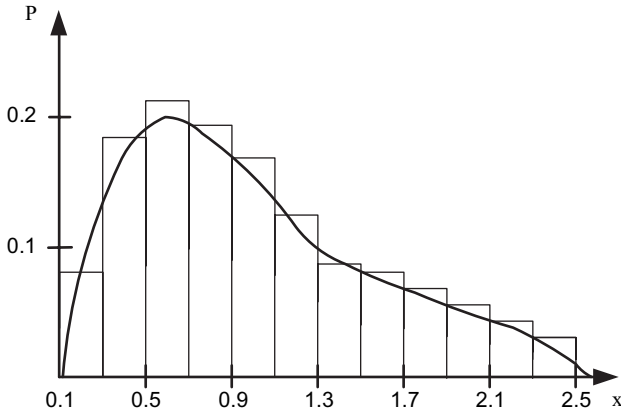
FIGURE 11.24. Distribution of signal strength amplitude $r(t)$ versus the normalized parameter $x = r(t)/rms$; histograms correspond to experiments and the continuous curve describes the general distribution of eqn. (11.44).

These probabilities were computed for the terrain parameters $\gamma_0 = 10\,\text{km}^{-1}$ and $d = 0.5$–$0.8\,\text{km}$ of an average city and for the ratio of $(\sigma_1/\sigma_2) \approx 12$–$13\,\text{dB}$ of losses between the single and double scattered waves [14–21].

It is clearly seen from Figure 11.24 that for $d < 1\,\text{km}$, the obtained distribution, calculated according to (11.44) with all the parameters obtained from measurement, strongly differs from Rayleigh or Rician statistics, presented in Figures 11.23(a) and 11.23(b). At the same time, using the other 2500–2600 samples selected separately and depicted in Figure 11.23(a) and Figure 11.23(b), we computed (11.44) for each specific condition occurring in the urban scene. Thus, for the histogram in Figure 11.23(a), we took the same condition of mean city with $\gamma_0 = 10\,\text{km}^{-1}$, but with the NLOS conditions at the distance of 1.5 km from the BS antenna. For the histogram, depicted in Figure 11.23(b), we took the same conditions of mean city with $\gamma_0 = 10\,\text{km}^{-1}$, but with the LOS and quasi-LOS conditions at the distance of 1.5 km from the BS antenna. The corresponding computations of general signal strength distribution (11.44) are shown by dashed curves in Figure 11.23(a) and Figure 11.23(b). It is obvious that general distribution (11.44) gives close solution both for Rician law (in LOS and quasi-LOS conditions) and for Rayleigh law (in NLOS conditions), at distances from the BS antenna where effects of multipath become predominant. Therefore, with a great accuracy we can use expression (11.44) to describe the fast fading phenomena for various situations occurring in multipath communication links for different elevations of base station antenna and subscriber antenna with respect to obstructions surrounding them. We propose a new tool to investigate fast spatial and temporal signal strength fading by using the general signal strength distribution (11.44) based only on propagation multipath phenomena, using measurements data and characteristic features of the built-up terrain, conditions of measurements, and antennas location compared with height profile of the buildings.

11.3. CHARACTERIZATION OF MULTIPATH RADIO CHANNEL BY RICIAN FACTOR

In this section, we present a simple physical explanation of multipath propagation effects that fit the Rician distribution. The K-factor of Rician distribution also can be a very useful tool for multiplicative noise description (see definitions in Chapter 1). We will show in Chapters 12 and 13 how to use this fading factor to predict information data stream parameters, such as capacity and spectral efficiency, as well as the maximum radius of cell during cellular maps design in different terrestrial environments.

According to the definition presented in Section 11.2, the Rician parameter can be defined according to the stochastic model as the ratio of the coherent and incoherent component of the signal intensity, $K = \frac{\langle I_{co} \rangle}{\langle I_{inc} \rangle}$. Where the coherent component, $\langle I_{co} \rangle$, describes line-of-sight (LOS) conditions, and the incoherent component, $\langle I_{inc} \rangle$, describes the clutter or obstructive conditions in the propagation channel. As was also shown in References [28,64,65], the later component determines the multiplicative noise inside the communication channel, and we can determine K as a ratio between the signal and the multiplicative noise, $K \equiv \frac{S}{N_{mult}}$. It has different physical meaning in different environments.

In fact, for the mixed residential area using results obtained in Chapter 5, we get the expression for the K-factor along the radio path d between two terminal antennas:

$$K = \frac{I_{co}}{I_{inc}}$$

$$= \frac{\exp\left\{ -\gamma_0 d \dfrac{\bar{h} - z_1}{z_2 - z_1} \right\} \left[\dfrac{\sin(k\, z_1 z_2 /d)}{2\pi d} \right]^2}{\dfrac{\Gamma}{8\pi} \dfrac{\lambda\, l_h}{\lambda^2 + [2\pi l_{h\bar{L}}\gamma_0]^2} \dfrac{\lambda\, l_v}{\lambda^2 + [2\pi l_v \gamma_0 (\bar{h} - z_1)]^2} \dfrac{[(\lambda d/4\pi^3)^2 + (z_2 - \bar{h})^2]^{1/2}}{d^3}} \tag{11.45}$$

For the urban and suburban environments following Chapter 5, we finally get

$$K = \frac{I_{co}}{I_{inc_1} + I_{inc_2}}$$

$$= \frac{\exp\left\{ -\gamma_0 d \dfrac{(z_1 - \bar{h})}{(z_2 - z_1)} \right\} \dfrac{\sin^2(kz_1 z_2 /d)}{4\pi^2 d^2}}{\dfrac{\Gamma\lambda l_v [(\lambda d/4\pi^3) + (z_2 - \bar{h})^2]^{1/2}}{8\pi[\lambda^2 + (2\pi l_v \gamma_0 (z_1 - \bar{h}))^2]\, d^3} + \dfrac{\Gamma^2 \lambda^3 l_v^2 [(\lambda d/4\pi^3) + (z_2 - \bar{h})^2]}{24\pi^2 [\lambda^2 + (2\pi l_v \gamma_0 (z_1 - \bar{h}))^2]^2 d^3}} \tag{11.46}$$

where, as in Chapters 5 and 10, $\gamma_0 = 2\bar{L}v/\pi \,\mathrm{km}^{-1}$ is the density of the building contours, v is the density of buildings in the investigated area per square kilometer, and $\bar{L}$ is the average length (or width) of buildings in meters. l_v and l_h are the vertical and horizontal coherence scales of reflections from building walls in meters,
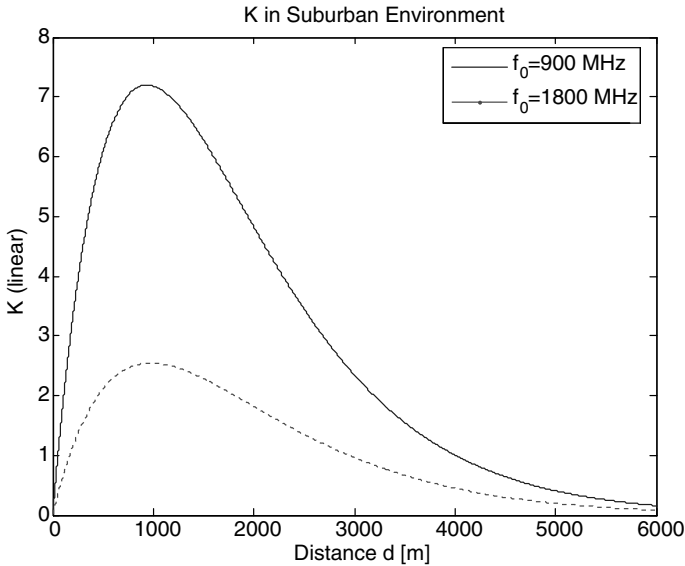
FIGURE 11.25. K-factor versus distance between BS and MS at $f_0 = 900$ and 1800 MHz.

and $\bar{h}$ is the average buildings' height in meters. Finally, $\Gamma \equiv |\Gamma|$ is the absolute value of the reflection coefficient, and z_2 and z_1 are the BS and MS antenna heights in meters.

For one of the mixed residential area, that we used as an experimental site in References [15–18], we have obtained the following parameters based on the corresponding topographic map: $\bar{h} = 12$ m, $z_1 = 2$ m, $z_2 = 22$ m, $f_0 = 900$ MHz and $f_0 = 1800$ MHz, $\gamma_0 = 2 \cdot 10^{-3}$ m^{-1}, $d = (1\text{–}6000)$ m, $l_v = 1$ m, $l_h = 1$ m, $|\Gamma| = 0.6$. Results of numerical calculation are shown in Figure 11.25.

As follows from the results of this calculation, the ratio between a signal and the noise caused by fast fading can achieve magnitude of 6–7 at the ranges of 1–2 km, that is, for microcell environment. Decrease of the LOS (dominant) component at far distances can be explained by the increase of the multipath component due to multiple scattering from obstructions, which are sufficient in far zones.

For the numerical analysis of the K-factor variations along radio path in urban area, we used the parameters obtained from one of experimental site described in References [22–26]: $\bar{h} = 18.3$ m, $z_1 = 2$ m, $z_2 = 50$ m, $\gamma_0 = 1 \cdot 10^{-2}$ m^{-1}, $d = 1\text{–}1600)$ m, $l_v = 2$ m, $|\Gamma| = 0.8$. Results of calculations are shown in Figure 11.26 for 900 MHz and 1800 MHz. As follows from Figure 11.26, the results of simulations fully repeat the previous results obtained for mixed residential area; only the K-factor in urban environment can achieve magnitude of 15–18, the effect of which depends on the density of obstructions and the height of the BS antenna. This effect also depends on the frequency of the system. Thus, when doubling the frequency, the magnitude of the K-factor is also increased more than twice (see Figures 11.25 and 11.26). The obtained results are not in contradiction with those
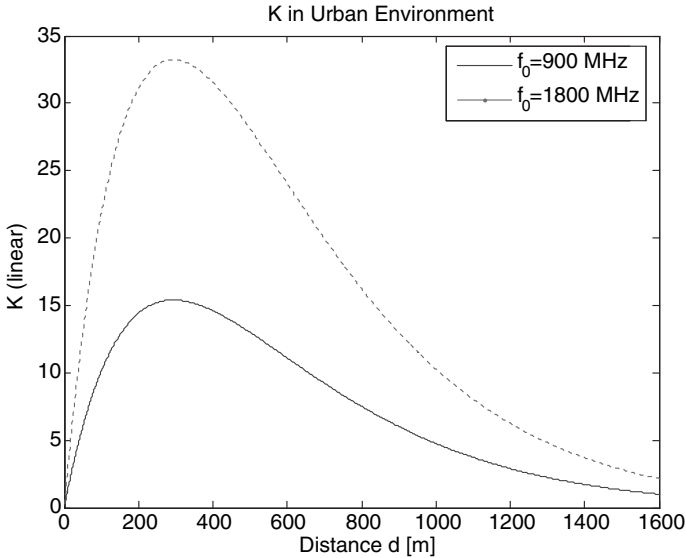
FIGURE 11.26. *K*-factor versus distance between BS and MS at $f_0 = 900$ and 18 MHz.

obtained in References [64,65], where with increase of the radiated frequency of the source, the coherent component becomes predominant compared with the incoherent component of the total signal intensity.

As was mentioned in References [64,65], this result has a physically vivid explanation. Thus, with the increase of the radiated frequency, that is, the decrease of the wavelength with respect to the dimensions of rough structures and obstructions surrounding a transmitter, the effects of scattering (e.g. stochastic effects) become weaker, whereas the effects of reflection and diffraction from obstructions (e.g., deterministic effects) become predominant.

11.4. MAIN ALGORITHM OF RADIO COVERAGE (RADIO MAP) DESIGN

The physical–statistical multiparametric models proposed in Chapter 5 for various land environments are based on the stochastic approach and require, as initial data, statistical parameters of the terrain and environment such as the law of the distribution of the buildings at the rough terrain, their density, average length and height, as well as the locations of terminals, the transmitter and receiver, to obtain loss characteristics in various situations in the built-up areas. In addition to that, this approach provides an estimate of the total path loss and finally, allows us to obtain the radio coverage of the area of service for various built-up environments. In turn, we propose the following algorithm to obtain the radio coverage and the corresponding radio map. First, we need information about the terrain features, such as [15–28]

- Terrain elevation data, digital terrain map, consisting of ground heights as grid points $h_q(x, y)$;
- A clutter map, the ground cover of artificial and natural obstructions as a distribution of grid points, $h_0(x, y)$ for built-up areas. This is the overlay profile of the buildings $F(z_1, z_2)$; the average length or width of obstructions, $\bar{L}$ or $\bar{d}$; the average height of obstructions in the test area, $\bar{h}$; the obstructions density per square kilometer, v;
- The effective antenna height, which is the antenna height plus a ground or obstruction height, if the antenna is assembled on a concrete obstruction: z_1 for the transmitter and z_2 for the receiver;
- The antenna pattern or directivity and its effective radiated power (ERP); the operating frequency, f.

According to the data obtained above, we perform a prediction algorithm consisting of several steps of analysis [25–28]:

First Step. We introduce the built-up terrain elevation data for a three-dimensional radio path profile construction. As a result, there is a digital map (cover) with actual heights of obstructions in the computer memory.

Second Step. Using all parameters of built-up terrain and antennas, the transmitter and receiver, the three-dimensional digital map is analyzed for estimations of the following parameters and features of the built-up terrain: the typical correlation scales of the obstacles, ℓ_v and ℓ_h, and the type of building material dominant in the test area to evaluate the absolute value of reflection coefficient in each "cell" of computation.

Finally, all these parameters allow us to obtain the density of building contours at the plane $z = 0$ (the ground level), $\gamma_0 = 2\bar{L}v/\pi$, and then the clearance conditions between the receiver and the transmitter, for example the average horizontal distance of the line-of-sight $\langle\rho\rangle$: $\langle\rho\rangle = \gamma_0^{-1}$.

Third step. The various factors obtained earlier must then be used for the computer program based on the 3D multiparametric model for different types of irregular terrain. In the case of mixed residential rural areas, expressions (5.98) and (5.99) with (5.59) and (5.60) must be used. In the case of *built-up* (urban and suburban) terrain, expressions (5.63) to (5.67) [straight crossing grid-street structure] or (5.94), (5.96), and (5.97) [randomly distributed buildings], or combination of both structures, as was shown in Chapter 10, must be used. As a result, the signal path loss distribution can be obtained for both isotropic and directive antennas by introducing their EPR.

These data must be constructed as a two-dimensional radio map, which describes the ground coverage of the radio signal for the built-up area being tested for service. The example of such radio coverage for one concrete experimental site with straight crossing streets described in Reference [20] is shown in Figure 11.27.

Here, the curves are the path loss obtained experimentally by direct measurements along various routes of moving antenna. The numbers inside the circles are computed using formulas (5.63) to (5.67) according to crossing-waveguide model described in Chapter 5. An agreement between theoretical prediction and measured data is clearly seen.

FIGURE 11.27. Radio coverage of experimental site with straight crossing streets according to [20]; the curves are the results of computation of (5.63)–(5.67) and the circles are the measured data.

Another example of the radio map can be presented for the Stockholm city following results obtained in Section 11.1. On the basis of theoretical results, the radio map of the experimental site can be presented as 2D and 3D pictures, as shown in Figure 11.28.

The vivid radio coverage of the service site of Stockholm is obtained to analyze propagation situation and possibility to communicate with the BS antenna for any subscriber's access point located in the area of service.

According to the general algorithm presented above, we had designed radio coverage of Ramat-Gan market area in Israel following only its topographic map and building height profile presented in Figure 11.29.

It can be easily prototyped as a typical "Down-Town" area with tall buildings that are very dense. The first stage of the simulation was to process the physical data.
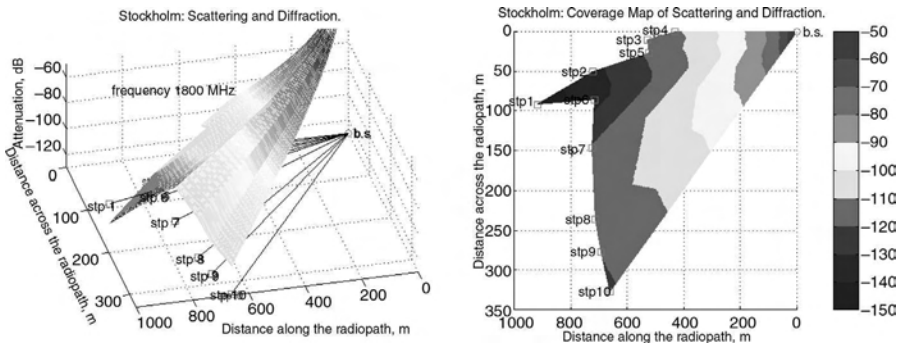
FIGURE 11.28. Radio map of Stockholm city: in 3-D (left) and 2-D (right) domains.

FIGURE 11.29. Topographic map of the stock market area in Ramat-Gan.

We have measured the dimensions of each building near the antenna and calculated the average height of the buildings for every path stretched at 5° intervals. We then estimated the number of buildings per square kilometer in the test-site area, their average length or width (related to the direction of the antenna main loop orientation), and the contour density of the buildings, γ_0. The antenna characteristics, such as "sector", tilt, height (z_2), effective power ("Eff"), and gain ("G"), as well as the terrain parameters, such as γ_0, the distance d between BS and MS, and step Δd along the radio path between BS and MS used for this simulation are presented in Table 11.1

Table 11.1. The Terrain and Antenna Parameters of Ramat-Gan Experimental Site.

Sector [deg]	γ_0 (gamma) $[m^{-1}]$	z_2 [m]	d [m]	Δd [m]	Tilt (α) [deg]	Eff [dB]	G dBi
90	10^{-3}	50	200	5	4	8.8	12.5
220	10^{-3}	50	1500	20	6	8.8	12.5
330	10^{-3}	50	500	10	4	8.8	12.5
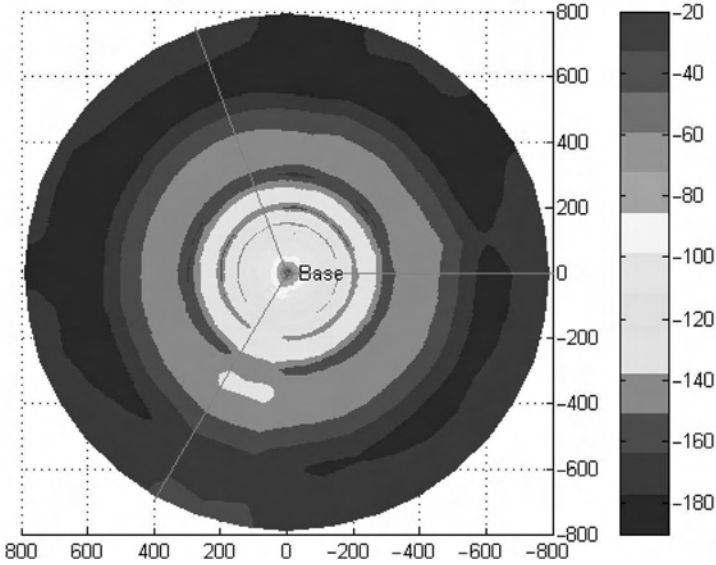
FIGURE 11.30. Radio map of the stock market area in Ramat-Gan.

We notice that in the first column, the values represent the angle of the sector with reference to $0°$ (North). The simulation running constants and variables are as follows:

$$z_1 = 2[m]; l_v = 2[m]; f_0 = 900[MHz]; |\Gamma| = 0.7 - 0.8; \lambda = \frac{3 \cdot 10^8}{f_0} \approx 0.33[m].$$

The BS antenna was elevated above the built-up profile with the average building of $\bar{h} = 18.3$ m. Finally, using the stochastic model we have created a radio map for the test-site area of -800 m to 800 m, depicted in Figure 11.30, where at the right-side the path loss (in dBm) is presented by colored segments corresponding to the obtained magnitudes of loss.

As is seen in Figure 11.30, at the ranges close to BS antenna (100–300 m) the path loss is varied from -100 dBm to -120 dBm, whereas far from BS antenna (at 500–800 m) it varies from -150 dBm to -180 dBm.

The same computation process was done to simulate the premises of Ben-Gurion University, with one major difference. Here, we have divided the university into five major parts, as depicted in Figure 11.31, which are different in their buildings density.

This decision was made, on the basis of university's topographic plan and the values of the building contour density γ_0: for section II, $\gamma_0 = 6 \cdot 10^{-3} m^{-1}$, for sections I, III, and IV, $\gamma_0 = 3 \cdot 10^{-3} m^{-1}$, and for section V, $\gamma_0 = 4 \cdot 10^{-3} m^{-1}$. The heights of two antennas were 25 m and 22 m (compared to the average buildings height of $\bar{h} = 14.5$ m).
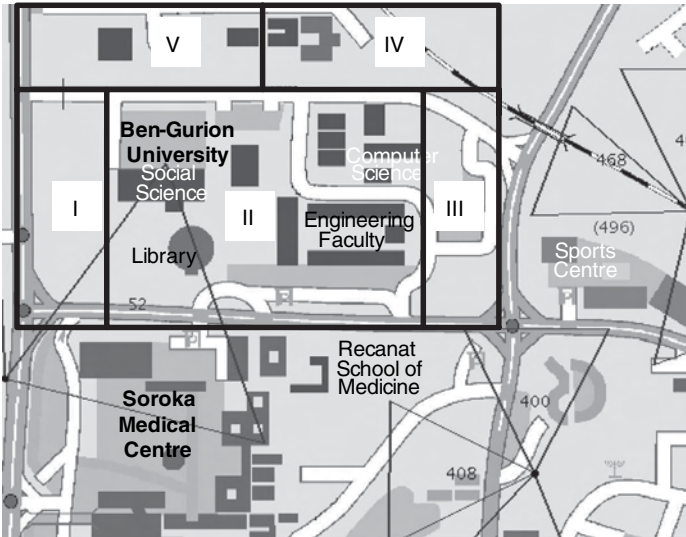
FIGURE 11.31. Topographic plan of Ben Gurion university campuses.

Two sectoral antennas, with three sectors 52, 408, and 400, arranged only according to preliminary experiments, cover an area of the university and together give the pure coverage of radiated energy (see Fig. 11.32). Results presented in Figure 11.32 show that the three sectors cannot fully cover the university's
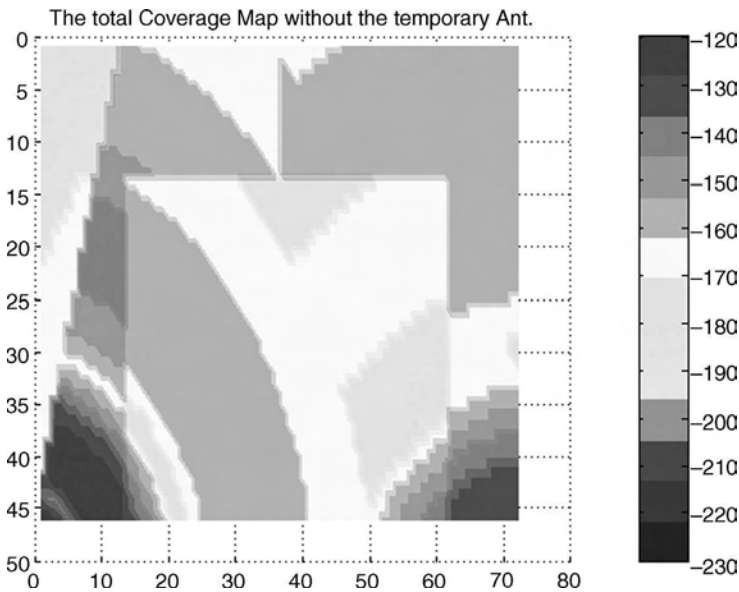
FIGURE 11.32. Radio coverage of two sectoral antennas, numbered 52 and 400, and shown in Fig. 11.31.

campuses, and more than 40% of the area of service are in shadow zones. Therefore, an effective service of subscribers cannot be achieved in more than 40% of the university area.

Therefore, we proposed another arrangement of three sectoral antennas, on the basis of our stochastic approach and the corresponding algorithm described in Chapter 10, according to which specific tilts and heights of two sectoral antennas, and power distribution within each sector, were found according to strict analysis of topographic map of the university area. Now, using the same three more strictly assembled sectors, according to the theoretical prediction, based only on topography of the tested area and the data of antennas, more than 90% of radio coverage was obtained (see Fig. 11.33) to allow each subscriber located in the university area a stable and effective radio service. We notice that because the obtained data corresponds to the technical requirements of our customers, we cannot present here full information about our derivations according to proposed algorithm. The result is evident: about 93% of the university area is now covered. The corresponding decrease of the overall loss is now about 30–40 dBm compared with that obtained by the use of three nonarranged sectoral antennas (see Fig. 11.32).

This example shows that using the proposed theoretical algorithm on how to predict link budget for various built-up areas, described for different scenarios occurred in the urban scene, each designer of cellular networks can achieve the effective arrangement of antennas in such a manner to give full radio coverage to the area of service with minimum path loss for the corresponding users located in this area.
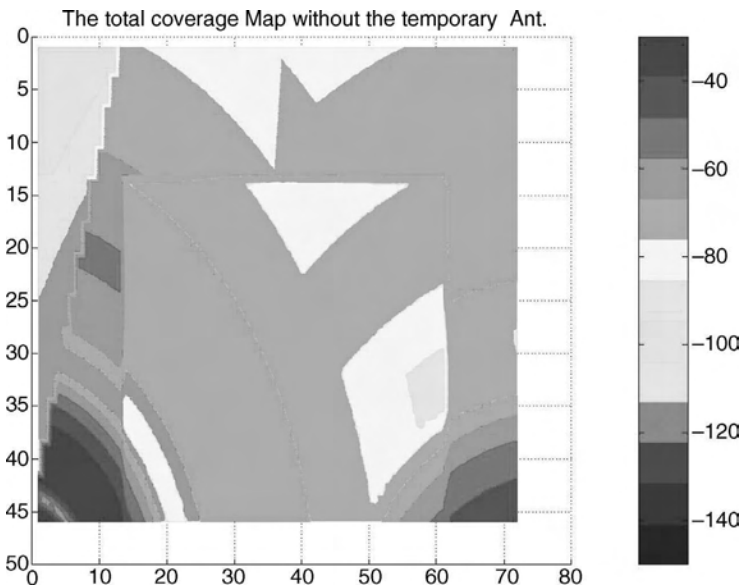
FIGURE 11.33. Radio coverage of three sectoral antennas, numbered 52, 400 and 408, according to the theoretical prediction of their new parameters.

BIBLIOGRAPHY

[1] Anderson, H. R., "A ray-tracing propagation model for digital broadcast systems in urban areas," *IEEE Trans. on Broadcasting*, vol. 39, no. 3, 1993, pp. 309–317; *Trans. Select. Areas in Communic.*, vol. 10, no. 4, 1992, pp. 665–668.

[2] Bertoni, H. L., *Radio Propagation for Mobile Wireless Systems*, Prentice Hall PTR, New Jersey, 2000.

[3] Bertoni, H. L., P. Pongsilamanee, C. Cheon, and G. Liang, "Sources and statistics of multipath arrival at elevated base station antenna," *Proc. IEEE Veh. Technol. Conference*, vol. 1, Houston, Texas, 1999, pp. 581–585.

[4] Liang, G., and H. L. Bertoni, "A new approach to 3D ray tracing for propagation prediction in cities," *IEEE Trans. Anten. Propagat.*, vol. 46, 1998, pp. 853–863.

[5] Lebherz, M., W. Weisbeck, and K. Krank, "A versatile wave propagation model for the VHF/UHF range considering three dimensional terrain," *IEEE Trans. Antennas Propagat.*, vol. AP-40, 1992, pp. 1121–1131.

[6] Lee, W. Y. C., *Mobile Communication Engineering*, McGraw Hill, New York, 1985.

[7] Kouyoumjian, R. G., and P. H. Pathak, "A uniform geometrical theory of diffraction for an edge in a perfectly conducting surface," *Proc. IEEE*, vol. 62, no. 9, 1974, pp. 1448–1469.

[8] L. E. Vogler, "An attenuation function for multiple knife-edge diffraction," *Radio Sci.*, vol. 19, no. 8, 1982, pp. 1541–1546.

[9] Walfisch, J., and H. L. Bertoni, "A theoretical model of UHF propagation in urban environments," *IEEE Trans. Antennas Propagat.*, vol. AP-38, 1988, pp. 1788–1796.

[10] Xia, H. H., and H. L. Bertoni, "Diffraction of cylindrical and plane waves by an array of absorbing half screens," *IEEE Trans. Antennas and Propagation*, vol. 40, 1992, pp. 170–177.

[11] Bertoni, H. L., W. Honcharenko, L. R. Maciel, et al., "UHF propagation prediction for wireless personal communications," *Proc. IEEE*, vol. 82, no. 9, Sept. 1994, pp. 1333–1359.

[12] Rustako, A. J. Jr., N. Amitay, M. J. Owens, et al., "Radio propagation at microwave frequencies for line-of-sight microcellular mobile and personal communications," *IEEE Trans. Veh. Technol.*, vol. 40, no. 2, February 1991, pp. 203–210.

[13] Tan, S. Y., and H. S. Tan, "UTD propagation model in an urban street scene for microcellular communications," *IEEE Trans. Electromag. Compat.*, vol. 35, no. 4, November 1993, pp. 423–428.

[14] Ponomarev, G. A., A. N. Kulikov, and E. D. Telpukhovsky, *Propagation of Ultra-Short Waves in Urban Environments*, Tomsk, Rasko, Russia, 1991.

[15] Blaunstein, N., and M. Levin, "VHF/UHF wave attenuation in a city with regularly spaced buildings," *Radio Sci.*, vol. 31, no. 2, 1996, pp. 313–323.

[16] Blaunstein, N., and M. Levin, "Propagation loss prediction in the urban environment with rectangular grid-plan streets," *Radio Sci.*, vol. 32, no. 2, 1997, pp. 453–467.

[17] Blaunstein, N., "Wireless Communication Systems," in *Handbook of Engineering Electromagnetics*, ed. R. Bansal, chap. 12 Marcel Dekker, New York, 2004, pp. 417–481.

[18] Blaunstein, N., "Average field attenuation in the non-regular impedance street waveguide," *IEEE Trans. Anten. and Propagat.*, vol. 46, no. 12, 1998, pp. 1782–1789.

[19] Blaunstein, N., and M. Levin, "Loss characteristics prediction in urban environments with randomly distributed buildings,". *Proc. of IEEE/URSI International Conference*, Atlanta, USA, July 15–21, 1998, pp. 23–26.

[20] Blaunstein, N., "Prediction of cellular characteristics for various urban environments," *IEEE Anten. Propagat. Magazine*, vol. 41, no. 6, 1999, pp. 135–145.

[21] Blaunstein, N., and E. Tsalolihin, "Angle-of-arrival and time delay distribution in urban areas with street guiding structures," *WSEAS Trans. on Circuits.*, vol. 2, 2003, pp. 202–206.

[22] Blaunstein, N., "Distribution of angle-of-arrival and delay from array of buildings placed on rough terrain for various elevations of base station antenna," *Journal of Communications and Networks*, vol. 2, no. 4, 2000, pp. 305–316.

[23] Blaunstein, N., D. Katz, A. Freedman, et al., "Prediction of loss characteristics in rural and residential areas with vegetation," *Proc. of Int. Conf. on Electromagnetics in Advanced Applications*, Torino, Italy, 2001, pp. 667–670.

[24] Blaunstein, N., D. Katz, and D. Censor, "Loss characteristics in urban environment with different buildings' overlay profiles," *Proc. 2001 IEEE Anten. Propag. Int. Symp.*, Boston, Massachusetts, vol. 2, 2001, pp. 170–173.

[25] Blaunstein, N., D. Katz, D. Censor, et al., "Prediction of loss characteristics in built-up areas with various buildings' overlay profiles," *IEEE Anten. Propagat. Magazine*, vol. 43, no. 6, 2001, pp. 181–191.

[26] Blaunstein, N., D. Censor, D. Katz, et al., "Radio propagation in rural residential areas with vegetation," *J. Electromagnetic Waves and Applications*, vol. 17, no. 7, 2003, pp. 1039–1041; *Progress In Electromag. Research*, PIER 40, 2003, pp. 131–153.

[27] Blaunstein, N., and Y. Ben-Shimol, "Frequency dependence of pathloss characteristics and link budget design for various terrestrial communication links," *IEEE Trans. on Antennas and Propagat.*, vol. 52, no. 10, 2004, pp. 2719–2729.

[28] Blaunstein, N., and Y. Ben-Shimol, "Spectral Properties of Signal Fading and Doppler Spectra Distribution in Urban Communication Mobile Links," *Wireless Communic. and Mobile Computing*, vol. 6, no. 1, 2006, pp. 113–126.

[29] Reudink, D. O., and M. F. Wazowicz, "Some propagation experiments relating foliage loss and diffraction loss at X-band and UHF frequencies," *IEEE Trans. on Commun.*, vol. COM-21, November 1973, pp. 1198–1206.

[30] Barton, F. A., and G. A. Wagner, "900 MHz and 450 MHz - mobile radio performance in urban hilly terrain," *Veh. Technol. Confer. Rec.*, Clevelend, Ohio, USA, June 1973, pp. 1–8.

[31] Okumura, Y., E. Ohmori, T. Kawano, et al., "Field strength and its variability in the VHF and UHF land mobile radio service," *Review Elec. Commun. Lab.*, vol. 16, no. 9–10, 1968, pp. 825–843.

[32] Wells, P. J., "The attenuation of UHF radio signal by houses," *IEEE Trans. Vech. Technol.*, vol. 26, no. 4, 1977, pp. 358–362.

[33] Bramley, E. N., and S. M. Cherry, "Investigation of microwave scattering by tall buildings," *Proc. IRE*, vol. 120, no. 8, 1973, pp. 833–842.

[34] Allsebrook, K., and J. D. Parsons, "Mobile radio propagation in British cities at frequencies in the VHF and UHF bands," *IEEE Proc.*, vol. 124, 1977, pp. 95–102.

[35] Trubin, V. N., "Urban and suburban radio propagation characteristics in the VHF and UHF bands," *7-th Int Symp. Electromagn. Compat.*, Wroclaw, Poland, 1984, vol. 1, pp. 393–402.

[36] Kovacs, I. Z., P. C. F. Eggers, and K. Olesen, ''Radio channel characterization for forest environments in the VHF and UHF frequency bands,'' *Proc. VTC'99*, Amsterdam, Netherland, September 1999, pp. 1387–1391.

[37] Pedersen, K. I., P. E. Mogensen, and B. H. Fleury, ''Power azimuth spectrum in outdoor environments,'' *IEE Electron. Lett.*, vol. 33, no. 18, 1997, pp. 1583–1584.

[38] Pedersen, K. I., P. E. Mogensen, and B. H. Fleury, ''A stochastic model of the temporal and azimuthal dispersion seen at the base station in outdoor environments,'' *IEEE Trans. Veh. Technol.*, vol. 49, no. 2, 2000, 437–447.

[39] Jakes, W. C., *Microwave Mobile Communications*, John Wiley and Son, New York, 1974.

[40] Steele, R., *Mobile Radio Communication*, IEEE Press, NY, 1995.

[41] Saunders, S. R., *Antennas and Propagation for Wireless Communication Systems*, John Wiley & Sons, New York, 1999.

[42] Rappaport, T. S., *Wireless Communications*, Prentice Hall PTR, New York, 1996.

[43] Faruque, S., *Cellular Mobile Systems Engineering*, Artech House, London, 1994.

[44] Cox, D. C., ''910 MHz urban mobile radio propagation: multipath characteristics in New York City,'' *IEEE Trans. Communic.*, vol. 21, no. 11, 1973, pp. 1188–1194.

[45] Lin, S. H., ''Statistical behaviour of a fading signal,'' *Bell Syst. Tech. J.*, vol. 50, no. 10, 1971, pp. 3211–3270.

[46] Black, D. M., and D. O. Reudink, ''Some characteristics of mobile radio propagation at 836 MHz in the Philadelphia area,'' *IEEE Trans. Vehicular Technol*, vol. 21, no. 2, 1972, pp. 45–51.

[47] Reudink, D. O., ''Comparison of radio transmission at X-band frequencies in suburban and urban areas,'' *IEEE Trans. Anten. Propagat.*, vol. 20, no. 4, 1972, pp. 470–473.

[48] Ikegami, F., and S. Yoshida, ''Analysis of multipath propagation structure in urban mobile radio environments,'' *IEEE Trans. Anten. Propagat.*, vol. 28, no. 4, 1980, pp. 531–537.

[49] Fumio, J., and J. Susumi, ''Analysis of multipath propagation structure in urban mobile radio environments,'' *IEEE Trans Anten. Proagat.*, vol. 28, no. 4, 1980, pp. 531–537.

[50] Lee, W. C. Y., and Y. S. Yeh, ''On the estimation of the second-order statistics of lognormal fading in mobile radio environment,'' *IEEE Trans. on Communic.*, vol. 22, no. 6, 1974, pp. 869–873.

[51] Lee, W. C. Y., ''Estimate of local average power of a mobile radio signal,'' *IEEE Trans. Vehic. Technol.*, vol. 34, no. 1, 1985, pp. 22–27.

[52] Hata, M., and T. Nagatsu, ''Mobile location using signal strength measurements in a cellular system,'' *IEEE Trans. Vehic. Technol.*, vol. 29, no. 2, 1980, pp. 245–252.

[53] Mockford, S., A. M. D. Turkmani, and J. D. Parsons, ''Local mean signal variability in rural areas at 900 MHz,'' *Proc. of the 40th Vehic. Technol. Conference*, 1990, pp. 610–615.

[54] Gudmunson, M., ''Correlation model of shadow fading in mobile radio systems,'' *Electronic Letters*, vol. 27, no. 23, 1991, pp. 2145–2146.

[55] Goldsmith, A. J., L. J. Greenstein, and G. J. Foschini, ''Error statistics of real-time power measurements in cellular channels with multipath and shadowing,'' *IEEE Trans. Vehic. Technol.*, vol. 43, no. 3, 1994, pp. 439–446.

[56] Holtzman, J. M., and A. Sampath, ''Adaptive averaging methodology for handoffs in cellular systems,'' *IEEE Trans. Vehic. Technol.*, vol. 44, no. 1, 1995, pp. 59–66.

[57] Giancristofaro, D., "Correlation model for shadow fading in mobile radio channels," *Electronic Letters*, vol. 32, no. 11, 1996, pp. 958–959.

[58] Chockalingam, A., P. Dietrich, L. Milstein, et al., "Performance of closed-loop power control in DS-CDMA cellular systems," *IEEE Trans. Vehic. Technol.*, vol. 47, no. 3, 1998, pp. 774–789.

[59] Wong, D., and D. C. Cox, "Estimating local mean signal power level in a Rayleigh fading environment," *IEEE Trans. Vehic. Technol.*, vol. 48, no. 3, 1999, pp. 956–959.

[60] Greenstein, L. J., D. G. Michelson, and V. Erceg, "Moment-method estimation of the Rician factor," *IEEE Communic. Letters*, vol. 3, no. 6, 1999, pp. 175–176.

[61] Clarke, R. H., "A statistical theory of propagation in the mobile radio environment," *BSTI*, vol. 47, no. 7, 1968, pp. 957–1000.

[62] Aulin, T. A., "A modified model of the fading signal at a mobile radio channel," *IEEE Trans. Veh. Technol.*, vol. 28, no. 3, 1979, pp. 182–203.

[63] Tepedelenlioglu, C., A. Abdi, G. B. Giannakis, et al., "Estimation of Doppler spread and signal strength in mobile communications with applications to handoff and adaptive transmission," *J. Wireless Communicat. and Mobile Computing*, vol. 1, no. 2, 2001, pp. 221–242.

[64] Blaunstein, N., N. Yarkoni, and D. Katz, "Link budget performance for various outdoor scenarios taking into account fading phenomena," *Proc. of 13th Conf. on Microwave Technologies*, Prague, Chech Republic, September 26–28, 2005, pp. 56–59.

[65] Blaunstein, N., N. Yarkoni, and D. Katz, "Innovative approach to radio propagation modeling in urban and suburban areas," *Proc. of Int. Conf. on Electromagnetics In Advanced Applications* (*ICEAA*'05), Torino, Italy, September 12–16, 2005, pp. 293–298.

Cellular Communication Networks Design Based on Radio Propagation Phenomena

As was mentioned in Chapter 1, wireless systems are an enhancement of the traditional wire-line telephone systems. However, unlike the wire-line systems, they suffer from a poor grade of service (GOS) and low quality of service (QOS) because of low link reliability caused by propagation characteristics of the radio environment. Furthermore, most characteristics of wireless network design strongly depend on the sensitivity of receivers due to high service demand, on a low number of call resources due to limited frequency band of each network, and on degradation in the information data stream transmitting within each individual subscriber radio communication link. Important statistical characteristics that must be predicted are the path loss, and slow and fast fading. These allow designers of such networks to improve the grade of service (GOS) and quality of service (QOS) characteristics, to create cellular maps of areas of service, and to optimize the information data stream within each radio communication channel.

In order to avoid measuring channel statistics for all operating environments and for all networks design, we introduced in Chapters 5 and 10 a unified stochastic approach for multipath radio channel description based on real physical phenomena, such as multiple reflection, diffraction, and scattering from various nontransparent obstructions (trees, hills, houses, buildings). In this chapter we describe elements of wireless networks design via this unified statistical approach comparing it with existing standard methods of network designs.

Thus, in Section 12.1, we describe the unified concept of GOS design in multipath radio channels caused by fading phenomena. In Section 12.2, we discuss the strategies to create cellular maps, uniform, and nonuniform, for various built-up environments, referring the reader to the channel (frequency) assignment technique. Then, Section 12.3 describes the prediction mechanism of main parameters of information data stream, such as bit error rate (BER), capacity, and spectral efficiency versus Ricean parameter K that determines fading effects within the multipath radio channel.

12.1. GRADE OF SERVICE (GOS) DESIGN OPERATING IN MULTIPATH FADING ENVIRONMENT

The classical GOS analysis, that is the analysis of the probability of working without call congestion, of wireless networks, uses the Erlang B model that is a private case of the birth and death (B&D) equations of the statistical traffic theory [1–5]. Also, the Erlang B model is usually used for a calculation of the total system capacity. This gives a calculation of the estimated GOS, which is the probability of a user trying to initiate a call and the call failing. However, this model is justified only in cases where all users have access to all resources of the system (a situation of full availability). In wireless systems, due to propagation limitation such as obstacles and wave fading, a user has limited access to system resources. This refers to a limited availability and therefore we cannot use the classical approach of this traditional model.

In wireless systems, a user gets service from one cell. The user is part of a group that is covered by one or more cells. If the user has optional access to more then one cell, the system has to allocate the user to one of these cells in order to achieve an optimal GOS - referring to load balancing. The decision rule of user allocation refers to the *load balancing algorithm*. Hence, the goal of the wireless system operator is to deploy a system such that the GOS will be maximized, while the number of cells serving a certain number of users is minimal. In fact, some studies that have been done to explore this type of the GOS problem have found a strict effect of the coverage overlapping between cells and the effect of the decision rules of user allocation [6–8].

In the following section, we will briefly explain the approach of how to define an effective methodology of the GOS estimation by calculating the fading and its statistical characteristics, according to the concept of the link budget design described in Section 11.2. We compare the generalized GOS that takes into account the fading as well as the congestion probability due to high load, with the traditional GOS calculation. We also compare the results for different land area types (mixed residential and urban) and for different hands-off decision rules, in order to show the destructive effects of the slow fading due to shadowing and those of the fast fading due to multipath phenomena in order to recommend an optimal deployment methodology.

12.1.1. The Concept

Till date now, existing wireless systems considered only elements of the traditional deployment methodology that do not take into account the real propagation characteristics of the environment. The most elementary stage of a system deployment is the link budget design, which is the main parameter of wireless communication links (see Section 11.2). It is based on propagation characteristics of the channel and describes the signal power distribution along the radio path between the base station antenna and the user antenna [9,10]. The link budget is a balanced sheet of gains and losses [11]. Some of the link budget parameters such as antenna gain, are fixed and some are statistical such as fading (see Chapter 1). So, by calculating link budget, we evaluate the link performance. Section 11.2 (see Chapter 11) explains briefly the link performance considering the wave path loss and taking into account a fade margin, which is the average of the slow and fast fading due to shadowing and multipath phenomena in the entire area. As in Section 11.2, in our estimations of the GOS, we take into account two types of areas: *mixed residential areas,* as low buildings with trees around and *urban areas,* as mostly high buildings in a dense built-up area. For each type of area, we may calculate the average path loss and estimate the statistics of slow and fast fading effects according to the corresponding algorithm presented in Section 11.2. The proposed model is adapted to use a known number of subscribers located in an area of service, which is assumed to be distributed equally over this area, with a known statistical distribution.

In our description, we concentrate on a model of two cells that are deployed in two ways: *contained*, when one cell's coverage area is fully contained in the other cell (see Fig. 12.1, case A) and *overlapped*, when two cells have a common area (see Fig. 12.1, case B).

If the user is in the common area, then it is allocated to one cell upon *predefined algorithms*

a) random assignment (denoted *random*);
b) assign to site with higher signal strength (denoted *by_ss*);
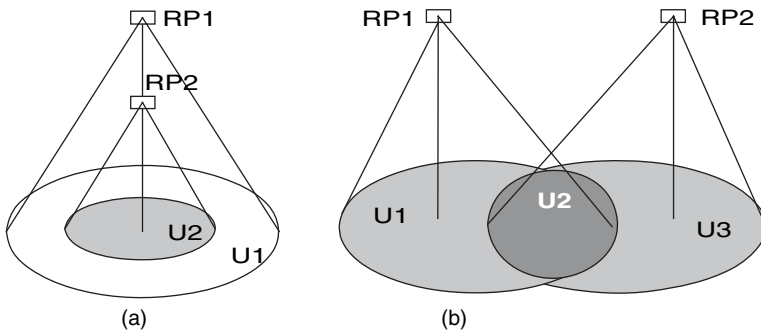
FIGURE 12.1. Unbalanced availability scenario: [A]-contained, [B]-overlapping.
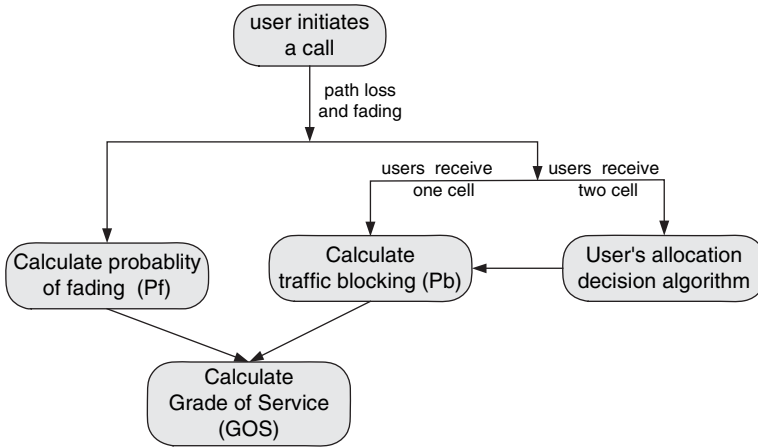
FIGURE 12.2. Unbalanced availability scenario.

c) assign user to the less loaded cell (denoted *min-load*), investigated in detail in Reference [7].

For each user who initiates an outgoing call, it calculates its chance of not succeeding. All the steps of the corresponding algorithm are described by the block-scheme shown in Figure 12.2.

12.1.2. Simulation Tests

The simulation includes two scenarios, as shown in Figure 12.1 according to Reference [8]. In both cases, there are two radio ports (RP); each with eight channels. In the contained scenario A, RP2 serves the user group U2, and RP1 serves both groups U1 and U2. In the overlapped scenario B, RP1 serves groups U1 and U3, and RP2 serves groups U2 and U3; the coverage area by the group U3 is called the overlapped area.

In both scenarios, A and B, each user can initiate a call randomly, and if the signal level is high enough, it can request for a channel allocation. Here, it is clear that if the fading effect is high, that is low signal is received, then there is degradation in service quality. If the user is in the overlapped area, a decision on which RP to allocate to it is taken by the following load balancing algorithms [7]:

- random (*random*)—the user selects randomly one RP;
- best signal strength (*by_ss*)—the user selects the RP that is received with a highest signal strength;
- controlled load (*min_load*)—the user selects the RP that has the less occupied channels.
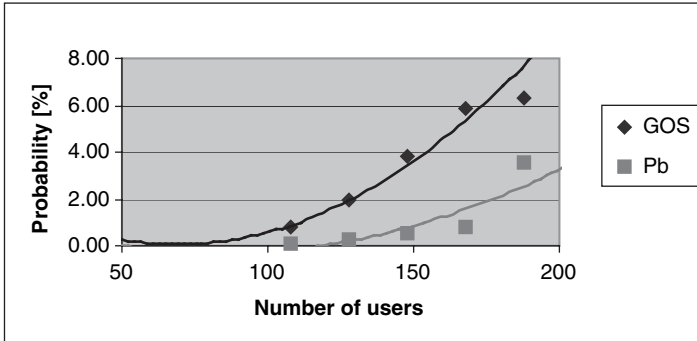
FIGURE 12.3. [Pb] is traffic blocking without fading effect; [GOS] is traffic blocking with fading effect.

The goal of our simulations presented in the next section is to demonstrate the decrease of traffic as an effect of fading or load balancing algorithm.

12.1.3. Traffic Computation in Wireless Channels with Fading

For each single scenario, overlapped or contained, and an algorithm we have scattered various numbers of users that have a call statistics of Poisson distribution with an average arrival process of one hour and an average call time of four minutes in order to measure the probability of dropped calls (call blocking). It is possible to measure the same results with and without considering the fading effect.

We now consider how the fading affects the results. In Figure 12.3, two graphs are presented showing the blocking rate (Pb) as a function of the number of users as well as the traffic loss when considering the fading effects (GOS).

In this example, a system that has 2% blocking carried 180 users, while taking into account the fading, we get for a GOS of 2% with only 130 users. The fading therefore has an effect that reduces the system capacity by 50 users.

Results of Simulations. Our test and simulation results measured three parameters

- – the effect of fading on the average increase of the overlapping area;
- – the increase of probability of call blocking when considering the fading effect;
- – the effect of overlapping on the GOS.

In the numerical experiment we checked the GOS for 128 users only. Figures 12.4 and 12.5 depict the results achieved by computing the problem concerning the last two scenarios.

Mixed Residential Area. Figure 12.4 depicts situation when the GOS was computed taking into account fading phenomena. Without fading, the probability of blocking was not more than 3%. As can be seen, the effects of fading can increase
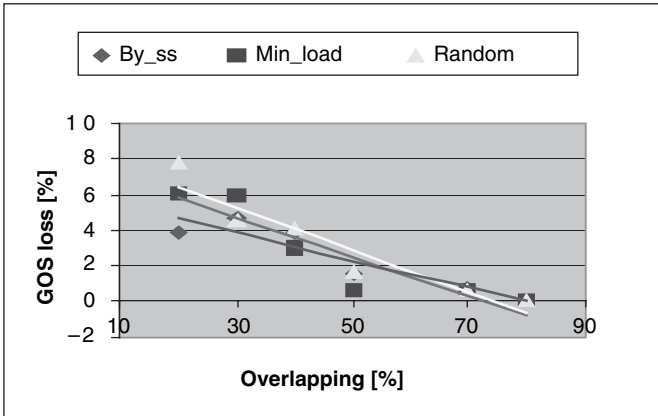
FIGURE 12.4. Mixed residential area: GOS versus overlapping (in %) for three load balancing algorithms.

the probability of blocking (GOS) up to 5–7%, as well as an increase of the overlapping area for the same GOS.

Urban Area. Figure 12.5 depicts situation when GOS was computed taking into account the fading phenomena. Here, without accounting for the fading effect we get not more than 5% of the blocking probability, whereas in the overlapping scenario in urban environments fading has tremendous effect on the GOS (up to 20–30%) and in low overlapping, it is so large that an unacceptable GOS was obtained (for overlapping of 50% it can achieve 50–70%).

Some Specific Example. Finally, we will present some specific example of a cellular system arranged in the mixed residential area to show the loading effect on
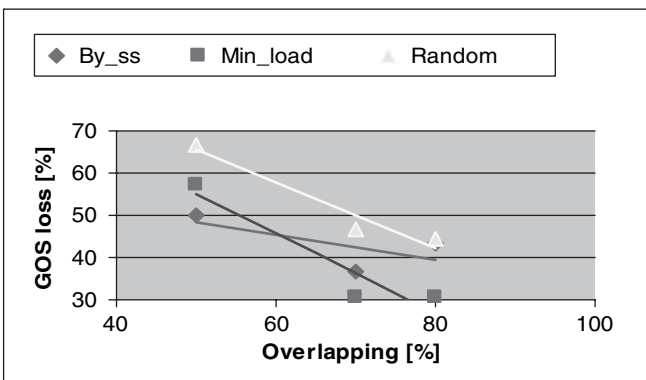
FIGURE 12.5. Urban area: GoS versus overlapping.
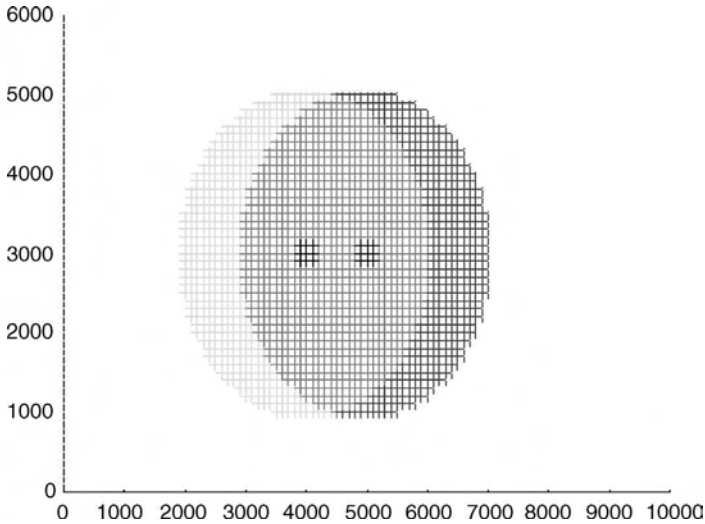
FIGURE 12.6. An example of two cells propagation map in an overlapping case.

each cell constructed according to the overlapping scenario. We use the following testing area configuration:

- two cells located at a distance of 1 km;
- number of users is 128;
- average arrival time is 60 min;
- average holding time is 4 min;
- decision rule is *random* with decision probability $P_1 = 35\%$.

After the corresponding simulation, we get the following overlapping map shown in Figure 12.6. The overlapping area (red area in the middle) is 53% of the entire service coverage area. Finally, we get two histograms that represent the load on each cell (see Fig. 12.7). These histograms show the percentage of time of occupancy for a certain number of channels. As it is seen, as we took the probability of decision of $P_1 = 35\%$, the common users had higher probability to be in Cell #2, because we decided more time of occupancy of eight channels being in Cell #2 compared to Cell #1. We also get from this simulation the following results: the probability of fading (P_f) is 0.6%, that is it is low, for the high overlapping, and the probability of blocking (P_{bl}) is 1.8%. Finally we get according to Reference [8] that

$$GOS = P_{bl}(1 - P_f) + P_f(1 - P_{bl}) \tag{12.1}$$

Substituting probabilities mentioned above, we get

$$GOS = 0.018\,(1 - 0.006) + 0.006\,(1 - 0.018) = 0.023\ \text{or}\ 2.3\%$$
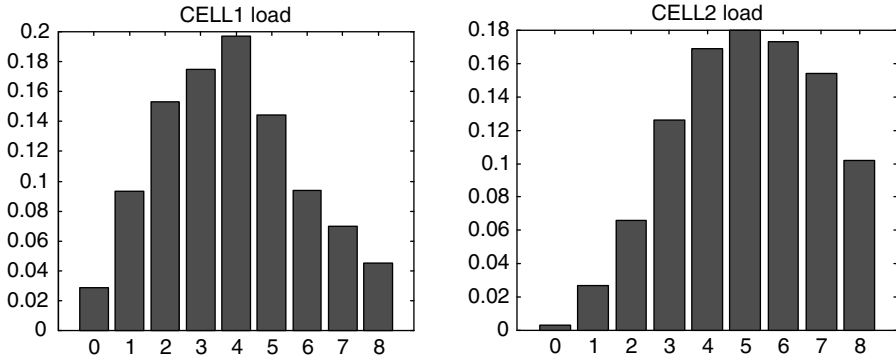
FIGURE 12.7. Traffic histograms of an overlapping case versus number of channels.

So, for the presented configuration of the system, the fading effect is of 2.3% $-1.8\% = 0.5\%$ on GOS, which is in agreement with results obtained for mixed residential areas and shown in Figure 12.4.

12.2. PROPAGATION ASPECTS OF CELL PLANNING

In the previous section, we analyzed two scenarios of two cells assembling for allocation of subscribers in an area of service: overlapping scenario and contained scenario. Now we will briefly consider what we mean by *cellular* and how the strategy of *cell splitting* depends on conditions of radio propagation in different built-up areas.

The cellular concept was proposed to help the designers of land wireless systems to eliminate noise within the propagation channels, and to minimize the effects of interference that occurs in a multiuser environment within band-limited channels. These phenomena are mostly manifested for moving subscribers, that is for mobile communication systems due to the Doppler effect, which causes time-dependent and frequency-dependent fading effects (see Chapter 1). So, most problems are to use the cellular concept for the purposes of mobile communications.

As was shown in the previous section, the simplest *radio cell* can be constructed by using a base station (BS) at the center (or inside) of such a cell and predicts the coverage area from BS antenna. The range defines this coverage area where a stable signal from this station can be received. There are several methods to construct the cell pattern or usually called the cell map. We start with the regular case based on the presentation of each cell in the form of hexagon as shown in Figure 12.8, which illustrates the pattern of such cells. It can be seen that some regions overlap with neighboring radio cells, where stable reception from neighboring base stations can be obtained. From this scheme it is obvious that different frequencies should be used in these cells that surround the tested central cell. On the other hand, the same frequencies can be used for the cells farthest from the

Region of overlap

A — Radio base station for each frequency set

☐ Idealised coverage per cell

------- Actual radio range
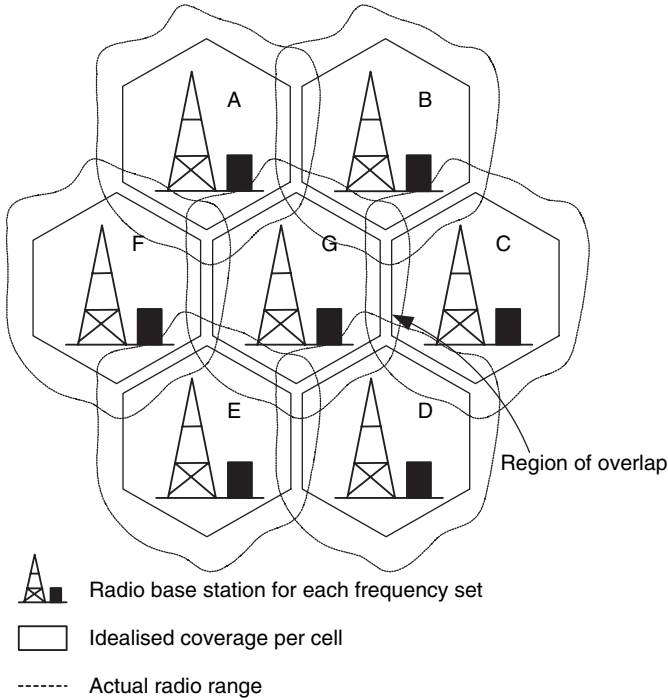
FIGURE 12.8. Cellular map pattern with overlapped hexagons.

central one. This is the so-called *cells repeating* or *reuse of operating frequencies* principle. At the same time, the reuse of the same radio channels and frequencies within the neighboring cells is limited by preplanned *co-channel interference*. Moreover, in the process of cellular systems design in various built-up areas, it is very important to predict the influence of propagation phenomena within the corresponding communication channels on variations of the main parameters of the cellular system, on the construction and splitting of cellular maps. All these points will be briefly discussed in the following sections on the basis of some classical aspects described in the corresponding literature [10–19] and the results of recent investigations carried out by the authors of this book, as well as by other researchers dealing with modern configuration of cellular pattern performance.

12.2.1. Main Characteristics of Uniform Cellular Pattern

As was mentioned in References [16–19], the *cellular pattern* concept for land wireless communications has been introduced to account for the numerous cells within a small radius, which provide a sufficient signal-to-noise ratio (SNR) and a low level of interference with received signals within the communication channel. As follows from the literature regarding cellular splitting strategy [10–19], this

strategy at early stages of cellular communications has been based on the following principles:

  – use regular hexagon-shaped cells, as the hexagon-shaped cell is more geometrically attractive than the circle-shaped cell, but at the same time hexagon shape is very close to circle shape;
  – with an increase in the number of subscribers, the dimensions of the cells must be smaller, usually occurring in the center of cities, where the amount of traffic is bigger and density of the buildings is higher;
  – cells are arranged in *clusters*. The cluster size is designated by the letter *N* and is determined by the [16–19]

$$N = i^2 + ij + j^2 \tag{12.2}$$

where $i, j = 0, 1, 2, \ldots$, that is only the cluster sizes 3, 4, 7, 9, 12 and so on, are possible. Thus, each hexagonal cell can be packed into clusters "side-to-side" with neighboring cells, as shown in Figure 12.8.

The size of such a hexagonal cell can be defined by the use of its radius R_{cell}. The installation of additional base stations within each cell depends on the degree of the cell density in each cluster and on the coverage effect of each base station antenna.

There is another main parameter of cellular pattern called *reuse distance*, *D*, which defines the distance between two cells utilizing the same limited bandwidth called *reuse frequencies* or *repeating frequencies*. We will explain these definitions focusing on the popular 7-cell cluster pattern [16–19], which is depicted in Figure 12.9. First, we notice that the allocation of frequencies into seven sets is required. In Figure 12.9, the mean reuse distance is explained in which the cells (denoted by dark color) use the *same frequency bandwidth*. This is a simple way to
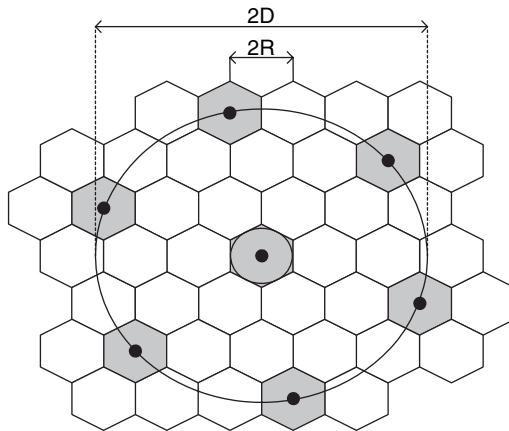
FIGURE 12.9. Frequency reuse plan with reuse factor $N = 7$.

use the repeat frequency set in the other clusters. Between D and the cell radius R_{cell} there is a relationship that is called the *reuse ratio*. This parameter, denoted by Q, for a hexagonal cell is a function of the cluster size, that is [16–19],

$$Q = \frac{D}{R_{cell}} = \sqrt{3N} \qquad (12.3)$$

Within other cells in a cluster, interference inside the communication channel can be expected at the same frequencies. Hence, for a 7-cell cluster there could be up to six immediate interferers, as it is shown in Figure 12.9. So, it is apparent that the cellular system concept is closely connected with the so-called *co-channel interference* caused by the frequent reuse of channels within the cellular communication system. To illustrate the concept of the co-channel interference, let us consider a pair of cells with radius R, separated by a reuse distance D, as shown in Figure 12.9. As the co-channel site is located far from the transmitter ($D \gg R$), which is located within the initial cell, its signal at the servicing site will suffer multipath attenuation. To predict the degree of co-channel interference in such a situation with moving subscribers within the cellular system, a new parameter, *carrier-to-interference ratio C/I*, is introduced in References [10–19]. A co-channel interferer has the same nominal frequency as the desired frequency. It arises from multiple use of the same frequency band. For omnidirectional or isotropic antennas (see definitions in Chapter 2) located inside each site, the theoretical co-channel interference in decibal is given by References [16–19]

$$\frac{C}{I} = 10 \log \left[\frac{1}{j} \left(\frac{D}{R} \right)^{\gamma} \right] \qquad (12.4)$$

where j is the number of co-channel interferers ($j = 1, 2, \ldots, 6$), γ is the path-loss slope constant introduced and defined in Chapter 5. It determines the signal decay in various propagation environments. For a typical seven-cell cluster ($N = 7$) with one cell as basic (with the transmitter inside it) and with six other interferers ($j = 6$, as seen from Fig. 12.9) as the co-channel sites, this parameter depends on the conditions of wave propagation within the urban communication channel. As a simple example, presented in Reference [19] for two-ray propagation model above a flat terrain with $\gamma = 4$ (see also Chapter 5), we can rewrite (12.4) as

$$\frac{C}{I} = 10 \log \left[\frac{1}{6} \left(\frac{D}{R} \right)^{4} \right] \qquad (12.5)$$

Namely, for $N = 7$, that is $D/R_{cell} = \sqrt{3N} = 4.58$, we get $C/I = 18.6$ dB. Using (12.3), we can simplify (12.5) as

$$\frac{C}{I} = 10 \log \left[\frac{1}{6} (3 \cdot N)^{2} \right] = 10 \log \left(1.5 \cdot N^{2} \right) \qquad (12.6)$$

meaning that the carrier-to-interference ratio is also a function of the cluster size N and increases with the increase in the number of cells in each cluster or with the decrease of the cell radius R_{cell}.

Now we will discuss the problem of how to predict the optimal cell size. That is we will discuss how to define its radius and how to efficiently design a cellular map based on the law of signal decay as was shown in Chapter 5. The law of signal decay is changed for different propagation situations in the urban scene and for different land wireless communication channels, outdoor and indoor.

12.2.2. Methods of Cellular Map Design

To arrange the effective splitting of a tested built-up area at cells, the designers need strict information about the law of signal power decay for the concrete situation in the site of consideration. Specifically, they need the strict link budget analysis of propagation situation within each communication channel, as well as full radio coverage of each subscriber located at LOS or NLOS conditions in areas of service, giving exact clearance between subscribers within each cell. On the basis of precise knowledge of the propagation phenomena inside the cellular communication channels, it is easy to optimize cellular characteristics, such as the radius of a cell, reuse factor Q, channel interference parameter C/I, and so on.

Standard Definition of the Radius of Cells. As follows from Chapter 5, a better clearance between the base station (BS) and the moving subscribers (MS) in cluttered conditions may be reached only for LOS conditions (or direct visibility) between them. In this case, as follows from the two-ray model and the waveguide street model (see Chapter 5), the cell size, R_{cell}, cannot be larger than the break point range, r_B, at which the decay of the signal is changed from $\gamma = 2$ (as in free space propagation) to $\gamma = 4$ (propagation above flat terrain). If so, the law of signal decay between BS and each MS in the cell of radius $R_{cell} \leq r_B$ is R_{cell}^{-2}. Generally speaking, beyond the break point the law of signal decays versus the range between terminal antennas, described by path-loss slope parameter γ, depends on the concrete situation in the urban scene and may be proportional to $R^{-\gamma}$ with $\gamma > 2(\gamma = 4 - 7$, see discussions in Chapter 5). Such a distance dependence of signal decay law inside and outside the cell is shown in Figures 12.10a and 12.10b for two typical situations in regular cell splitting.

So, we can conclude that the best clearance between each BS and any subscriber inside the cell determines the minimum radius of the concrete cell.

Wave propagation phenomena in urban environments with both antennas in NLOS (clutter) conditions were described earlier in Chapter 5 by using two physical – statistical models, street waveguide, and multiparametric stochastic. As follows from the models described there, in rural and mixed residential areas with a rare building distribution, the path-loss slope parameter γ describing the received signal decay is changed from $\gamma = 2.5$ to $\gamma = 4.0$ (see Chapter 5). In other words, in such an area field attenuation is faster than that in LOS conditions of free space.
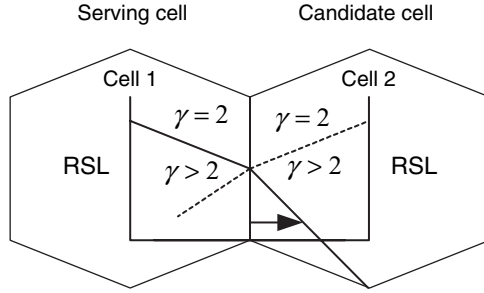
FIGURE 12.10(a). LOS hand-off scenario.
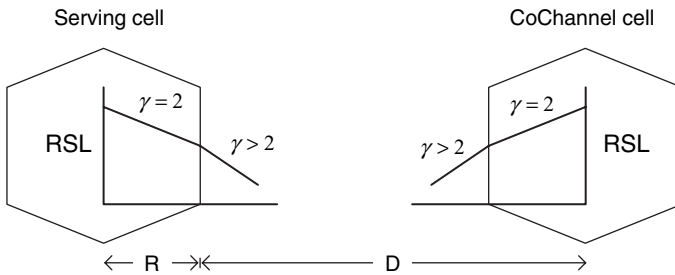
FIGURE 12.10(b). LOS co-channel interference.

From the multiparametric model, described in Chapter 5, when both antennas are placed in a built-up area with a high density of irregularly distributed buildings, the law of signal power decay is changed with distance d between the antennas. It changes from $\sim d^{-\gamma}$ ($\gamma = 2$) before the break point r_B (where the coherent part of total field is dominant) to $\sim d^{-\gamma}$ ($\gamma = 2.5 - 4$) beyond the break point r_B (where the incoherent part of total field is dominant). Therefore, it is easier to obtain the minimum cell size, R_{cell}, defined as the break point r_B, in a variety of cities with crossing-street grid plan. In fact, for urban areas with a rectangular grid plan of straight crossing streets, when the multislit street waveguide model (described in Chapter 5) is successfully used [20–22], the cell size can be described by the following formula, where we eliminate the effects of diffraction from building corners, as in Chapter 5:

$$R_{cell} \equiv r_B = \frac{4h_T h_R}{\lambda} \frac{(1+\chi)}{(1-\chi)} \frac{\lfloor 1 + h_b/a + h_T h_R/a^2 \rfloor}{|R_n|^2} \tag{12.7}$$

where all parameters in (12.7) are described in Chapter 5. As follows from (12.7), using information about street geometry, such as the street width a, the average height of buildings h_b, and the mean gaps between buildings lining the street, that is, the parameter of brokenness χ. As well as geometry about both antennas height,

h_T and h_R, and the material of the building walls (which determines the absolute value of reflection coefficient R_n), we can easily obtain the cell radius along the crossing streets.

In the case of built-up areas with non regularly distributed buildings placed on rough terrain, consisting of hills, buildings, and other obstructions located in residential zones, the cell size can be obtained by using the probabilistic approach presented in Chapter 5 according to the multiparametric stochastic model. As follows from this approach, the average distance of the direct visibility $\bar{\rho}$ between two arbitrary points, the source and the observer, is described by the following formula:

$$\bar{\rho} = (\gamma_0 \gamma_{12})^{-1} \text{ [km]} \tag{12.8}$$

where γ_{12} is a dimensionless parameter describing effects of overlay the profile of the buildings, $0 < \gamma_{12} \leq 1$ and $\gamma_0 = 2\bar{L}v/\pi \, (\text{km}^{-1})$ is the 1D density of contours of the buildings. For uniform distribution of buildings height, when $\gamma_{12} = 1$, (12.8) can be simplified as

$$\bar{\rho} = (\gamma_0)^{-1} = \frac{\pi}{2\bar{L}v} \text{ [km]} \tag{12.9}$$

If now one obtains the information about the service area, that is about the overlay profile of the buildings with parameters of building height pattern n and $\bar{h}$ (as was done for Lisbon, see Section 11.1.3) and about length of the average buildings $\bar{L}$, as well as the density of the buildings per square kilometer. It is easy to estimate the cell radius within the tested area by use of formulas (12.8) or (12.9).

So, by the use of formulas (12.7) to (12.9) for specific scenarios occurring in the land communication environment, we can easily obtain the *minimum cell radius* for different built-up areas with various situations of the terminal antennas, BS and MS [23–26].

Definition of Cell Radius via the K-factor. Taking into account the fading phenomena, we can also estimate the maximum cell radius based on the definition of Ricean K-factor and the corresponding evaluation of this parameter presented in Section 11.3. Thus, for the experiment carried out in a mixed residential area and the results of the K-factor computation shown in Figure 11.23 for $f = 900\,\text{MHz}$, the criteria to use the maximum radius of cell can be determined by the maximal value of K versus the distance. From the illustration in Figure 11.23 this radius can be estimated as about 1–1.2 km. Whereas, for the same conditions, formula (12.8) gives the minimum cell radius value of 570 m. The same computations made for the urban area ("market-site" of Ramat-Gan) according to illustration presented in Figure 11.24 allow us to estimate the maximum cell radius of about 320–350 m. Whereas, for the same conditions using formula (12.9), the minimum radius is an estimated value of 170–180 m. Real experiments carried out in both areas showed that the stable communication between the BS and any user located

in the area of service can be achieved for the mixed area up to 1 km and for the tested urban area at about 400–450 m. We notice, according to the experiment described in Section 11.4, that the tested area of Ramat-Gan is a high dense area with tall buildings. These estimations again show that using the proposed stochastic approach with definitions of the minimum cell radius by (12.9) and of the maximum cell radius by K-parameter from (11.45) to (11.46), we can predict a priori the cell radius of the area where stable communication between users and BS antenna can be achieved.

Definition of Cell Radius via Maximum Acceptable Path Loss. Another method of cell radius estimation is to use information about the total link budget in the channel accounting for both slow and fast fading. We discussed in Chapter 11 how to estimate this parameter. Now using formula (11.36) with (11.33) to (11.35) for slow fading and formula (11.39) with (11.37) and (11.38), on the basis of the results obtained from the stochastic model, we can estimate the maximum and minimum cell radius. Let us again use data from experiment carried out in the Ramat-Gan experimental site described in Chapter 11. Following the same approach as was done for link budget design and K-factor estimation for this propagation scenario, we have found the following results. The attenuation loss according to slow fading is changed from 7.1 to 7.2 dB, which is approximately constant with the range between the BS and MS antennas. At the same time the probability to obtain this loss is changed from about 0.4 at 100 m from the BS station to about 0.9 at 500 m from the base station.

The same computations for the attenuation loss due to fast fading give about 32 dB at the distance of 100 m from the BS antenna and about 42 dB at the 500 m from the BS antenna with the corresponding probability of 0.7 and about 1. Then, according to estimations made in Chapter 11 for link budget design in the Ramat-Gan experimental area, the total loss is changed from about 105 dB at the distance of 100 m to about 140 dB at the distance of 500 m. Taking into account the acceptable path loss of the system, which was used in the corresponding experiment is 138 dB, we have found that the maximum radius of the cell can not be more that 420 m. Therefore, according to these estimations one can see that instead of using the formulas for K-factor estimations presented in Section 11.3, which give us the cell radius $R_{min} \approx 320$ m, we have $R_{max} \approx 420$ m accounting maximum acceptable signal loss with the corresponding probability of fast and slow fading phenomena. Of course, this radius is larger than the minimum one, but smaller or about the same as that of about 400–450 m obtained experimentally in the Ramat–Gan experimental area.

So, using information of the K-factor describing the fast fading phenomena, its probability and the corresponding loss, or using the maximum accepted path loss, accounting for both kinds of fading with their corresponding probabilities and loss, one can estimate more precisely the cell radius instead of using the simple formulas (12.8) or (12.9) following the stochastic model. Using the more precise approach described above, we can increase the radius of a cell, which allows designers of cellular maps to increase the areas of service for each individual base

station, and finally the number of users located in such areas, that is increasing both the quality and capacity of service.

Co-channel Interference Parameter Definition. The same detailed analysis based on propagation phenomena in different built-up areas can be done to determine the *co-channel interference parameter* (C/I) defined above. According to the propagation situation in the urban scene for cell sites located beyond the break point range r_B, as shown in Figure 12.10b, the Equation (12.4) can be modified taking into account the multipath phenomena and obstructions that change the signal decay law from D^{-2} to $D^{-\gamma}$, $\gamma = 2 + \Delta\gamma$, $\Delta\gamma \geq 1$. Hence, instead of (12.4) we finally have

$$\frac{C}{I} = 10\log\left[\frac{1}{6}\left(\frac{D^{(2+\Delta\gamma)}}{R^2_{\text{cell}}}\right)\right] \tag{12.10}$$

According to the concepts of cellular map construction presented above, the signal strength decay is weaker within each cell (with path-loss slope parameter $\gamma = 2$) and corresponds to that in free space. At the same time, due to obstructions, the signal strength decay is stronger in regions outside the servicing cell and within the co-channel site (with path-loss slope parameter $\gamma = 2 + \Delta\gamma$, $\Delta\gamma \geq 1$). Therefore, we can rewrite (12.10) in terms of the number of cells in cluster N, and of radius of the individual cell R_{cell}, by the use of (12.3):

$$\frac{C}{I} = 10\log\left[\frac{N}{2}(3N)^{\frac{\Delta\gamma}{2}}R^{\Delta\gamma}_{\text{cell}}\right] \tag{12.11}$$

Let us examine these equations for the two typical cases described above. In the case of typical *crossing straight wide avenues*, for which according to multislit street waveguide model $\Delta\gamma = 2$ ($\gamma = 4$) (see Chapter 5), we get

$$\frac{C}{I} = 10\log\left[\frac{3}{2}(N)^2R^2_{\text{cell}}\right] \tag{12.12}$$

For the case of narrow streets, which is more realistic in cases of the urban scene, one can put in (12.11) $\Delta\gamma = 3 - 7$ ($\gamma = 5 - 9$). This is close to the exponential signal decay that follows from the street waveguide model [20–22].

For the case of propagation over *irregular built-up terrain*, following the probabilistic approach presented in Chapter 5, $\Delta\gamma = 1$ and the C/I-ratio prediction equation

$$\frac{C}{I} = 10\log\left[\frac{N}{2}(3N)^{1/2}R_{\text{cell}}\right] \tag{12.13}$$

From (12.11) to (12.13), the C/I-ratio strongly depends on conditions of wave propagation within the urban communication channels (on path-loss slope parameter

$\gamma = 2 + \Delta\gamma, \Delta\gamma \geq 1$) and on the cellular map splitting strategy (on parameters N and R_{cell}). In fact, from the formulas presented above, the C/I performance is enhanced if the cell radius R_{cell} is within the break point range and the reuse distance D is beyond this range. At the same time, stated differently, for a given C/I-ratio, a channel can be reused more often, enhancing the cellular system capacity. This is a pure engineering subject as the same engineering questions of cellular system performance, which lie outside the purpose and main goal of this book. The reader can find all these questions described in detail in References [16–19].

12.2.3. Strategy of Non Uniform Cellular Maps Design

In the previous section, we considered the classical strategy of how to split the radio map into regular cell lattice using hexagon-cell configuration with periodic constant frequency reuse pattern, that is cluster layout concept by using the same frequencies at those cells, the ranges of which between their BS equal the reused distance D. This concept is good for uniform distribution of users/subscribers and calls, for uniform traffic (see Section 12.1). However, due to the demand to keep on increasing the network traffic capacity, designers of the most modern cellular networks started looking for new strategies and some alternative concepts to deal with inhomogeneous traffic. Moreover, in such modern approaches the base station positioning within the cell pattern was stated to be nonuniform with relocation in real time according to propagation conditions within the traffic hot spots, as shown in Figure 12.11. The corresponding approaches and models are fully discussed in References [27–36]. Below, we briefly will show how to introduce a flexible concept of cell splitting and propagation effects in a new strategy of cellular maps design. Then, we base on a specific experiment, described in Reference [28], and use for comparison with theoretical predicting model proposed in References [31–33]. We compare the obtained theoretical and experimental results with those obtained by using the proposed stochastic approach of radio propagation in different scenarios in the urban scene.
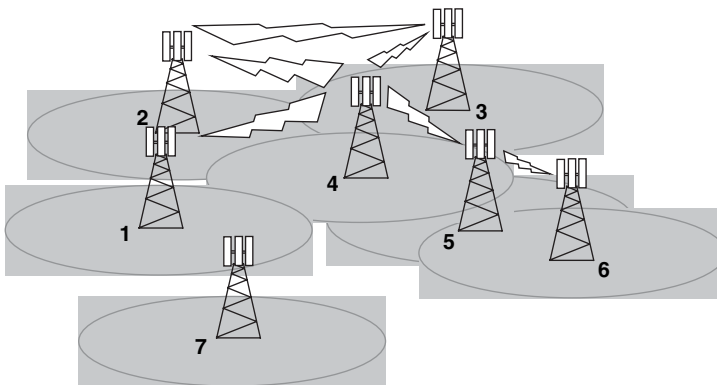
FIGURE 12.11. Non-homogeneous cellular pattern.

A Heuristic Approach for Channel Assignment Performance. Let us briefly introduce a modern heuristic algorithm developed in References [31–33] on how to obtain C/I-ratio based on mathematical models proposed in References [27–30,34–36] by accounting for the Walfisch–Ikegami model (WIM) of signal power decay in the urban environment [37].

The frequency assignment problem, was represented in References [31–33] in the form of the heuristic algorithm developed on the basis of cell configuration, which does not follow the classical hexagonal-cell homogeneous concept with a periodic frequency reuse pattern. This algorithm is based on the binary constraints between a pair of the transmitters presented in References [31–33] that appear in the following form:

$$|f_i - f_j| > k, \qquad k \geq 0 \tag{12.14}$$

where f_i and f_j are the frequencies assigned to transmitters i and j. In References [31–38], different configurations of the cellular pattern were analyzed for channel (frequency) assignment with applications to real nonregular, nonuniform radio networks, mobile and stationary, considering

– cellular maps with different dimensions of cells;
– cellular maps with irregular shapes of cells;
– cellular maps with certain level of intercell overlapping.

An example of nonuniform cell pattern distribution with different shapes and sizes of cells is presented in Reference [38] for a city in Germany [34], where the location of the BS, the cell-shape, and dimensions of each cell were taken to be nonregular. It was then redesigned in References [31–33] by using the new heuristic approach. In its redesigned form, this nonregular cell pattern is shown in Figure 12.12, according to References [31–33]. For such a configuration of cells we need to use the following formula:

$$\left(\frac{C}{I}\right)_i = \frac{R_i^{-4}}{\sum\limits_{j \in M_i} d_{ij}^{-4}} \tag{12.15}$$

Here, following Reference [38] we take a simple two-ray propagation model with $\gamma = 4$ (see Chapter 5). Notice that all notations are changed here from those used in References [32,34,38] to be unified with those used in this section. Here R_i is a radius of cell i; M_i is the set of all the cells (excluding cell i) that uses the same bandwidths (channels) as cell i; d_{ij} is the worst-case distance between interfering cell j and cell i. The latter can be found as [38]

$$d_{ij} = \sqrt{(x_i - x_j)^2 + (y_i - y_j)^2} - R_i \tag{12.16}$$
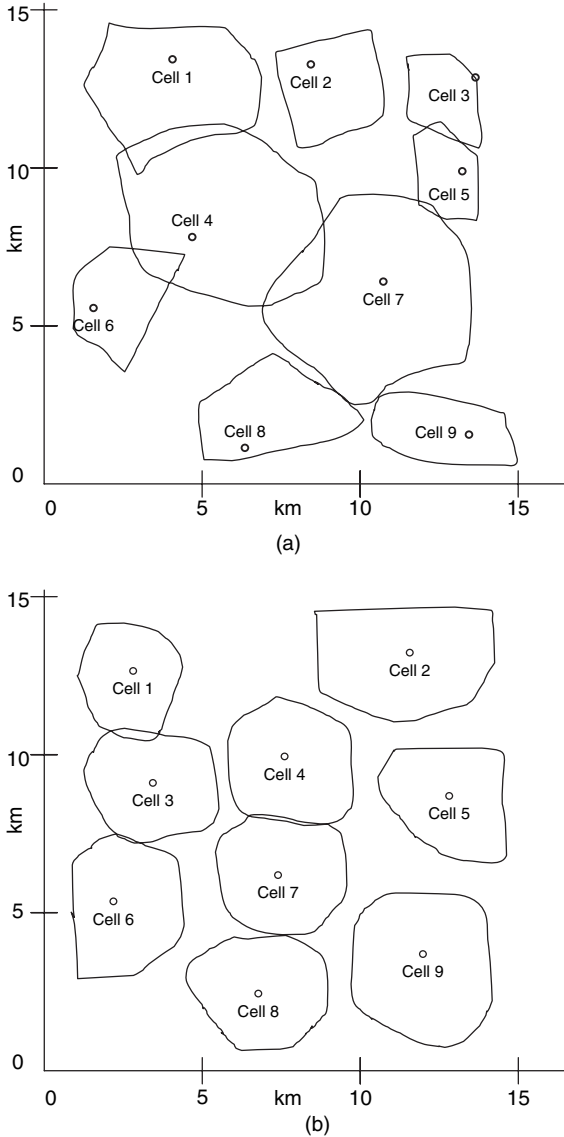
FIGURE 12.12. Nonuniform cell pattern. (Source [31]: Reprinted with permission © 2004 IEEE)

where (x_i, y_i) and (x_j, y_j) are the Cartesian coordinates of the base stations (BSs) of cells i and j. Using the simplest propagation model, in Reference [38] the co-channel interference constraint was obtained for C/I threshold $\alpha = 1/\beta = 18\,\text{dB}$

$$\sum_{j \in M_i} \frac{d_{ij}^{-4}}{R_i^{-4}} \leq \beta \tag{12.17}$$

In Reference [32], sufficient improvements of the model [38] were obtained by introducing adjacent channel interference $adj\_factor_k = -a(1 + \log_2 k)$. Where k is the bandwidth separation (in number of channels) between the adjacent channel frequency and central frequency of the corresponding filter (see the strict explanations in Reference [32]). A typical value for a is 18 dB (as $\alpha = 18$ dB in Reference [38]), and for $k = 1$ an adjacent channel is attenuated by a factor equal to 0.015 [32].

Channel Assignment Strategy Accounting for the Propagation Loss Law.
Using such definitions, the co-channel interference constraint (12.16), accounting for the simple law of the received power attenuation $P_{Ri} \propto P_{Ti} d^{-4}$, can be rewritten as [32]

$$\sum_{j \in M_i} \frac{P_{Tj} d_{ij}^{-4}}{P_{Ti} R_i^{-4}} + \sum_{k=1}^{n} adj\_factor_k \sum_{j \in M_i} \frac{P_{Tk} d_{ik}^{-4}}{P_{Ti} R_i^{-4}} \leq \beta \qquad (12.18)$$

Using the two-ray model presentation (see Chapter 5), we can also express this constraint as [32]

$$\sum_{j \in M_i} \frac{P_{Tj} L(d_{ij}, f)}{P_{Ti} L(R_i, f)} + \sum_{k=1}^{n} adj\_factor_k \sum_{j \in M_i} \frac{P_{Tk} L(d_{ik}, f)}{P_{Ti} L(R_i, f)} \leq \beta \qquad (12.19)$$

In Reference [32], the Walfisch–Ikegami propagation model (WIM) with a slope-attenuation parameter of $\gamma = 2.6$ (i.e., $P_{Ri} \propto P_{Ti} d^{-2.6}$), was also taken into consideration. Let us now compare results obtained according to Reference [32], using a simple two-ray model and the WIM model, with those obtained using the stochastic approach with a slope-attenuation parameter of $\gamma = 3.0$ (i.e., $P_{Ri} \propto P_{Ti} d^{-3.0}$). To compare the effects of these three laws of propagation loss on the strategy of frequency assignment, in computations, following References [31–33], we take into account the interference effects of first ($n = 1$) and second ($n = 2$) adjacent channels. During computations we considered only co-channel interference ($n = 0$) and also considered a practical example of a 21 cell network, by varying the radii of the cells without changing the base station locations in order to produce three different configurations:

a) nonoverlapping cells;
b) adjacent cells; and
c) overlapping cells.

Finally, the channel assignment, *span* and *order*, which guarantees a *C/I* of at least 18 dB in every point in an urban environment, was computed and presented in Figures 12.13(a,b)–12.15(a,b) for *span* (a) and *order* (b) assignment. Here, three kinds of laws of path loss according to two-ray ($d^{-4.0}$), WIM ($d^{-2.6}$) and stochastic

**Frequency assignment span (Radius 100 m)
nonoverlapping cells**

**Frequency assignment order (Radius 250 m)
nonoverlapping cells**
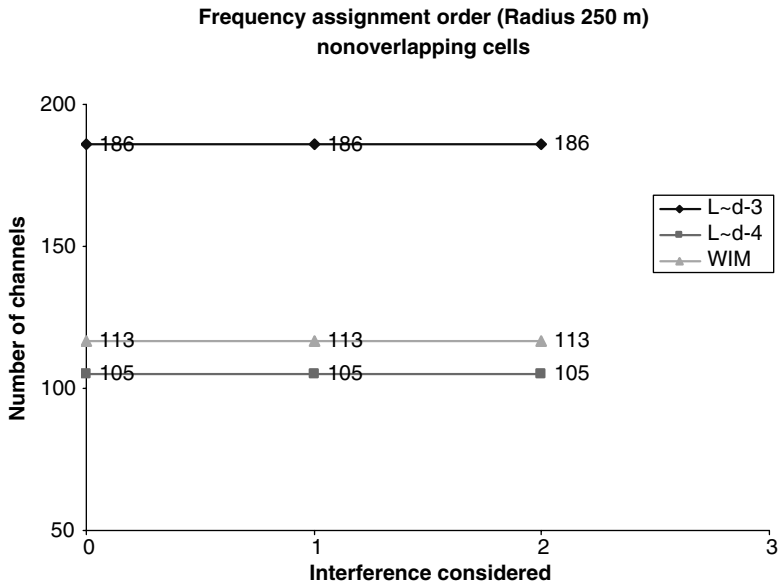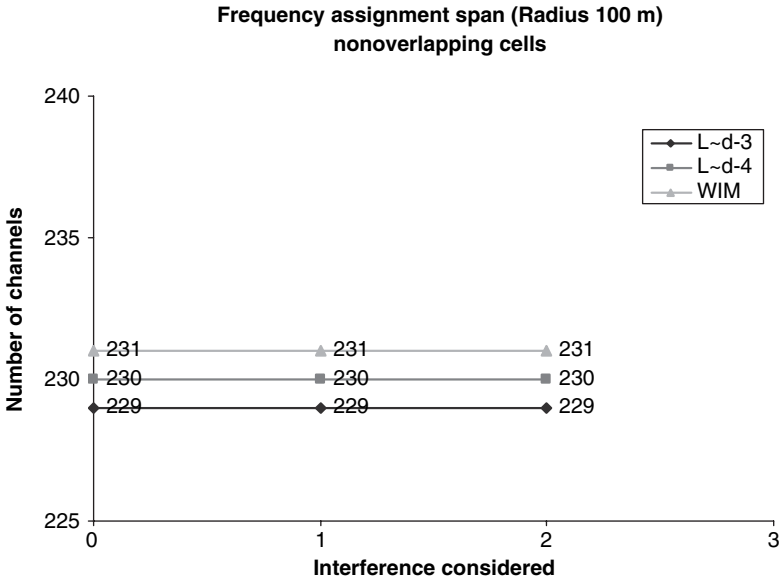
FIGURE 12.13. Frequency assignment for nonoverlapping cells.

$(d^{-3.0})$ models for nonoverlapping (Fig. 12.13), adjacent (Fig. 12.14), and overlapping (Fig. 12.15) configurations of nonuniform cellular patterns are shown.

As it is clearly seen from the presented illustrations, the multiparametric model and the Walfisch–Ikagami model (WIM) give higher channel (frequency)
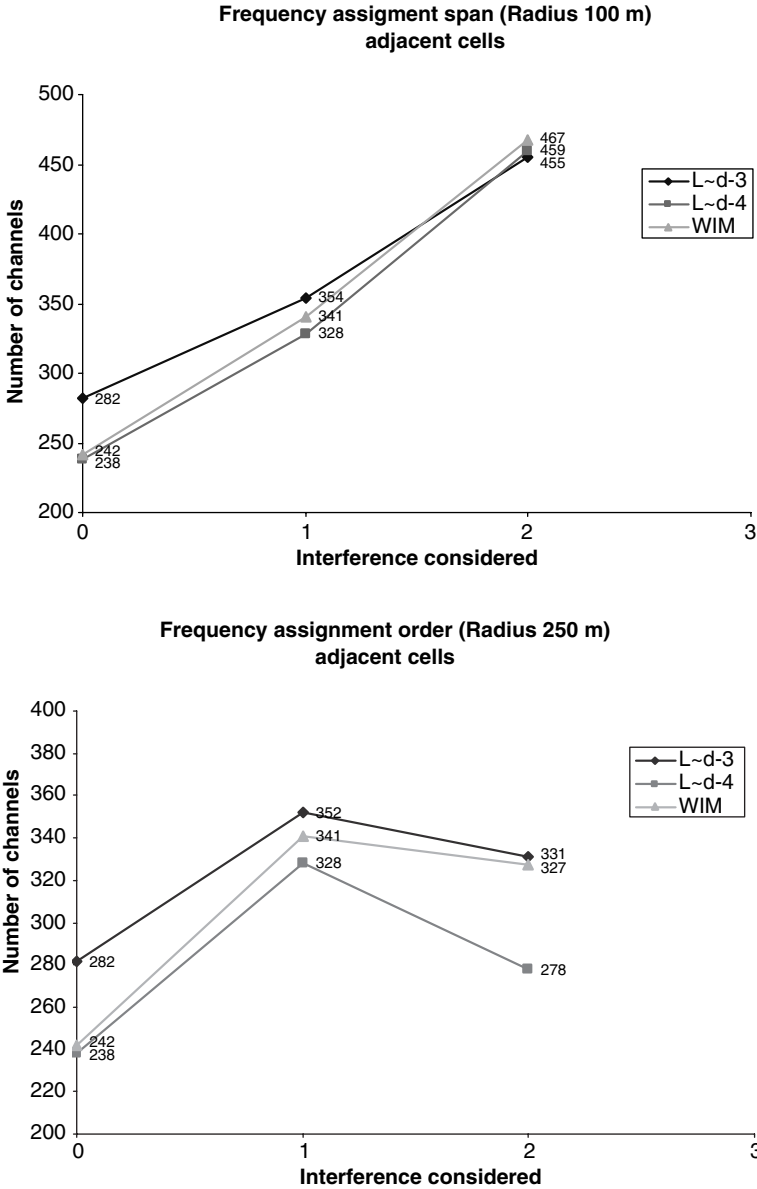
FIGURE 12.14. Frequency assignment for adjacent cells.

assignments for the worst situations with a configuration of cellular pattern planning, such as overlapped and adjacent, where the two-ray model is a weaker predictor. Consequently, for nonuniform and nonregular radio cellular networks it is more realistic to use the stochastic model (which also predicts a distance dependence of $d^{-2.5}$ in the presence of the diffraction phenomena, that is close to that for
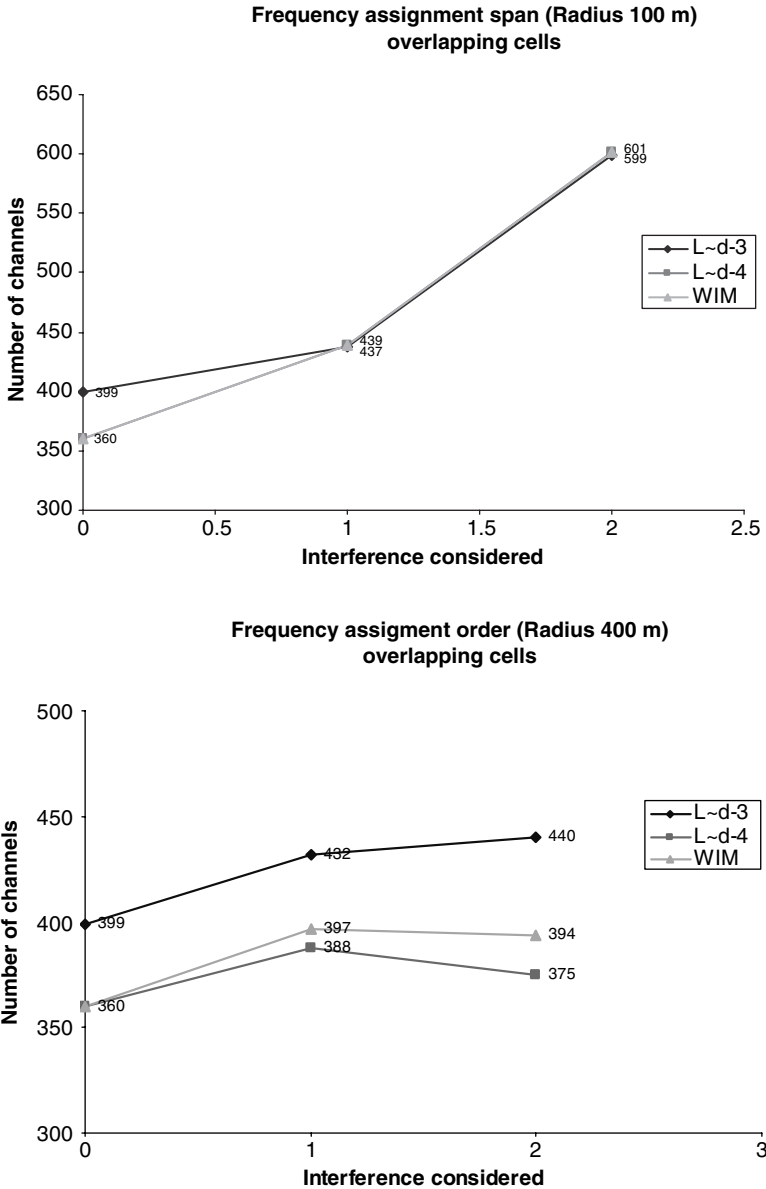
FIGURE 12.15. Frequency assignment for overlapping cells.

WIM $\sim d^{-2.6}$) compared with that predicted by the simple two-ray model usually used by other authors [34,38]. So, we show again, as was done in above discussions of how to predict the efficiency and increase performance of cellular networks, that the strict description of propagation phenomena occurred in specific urban radio communication channels allow designers to better and more precisely resolve both

the base station location problem and the frequency assignment problem, which must be considered simultaneously. We may conclude that the receipt based on the heuristic model, which was discussed in References [31–33] is fully verified by existing experimental data described in Reference [34], as well as by other theoretical models [35–38]. It can be used for the purposes of nonuniform cellular maps design and channel (frequency) assignment within different land radio links by the use of the more realistic propagation models, the WIM (as the COST-231 standard) and the stochastic multiparametric model. The results shown in Figures 12.13–12.15 fully illustrate the actuality of these conclusions.

12.3. PREDICTION OF PARAMETERS OF INFORMATION DATA STREAM

In the literature for wireless communications, the term "capacity" has different meanings: determining the user capacity in cellular systems in users per channel, information stream capacity inside the communication channel in bits per second, or considering data in bits per second per hertz per base station dealing with the spectral efficiency of the communication channel. Let us determine the main parameters of the information data stream sent through any wireless communication link.

Channel Capacity and Spectral Efficiency

According to standards utilized in information science, a *channel capacity*, denoted by C, is referred to the maximum data rate of information in a channel of a given bandwidth, which is measured in bits per second (bps). Whereas the *spectral efficiency*, denoted by $\widetilde{C} = C/B_w$, is considered as a measure in bits per second per hertz (bps/Hz). Both these terms are used in the well-known Shannon–Hartley equation, which for one channel with the given signal-to-noise ratio (SNR) S/N_0B_w, where S is the signal power in $W = J/\text{sec}$, B_w is the channel bandwidth (in Hertz) and N_0 is the noise power spectral density in W/Hz, can be written as [39]

$$C = B_w \log_2\left(1 + \frac{S}{N_0B_w}\right) \tag{12.20}$$

If we denote $\widetilde{C}$ as the spectral efficiency, as the ratio $\frac{C}{B_w}$, we get instead of (12.20)

$$\widetilde{C} = \log_2\left(1 + \frac{S}{N_0B_w}\right) \tag{12.21}$$

These two formulas for the capacity and spectral efficiency estimation are valid only for the channels with additive white Gaussian noise (AWGN-channels), which is also called additive noise (see definitions in Chapter 1). In this case the power of the additive noise equals $N_{\text{add}} = N_0B_w$, which is simply defined in the literature as the signal-to-noise ratio (SNR). Usually, AWGN channels are called the ideal

channels and all practical radio channels are compared to the ideal channel by selecting detection error probability of 10^{-6} and finding SNR necessary to achieve it. Effects of interference can be regarded as another source of effective noise, which raises the noise level for calculating the error rate. In this case, we must also introduce in (12.20) and (12.21) together with N_{add} the noise caused by interference N_{int}

$$\widetilde{C} = \log_2\left(1 + \frac{S}{N_0 B_w + N_{\text{int}}}\right) \tag{12.22}$$

Above, we discussed the channels in which only white or Gaussian noise was taken into account. What will happen if there is additional noise called multiplicative (see definitions in Chapter 1), which usually occurs in the wireless communication channel, land, atmospheric, and ionospheric due to multipath fading phenomena? In this case, on the basis of a unified algorithm of how to estimate fading effects, described in Chapter 11, we can account for all kinds of noise in the Shannon–Hartley formula (12.20). To do that, we propose now a simple approach, which can be used only if LOS component is predominant with respect to the NLOS component, that is, when the Ricean parameter $K > 1$ [40]. Taking into account the fading phenomena, described by the Ricean distribution with parameter $K > 1$ (see Chapters 1, 5, and 11), we can estimate the multiplicative noise by introducing its spectral density, N_{mult}, with its own frequency band, B_Ω, into (12.20) or (12.21)

$$\widetilde{C} = \log_2\left[1 + \frac{S}{N_0 B_w + N_{\text{mult}} B_\Omega}\right] \tag{12.23}$$

This formula can be rewritten as

$$\widetilde{C} = \log_2\left(1 + \frac{S}{N_{\text{add}} + N_{\text{mul}}}\right) = \log_2\left(1 + \left(\frac{N_{\text{add}}}{S} + \frac{N_{\text{mul}}}{S}\right)^{-1}\right) \tag{12.24}$$

where, according to our definitions introduced in Chapters 5 and 11 following the proposed stochastic approach, $\frac{S}{N_{\text{mult}}} = \frac{\langle I_{\text{co}} \rangle}{\langle I_{\text{inc}} \rangle}$. Using now the definition of K, introduced in these chapters, we get

$$\frac{S}{N_{\text{mult}}} = \frac{\langle I_{\text{co}} \rangle}{\langle I_{\text{inc}} \rangle} = K \tag{12.25}$$

Combining together all these notations, we finally get the capacity as a function of the Recean K-factor

$$C = B_w \log_2\left(1 + \left(\frac{N_{\text{add}}}{S} + K^{-1}\right)^{-1}\right) = B_w \log_2\left(1 + \frac{K \cdot \text{SNR}_{\text{add}}}{K + \text{SNR}_{\text{add}}}\right) \tag{12.26}$$

where we denoted signal-to-additive-noise ratio as $\text{SNR}_{\text{add}} = \frac{S}{N_{\text{add}}}$.

This approximate formula can be used to estimate the capacity of the wireless communication channel with fading, additive, and multiplicative phenomena, only when the coherent component of the total signal power will exceed the incoherent component and a direct visibility for each subscriber take place. As follows from (12.26), a decrease of the *K*-factor in one order leads to a decrease of the capacity maximum twice. To compensate for this decrease caused by fading, array antennas can be used in a MIMO communication link consisting of an *M*-element (or *M*-beam) antenna at one end and an *N*-element (or *N*-beam) antenna at the other.

Thus, for the MIMO communication links consisting of the *M*-element (or *M*-beams) antenna at the one end and *N*-element (or *N*-beam) antenna at the other end, the link capacity and spectral efficiency depend on the degree of correlation between channels corresponding to each element or beam. Thus, if the channels are uncorrelated, their capacity and spectral efficiency may be added. For $M > N$ the following expression can be used in pure AGWN channel without multiplicative noise [39,45,46]

$$\widetilde{C}_{\text{uncor}} = N \, \log_2 \left(1 + \frac{M \cdot S}{N \cdot B_W \cdot N_0} \right) \tag{12.27}$$

We can interpret this formula as follows: the output signal power is divided equally between *N* channels, as they have the same gain as *M*. As the capacities of the channels are the same, we get a factor *N* outside the logarithm. In the case of correlated antennas within the array, we have only one channel with gain *MN* [39,45,46] and:

$$\widetilde{C}_{\text{corr}} = \log_2 \left(1 + \frac{MNS}{B_W N_0} \right) \tag{12.28}$$

In the case of uncorrelated element antenna array, the channel capacity or spectral efficiency increases linearly with the increase of the number of channels *N*. While for correlated antenna elements, this increase is lesser according to logarithmic law. Nevertheless, in both cases, an adaptive array can significantly increase the data rate between the mobile and a base station in multiple spatial channels, as was shown in Reference [47]. For example, in an IS-136 system, an omni-antenna gives 48.6 kilobit per second (kbps) in a single 30 kHz channel, whereas the *M* spatially separated channels corresponded to the *M* antenna elements at the base station can yield data rates of $\approx M \cdot 30$ kHz [47]. Use of the additional techniques for space-time coding or space-time processing offer the potential to make practical spectral efficiency of many bits per second per hertz to each mobile users (in the above example of hundreds of kilobits per second in a 30 kHz channel).

Now, comparing (12.26) with (12.27) or (12.28), we can obtain the compensation of fading effects for link capacity in linear order of *N* for the adaptive antenna array with uncorrelated elements or in logarithmical order of *NM* for adaptive antenna array with the correlated elements.

Bit Error Rate. The bit error rate (BER) is another main parameter that determines the quality of the communication channel, that is, the relative quantity of the received data versus the sent data. BER is measured in the percentage of bits that have an error relative to the total bits received in a transmission. To estimate this parameter, the following formula is usually used [48]

$$\text{BER} = \frac{1}{2} \int_0^\infty p(x) erfc \left(\frac{\text{SNR}}{2\sqrt{2}} x \right) dx \tag{12.29}$$

Here $p(x)$ is the probability density function and $erfc(\bullet)$ is the well-known error function [47]. Now using the BER definition (12.29), where $p(x)$ is Ricean PDF with the standard deviation σ (see definitions in Chapter 1) and taking into account multiplicative noise, we finally get for BER the following general equations:

$$\text{BER}(K, \text{SNR}, \sigma) = \frac{1}{2} \int_0^\infty \frac{x}{\sigma^2} e^{-\frac{x^2}{2\sigma^2}} e^{-K} I_0 \left(\frac{x}{\sigma} \sqrt{2K} \right) erfc \left(\frac{K SNR_{\text{add}}}{2\sqrt{2}(K + SNR_{\text{add}})} x \right) dx \tag{12.30}$$

Relations Between Main Parameters

To understand a problem on how noise characteristics caused by fading phenomena affect situations with information data rate and capacity within various land radio communication links, we must obtain the convenient formulas describing relations with the main parameters of data stream. Therefore, in order to derive BER versus capacity or spectral efficiency, we express K-factor as a function of C or $\widetilde{C}$ using (12.26)

$$K = \frac{\text{SNR}_{\text{add}} \left(2^{\frac{C}{B_w}} - 1 \right)}{\text{SNR}_{\text{add}} - \left(2^{\frac{C}{B_w}} - 1 \right)} = \frac{\text{SNR}_{\text{add}} (2^{\tilde{C}} - 1)}{\text{SNR}_{\text{add}} - (2^{\tilde{C}} - 1)} \tag{12.31}$$

Then using (12.29) and (12.31), we get the *BER* as a function of $\widetilde{C}$:

$$\text{BER}(\widetilde{C}) = \frac{1}{2} \int_0^\infty \frac{x}{\sigma^2} e^{-\frac{x^2}{2\sigma^2}} e^{-\frac{W_1(\tilde{C})}{W_2(\tilde{C})}} I_0 \left(\frac{x}{\sigma} \sqrt{2\frac{W_1(\widetilde{C})}{W_2(\widetilde{C})}} \right) erfc \left(\frac{\frac{W_1(\widetilde{C})}{W_2(\widetilde{C})} \text{SNR}_{\text{add}}}{2\sqrt{2} \left(\frac{W_1(\widetilde{C})}{W_2(\widetilde{C})} + \text{SNR}_{\text{add}} \right)} x \right) dx \tag{12.32}$$

where $W_1(\widetilde{C}) = \text{SNR}_{\text{add}} (2^{\tilde{C}} - 1)$ and $W_2(\widetilde{C}) = \text{SNR}_{\text{add}} - (2^{\tilde{C}} - 1)$.
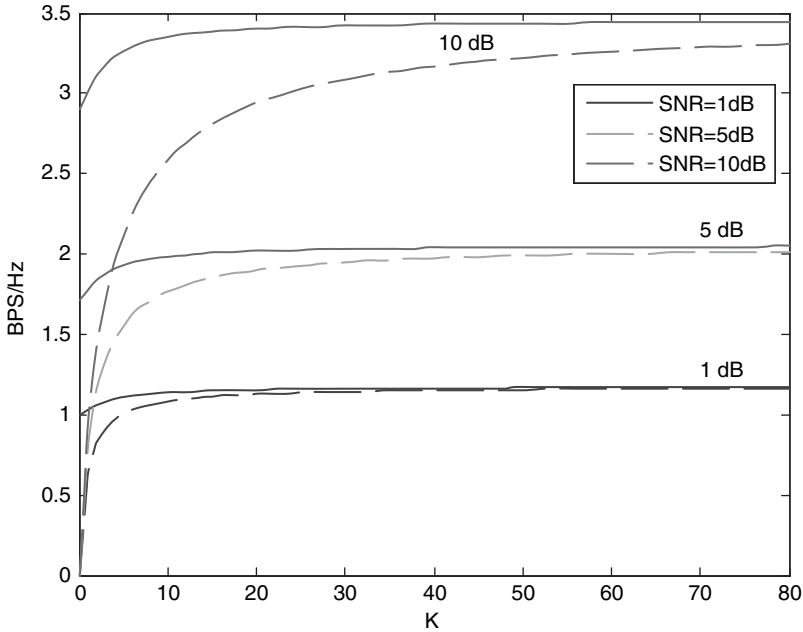
FIGURE 12.16. Spectral efficiency as a function of K-factor.

This is a very important formula, which gives the relation between the spectral efficiency of the multipath communication channel, caused by fading phenomena, and the probability of BER of the information data stream inside such a channel.

To show the reader how to minimize the BER and maximize the capacity or the spectral efficiency for different wireless networks (with the corresponding bandwidth of each channel), we created a special program based on the above formulas. First, we have analyzed the changes of the capacity as a function of K, that is, as a function of different conditions of the channel allocation, using Equations (12.23) to (12.26). Results are shown in Figure 12.16. Here, we have examined the spectral efficiency for three different typical values of SNR_{add}, which are shown in Figure 12.16. It is obvious, that with the increase in SNR (from 1 dB to 10 dB) the spectral efficiency is increased by more than three times; this effect is more significant for the worst case of multipath fading channels (for $K < 5$).

Then, we made computations to estimate the capacity that can be used by various wireless networks with a given $\frac{S}{N_{add}}$ ratio of 5 dB, using in (12.26) different bandwidths, corresponding to several well used networks; such as the CDMA-system with the bandwidth $B_w = 25$ MHz, the TDMA-system ($B_w = 40$ MHz), the TDMA1-system (15 MHz), the TDMA2-system (5 MHz), and the GSM, as a combination of the TDMA and FDMA ($B_w = 12.5$ MHz). As is seen from Figure 12.17, where the capacity in bits per second is shown versus the K-factor, the fading effect is dominant for $K < 5$, when the multipath component may play some significant role. This effect depends on parameter K, which characterized fading effects within the wireless
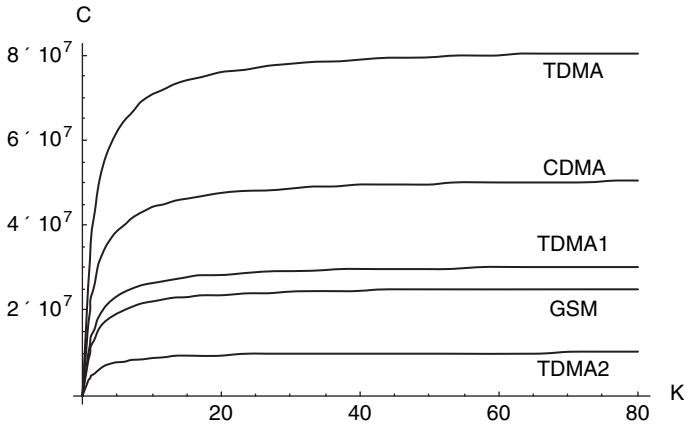
FIGURE 12.17. Capacity of various systems vs. the K-factor.

channel. Furthermore, a network that uses larger bandwidths gives better throughput of data streams. Usually the TDMA systems have bandwidths containing not more than 20 MHz, therefore, their capacity is larger than that for CDMA systems.

As is known from References [49–52], the TDMA and CDMA systems result in an increase in channel capacity over the standard FDMA system, allowing different time slots and different codes, to be assigned to different users. Each increase is in the order of five to ten [53–56].

Finally, we ran two simulations, the first one was BER as a function of K using Equation (12.30), and the second was BER as a function of spectral efficiency, using Equation (12.32). The parameters we used for the computations are the following: $\sigma = 2$ and $\mathrm{SNR_{add}} = \frac{S}{N_{add}} = 1\,\mathrm{dB}$. The results of the computation are shown in Figure 12.18 and Figure 12.19, respectively. As seen from Figures 12.18 and 12.19, with an increase of K-factor, that is when LOS component becomes predominant compared to NLOS multipath component of signal total intensity, the BER
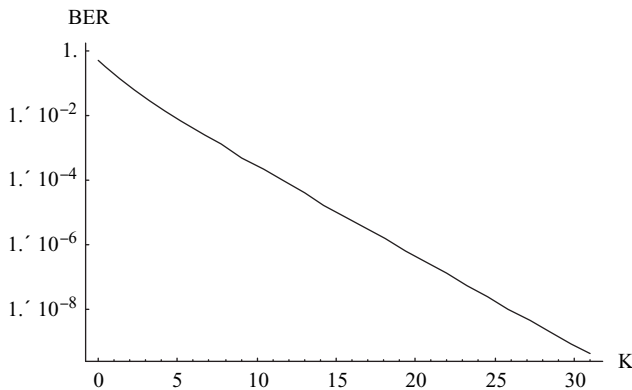
FIGURE 12.18. BER as a function of K.
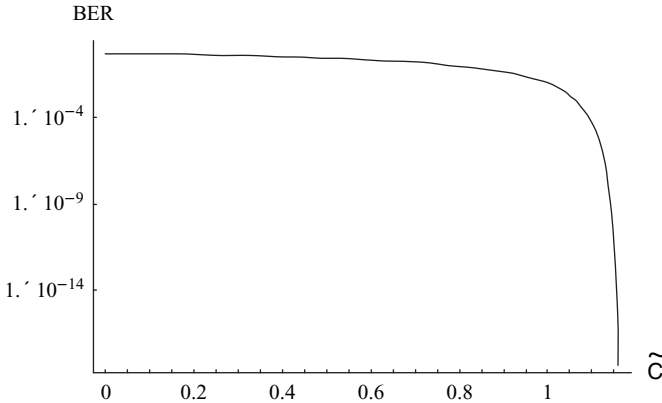
FIGURE 12.19. BER as a function of $\widetilde{C}$.

parameter is decreased, from 10^{-2} for $K \approx 5$ to 10^{-6} for $K \approx 20$ (corresponding to communication channels with high BS antenna and quasi-LOS for any user located in the area of service). At the same time, as expected, the spectral efficiency is also increased (see Fig. 12.19). Hence, with the increase of the spectral efficiency of the data stream a simultaneous sharp decrease of BER is also observed.

BIBLIOGRAPHY

[1] Syski, R., *Introduction to Congestion Theory in Telephone Systems*, 2nd edition, New York, 1986.

[2] Nelson R., *Stochastic Processes and Queuing Theory*, Springer-Verlag, 1994.

[3] Alanyali, M., and B. Hajek, ''On simple algorithm for dynamic load balancing,'' *Proc. IEEE INFOCOM*, vol. 1, 1995, pp. 230–238.

[4] Yuan, W. et al., ''Loading balancing in wireless networks,'' *Proc. GLOBECOM*, 1997, pp. 1616–1620.

[5] Papavassiliou, S., and L. Tassiulas, ''Joint optimal channel base station and power assignment for wireless access,'' *IEEE Trans. Network.*, vol. 4, 1996, pp. 857–872.

[6] Freedman, A., A. Gil, and R. Giladi ''An impact of unbalanced availability on GOS of wireless systems,'' *Wireless Personal Communications*, vol. 20, 2002, pp. 21–40.

[7] Blaunstein N., A. Freedman, R. Giladi, and M. Levin, ''Unified approach of GOS optimization for fixed wireless access,'' *IEEE Trans. on Veh. Technolog.,* vol. 51, 2002, pp. 101–110.

[8] Blaunstein N., and R. Hassanov, ''Grade of service design in wireless systems operating in multipath fading environments,'' *J. Business Briefing: Wireless Technology 2004*, 2004, pp. 121–124.

[9] Lee, W. Y. C., *Mobile Communication Engineering*, New York, McGraw Hill, 1985.

[10] Jakes, W. C., *Microwave Mobile Communications*, J. Wiley & Sons, New York, 1974.

[11] Blaunstein, N., and Y. Ben-Shimol, ''Frequency dependence of path loss characteristics and link budget design for various terrestrial communication links,'' *IEEE Trans. on Antennas and Propagat.*, vol. 52, no. 10, 2004, pp. 2719–2729.

[12] Steele, R., *Mobile Radio Communication*, IEEE Press, New York, 1995.

[13] Saunders, S.R., *Antennas and Propagation for Wireless Communication Systems*, John Wiley & Sons, New York, 1999.

[14] Rappaport, T. S., *Wireless Communications*, Prentice Hall PTR, New York, 1996.

[15] Faruque, S., *Cellular Mobile Systems Engineering*, Artech House, Boston-London, 1994.

[16] Feuerstein, M. L., and T. S. Rappaport, *Wireless Personal Communication*, Artech House, Boston-London, 1992.

[17] Lee, W. Y. C., *Mobile Cellular Telecommunications Systems*, McGraw Hill Publications, New York, 1989.

[18] Linnartz, J. P., *Narrowband Land-Mobile Radio Networks*, Artech House, Boston-London, 1993.

[19] Mehrotra, A., *Cellular Radio Performance Engineering*, Artech House, Boston-London, 1994.

[20] Blaunstein, N., and M. Levin, ''Propagation loss prediction in the urban environment with rectangular grid-plan streets,'' *Radio Sci.*, vol. 32, no. 2, 1997, pp. 453–467.

[21] Blaunstein, N., ''Average field attenuation in the non-regular impedance street waveguide,'' *IEEE Trans. Anten. and Propagat.*, vol. 46, no. 12, 1998, pp. 1782–1789.

[22] Blaunstein, N., ''Prediction of cellular characteristics for various urban environments,'' *IEEE Anten. Propagat. Magazine*, vol. 41, no. 6, 1999, pp. 135–145.

[23] Xia, H. H., and H. L. Bertoni, ''Diffraction of cylindrical and plane waves by an array of absorbing half screens,'' *IEEE Trans. Antennas and Propagation*, vol. 40, 1992, pp. 170–177.

[24] Bertoni, H. L., W. Honcharenko, L.R. Maciel, and H.H. Xia, ''UHF propagation prediction for wireless personal communications,'' *Proc. IEEE*, vol. 82, no. 9, Sept. 1994, pp. 1333–1359.

[25] Rustako, A. J., Jr., N. Amitay, M.J. Owens, et al., ''Radio propagation at microwave frequencies for line-of-sight microcellular mobile and personal communications,'' *IEEE Trans. Veh. Technol.*, vol. 40, no. 2, Feb. 1991, pp. 203–210.

[26] Tan, S.Y., and H. S. Tan, ''UTD propagation model in an urban street scene for microcellular communications,'' *IEEE Trans. Electromag. Compat.*, vol. 35, no. 4, Nov. 1993, pp. 423–428.

[27] Gamst, A., and E. G. Zinn, ''Cellular radio network planning,'' *IEEE Aerosp. Electron. Syst. Magazine*, vol. 1, no. 1, 1985-1986, pp. 8–11.

[28] Akl, R. G., M.V. Hegde, M. Naraghi-Pour, and P. S. Min, ''Cell placement in CDMA network,'' in *Proc. of the IEEE Wireless Communic. and Networking Conf.*, vol. 2, 1999, pp. 903–907.

[29] Eisenblatter, A., A. Fugenschuh, T. Koch, et al., ''Modeling feasible network configurations for UMTB,'' ZIB, Berlin, *Tech. Rep.* March 2002, pp. 02–16.

[30] Hurley, S., ''Planning effective cellular mobile radio networks,'' *IEEE Trans. Veh. Technol.*, vol. 51, No.2, 2002, pp. 48–56.

[31] Santiago, R. Ch., and V. Lyandres, ''A sequential algorithm for optimal base station location in a mobile radio network,'' in *Proc. of 2004 IEEE 15th Int. Symp. on Personal, Indoor and Mobile Radio Communic.*, Barcelona, Spain, Sept. 2004, pp. 5–8.

[32] Santiago, R. Ch., A. Raymond, V. Lyandres, et al., ''Effective base stations location and frequency assignment in mobile radio networks,'' in *Proc. of 2003 IEEE Int. Symp. on Electromagn. Compatibility.* Istanbul, Turkey, 2003.

[33] Santiago, R. Ch., E. Gigi, and V. Lyandres, ''An improved heuristic algorithm for frequency assignment in non-homogeneous cellular mobile networks,'' in *Proc.of 2004 IEEE 60th Veh. Technol. Conf.*, Los Angeles, California, September 2004, pp. 26–29.

[34] Tutschku, K., and P. Tran-Gia, ''Spatial traffic estimation and characterization for mobile communication network design,'' *IEEE J. Select. Areas Communic.*, vol. 16, no. 5, 1998, pp. 804–811.

[35] Hurley, S., R. M. Whitaker, and D. H. Smith, ''Channel assignment in cellular networks without channel separation constraints,'' in *Proc. of 2000 IEEE Veh. Technol. Conf.*, Boston, Massachusetts, Sept. 2000, pp. 24–28.

[36] Hurley, S., ''Automatic base station selection and configuration in mobile networks,'' in *Proc. of 2000 IEEE Veh. Technol. Conf.*, Boston, Massachusetts, Sept. 2000, pp. 24–28.

[37] Lee, J. S., and L. E. Miller, ''Walfisch-Ikegami Formula,'' in *CDMA Systems Enginnering Handbook*, Boston-London, Artech House, 1988, pp. 190–199.

[38] Wu, J. -L. C., and L.-Y. Wey. ''Channel assignment for cellular cellular mobile networks with non-uniform cells,'' *IEE Proc. Communic.*, vol. 145, Dec. 1998, pp. 451–456.

[39] Andersen, J. B., ''Antenna arrays in mobile communications,'' *IEEE Antenna Propagat. Magazine*, vol. 42, no. 2, 2000, pp. 12–16.

[40] Blaunstein, N., ''Wireless Communication Systems,'' in *Handbook of Engineering Electromagnetics*, Ed. R. Bansal, Marcel Dekker, New Jersey, 2004, pp. 417–481.

[41] Anderson, H. R., ''A ray-tracing propagation model for digital broadcast systems in urban areas,'' *IEEE Trans. on Broadcasting*, vol. 39, no. 3, 1993, pp. 309–317. *Trans. Select. Areas in Communic.*, vol. 10, no. 4, 1992, pp. 665–668.

[42] Bertoni, H., L. *Radio Propagation for Mobile Wireless Systems*, Prentice Hall PTR, New Jersey, 2000.

[43] Liang, G., and H. L. Bertoni, ''A new approach to 3D ray tracing for propagation prediction in cities,'' *IEEE Trans. Anten. Propagat.*, vol. 46, 1998, pp. 853–863.

[44] Lebherz, M., W. Weisbeck, and K. Krank, ''A versatile wave propagation model for the VHF/UHF range considering three dimensional terrain,'' *IEEE Trans. Antennas Propagat.*, vol. AP-40, 1992, pp. 1121–1131.

[45] Andersen, J. B., ''Array gain and capacity for known random channels with multiple element arrays at both ends,'' *IEEE J. Select. Areas in Communic.*, vol. 18, no. 11, 2000, pp. 2172–2178.

[46] Andersen, J. B., ''Role of antennas and propagation for the wireless systems beyond 2000,'' *J. Wireless Personal Communic.*, vol. 17, 2001, pp. 303–310.

[47] Alouini, M.-S., M. K. Simon, and A. J. Goldsmith, ''Average BER performance of single and multi carrier DS-CSMA systems over generalized fading channels,'' *J. Wireless Systems and Mobile Comput.*, vol. 1, no. 1, 2001, pp. 93–110.

[48] Andrews, L. C., R. L. Philips, and C. Y. Hopen, *Laser Beam Scintillations with Applications*, SPIE Press, New York, 2001.

[49] Jung, P., Z. Zvonar, and K. Kammerlander (Editors), *GSM: Evolution Towards 3rd Generation*, Kluwer Academic Publishers, PL, 1998.

[50] Rappaport, *Wireless Communications: Principles and Practice*, Prentice Hall, Englewood Cliffs, New Jersey, 1996.

[51] Prasad, R., *CDMA for Wireless Personal Communications*, Artech House, Boston-London, 1996.

[52] Saunders, S. R., *Antennas and Propagation for Wireless Communication Systems*, J. Wiley & Sons, New York, 1999.

[53] Raith, K., and J. Uddenfeldt, ''Capacity of digital cellular TDMA systems,'' *IEEE Trans. Veh. Technol.*, vol. 40, 1991, no. 2, pp. 323–332.

[54] Gilhousen, K. S., I. M. Jacobs, R. Padovani et al., ''On the capacity of cellular CDMA system,'' *IEEE Trans. Veh. Technol.*, vol. 40, no. 2, 1991, pp. 303–312.

[55] Sivanand, S., ''On adaptive arrays in mobile communication,'' in *Proc. IEEE Nat. Telesystems Conf.*, Atlanta, Georgia, 1993, pp. 55–58.

[56] Balaban, P., and J. Salz, ''Dual diversity combining and equalization in digital cellular mobile radio'', *IEEE Trans. Veh. Technol.*, vol. 40, no. 2, 1991, pp. 342–354.

Prediction of Operational Characteristics of Adaptive Antennas

In adaptive antenna performance, as was mentioned in Chapters 9 and 10, it is very important to predict any desired subscriber position in the tested area. To obtain information about the direction to the subscriber as well as about the range to the subscriber, designers of the wireless networks need to carry out some special experiments. The direction of the subscriber is determined by the distribution of the recording signal in the azimuth and elevation domains. The range to the subscriber is determined by the time delay distribution of the arriving signal. Furthermore, when the adaptive antenna ''searches'' the moving subscriber (MS), it is very important to obtain information about its velocity based on signal distribution in the Doppler shift domain. In Chapter 10, we showed that this can be done theoretically using the proposed unified stochastic multiparametric approach. In the following section, we will verify the theoretical results described in the Chapter 10 by using more precisely arranged experiments carried out in different urban sites that focused our attention on adaptive antenna operational characteristics in the space, angle, time, and frequency domains.

13.1. EXPERIMENTAL VERIFICATION OF SIGNAL DISTRIBUTION IN AZIMUTH, TIME DELAY, AND DOPPLER SHIFT DOMAINS

Signal Azimuth Distribution. First, we verify results of theoretical prediction described in Chapter 10 via special experiments carried out in microcell urban

environments that are fully described in References [1,2]. In these experiments, the pulse signals were sent by using directive rotating antennas arranged at terminals— the transmitter and the receiver—at radio paths up to 1.5–2 km. The width of the loops of both antennas was 3° (at the half power points); measurements are based on the same method described in References [1,2].

The height of the BS transmitter antenna was changed from $z_2 = 6\,\text{m}$ to $z_2 = 12\,\text{m}$, and therefore the MS receiver antenna became $z_1 = 2\,\text{m}$. During its movement, the MS passed streets with different orientations with respect to the BS antenna, with various density and overlay profiles of the buildings. The receiving antenna with mechanical rotations on the vehicle had registered N multipath components of the wideband signal, each of which corresponded to one of the possible angular positions on the axis of the MS directive antenna. Because the antenna loop width was initially smaller than the integral scale width $\widetilde{\theta}$ of the energetic spectrum $\widetilde{W}(\varphi)$ described in Chapter 10, we can discuss the registration of realizations, having delta-function kind of shape on the angle energetic spectrum $\widetilde{W}(\varphi)$. The schematic geometry of the experiment is shown in Figure 13.1, where φ_T is the angle between the transmitter antenna axis and the direction to the receiver, φ_R^i is the current angle of observation of the vehicle receiving antenna, $i = 1, 2, \ldots, 360°$. According to the conditions of the experiments, $\varphi_R^i = \Delta\varphi(i-1)$, $\Delta\varphi = 1°$.
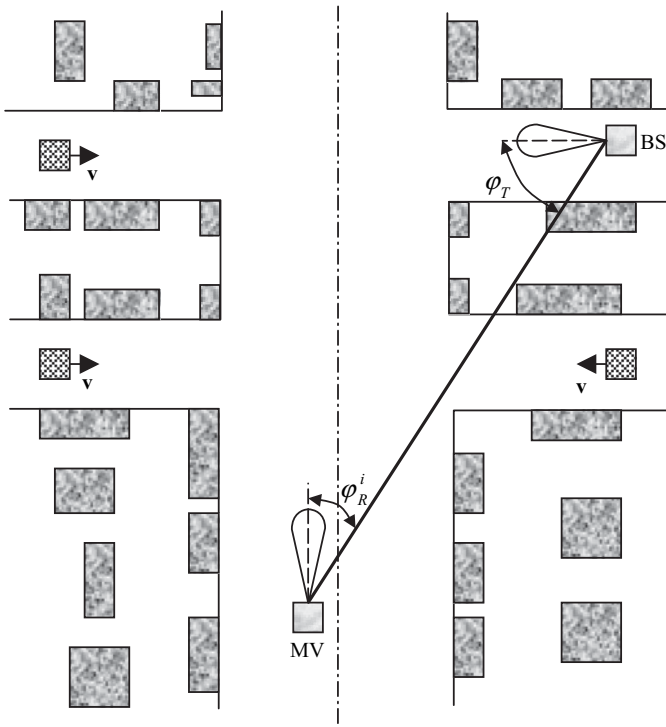
FIGURE 13.1. Geometry of the experimental site and the experiment.
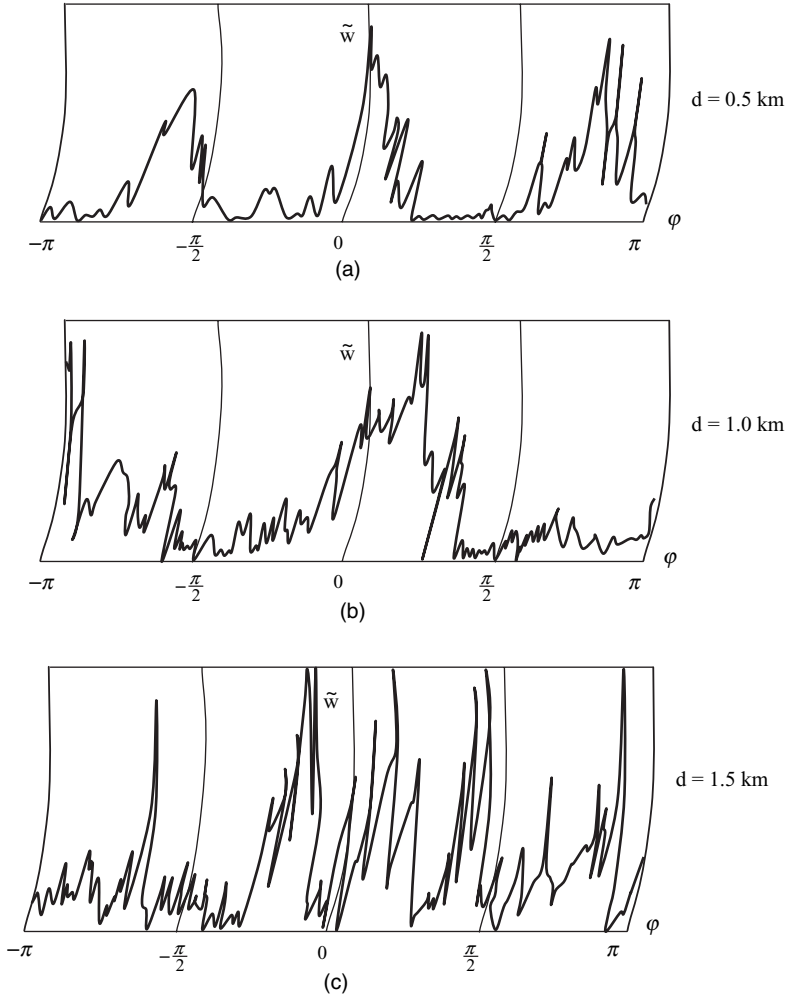
FIGURE 13.2. The results of measurements of the normalized signal power spectrum, $\tilde{w} = W(\varphi)/W(\varphi_T)$ for various ranges between the terminal antennas: $d = 0.5\,\text{km}$ (a), $d = 1.0\,\text{km}$ (b), $d = 1.5\,\text{km}$ (c).

In Figure 13.2, results of measurements of the normalized signal power spectrum, $\tilde{w} = W(\varphi)/W(\varphi_T)$, where $W(\varphi_T) = W_{\max}$, are presented for the case where the height of the BS antenna is lower than the level of the average rooftop $\bar{h}$ (i.e., $z_2 = 6\,\text{m} < \bar{h} = 8\,\text{m}$), for the following distances from BS: (a) $d = 0.5\,\text{km}$, (b) $d = 1.0\,\text{km}$, and (c) $d = 1.5\,\text{km}$. All data are presented for the case when the BS antenna axis is directed to the MS receiver antenna, that is, $\varphi_T \equiv 0°$. As follows from these measurements, when the two terminal antennas are lower than the rooftop, the maximal level of signal power at small ranges from the source
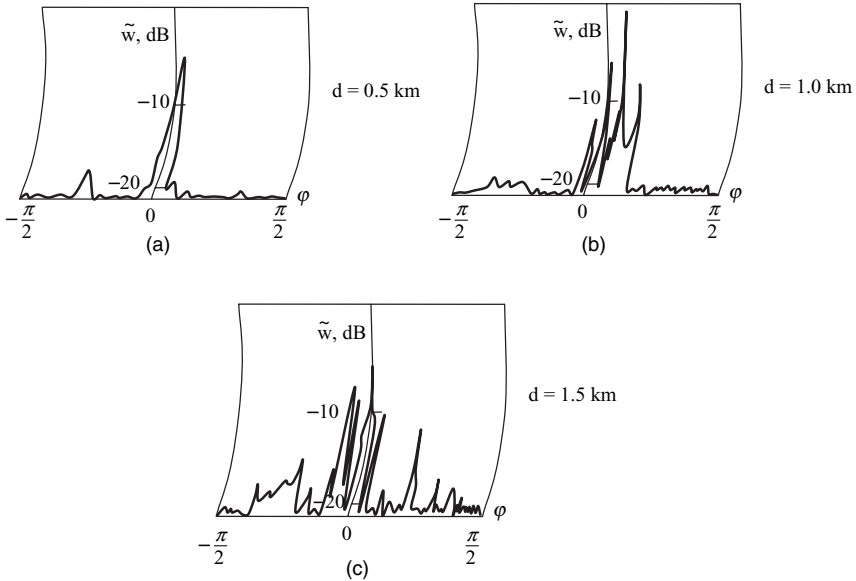
FIGURE 13.3. The same as in Fig. 13.2, but for the base station antenna higher than building rooftops.

is concentrated in the direction of the source. Simultaneously, some multipath signal components with a power of the same order are registered from angles close to back scattering and reflection (see Fig. 13.2a, $\varphi_R^i \in (-\pi, -\frac{\pi}{2}) \cup (\frac{\pi}{2}, \pi)$).

This effect is increased with an increase of range between the two terminal antennas. At far zones from the BS, multiray effects are observed, with quasi-uniform distribution of signal spectrum within the range of $[0, 2\pi]$ angles to the BS antenna, and with minimum energy from the direction to the MS (see Figs. 13.2b and 13.2c). Quite a different picture is observed for the case of the base station antenna higher than the overlay profile of the building, for example, $\bar{h} = 8\,\text{m} < z_2 = 12\,\text{m}$. In this case, as follows from Figures 13.3(a)–(c) measured for the same conditions and ranges between both antennas, despite the fact that far from the BS, due to an increase in the number of obstructions, the multipath components of the total signal are also presented with approximately the same power, the maximum of the power spectrum is concentrated near the direction to the BS. All these features are clearly understood by using the theoretical results that follow from the proposed multiparametric stochastic model described in Chapter 10 (see full description in References [1–3]).

In fact, as obtained in Chapter 10 with an increase of the BS antenna height and for the low elevated MS antenna, the area, where all obstructions are located around the MS, becomes smaller, that is fewer obstructions are involved in the multiple scattering and reflection process. It means that for a high BS antenna the multiray phenomena become weaker.
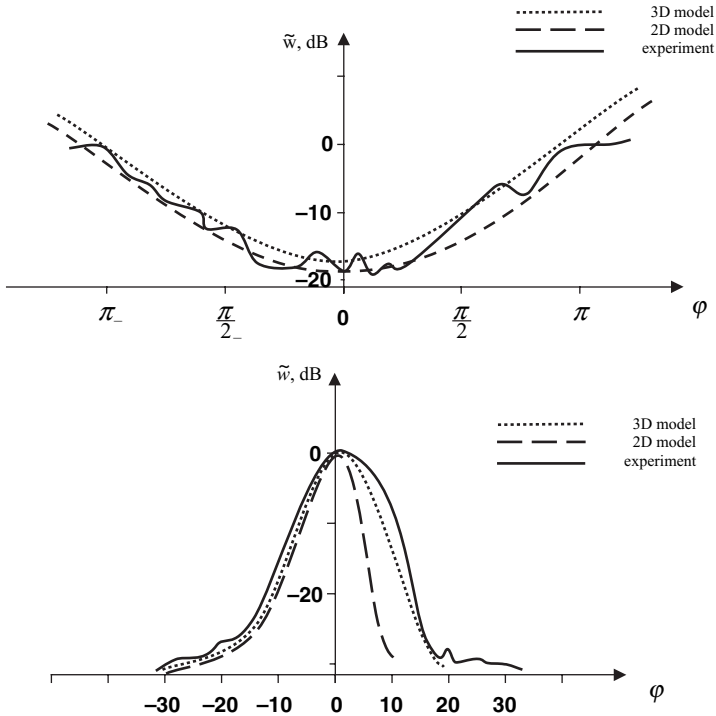
FIGURE 13.4. $\widetilde{w}(\varphi) = W(\varphi)/W_{\max}$ vs. φ for $z_2 = 5\,\mathrm{m}$ (top) and $z_2 = 12\,\mathrm{m}$ (bottom).

These results can be clearly seen from a comparison between the measurements presented in Figures 13.2(a)–(c) and in Figures 13.3(a)–(c). To obtain enough statistical data for theoretical prediction and better verification, averaged results of the pulse signal power spectrum distribution measurements were obtained in References [1,2] by using approximately ten local positions of the MS.

The normalized signal power $\widetilde{w}(\varphi) = W(\varphi)/W_{\max}$ (in decibel) is obtained after the averaging procedure is presented by a continuous curve in Figure 13.4 for $z_2 = 5\,\mathrm{m}$ (top figure) and for $z_2 = 12\,\mathrm{m}$ (bottom figure), respectively. Here, the results of the calculations according to the proposed combined 3D multiparametric model, which takes into account the effects of diffraction, street orientations, and buildings overlay profile of the building (see Chapter 1, 2, and 10), are presented in both figures by a dotted curve. Whereas the same calculations according to the regular 2D stochastic model obtained in Reference [3] without accounting for all these propagation phenomena are presented by dashed curves.

All parameters of the calculations are mentioned above and also follow from the topographical map and the geometry of the experiments of the tested area described in Reference [1]. As follows from the presented illustrations, the

proposed model can, with a great accuracy, predict the asymmetric shape of the signal PAS' distribution obtained experimentally, because of diffraction phenomenon and nonuniform height distribution of the building, the effects that cannot be explained by using the simple statistical models developed in References [3–7].

Signal Distribution in Time Delay Domain. The same dependence on the antenna height, predicted theoretically in Chapter 10, was obtained during experimental investigations of the signal power spectrum in the time delay domain. The method of experimental investigation of the time delay spectrum distribution is based on recording the wideband channel response at the same ten points of the MS schematically presented in Figure 13.1 by recording the unit pulse responses of the channel. The transmitter pulse duration was 60 ns at the level of -3 dB from the maximum signal amplitude. The same geometry of the experiment, the same parameters of both the antennas (MS and BS) and of the built-up terrain were used [1]. The results of measurements using two low terminal antennas of 5 m and 2 m (see above) are shown in Figure 13.5 for the range between both terminals: (a) $d = 1.0$ km, and (b) $d = 1.5$ km.

As follows from the given illustration in the, multipath pulse propagation—the number of incoming pulses exceeds 10–15 at all ranges from the base station—because of the effects of multiple scattering and reflection from the obstructions
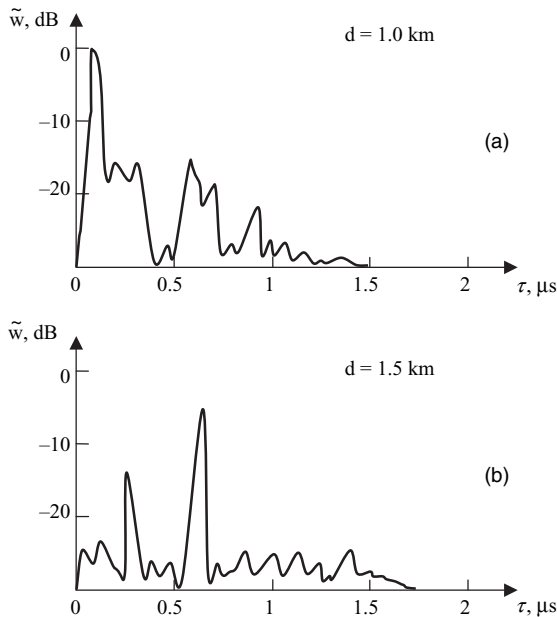
FIGURE 13.5. The results of measurements of time delay distribution for the range between both terminals: (a) $d = 1.0$ km and (b) $d = 1.5$ km.
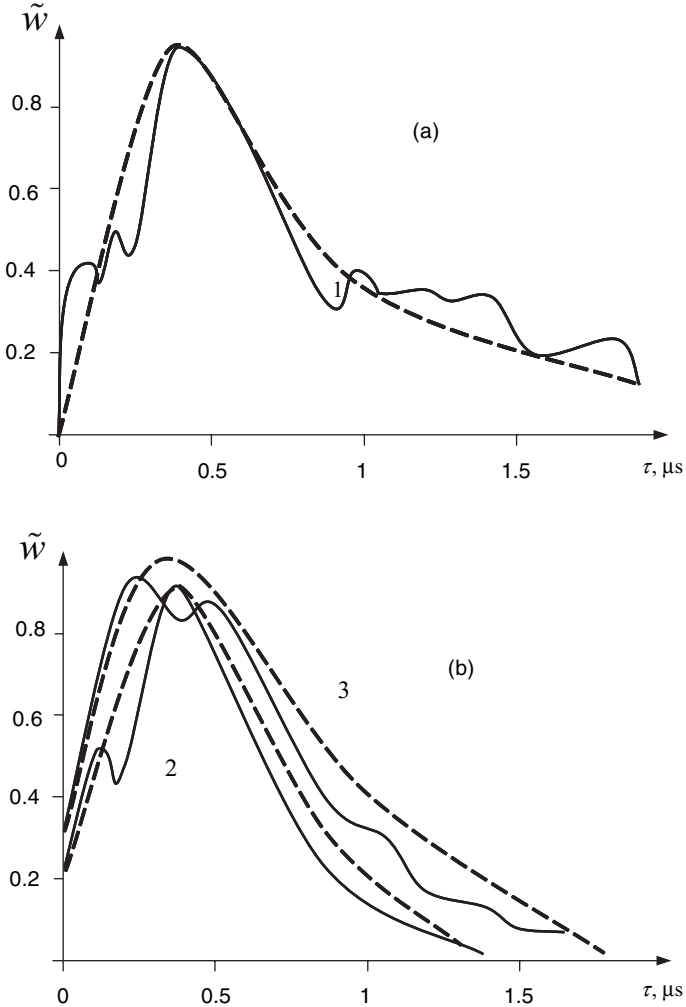
FIGURE 13.6. Comparison between measurements (continuous curves) and theoretical prediction (dashed curves) for time delay distributions for three position of vehicle antenna denoted by 1, 2 and 3, which correspond the antenna height of 2, 5 and 12 m, respectively.

surrounding the moving vehicle are observed. The impulse (wideband) signal power distribution over the time delay is quasi-homogeneous and unified. A different picture is observed for the high BS antenna ($\sim$12 m) with respect to building roofs. In fact, as follows from the results of the normalized power spectrum distribution measurements in the time delay domain (presented in Figures 13.6a,b), for this case the shape of the spectrum has an obvious maximum

that corresponds to the direct pulse arriving from the BS at the moving vehicle receiving antenna. Only a few arriving pulses as multipath components due to multiple reflection and scattering are distributed close to the initial pulse and their power is less than that of the main pulse. Here, three different positions of antennas, denoted by 1, 2, 3 near each curve, are presented. We also present by dashed curves in Figures 13.6a,b the results of calculations according to theoretical results for different situations of the experiment (denoted by 1 in 13.6a and 2, 3 in Fig. 13.6b, respectively).

Again, as seen for the spectrum distribution in the azimuth domain, the theoretical predictions are in agreement with the experimental data.

Signal Distribution in Doppler Domain. To verify the theoretical signal power spectrum distribution in the Doppler shift domain, a special experiment was carried at $f = 920\,\text{MHz}$ using the same experimental site described in References [1,2]. This tested site contains mostly three-five-floor buildings, which are homogeneously distributed around both terminal antennas. The range between mobile antenna and the fixed BS antenna varied from 200 m to 2 km. The transmitter antenna was assembled at the top of the mobile vehicle at the height of 2 m; the receiver antenna was assembled on the roof of the building, the first time at the height of 30 m, and then at the height of 3 m. The mobile vehicle speed varied from 10 km/h to 40 km/h.

In Figure 13.7 the signal power spectrum distribution relative to that for $\varphi_0 = 0°$ is presented for the mobile trajectory orientated to the radio path between antennas upon the angle $\varphi_0 = 60°$ and for mobile speed of 32 km/h, from which we get that $f_d = \frac{v}{\lambda}\cos\varphi_0 \approx 15\,\text{Hz}$ in the case where both antennas are below the rooftop.

Figures 13.7a and 13.7b correspond to opposite directions of the same mobile vehicle along the experimental path. Both the spectra illustrated in Figure 13.7(a) and Figure 13.7(b) are the mirror transformation of each other. This is because of the opposite direction of the movement of the vehicle antenna. The same picture follows from an experiment when the receiver antenna was above the rooftop ($z_2 = 30\,\text{m}$) for opposite directions of movements of the vehicle antenna. It is shown in Figures 13.8(a) and (b).

In this case the mobile vehicle path was oriented upon the angle $\varphi_0 = 65°$ to the radio path between terminals. Again, asymmetry of the spectrum shape corresponds to the direction of the moving vehicle. Moreover, because of the existence of the LOS component of the total signal (BS antenna is higher than the building roof), the sharp component is clearly seen in the signal spectrum at the frequency, which corresponds to source movement in free space $f_{d_0} = \frac{v}{\lambda}\cos\varphi_0 \approx 7\text{Hz}$. In both cases presented in Figures 13.7 and Figure 13.8, the power spectrum is limited by the maximum Doppler frequency, which is around $\pm(15–17)\text{Hz}$.

Comparisons between experimentally obtained signal spectrum distribution in the Doppler spread domain and the Doppler power spectrum distribution
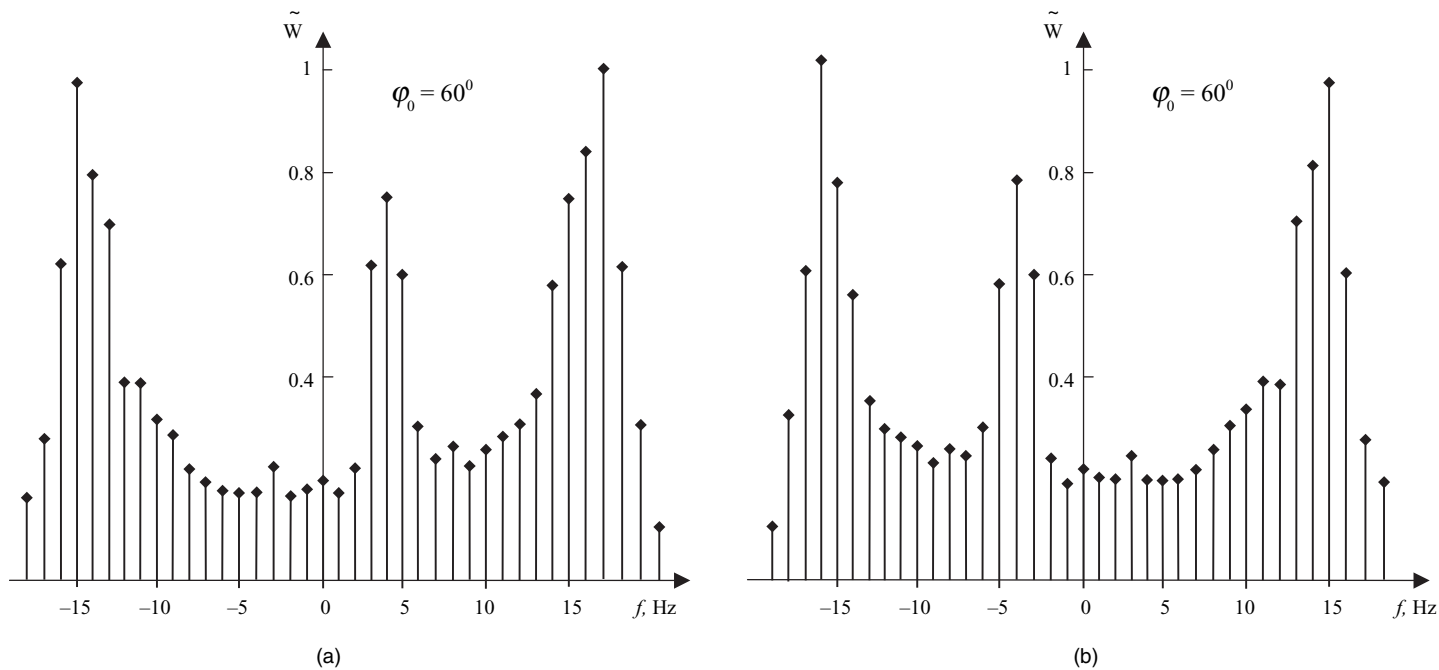
FIGURE 13.7. Power spectrum distribution in the Doppler shift domain obtained experimentally for low-elevated BS and vehicle antennas.
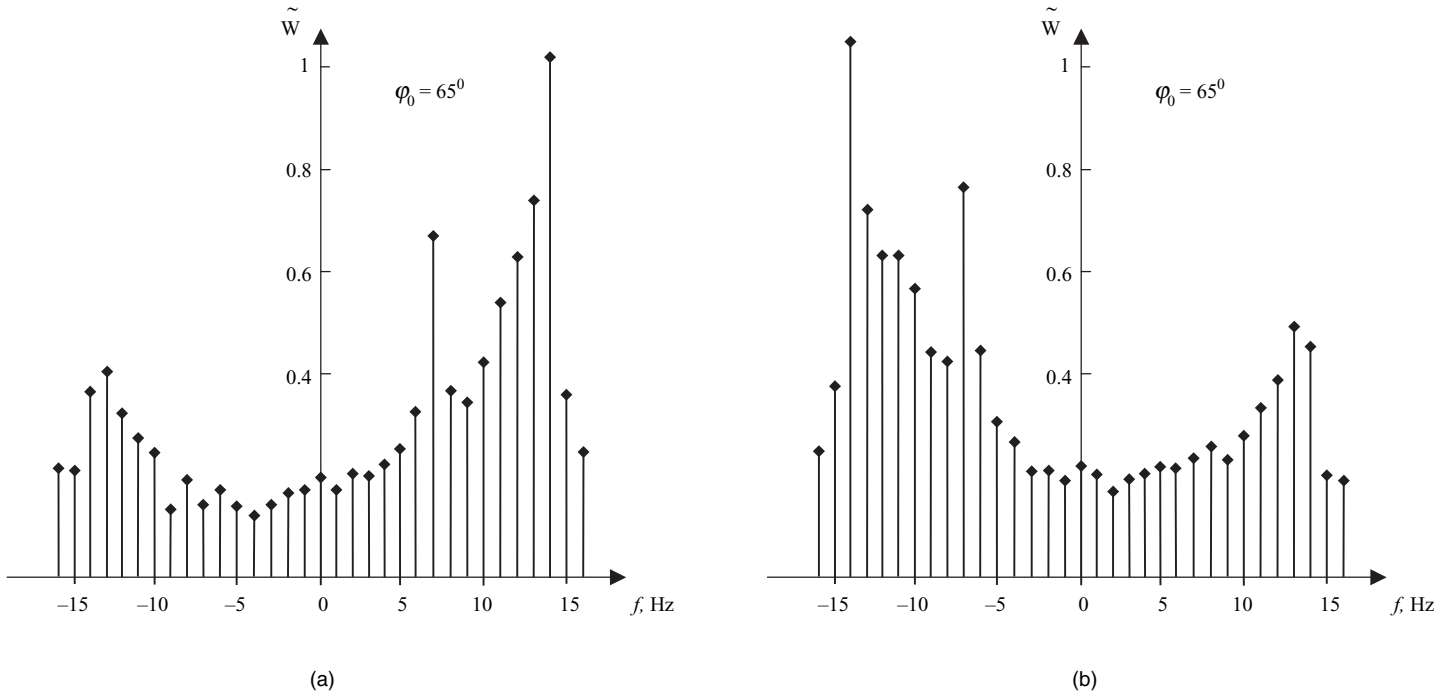
FIGURE 13.8. Power spectrum distribution in the Doppler shift domain obtained experimentally for a high-elevated BS antenna.

obtained from theoretical analysis presented in Chapter 10, allow us to conclude that the data obtained experimentally fully confirm results of theoretical prediction.

Finally, we must conclude that the 3D stochastic model of wave scattering and diffraction from randomly distributed buildings placed on rough terrain leads to a more accurate description of the signal loss effects. This makes the model extremely useful for fixed wireless access applications, where the subscriber antenna deployment can be made on rooftops. At the same time, taking into account effects of shadowing and multipath fading, the algorithm of how to evaluate these effects for concrete situation in the urban scene is described in Chapter 11. We can improve accuracy of the proposed stochastic approach even though some of the subscribers will be located in the shadow zones behind buildings. It means that, for a uniform angle-of-arrival distribution of signal, an additional slow- or long-term fading in link budget due to shadowing can be estimated according to methods described in Reference [1] (see also Chapter 11).

We obtained from the proposed stochastic model a general description of the signal power distributions in the angle-of-arrival (PAS) and time delay (PDS) domains for various BS antenna elevations with the continuous transition to both limiting cases of multipath phenomena. Either the diffraction or the multiple scattering component of the total field is predominant, and the PAS and PDS distributions are closer to the classical Laplacian theory or to the Gaussian theory, respectively. This fact was obtained experimentally and theoretically in References [1–7] and briefly described in Chapter 10. The proposed stochastic model predicts with great accuracy the nonuniform and nonregular distribution of the narrowband (CW) and wideband (pulse) signal power spectra in the azimuth, elevation, time delay, and Doppler shift domains for the cases where the base station and moving vehicle antennas are lower than the rooftops [16–20]. By increasing the base station antenna height compared to the rooftops of the building, the power spectra shape in the angle, time, and frequency domains tend to approach the regular and uniform distribution. Using the unified statistical multiparametric model, we obtain clear relations between the parameters of the built-up terrain, the conditions of propagation, and the multipath signal characteristics, investigated in Chapters 5 and 10. These characteristics of radio channel cannot be obtained from the simple empirical, semiempirical, and the so-called ray tracing models proposed by References [8–10], as well as from those that are ever based on the statistical description of propagation effects [11–15].

13.2. PREDICTION OF ADAPTIVE ANTENNA CHARACTERISTICS BASED ON UNIFIED STOCHASTIC APPROACH

In Section 10.2, we showed results of numerical simulation of the proposed unified stochastic approach [1–3, 16–20] through comparisons with real experiments carried out in downtown Helsinki [13–15]. An agreement between theoretical prediction and measured data for different built-up areas allows us to create a virtual numerical

experiment with the specific antennas assembled at the base station. In our virtual numerical experiment we will use, for example, the experimental site RX1, shown by Figure 10.11, in which we will change the BS antenna directivity κ, azimuth φ, and tilt β and will analyze how the changes to these parameters change the signal power redistribution in such an urban area.

13.2.1. Tilt-Dependence of the Base Station Antenna

In this case we will take into account four different tilts of the RX antenna $\beta = -20°, -10°, 10°, 20°$. Here again, the condition of $\beta > 0$ corresponds to the tilt up and $\beta < 0$ is to the tilt down from the horizon. Figures 13.9a to 13.9b show these variants in the 2D- and 3D-planes, respectively.
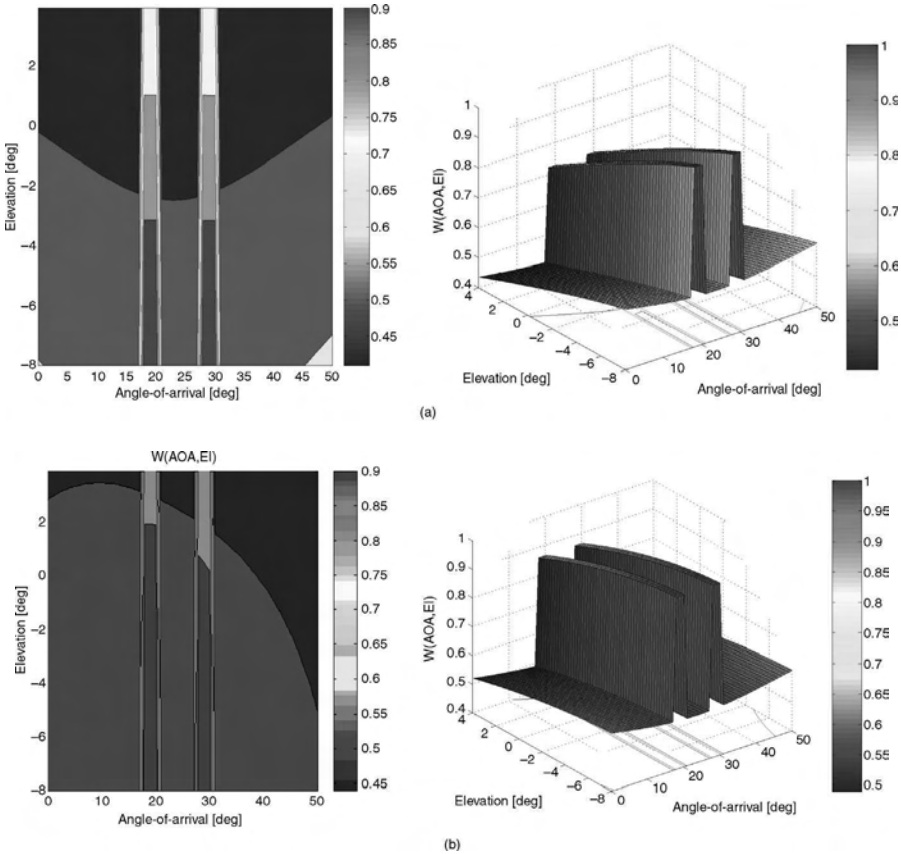
FIGURE 13.9. (a) The relative power, $\widetilde{W}(\theta, \varphi)$, $\beta = -20°$: 2D and 3D plane. (b) The relative power, $\widetilde{W}(\theta, \varphi)$, $\beta = -10°$: 2D and 3D plane. (c) The relative power, $\widetilde{W}(\theta, \varphi)$, $\beta = 10°$: 2D and 3D plane. (d) The relative power, $\widetilde{W}(\theta, \varphi)$, $\beta = 20°$: 2D and 3D plane.

(c)

(d)
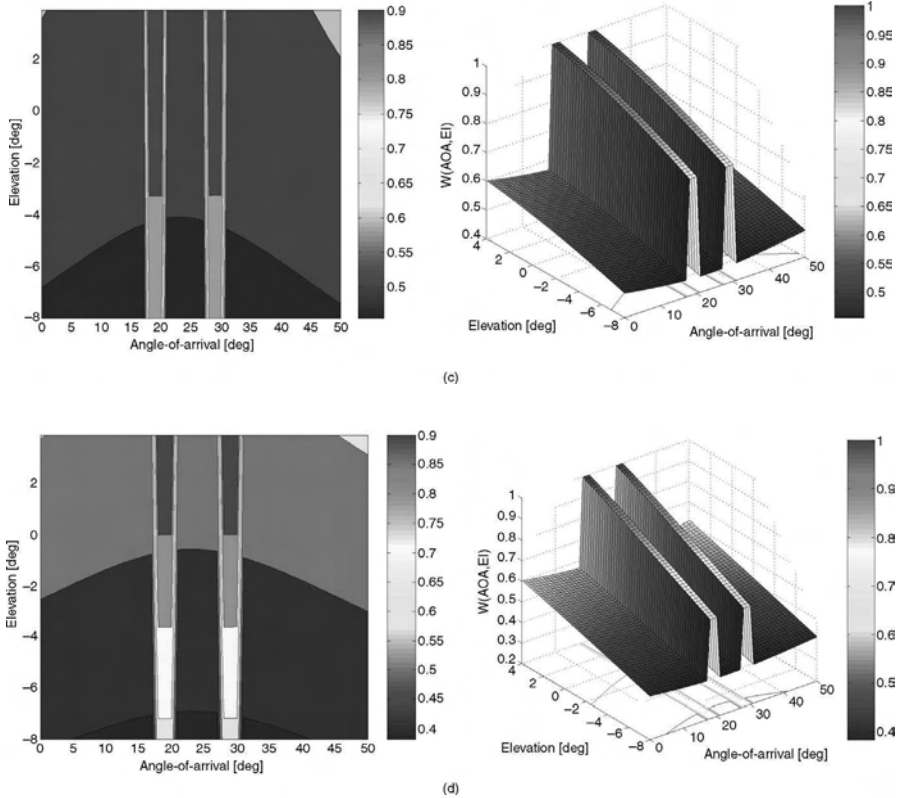
FIGURE 13.9. (*Continued*)

From changes to the antenna tilt from a negative to a positive direction in the vertical (elevation) plane, it is clearly seen that when the tilt is directed up from the horizon ($\beta > 0$), most of the energy arrives from the areas located far from the RX antenna. This is caused by multipath components of the total signal because of the propagation along the two streets. At the same time, when the tilt is directed down from horizon ($\beta < 0$) most of the energy arriving at the receiving (RX) antenna is located in the direction of the receiver (i.e., around the pseudo-LOS direction).

13.2.2. Azimuth-Dependence of the Base Station Antenna Maximum Loop

Now we will turn the array of the antenna to the maximum azimuth direction angle of $\varphi_0 = 5°$ and $50°$ from the north direction. These simulated variants are shown in Figures 13.10a,b by the 2D and 3D radio maps for $\varphi_0 = 5°$ and $\varphi_0 = 50°$, respectively.

(a)

(b)
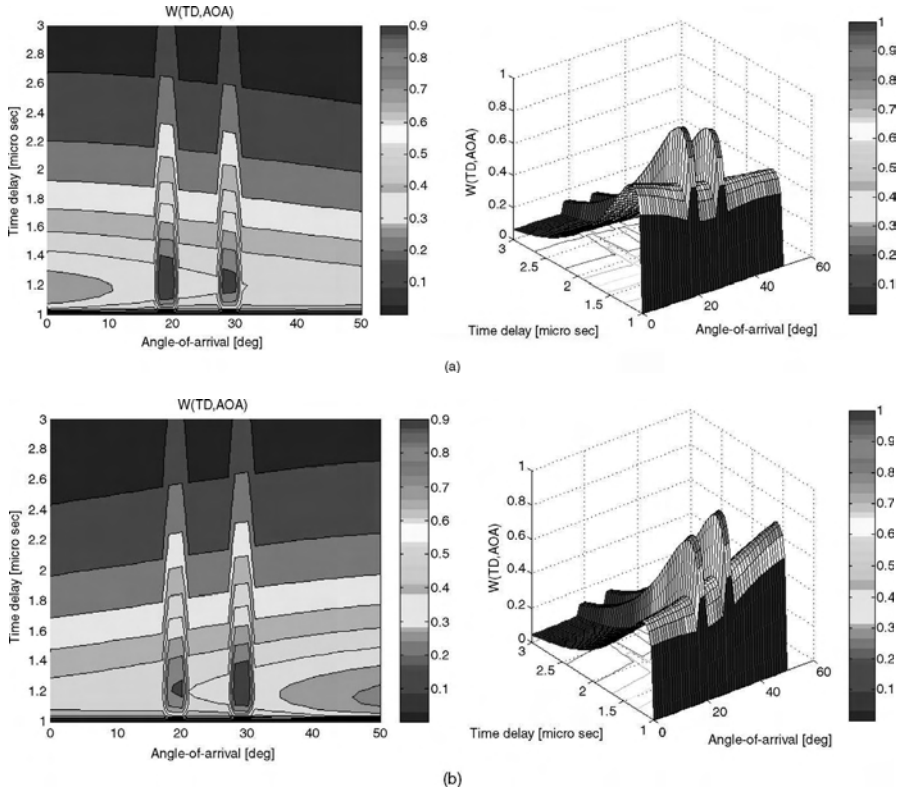
FIGURE 13.10. (a) The normalized power, $\widetilde{W}(\tau, \varphi)$, $\varphi_0 = 5°$: 2D and 3D plane. (b) The normalized power, $\widetilde{W}(\tau, \varphi)$, $\varphi_0 = 50°$: 2D and 3D plane.

Figure 13.10a shows the situation when the RX antenna is turned left from the original direction and most of the energy is received from the azimuth direction of $\varphi_0 = 5°$; more energy comes from street #1 and less energy is arriving from the street #2 (see Fig. 13.11). This result differs from that obtained in the real situation shown by Figures 10.11 and 10.12. In the situation described by Figure 13.10b, the energy, arriving from the azimuth direction of $\varphi_0 = 50°$, is about 0.8–0.9 (compared to W_{max}), that is, at the same order with the rays energy arriving from the street #1. In this situation, as shown by Figure 13.12, a significant part of the total energy comes from directions far from street #1 and street #2. The "side" effect, when the antenna is oriented as shown in Figure 13.12, gives the same strong influence on signal energy azimuth redistribution as in the cases described by Figures 10.11 and 10.12.

13.2.3. Directivity-Dependence of the Base Station Antenna

Now, we will analyze the normalized signal power spectrum $\widetilde{W}(\theta, \varphi)$ for different values of the directivity of the antenna $\kappa = 10, 20, 30$. Figures 13.13a–13.13c show
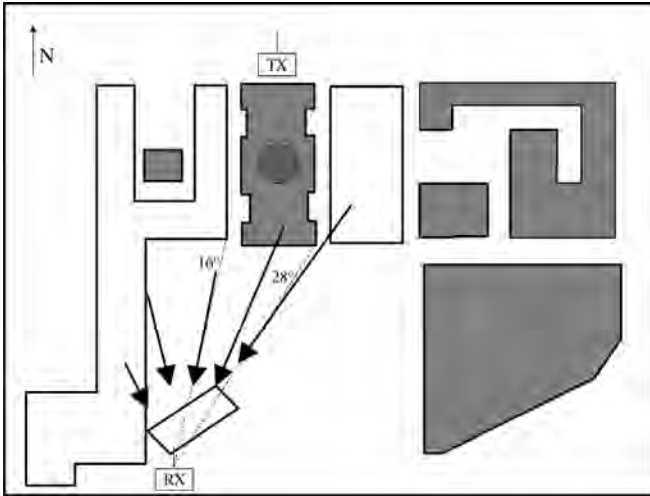
FIGURE 13.11. Detailed map for the situation where the azimuth direction is $\varphi = 5°$.

these cases. From this virtual numerical experiment, we can understand how the increment of directivity of the RX antenna affects the decrease of the arriving power of the multipath components in the total signal power received by the base station antenna. It is clearly seen that with an increase in the directivity of the antenna κ in
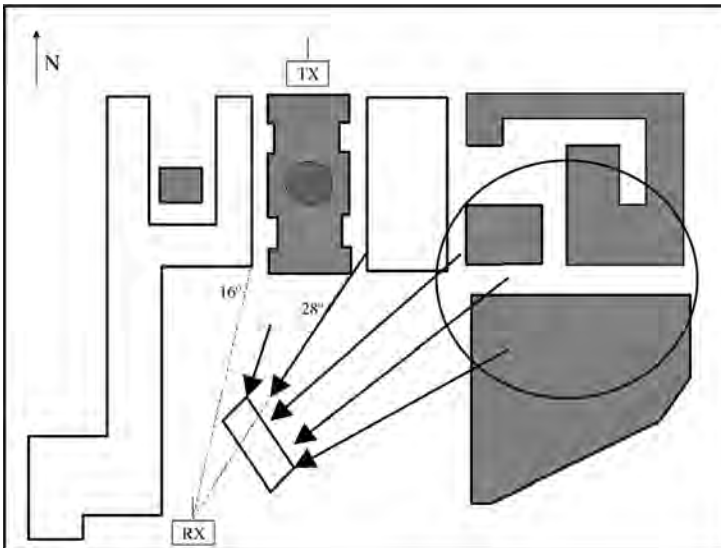
FIGURE 13.12. Detailed map for the situation where the azimuth direction is $\varphi = 50°$.
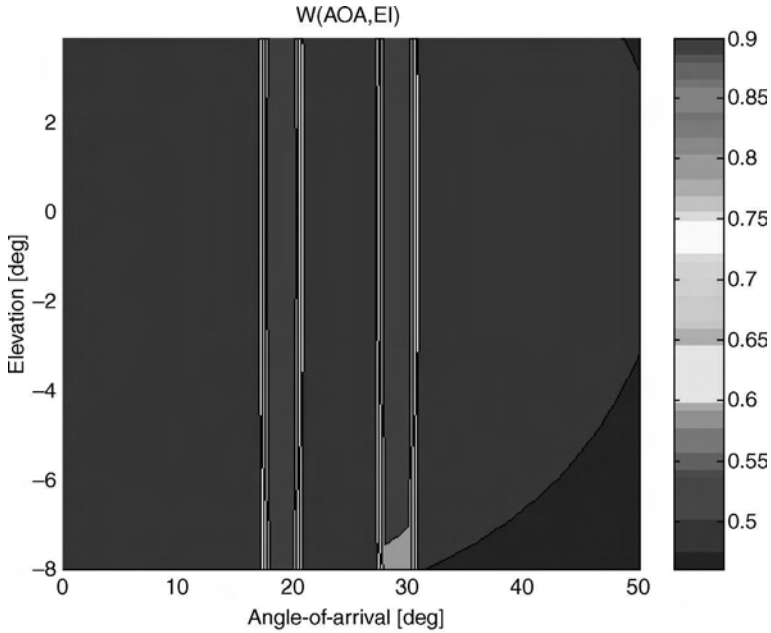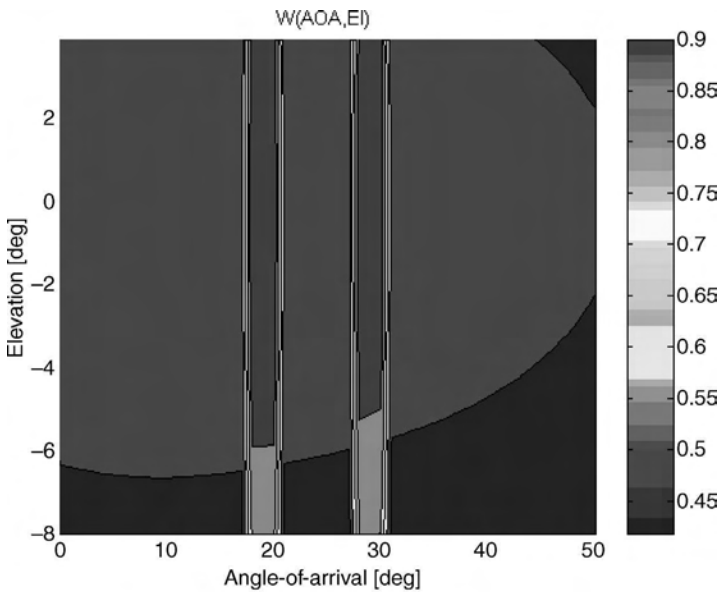
FIGURE 13.13. (a) The normalized signal power, $\widetilde{W}(\theta, \varphi)$, $\kappa = 10$. (b) The same, as in Fig. 13.13a, but for $\kappa = 20$. (c) The same, as in Fig. 13.13a, but for $\kappa = 30$.
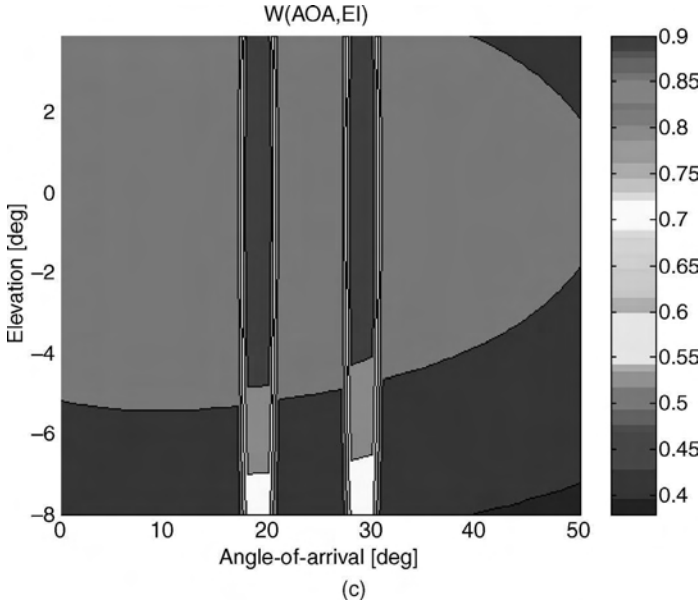
FIGURE 13.13. (*Continued*)

the vertical (elevation) plane, most of the energy arrives at the base station antenna from the direction closest to the zero degree elevation angle, working as a spatial filter to eliminate multipath components arriving from other direction in the EOA plane.

BIBLIOGRAPHY

[1] Blaunstein, N., and J. Bach Andersen, *Multipath Phenomena in Cellular Networks*, Artech House Boston-London, 2002.

[2] Blaunstein, N., and Y. Ben-Shimol, "Spectral properties of signal fading and Doppler spectra distribution in urban mobile communication links," *Wireless Communic. and Mobile Computing*, vol. 5, no. 1, 2006, pp. 113–116.

[3] Ponomarev, G. A., A. N. Kulikov, and E. D. Telpukhovsky, *Propogation of Ultra – Short Waves in Urban Environments*, Tomsk, Rasko, USSR, 1991.

[4] Pedersen, K., P. E. Mogensen, and B. Fleury, "Power azimuth spectrum in outdoor environments," *IEE Electron. Letters*, vol. 33., 1997, pp. 1583–1584.

[5] Pedersen, K. I., B. H. Fleury, and P. E. Mogensen, "High resolution of electromagnetic waves in time-varying radio channels," *IEEE Proc. Personal, Indoor, and Mobile Radio Communic. (PIMRC '97)*, Helsinki, Finland, Sept. 1997, pp. 650–654.

[6] Pedersen, K. I., P. Mogensen, and B. H. Fleury, "Experimental analysis of the joint statistical properties of azimuth spread, delay spread, and shadow fading," *IEEE J. Select. Areas Communic.*, vol. 20, no. 3, 2002 pp. 523–531.

[7] Pedersen, K., P. Mogensen, and B. Fleury, "A stochastic model of the temporal and azimuthal dispersion seen at the base station in outdoor propagation environments," *IEEE Trans. Veh. Technol.*, vol. 49, no. 2, 2000, pp. 437–447.

[8] Ertel, R. B., P. Cardieri, K. W. Sowerby et al. "Overview of spatial channel models for antenna array communications systems," *IEEE Personal Communic.*, vol. 5, no. 1, 1998, pp. 10–22.

[9] Fuhl, J., J. P. Rossi, and E. Bonek, "High resolution 3-D direction-of-arrival determination for urban mobile radio," *IEEE Trans. Antennas Propagat.*, vol. 44, no. 4, 1997, pp. 672–682.

[10] Kuchar, A., J. P. Rossi, and E. Bonek, "Directional macro-cell channel characterization from urban measurements," *IEEE Trans. Antennas Propagat.*, vol. 48, no. 1, 2000, pp. 137–146.

[11] Kalliola, K., H. Laitenen, L. Vaskelainen et al., "Real-time 3-D spatial-temporal dual-polarized measurement of wideband radio channel at mobile station," *IEEE Trans. Instrum. Measurements*, vol. 49, no. 3, 2000, pp. 439–448.

[12] Kalliola, K., and P. Vainikainen, "Characterization system for radio channel of adaptive array antennas," *Proc. Int. Symp. Personal Indoor Mobile Radio Conf. (PIRMC'97)*, Helsinki, Finland, 1997, pp. 95–99.

[13] Laurila, J., K. Kalliola, M. Toeltsch et al., "Wide-band 3-D characterization of mobile radio channels in urban environment," *IEEE Trans. Antennas Propagat.*, vol. 50, no. 2, 2002, pp. 233–243.

[14] Toeltsch, M., J. Laurila, K. Kalliola et al., "Statistical characterization of urban spatial radio channels," *IEEE J. Select. Areas Communic.*, vol. 20, no. 3, 2002, pp. 539–549.

[15] Blaunstein, N., M. Toeltsch, E. Benek et al., "Signal power distribution in the azimuth, elevation and time delay domains in urban environments for various elevations of base station antenna," *IEEE Trans. Antennas and Propagation*, vol. 54, August 2006.

[16] Blaunstein, N., and E. Tsalolihin, "Angle-of-arrival and time delay distribution in urban areas with street guiding structures," *WSEAS Trans. on Circuits.*, vol. 2, 2003, pp. 202–206.

[17] Blaunstein, N., and E. Tsalolihin, "Signal distribution in the azimuth, elevation and time delay domains in urban radio communication links," *IEEE Antennas and Propagat. Magazine*, vol. 46, no. 5, 2004, pp. 101–109.

[18] Blaunstein, N., "Distribution of angle-of-arrival and delay from array of building placed on rough terrain for various elevation of base station antenna," *Journal of Communic. and Networks*, vol. 2, no. 4, 2000, pp. 305–316.

[19] Blaunstein, N., and Y. Ben-Shimol, "Frequency dependence of pathloss characteristics and link budget design for various terrestrial communication links," *IEEE Trans. on Antennas and Propagat.*, vol. 52, no. 10, 2004, pp. 2719–2729.

[20] Blaunstein, N., M. Toeltsch, C. Christodoulou et al., "Azimuth, elevation and time delay distribution in urban wireless communication channels," *Antennas and Propagat. Magazine*, vol. 48, no. 1, 2006, pp. 160–167.

Land–Satellite Communication Links

14.1. OBJECTIVE

The Space Age was started on October 4, 1957, when the first artificial satellite, Sputnik 1, was placed in orbit by the Soviet Union. Before October 1957, the term satellite referred to essentially a small body that revolved around a larger astronomical object. Thus, all the moons circling the planets of the solar system were called *satellites*. Today these bodies are specifically called *natural satellites*, and any artificial object that revolves around a larger astronomical object is called an *artificial satellite*.

The main task of the artificial satellite is to allow stable wireless communication among users located on the Earth using physical device, simply called satellite located in the upper atmosphere, on the basis of mechanism of radio propagation [1,2]. During the last four decades, the satellites have been used for wireless communication, weather study, navigation, military observation, and other purposes. In this book, as was mentioned in the Chapter 1, we deal only with the aspects of radio communication between various terminals, personal, stationary or moving, portable telephone or ground-based facilities, which will secure a satisfactory quality of service for each subscriber located within such a channel (see Fig. 14.1).

More than forty years ago, J. R. Pierce and R. Kompfner (see [1,2]) discussed a number of alternatives, problems, and potential solutions for transoceanic communication by means of satellites, addressing the following subjects:

- alternative satellite repeater schemes; orbits, mutual visibility, and distances;
- number of satellites;
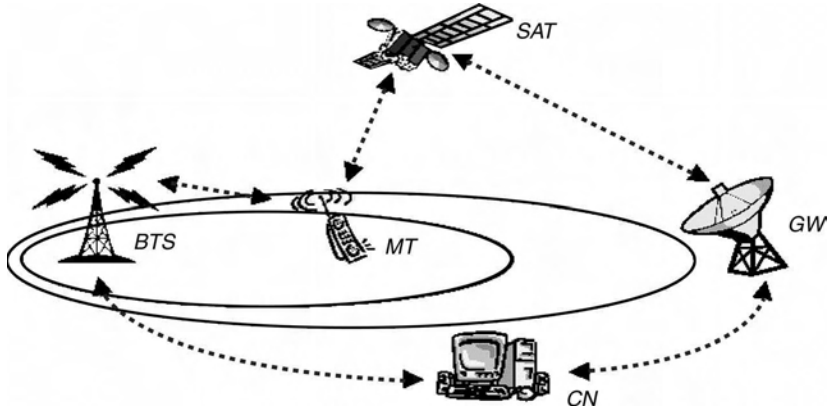
FIGURE 14.1. Satellite–Land service terminals.

- path-loss calculations;
- modulation systems;
- unknowns in satellite communications.

Surprisingly, after 40 years the fundamental ideas have not changed much. Generally, there are differentiations between satellite orbits. They called "far" geosynchronous orbit (GEO) and "near" low earth orbit (LEO); between these two orbits, there is medium altitude earth orbit (MEO). In terms of transponders, or repeaters, Pierce and Kompfner mentioned *active* and *passive*.

Signal propagation in land–satellite communication (LSC) systems for the last several decades has become an essential consideration, especially when high-rate data services are involved [1–19]. Path conditions may yield harmful impairments, severely degrading the system performance and availability. As far as urban or suburban built-up areas are concerned, the extent of the influence is mainly restricted to the roadside obstacles, because the satellite is positioned at relatively high elevation angles in most practical situations. The advantages of satellite communication compared to local land are [1–4]:

(1) large capacity; the total transmission capacity can exceed 1 *Gbit per second*;
(2) distance insensitive cost;
(3) wideband service that allows transmission of high bit rate multimedia information: video, audio, voice, digital, and so on;
(4) broadcast transmission capability that allows distribution of any information from one point to multipoint users located on the Earth.

The GEO is a circular orbit in the equatorial plan. The angular velocity of the satellite is the same as that of the Earth. Therefore, the satellite seems to

TABLE 14.1. A Comparison of the LEO, MEO, and GEO Orbits [3]

	LEO	MEO	GEO
Altitude	700–1,000 km	10,354 km	35,786
Orbital period	100 minutes	6 hours	Stationary
Number of satellite for global coverage	48–66	10–12	3
Space segment cost	Highest	Lowest	Medium
Satellite lifetime (Years)	Imperceptible	Imperceptible	Long
Propagation delay call handover	Frequent	Infrequent	None

remain stationary in the sky. The LEO and MEO orbits are lower altitude orbits. They are particularly suitable for the personal communications systems satellite because of their low path loss, fading effects, and low propagation delays. A comparative analysis of the main parameters of the LEO, MEO, and GEO orbits is shown in Table 14.1 after analysis of several tables presented in [3].

Let us briefly consider advantages and disadvantages of each kind of satellite following Reference [1–4].

(a) *GEO satellites*

Advantages:
1. The satellite appears to be fixed (immovable) when viewed from the Earth, which means no tracking is required for each Earth station antenna;
2. About 40% of the Earth's surface is in view from the satellite.

Disadvantages:
1. High power loss of about 200 dB over the radio path.
2. Large signal delay of 238–284 ms.
3. Polar region of the Earth with latitudes more than 81° are not covered by GEO satellite.

(b) *LEO and MEO satellites*

Advantages:
1. Much smaller path loss compared to GEO satellites.
2. Lower signal delay (about 10 ms).
3. The reduction in range provides a large decrease in path loss resulting in much smaller receiving antennas.
4. The reduction in range provides a significant reduction in propagation delay, making voice conversation more pleasing to the user and increasing most data communication protocols.

TABLE 14.2. Frequency Allocations for Satellite Communications [4]

Band	Uplink (GHz)	Downlink (GHz)
C	6	4
X	8.2	7.5
Ku	14	12
Ka	30	20
S	40	20
Q	44	21
L (mobile)	1.525 to 1.559	1.626 to 1.660

Disadvantages:

(1) Short period of satellite observation both visual and radio.

(2) Doppler effects are significant because of the high speed of the satellite.

(3) Many satellites are required to establish continuous transmission and full radio coverage for subscribers.

The notion of "free space" has long passed for satellite communications. For minimizing satellite-to-satellite interference and sharing the limited frequency spectrum among the ever-increasing number of operational or proposed satellites, regulations become a main part of channel design. The coordination of frequency and orbit is necessary to ensure a noninterfering satellite operation.

In the same manner, as was defined for land communication links (see Chapters 1 and 5), one can define the transmitted path from an Earth's terminal antenna to the satellite as *uplink* and the transmitted path from the satellite to an Earth's station as *downlink*. Table 14.2 presents the "working frequencies" that are commonly used both in uplink and downlink land–satellite communications.

Land–satellite communication (LSC) systems enable users of handle wireless phones, portable computers, or mobile phones to communicate with one another from any two points worldwide. Signal propagation for such systems has become an essential consideration. Path conditions may indeed cause harmful impairments that severely corrupt the system availability and performance. Hence, propagation considerations are very important for successful operation. Most satellites employ fixed not mobile terminals as in LSC systems. Whereas terrestrial land mobile systems are often able to exploit relatively strong multipath, it will be power limited and dependent on the line-of-sight (LOS) component. Such reliability of the mobile systems will largely be determined by propagation-induced fading (see definitions in Chapter 1). Satellite-mobile links operate with low signal margins, and obstructions due to overpasses and vegetation will cause outages and reduce communication quality.

Therefore, to design successful wireless LSC links, stationary or mobile, it is very important to predict all propagation phenomena occurring in such links, to give a satisfactory physical explanation of main parameters of the channel, such as path loss and slow and fast fading, and finally, to develop a link budget compared to total noise at the outputs of the terminals of the channel (called signal noise figures or

maximum acceptable path loss, see Chapters 1 and 5). Moreover, in land satellite communications, we must divide the channel into three parts. The upper channel covers the ionospheric radio propagation, as was shown in Chapter 7, for frequency bands useful for satellite communications (see Table 14.2). Fading phenomena is not so significant if we deal with the regular ionosphere without any fluctuations caused, namely by magnetic storms, disturbances on the Sun, cosmic rays, and so on. Taking into account such effects, for the frequency band (see Table 14.2), as was obtained from computations made in Chapter 7, we can say that the fast fading phenomena effects change the link budget only on several decibels. The same situation is observed in the turbulent troposphere (see Chapter 6), as the middle part of the land–satellite channel, at frequencies in C/Q band (see Table 14.2), taken into account the effects of hydrometeors (rain, snow, smoke etc.). Here, all features together give a cumulative effect in fast fading of about a few decibels in the total path loss (see estimations in tables of Chapter 6). The main effect in link budget and the total path loss come from the bottom part of the land–satellite channel, where effects of the terrain profile, which cause shadowing (or slow fading), become more appropriate. In the land subchannel, *local shadowing effects*, caused by multiple diffraction from numerous wedges and corners of obstructions, become predominant and can significantly corrupt information sent from the ground-based terminal to the satellite and conversely. Furthermore, in the LSC typical land built-up scenarios, the line-of-sight (LOS) path between the satellite and the land terminal (stationary or mobile) can be affected by multipath mechanisms arising from reflection on rough ground surfaces and wall surfaces, multiple scattering from trees and obstacles. As was mentioned by Saunders [2], in such very complicated environments, accounting high speed satellite movements, it is very complicated to differentiate slow fading and fast fading effects, as was done for land communication links (see Chapter 5); they must be accounted for together.

Therefore, below we will try to show the reader how to take into account effects of the terrain built-up profile and multiple diffraction and scattering effects for fading description and for link budget design within the LSC channel. All these elements will allow us to obtain the radio coverage of the areas of service. Finally, we will present a complete algorithm for the mega-cell radio map construction for different areas of the Earth, depending on the propagation situation within each LSC channel, position of each subscriber and elevation of the satellite above the horizon with respect to position and location of the desired subscriber.

In this chapter, we will analyze two main concepts on how to account for the terrain effects on land–satellite communications. The first is based on the *statistical* models, whereas another is based on the *physical-statistical* models. To unify these models and to use them together in our analysis, we assume that the radio signal is moving within a channel only between two states: *good* and *bad*, as is shown in Figure 14.2.

The good state occurs when the LOS component is predominant, whereas the bad state occurs when the LOS component is absent and only the NLOS component is present because of shadowing and/or multipath phenomena. This scheme is called the Markov's chain [5,19]. Then, the statistical models, which we will present here,
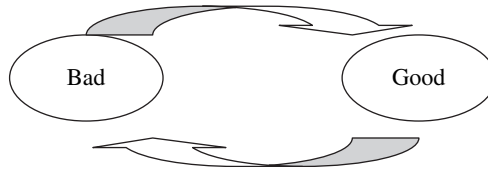
FIGURE 14.2. Markov's chain.

are based on the transfer from bad to good states and vice versa. At the same time, the physical-statistical models are based on the classical aspects of radio propagation over the terrain and on the statistical description of obstructions placed randomly on the rough terrain. As will be shown below, such models can also be adapted to use the Markov's chain, as a basic aspect of pure statistical models. So, despite the fact that some researchers separate statistical and physical-statistical models and show them separately, we will show how to unify these approaches. Both statistical parameters of Markov's stochastic process, statistical distributions of the built-up terrain features and propagation phenomena can be used to predict the radio coverage of the Earth's surface and satellite constellation for the mega-cell maps design.

14.2. TYPE OF SIGNALS IN LAND–SATELLITE COMMUNICATION LINKS

Propagation between a satellite and a mobile receiver can be classified as either *nonshadowed*, when the mobile or stationary subscriber has an unobstructed LOS path to the satellite, or *shadowed*, when the LOS path to the satellite is obstructed by either feature placed at the terrain, natural or man-made.

The nonshadowed signal received at the mobile receiver is composed of three signal components: direct, specular, and diffuse (see Fig. 14.3). Propagation measurements indicate that a significant fraction of the total energy arrives at the receiver by way of a direct path.

The remaining power is received by the specular ground reflected path and the many random scattering paths that form the diffuse signal component.

The shadowed signal occurs when the signal fade is caused primarily by scattering and absorption from both branches and foliage where the attenuation path length is the interval within the first few Fresnel zones intersected by the canopies or building roofs.

Measured results indicate that shadowing is the most dominating factor determining slow signal fading. Its effect depends on the signal path length through the obstruction, type of obstruction, elevation angle, direction of traveler, and carrier frequency. The shadowing is more severe at low elevation angles where the projected shadow of the obstacle is high. The effect of shadowing due to diffraction from buildings can be clearly understood on the basis of the results discussed in
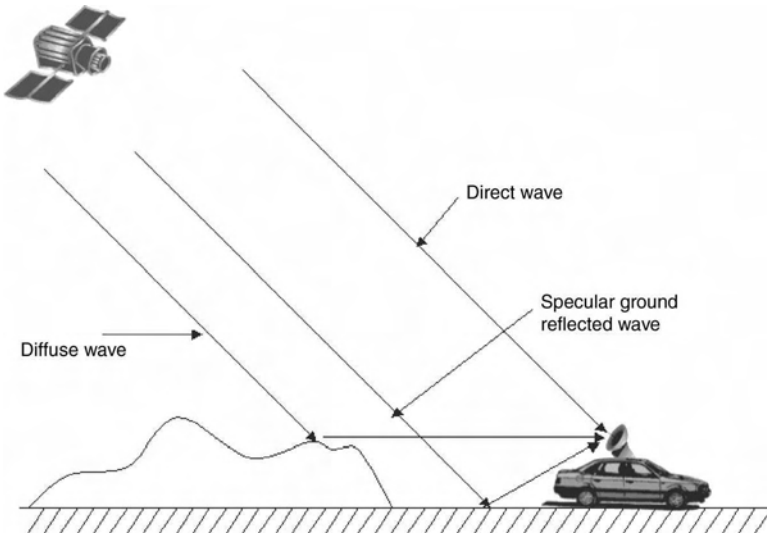
FIGURE 14.3. LOS propagation in land-satellite communications.

Chapter 5. The effect of shadowing induced by vegetation is more complicated and depends on how frequently trees intercept, the path length through the trees, and the density of branches and foliage. Some typical scenarios, in which shadowing occurs due to tree canopies, is depicted in Figure 14.4. At frequencies lower than 1 GHz, trees are virtually transparent to the signal. For higher frequencies, trees are regarded as ideal edge refractors in order to estimate the amount of signal attenuation. The shadowed signal received at the mobile receiver is composed of two components: a shadowed *direct* component and a *diffuse* component.

The shadowed direct component is generated when the LOS signal from the satellite passes through roadside vegetation and is attenuated and scattered by the leaves, branches, and limbs of the vegetation. The attenuation of the direct component depends on the path length through the vegetation. Scattering by the vegetation generates a random forward scattered field that interferes with the direct component causing it to fade and lose its phase coherency. Thus, the shadowed direct
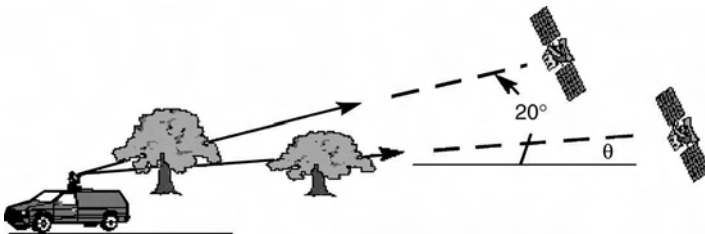
FIGURE 14.4. Shadowing caused by trees are more serious at low satellite elevation angles.

component can be modeled as the sum of an attenuation LOS signal and a random forward scattered field [6]:

$$P_{\text{shadowed}} = \alpha_{\text{att}} P_{\text{direct}} + P_{\text{scattered}} \tag{14.1}$$

Here, α_{att} represents the attenuation factor of the direct component of the signal power, and $P_{\text{scattered}}$ is the scattered signal power from the vegetation. A typical shadowing attenuation from a building, bridge, or trees is on the order of 8–20 dB relative to the signal mean value.

The diffuse component results from various reflections from the surrounding terrain. This component varies randomly in amplitude and phase. Multipath propagation does not cause significant losses for land mobiles.

The shadowed diffuse component from vegetation is identical in form to the diffuse component for nonshadowed propagation. The diffuse component is assumed to be received randomly from all angular directions.

Hence, the total shadowed signal is the sum of the shadowed direct component and the diffuse component [6]:

$$P_{\text{shadowed}} = \alpha_{\text{att}} P_{\text{direct}} + P_{\text{scattered}} + P_{\text{diffuse}} \tag{14.2}$$

We can use this formula to calculate the total path loss within the LSC link. For this purpose we need to use the corresponding models, pure statistical or physical-statistical, based on some special experiments and numerous measurements.

14.3. STATISTICAL MODELS

Models of these types correspond to the cases for which multipath fading alone or with line-of-sight are simultaneously presented.

14.3.1. Loo's Model

Loo's model [7,9] is a statistical model for a land mobile-satellite link with applications to rural environments. The model assumes that the amplitude of the LOS component under foliage attenuation is distributed according to lognormal PDF and the received multipath component is described by a Rayleigh PDF. The model is statistically described in terms of its PDF or CDF functions, which were obtained under the hypothesis that foliage not only attenuates but also scatters radio waves. In such assumptions, the total complex fading signal is the sum of a lognormally distributed random signal and a Rayleigh signal [7,9]:

$$r \exp(j\theta) = z \cdot \exp(j\phi_0) + w \cdot \exp(j\phi), \qquad z, w > 0 \tag{14.3}$$

where the phase ϕ_0 and ϕ are uniformly distributed between 0 and 2π, z is lognormal distributed amplitude, and w is a Rayleigh distributed amplitude. If z is

TABLE 14.3. Statistical Model Parameters

Conditions	Standard deviation	Mean	Multipath power
Infrequent: Light shadowing	0.5	0.5	−8
Frequent: Heavy shadowing	3.5	−14	−12
Overall results	1.0	−3	−6

temporally kept constant, it can be assumed that PDF $p(z)$ is lognormal. Signal random envelope r is lognormal distributed for large values and Rayleigh distributed for small values [7,9]:

$$p(r) \approx \begin{cases} \dfrac{1}{r\sqrt{2\pi d_0}} \exp\left[-\dfrac{(\ln r - \mu)^2}{2d_0}\right] & \text{for } r \gg \sqrt{b_0} \\[3mm] \dfrac{r}{b_0} \exp\left[-\dfrac{r^2}{2b_0}\right] & \text{for } r \ll \sqrt{b_0} \end{cases} \qquad (14.4)$$

In this equation $\sqrt{b_0}$ and μ are the standard deviation and mean, respectively. The parameter b_0 represents the average scattered power caused by multipath effects.

Many calculations with different values for b_0, d_0, and μ were carried out by Loo with the objective of fitting results from the model to those derived from measurements made on simulated satellite paths. The measurement site was a rural area with about 35% tree coverage. The model parameters were obtained by trial and error to fit measured values. The parameters in decibels [dB] are shown in Table 14.3.

As results of computations, according to Loo's model, the signal envelope was compared to measurements obtained in References [7,9] and presented in Figure 14.5.

As was mentioned in Chapter 1, the signal envelope PDF of the model facilitates the calculation of fade margins in the design of communication systems. As for the signal envelope phase distribution, Figure 14.6 shows a comparison of the complementary cumulative distribution function (CCDF) for the received signal phase calculated using the well-known equation (see Chapter 1):

$$\text{CCDF}(r) \equiv p(r > R) = 1 - \text{CCD}(r) = 1 - \int_0^R p(r)dr \qquad (14.5)$$

where R is either the maximum accepted path loss or the noise floor figure of the system. We must note that for the case of infrequent light shadowing, the model shows the best fit around the median region and some deviation near the tails of the distribution (see Fig. 14.5). The results of the model showed a slightly higher shadowing effect than those from measured data. For the combined results (see both Figs. 14.5 and 14.6), the fit was poor about the median but reasonably good in the
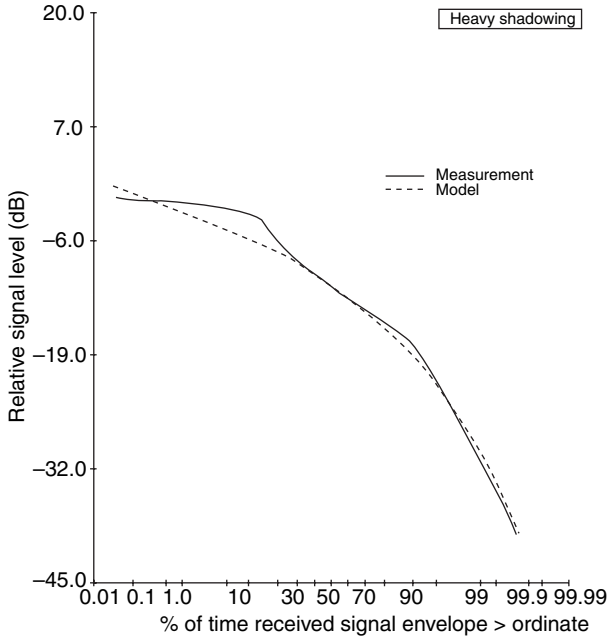
FIGURE 14.5. Loo's envelope model and measurement for heavy shadowing at $f = 18.925\,\text{GHz}$.
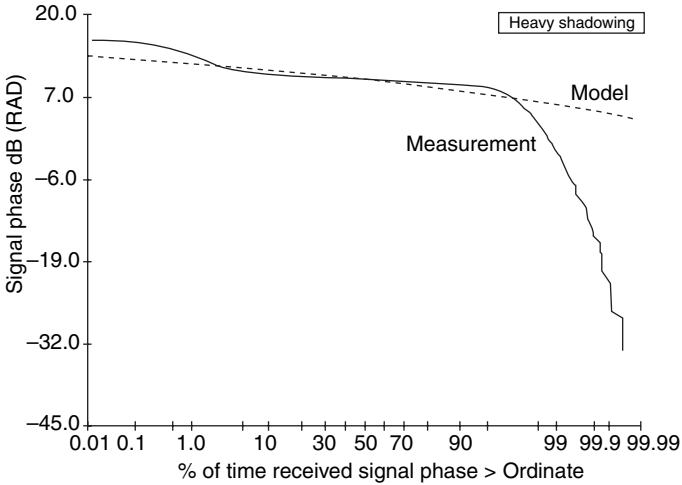
FIGURE 14.6. Loo's phase model and measurement for heavy shadowing at $f = 18.925\,\text{GHz}$.

weak signal range, which is most important for fade margin calculations. The model parameters were obtained by trial and error to fit the measured values.

The results indicate that the model shows a correlation between the rate of change of the envelope due to multipath and foliage attenuation both for heavy shadowing and for light shadowing. The disadvantage of this model is that the measurements were made up to 30°, model parameters for higher elevation angles are not available.

14.3.2. Extended Suzuki Model

In literature, the product of a Rayleigh process combined with a lognormal process is defined as the Suzuki process [10]. It is well known that such a process is a suitable and widely accepted statistical model for the random variations of the envelope of the received signal of frequency nonselective macrocell land mobile terrestrial channel.

The Suzuki process is an adequate statistical model [10], which is usually used in land mobile communication channels, where often it is assumed that a direct line-of-sight component is absent. For mobile-satellite communication channels, where for most of the time a direct line-of-sight component is present, an extension of the Suzuki process was proposed as combination of Rician and lognormal processes. The extended Suzuki process $\eta(t)$ will be introduced here as a product process of the Rician process $\xi(t)$ (see definitions in Chapter 1) with cross-correlated components and the lognormal process $\zeta(t)$, that is,

$$\eta(t) = \xi(t) \cdot \zeta(t) \tag{14.6}$$

Then the PDF of the extended Suzuki process, $\eta(t)$, $p_\eta(z)$, is [10]

$$p_\eta(z) = \int_{-\infty}^{\infty} \frac{1}{|y|} p_{\xi\zeta}\left(\frac{z}{y}, y\right) dy \tag{14.7}$$

where $p_{\xi\zeta}(x, y)$ denotes the joint PDF of the processes $\xi(t)$ and $\zeta(t)$ at the same time t, y is the variable of integration, and $x = z/y$. The Rician process, x, and the lognormal process, y, are statistically independent, that is,

$$p_{\xi\zeta}(x, y) = p_\xi(x) \cdot p_\zeta(y) \tag{14.8}$$

Thus, (14.7) can be written using the PDF of the Rician process and the PDF of the lognormal process:

$$p_\eta(z) = \frac{z}{\sqrt{2\pi}\psi_0\sigma} \int_0^{\infty} \frac{1}{y^3} e^{-\{[(z/y)^2+p^2]/(2\psi_0)\}} I_0\left(\frac{zp}{y\psi_0}\right) e^{-[(\ln y-m)^2/(2\sigma^2)]} dy, \qquad z \geq 0$$

$$\tag{14.9}$$

Here, ψ_0 is a mean of the Rician random variable x, p is a LOS component, m and σ are the mean and standard deviation of random variable y.

To test the accuracy of this model, a special experiment was carried out where the transmitter with a radiated frequency of 870 MHz was assembled on a helicopter at a fixed elevation angle of 15° with respect to the receiver. As the test route, a rural area was chosen with about 35% tree coverage, and the rest was cleared land. A test was performed for two different situations. In one, the test route was lightly shadowed and in the other it was heavily shadowed by a dense tree cover.

It was shown that, using the extended Suzuki model, the cumulative distribution function $\widetilde{P}_\eta(x/y)$ is in agreement with the measurements [10]. For both situations, light and heavy shadowing, the simulation results of the cumulative distribution function $\widetilde{P}_\eta(x/y)$ of the simulation system are in an extremely good agreement with the analytical results. As was mentioned in Reference [10], an extended Suzuki process is proposed for modeling frequency of nonselective fading mobile-satellite radio channels. Such an extended Suzuki process is a product of a Rician process and a lognormal process, where the in-phase and quadrature components describing the Rician process are mutually correlated. In addition, the model can also take into consideration a Doppler shift of the direct line-of-sight component.

14.3.3. Corazza–Vatalaro Model

This model may be considered as an extension of the Loo's model for the case, where the direct and the multipath (diffuse) components of the shadowed signal are lognormally distributed [11]. In particular, the model is applied to nongeostationary satellite channels, such as low-Earth orbit (LEO) and medium-Earth orbit (MEO) channels, in which for a given user located in a generic site the elevation angle changes continuously.

Again, it combines a Rician and lognormal statistics, with shadowing affecting both direct and diffuse components. Therefore, it is suitable for all types of environment (rural, suburban, urban) simply by tuning the model parameters. The PDF of the received signal envelope, r, can be presented as [11]:

$$p_r(r) = \int_0^\infty p(r\,|\,S)p_S(s)\mathrm{d}s \qquad (14.10)$$

where $p(r\,|\,S)$ is a Rician PDF conditioned on shadowing, S. It can be rewritten as [11]:

$$p(r\,|\,S) = 2(K+1)\frac{r}{S^2}\exp\left[-(K+1)\frac{r^2}{S^2} - K\right] \cdot I_0\left(2\frac{r}{S}\sqrt{K(K+1)}\right), \quad r \geq 0$$

$$(14.11)$$

where $I_0(*)$ is the zero order modified Bessel function and K is the Rician factor defined earlier in Chapter 1. The shadowing amplitude, S, is lognormal with PDF:

$$p_S(S) = \frac{1}{\sqrt{2\pi}h\sigma S}\exp\left\{-\frac{1}{2}\left(\frac{\ln S - \mu}{h\sigma}\right)^2\right\} \qquad (S \geq 0) \tag{14.12}$$

where $h = (\ln 10)/20$ is the mean, μ and $(h\sigma)^2$ is the variance of the associated normal variance.

When $K = 0$ (14.10)–(14.12) provide the Suzuki PDF. In the limit of $\sigma \to 0$, $p_S(S)$ tends to a Dirac pulse located at the mean value of the distribution. Therefore $p_r(r)$ finally limits to $p(r \,|\, e^\mu)$, and the channel is Rician.

The signal envelope, which is described by the channel model defined by (14.10)–(14.12), can be interpreted as the product of two independent processes $r = RS$, where R is a Rician process, and S is a lognormal process. Due to the independence between R and S, we have:

$$p_r(r) = \int\limits_0^\infty \frac{1}{S}p_S\left(\frac{r}{S}\right)p_S(S)\mathrm{d}s = \int\limits_0^\infty \frac{1}{R}p_S\left(\frac{r}{S}\right)p_R(R)\mathrm{d}R \tag{14.13}$$

The CDF of the signal envelope is [11]

$$P_r(r_0) \equiv P\{r < r_0\} = \int\limits_0^{r_o}\int\limits_0^\infty \frac{p_S(S)}{S}p_R\left(\frac{r}{S}\right)\mathrm{d}S\,\mathrm{d}r = 1 - E_S\left\{Q\left(\sqrt{2K}, \frac{r_0}{S}\sqrt{2(K+1)}\right)\right\} \tag{14.14}$$

The fitting of the data was conditioned on the following intuitive indications: the greater is α, the larger is K, and the smaller is σ. The resulting empirical formulas allow interpolation for any α at the range with a satellite angle elevation $20° < \alpha < 80°$:

$$\begin{align} K(\alpha) &= K_0 + K_1\alpha + K_2\alpha^2 \\ \mu(\alpha) &= \mu_0 + \mu_1\alpha + \mu_2\alpha^2 + \mu_3\alpha^3 \\ \sigma(\alpha) &= \sigma_0 + \sigma_1\alpha \end{align} \tag{14.15}$$

This model allows us to estimate the information data stream error sent over such LSC channels. Thus, the symbol error probability for transmission changing affected by frequency nonselective fading is [11]

$$P_e = \int\limits_0^\infty P(e\,|\,r)p_r(r)\mathrm{d}r \tag{14.16}$$

where $P(e \mid r)$ is the symbol error probability conditioned on a certain value of r, and $p_r(r)$ is given by (14.13). The average error probability in the presence of Rician fading is now represented by

$$E_R\{P(e \mid RS)\} = \int\limits_0^\infty P(e \mid RS)p_R(R)\mathrm{d}R = f(S) \qquad (14.17)$$

Then, the total probability of the error is

$$P_e = E_s\{f(S)\} = E_S\{E_R[P(e \mid r)]\} \qquad (14.18a)$$

In the case of nongeostationary orbit systems, the probability P_e must be additionally averaged with respect to the angle PDF:

$$\overline{P_e} = E_\alpha\{P_e\} \qquad (14.18b)$$

The advantage of this model is that it is suitable for different propagation environments and a wide range of elevation angles. Therefore, the model is proposed for the statistical characterization of LEO and MEO satellite communications. The model allows for predictions of communication performance under different access.

14.3.4. The Xie-Fang Model

This is a general statistical model for mobile communication systems based on the propagation scattering theory [12]. With the first launches of the "Iridium" spacecraft in 1997 and 1998, a significant new architecture was introduced into the field of satellite communications (see next Section). These systems were based upon the use of LEO and MEO systems. The experimental test of this approach for Ka-band propagation using special measurements was presented in Reference [13], where only some empirical data have been formulated without entering into model discussions.

The use of the small antennas as well as the motion of the transmitter and the receiver introduces the possibility of multipath and path blockage into the link budget of these satellite systems. Because of the movement of receivers or transmitters, the received signals may fluctuate very rapidly from time to time. This fluctuation results from the combining effects of random multipath signals and obstruction of the line-of-sight path, which induces various fading phenomena. We must quantitatively know the propagation characteristics such as

(1) Signal fading due to reflection; shadowing from trees, buildings, utility poles, and terrain
(2) Doppler effects due to movement of mobile terminals, satellites, or the communication effects
(3) Other effects such as the rainfall and hydrometeors in the troposphere (Chapter 6).

The lognormal distribution is the optimum model for the long-term fading, whereas the Rician distribution is only good for some fading environments. This general statistical model for mobile-satellite communication systems is based on the propagation scattering theory, which describes the received signal as product of two independent processes: large- and small-scale fading. In this model the lognormal distribution is used to describe the large-scale fading. As for the small-scale fading, the model uses a more general distribution than Rician distribution.

The model concentrates on the evaluation of small-scale fading phenomena. In many mobile communication systems, as was mentioned in Chapter 1, the small-scale fading is caused by multiple reflections from different paths. In particular, when the elevation angle is low for land mobile-satellite communications systems, many land obstructions cross the radio path. Any transmitted signals will experience signal fluctuations. In general, the fluctuations are caused by the combination of multipath received signals that have different amplitudes and phases. In Reference [12], the received electrical field was presented as the sum of such multipath signals

$$E = re^{j\psi} = \sum_{i=1}^{n} A_i e^{j\phi_i} \tag{14.19}$$

where n is the number of multipath signals, A_i is the amplitude, and ϕ_i is the phase of the ith-path component. In many situations, a different path signal will experience different attenuation and different phase shift. The asymmetrical Doppler spectrum observation showed the correlated characteristics of A_i and ϕ_i.

$$\text{Re}(E) = x = r\cos(\psi) = \sum_{i=1}^{n} A_i \cos(\phi_i)$$

$$\text{Im}(E) = y = r\sin(\psi) = \sum_{i=1}^{n} A_i \sin(\phi_i) \tag{14.20}$$

from which follows:

$$\alpha = \langle x \rangle = \sum_{i=1}^{n} \int_{-\infty}^{\infty} \int_{0}^{\infty} w_i(A, \phi) A \cos(\phi) dA \, d\phi$$

$$\beta = \langle y \rangle = \sum_{i=1}^{n} \int_{-\infty}^{\infty} \int_{0}^{\infty} w_i(A, \phi) A \sin(\phi) dA \, d\phi$$

$$S_1 = D\{x\} = \langle x^2 \rangle - \alpha^2 = \sum_{i=1}^{n} \int_{-\infty}^{\infty} \int_{0}^{\infty} w_i(A, \phi) A^2 \cos^2(\phi) dA \, d\phi - \alpha^2 \tag{14.21}$$

$$S_2 = D\{y\} = \langle y^2 \rangle - \beta^2 = \sum_{i=1}^{n} \int_{-\infty}^{\infty} \int_{0}^{\infty} w_i(A, \phi) A^2 \sin^2(\phi) dA \, d\phi - \beta^2$$

where brackets denote the expectation, $w_i(A, \phi)$ is the fade factor for each ith-path component, and $D\{\bullet\}$ denotes the variance. The received signal envelope is given by

$$r = \sqrt{x^2 + y^2} \tag{14.22}$$

It is well known [20] that for infinite n the signal components, x and y, are distributed according to Gaussian law with means α and β and with variances S_1 and S_2, respectively. Thus, the PDF of signal envelope r will equal

$$p_r(r) = \frac{r}{\sqrt{S_1 S_2}} \exp\left[-\frac{S_1 r^2 + S_2 \alpha^2 + S_1 \beta^2}{2 S_1 S_2} \right]$$

$$\times \frac{1}{2\pi} \int\limits_0^{2\pi} \exp\left(\frac{2 S_2 \alpha r \cos\theta + 2 S_1 \beta r \sin\theta + (S_1 - S_2) r^2 \cos^2\theta}{2 S_1 S_2} \right) d\theta \tag{14.23}$$

The conclusion is that the received signal from a satellite can be treated as a product of two independent processes:

$$R(t) = L(t) \cdot S(t) \tag{14.24}$$

where $R(t)$ is the received signal, $L(t)$ is the large-scale fading that characterizes the signal attenuation over large transmitter–receiver separation distance, and $S(t)$ is the small-scale fading that characterizes the rapid fluctuations of the received signal over short time duration. Large-scale fading is lognormal distributed with PDF:

$$p_l(l) = \frac{1}{\sqrt{2\pi}\sigma l} \exp\left[-\frac{1}{2} \left(\frac{\ln l - \mu}{\sigma} \right)^2 \right] \tag{14.25}$$

where μ and σ^2 are the mean and variance of the associated Gaussian variable. The general PDF of a received signal envelope in the mobile-satellite communication systems:

$$p(r) = \int\limits_0^\infty \frac{1}{l} p_r\left(\frac{r}{l} \right) p_l(l) dl \tag{14.26}$$

In the same manner we can derive the probability density function of received signal power ($w = r^2$). Here, the small-scale PDF for the received signal power is $p_p(w)$ and large-scale fading is lognormal distributed with PDF $p_{l_0}(l_0)$. The PDF of the

received power $p(w)$ [12] is

$$p_p(w) = \frac{1}{2\sqrt{S_1 S_2}} \exp\left(-\frac{S_2 w + S_2 \alpha^2 + S_1 \beta^2}{2 S_1 S_2}\right)$$

$$\times \frac{1}{2\pi} \int_0^{2\pi} \exp\left(\frac{2 S_2 \alpha \sqrt{w} \cos\theta + 2 S_1 \beta \sqrt{w} \sin\theta + (S_1 - S_2) w \cos^2\theta}{2 S_1 S_2}\right) d\theta$$

$$(14.27)$$

So, we finally get

$$p_{l_0}(l_0) = \frac{1}{\sqrt{2\pi}\sigma l_0} \exp\left[-\frac{1}{2}\left(\frac{\ln l_0 - \mu}{\sigma}\right)^2\right]$$

and $$(14.28)$$

$$p(w) = \int_0^\infty \frac{1}{l_0} p_p\left(\frac{w}{l_0}\right) p_{l_0}(l_0) dl_0$$

The proposed model is more general because it contains all one-state statistical model modes described above: Rician and Rayleigh, Suzuki, Corazza–Vatalaro, and lognormal distributions.

14.3.5. Three-State Propagation Channel

This model focuses on the analysis of availability improvement by means of satellite diversity in land mobile satellite system (LMSS) with a LEO or MEO constellation. The model first presents an LMSS propagation model suitable for assessing the diversity effect in various propagation environments [15,19]. The classification of general fading conditions by use of three states was done for LMSS:

(State A) the line-of-sight (LOS),
(State B) slightly blocked by trees or small obstructions, and
(State C) fully shadowed by obstructions.

By taking into account the occurrence probability of each state, a new fading channel model was developed. The validity of the model was identified by comparing its predicted values in terms of the CDF with measured data obtained in experiments using an "Inmarsat" satellite at 1.5 GHz (see the next Section) and other available data. Then, on the basis of this model, the satellite diversity effect was computed while assuming that the area is illuminated simultaneously by at least two satellites moving in LEO over urban and suburban environments. In addition,
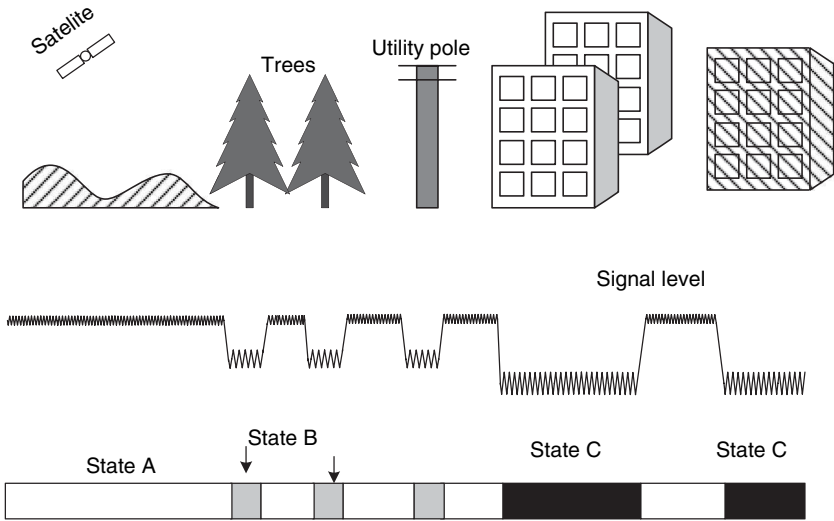
FIGURE 14.7. An LMSS propagation environment and classification of propagation states [19].

state transition characteristics based on a Markov model were obtained by this approach.

States *A*, *B*, and *C* represent the LOS condition, *slight shadowing* by trees and/or small obstacles such as utility poles, and *full shadowing* by large obstacles such as buildings as is shown in Figure 14.7 prepared according to Reference [19].

A fading channel model is discussed in Reference [19] for the quantitative assessment of signal degradation due to shadowing and multipath propagation in various fading environments. On the basis of previously developed channel models and taking the three states into account, we will present an improved channel model. Each state consists of various propagation elements. In Figure 14.8(a), notation *a*1 represents a case of the direct wave component, without shadowing, *a*2 denotes the slight shadowing, and *a*3 denotes perfect shadowing. Similarly, *b* represents the multipath wave component caused by the ground (*b*1) and scattered waves from land obstructions (*b*2). Notice that both kinds of waves, *b*1 and *b*2, contain a coherently reflected component and an incoherently scattered component, which were defined in Chapter 5.

Now, we consider statistical signal level characteristics in terms of the PDF. A few useful PDF models have been developed for LMSS. State *A* can be expressed by the Nakagami–Rician fading model (also called the Rician model). As for Loo's model, it presents the PDF of the direct wave component following a lognormal distribution and PDF of the reflected wave component following the Rayleigh distribution. Loo's model can be a good representation of State *B*. Moreover, we can assign a Rayleigh fading model for the PDF of State *C*. As the model we present is characterized by a three states, it can be expected to have a more flexible expression
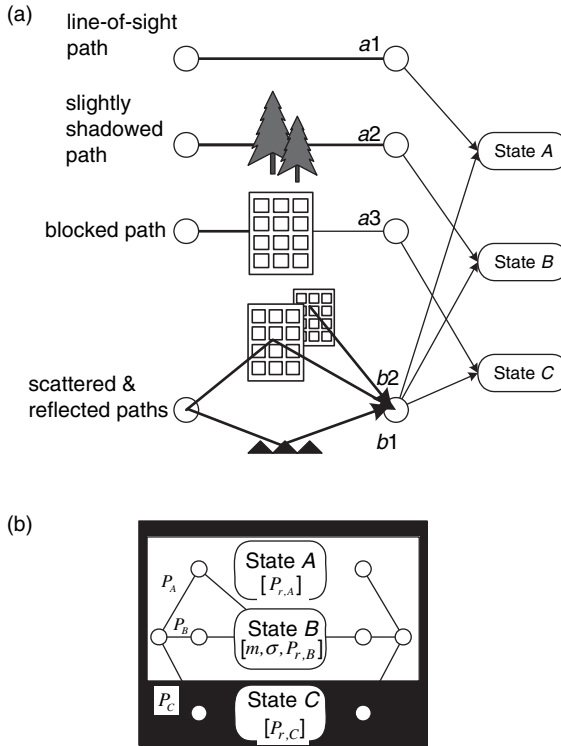
FIGURE 14.8. A three-state propagation channel model according to [19]: (a) Propagation impairment factor. (b) Statistical channel model. (Reprinted with permission © 1997 IEEE)

for LMSS propagation environments composed to States *A*, *B*, and *C*. So, the resultant channel model proposed in Reference [19] can be written as shown in Figure 14.8(b) with the state occurrence probability functions, p_A, p_B, p_C, where $p_A + p_B + p_C = 1$. The calculations of *A*, *B*, and *C* are following:

$$p_A = 1 - (90 - \theta)^2/a, \tag{14.29a}$$

$$p_C = \begin{cases} p_C/4, & \text{for urban areas} \\ 4p_C, & \text{for suburban areas} \end{cases} \tag{14.29b}$$

where θ is the elevation angle of the satellite, $10° \leq \theta \leq 90°$, and

$$a = \begin{cases} 7.0 \times 10^3, & \text{for urban areas} \\ 1.66 \times 10^4, & \text{for suburban areas} \end{cases} \tag{14.30}$$

In order to understand the state duration statistics, such as the mean duration of State *A* during which high quality communication is maintained, a model capable of
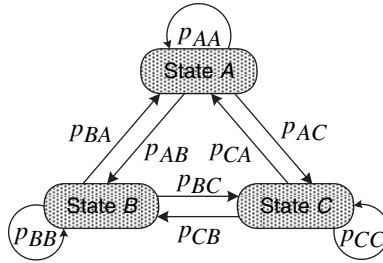
FIGURE 14.9. The three-state Markov model.

expressing time-variant characteristics is necessary. A Markov model is useful for this purpose. Since the model we are proposing is a three-state model, the Markov model can also be expressed as a three-state model as shown in Figure 14.9 according to Reference [19].

According to our definitions of fading (see Chapter 1), there are two types of signal level variations: short-term variations in terms of instantaneous fluctuations followed by the given PDF in each state and long-term variations represented by state transitions. For the purpose of satellite diversity assessment, understanding of the long-term variations is adequate at the first stage of assessment as mentioned before. Therefore, we formulate a Markov model for simulating the long-term variations (namely, state-to-state variations).

Figure 14.10(a)–(c) shows examples of satellite constellations where at least one, two, and three satellites simultaneously cover every point on the Earth's surface
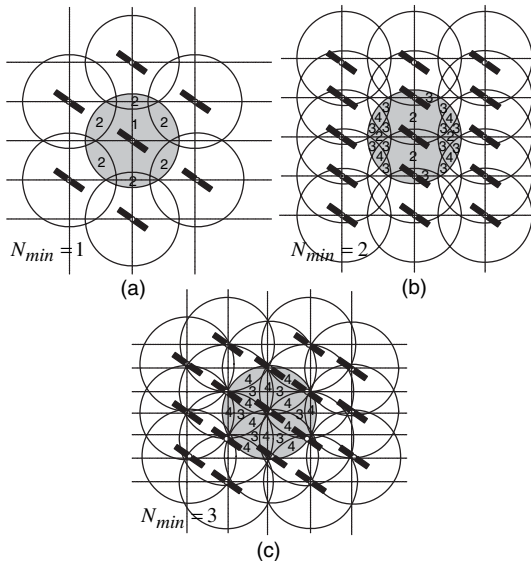
FIGURE 14.10. Foot print patterns on the ground where at least (a) one, (b) two, and (c) three satellite zones overlap according to [19].

(N_{min} = 1, 2, and 3). At the beam edge regions where the propagation condition seems the worst in single coverage operation, larger number of satellites can be used for the diversity. In the case of $\theta = 30°$ with H = 1000 km, for example, 200 satellites are necessary for achieving $N_{min} = 1$. To improve the service quality by means of the satellite diversity in this case, more than 400 satellites (corresponding to $N_{min} > 2$) are desirable. This value is not unrealistic, a system having 840 satellites has already been proposed.

Considering the effective use of a limited number of satellites, a beam footprint pattern is more or less uniquely determined. However, there are several choices concerning the direction of the orbit. For example Orbit *a* and Orbit *b*, as indicated by each arrow in the Figure 14.10. The scheme of "Orbit *a*" involves many satellites in the same orbit; the "Orbit *b*" scheme has fewer satellites in the same orbit, but the distance between the adjacent orbits is small.

14.3.6. Lutz Statistical Model

In this model, the simple statistics of LOS and NLOS are modeled by two distinct states, *good* and *bad* as shown by Figure 14.2; appropriate for the description of propagation situation in urban and suburban areas where there is a large difference between the shadowed and nonshadowed statistics. The parameters associated with each state and the transition probabilities for evolution between states are empirically derived. The line-of-sight condition is represented by a good state, and the non-line-of-sight condition by a bad state. In the good state, the signal is assumed to be Rician distributed with K-factor, which depends on the satellite elevation angle and the carrier frequency, so that the PDF of the signal amplitude is given by $P_{good} = P_{Rice}$. In the bad state, the fading statistics of the signal amplitude are assumed to be Rayleigh, with a mean power $S_0 = \sigma^2$, which varies with time. So the PDF of amplitude is specified as the conditional distribution $p_{Rayl}(S \mid S_0)$, where S_0 varies slowly with a lognormal distribution $p_{LN}(S_0)$, representing the varying effects of shadowing with the NLOS component. For detailed formulas, we refer the reader to the original [16].

Transitions between states are described by a first-order Markov chain. This is a state transition system in which the transition from one state to another depends only on the current state rather than on any more distant history of the system. The transition probabilities, which summarize all mentioned models based on Markov chain, are (see Fig. 14.11 according to References [2,14–16]):

probability of transition from good state to good state P_{gg};
probability of transition from good state to bad state P_{gb};
probability of transition from bad state to bad state P_{bb};
probability of transition from bad state to good state P_{bg}.

For a digital communication system, each state transition is taken to represent the transition of one symbol. The transition probabilities can then be found in terms of the mean number of symbol duration spent in each state [2,14–16]:
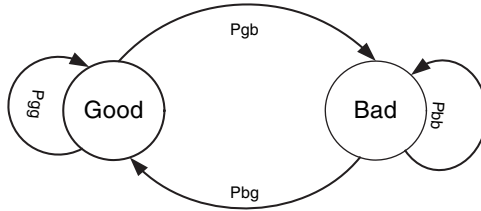
FIGURE 14.11. Markov's model of channel state.

$$P_{\text{gb}} = \frac{1}{D_{\text{g}}} \text{ where } D_{\text{g}} \text{ is the mean number of symbol duration in the good state;}$$

$$P_{\text{bg}} = \frac{1}{D_{\text{b}}} \text{ where } D_{\text{b}} \text{ is the mean number of symbol duration in the bad state.}$$

The sum of the probabilities leading from any state must be equal to the sum of the unit, so

$$P_{\text{gg}} = 1 - P_{\text{gb}} \quad \text{and} \quad P_{\text{bb}} = 1 - P_{\text{bg}} \tag{14.31}$$

The time share of shadowing (the proportion of a symbol in the bad state) is

$$A = \frac{D_{\text{b}}}{D_{\text{g}} + D_{\text{b}}} \tag{14.32}$$

Below we will use this formula to find the parameter A, denoted as *the time share of shadowing*, during comparison with physical-statistical approach, where this parameter is derived in other manner. In this comparison we will use the Lutz model as a classical statistical approach.

14.3.7. Abdi's Model

This model deals with a new shadowed Rician distribution for land mobile satellite channels [13]. In this model, the amplitude of the line-of-sight (LOS) component of the total signal envelope is characterized by the Nakagami distribution:

$$p_Z(z) = \frac{2m^m}{\Gamma(m) \cdot \Omega^m} z^{2m-1} \exp\left[-\frac{mz^2}{\Omega}\right], \quad z \geq 0 \tag{14.33}$$

where the multipath component (due to scattering effects) of the total signal envelope is characterized by the Rayleigh distribution:

$$p_A(a) = \frac{a}{b_0} \exp\left[-\frac{a^2}{2b_0}\right], \quad a \geq 0 \tag{14.34}$$

Here, a is the amplitude of the LOS, and z is the multipath components of the total signal; $2b_0 = E[A^2]$ is the average power of the multipath component; $\Omega = E[Z^2]$ is the average power of the LOS component. The Nakagami parameter m with variance $Var[Z^2]$ can be presented as

$$m = \frac{(E[Z^2])^2}{Var[Z^2]} \tag{14.35}$$

and $\Gamma(m)$ is the gamma function. The major advantage of this model is that it leads to a closed-form and mathematically tractable expressions for the fundamental channel statistics such as the envelope probability density function, moment generating function of the instantaneous power (the so-called *first-order statistics*), the level crossing rate (LCR), and the average fade duration (ADF) (the so-called *second-order statistics*) [13]. Below, we will discuss the first-order statistics only, on the basis of derivation of the PDF of the signal envelope in LSC channel.

The model is very convenient for analytical and numerical performance predictions of complicated narrowband and wideband land mobile satellite systems, with different types of decoded/encoded modulations, with or without diversity. Comparisons of the first- and second-order statistics of the proposed model with different sets of published statistics demonstrate the flexibility of the new model in characterizing a variety of channel conditions and propagation mechanisms over satellite links. At the same time, the proposed model provides a similar fit to the experimental data as the well-accepted Loo's model, which is characterized by significantly less computational operations. The model mainly focuses on narrowband models, which are the basic building blocks of wideband models.

The available statistical models for narrowband LMS channels can be placed into two categories: single and mixture models. In a single model, the channel is characterized by a single statistical distribution, whereas a mixture model refers to a combination (weighted summation) of several statistical distributions. Single models are valid for stationary conditions, where the channel statistics remain approximately constant over the time period of interest in a small area. On the contrary, the mixture models are developed for nonstationary channels, where the signal statistics vary significantly over the observation interval in large areas. The random fluctuations of the signal envelope in a narrowband LMS channel can be attributed to two types of fading: multipath (fast) fading and shadow (slow) fading. LOS shadow fading (called *flat*, see Chapter 1) comes from the complete or partial blockage of the LOS by buildings, trees, hills, mountains, and so forth, which in turn makes the amplitude of the LOS component a random variable. In comparison, multiplicative fading (see definition in Chapter 1) refers to the random variations of the total power of the multipath components, both the LOS and scatter components.

As for the first-order statistic of the model, the shadowed Abdi's PDF for the signal envelope in an LMS channel can be written as [13]

$$p_R(r) = \left(\frac{2b_0 m}{2b_0 m + \Omega}\right)^m \frac{r}{b_0} \exp\left\{-\frac{r^2}{2b_0}\right\} {}_1F_1\left[m, 1, \frac{\Omega r^2}{2b_0(2b_0 m + \Omega)}\right], \; r \geq 0 \quad (14.36)$$

where ${}_1F_1(*)$ is the confluent hypergeometric function.

As was shown in Reference [13], the Loo's signal envelope distribution and the above distribution (14.36) closely match each other. This is particularly useful when we wish to apply the new model with unknown parameters to a set of data collected previously, but the measured data is not available for parameter estimation, or we may not want to go through the time-consuming procedures of parameter estimation.

Now we want to show the equivalency of the proposed pure stochastic models based on the well-known statistical distributions and their combinations. Let us compare the model proposed by Abdi [13] with that proposed by Loo [7,9]. In Figure 14.12, we plotted the envelope complementary CDF(CCDF = 1 − CDF) for Loo's PDF and Abdi's PDF, together with the measured data (points) according to Reference [13].
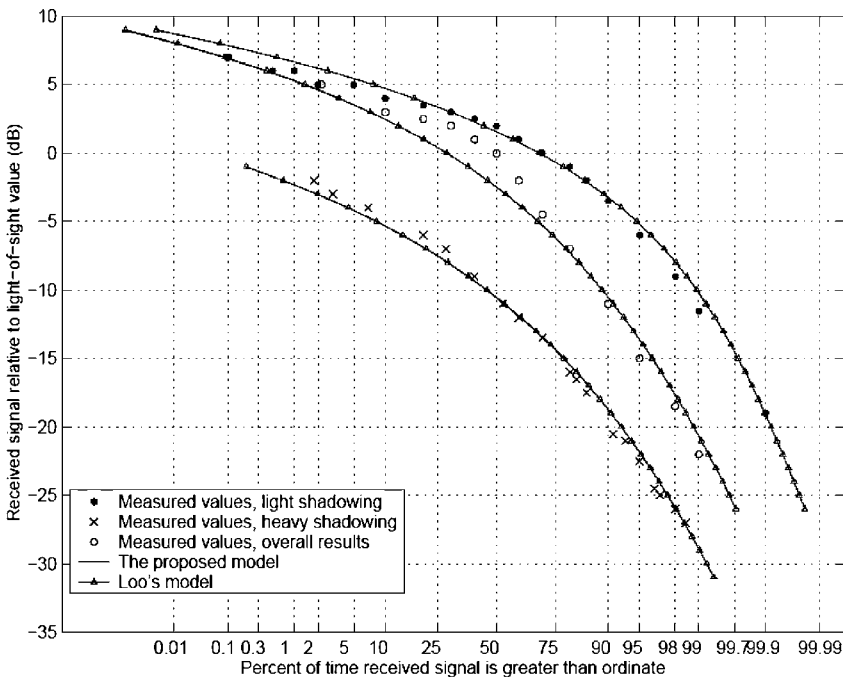
FIGURE 14.12. CCDF of the signal envelope in a land mobile satellite channel in Canada, under different shadowing conditions: measured data [13], Loo's model [7–9], and the Abdi's model [13]. (Reprinted with permission © 2003 IEEE)

From the presented illustration, it follows that the Loo's curve and the Abdi's curve, both are close to the measured data for different cases and channel conditions and cannot be distinguished. This is very important for link budget design. These empirical results indicate the utility of an Abdi's model [13] for LMS channels.

14.4. PHYSICAL–STATISTICAL MODELS

In pure statistical models, the input data and computational effort are quite simple, as the model parameters are fitted to measured data. Because of the lack of physical background, such models only apply to environments that are very close to the one they have been inferred from. On the contrary, pure deterministic physical models provide high accuracy, but they require actual analytical path profiles and time-consuming computations.

A combination of both approaches has been developed by the authors. The general method relates any channel simulation to the statistical distribution of physical parameters, such as building height, width and spacing, street width or elevation and azimuth angles of the satellite link. This approach is henceforth referred to as the ''*Physical-Statistical*'' approach [2,14,15]. The main concept of such an approach is sketched in Figure 14.13.

As for physical models, the input knowledge consists of electromagnetic theory and a full physical understanding of the propagation processes. However, this knowledge is then used to analyze a *statistical* input data set, yielding a *distribution* of the output predictions. The output predictions are not linked to specific locations. Physical-statistical models therefore require only simple input data such as distribution parameters (e.g., mean building height and building height variance, as was done in Chapter 5 for land communication links).

This modeling describes the geometry of mobile satellite propagation in built-up areas and proposes statistical distributions of building heights, which are used in the subsequent analysis. We will consider only two of them, which have been fully proved by numerous experiments for land–land and land–satellite communication links:
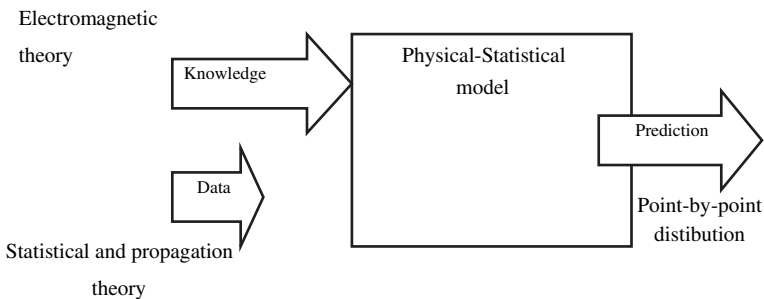
FIGURE 14.13. Algorithm of the physical-statistical model.
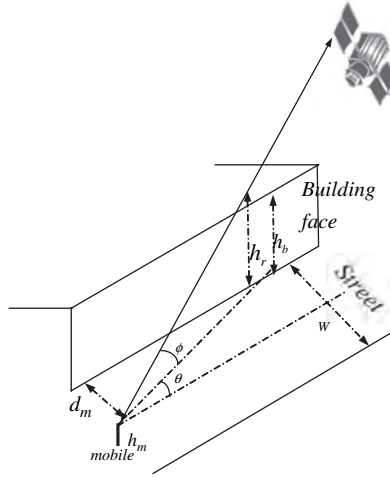
FIGURE 14.14. Geometry for mobile-satellite communication in built-up areas.

- a model of shadowing based on the two-state channel Lutz model;
- a multiparametric stochastic model.

14.4.1. The Model of Shadowing

The geometry of the situation, which was analyzed in References [2,14,15] by Saunders and his colleagues, is illustrated in Figure 14.14. It describes a situation where a mobile is situated on a long straight street with the direct ray from the satellite impinging on the mobile from an arbitrary direction. The street is lined on both sides with buildings whose height varies randomly. In the presented model, the statistics of the building height in typical built-up areas will be used as input data. A suitable form was sought by comparing it with geographical data for the cities of Westminster and Guildford, UK [14,15]. The PDFs that were selected to fit the data are the lognormal and Rayleigh distributions with unknown parameters of a mean value, m, and standard deviation, σ_b. The PDF for the lognormal distribution is [2,15]

$$p_b(h_b) = \frac{1}{h_b\sqrt{2\pi}\sigma_b} e^{-\frac{\ln^2(h_b/m)}{2\sigma_b^2}} \tag{14.37}$$

The PDF for the Rayleigh distribution is presented in Chapter 1. We will repeat it using notations made in References [2,15]:

$$p_b(h_b) = \frac{h_b}{\sigma_b^2} e^{-\frac{h_b^2}{2\sigma_b^2}} \tag{14.38}$$

TABLE 14.4. Best-fit Parameters for the Theoretical PDFs

| City | Lognormal PDF | | Rayleigh PDF |
	Mean (m)	Standard deviation	Standard deviation
Westminster	20.6	0.44	17.6
Guildford	7.1	0.27	6.4

To find the appropriate parameters for these functions in order to fit the data measurements as accurately as possible, the probability density function was found by minimizing the maximum difference between the two cumulative distribution functions. The parameters for each PDF are quoted in Table 14.4 from References [14,15], where all parameters are in meters.

The direct ray is judged to be shadowed when the building height h_b exceeds some threshold height h_T relative to the direct ray height h_r (see Figure 14.14). The shadowing probability, P_s, can then be expressed in terms of the probability density function of the building height, $p_b(h_b)$ as in References [2,15]:

$$P_s = \Pr(h_b > h_T) = \int_{h_T}^{\infty} p_b(h_b) dh_b \qquad (14.39)$$

The shadowed model estimates the probability of shadowing for Lutz two-state model [16]. The same Markov chain (as shown in Fig. 11.11) is used, but parameters A, P_{bad}, and P_{good} are obtained from actual random distribution of the obstructions above the terrain. Thus,

$$A = \int_{z_1}^{z_2} P_b(h) dh \qquad (14.40)$$

where h is different heights of obstacles, Z_1 and Z_2 are the minimum and maximum height of the built-up layer;

$$P_b = \begin{cases} lognormal + Ricean \\ lognormal + Rayleigh. \end{cases} \qquad (14.41)$$

where lognormal PDF is pure NLOS shadowing, Rician's PDF describes both the LOS and the multipath component, and Rayleigh's PDF describes the multipath component of the total signal, when the LOS component is absent (see Chapter 1).

14.4.2. Multiparametric Stochastic Approach

As an example of the physical-statistical model, we present the same stochastic approach that was used successfully for land communication channels, rural, suburban, and urban (see Chapters 5 and 10).
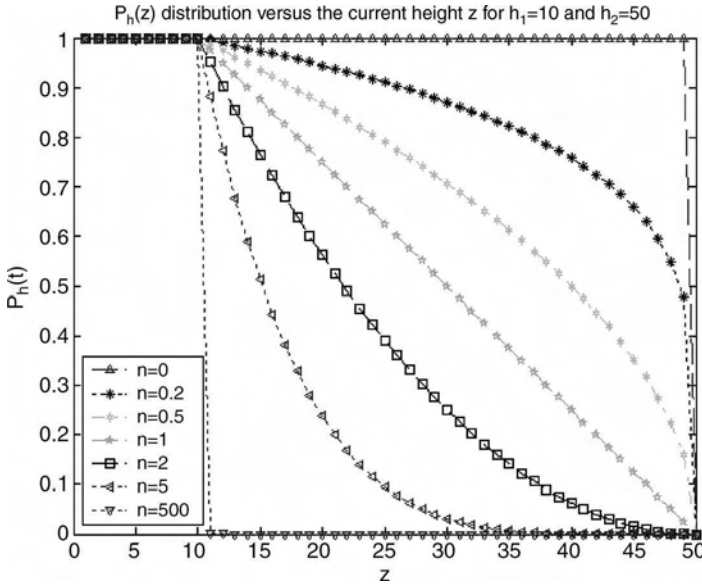
FIGURE 14.15. Buildings' overlay profile PDF.

Overlay Profile of the Buildings. Taking into account the fact that real profiles of urban environment are randomly distributed, the probability function $P_h(z)$, which describes the overlay profile of the buildings, can be presented in the following form [20] (see also Chapter 5):

$$P_b(z) = H(h_1 - z) + H(z - h_1) \cdot H(h_2 - z) \cdot \left[\frac{(h_2 - z)}{(h_2 - h_1)} \right]^n \quad n > 0, \qquad 0 < z < h_2$$

(14.42)

where the function $H(x)$ is the Heaviside step function, which is equal to 1, if $x > 0$, and is equal to 0, if $x < 0$. The graph of this function versus height z of a built-up overlay is presented in Figure 14.15, for $h_1 = 10$ m and $h_2 = 50$ m.

For $n \gg 1$ $P_b(z)$ describes the case where buildings higher than h_1 (minimum level) very rarely exist. The case, where all buildings have heights close to h_2 (maximum level of the built-up layer), is given by $n \ll 1$. For n close to zero, or n approaching infinity, most buildings have approximately the same level that equals h_2 or h_1, respectively. For $n = 1$, we have the case of building height uniformly distributed in the range of h_1 to h_2. The average height of the buildings $\bar{h}$, can be found as [20] (see also Chapter 5)

$$\bar{h} = h_2 - n \cdot \frac{(h_2 - h_1)}{n + 1}$$

(14.43)

Combination of Physical and Statistical Modes. Now, using theoretical results obtained from the pure statistical Lutz model and the physical-statistical Saunders model with two methods of overlay profile derivation of the buildings, we can propose the unified model that is based on results discussed above. Thus, taking into account the Markov's chain (Fig. 14.11), we consider the bad status by using the Rayleigh PDF and the good status by using the Rician PDF, as well as shadowing by using the lognormal PDF. Combine all these PDFs in the Markov chain, we finally can obtain the total PDF that describes effects of different kinds of fading occurred within the land–satellite communication link, caused by terrain obstructions, natural and man-made. As a result we get

$$p(S) = (1 - A) \cdot P_{good} + A \cdot P_{bad} = (1 - A) \cdot P_{Rice}(S)$$
$$+ A \int_0^\infty p_{Rayleigh}(S \mid S_0) \cdot p_{\log norm}(S_0) \mathrm{d}S_0 \qquad (14.44)$$

Then, the corresponding complementary cumulative distribution function, CCDF, which describes the signal stability, being the received signal with amplitude r prevails upon the maximum accepted path loss, R, in the multipath channel, caused by fading phenomena; it can be presented in the following form:

$$\mathrm{CCDF} = \Pr(r > R) = \int_0^R p(S) \mathrm{d}S \qquad (14.45)$$

All above formulas allow us to present the unified algorithm for fading phenomena estimation in land–satellite communication links, stationary and mobile.

14.5. THE UNIFIED ALGORITHM FOR FADING PHENOMENA PREDICTION

Now we will present the unified algorithm, which is created to estimate and examine the different models for predicting fading in satellite communication links. The unified algorithm is a dynamic model based on the combination of the physical-statistical (Saunders) model and the pure statistical (Lutz) model of the mobile-satellite communication channel; it is shown in Figure 14.16. This figure shows a dynamic model for the land mobile satellite channel that reproduces the probability density function of the received signal power as well as the dynamic behavior of the fading and shadowing processes. The transmitted signal $s(t)$ is corrupted by multiplicative $a(t)$ and additive (white) Gaussian noise $n(t)$ with power spectral density No (see all definitions in Chapter 1).
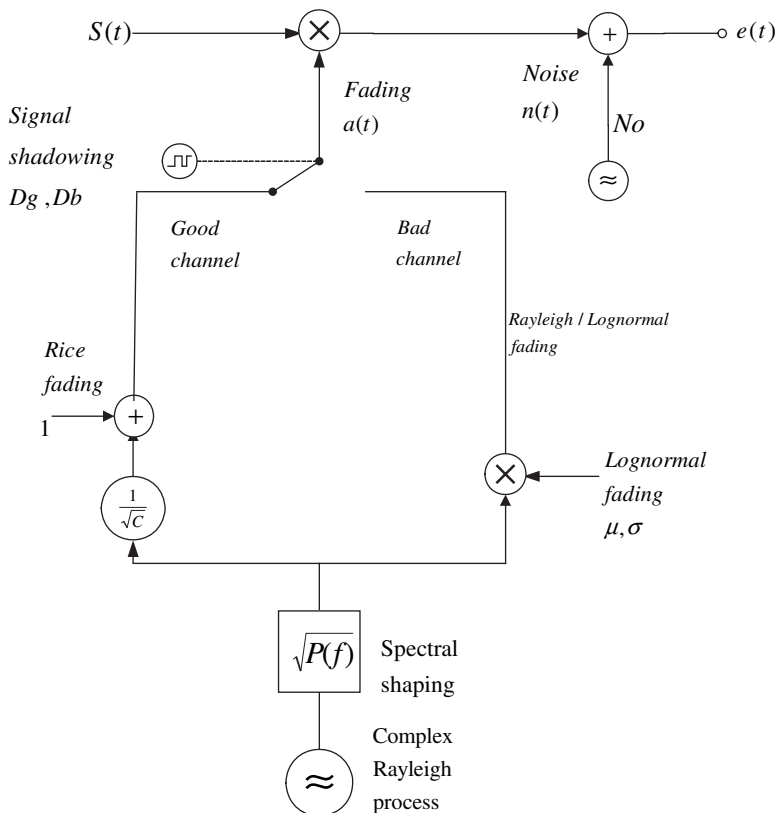
FIGURE 14.16. Dynamic model of the mobile-satellite communication channel.

This algorithm uses several probability density functions, which we will repeat once again. The Rician PDF, which is given by

$$p_{\text{good}} = p_{\text{Rice}}(S) = \frac{S}{\sigma^2} \exp\left\{\frac{-(S^2 + C^2)}{2\sigma^2}\right\} I_0\left(\frac{SC}{\sigma^2}\right), \quad r > 0 \qquad (14.46)$$

where σ^2 is the standard deviation and $Io(*)$ is the modified Bessel function of order zero. The Rayleigh PDF is given by

$$p_{\text{Rayleigh}}(S) = \frac{S}{\sigma^2} \exp\left\{-\frac{S^2}{2\sigma^2}\right\} \qquad (14.47)$$

and, the lognormal PDF is

$$p_{\text{LN}}(S) = \frac{1}{S\sigma\sqrt{2\pi}} \exp\left\{-\frac{(\ln S - \mu)^2}{2\sigma^2}\right\} \qquad (14.48)$$

In the bad state, the fading statistics of the signal amplitude are assumed to be Rayleigh but with a mean power $S_0 = \sigma^2$, which varies with time, so the PDF of amplitude is specified as the Rayleigh conditional distribution $p_{Ray}(S \mid S_0)$. The parameter S_0 varies slowly with a lognormal distribution $p_{LN}(S_0)$, representing the varying effects of shadowing in a NLOS situation. The overall PDF in the bad state is then found by integrating the Rayleigh distribution over all possible values of S_0, so that

$$p_{bad}(S) = \int_0^\infty p_{Ray}(S \mid S_0) \cdot p_{LN}(S_0) dS_0 \qquad (14.49)$$

The proportion of time, for which the channel is in the bad state, is called the *time-share of shadowing A*. Finally, the overall probability density function $p(s)$ is given by

$$p(S) = (1 - A)p_{Rice}(S) + A \cdot \int_0^\infty p_{Ray}(S \mid S_0) \cdot p_{LN}(S_0) dS_0 \qquad (14.50)$$

where S is the received power amplitude.

Next, the model estimates the time-share of shadowing A and is expressed in terms of the probability density function of the building height $p_b(h_b)$ according to

$$P_S = \Pr(h_b > h_T) = \int_{h_T}^\infty p_b(h_b) dh_b \qquad (14.51)$$

using the built-up profile distributions in (14.37), (14.38), and (14.42). The definition of h_T is obtained by considering shadowing to occur exactly when the direct ray is geometrically blocked by the building face. Using a simple geometry, the following expression is extracted for h_T [2,14]:

$$h_T = h_r = \begin{cases} h_m + \dfrac{d_m \tan \phi}{\sin \theta} & \text{for } 0 < \theta < \pi \\[3mm] h_m + \dfrac{(w - d_m) \tan \phi}{\sin \theta} & \text{for } -\pi < \theta < 0 \end{cases} \qquad (14.52)$$

All notations and geometrical parameters in (14.52) are explained in Figure 14.14. In our simulations we used the measured data from References [17,18], done in several cities in Europe. These tests were narrowband measurements at a single frequency, representing the channel within its coherence bandwidth. The test was transmitted from the ESA ground station in Villafranca, Spain and relayed by the geostationary satellite MARECS at L-band (1.54 GHz). The measurements were conducted in areas with different satellite elevations (see Table 14.5).

TABLE 14.5. Parameters of Channel Model Measured by [17,18]

Satellite elevation	A	10 log(c) [dB]	μ [dB]	σ [dB]
13° Stockholm	0.24	10.2	−8.9	5.1
18° Copenhagen	0.8	6.4	−11.8	4.0
24° Munich	0.66	6.0	−10.8	2.8
34° Barcelona	0.58	6.0	−10.6	2.6
43° Cadiz	0.54	5.5	−13.6	3.8

Using these measurements and using a Rayleigh PDF for building distribution heights and Equation (14.52), we constructed a corresponding numerical code to see if there is an agreement of the theoretical time share factor A with the measured data. We examined two main functions: PDF and CCDF. CCDF gives us the knowledge of stability of a received signal with respect to noise caused by the fading phenomena. The results of our simulation using the CCDF, given by the physical-statistical Saunders model [2,14], is shown in Figures 14.17(a)–(e) for various elevations of the satellite and different cities. We can see by this simulations that there is a good agreement between the measured and physical-statistical model outputs.

The same was done using the multiparametric model in (14.51) and the corresponding PDF in (14.42) for each city. The results of *fading* estimations were also compared with the pure statistical Lutz model based on Markov's chain, and
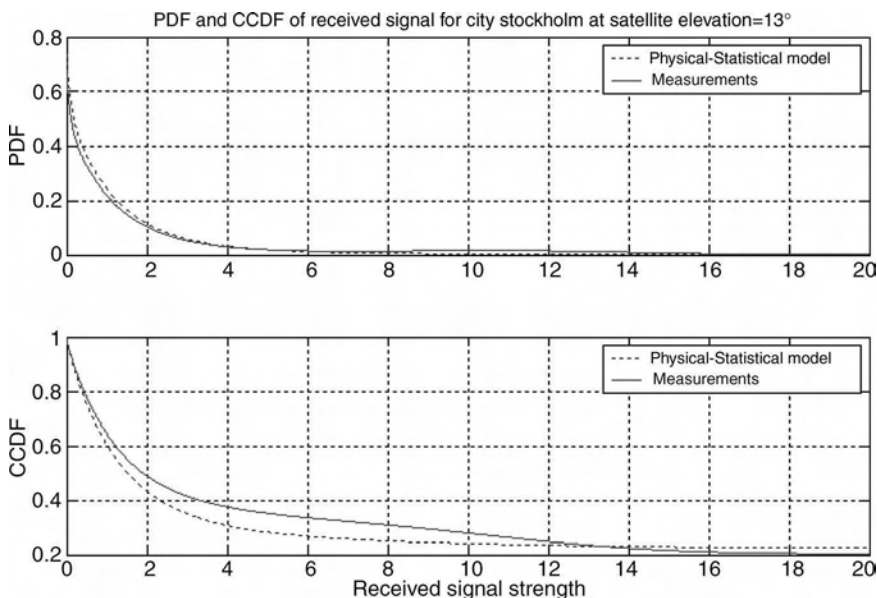
FIGURE 14.17(a). PDF and CCDF of received signal for Stockholm at satellite elevation of 13°.
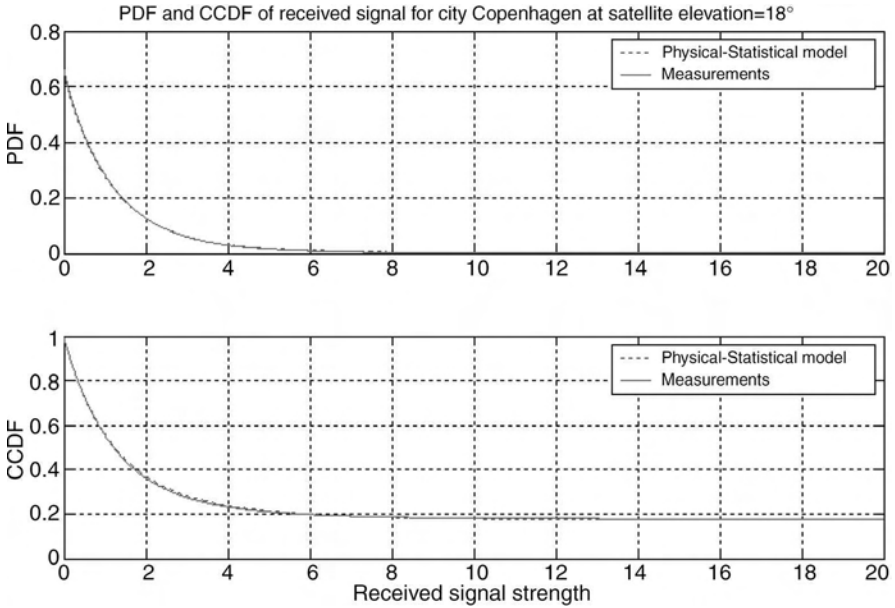
FIGURE 14.17(b). PDF and CCDF of received signal for Copenhagen at satellite elevation of 18°.
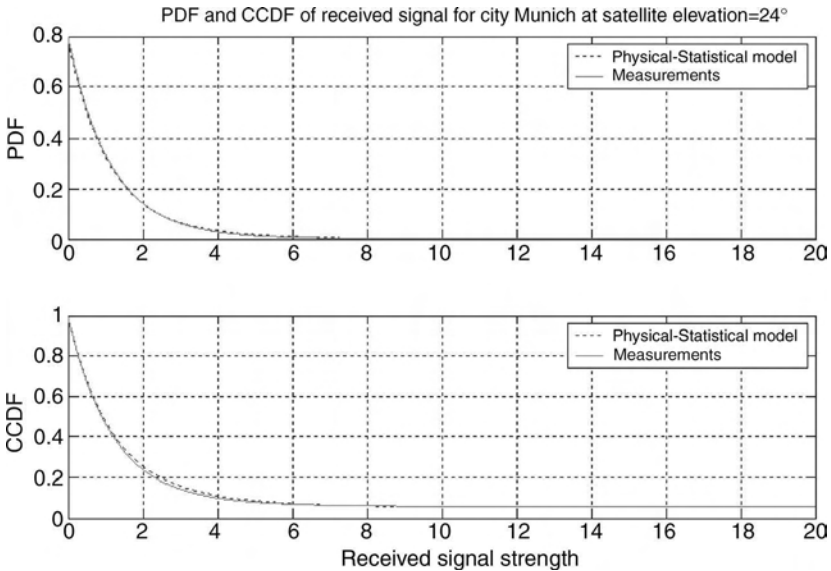
FIGURE 14.17(c). PDF and CCDF of received signal for Munich at satellite elevation of 24°.
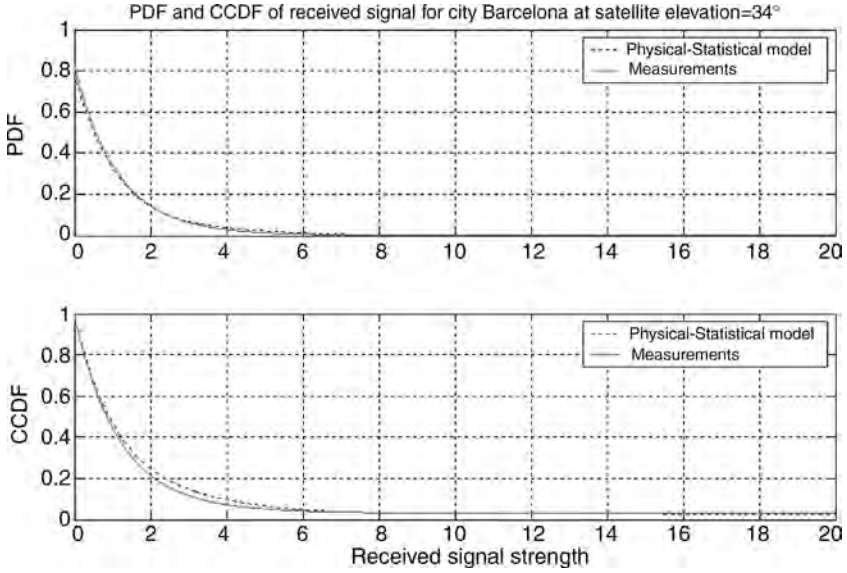
FIGURE 14.17(d). PDF and CCDF of received signal for Barcelona at satellite elevation of 34°.
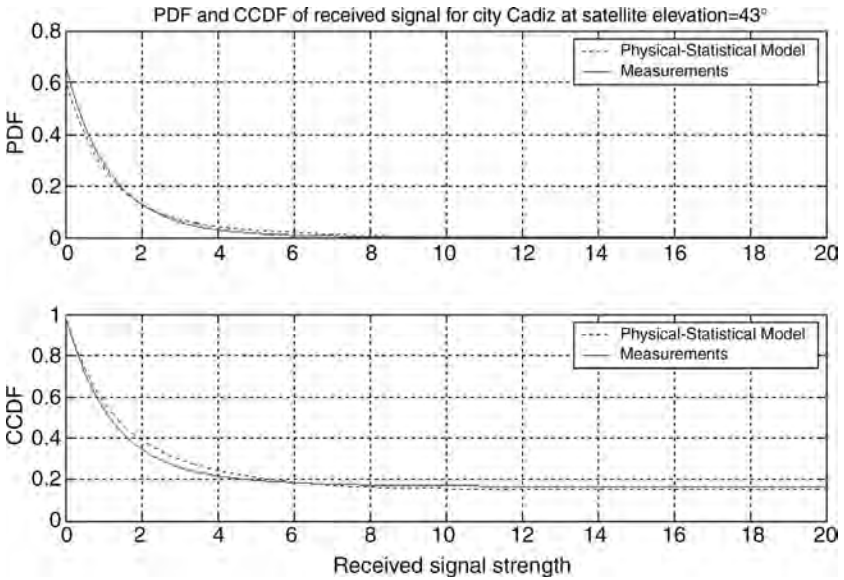
FIGURE 14.17(e). PDF and CCDF of received signal for Cadiz at satellite elevation of 43°.

with Saunders model described above. All three approaches were compared with measured data obtained for various elevation angles and different urban environments. To compare the measured data with the three different models, the probabilities P_{gg} and P_{bb} were changed to best fit the measured data. Five tests were run:

Simulation 1: $P_{gg} = (0.7, 0.92, 0.9, 0.9, 0.7)$ and
$\quad\quad\quad\quad\quad\quad P_{bb} = (0.05, 0.1, 0.08, 0.2, 0.4).$

Simulation 2: $P_{gg} = (0.8, 0.95, 0.85, 0.83, 0.7)$ and
$\quad\quad\quad\quad\quad\quad P_{bb} = (0.08, 0.15, 0.25, 0.22, 0.5)$

Simulation 3: $P_{gg} = (0.87, 0.85, 0.8, 0.75, 0.65)$ and
$\quad\quad\quad\quad\quad\quad P_{bb} = (0.17, 0.22, 0.25, 0.3, 0.35)$

Simulation 4: $P_{gg} = (0.86, 0.82, 0.79, 0.75, 0.7)$ and
$\quad\quad\quad\quad\quad\quad P_{bb} = (0.15, 0.2, 0.17, 0.2, 0.3)$

Simulation 5: $P_{gg} = (0.9, 0.89, 0.85, 0.8, 0.77)$ and
$\quad\quad\quad\quad\quad\quad P_{bb} = (0.13, 0.2, 0.25, 0.3, 0.35)$

The results of such comparisons, for five different cities and, therefore, for five elevation angles are presented in Figures 14.18(a)–(e).

From the results of these simulations, we can conclude that the pure statistical model does not match the measured data. A better fit can be found by using both the Saunders model and the multiparametric model.

Let us now examine all three models with measurements to try and define which one presented the best fit to the measured data and also the simplest one. In such a
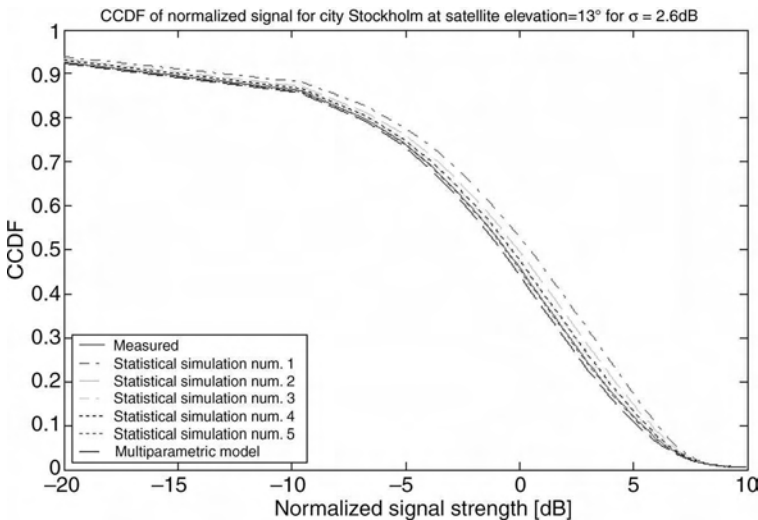
FIGURE 14.18(a). CCDF of normalized signal for Stockholm at satellite elevation of 13° for different bad and good states.
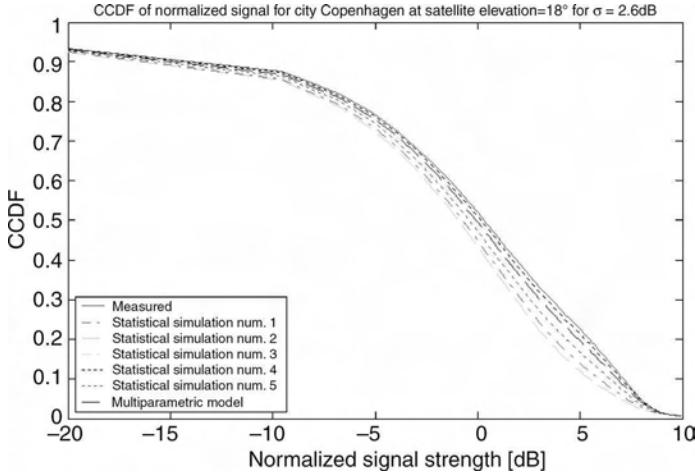
FIGURE 14.18(b). CCDF of normalized signal for Copenhagen at satellite elevation angle of 18° for different bad and good status.
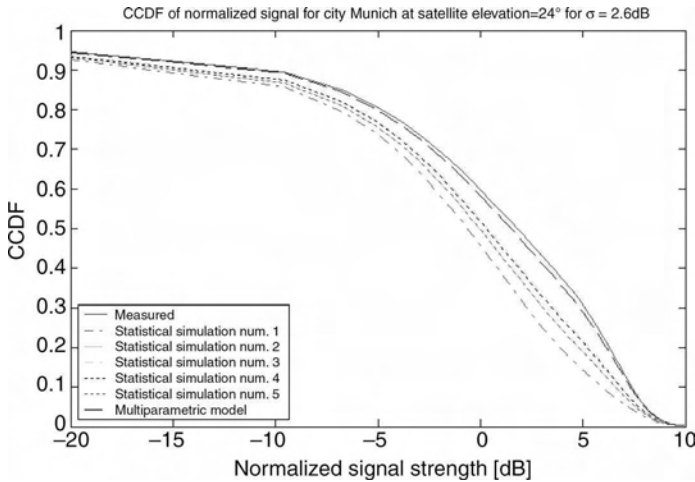
FIGURE 14.18(c). CCDF of normalized signal for Munich at satellite elevation angle of 24° for different bad and good states.

comparison we use the Lutz statistical model simulation with $P_{gg} = (0.8, 0.95, 0.85, 0.83, 0.7)$ and $P_{bb} = (0.08, 0.15, 0.25, 0.22, 0.5)$. These results are shown in Figures 14.19(a)–(e).

The standard deviation, σ, was taken not more than 2.6 dB, obtained from our estimations of each built-up profile. Nevertheless, in Reference [16] the authors took $\sigma = 3 - 4$ dB, which is not a realistic case when the NLOS regime is very small compared with the LOS component of the total filed strength. We also checked this
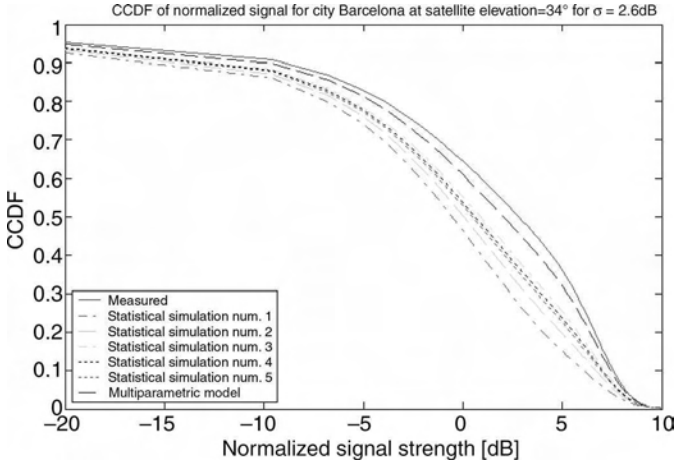
FIGURE 14.18(d). CCDF of normalized signal for Barcelona at satellite elevation of 34° for different bad and good states.
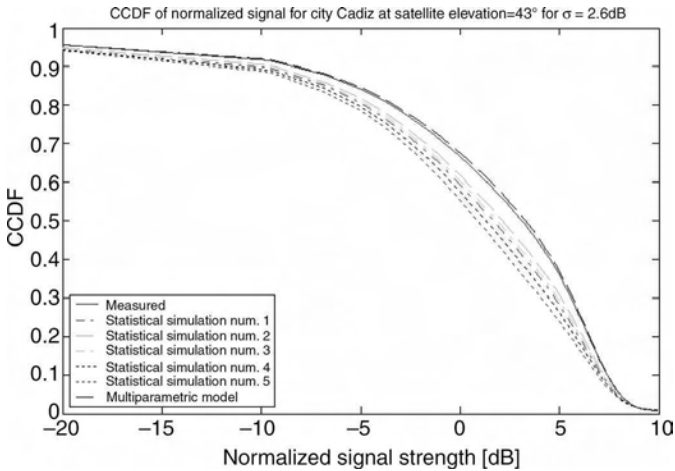
FIGURE 14.18(e). CCDF of normalized signal for Cadiz at satellite elevation angle of 43° for different bad and good states.

situation in our numerical evaluations. Thus, in Figure 14.20, the CCDF of the received signal for the city Stockholm [20], at a satellite elevation angle of 13°, for all three different models is shown for $\sigma = 4\,\mathrm{dB}$. It is clearly seen that the results of fading estimation obtained from the multiparametric model are closer to the experimental data compared to the other two models, the statistical and physical-statistical.

CCDF of normalized signal for city Stockholm at satellite elevation=13° for σ = 2.6dB
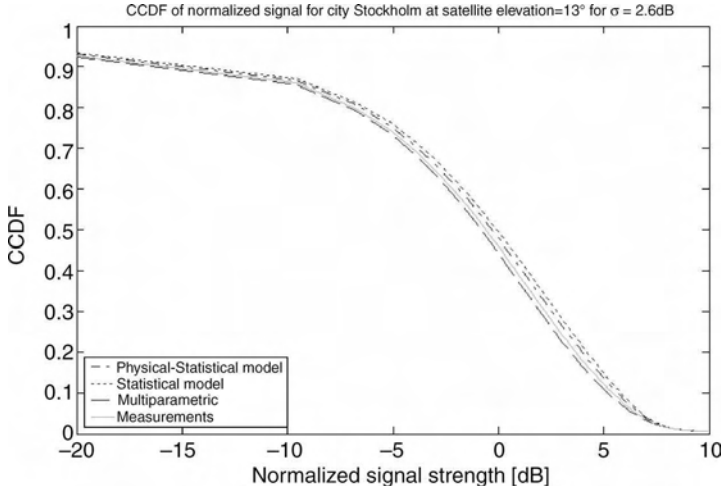
FIGURE 14.19(a). CCDF of normalized signal for Stockholm at satellite elevation angle of 13° for three different models.

CCDF of normalized signal for city Copenhagen at satellite elevation=18° for σ = 2.6dB
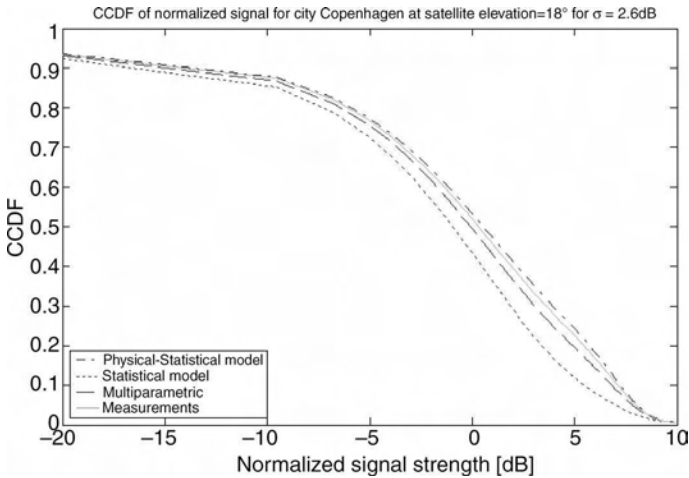
FIGURE 14.19(b). CCDF of normalized signal for Copenhagen at satellite elevation angle of 18° for three different models.

14.6. MEGA-CELL CONCEPT FOR LAND SATELLITE COMMUNICATION LINKS

To give full radio coverage of the Earth and the corresponding mega-cell map, a net of satellites, assembled into global satellite networks with specific constellations, was developed. Modern global satellite systems were built both for personal and
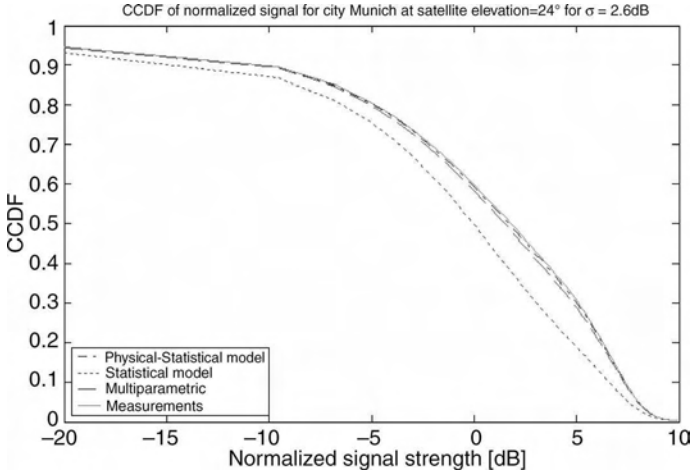
FIGURE 14.19(c). CCDF of normalized signal for Munich at satellite elevation angle of 24° for three different models.
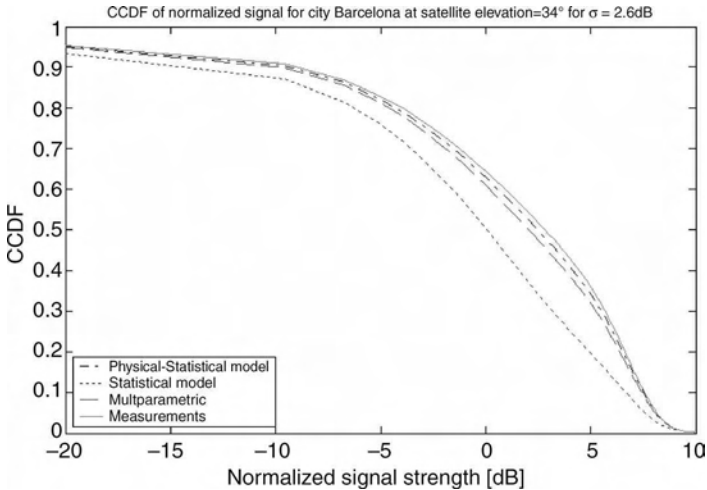
FIGURE 14.19(d). CCDF of normalized signal for Barcelona at satellite elevation angle of 34° for three different models.

mobile communications. Presently, a strong effort is being made toward the assessment of main specifications for the IMT-2000 system for mobile and personal multimedia communications worldwide, which in Europe is named UMTS (Universal Mobile Telecommunication System). IMT-2000 is intended as a 'family' of interoperable systems capable of assisting the roaming/desired user in any mobile network where it may be temporarily present. This system is called a third-generation (3G) system, after the first-generation (1G) incompatible analog cellular
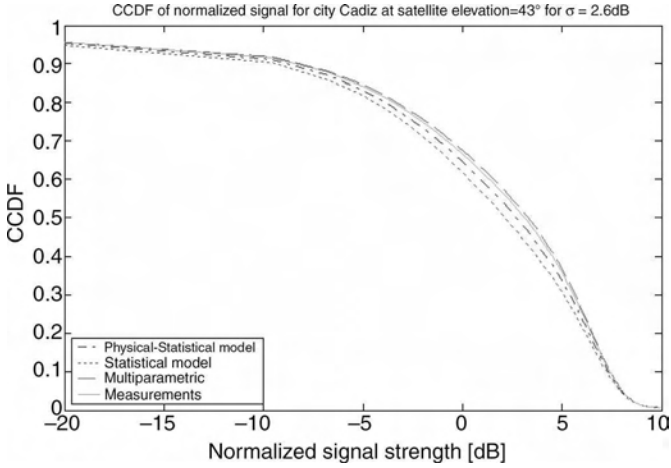
FIGURE 14.19(e). CCDF of normalized signal for Cadiz at satellite elevation angle of 43° for three different models.

systems and the second-generation (2G) digital systems, the most successful one being GSM (Global System for Mobile) communication [1–4].

14.6.1. Existing Land–Satellite Personal and Mobile Systems

In order to understand the operational characteristics of land–satellite mobile communication system, we start, first of all, with existing systems [3]. Earlier mobile
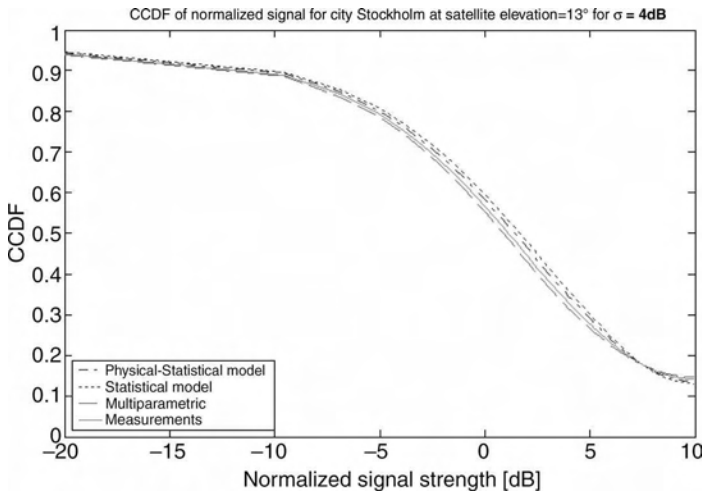
FIGURE 14.20. CCDF of normalized signal for Stockholm at satellite elevation angle of 13° for $\sigma = 4\,\mathrm{dB}$.

FIGURE 14.21. Shipboard Inmarsat terminal radome-enclosed antenna. (Source [3]: Reprinted with permission © 1998 IEEE)

satellite communications systems employed geostationary satellites with modest effective isotropic radiated power (EIRP), which restricts their use to mobile terminals with an antenna gain of approximately 8 dB (considerably more than can be achieved with a handheld unit, which might be only on the order of 2 dB). These terminals are most frequently mounted on vehicles, although fixed and transportable versions can also be provided.

Inmarstat. The commercial use of satellites for mobile communications began with the COMSAT/Marisat system in 1976 [21]. Satellites operating at UHF (∼800 MHz) and at L band (∼1,600 MHz) were launched on February 19 and June 9 of 1976 into positions over the Atlantic and Pacific Oceans, respectively. The UHF capacity was utilized by the U.S. Navy, whereas the L-band capacity was intended to inaugurate a commercial service for mariners. Shipboard terminals typically consisted of an above-deck 1-m-diameter specific antenna to remain locked on the satellite (see Fig. 14.21, according to Reference [3]).

To increase the efficiency of this system, as well as to create more channels, "Inmarsat" introduced three new services [3,4]. In 1996, the first two of five Inmarsat-3 satellites were launched. These satellites reuse the authorized frequencies in up to five spot beams, which can be selected for their coverage over land, as shown in Figure 14.22 according to Reference [3].

North American MSAT System. The most advanced satellite system providing mobile satellite communications over the land is a system implemented by the United States and Canada that covers those two countries (including Alaska), Mexico, and the Caribbean using two essentially identical satellites. Early designs focused on a UHF system; however, an FCC proceeding concluded that any U.S. system should operate at L band. Moreover, as the mobile terminals could not readily discriminate between satellites placed in the longitude sector that covers North America, there could only be a single system. The contenders to provide this service were thus forced into a consortium, which became known as the American Mobile Satellite Corporation (AMSC) [3,4].
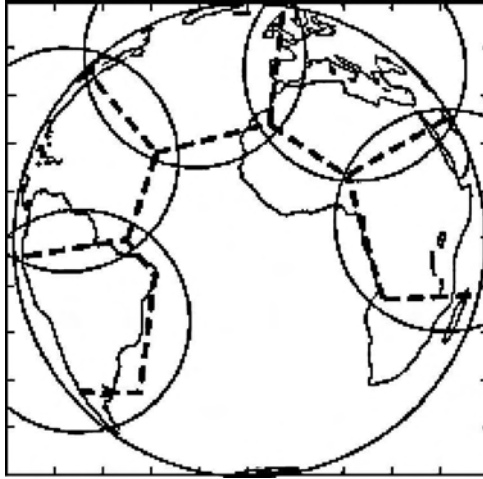
FIGURE 14.22. Mega-cell patterns of an Inmarsat-3 satellite system with five possible spot beams, four of which can be activated to provide coverage of land areas. (Source [3]: Reprinted with permission © 1998 IEEE)

In Canada, Telesat Mobile (TMI) was licensed to provide service, and these two companies, TMI and AMSC, agreed on a common set of specifications and an arrangement for sharing the available bandwidth. The ground segment for the AMSC/TMI system is depicted in Figure 14.23 according to Reference [3]. This system differs from that employed in the ''Inmarsat'' system in that provision is made for separate Earth's stations providing public switched network services, private network services, and data services, all under the command of a network control center.

Australian Mobile Satellite System (OPTUS). Australia has implemented a mobile satellite service using a L-band transponder carried on the Aussat-B series spacecraft [22–23]. Because of Australia's relatively high latitude, the elevation of the satellite, as seen from the more populated parts of Australia, was over 40°, somewhat simplifying the design of the mobile antenna. The services offered by this system include telephony using 4.8-kb/s voice encoding in 5-kHz channels (similar to the ''Inmarsat-M'' system), as well as a data service at 2.4 kb/s and fax at 4.8 kb/s [3,22,23]. Figure 14.24, according to Reference [22], presents the land coverage of Aussat B-1 satellite by use of single spot beam.

Japanese N-Star Mobile Communications System. The Japanese NTT Mobile Communications Network, (NTT DoCoMo), initiated mobile service in March 1996 using the *N*-Star satellites, offering both fixed and mobile services. These satellites provide mobile services to the Japanese islands and surrounding waters via four 1200-km-diameter spot beams, as illustrated in Figure 14.25 according to Reference [24].
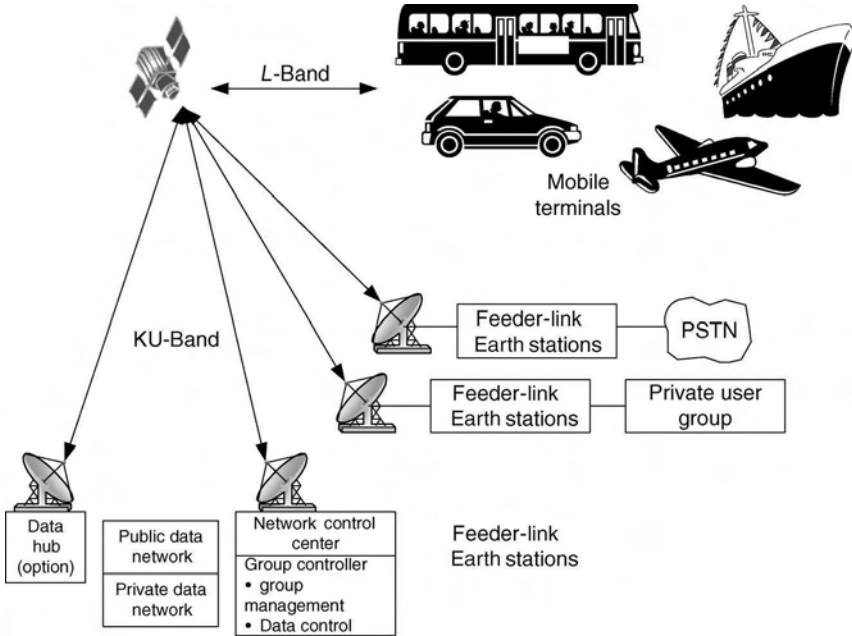
FIGURE 14.23. Arrangement of the ground segment for the AMSC/TMI system.

Three kinds of mobile terminals have been developed: portable, maritime, and car mounted. The maritime terminals use this satellite exclusively, and the car-mounted terminals provide access to both the terrestrial cellular network and the satellite system. The portable units are available in this dual-mode version also, or in a
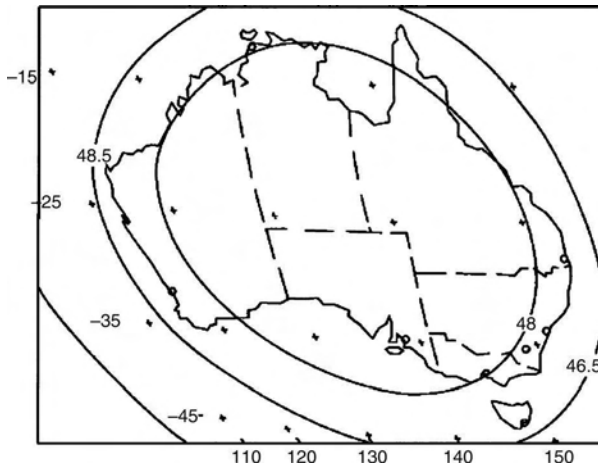
FIGURE 14.24. Coverage of Australia by the Aussat B-1 satellite, according to [3]. (Source [3]: Reprinted with permission © 1998 IEEE)
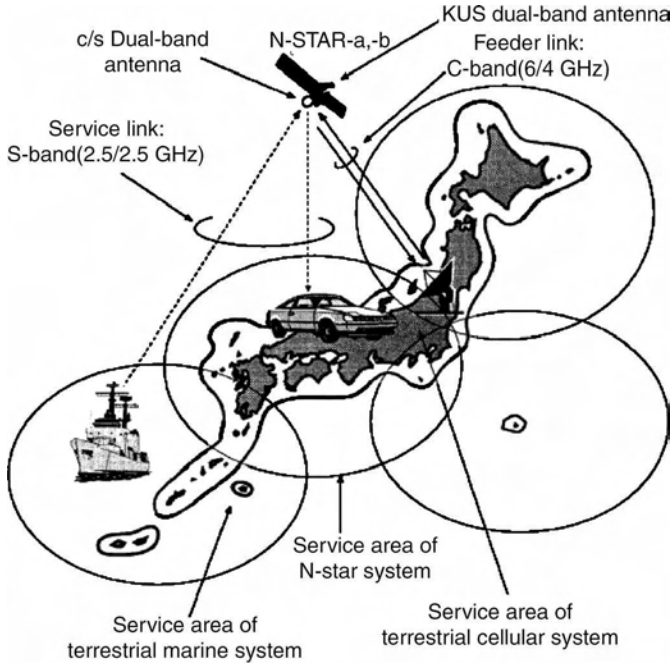
FIGURE 14.25. Overview of the Japanese N-Star mobile communications system according to [3]. (Reprinted with permission © 1998 IEEE)

satellite-only version. The system provides voice service using a 5.6 kb/s codec, which results in a transmission rate of 14 kb/s. Fax and data are sent at 4.8 kb/s rates.

Channel spacing is 12.5 kHz. Each of the two satellites is accessed by separate base stations, each of which has dual redundant equipment for high reliability [3,24].

Other Mobile Satellite Systems. Mexico is in the process of implementing a mobile satellite service employing L-band transponders on each of two Solidaridad satellites launched in 1994 [25]. To take advantage of the work performed by AMSC/TMI in developing their system and associated terminals, it is clear that the Mexican system will provide the same service dealing with identical equipment.

India is planning a mobile satellite service using an S-band (2 GHz) transponder placed on the INSAT 2 spacecraft [26]. This service will consist of voice, data, and fax using essentially the same parameters as the Inmarsat-*M* service.

14.6.2. Global Land–Satellite Personal Communication Systems (PCS)

Proposed new global satellite PCS and their communication characteristics are presented according to References [27–30] in Table 14.6a and Table 14.6b, respectively. Let us briefly discuss these new PCS following References [3,27–30].

TABLE 14.6(a). New Satellites for New Satellite PCS (Source [3]: Reprinted with permission © 1998 IEEE)

Parameter	Iridium	Globalstar	lCO-global	Ellipso	Aires (ECCO)
Company	Motorola	Loral Qualcomm	ICO-Global	Mobile Communication Holdings. Inc.	Constellation Communications, Inc.
No. of active satellites	66	48	10	17	46
Orbit planes	6 circular polar (86.5°)	6 circular inclined (52°)	2 circular inclined (45°)	2 elliptical inclined (116.6°) I circular equatorial	7 circular inclined I circular equatorial
Orbit altitude (km)	780	1,414	10,355	N.A. 8.060 equatorial	? 2,000 equatorial
Satellites per orbit plane	11	8	5	5 in each elliptical orbit 7 in equatorial orbit	5 in each inclined orbit 11 in equatorial orbit
Beams per satellite	48	16	163	61	1
Reported cost ($B)	4.7	2.5	4.6	0.56	1.15

TABLE 14.6(b). Communication Characteristics of the New Satellite PCS (Source [3]: Reprinted with permission © 1998 IEEE)

Parameter	Iridium	Globalstar	ICO-global	GEO regionals
Mobile User Link				
Frequency, Up/Down (GHz)	1.62135–1.6265	1.6100–1.62135/2.4835–2.49485	1.980–2.010/2.170–2.200	1.525–1.559/1.6265–1.6605
Bandwidih (MHz)	5.15	11.35	30	34
Spot beams per satellite	48	16	163	>240
Voice bit rate (coded) (kb/s)	4.8 (6.25)	1–9	4.8 (6.0)	3.6 (5.2)
Feeder link				
Frequency Up/Down (GHz)	30/20	5.1/6.9	5.2/6.9	14/12
Gateway antenna G/T (dB/K)	24.5	28.5	26.6	37.0
User terminal				
Multiple access	TDMA–FDMA	CDMA–FDMA	TDMA–FDMA	TDMA–FDMA
Carrier bandwidth (kHz)	TDD, 31.5	1250	25.2	27
Carrier bit rate (kb/s)	50	2.4	36	45
Mudulation	DQPSK	PN/QPSK	QPSK	QPSK
RF power (W)	0.45	0.5	0.625	0.5
G/T (dB/K)	−23.0	−22.0	−23.8	−23.8
Nominal link margin (dB)	16.5	11	10	10
Nominal capacity per satellite (ckts)	1,100	2,400	4,500	16,000
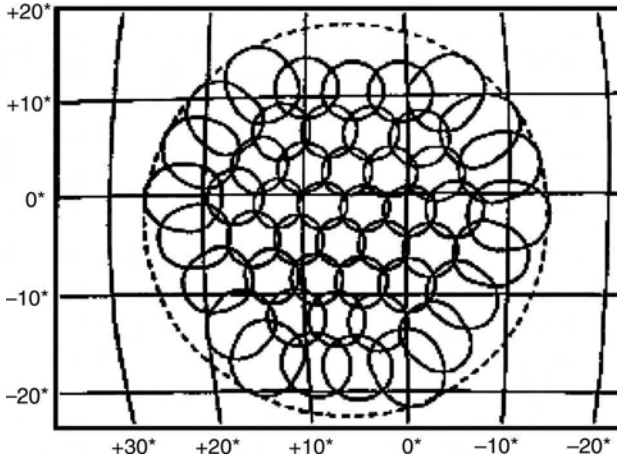
FIGURE 14.26. Service (L-band) spot beams formed by an Iridium satellite. (Source [3]: Reprinted with permission © 1998 IEEE)

Iridium. The design employs 66 satellites placed in circular polar orbits at 780 km altitude [29,30]. The satellites are deployed into six orbital planes, with 11 satellites equally separated around each orbit. Satellites in adjacent planes are staggered with respect to each other to maximize their coverage at the equator, where a user may be required to access a satellite that is as low as 10° above the horizon.

Users employ small handsets operating in frequency division-multiplexed/ time-division multiple access (FDM/TDMA) fashion to access the satellite at L-band. Eight users share 45 ms transmit and 45 ms receive frames in channels that have a bandwidth of 31.5 kHz and are spaced 41.67 kHz. That is, users are synchronized so that they transmit and receive in the same time using time-windows alternately. This approach is necessary because three phased-array adaptive antennas are used for both transmitting and receiving information. Figure 14.26 shows the 48 spot beams formed at L-band projected onto the earth at the equator. The satellite cross-links operate at 23 GHz, whereas the links to the gateway earth stations are at 20 GHz. The use of cross-links greatly complicates the design of the system but allows global service to be provided with a small number (11 are planned) of gateway earth stations. To properly route traffic, each satellite must carry a set of stored routing tables from which new routing instructions are called every 2.5 min.

The cross-links to the satellites in the adjacent orbital planes have constantly changing time delays and antenna pointing requirements. To mitigate this problem, a circular polar orbit (actually an inclination of 86.5°) was chosen. Even so, these cross-links are dropped above 68° latitude as the angular rates for the tracking antennas become high and little traffic is expected at these latitudes. Each satellite is capable of handling as many as 1100 simultaneous calls.

Services to be provided include voice (at 2.4 kb/s and 4.8 kb/s encoding), data at 2.4 kb/s, and high-penetration paging, which affords 11 dB more power than the
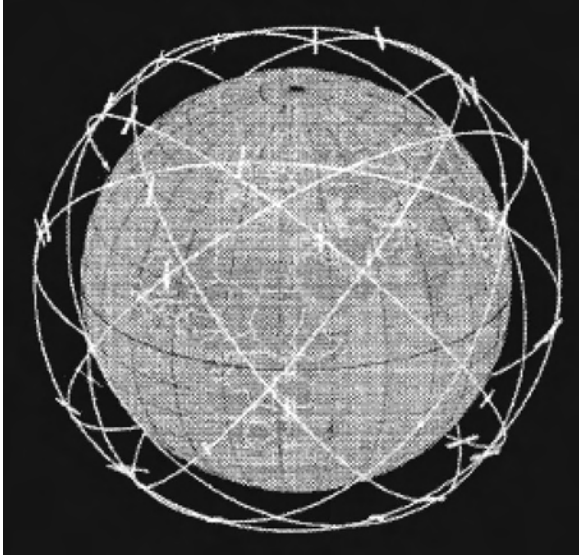
FIGURE 14.27. The Globalstar constellation according to [32].

regular signal. The design, however, already provides a link margin (16 dB) that is higher than any of the competing systems.

One of the complicating aspects of the Iridium system is the need to hand off a subscriber from beam to beam as a satellite flies by. As a typical satellite pass takes less than 9 min, and the average international call duration is about 7 min, there is also a need to hand off some calls to the next satellite to appear above the horizon. This will be in one of the adjacent orbits, and hence in a somewhat different direction from the first, raising the possibility of the calls being dropped if buildings block the view. Other systems, such as Globalstar, attempt to exploit dual-satellite visibility as a means of mitigating shadowing effects and claim that this is preferable to designing for high link margins.

Globalstar. The Globalstar system has 48 satellites organized in eight planes of six satellites each (see Figure 14.27 [32]). The satellite orbits are circular, at 1414 km and 52° inclination. The Globalstar satellite is simple. Each satellite consists of an antenna, a trapezoidal structure, two solar arrays, and a magnetometer (see Fig. 14.28). As was shown in References [3,32], the use of an inclined orbit concentrates the available satellite capacity at lower latitudes where the largest populations exist; little or no coverage is provided beyond 70° latitude (see Fig. 14.29). Like the Iridium satellites, the Globalstar spacecrafts are three-axis-stabilized, with a mission life of 7.5 years (minimum). As the Globalstar system does not employ satellite cross-links, a subscriber can gain access to the system only when a satellite in view can also be seen by a gateway Earth station. Typically, this means that service areas are within 1000 miles of each gateway Earth station. To achieve truly global
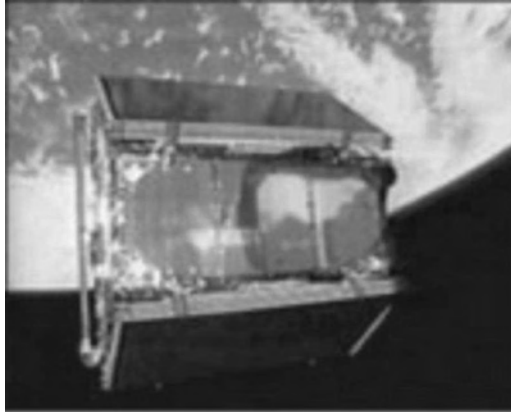
FIGURE 14.28. The Globalstar view according to [32].

coverage would require the construction of more than 200 Earth stations, which seems unlikely to happen.

In contrast to Iridium, each Globalstar satellite covers a comparable area of the earth's surface with only 16 spot beams. Thus, Globalstar is more likely to serve national roamers than international business travelers. This, together with the
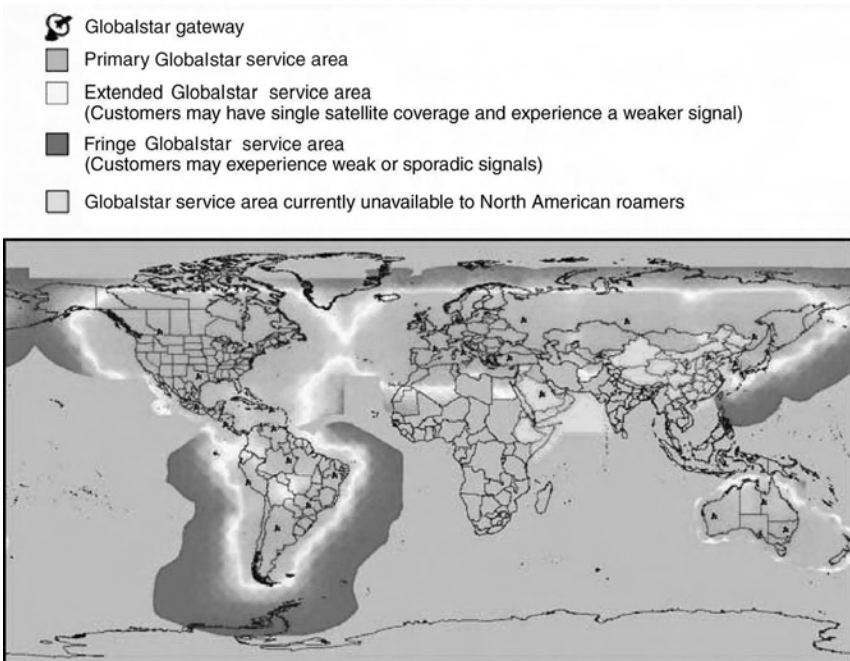
FIGURE 14.29. Up-to-date coverage map of Globalstar (according to Globalstar website).
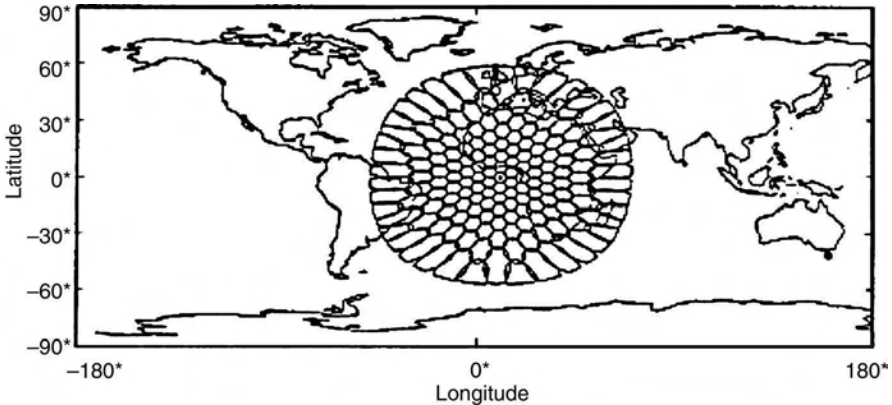
FIGURE 14.30. Coverage provided by the 163 spot beams of an ICO satellite over the equator according to [3]. (Reprinted with permission © 1998 IEEE)

sharing of the receive channels on board the satellite by many more users, reduces the available link margins to about 3–6 dB, although for a small number of users, this can be increased to 11 dB. Access to and from the satellite is at and band, respectively, utilizing code-division multiple access (CDMA) in channels that are 1.25 MHz in bandwidth. Voice is encoded at rates of 1–9 kb/s, depending on speaker activity. A problem for such satellite system is that while frequency reuse can be employed at L and S band, the feeder links must occupy the full band of all of the signals that can be transmitted through the satellite. Therefore, securing an adequate feeder link allocation becomes almost as critical as an L- and S-band allocation.

ICO-Global. ICO-Global has chosen an intermediate circular orbit for its system (10,355 km altitude), with 10 satellites arranged five in each of two inclined circular orbits [35]. The inclination of the orbits is 45°, making it the lowest of the systems described. This reduces the coverage at high latitudes but allows for the smallest number of satellites. Actually, 12 satellites are to be launched in order to provide a spare in each orbital plane.

To improve the link margins on the ICO satellites, Inmarsat chose a satellite design that employs 163 spot beams (see Fig. 14.30, according to Reference [35]). Therefore, to access a given spot beam, the gateway Earth station must transmit at a particular frequency. Given that a large digital signal processor is required on board the ICO satellites, it is expected to greatly simplify the checkout and calibration of the adaptive antenna systems. In principle, this arrangement would also permit the beams to be steered to increase the amount of time a given subscriber remains in a given spot beam.

ICO differs from both Iridium and Globalstar in that a true TDMA scheme has been adopted for the service links, with six subscribers multiplexed into channels 25.2 kHz in width at a bit rate of 36 kb/s. A disadvantage of this access scheme is that a soft handoff (e.g., from beam to beam) is not automatic, and it is more difficult to exploit dual-satellite visibility. One method being considered would be to send a

burst via an alternate satellite (say) every fifth burst. By noting the strengths of the regular and alternate bursts, the subscriber terminal could determine which satellite presently affords the best path to the gateway Earth station and could adjust its own burst time and frequency to select that satellite.

For more coverage on other existing land–satellite PCS, the reader is referred to the original papers [34–36].

14.7. "MEGA-CELL" GLOBAL NETWORKS DESIGN

Prediction of radio and cellular maps for full coverage of the Earth's surface, using determined constellations of satellites, CEO, MEO, or LEO, is based on most strict statistical and physical-statistical propagation models. The models take into account the average path loss along all three "sub-links": land, atmospheric, and ionospheric. These effects can be postulated as worst (or bad) or convenient (or good) with intermediate variants "good-bad" and "bad-good," obtained from numerous measurements carried out in these three "sub-links." In Chapters 6 and 7, we showed how to take into account fading phenomena for a link budget design and how to predict radio coverage for the atmospheric and ionospheric links. It was also shown that for the frequencies of interest operated in land–satellite links, the effects of these two "sub-channels" on total path loss and fading are not so significant. More essential fading effects are observed in the land communication "sub-channel."

To show the reader how to predict the land-link total path loss and to obtain a "mega-cell" radio coverage using specific satellite constellations, we developed a mathematical tool. This planning tool is based on results obtained in References [29–33] and is able to show the efficiency of the general approach proposed in previous sections to resolve the problem of link budget design and outage probability of path loss prediction within any LSC link. Thus, in our calculations we combine two models, Loo's model and the three-state Markov model, that account for the effects of overlay profile of the buildings. For this purpose, we introduced the PDFs, $P_a(r)$, $P_b(r)$, and $P_c(r)$, for LOS, multipath and shadow effects description, respectively. Here, each status, a, b, and c, corresponds to a transaction from bad to good situations within a wireless link, depending on environment phenomena. Then, for each situation within the channel, we took the corresponding PDF, $P(a)$, $P(b)$, and $P(c)$, (the lognormal, Rayleigh, and Rician, respectively). Next, the following cumulative formula for determining the probability of fading phenomena within the satellite link is found as

$$P_{\text{total}}(r) = P(a)P_a(r) + P(b)P_b(r) + P(c)P_c(r) \qquad (14.53)$$

Below, we present the different coverage maps based on the planning tools developed in References [29–33] in order to understand the differences between satellite networks and their effect on the network's *foot print*. Thus, in Figure 14.31, the cellular map of "Iridium" network [29,30] with uniform radio coverage of the Earth's surface is presented.
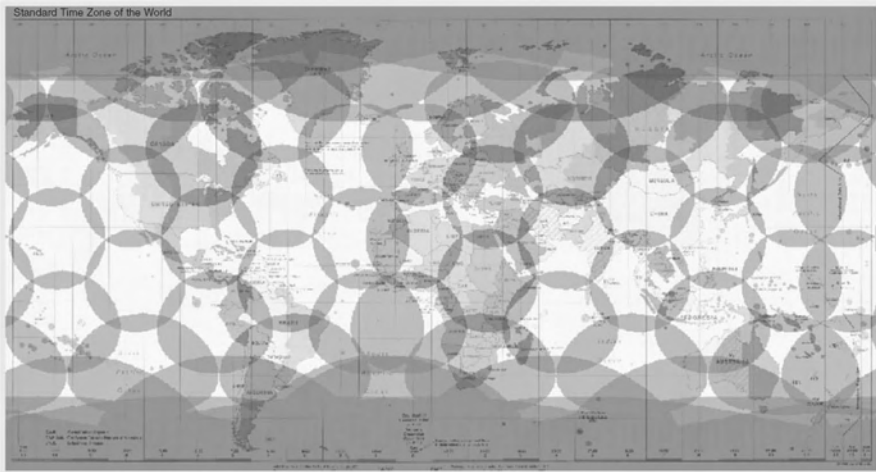
FIGURE 14.31. Computed foot print patterns of the ''Iridium'' network. (Source [29]: Reprinted with permission © 1991 IEEE)

Figure 14.32 illustrates the cellular map for ''GlobalStar'' network [31,32]. The corresponding constellation covers most of the populated area of the Earth. But the polar areas of the Earth cannot be covered by this system.

It is seen that a medium orbit satellite (MEO) constellation covers the Earth with only 12 satellites with great overlapping, which is caused by their relatively high altitude.
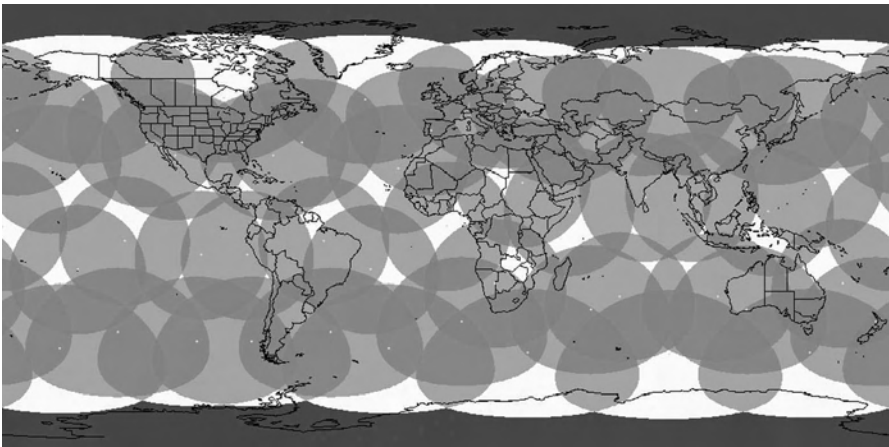
FIGURE 14.32. Computed foot print patterns of the Globalstar network. (Reprinted with permission from Globalstar)
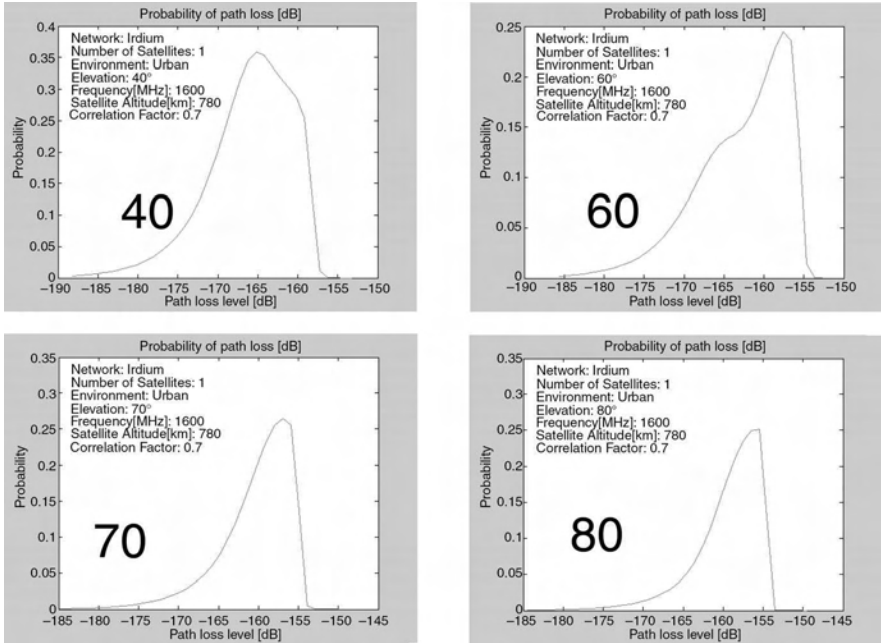
FIGURE 14.33. Simulation output of probability to obtain a smaller acceptable path loss for varying satellite elevation angles.

Now we present some outputs derived from our calculation of the general physical-statistical model described by the cumulative formula (14.53) to demonstrate the actions of our own simulation tool and its ability to be adapted to different cellular network and various environments: urban, suburban, rural, and open. The output parameters computed by the proposed tool are probability of fading, path loss, link budget, radio and cell coverage, LCR, AFD, and BER. First, we varied the satellite elevation angle; Figure 14.33(a)–(d) shows the increase of the probability to obtain a smaller path loss with an increase in the number of satellites or with a decrease in the elevation angle. Second, we investigated the same probability versus the maximum accepted path loss for different satellite networks. Results are presented in Figure 14.34(a)–(d), where one network is virtually created by us. The difference between the networks is seen in the x-axis. It is clear that the differences in results are due to the varying satellite altitudes and the downlink operational frequency.

Finally, we showed how the terrain, as the land channel environment, affects the probability to obtain a smaller acceptable path loss. Figure 14.35(a)–(d) shows a difference between obtained results for different land environments. Results were obtained for a low elevation satellite. As expected, the main difference is noticeable in the urban environment, due to its special propagation features such as multiple diffraction, scattering, and reflection.
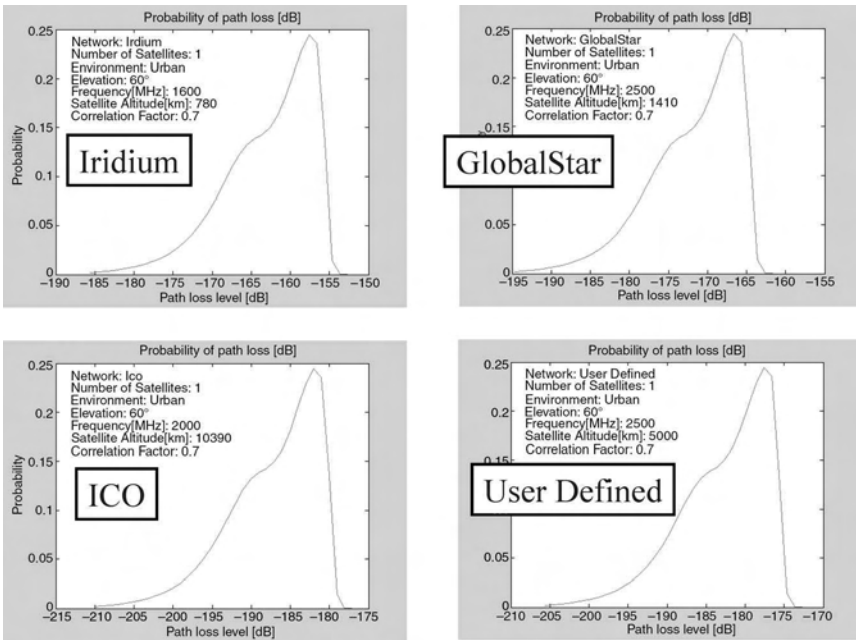
FIGURE 14.34. Simulation output of probability to obtain a smaller acceptable path loss for varying global networks.
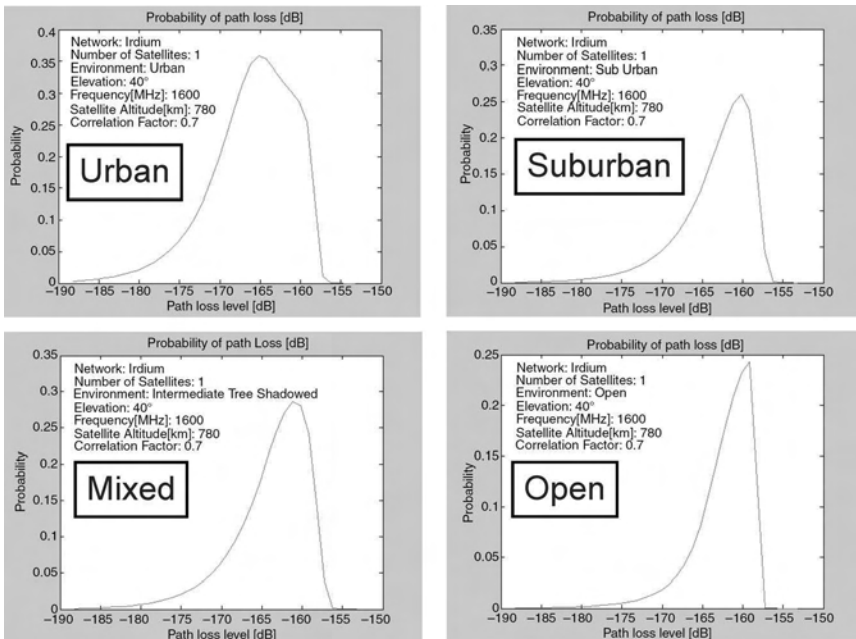
FIGURE 14.35. Simulation output of probability to obtain smaller acceptable path loss for varying land environments.

SUMMARY

- From our simulation results, we can conclude that the statistical model is the worst model with respect to physical-statistical models in predicting fading phenomena and link budget in land–satellite communication links.

- Also, we must state that almost in all simulations the physical-statistical model based on built-up profiles described by the corresponding PDFs (14.37) and (14.38), as well as by (14.42), are the best fit to measurements with respect to pure statistical models. Furthermore, the difference between two physical-statistical approaches on how to describe the overlay profile of the buildings is small, but the multiparametric model is much simpler to use and implement. The reason for this is the fact that for physical-statistical model we need exact knowledge of the distribution of the height of the buildings in each city, information that is difficult to measure at every land site. On the contrary for the multiparametric model we need to know only the heights of the smaller and higher buildings in the city and also the average height of buildings in the tested area. From these values we could easily find the ''relief'' parameter n, using Equation (14.43).

- So, both the Saunders physical-statistical and multiparametric stochastic approaches are more accurate models, which can be used in predicting fading phenomena and link budget both for personal and mobile land satellite radio communication links.

- A simulation tool, based on the combination of pure statistical and physical-statistical models was developed for the link budget performance and for the outage probability of path loss prediction for more applicable satellite networks based on radio propagation characteristics within each communication channel.

- The simulation tool is designed to be used both by LMS designers and by customers. The designers can determine, using the simulator, the best satellite constellation and channel characteristics for each satellite system, in terms of desired performance and cost. The customers of the LMS systems can use the tool to determine which system is best suited for their needs, at their specific location in the world.

We can outline some practical conclusions and remarks, which emphasize the advantages in LMS systems. They are

- a high elevation angle between the satellite and the LMS customer increases the link quality significantly. The main advantage in using the LMS system is emphasized dramatically in urban environments, where one satellite in a high elevation angle eliminates the use of dozens of base stations;

- LEO satellites provide better link quality than MEO satellites but demand more satellites to fully cover the Earth's surface. The main obstacle in designing an LMS system is determining the best-suited satellite constellation for the potential customers;

- a system designed for personal stationary subscriber will be very much different from a system designed for moving subscribers. The proposed tool gives the designer the option to set its own user-defined system and check if it suits its customer;
- all present LMS systems simulated can provide only voice, messages, and slow data today. Our calculations showed that even in the best conditions, current systems can deliver only basic services to global customers;
- in order to develop systems that can compete with third generation (3G) and future fourth generation (4G) cellular systems, the LMS system should overcome the obstacles of low SNR and of a large number of satellites to cover highly populated areas. Simulations proved that systems using current technology should deploy over 280 satellites in order to compete in the market. Another way is to improve transceiver technology by use smart/adaptive antennas and to develop wideband technology for LMS use.

BIBLIOGRAPHY

[1] Farserotu, J., and R. Prasad, *IP/ATM Mobile Satellite Networks*, Artech House, Boston-London, 2002.

[2] Saunders, S. R., *Antennas and Propagation for Wireless Communication Systems*, John Wiley & Sons, Chichester, England, 2001.

[3] Evans, J. V., "Satellite systems for personal communications," *Proc. IEEE*, vol. 86, no. 7, 1998, pp. 1325–1341

[4] Wu, W. W., "Satellite communication," *Proc. IEEE*, vol. 85, no. 6, 1997, pp. 998–1010.

[5] Fontan, F. P., J. P. Gonzalez, M. J. S. Ferreiro, et al., "Complex envelope three-state Markov model based simulator for the narrow-band LMS channel," *Int. J. Satellite Communications*, vol. 15, no. 1, 1997, pp. 1–15.

[6] Barts, R. M., and W. L. Stutzman, "Modeling and simulation of mobile satellite propagation," *IEEE Trans. Antennas Propagat.*, vol. 40, no. 4, 1992, pp. 375–382.

[7] Loo, C., and J. S. Butterworth, "Land mobile satellite channel measurements and modeling," *Proc. IEEE*, vol. 86, no. 7, July 1998, pp. 1442–1462.

[8] Vatalaro, F., and F. Mazzenga, "Statistical channel modeling and performance evaluation in satellite personal communications," *Int. J. Satellite Communications*, vol. 16, no. 2, 1998, pp. 249–255.

[9] Loo, C., "A statistical model for land mobile satellite link," *IEEE Trans. Veh. Technol.*, vol. VT-34, no. 3, 1985, pp. 122–127.

[10] Patzold, M., U. Killat, and F. Laue, "An extended Suzuki model for land mobile satellite channels and its statistical properties," *IEEE Trans. Veh. Technol.*, vol. 47, no. 2, 1998, pp. 617–630.

[11] Corazza, G. E., and F. Vatalaro, "A statistical model for land mobile satellite channels and its application on nongeostationary orbit systems," *IEEE Trans. Veh. Technol.*, vol. 43, no. 3, 1994, pp. 738–741.

[12] Xie, Y., and Y. Fang, "A general statistical channel model for mobile satellite systems," *IEEE Trans. Veh. Technol.*, vol. 49, no. 3, 2000, pp. 744–752.

[13] Abdi, A., W. C. Lau, M.-S. Alouini, et al., "A new simple model for land mobile satellite channels: First- and second-order statistics," *IEEE Trans. Wireless Communications.*, vol. 2, no. 3, 2003, pp. 519–528.

[14] Saunders, S. R., and B. G. Evans, "A physical model of shadowing probability for land mobile satellite propagation," *Electronics Letters*, vol. 32, no. 17, 1996, pp. 1548–1549.

[15] Tzaras, C., S. R. Saunders, and B. G. Evans, "A tap-gain process for wideband mobile satellite PCN channels," *Proc. COST 252/259 Joint Workshop*, Bradford, UK, April 21-22, 1998, pp. 156–161.

[16] Lutz, E., D. Cygan, M. Dippold, et al., "The land mobile satellite communication channel-recording, statistics and channel model," *IEEE Trans. Veh. Technol.*, vol. 40, no. 2, 1991, pp. 375–385.

[17] Butt, G., G. Evans, and M. Richharia, "Narrowband channel statistics from multiband propagation measurements applicable to high elevation angle land-mobile satellite systems," *IEEE Trans. Select. Areas Communic.*, vol. 10, no. 8, 1992, pp. 1219–1226.

[18] Parks, M. A. N., B. G. Evans, G. Butt, et al., "Simaltaneous wideband propagation measurements for mobile satellite communication systems at L- and S-bands," *Proc. 16th Int. Communic. Systems Conf.*, Washington, DC, 1996, pp. 929–936.

[19] Karasawa, Y., K. Kimura, and K. Minamisono, "Analysis of availability improvement in LMSS by means of satellite diversity based on three-state propagation state model," *IEEE Trans. Veh. Technol.*, vol. 46, no. 4, 1997, pp. 1047–1056.

[20] Blaunstein, N., "Wireless Communication Systems," in *Handbook of Engineering Electromagnetics*, ed. R. Bansal, Chap. 12, Marcel Dekker, New York, 2004.

[21] Lipke, D. W., D. W. Swearingin, J. F. Parker, et al., "MARISTAT – A maritime satellite communication system," *COMSAT Tech. Rev.*, vol. 7, 1977, pp. 351–391.

[22] Newland, W., "AUSSAT mobilesat system description," *Space Communications*, vol. 8, no. 1, 1990, pp. 37–52.

[23] Wagg, M., "MOBILESAT, Australia's own," *Proc. Int. Mobile Satellite Conf.*, Ottawa, Canada, June 1990, JPL Publication 90–97, pp. 3–7.

[24] Furukawa, K., Y. Nishi, M. Kondo, et al., "N-STAR mobile communications satellite systems," *IEEE Global Telecommunications Conf. Rec.*, London, UK, November 1996, pp. 390–395.

[25] Moncayo, J. M. R., "Mobile satellite communications in Mexico," *Int. Mobile Satellite Conf.*, Paris, France, October 1993, pp. 559–563.

[26] Taylor, S. C., and A. R. Adiwoso, "The Asia cellular satellite system," *AIAA 16th Int. Communications Satellite Systems Conf., Collection of Technical Papers*, Washington, DC, February 1996, pp. 1239–1249.

[27] Johannsen, K. G., "Mobile P-service satellite system comparison," *Int. J. Satellite Communic.*, vol. 13, 1995, pp. 453–471.

[28] Comparetto, G. M., and N. D. Hulkower, "Global mobile satellite communications: A review of three contenders," *AIAA 15th Int. Communications Satellite Systems Conf., Collection of Technical Papers*, San Diego, California, February/March 1994, pp. 1507–1515.

[29] Sterling, D. E., and J. E. Harlelid, "The Iridium[TM] System – A revolutionary satellite communications system developed with innovative applications of technology," *Proc. IEEE Military Satellite Communications Conf.*, McLean, Virginia, 1991, pp. 436–440.

[30] Brunt, P., "IRIDIUM - Overview and status," *Space Communic.*, vol. 14, no. 1, 1996, pp. 61–68.

[31] Wiedeman, R. A., A. B. Salmasi, and D. Rouffet, "Globalstar: Mobile communications wherever you are," *AIAA 14th Int. Communications Satellite Systems Conf., Collection of Technical Papers*, Washington, DC, 1992, pp. 123–129.

[32] Smith, D., "Operational innovations for the 48-satellite Globalstar constellation," *AIAA 15th Int. Communications Satellite Systems Conf., Collection of Technical Papers*, San Diego, California, February/March 1994, pp. 1107–1112.

[33] Singh, J., "Project 21/Inmarsat-P: Putting reality into the handheld satphone vision," *Int. Mobile Satellite Conf.*, Paris, France, October 1993, pp. 834–839.

[34] Castiel, D., S. J. Brosius, and J. E. Draim, "Ellipso: The ELLIPSO mobile satellite system," *AIAA 15th Int. Communications Satellite Systems Conf., Collection of Technical Papers*, San Diego, California, February/March 1994, pp. 1235–1241.

[35] Draim, J. E., D. Castiel, S. J. Brosius, et al., "ELLIPSOTM-An affordable global, mobile personal communications system," *Proc. Int. Mobile Satellite Conf.*, Pasadena, California, 1997, pp. 153–158.

[36] Summers, R. A., and R. J. Lepkowski, "ARIES: Global communication through a constellation of low earth orbit satellites," *AIAA 14th Int. Communications Satellite Systems Conf., Collection of Technical Papers*, Washington, DC, 1992, pp. 628–638.

Index

WILEY SERIES IN MICROWAVE AND OPTICAL ENGINEERING

KAI CHANG, Editor
Texas A&M University